DEPARTMENT OF PHYSICS

TECHNISCHE UNIVERSITÄT MÜNCHEN

PhD thesis

Phenomenology of Baryogenesis and Neutrino Physics: From Effective Field Theory to Simplified Models

Karl Kåre Fridell

Technische Universität München
Fakultät für Physik

Phenomenology of Baryogenesis and Neutrino Physics: From Effective Field Theory to Simplified Models

Karl Kåre Fridell

Vollständiger Abdruck der von der Fakultät für Physik der Technischen Universität München zur Erlangung eines

Doktors der Naturwissenschaften (Dr. rer. nat.)

genehmigten Dissertation.

Vorsitz: Prof. Dr. Bastian Märkisch

Prüfer*innen der Dissertation:

1. TUM Junior Fellow Dr. Julia Harz
2. Prof. Dr. Andreas Weiler

Die Dissertation wurde am 11.08.2022 bei der Technischen Universität München eingereicht und durch die Fakultät für Physik am 08.09.2022 angenommen.

Phenomenology of Baryogenesis and Neutrino Physics: From Effective Field Theory to Simplified Models

Phänomenologie der Baryogenese und Neutrinophysik: Effektive Feldtheorien und vereinfachte Modelle

Karl Kåre Fridell

Abstract

This work focuses on lepton- and baryon-number-violating interactions in simplified models and effective field theory. Using both high- and low-scale observables, lepton number violation is constrained in dimension-7 operators and their tree-level UV-completions. Moreover, novel ways are proposed to disentangle the nature of neutrinos using rare kaon decays and coherent elastic neutrino-nucleus scattering. Finally, baryogenesis is studied in a model that induces baryon-number-violating neutron-antineutron oscillation.

Kurzfassung

Diese Arbeit untersucht Lepton- und Baryonzahlverletzung in vereinfachten Modellen und effektiven Feldtheorien. Es werden sowohl Observablen an großen sowie niedrigen Skalen genutzt, um Leptonzahlverletzung in Operatoren mit Massendimension 7 und deren UV-Vervollständigung zu beschränken. Des Weiteren werden neue Tests der Leptonzahlverletzung in Kaonzerfällen und Neutrino-Nukleus-Streuung präsentiert. Außerdem wird Baryogenese in einem Model untersucht in dem die Baryonzahl durch Neutron-Antineutron-Oszillationen verletzt wird.

Contents

1. Introduction

Matter and antimatter do not exist in equal quantities in the Universe. This fact is in conflict with leading theories of quantum field theory and cosmology, which predict that the inequality between matter and antimatter should be at least one billion times smaller than what we observe. Every structure we see, such as the Earth, the Sun, the Milky Way, etc., is made out of matter. Upon contact with antimatter, the two would annihilate and result in an output of energy in the form of radiation. We owe our very existence to the lack of antimatter in the Universe, but there has so far been no experimentally verified theory that explains its absence. Why is there more matter than antimatter?

To answer this question we can try to construct quantum field theory models that lead to mechanisms by which an asymmetry can arise dynamically. In doing so we may then predict the outcomes of different experiments, and if we are right we could have discovered something deep about nature. One problem is that the energy scales involved in the very early Universe, when the asymmetry between matter and antimatter is expected to have been generated, are up to a billion times higher than what can be probed in terrestrial experiments. To test such theories directly is therefore currently impossible, and we must resort to more indirect methods.

The role of phenomenology in particle physics is to bridge the gap between theory and experiment. A phenomenological study of the matter-antimatter asymmetry therefore asks how the different models can be experimentally identified, differentiated, or falsified. Different indirect signatures of models that could lead to an asymmetry generation include the violation of certain charges that are unique to matter particles, namely lepton number L or baryon number B. Experimentally, such signatures can be sought for in processes that involve low energy scales, substituting the high energy for large volumes and long exposure times. Examples of such experimental observables include e.g. neutrinoless double beta-decay, rare kaon decays, or coherent elastic neutrino-nucleus scattering for L-violation, and proton decay or neutron-antineutron oscillation for B-violation.

Lepton number violation can be studied model-independently in effective field theories, in which a higher quantum-field-theory model is assumed to lead to effective processes at lower energy scales. One advantage of this method is its general applicability, we can easily increase or decrease the complexity of the interactions such that it suits our analysis, without having to worry about the details of the underlying model. For a given set of effective-field-theory interactions, we can then derive a complete list of quantum-field-theory models that can generate them. In this way, connecting an experimental observable to effective-field-theory interactions can lead to the systematic analysis of a large set of high-scale models.

Our main line of investigation in this thesis is the question of how lepton- and baryon-number violation can be constrained using current and near-future observables. We ask how

the Standard Model can be extended in minimal ways that lead to distinct signals in future experiments, but that do not contradict existing experimental constraints. The study of lepton number violation is in particular interesting to us due to its connection to both the baryon asymmetry and neutrino masses.

In this thesis we discuss a wide range of different high- and low-scale lepton-number-violating observables. We present a new study of dimension-7 lepton number violation at the LHC, leading to the currently most stringent limits on the muon-flavour component of the corresponding Wilson coefficients. Furthermore, we describe a novel method of probing lepton number violation based on the distribution of final state particles in neutrino experiments. In two concrete examples, that of rare kaon decays and radiative coherent elastic neutrino-nucleus scattering, we show how the energy spectrum of final state particles can hint at the presence of lepton number violation, and thereby also reveal the Dirac/Majorana nature of neutrinos.

Lepton number violation is often studied in either effective field theories or in concrete models. In this thesis we combine these analyses by systematically deconstructing lepton-number-violating operators up to dimension-7. Using the full range of tree-level UV-completions, we show all simplified models that lead to dimension-7 lepton number violation. We demonstrate how the neutrino mass generated by such models differs from the conventional effective-field-theory-based estimation. A previously undefined dependence on the hierarchy between the different heavy degrees of freedom in a higher-dimensional operator leads to more accurate neutrino masses that can lie several orders of magnitude below earlier estimates. This new analysis opens up large regions of parameter space that were previously considered excluded.

As a compliment to our lepton-number based analysis we finally also consider baryon number violation. We derive a new set of Boltzmann equations that describe the evolution of baryon asymmetry in a generic simplified model connected to neutron-antineutron oscillation. By systematically analysing different washout channels we show how successful baryogenesis can be realised in models that can lead to observable neutron-antineutron oscillation as well as future LHC signals. This new result goes beyond the effective-field-theory based result that a neutron-antineutron oscillation signal is incompatible with high-scale baryogenesis due to severe washout. Instead, we find that an observation of neutron-antineutron oscillation could hint at new physics around 10^{14} GeV that can lead to the successful generation of a baryon asymmetry.

This thesis covers a wide range of different aspects regarding the phenomenology of a matter-antimatter asymmetry. It is based on original work, Refs. [1–9], presented in existing publications

[1] F. F. Deppisch, K. Fridell and J. Harz, *Constraining lepton number violating interactions in rare kaon decays*, JHEP **12** (2020) 186, [2009.04494].

[2] K. Fridell, J. Harz and C. Hati, *Probing baryogenesis with neutron-antineutron oscillations*, JHEP **11** (2021) 185, [2105.06487].

[3] P. D. Bolton, F. F. Deppisch, K. Fridell, J. Harz, C. Hati and S. Kulkarni, *Probing active-sterile neutrino transition magnetic moments with photon emission from CEνNS*, *Phys. Rev. D*

106 (2022) 035036 [2110.02233].

material to be published

[4] K. Fridell, L. Graf, J. Harz and C. Hati, in preparation.

and conference proceedings

[5] F. F. Deppisch, K. Fridell and J. Harz, *Implications of Rare Kaon Decays on Lepton Number Violating Interactions*, PoS **ICHEP2020** (2021) 130, [2012.14825].

[6] K. Fridell, J. Harz and C. Hati, *Neutron-antineutron oscillations as a probe of baryogenesis*, J. Phys. Conf. Ser. **2156** (2021) 012015.

[7] P. D. Bolton, F. F. Deppisch, K. Fridell, J. Harz, C. Hati and S. Kulkarni, *Transition neutrino magnetic moments in CEvNS*, J. Phys. Conf. Ser. **2156** (2021) 012218.

[8] K. Fridell, J. Harz and C. Hati, *Probing Baryogenesis using Neutron-Anti-Neutron Oscillation*, PoS **ICHEP2020** (2021) 243.

[9] C. Hati, P. Bolton, F. F. Deppisch, K. Fridell, J. Harz and S. Kulkarni, *Distinguishing Dirac vs Majorana Neutrinos at CEvNS experiments*, PoS **EPS-HEP2021** (2022) 225.

In Ch. 2 we cover the background relevant for subsequent chapters by first introducing the Standard model and the Λ Cold dark matter model, after which we describe different directions in which New Physics beyond these well-established theories may lead. In Ch. 3 we introduce the concept of baryogenesis, the dynamical generation of a matter-antimatter asymmetry, and describe different models in which it can be accommodated. In Ch. 4 we set up a formalism to describe lepton number violation using effective field theories, and present new limits coming from collider searches that are subject for publication in Ref. [4]. In Ch. 5, which also stems from the work to appear in Ref. [4], we systematically analyse all models coming from the second-to-most simple realisations of lepton-number-violating effective-field-theory interactions, and for the first time show how a hierarchy in the internal degrees of freedom of such models can affect the phenomenology of lepton number violation and neutrino masses. In Ch. 6 we show how the details of the rare kaon decay dynamics can reveal the presence of lepton-number-violating interactions. This work led to the publication in Ref. [1]. In Ch. 7 we propose a novel search method for potentially detecting the presence of lepton number violation in coherent elastic neutrino-nucleus scattering, which led to the publication in Ref. [3]. In Ch. 8 we derive new equations that describe the dynamical generation of a matter-antimatter asymmetry in a model that also induces B-violating neutron-antineutron oscillation. These results were published in Ref. [2]. Finally, we conclude in Ch. 9.

2. The Standard model and beyond

In this introductory chapter, we cover background topics relevant for the subsequent chapters. In Sec. 2.1 we introduce the Standard model, with a discussion of the relevant particle content in Secs. 2.1.1 to 2.1.4, followed up with anomaly cancellation in Sec. 2.1.5, sphalerons in Sec. 2.1.6, and finally electroweak symmetry breaking in Sec. 2.1.7. In Sec. 2.2 we review the relevant modern cosmology, with a thermal timeline of our Universe given in Sec. 2.2.2. Lastly, in Sec. 2.3 we discuss theories beyond the current framework, by first motivating extensions to the Standard model in Sec. 2.3.1, after which we discuss the relevant phenomenology in Secs. 2.3.2 and 2.3.3.

2.1. The Standard model

The Standard model (SM) [10–12] is a model based on quantum field theory that has a very firm phenomenological footing. It predicts to a great accuracy different properties of particles and particle interactions such as e.g. dipole moments [13] and branching ratios (BRs) of decays [14]. After the observation of the Higgs boson [15, 16], all fundamental particles of the SM had been discovered, and not one particle more. Whether the SM is *beautiful and elegant* [17] or *hässlich*[1] [18] is an open question, but irrespective of that, it has withstood a thorough experimental scrutiny and therefore remains an accurate description of high energy physics to date.

2.1.1. Field content of the Standard model

In the SM, three of the four fundamental forces of nature are described as arising from interactions via gauge bosons. The electromagnetic force is mediated via the electromagnetic gauge field A_μ corresponding to the symmetry group $U(1)_{\text{em}}$. The weak nuclear force is mediated via $W^\pm_\mu$ and Z_μ fields. At energies above the scale of electroweak symmetry breaking (EWSB), corresponding to the vacuum expectation value (vev) of the Higgs boson[2] $v = 174$ GeV, these two forces are united into a single electroweak force with the gauge fields B_μ and $W_{a\mu}$, for $a \in \{1, 2, 3\}$, which is described by the symmetry group $SU(2)_L \times U(1)_Y$. Here L stands for *left*, stressing that only the left-handed chiral fermions of the SM have an $SU(2)_L$ structure, an Y stands for *hypercharge*. When the electroweak symmetry is broken, $W_{3\mu}$ and B_μ mix to create the Z boson and photon fields, and $SU(2)_L \times U(1)_Y$ is then no

[1] German for *ugly* or *hideous*.

[2] Note that the Higgs vev is often taken as $v = 246$ GeV $= 174 \times \sqrt{2}$ GeV. This is a matter of convention, and we here choose $v = 174$ GeV to best match with the most relevant literature.

longer a valid symmetry. Instead, there is a new symmetry described by $U(1)_{\text{em}}$, where *em* stands for *electromagnetic*. The strong nuclear force is mediated via the gluon field $G_{a\mu}$, for $a \in \{1, 2, \ldots, 8\}$, and is related to the symmetry group $SU(3)_c$, where c stands for *colour*, the charge corresponding to the strong force. A quanta of the electromagnetic field A_μ is called a photon and is represented by γ, while a quanta of the gluon field $G_{a\mu}$ is called a gluon, and is represented by g. The fields $G_{a\mu}$, $W_{a\mu}$ and B_μ are all vector boson fields related to gauge symmetries, where the total gauge symmetry group of the SM is $G_{\text{SM}} = SU(3)_c \times SU(2)_L \times U(1)_Y$. Of the fundamental forces, only gravity is not described by the SM.

All fermion fields in the SM are chiral, implying that there is a distinction between fields that transform as the left- or right-handed representations of the Poincaré group (such fields are then respectively called *left-* or *right-handed*). Furthermore, they all have three generations or families, and to each fermion there exists a corresponding anti-fermion with the opposite charges under the G_{SM} symmetry group, as well as opposite baryon number B and lepton number L. There are two types of SM fermions: leptons and quarks, with one major difference being that leptons are not charged under the $SU(3)_c$ symmetry while quarks are. Leptons have a non-zero lepton number L, and they can be classified into charged leptons (e, μ, τ) and neutrinos (ν_e, ν_μ, ν_τ). Quarks have a non-zero baryon number B and can be classified into up-type quarks (u, c, t) and down-type quarks (d, s, b). Left-handed fermions combine to form $SU(2)_L$ doublets in the following way

$$L = \begin{pmatrix} \nu_L \\ e_L \end{pmatrix}, \quad Q = \begin{pmatrix} u_L \\ d_L \end{pmatrix}. \tag{2.1}$$

For all SM fermions except for the neutrinos there also exist right-handed analogue fields. In Tab. 2.1, the different fermion fields of the SM are summarised, including their representations under the relevant subgroups of the SM gauge group as well as their baryon and lepton numbers.

The shorthand notation we use for describing the representation in which a particle resides goes as follows: a field ψ is written as belonging to a set of digits $\psi \in (X, Y, Z)$, where X, Y and Z describe the fields representation under $SU(3)_c$, $SU(2)_L$ and $U(1)_Y$ respectively, unless otherwise stated. For example, the quark doublet Q is described as $Q \in (3, 2, \frac{1}{6})$ (c.f. Tab. 2.1). If a parenthesis is written after the representation, it corresponds (unless otherwise stated) to the baryon number B multiplied by 3, such that $Q \in (3, 2, \frac{1}{6})(1)$. For more details regarding the notations used in this thesis, see Appendix A.

Finally, the only scalar field of the SM is the Higgs boson. Above the scale of EWSB, the Higgs field is a complex scalar field ϕ that is a doublet under $SU(2)_L$. Below the EWSB scale, the Higgs field $\langle\phi\rangle$ has settled into the minimum of its potential, and the neutral component acquires a vacuum expectation value (vev) v, with a small perturbation h denoting the real physical Higgs in the unitarity gauge, such that

$$\phi = \begin{pmatrix} \phi^+ \\ \phi_0 \end{pmatrix}, \quad \langle\phi\rangle = \begin{pmatrix} 0 \\ v + h \end{pmatrix}. \tag{2.2}$$

The boson fields of the SM are summarised in Tab. 2.2.

	$SU(3)_c$	$SU(2)_L$	$U(1)_Y$	B	L
Q	3	2	1/6	1/3	0
L	1	2	-1/2	0	1
u	3	1	2/3	1/3	0
d	3	1	-1/3	1/3	0
e	1	1	-1	0	1

Table 2.1.: Representations of the SM fermion fields under the SM gauge group $G_{\text{SM}} = SU(3)_c \times SU(2)_L \times U(1)_Y$, as well as their baryon- and lepton numbers.

	$SU(3)_c$	$SU(2)_L$	$U(1)_Y$	B	L
$G_{a\mu}$	8	1	0	0	0
$W_{a\mu}$	1	3	0	0	0
B_μ	1	1	0	0	0
ϕ	1	2	1/2	0	0

Table 2.2.: Representations of the SM boson fields under the SM gauge group $G_{\text{SM}} = SU(3)_c \times SU(2)_L \times U(1)_Y$, as well as their baryon- and lepton numbers.

2.1.2. The Standard model Lagrangian

The Standard model Lagrangian is given by [17]

$$\begin{aligned}\mathcal{L}_{\text{SM}} = &-\frac{1}{4}B_{\mu\nu}B^{\mu\nu} - \frac{1}{4}W_{a\mu\nu}W_a^{\mu\nu} - \frac{1}{4}G_{a\mu\nu}G_a^{\mu\nu} \\ &+ i\bar{Q}_i \not{D} Q_i + i\bar{u}_{Ri}\not{D}u_{Ri} + i\bar{d}_{Ri}\not{D}d_{Ri} + i\bar{L}_i\not{D}L_i + i\bar{e}_{Ri}\not{D}e_{Ri} \\ &+ \left(-y^\ell_{ij}\bar{L}^a_i\phi^a e_{Rj} - y^d_{ij}\bar{Q}^a_i\phi^a d_{Rj} - y^u_{ij}\bar{Q}^a_i\tilde{\phi}^a u_{Rj} + \text{h.c.}\right) \\ &+ \left(D_\mu\phi\right)^\dagger\left(D^\mu\phi\right) - \mu^2\phi^\dagger\phi - \lambda(\phi^\dagger\phi)^2\,.\end{aligned} \tag{2.3}$$

Here several things need clarification. To begin with, the first row contains the field strengths

$$\begin{aligned}B_{\mu\nu} &= \partial_\mu B_\nu - \partial_\nu B_\mu, \\ W_{a\mu\nu} &= \partial_\mu W_{a\nu} - \partial_\nu W_{a\mu} - g\epsilon_{abc}W_{b\mu}W_{c\nu}\,, \\ G_{a\mu\nu} &= \partial_\mu G_{a\nu} - \partial_\nu G_{a\mu} - g_s f_{abc}G_{b\mu}G_{c\nu}\,,\end{aligned} \tag{2.4}$$

where ϵ_{abc} is the Levi-Civita symbol, which is the structure constant for $SU(2)$, and similarly f_{abc} is the structure constant for $SU(3)$, such that

$$[l_a, l_b] = i\epsilon_{abc}l_c\,, \quad [t_a, t_b] = if_{abc}t_c\,, \tag{2.5}$$

where l_i and t_i are the generators of $SU(2)$ and $SU(3)$ respectively, which in the fundamental representation are given by $\frac{1}{2}$ times the Pauli matrices σ_i for $SU(2)$ and $\frac{1}{2}$ times the Gell-Mann

matrices λ_i for $SU(3)$. Furthermore, g is the coupling constant for the weak interaction, and g_s is the coupling constant for the strong interaction.

The second row of Eq. (2.3) contains terms called *kinetic terms* for the quarks and leptons[3]. Covariant derivatives D_μ include terms coming from the three gauge interactions,

$$D_\mu \equiv \partial_\mu + ig' B_\mu Y + igW_{a\mu} l_a + ig_s G_{a\mu} t_a \,. \tag{2.6}$$

Here g' is a coupling constant corresponding to the hypercharge symmetry group[4] $U(1)_Y$, and Y is the hypercharge of the field that the covariant derivative acts on. Furthermore, l_a and t_a are the generators of the fundamental representation for $SU(2)_L$ doublets and $SU(3)_c$ triplets, and as the structure constants for $SU(2)_L$ adjoints (triplets) and $SU(3)_c$ adjoints (octets), respectively. For covariant derivatives acting on $SU(2)_L$ or $SU(3)_c$ singlet fields, l_a or t_a should correspondingly be taken as to be zero (trivial representation). For example, a covariant derivative acting on a quark doublet gives

$$D_\mu Q_i = \left(\partial_\mu + \frac{i}{6} g' B^\mu + \frac{i}{2} g W_a^\mu \sigma_a + \frac{i}{2} g_s G_a^\mu \lambda_a\right) Q_i \,. \tag{2.7}$$

Next, y^ℓ_{ij}, y^d_{ij}, and y^u_{ij} are the charged lepton, down-type quark and up-type quark Yukawa coupling constants, respectively. Terms involving these couplings describe interactions between the fermions with the Higgs boson, such that e.g.

$$-y^\ell_{ij} \bar{L}^a_i \phi^a e_{Rj} = -y^\ell_{ij} \left(\bar{\nu}^a_{Li} \phi^+ e_{Rj} + \bar{e}^a_{Li} \phi^0 e_{Rj}\right) \,. \tag{2.8}$$

After EWSB, when the Higgs acquires a vev, ϕ should be replaced by $\langle\phi\rangle$, such that the Yukawa terms lead to mass terms for the respective fermions[5], as well as interactions between the fermions and the physical Higgs field h.

The last row in Eq. (2.3) describes the Higgs self-interaction and gauge interactions, where ϕ with a tilde is given by $\tilde{\phi}^a = \epsilon_{ab} \phi^{*b}$. A covariant derivative acting on the Higgs field is given by

$$D_\mu \phi = \left(\partial_\mu + \frac{i}{2} g W_{a\mu} \sigma_a + \frac{i}{2} g' B_\mu\right) \phi \,, \tag{2.9}$$

and when the Higgs gets its vev, we have

$$D^\mu \langle\phi\rangle = (v+h) \begin{pmatrix} \frac{i}{2} g W_1^\mu - \frac{1}{2} g W_2^\mu \\ \partial^\mu - \frac{i}{2} g W_3^\mu + \frac{i}{2} g' B^\mu \end{pmatrix} \,, \tag{2.10}$$

leading to

$$\left(D^\mu \langle\phi\rangle\right)^\dagger D^\mu \langle\phi\rangle = (v+h)^\dagger (v+h) \left(\frac{1}{4} g^2 W_2^2 + \frac{1}{4} g^2 W_1^2 + \partial^2 + \frac{g^2}{4} W_3^2 + \frac{g'^2}{4} B^2 - \frac{g g'}{2} W_{3\mu} B^\mu\right) \,. \tag{2.11}$$

[3]The first term in the last row of Eq. (2.3) is the kinetic term for the Higgs boson.

[4]The coupling constants g and g' mix to form the electromagnetic coupling constant e in EWSB. For details see e.g. Refs. [17, 19–21].

[5]Note that, in the SM, neutrinos do not acquire a mass term in this way. However, by a small extension to the SM, a Yukawa term for neutrinos could be introduced along with a new field $\nu_R \in (1, 1, 0)$, see Sec. 2.3.

Now identifying

$$W_\mu^\pm = \frac{1}{\sqrt{2}} \left(W_1 \pm i W_2\right)_\mu , \quad Z_\mu = \cos\theta_W W_{3\mu} - \sin\theta_W B_\mu, \quad A_\mu = \sin\theta_W W_{3\mu} + \cos\theta_W B_\mu , \tag{2.12}$$

where

$$\tan\theta_W \equiv \frac{g'}{g} \tag{2.13}$$

for the Weinberg angle θ_W[6], we find the masses of the different bosons to be

$$m_{W^\pm} = \frac{1}{2} g^2 v^2, \qquad m_Z = \frac{1}{2}\left(g^2 + g'^2\right) v^2, \qquad m_A = 0 . \tag{2.14}$$

In this procedure, the symmetry group of the SM has broken,

$$SU(3)_c \times SU(2)_L \times U(1)_Y \to SU(3)_c \times U(1)_{\text{em}} . \tag{2.15}$$

The gauge boson A_μ (photon) remains massless and corresponds to the unbroken electromagnetic symmetry.

Lastly, by writing

$$v^2 = -\frac{\mu^2}{2\lambda} , \tag{2.16}$$

we can rewrite the last two terms of the last row in Eq. (2.3), up to a constant, as

$$-\mu^2(\phi^\dagger\phi) - \lambda(\phi^\dagger\phi)^2 \to -\lambda\left(\phi^\dagger\phi - v^2\right)^2 . \tag{2.17}$$

After EWSB, when the Higgs field acquires a vev and ϕ is replaced by $\langle\phi\rangle$, the above term describes a quartic coupling of the physical Higgs h.

2.1.3. Flavour in the Standard model

All fermions of the SM come in three *generations* or *families*, as indicated by the indices $i \in \{1,2,3\}$ and $j \in \{1,2,3\}$ in Eq. (2.3). After EWSB, the quark Yukawa terms of the SM Lagrangian give masses to the quarks,

$$\mathcal{L}_{\text{SM}} \supset -y^d_{ij}\bar{Q}^a_i \phi^a d_{Rj} - y^u_{ij}\bar{Q}^a_i \tilde{\phi}^a \bar{u}_{Rj} + \text{h.c.} \to -m^d_{ij}\bar{d}_{Li} d_{Rj} - m^u_{ij}\bar{u}_{Li} u_{Rj} + \text{h.c.} , \tag{2.18}$$

where

$$m^u_{ij} = y^u_{ij} v, \qquad m^d_{ij} = y^d_{ij} v . \tag{2.19}$$

We can diagonalise both mass matrices m^u_{ij} and m^d_{ij},

$$m^u \;\to\; \hat{m}^u = V_{uL} m^u V^\dagger_{uR}, \qquad m^d \;\to\; \hat{m}^d = V_{dL} m^d V^\dagger_{dR} , \tag{2.20}$$

[6]The value of the Weinberg angle is usually given in the form $\sin^2\theta_W = 1 - (m_W/m_Z)^2 \approx 0.22$ [14].

such that the mass eigenstates correspond to flavour eigenstates for the quarks. In doing this we are redefining the quark fields as

$$\begin{aligned} u_{Li} &\to (V_{uL})_{ij} u_{Lj}, \qquad d_{Li} \to (V_{dL})_{ij} d_{Lj} \\ u_{Ri} &\to (V_{uR})_{ij} u_{Rj}, \qquad d_{Ri} \to (V_{dR})_{ij} d_{Rj} \,. \end{aligned} \tag{2.21}$$

Up-type quarks have the families *up* (u), *charm* (c), and *top* (t); down-type quarks have *down* (d), *strange* (s), and *bottom* (b) flavour states,

$$u_i \in \{u, c, t\}, \quad d_i \in \{d, s, b\} \,, \tag{2.22}$$

and their respective masses are given by

$$m_{u/c/t} = y_{u/s/t} v, \qquad m_{d/s/b} = y_{d/s/b} v \,. \tag{2.23}$$

Diagonalising the quark mass matrices has consequences for the charged current interaction matrix between quarks and $W^{\pm}_{\mu}$ bosons in the broken SM. From the relation between $W^{\pm}_{\mu}$ and $W_{a\mu}$,

$$W^{\pm}_{\mu} = \frac{1}{\sqrt{2}} \left(W_1 \pm i W_2 \right)_{\mu} \,, \tag{2.24}$$

we note from the definition of the covariant derivative in Eq. (2.6) and the Pauli matrices

$$\sigma_1 = \begin{pmatrix} 0 & 1 \\ 1 & 0 \end{pmatrix}, \qquad \sigma_2 = \begin{pmatrix} 0 & -i \\ i & 0 \end{pmatrix} \tag{2.25}$$

that

$$D_{\mu} \supset i\frac{g}{2} W_{1\mu} \sigma_1 + i\frac{g}{2} W_{2\mu} \sigma_2 \to i\frac{g}{\sqrt{2}} W^{+}_{\mu} \begin{pmatrix} 0 & 0 \\ 1 & 0 \end{pmatrix} + i\frac{g}{\sqrt{2}} W^{-}_{\mu} \begin{pmatrix} 0 & 1 \\ 0 & 0 \end{pmatrix} . \tag{2.26}$$

From the matrices on the RHS of Eq. (2.26) and the appearance of the kinetic term for the quark doublet in the SM Lagrangian,

$$\mathcal{L}_{\text{SM}} \supset i \bar{Q}_i \not{D} Q_i \,, \tag{2.27}$$

it is evident that the $W^{\pm}_{\mu}$ bosons act on the pairs of quarks in the broken SM Lagrangian through the terms (in the old definition of the quarks)

$$\mathcal{L}_{\text{SM, broken}} \supset i\frac{g}{\sqrt{2}} \bar{u}_{Li} \gamma_{\mu} d_{Li} W^{+\mu} + i\frac{g}{\sqrt{2}} \bar{d}_{Li} \gamma_{\mu} u_{Li} W^{-\mu}. \tag{2.28}$$

We see that, in the interactions between $W^{\pm}$ bosons and quarks, there is always one up-type and one down-type quark involved, never two of the same type[7]. Now redefining the quarks as in Eq. (2.21) we have

$$\mathcal{L}_{\text{SM, broken}} \supset i\frac{g}{\sqrt{2}} \bar{u}_{Lj} \gamma_{\mu} \left(V_{dL} V^{\dagger}_{uL} \right)_{ji} d_{Li} W^{+\mu} + i\frac{g}{\sqrt{2}} \bar{d}_{Lj} \gamma_{\mu} \left(V_{uL} V^{\dagger}_{dL} \right)_{ji} u_{Li} W^{-\mu} \,. \tag{2.29}$$

[7]This can of course also be seen from the $U(1)_{em}$ charge: it is impossible to combine two instances of $\pm\frac{2}{3}$ or $\mp\frac{1}{3}$ from the quarks with the ± 1 charge from the $W^{\pm}$ bosons to create a term that preserves electromagnetic charge by having a vanishing total charge.

Here we encounter a matrix

$$V \equiv V_{dL} V_{uL}^{\dagger} = V_{uL} V_{dL}^{\dagger} \,, \tag{2.30}$$

which is called the Cabibbo-Kobayashi-Maskawa (CKM) matrix [22, 23]. Unlike the redefined Yukawa matrices, the CKM matrix is not diagonal[8]. It therefore connects different quark flavours to each other, and we can conclude that quark flavour transitions are mediated by $W^{\pm}$-bosons in the SM.

In the leptonic sector of the SM, upon EWSB, the Yukawa term can, as with the quarks, be written as a mass term,

$$\mathcal{L}_{\text{SM}} \supset -y^{\ell}_{ij} \bar{L}^{a}_{i} \phi^{a} e_{Rj} + \text{h.c.} \to -m^{\ell}_{ij} \bar{d}_{Li} d_{Rj} + \text{h.c.} \,, \tag{2.31}$$

where

$$m^{\ell}_{ij} = y^{\ell}_{ij} v \,. \tag{2.32}$$

In the SM, there is no Yukawa term for the neutrinos, therefore we only have the charged lepton term in the leptonic sector. We can again diagonalise the mass matrix,

$$m^{\ell} \;\to\; \hat{m}^{\ell} = V_{eL} m^{\ell} V_{eR}^{\dagger} \,, \tag{2.33}$$

and subsequently redefine the charged lepton fields,

$$e_{Li} \to (V_{eL})_{ij} e_{Lj}, \qquad e_{Ri} \to (V_{eR})_{ij} e_{Rj} \,. \tag{2.34}$$

From the kinetic term

$$\mathcal{L}_{\text{SM}} \supset i \bar{L}_i \not{D} L_i \,, \tag{2.35}$$

we then find

$$\mathcal{L}_{\text{SM, broken}} \supset i \frac{g}{\sqrt{2}} \bar{\nu}_{Lj} \gamma_{\mu} \left(V_{eL}\right)_{ji} e_{Li} W^{+\mu} + i \frac{g}{\sqrt{2}} \bar{e}_{Lj} \gamma_{\mu} \left(V_{eL}^{\dagger}\right)_{ji} \nu_{Li} W^{-\mu} \,. \tag{2.36}$$

Here we have ended up with a matrix V_{eL} that is not necessarily unitary like the CKM matrix. We can absorb it by also redefining the neutrinos,

$$\nu_{Li} \to (V_{eL}^{-1})^{\dagger}_{ij} \nu_{Lj} \,. \tag{2.37}$$

Now the leptonic kinetic term can be written as

$$\mathcal{L}_{\text{SM, broken}} \supset i \frac{g}{\sqrt{2}} \bar{\nu}_{Li} \gamma_{\mu} e_{Li} W^{+\mu} + i \frac{g}{\sqrt{2}} \bar{e}_{Li} \gamma_{\mu} \nu_{Li} W^{-\mu} \,, \tag{2.38}$$

where the charged lepton mass states correspond one-to-one to their flavour states, and the neutrinos only have flavour states since they are massless in the SM. In case the neutrinos were massive, their flavour states and mass states would not align, but rather mix, where

[8] In principle, we *could* have chosen to only diagonalise one of the Yukawa matrices. We would then be free to also diagonalise the CKM matrix, but for one type of quark the flavour states would not directly correspond to the mass states [24]. This strategy is employed for the leptonic sector of the SM, as can be seen later in this section.

the mixing is described by a leptonic equivalent of the CKM matrix called the Pontecorvo-Maki-Nakagawa-Sakata (PMNS) matrix. As discussed in Sec. 2.3.1, observations of neutrino oscillations indeed lead to the conclusion that non-zero neutrino masses are realised in nature. For the charged leptons and neutrinos, the flavour states are *electron* e, *muon* μ, and *tau* τ,

$$e_i \in \{e, \mu, \tau\}, \quad \nu_i \in \{\nu_e, \nu_\mu, \nu_\tau\}\,. \tag{2.39}$$

Unlike in the quark sector, the leptons always conserve flavour as they interact with the $W^\pm$ boson in the SM.

2.1.4. Mesons and baryons

In Eq. (2.7) we see the covariant derivative acting on a quark doublet, with the gauge fields B^μ, $W_a^\mu \sigma_a$ and $G_a^\mu \lambda_a$ shown explicitly, along with their corresponding couplings g', g, and g_s, respectively. From renormalisation group evolution we know that these couplings run, i.e. their values do not stay constant as the energy at which they are evaluated changes. With increasing energy, the $U(1)_Y$ and $SU(2)_L$ gauge interactions grow stronger, while the $SU(3)_c$ interaction gets weaker. Since $SU(3)_c$ remains unbroken in the SM all the way down to low scales, this means that there is some scale $\Lambda_{\text{QCD}} \sim 200$ – 300 MeV where the strong interaction diverges, and becomes very strong indeed. Below this scale, the quarks are so attracted to each other that it is not possible to observe them individually, instead they are all locked up in colour-neutral bound states called hadrons[9] (see e.g. Refs. [14, 19, 24, 25]). This isolation of quarks inside bound states is called *confinement*, which is a condition that the only free states are those that are colour singlets.

Hadrons can be subdivided into mesons (containing a quark and an antiquark), (anti)baryons (containing three (anti)quarks), and exotic hadrons (with more than three quarks, i.e. tetraquarks with two quark-antiquark pairs, pentaquarks with three quarks plus one quark-antiquark pair, and so on[10]). The commonest hadrons are the nucleons, which are the first generation spin-$\frac{1}{2}$ baryons, namely protons p and neutrons n. They approximately[11] preserve an $SU(2)$ symmetry called *isospin*, where a π-rotation in isospin space takes a proton to a neutron and vice versa. Baryons are made up of three quarks, and antibaryons of three antiquarks. In the case of nucleons these are the u and d quarks, which in terms of isospin I and its third component I_3 can be written as

$$\begin{aligned} u &= \left|\tfrac{1}{2} \quad \tfrac{1}{2}\right\rangle, & d &= \left|\tfrac{1}{2} \quad -\tfrac{1}{2}\right\rangle, \\ \bar{u} &= \left|\tfrac{1}{2} \quad -\tfrac{1}{2}\right\rangle, & \bar{d} &= -\left|\tfrac{1}{2} \quad \tfrac{1}{2}\right\rangle. \end{aligned} \tag{2.40}$$

[9] Hadrons can also form from quarks who's individual masses are above Λ_{QCD}, the relevant condition for bound state formation is rather that the kinetic energies of the quarks be sufficiently low.

[10] Note however that this is a simplified picture. In principle, a bound state of hadrons also consists of a lot of gluons and quark-antiquark pairs, in what can be described as a *quark sea*, or *quark-gluon plasma*. In addition to this sea are the valance quarks, which in common speech is what is said to make up the hadron, but which due to confinement are impossible to observe on their own at low energies, where the bound state lies. The term *valance* quark here draws analogies to valance nucleons in the shell model of nuclear physics, or valance electrons in atomic physics.

[11] Isospin symmetry in nucleons is broken by the mass difference between p and n as well as the difference in electromagnetic charge.

Here the quark with the largest electromagnetic charge is assigned the positive I_3. Note that the minus sign on $\bar{d}$ comes from our desire to have a π-rotation of the antiquark isopsin doublet around the 2-axis

$$\begin{pmatrix} -\bar{d}' \\ \bar{u}' \end{pmatrix} = \begin{pmatrix} 0 & -1 \\ 1 & 0 \end{pmatrix} \begin{pmatrix} -\bar{d} \\ \bar{u} \end{pmatrix} \tag{2.41}$$

behave in the same way as the quark doublet

$$\begin{pmatrix} u' \\ d' \end{pmatrix} = \begin{pmatrix} 0 & -1 \\ 1 & 0 \end{pmatrix} \begin{pmatrix} u \\ d \end{pmatrix} . \tag{2.42}$$

In terms of the quarks, the proton and neutron can then be written as uud and udd respectively[12], while antiprotons and antineutrons can be written as $\bar{u}\bar{u}\bar{d}$ and $\bar{u}\bar{d}\bar{d}$, respectively. Simpler hadrons can be formed out of a quark-antiquark pair rather than three quarks or antiquarks, where the first generation spin-0 isospin $I = 1$, $I_3 = -\frac{1}{2}, 0, +\frac{1}{2}$ triplet of states are the pions[13]

$$\begin{aligned} \left|\pi^+\right\rangle &= \left|u\bar{d}\right\rangle , \\ \left|\pi^0\right\rangle &= \frac{1}{\sqrt{2}} \left(|u\bar{u}\rangle - \left|d\bar{d}\right\rangle\right) , \\ \left|\pi^-\right\rangle &= |\bar{u}d\rangle . \end{aligned} \tag{2.43}$$

The mesons above constitute the charged and neutral pions. The $SU(2)$ equation $2 \otimes 2 = 1 \oplus 3$ tells us that there should also be an isospin singlet state, which indeed is given by

$$|00\rangle = \frac{1}{\sqrt{2}} \left(|u\bar{u}\rangle + \left|d\bar{d}\right\rangle\right) . \tag{2.44}$$

This state does not, however, directly correspond to a meson. Instead, the situation is changed due to a member of the next generation of SM fermions, namely the s-quark. Firstly, the u-, d-, and s-quarks are the only coloured SM fermions with masses below Λ_{QCD}, such that the hadrons they form mainly get their mass from the binding energy rather than the individual quark masses[14]. Secondly, in quantum mechanics any two states that have the same quantum numbers generally mix, where the degree to which the mixing occurs depends on the mass splitting between the two states. The relevant quantum numbers for quarks are: electric charge Q, isospin I, third component of isospin I_3, strangeness S, charm C, bottomness $\mathcal{B}$, and topness T, where the different flavour quantum numbers (I_3, S, C, $\mathcal{B}$, and T) have an absolute

[12] Note that protons and neutrons are both spin-$\frac{1}{2}$ particles, therefore the spins if the individual quarks have to partially cancel, such that, for a $|\uparrow\rangle$ nucleon, the allowed spin combinations of the quarks are $|\uparrow\uparrow\downarrow\rangle$, $|\uparrow\downarrow\uparrow\rangle$, and $|\downarrow\uparrow\uparrow\rangle$. Writing out the full states $|p\rangle$, and $|n\rangle$ requires combining these different spin possibilities which yields quite long expressions. For details see e.g. Ref. [26]. Having all quark spins aligned yields spin-$\frac{3}{2}$ baryons, which are generally less stable than spin-$\frac{1}{2}$ ones [14].

[13] Similarly to the baryons, mesons may be divided into spin-0 and spin-1, corresponding to spin combinations $|\uparrow\downarrow\rangle$ or $|\downarrow\uparrow\rangle$ and $|\uparrow\uparrow\rangle$ (or $|\downarrow\downarrow\rangle$ depending on the spin state of the meson) respectively.

[14] Note that, in gauge interactions that lead to confinement, such as QCD, the mass of a bound state is generally greater than the mass of the constituent particles. This is in opposition to e.g. atomic physics, where the binding of an electron very slightly reduces the mass of the bound state as compared to the sum of the ion and electron masses.

value 1 and the same sign as the electric charge Q for each quark. In an overcomplete basis we can also include baryon number B which can be solved for via

$$B = 2Q - 2I_3 - S - C - \mathcal{B} - T\,. \tag{2.45}$$

For mesons we additionally have the principal quantum number n, orbital angular momentum ℓ, spin J (where $|\ell - s| \leq J \leq |\ell + s|$, and where $s = 0$ and $s = 1$ for antiparallel and parallel quark spins respectively), parity $P = (-1)^{\ell+1}$, and charge conjugation parity $C = (-1)^{\ell+s}$. Note however that C is only defined for mesons where the quark and antiquark are the antiparticles of each other. For $u\bar{d}$ and $d\bar{u}$ bound states one can similarly define another parity $G = (-1)^{I+\ell+s}$. Conventionally these meson-specific quantum numbers are written in the form $I^G(J^{PC})$ (with G and/or C omitted when not applicable), such that e.g. the charged and neutral pions $\pi^\pm$ and π^0 have $I^G(J^P) = 1^-(0^-)$ and $I^G(J^{PC}) = 1^-(0^{-+})$, respectively. For mesons, it is enough to have them same I and J^{PC} in order for two states to mix, their flavour quantum numbers are only conserved to the extent that the mass splitting between two states is large, such that for mesons $q\bar{q}'$ with $m_q + m_{\bar{q}'} \ll \Lambda_{QCD}$ their flavour is not well preserved (making isospin a relatively good symmetry). Note that not all combinations of quantum numbers lead to mesons that can be observed as such. Some quark-antiquark bound states decay so quickly that they are seen as resonances in a detector rather than having a certain lifetime. These resonances are nevertheless referred to as mesons[15]. Now, the reason that the state in Eq. (2.44) is not a good description of any meson is that this state mixes with $|s\bar{s}\rangle$. Since also the mesons containing s-quarks (but no heavier quarks) mainly get their mass from Λ_{QCD}, same as for the u- and d-quarks, this mixing should be significant. Now that we are considering three quarks instead of just two, the $SU(2)$ isospin symmetry should be promoted to a (also broken) $SU(3)$ symmetry, where $3 \otimes \bar{3} = 1 \oplus 8$ tells us that we should expect 9 mesons, where one of them is a singlet. This singlet ψ_1 mixes with one of the $I = 0$ states ψ_8 from the octet such that

$$\begin{pmatrix} \eta \\ \eta' \end{pmatrix} = \begin{pmatrix} \cos\theta & -\sin\theta \\ \sin\theta & \cos\theta \end{pmatrix} \begin{pmatrix} \psi_8 \\ \psi_1 \end{pmatrix}\,, \tag{2.46}$$

where

$$\begin{aligned} \psi_8 &= \frac{1}{\sqrt{6}}\left(u\bar{u} + d\bar{d} - 2s\bar{s}\right)\,, \\ \psi_1 &= \frac{1}{\sqrt{3}}\left(u\bar{u} + d\bar{d} + s\bar{s}\right)\,. \end{aligned} \tag{2.47}$$

Together with the three pions, the mesons η and η' make up five out of the nine mesons. The remaining four are the charged and neutral kaons

$$\begin{aligned} K^0 &= |d\bar{s}\rangle, \quad K^+ = |u\bar{s}\rangle\,, \\ K^- &= |s\bar{u}\rangle, \quad \overline{K}^0 = \left|s\bar{d}\right\rangle\,. \end{aligned} \tag{2.48}$$

[15] One rule of thumb in order to determine whether a meson is stable on detector timescales, due to Ref. [24], is that if the $U(1)_Y$ and $SU(2)_L$ interactions are turned off such that $g, g' \to 0$, mesons that now have infinite lifetime are otherwise also stable on detector timescales, while mesons that can still decay are resonances.

We may now suspect that K^0 and $\overline{K}^0$ also mix. To the extent that our $SU(3)$ flavour symmetry is obeyed, the neutral kaons are both negative under parity conjugation P and positive under charge parity conjugation C. We may then form eigenstates $|K_1\rangle$ and $|K_2\rangle$ of the combined transformation CP such that

$$\begin{aligned} |K_1\rangle &= \tfrac{1}{\sqrt{2}}\left(|K^0\rangle - |\overline{K}^0\rangle\right), \quad CP\,|K_1\rangle = |K_1\rangle \ , \\ |K_2\rangle &= \tfrac{1}{\sqrt{2}}\left(|K^0\rangle + |\overline{K}^0\rangle\right), \quad CP\,|K_2\rangle = -\,|K_2\rangle \ . \end{aligned} \tag{2.49}$$

Assuming that CP is conserved in kaon decays, K_1 can only decay to CP positive states (such as two pions) and K_2 can only decay to CP negative states (such as three pions). The departure from this ideal K_1–K_2 picture is parametrised by the CP-violating parameter ϵ, such that experimentally the states $|K_L\rangle$ and $|K_S\rangle$ are found[16], where

$$\begin{aligned} |K_L\rangle &= \frac{1}{\sqrt{1+|\epsilon|^2}}\left(|K_2\rangle + \epsilon\,|K_1\rangle\right) , \\ |K_S\rangle &= \frac{1}{\sqrt{1+|\epsilon|^2}}\left(|K_1\rangle + \epsilon\,|K_2\rangle\right) . \end{aligned} \tag{2.50}$$

This completes the $s = 0$ nonet of $n = 1$, $\ell = S$ mesons. For $s = 1$, the $I = 1$ mesons are correspondingly called ρ, the $I = \frac{1}{2}$ mesons[17] K^*, and the $I = 0$ mesons ϕ and ω. For higher n and ℓ the mesons quickly become very unstable. A similar statement can be made for non-nucleonic baryons, where the most stable $SU(3)$ flavour symmetric ones have $J = \frac{1}{2}$, and they are are[18] $\Lambda^0 = uds$, $\Sigma^+ = uus$, $\Sigma^0 = uds$, $\Sigma^- = dds$, $\Xi^0 = uss$, $\Xi^- = dss$, and $\Omega^- = sss$. Involving also the next two quarks in the mass hierarchy (now leaving any kind of flavour symmetry behind us), namely the c- and b-quarks, yields many more mesons. For example, including the c-quark gives the $s = 0$ charmed $D^+ = c\bar{d}$, $D^0 = c\bar{u}$, $\overline{D}^0 = \bar{c}u$ and $D^- = \bar{c}d$ mesons, as well as strange charmed mesons D_s exchanging d for s. Similar constructions with the b-quark yields bottom mesons B, strange bottom mesons B_s, and charmed bottom mesons B_c, as well as charmonium $\eta_c = c\bar{c}$ and bottomonium $\eta_b = b\bar{b}$. For the baryons the naming convention including c- and b- quarks follows that of the $SU(3)$ flavour symmetric baryons, with indices c and b included to denote this modified quark content, such that we have e.g. $\Sigma_b^0 = udb$ and $\Xi_{cb}^+ = ucb$.

The t-quark does not form hadrons on detector timescales. In fact, the t-quark is so massive that it can decay into an *on-shell* $W^\pm$ boson, which significantly increases the decay rate with respect to the less massive quarks, since the final state phase space is that of a two-body rather than a three-body.

2.1.5. Anomaly cancellation

Chiral fermions require cancellation of chiral anomalies in order for the theory to be consistent. Classically, left- and right-handed fermion number are two separately conserved charges for

[16] The indices L and S here stand for *long* and *short*, since K_L has a long lifetime of $\tau_{K_L} \approx 5 \times 10^{-8}$ s while K_S has a short lifetime of $\tau_{K_S} \approx 9 \times 10^{-11}$ s.

[17] A star * typically denotes an excited state.

[18] Note that Λ^0 and Σ^0 do not mix since Λ^0 has $I = 0$ while Σ^0 has $I = 1$.

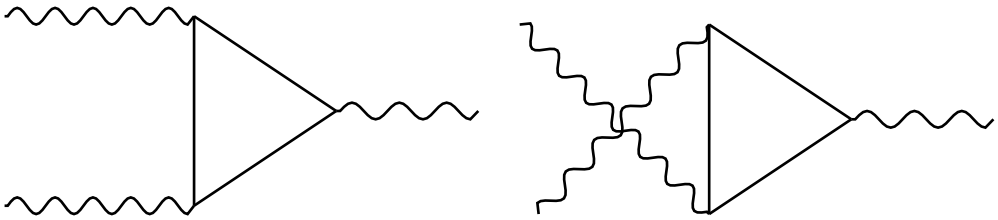

Figure 2.1.: Triangle diagrams that lead to the chiral anomaly. For any combination of gauge bosons in the three external legs, the sum of all diagrams (all possible fermions in the loop) must lead to an equal contribution from left- and right-handed fermions.

massless fermions, with the associated currents[19] $J^\mu = \bar{\psi}\gamma^\mu\psi$ and $J^{\mu 5} = \bar{\psi}\gamma^\mu\gamma^5\psi$. Note that J^μ and $J^{\mu 5}$ do not correspond directly to left- and right-handed fermion number respectively. Rather, left-handed fermion number is associated with the current $J^\mu_L = \frac{1}{2}(J^\mu - J^{\mu 5})$, and right-handed fermion number with $J^\mu_R = \frac{1}{2}(J^\mu + J^{\mu 5})$. Since the sign in front of $J^{\mu 5}$ differentiates J^μ_L from J^μ_R, the conservation of $J^{\mu 5}$ leads to what is known as a *chiral symmetry*. However, at one-loop level in the presence of a gauge coupling to the fermions, $J^{\mu 5}$ is no longer conserved, and the chiral symmetry is anomalously broken. For a non-abelian gauge theory, the divergence of the chiral current is given by [21]

$$\partial_\mu J^{a\mu 5} = -\frac{i}{64\pi^2}\,\mathrm{tr}\left(\gamma^5 t^a\{t^b, t^c\}\right)\epsilon^{\mu\nu\sigma\rho}F^b_{\mu\nu}F^c_{\rho\sigma}\,, \tag{2.51}$$

where t^α are the generators of the gauge theory, and where the anticommutator arises from the sum of two diagrams with their final legs crossed, as seen in Fig. 2.1. Loop diagrams like these lead to chiral anomalies for any combination of external bosons. The chiral current is given by

$$J^{a\mu 5} = ig\bar{\psi}t^a\gamma^\mu\gamma^5\psi, \tag{2.52}$$

where g is the gauge coupling. The factor γ^5 in Eq. (2.51) is given by $\gamma^5 = -\mathbb{1}$ for left-handed fermions and $\gamma^5 = +\mathbb{1}$ for right-handed fermions. For abelian gauge theories, the generators are simply replaced by the corresponding charge. In fact, in case the fermion ψ obeys several different gauge symmetries, the generators t^a, t^b, and t^c may not correspond to the same gauge group, in which case the trace containing the generators can be simplified using group theoretical relations [27]. In order for a given theory to be consistent, the sum of all chiral current divergences must vanish. That is, when evaluating the RHS of Eq. (2.51) for each fermion ψ that is part of the theory, the different contributions must cancel each other for each possible combination of generators from each gauge symmetry, including the mixing of different gauge symmetries. In the SM, this cancellation occurs consistently [28]. For the case where all generators correspond to $SU(3)_c$, the sum vanishes since there is no difference between left- and right-handed fermions in QCD. Furthermore, when there is only a single gluon present, each term vanishes individually due to the relation $\mathrm{tr}(t^a) = 0$, where t^a is now

[19] Note that the quantities J^μ etc. are technically current densities and not currents.

a generator of[20] $SU(3)$. The same is true for $SU(2)_L$, where we have $\mathrm{tr}(\tau^a) = 0$, where τ^a is a generator of $SU(2)$. For combinations where we have two $SU(3)_c$ bosons and one $U(1)_Y$ boson, the sum of divergences is proportional to

$$\sum_{\text{quarks}} \mathrm{tr}\left(t^a t^b Y\right) = \frac{1}{2}\delta^{ab} \sum_{\text{quarks}} Y\,, \tag{2.53}$$

where the sum only goes over the quarks since the leptons are uncharged under $SU(3)_c$. Evaluating the sum, including colour and $SU(2)_L$ multiplicities, and assigning a factor -1 to left-handed fields leads to

$$\sum_{\text{quarks}} Y = -3 \cdot 2 \cdot \tfrac{1}{6} + 3 \cdot \tfrac{2}{3} + 3 \cdot \left(-\tfrac{1}{3}\right) = 0\,. \tag{2.54}$$

Next, in the case where we have two $SU(2)_L$ bosons and one $U(1)_Y$ boson, the sum of divergences is proportional to

$$\sum_{\text{left-handed}} \mathrm{tr}\left(\tau^a \tau^b Y\right) = \frac{1}{2}\delta^{ab} \sum_{\text{left-handed}} Y\,, \tag{2.55}$$

where the sum goes over all left-handed fermions, since the right-handed ones are uncharged under $SU(2)_L$. This sum of hypercharges can be evaluated as

$$\sum_{\text{left-handed}} Y = -2 \cdot \left(-\tfrac{1}{2}\right) - 3 \cdot 2 \cdot \tfrac{1}{2} = 0\,. \tag{2.56}$$

For the case where all three bosons belong to $U(1)_Y$ we have the sum

$$\sum_{\text{fermions}} \left(Y^3\right) = -2 \cdot \left(-\tfrac{1}{2}\right)^3 + (-1)^3 - 3 \cdot 2 \cdot \left(\tfrac{1}{6}\right)^3 + 3 \cdot \left(\tfrac{2}{3}\right)^3 + 3 \cdot \left(-\tfrac{1}{3}\right)^3 = 0\,. \tag{2.57}$$

Finally, we need to also consider the case where we have one $U(1)_Y$ gauge boson and two gravitons[21] [29]. This leads to the sum[22]

$$\sum_{\text{fermions}} Y = -2 \cdot \left(-\tfrac{1}{2}\right) + (-1) - 3 \cdot 2 \cdot \left(\tfrac{1}{6}\right) + 3 \cdot \left(\tfrac{2}{3}\right) + 3 \cdot \left(-\tfrac{1}{3}\right) = 0\,. \tag{2.58}$$

Fantastically, each anomalous contribution vanishes, and the SM remains consistent.

[20] It is an unfortunate notation to use t^a as a general generator of an undetermined gauge group in Eqs. (2.51) and (2.52) while later using it specifically for $SU(3)_c$. However, this is the notation usually followed in the literature.

[21] Gravitons are not part of the SM but we know that the SM fermions must couple to gravity somehow.

[22] Note that we started out this section by assuming that the fermions are massless, but they can still couple to gravity by having a non-zero kinetic energy.

2.1.6. Sphalerons

Baryon number B and lepton number L are both classically conserved in the SM [30, 31]. These charges can be expressed as [32]

$$B = \int d^3x J_{B0}(x), \qquad L = \int d^3x J_{L0}(x)\,, \tag{2.59}$$

where the currents $J_{B\mu}$ and $J_{L\mu}$ are given by

$$\begin{aligned} J_{B\mu} &= \frac{1}{3}\sum_i \left(\bar{Q}_i\gamma_\mu Q_i - \bar{u}^c_{Ri}\gamma_\mu u^c_{Ri} - \bar{d}^c_{Ri}\gamma_\mu d^c_{Ri}\right), \\ J_{L\mu} &= \sum_i \left(\bar{L}_i\gamma_\mu L_i + \bar{e}_{Ri}\gamma_\mu e_{Ri}\right), \end{aligned} \tag{2.60}$$

where i denotes the flavour and a superscript c denotes the charge conjugate (see Appendix B). Classically the divergence of these currents vanishes,

$$\partial_\mu J^\mu_B = \partial_\mu J^\mu_L = 0\,, \tag{2.61}$$

but at one-loop level, the divergence is non-zero due to the Adler-Bell-Jackiw triangular[23] anomalies [34, 35] (c.f. Sec. 2.1.5),

$$\partial_\mu J^\mu_B = \partial_\mu J^\mu_L = \frac{N_f}{32\pi^2}\left(g^2 W_{a\mu\nu}\tilde{W}^{\mu\nu}_a - g'^2 B_{\mu\nu}\tilde{B}^{\mu\nu}\right), \tag{2.62}$$

where N_f is the number of fermion generations, and therefore B and L are anomalous[24] [36]. Since their divergences are equal, we know that $\partial_\mu J^\mu_B$ and $\partial_\mu J^\mu_L$ can cancel each other such that $B - L$ is still conserved at the quantum level. We can now write the RHS of Eq. (2.62) as the divergence of a current[25] K_μ,

$$\partial_\mu J^\mu_B = \partial_\mu J^\mu_L = N_f \partial_\mu K^\mu\,, \tag{2.63}$$

where

$$K^\mu = -\frac{g^2}{16\pi}\epsilon^{\mu\nu\rho\sigma} W_{av}\left(\partial_\rho W_{a\sigma} + \frac{g}{3}\epsilon^{abc} W_{b\rho} W_{c\sigma}\right) + \frac{g'^2}{32\pi}\epsilon^{\mu\nu\rho\sigma} B_\nu B_{\rho\sigma}\,. \tag{2.64}$$

The change in B and L over time can be obtained by integrating over the divergence of the current,

$$\Delta B = \Delta L = N_f \int_{t_0}^{t_1} dt \int d^3x K^\mu = N_f\left(N_{cs}(t_1) - N_{cs}(t_0)\right) \tag{2.65}$$

where N_{cs} is the Chern-Simons number

$$N_{cs}(t) = \frac{g^3}{96\pi^2}\int d^3x \epsilon^{ijk}\epsilon^{abc} W_{ai} W_{bj} W_{ck}\,, \tag{2.66}$$

[23] *Triangular* here refers to the fact that the one-loop diagrams look like triangles with the sides made up of fermions, and one boson sticking out of each vertex. See e.g. Fig. 6.3 in Ref. [33].

[24] An *anomalous* charge here means that it is conserved classically but not at the quantum level.

[25] Introducing K_μ is not necessary here for the purpose of showing the effect of the sphaleron, and is sometimes not done in the literature, but it is useful in solving the integral over the divergence of the current using Gauss's theorem by choosing a gauge where $\vec{K} = 0$ at spatial infinity.

for spatial indices i, j, k, it can be shown that [37]

$$\Delta N_{cs} = N_{cs}(t_1) - N_{cs}(t_0) = \nu\,, \tag{2.67}$$

where ν is an integer, and we therefore have

$$\Delta B = \Delta L = \nu N_f\,. \tag{2.68}$$

We see that baryon- and lepton number can change in the SM in units of[26] $\pm N_f = \pm 3$. Stable configurations of $B + L$ exist as the minima of the total potential energy of the system, with energy barriers separating the minima. A transition between different configurations can occur in two ways: tunnelling can occur through the barrier via instanton effects [38–40], or the energy of the system can be high enough such that the energy barrier can be surmounted, which is known as an electroweak sphaleron transition [41, 42]. The electroweak sphaleron, therefore, is an interaction involving one field each from the three lepton fermion doublets, and three each from the quark doublets, as seen in Fig. 2.2 (left). The Gauge fields configurations that give non-zero $\Delta\,(B + L)$ at zero temperature are instantons, and their rate[27]

$$\Gamma_{\text{Ins}} \propto e^{-4\pi/\alpha_W} \sim 10^{-170}\,, \tag{2.69}$$

where α_W is the weak analogy of the fine structure constant, is unobservably small [43]. If it were only due to instantons, the transition between different states of $B + L$ is so rare that it should never have happened a single time in the observable Universe [44]. At higher temperatures, $B + L$ transitions can occur more rapidly via electroweak sphalerons, as their rate is temperature dependent [45, 46],

$$\Gamma_{\text{Sph}} \propto e^{-E_{\text{Sph}}/T}\,, \tag{2.70}$$

where $E_{\text{Sph}} \sim \mathcal{O}(1) \times m_W/\alpha_W$, with m_W being the mass of the W boson. At high temperatures $m_W \lesssim T \lesssim 10^{12}$ GeV, the electroweak sphaleron rate is significant, and can be considered to be in equilibrium [47, 48].

Apart from electroweak sphalerons, there are also QCD sphalerons corresponding to the $SU(3)_c$ symmetry of the SM [49–51]. As illustrated in Fig. 2.2 (right), QCD sphalerons only involve the quarks, and they do not break B, L, or $B + L$.

2.1.7. Electroweak phase transition

As detailed in Sec. 2.1.2, the electroweak symmetry of the SM is broken at low temperatures, and restored at high temperatures. There is strong evidence that the Universe was hotter in the past than it is now[28], so hot in fact, that in the past the electroweak symmetry was

[26] Note that a change in L implies a change in B. For this reason, the sum $B + L$ is often considered for the change of baryon- and lepton number in the SM, rather than the two charges separately.

[27] The dimension of Γ is here inverse time. It is proportional to $e^{-4\pi/\alpha_W}$ due to this factor appearing in the cross section for this instanton transition.

[28] See Sec. 2.2.2 for more details.

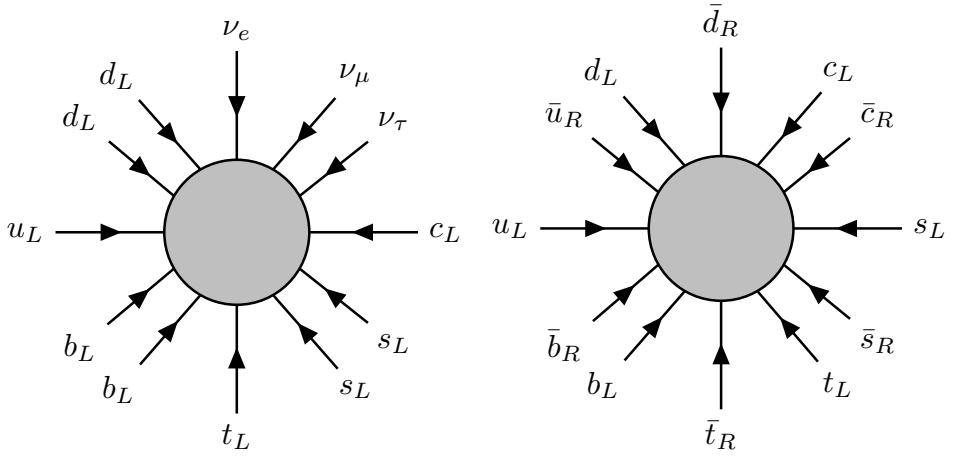

Figure 2.2.: Electroweak (left) and QCD (right) sphalerons. For the electroweak sphaleron, the $SU(2)_L$ indices can be changed so long as the vertex remains a singlet.

completely unbroken throughout the Universe. Since the Universe today is cool, and the electroweak symmetry is broken, there must have been some transition period when the electroweak symmetry went from being unbroken to being broken. This is the electroweak phase transition, and it is expected to take place around the weak scale[29].

The electroweak phase transition can be seen as arising as a consequence of the temperature dependence of the Higgs potential. For high temperatures, the minimum of the Higgs potential lies at the field value $\phi = 0$, while for low temperatures the minimum is at $\phi = v$. At zero temperature the Higgs potential at one-loop order is given by

$$V(\phi)\Big|_{T=0} = -\frac{1}{2}m_\phi^2\phi^2 + \frac{1}{4}\lambda\phi^4 + V_1(\phi)\,, \tag{2.71}$$

where $V_1(\phi)$ contains the one-loop corrections,

$$V_1(\phi) = \frac{g_i(-1)^{f_i}}{64\pi^2}M_i(\phi)^4 \ln\left(\frac{M_i(\phi)^2}{\mu^2}\right)\,. \tag{2.72}$$

Here f_i is the fermion number[30], μ is a cut-off scale, and $M_i(\phi)$ is the mass of particle i in terms of the Higgs field ϕ. For a particle i, the temperature-dependent contribution is given by [52]

$$V_T(\phi, T) = \frac{g_i(-1)^{f_i}T^4}{2\pi^2}\int_0^\infty dx x^2 \ln\left(1 - (-1)^{f_i}\exp\left[-\sqrt{x^2 + \frac{M_i(\phi)^2}{T^2}}\right]\right)\,. \tag{2.73}$$

The one-loop- and temperature-dependent contribution to the Higgs potential includes interactions with all particle species i that have couplings to the Higgs boson. However, the

[29]The *weak scale* is here loosely defined as an energy scale somewhere between the Higgs vev $v = 174$ GeV and the mass of the W boson $m_W = 80.4$ GeV.

[30]If i is a fermion we have $f_i = 1$, while if i is a boson $f_i = 0$.

effects are larger for more massive particles than for lighter ones. Therefore, we choose to only include contributions from the heaviest particles in the SM, namely the $W^{\pm}$, Z and Higgs bosons, as well as the top quark[31]. Explicitly, the ϕ-dependent masses of these particles are given by [53]

$$M_W(\phi)^2 = \frac{1}{2}g^2\phi^2\,, \tag{2.74}$$

$$M_Z(\phi)^2 = \frac{1}{2}\left(g^2 + g'^2\right)\phi^2\,, \tag{2.75}$$

$$M_\phi(\phi)^2 = -m_\phi^2 + 6\lambda\phi^2\,, \tag{2.76}$$

$$M_t(\phi)^2 = y_t^2\phi^2\,. \tag{2.77}$$

We then obtain the potential

$$\begin{aligned} V(\phi,T) = &-\frac{1}{2}m_\phi^2\phi^2 + \frac{1}{4}\lambda\phi^4 + \frac{1}{64\pi^2}\left(3\lambda\phi^2 - m_\phi^2\right)^2 \ln\left(\frac{3\lambda\phi^2 - m_\phi^2}{\mu^2}\right) \\ &+ \frac{3}{1024\pi^2}\left(2g^2 + (g^2+g'^2)^2\right)\phi^4\ln\left(\frac{\phi^2}{\mu^2}\right) - \frac{3}{64\pi^2}y_t^4\phi^4\ln\left(\frac{\phi^2}{\mu^2}\right) \\ &+ \frac{T^4}{2\pi^2}\left(6I^+\left(\frac{g^2\phi^2}{4}\right) + 3I^+\left(\frac{(g^2+g'^2)\phi^2}{4}\right) + I^+(-m^2+3\lambda\phi^2) + 12I^-\left(\frac{y_t^2\phi^2}{2}\right)\right), \end{aligned} \tag{2.78}$$

where

$$I^{\pm}(\Psi) = \pm\int_0^\infty x^2\ln\left(1 \mp \exp\left[-\left(x^2 + \frac{\Psi}{T^2}\right)^{1/2}\right]\right). \tag{2.79}$$

The minima of the Higgs potential, c.f. Eq. (2.78), are found via the conditions

$$V'(T,\phi)\Big|_{\phi=\phi_{\min}} = 0, \qquad V''(T,\phi)\Big|_{\phi=\phi_{\min}} > 0\,. \tag{2.80}$$

At high temperatures, the minimum of the Higgs potential is at $\phi_{\min} = 0$, while at low temperatures it is at $\phi_{\min} = v$. For some intermediate temperature, there are local minima at both $\phi = 0$ and $\phi = v$. If tunnelling effects are neglected, the electroweak phase transition occurs at a temperature T_2 when the potential barrier between the two local minima disappears. This temperature can be found via the condition

$$V''(0,T_2) = 0. \tag{2.81}$$

To find an expression for T_2, we simplify the temperature-dependent contribution to the potential using Taylor expansion,

$$f\left(\frac{\mu^2}{T^2}\right) = \ln\left(1 \pm \exp\left[-\sqrt{x^2 + \frac{\mu^2}{T^2}}\right]\right) \approx f(0) + \frac{\mu^2}{T^2}f'(0)\,. \tag{2.82}$$

[31] These particles, W, Z, ϕ and t, are commonly referred to as *The big four*, in reference to the heavy metal bands Anthrax, Megadeth, Metallica and Slayer, which are historically also known as *The big four*. These four particles all have masses of $\mathcal{O}(100\text{ GeV})$, which is significantly higher than the mass of the fifth most massive particle in the SM (the bottom quark at 4.18 GeV).

Now using the standard integrals

$$\int_0^\infty dx \frac{x}{2} \frac{e^{-x}}{1-e^{-x}} = \frac{\pi^2}{12}\,, \tag{2.83}$$

$$\int_0^\infty dx \frac{x}{2} \frac{e^{-x}}{1+e^{-x}} = \frac{\pi^2}{24}\,, \tag{2.84}$$

$$\int_0^\infty dx x^2 \ln\left(1-e^{-x}\right) = -\frac{\pi^4}{45}\,, \tag{2.85}$$

we find that

$$T_2 = \sqrt{\frac{12 m_\phi^2}{\frac{1}{4}\lambda + \frac{9}{4}g^2 + \frac{3}{4}g'^2 + 6y_t^2}}\,. \tag{2.86}$$

We see that the phase transition temperature T_2 depends on the couplings of the Higgs boson to the particles that we included in the one-loop and thermal effects. Furthermore, we expect the transition to occur at a temperature of roughly the same order of magnitude as the Higgs mass m_ϕ. However, the exact temperature at which the transition occurs depends on tunnelling effects, and on any other particles the Higgs interacts with which have not been included in deriving Eq. (2.86). Often the transition is simply assumed to occur at $\Lambda_{\text{EW}} \approx 100$ GeV.

2.2. The Λ Cold Dark Matter Model

In this section, we review the standard cosmological theory of modern times, the Λ Cold Dark Matter (ΛCDM) model. Here, the *cosmological constant* Λ refers to a term in Einstein's equations [54]

$$R_{\mu\nu} - \tfrac{1}{2} g_{\mu\nu} R + \Lambda g_{\mu\nu} = 8\pi G T_{\mu\nu}\,. \tag{2.87}$$

These equations[32] relate the curvature of spacetime (LHS) with the matter content of the Universe (RHS).

2.2.1. Modern cosmology

Our modern cosmology states that the Universe was created 13.787 ± 0.020 billion years ago [55] in an event known as the *Big Bang*. According to this view, the Universe evolved from a singularity by increasing its size and cooling down. Exactly from where our Universe came is not relevant to this thesis[33], and neither is the question of how the Universe might end.

As is described in more detail in Sec. 2.2.2, the term in Eq. (2.87) containing Λ describes what is known as *dark energy*, a constant expansion of space that dominates the energy content

[32] Even though it looks like a single equation, Eq. (2.87) actually contains $4 \times 4 = 16$ equations, since the indices μ and ν can take on one time dimension and three space dimensions each.

[33] With one exception, which is discussed briefly in the introduction to Ch. 3.

of the Universe at late times[34] [56, 57]. The *Cold Dark Matter* part of ΛCDM refers to an invisible form of matter, *dark matter*, that interacts via gravitation to form structures such as galaxies[35]. Dark matter is thought to be *Cold* in the sense that its velocity distribution is tilted towards the low end during the time of structure formation. The velocity distribution is affected by the mass of the individual dark matter components[36], as less massive particles are generally more relativistic than heavier ones[37].

Einstein's equations in Eq. (2.87) are central in General relativity and in cosmology. For a given metric $g_{\mu\nu}$, Einstein's equations reveal the details of the time evolution of the Universe. However, providing a metric that accurately describes our Universe is non-trivial, and usually some simplifying assumptions have to be made. On large enough scales[38], the Universe is often taken to be both homogeneous and isotropic, adhering to what is known as the *Cosmological principle*, which states that there are no special cosmological observers in the Universe: everyone should see the same thing when they look deep enough into space, no matter where they are. Isotropy and homogeneity are often seen as valid assumptions [58–60]. However, some large objects have been observed that brings into question at which scale the Universe should be seen as homogeneous [61–63], and the large scale structure of the Universe is being explored in large galaxy surveys [64]. Under the assumption of the cosmological principle, a good metric to use is the Friedmann–Lemaître–Robertson–Walker (FLRW) metric [65–68]

$$g_{\mu\nu} = \begin{pmatrix} 1 & 0 \\ 0 & -a(t)^2\left(\delta_{ij} + k\frac{x^i x^j}{1-kx^2}\right) \end{pmatrix}, \tag{2.88}$$

where $a(t)$ is a dimensionless time-dependent scale factor, and k is the Gaussian curvature of the Universe[39]. We can use Eq. (2.88) in the Ricci tensor

$$R_{\ \mu\nu} = \frac{\partial \Gamma^{\ \rho}_{\nu\ \mu}}{\partial x^\rho} - \frac{\partial \Gamma^{\ \rho}_{\rho\ \mu}}{\partial x^\nu} + \Gamma^{\ \eta}_{\eta\ \rho}\Gamma^{\ \rho}_{\nu\ \mu} - \Gamma^{\ \eta}_{\nu\ \rho}\Gamma^{\ \rho}_{\eta\ \mu}, \tag{2.89}$$

[34] In this chapter, *late times* or *late Universe* refers to a time comparable to present day, rather than something beyond present time (further in the future).

[35] The terms *dark matter* and *dark energy* are a bit unfortunate. Firstly, the two phenomena have little to do with each other apart from both being relevant to cosmology, and the fact that both are called *dark* is therefore misleading. Secondly, neither of them are strictly speaking *dark*, they can both more accurately be described as *invisible*, or *transparent*.

[36] Note that the nature of dark matter is not determined by the ΛCDM model. Dark matter may be a new particle beyond the SM, or it may be some compact object like black holes, or something else entirely.

[37] The temperature of dark matter, i.e. *hot* vs *cold*, may sound like it should refer to the kinetic energy of the individual dark matter components, rather than their velocity (at least if dark matter is in thermal equilibrium with the SM bath). Structure formation however relies on the ability of dark matter to form clumps, which in turn depends on the velocity of the dark matter components with respect to the escape velocity of the clumps, rather than the kinetic energy. Nevertheless it is conventional to use *hot* and *cold*, rather than something like *speedy* and *slow*, even if it could be thought that the latter more accurately captures the relevant physics.

[38] On scales larger than ~ 100 Mpc.

[39] If we drop the assumption of homogeneity but keep isotropy, the co-moving distance $a(t)$ and curvature k in the FLRW metric can be promoted to functions $A(r,t) = a(t)/r$ and $k(r) = kr^2$ that depend on the radial coordinate r. Such a metric is known as the Lemaître-Tolman-Bondi (LTB) metric [69–71].

and the Ricci scalar

$$R = g^{\mu\nu} R_{\mu\nu} \,, \tag{2.90}$$

where the Christoffel symbols $\Gamma^{\rho}_{\nu\,\mu}$ are given by

$$\Gamma^{\rho}_{\nu\,\mu} = \frac{1}{2} g^{\rho\eta} \left(\partial_\nu g_{\mu\eta} + \partial_\mu g_{\nu\eta} - \partial_\eta g_{\nu\mu} \right) \,. \tag{2.91}$$

The only remaining tensor to determine in Einstein's equations is the stress-energy tensor $T_{\mu\nu}$, which is given by

$$T_{\mu\nu} = \begin{pmatrix} \rho(t) & 0 \\ 0 & -p(t) g_{ij} \end{pmatrix} \,, \tag{2.92}$$

where g_{ij} is the spatial part of the FLRW metric at the origin $\vec{x} = 0$. Furthermore, $p(t)$ is the pressure, and $\rho(t)$ is the energy density. Plugging everything in, the time-component of Einstein's equations leads to [65,72]

$$\left(\frac{\dot{a}(t)}{a(t)} \right)^2 = \frac{8\pi G}{3} \rho(t) - \frac{k}{a(t)^2} + \frac{\Lambda}{3} \,, \tag{2.93}$$

and the spatial part leads to

$$\frac{\ddot{a}(t)}{a(t)} = -\frac{4\pi G}{3} \left(\rho(t) + 3p(t) \right) + \frac{\Lambda}{3} \,. \tag{2.94}$$

Eqs. (2.93) and (2.94) are known as the *Friedmann equations*, and they appear as a natural consequence of the cosmological principle applied to General relativity. Therefore, they are central components of the ΛCDM model. To interpret the Friedmann equations, we must first have an interpretation of the scale factor $a(t)$. From Eq. (2.88), we see that we would recover the standard Minkowski metric for $a(t) = 1$ and $k = 0$. A larger $a(t)$ would then mean that space is bigger with respect to time, and vice versa, such that a positive $\dot{a}(t)$ describes an expanding universe, and a negative $\dot{a}(t)$ describes a contracting universe. The Gaussian curvature $k = -1,\, 0,\, +1$ describes the geometry of the universe, whether it is a negatively curved 4-dimensional hyperboloid ($k = -1$, open universe), completely flat with no curvature into a 4th dimension ($k = 0$, flat universe), or a positively curved 4-dimensional sphere ($k = +1$, closed universe). Recently it has been claimed that there is evidence for a positive curvature [73,74] but this claim has also been disputed [75–77]. Historically, it has often been assumed that $k = 0$ applies to our Universe, which we also assume for the rest of this thesis. We can then interpret the first Friedmann equation (Eq. (2.93)) as showing that a positive energy density $\rho(t)$ leads to an expansion of the universe. In the second Friedmann equation (Eq. (2.94)), we see that a positive energy density, as well as pressure $p(t)$, leads to a deceleration of the expansion. The pressure and energy density may be related via the equation-of-state parameter

$$w(t) = \frac{p(t)}{\rho(t)} \,, \tag{2.95}$$

where for non-relativistic particles we have $w(t) = 0$, and for ultra-relativistic particles we have $w(t) = 1/3$. We see therefore that, for both matter and radiation, the energy density and

pressure act to slow down the expansion of the Universe. A positive cosmological constant Λ (dark energy) acts to increase the rate of expansion, as well as the acceleration of expansion.

Now, since we know that the Universe is expanding, we also know that the wavelength of light travelling from very distant sources is stretched, and visible colours are shifted towards red. This *redshift* is a useful tool to measure distances in cosmology, where the ridiculous length scales involved often make meters and even lightyears lose their intuitive connection[40]. The redshift is parametrised by z, which is given by[41]

$$z = \frac{\lambda_0}{\lambda_s} - 1\,, \tag{2.96}$$

where λ_0 is the wavelength of light at Earth, and λ_s is the wavelength at its source. The redshift z then describes the distance between Earth and the source of the light. We can now express the scale factor as[42]

$$a(z) = \frac{1}{1+z}\,. \tag{2.97}$$

Next, the the first law of thermodynamics gives us[43]

$$dU = -pdV\,, \tag{2.98}$$

where U is the energy that resides inside the volume V. We can rewrite this law in terms of our cosmological parameters such that

$$\begin{aligned} d(a^3\rho) &= -pdV \\ a^3 d\rho + 3\rho a^2 da &= -3w\rho a^2 da \\ d\ln\rho &= -3(1+w)d\ln a \\ \int_0^z dz' \frac{d\ln\rho(z')}{dz'} &= \int_0^z dz' 3(1+w)\frac{d\ln(1+z')}{dz'} \\ \frac{\rho(z)}{\rho(z=0)} &= \exp\left(3\int_0^z dz'(1+w(z'))(1+z')^{-1}\right)\,. \end{aligned} \tag{2.99}$$

For a constant w we get

$$\frac{\rho(z)}{\rho(z=0)} = \exp\left(3(1+w)\ln z\right) = z^{3(1+w)}\,. \tag{2.100}$$

Introducing the Hubble parameter

$$H(z) = \frac{\dot{a}(z)}{a(z)} \approx \sqrt{\frac{8\pi\rho(z)}{3}} \tag{2.101}$$

[40] Interestingly, it was the redshift of distant galaxies that led to the discovery of the expansion of the Universe [78, 79], which in turn led to the Big Bang theory.

[41] Unfortunately, z is also used as a time variable in astroparticle physics (see e.g. Appendix E). This time-variable z has nothing to do with redshift.

[42] Since light from far away was emitted at an earlier time and since light travels at a fixed velocity, the redshift z is a measure of both time and space.

[43] Here we have assumed that the Universe expands adiabatically.

and the Hubble constant

$$H_0 = \sqrt{\frac{8\pi\rho_{\text{crit}}}{3}}\,, \tag{2.102}$$

where ρ_{crit} is the critical energy density of the Universe[44], we can rewrite the first Friedmann equation as

$$\frac{H^2(z)}{H_0^2} = \sum_i \Omega_i \frac{\rho_i(z)}{\rho_i(z=0)}\,, \tag{2.103}$$

where the index i denotes different forms of energy. Using $w = 0, 1/3, -1$ for matter, radiation and dark energy, respectively, we have

$$\frac{H^2(z)}{H_0^2} = \Omega_m(1+z)^3 + \Omega_r(1+z)^4 + \Omega_\Lambda\,. \tag{2.104}$$

Due to their varying dependence on z, different forms of energy dominate at different times. Using the observed values $H_0 = 67.4$ (km/s)/Mpc, $\Omega_r = 8.5 \times 10^{-5}$, $\Omega_m = 0.3$, and $\Omega_\Lambda = 0.7$ [55], we see that radiation dominates from the beginning until $z \approx 3500$, then matter dominates until $z = 0.33$, after which dark energy dominates[45].

In Eq. (2.104), we neglected some forms of energy, e.g. gravitational waves and topological effects of phase transitions such as domain walls or cosmic strings, since their energy content is thought to be relatively small on large timescales. We also did not include inflation, which is a hypothetical process before radiation domination where the Universe undergoes rapid expansion [80, 81]. Inflation is conventionally not part of the ΛCDM model, but it does offer solutions to some of the problems that the ΛCDM model cannot explain, such as the *Flatness problem* (why is $k \approx 0$ so small, when even a very tiny deviation from zero in the early Universe would have led to a vastly different number today?) and the *Horizon problem* (why is the Universe almost the same temperature everywhere, when parts of it that are far from each other should never have been in thermal contact?). The details of inflation are not relevant for this thesis. However, the conditions for the end of inflation, known as *reheating*[46], play an important role. Unfortunately, the time of reheating, as well as the particle content of the Universe at that time, are both largely unknown. Therefore, even though it does play a role, from here on we neglect any effects coming from the details of reheating.

[44] This energy density is defined as the exact current energy density of the Universe that makes the first Friedmann equation hold using the observed value for H_0, as well as $k = 0$ and $\Lambda = 0$.

[45] The very recent (in cosmological terms) transition from matter domination to dark-energy domination highlights the so-called *Coincidence problem*. If dark energy continues to dominate more and more, light from distant sources (e.g. the Cosmic Microwave Background (CMB), see Sec. 2.2.2) will eventually not reach the Earth, because space expands faster than the light can travel (i.e. the photon wavelength is redshifted to infinity). There is a short window of time where dark energy is dominant enough to be detected, but weak enough such that we can still se light from very far away. The Coincidence problem then asks how it can be the case that we coincidentally happen to exist in this short window of time.

[46] Reheating contains the *re-* since the Universe should have at first been very hot when the inflatons are created (an inflaton is an inflation quanta), but later cooled down during inflation. As the inflaton decays, the decay products are hot, therefore the Universe is again heated.

T (GeV)	Process
$\gg 10^{13}$	Gauge interactions + t Yukawa
$> 10^{13}$	QCD sphaleron
$\sim 10^{13}$	EW sphaleron + b Yukawa
$\sim 10^{12}$	τ, c Yukawa
$\sim 10^{10}$	μ, s Yukawa
$\ll 10^{8}$	u, d, e Yukawa

Table 2.3.: Temperatures where different SM processes enter into equilibrium in the early Universe [86]. This table is taken from Ref. [2].

The ΛCDM model has many problems [82]. However, it is currently the leading theory of cosmology, and it does offer an explanation for many observed astrophysical phenomena. From here on we assume that the ΛCDM model is true.

2.2.2. Thermal history of the Universe

Here we briefly summarise the timeline of our Universe, from its creation until today. Since the Universe gradually became cooler as it aged, different stages of the evolution of the Universe can be described in terms of the temperature rather than how long ago they occurred. Furthermore, since physical processes often depend on the energy scale of the system in question, and since temperature is a form of energy, we categorise the different eras of cosmology in terms of the energy scale. This section follows Refs. [53] and [83].

Super-Planckian era: $T \gtrsim 10^{19}$ GeV

Quantum field theory applied to gravitation is non-renormalisable. This can be seen from dimensional arguments: the gravitational constant G has the dimensions m^{-2}, where m denotes mass. Therefore, any term proportional to G^n appearing in a probability density diverges as $\int dp p^{2n-1}$, where p is the momentum [84]. However, this is not a problem if the masses m of the particles that interact in the probability density are small, leading to a small dimensionless gravitational coupling constant $\alpha_G \propto Gm^2$, since we can then claim that the gravitational effect of the interaction is negligible. This assumption holds if $\alpha_G \ll 1$, leading to $m \ll G^{-1/2} \approx 1.2 \times 10^{19}$ GeV. Since, at high temperatures, the thermal mass of a particle is proportional to the temperature $m \propto T$ [85], the condition for neglecting quantum gravitational effects only holds for temperatures $T \lesssim 1.2 \times 10^{19}$ GeV. Above this temperature scale, in the super-Planckian era, there is no satisfactory theory to describe what is going on.

High-energy era: 10^{19} **GeV** $\gtrsim T \gtrsim 10^2$ **GeV**

The fundamental free variables of the SM, such as the coupling constants of the three gauge interactions, *run* with increasing or decreasing energy. This means that, due to renormalisation, the values of the coupling constants are different at different energy scales. In the presence of New Physics (NP), it is possible that this running is modified, such that the constants all meet in a single point at some high scale leading to a single gauge coupling. Such a scenario would correspond to a Grand Unified Theory (GUT), and is motivated from theoretical considerations of symmetry and simplicity of nature. If such a unification does occur, it should do so at a very high energy scale $\Lambda_{\text{GUT}} \sim 10^{16}$ GeV in order to avoid rapid proton decay, and there should be a plethora of Goldstone bosons coming from the broken generators of the GUT symmetry group.

Apart from the unification of forces, several unsolved problems of physics are thought to have solutions lying in the energy regime of the high-energy era. Inflation and reheating, the decoupling of DM with matter, as well as the generation of an asymmetry between matter and antimatter, could all occur in the high-energy era according to many theories (but there are several exceptions). It is also possible, as is discussed in Sec. 2.3.1, that the explanation for neutrino masses lies around the GUT scale. However, one reason why these problems are still unsolved is that the energy scales involved in the high-energy era are generally speaking outside current experimental reach. The LHC has a centre-of-mass energy of 13 TeV, which is not enough to probe the GUT scale, and low-scale observables do not have the sensitivity required to see the subtle effects of some GUT-scale particles directly.

Different SM processes come into equilibrium at different times, due to the different size of the corresponding coupling constants (larger coupling constants imply that the interaction is stronger and therefore it comes into equilibrium earlier). In Tab. 2.3, different SM processes can be seen along with the temperature at which they reach chemical equilibrium. All particles which are in equilibrium quickly thermalise among each other (this also includes the massless gluons, W^a, and B bosons), such that they become part of what is called the *thermal bath*. Radiation is the dominant energy content of the Universe during this era, apart from a possible inflationary period during which the inflaton should dominate.

At the end of the high-energy era there is the EWSB, which is known to occur, but apart from this the high-energy era is veiled in mystery. According to most theories, an asymmetry between matter and antimatter, with a ratio of about 1.000000001:1, is generated sometime during the high-energy era. A large part of this thesis deals with possible effects of NP during the high-energy era that leads to an asymmetry between matter and antimatter, and how they could possibly be probed experimentally.

Era of quark-gluon plasma: 10^2 **GeV** $\gtrsim T \gtrsim 1.5 \times 10^2$ **MeV**

After the electroweak symmetry has broken into the electromagnetic symmetry, quarks are part of the thermal bath, along with all other particles of the broken SM. There are distinct up- and down-type quarks, as the doublet $Q = (u_L \; d_L)^T$ no longer exists. The number densities of the massive gauge bosons $W^\pm$ and Z, along with that of the Higgs boson and the top

quark, significantly drop towards the end of the era of quark-gluon plasma.

Hadron era: 1.5×10^2 **MeV** $\gtrsim T \gtrsim 10^2$ **keV**

At a temperature around 1.5×10^2 MeV, quarks bind into hadrons. Instead of quarks, the Universe is now filled with mesons and baryons. However, the number densities of mesons drop heavily towards the end of the hadron era, as do the number densities of tau and muons. Neutrinos decouple from their chemical equilibrium with the SM thermal bath, and from here on they have a separate temperature as compared to the rest of the SM particle content.

BBN era: 10^2 **keV** $\gtrsim T \gtrsim 1$ **keV**

Eventually the temperature drops low enough for protons and neutrons to bind into nuclei, which denotes the start of Big Bang nucleosynthesis (BBN). A nucleus i can form if the temperature is low enough, according to the relation [53]

$$T_{\mathrm{NUC}} = \frac{B_i/(A_i - 1)}{\ln\left(\eta_B^{-1}\right) + 1.5\ln\left(m_p/T\right)}\,, \tag{2.105}$$

where B_i is the binding energy and $\eta_B = n_B/n_\gamma$ is the ratio of baryons to photons. The binding energy per nucleon is given by

$$B_i/A_i = \left(Z_i m_p + \left(A_i - Z_i\right) m_n - m_i\right)/A_i\,. \tag{2.106}$$

Here Z_i and A_i are the number of protons and nucleons, and m_p, m_n, m_i are the masses of protons, neutrons and the nucleus i, respectively. For deuterium ^{2}H, being the first nucleus to form, the binding energy $B_{^2\mathrm{H}}//2 \approx 1.1$ MeV is quite low in comparison to the next nuclei to form, which are ^{3}He with $B_{^3\mathrm{He}}/3 \approx 2.5$ MeV and ^{4}He with $B_{^4\mathrm{He}}/4 \approx 7$ MeV. We could then naively expect deuterium to start forming much later than helium. However, helium cannot fuse without deuterium, as it is created in e.g. $^2\mathrm{H} + p \rightarrow {}^3\mathrm{He}$ and $^2\mathrm{H} + {}^3\mathrm{He} \rightarrow {}^4\mathrm{He} + n$. Therefore, synthesis of helium is delayed until there is a sufficient abundance of deuterium in the Universe. At the end of BBN, the matter in the Universe consists of 75% hydrogen, 25% helium, and trace amounts of lithium [83].

Era of electron-ion plasma: 1 **keV** $\gtrsim T \gtrsim 0.4$ **eV**

Right after the primordial elements have formed, the Universe was too hot for electrons to settle into atomic shells around nuclei, and it remained so for several hundred thousand years (in contrast, BBN ended roughly 3 minutes after the Big Bang). During this time, in which the matter content of the Universe consisted of an electron-nucleus plasma, DM was forming haloes that would later serve as seeds for galaxies. Depending on the mass of the dark matter particle, these haloes either formed in the disintegration of bigger DM haloes (*top-down* structure formation, light DM particles) or by coalescence of smaller clumps (*bottom-up* structure formation, heavy DM particles). The visible matter consisted of charged

particles (positive nuclei and negative electrons), and could not form structures due to the repelling effect of Compton scattering. The rate of atomic hydrogen formation is described by the Saha equation [83, 87]

$$\frac{1-X}{X^2} = \frac{4\sqrt{2}\times 1.2}{\sqrt{\pi}}\eta_B \frac{T}{m_e} e^{B/T}, \tag{2.107}$$

where

$$X \equiv \frac{n_p}{n_B} = 1 - \frac{n_H}{n_B} \tag{2.108}$$

is the relative abundance of protons to baryons, and where $B = m_p + m_e - m_H = 13.6$ eV is the binding energy of hydrogen. Solving Eq. (2.107) gives a temperature of around 4000 K, or 0.4 eV, as the transition temperature from a plasma to a hydrogen gas. We see the light from the plasma at the time around this transition ($z \sim 1100$) as the Cosmic Microwave Background (CMB).

During the era of electron-ion plasma, at a temperature around 1 eV, radiation stops being the dominant form of energy in the Universe, being overtaken by matter (DM + visible matter).

Hydrogen era: 0.4 **eV** $\gtrsim T$

After the transition from a plasma to a gas, the Universe becomes transparent, and visible matter can fall into the DM haloes. This initiates star formation, which continues until present day. At 9.8 billion years after the Big Bang, dark energy takes over as the dominant energy source of the Universe. Presently, 13.8 billion years have passed since the Big Bang, and the Universe has reached a temperature of 2.7 K, or 2×10^{-4} eV.

2.3. Neutrino masses and physics beyond the Standard model

In Secs. 2.1 and 2.2, we outlined the most commonly accepted theories for particle physics and cosmology. In this chapter we go through the reasons why the former is not enough for a full description of nature. We also show some of the possible extensions that could solve issues in the current framework, focusing mainly on the particle physics aspect of the modern theories, rather than cosmology.

2.3.1. Motivations to go beyond the Standard model

To many physicists, the SM is simultaneously both exciting and boring. It's exciting in the sense that it accurately predicts the outcome of experiments, and provides us with a picture of how nature works on very short distances. The boring part comes from this ability to predict: the SM is so good that very few observations are left unexplained. Yet there are a plethora of theoretical problems that motivate the venture beyond the SM into different extensions.

Baryon asymmetry of the Universe

As is discussed at some length in Ch. 3, the observed difference in the number density of baryons vs antibaryons in the Universe motivates the search for New Physics (NP), as the SM does not explain how such an asymmetry came about. This problem has many solutions, which are also covered in Ch. 3.

Neutrino mass

Neutrinos are massless in the SM, but as inferred from neutrino oscillation experiments [88,89] at least two of the neutrinos have non-zero masses. The SM charged lepton weak gauge interactions and Yukawa interactions are both diagonalised, at least conventionally, and therefore it is not possible to diagonalise the neutrino mass matrix (c.f. Sec. 2.1.3). The connection between the neutrino flavour states and mass states is parametrised by the Pontecorvo–Maki–Nakagawa–Sakata (PMNS) matrix U [90,91], such that

$$|\nu_i\rangle = U_{i1}^* |\nu_1\rangle + U_{i2}^* |\nu_2\rangle + U_{i3}^* |\nu_3\rangle \ , \tag{2.109}$$

where $i \in \{e, \mu\, \tau\}$ denotes the neutrino flavour, ν_1, ν_2, ν_3 are the neutrino mass eigenstates, and U_{ab} is an element of the unitary PMNS matrix. The connection between masses and oscillations can be seen by letting the state in Eq. (2.109) travel a distance L in the direction $\hat{x}$,

$$|\psi_i(L\hat{x}, t)\rangle = U_{i1}^* |\nu_1\rangle\, e^{-i\phi_1} + U_{i2}^* |\nu_2\rangle\, e^{-i\phi_2} + U_{i3}^* |\nu_3\rangle\, e^{-i\phi_3} \,, \tag{2.110}$$

where $\phi_a = p_a^\mu x_\mu$, and where p_a is the 4-momentum of particle a. We can also express Eq. (2.110) in terms of the flavour states,

$$|\psi_i(L\hat{x}, t)\rangle = c_{ie} |\nu_e\rangle + c_{i\mu} \left|\nu_\mu\right\rangle + c_{i\tau} |\nu_\tau\rangle \ , \tag{2.111}$$

for coefficients

$$c_{ij} = (U_{i1}^* U_{j1} e^{-i\phi_1} + U_{i2}^* U_{j2} e^{-i\phi_2} + U_{i3}^* U_{j3} e^{-i\phi_3}) \,. \tag{2.112}$$

The probability to oscillate from ν_i to ν_j is now given by

$$P(\nu_i \to \nu_j) = |\left\langle \nu_j \middle| \psi_i(L\hat{x}, t) \right\rangle|^2 = c_{ij} c_{ij}^* \,. \tag{2.113}$$

From the structure in Eq. (2.113), the oscillation probability is proportional to the differences between the phases ϕ_1, ϕ_2 and ϕ_3, which can be expressed as

$$\phi_i - \phi_j = (p_i^0 - p_j^0)t - (\vec{p}_i - \vec{p}_j)L = \left((E_i - E_j)t - \left(\frac{p_i^2 - p_j^2}{p_i + p_j} \right) L \right) = \frac{(m_j^2 - m_i^2)L}{2E_\nu} \,, \tag{2.114}$$

where we have assumed $E_i = E_j = E_\nu$ and $p_i + p_j = 2E_\nu$. Clearly, Eq. (2.114) depends on the mass difference between ν_i and ν_j. The observed neutrino oscillation involves three flavours, which necessitates two mass splittings, implying that at least two out of the neutrinos are massive.

Solutions to the neutrino mass problem may involve introducing BSM fields, which can generate a neutrino mass via tree- or loop-level diagrams. Perhaps the simplest solution is to introduce to the SM a coupling

$$\mathcal{L} \supset -y^{\nu}_{ij} \bar{L}^{a}_{i} \tilde{\phi}^{a} \nu_{Rj} + \text{h.c.}\,, \tag{2.115}$$

where $\nu_R \in (1,1,0)$ is a right-handed neutrino. A problem with this solution is that in order to get the correct neutrino mass $m_\nu \sim \mathcal{O}(10^{-2})$ eV, the coupling $y^{\nu}_{ij} \sim \mathcal{O}(10^{-13})$ has to be very small[47]. Another problem is that the field ν_R, being a complete SM singlet, has the potential to participate in a Majorana term

$$\mathcal{L} \supset -\frac{1}{2} M^{\nu}_{ij} \bar{\nu}^{c}_{Ri} \nu_{Rj} + \text{h.c.}\,, \tag{2.116}$$

where M^{ν}_{ij} can in principle be quite large. This is a problem because Eq. (2.116) induces lepton number violation (LNV), which has not been observed, though it can easily be solved by assuming that the scale of LNV is simply inaccessible to current experiments.

Dark matter

As detailed in Sec. 2.2, many of the most established modern theories of cosmology include a DM component, but the detailed nature of DM is often not directly relevant. The experimental evidence for the existence of DM is overwhelming: there is a wide range of astrophysical observations that can be simultaneously explained by the introduction of a non-interacting matter component (see Ref. [92] for an historical overview). It is not necessary for cosmology that DM is a new particle, it could e.g. be made up of black holes [93, 94]. Alternatively, some of the effects of DM could also be due to modified gravity [95, 96]. Many BSM theories (often by construction) include a particle or a set of particles that can act as DM, by being sufficiently non-interacting and stable, as well as having the correct mass. If DM does have a particle nature, it could be involved in the solution to other unsolved problems of particle physics, such as the origin of the matter-antimatter asymmetry or the generation of neutrino masses. One motivation to consider DM as a particle is being able to explain the correct DM abundance via thermal freeze-out or freeze-in. This provides a relatively simple explanation for how the DM energy density came about. The energy density of DM is very close to that of baryons [55]

$$\Omega_{\text{DM}} \approx 5 \times \Omega_B\,, \tag{2.117}$$

and many theories therefore postulate that they have a common origin [97–100]. Since baryons have a particle nature, it is, in such a scenario, often believed that DM does as well. Finally, the weak interaction strength between DM and visible matter could explain why neutrinos have such a small mass. The generation of neutrino masses could occur via loop diagrams involving DM particles [101], where the small coupling between DM and neutrinos, necessary to explain the experimental non-detection of DM, naturally leads to a tiny neutrino mass.

[47] It can be argued that the smallness of the neutrino Yukawa coupling is not a problem at all, and that there is no inherit reason to expect that all free parameters of the next theory beyond the SM are $\mathcal{O}(1)$.

Anomalies

The above mentioned motivations to look for theories beyond the SM all have to do with extending the currently established framework to explain observed phenomena, such as neutrino oscillations or the gravitational effects of some invisible matter component. A more straight-up version of this approach is to actively look for experimental results that deviate from theoretical expectations, and find extensions to the SM that explain the discrepancy. Historically this hunting for anomalies[48] has been unsuccessful, the SM has prevailed through very thorough scrutiny. For example, in 2015 both the ATLAS and CMS experiments at the LHC in CERN reported an excess of diphoton events at an invariant mass of 750 GeV [102,103]. What looked like a signal of NP disappeared a few years later [104,105]. More recently, in 2020, preliminary results from the KOTO experiment at J-PARC showed an excess of events in the rare meson decay $K_L \to \pi\nu\bar{\nu}$ [106], and later the same year this excess also disappeared [107]. We discuss this rare decay mode in more detail in Chs. 4 and 6.

There are further anomalies in the semileptonic decays of B-mesons that are still standing to this day [108, 109]. In 2012, the BaBar collaboration reported a deviation from the expected value in the ratio $R_{D^{(*)}} \equiv \text{BR}(\overline{B} \to D^{(*)}\tau^-\bar{\nu}_\tau)/\text{BR}(\overline{B} \to D^{(*)}\ell^-\bar{\nu}_\ell)$ [110], where a superscript $*$ denotes an excited meson. Similarly, in 2014, the LHCb collaboration reported an anomaly in $R_K \equiv \text{BR}\left(B^+ \to K^+\mu^+\mu^-\right)/\text{BR}\left(B^+ \to K^+e^+e^-\right)$ [111]. For the former mode, a more recent experimental result from the Belle collaboration is in less tension with the SM [112]. However, combined with the initial results, $R_{D^{(*)}}$ still remains anomalous. For R_K the story is different. The 2021 result from LHCb $R_K = 0.846^{+0.042+0.013}_{-0.039-0.012}$ [113] is consistent with the 2019 result $R_K = 0.846^{+0.060+0.016}_{-0.054-0.014}$ [114], while in the SM, R_K should be equal to 1 up to $\mathcal{O}(1\%)$ corrections from electromagnetic effects and the mass difference between e and μ [115,116]. This leads to a discrepancy between the SM expectation and LHCb experimental result with a statistical significance[49] of 3.1σ [113]. The consistent discrepancy between theory and experiment has led to R_K being one of the more well-studied anomalies.

Another anomaly related to muons is the discrepancy between the theoretical and experimental values for the anomalous muon magnetic moment $a_\mu \equiv (g_\mu - 2)/2$, where g_μ is the gyromagnetic ratio of the muon[50]. In 2006 the Muon g-2 collaboration obtained an experimental value for a_μ that differed from the SM with a significance of 3.7σ [117]. This deviation was confirmed in 2021, increasing the significance to 4.2σ [118,119]. However, a recent result from the Budapest-Marseilles-Wuppertal (BMW) collaboration regarding the calculation of the leading hadronic contribution to the muon magnetic moment significantly reduced the tension between the experimental result and the SM [120], turning the significance of the

[48] Note that the type of anomaly that is referred to here has little to do with the anomalies that are discussed in Sec. 2.1.5.

[49] The statistical significance of an experimental result in particle physics is usually given in terms of standard deviations (σ). For a result to be claimed as a discovery, a significance of 5σ is usually required.

[50] The gyromagnetic ratio is related to the magnetic moment $\vec{M}$ via $\vec{M} = \frac{g_\mu e}{2m_\mu}\vec{S}$, where $\vec{S}$ is the spin vector. At tree-level it has the value $g_\mu = 2$, such that $a_\mu \equiv (g_\mu - 2)/2$ only captures the loop-induced effects. Magnetic moments are generated at loop level because none of the SM particles have a magnetic charge (i.e. there are no magnetic monopoles). An excess in the magnetic moment of the muon can therefore be seen as a hint that there are more particles running in the loop than we have accounted for, leading to evidence for BSM particles.

anomaly into 1.5σ.

Regarding neutrinos, there is an anomaly that started with a result from the LSND experiment in 2001 [121]. In this experiment, a search was conducted to observe $\bar{\nu}_\mu \to \bar{\nu}_e$ oscillations, and the number of observed events was consistent with an oscillation probability $P = (0.264 \pm 0.112)$. However, this oscillation probability implied a mass squared difference $\Delta m^2 \sim 1$ eV^2 in the three-flavour model, inconsistent with solar and atmospheric data [122]. The MiniBooNE experiment was built to investigate the LSND anomaly, and it eventually lead to a confirmation of the excess [123, 124]. However, in MiniBooNE the observed excess could be caused by a range of different processes. Being a Cherenkov detector, MiniBooNE cannot distinguish between a single electron and an electron-positron pair coming from a converted photon [125]. To resolve this issue, the liquid argon time projection chamber experiment MicroBooNE was commissioned, sitting upstream of MiniBooNE in the very same neutrino beam but featuring superior event reconstruction capabilities [126]. A first result from MicroBooNE rules out the underestimation of Δ-baryon production as the source of the MicroBooNE excess at 94.8% CL [127]. One of the most common explanations for the LSND/MiniBooNE anomaly is the existence of a light sterile neutrino [128–130], and this explanation is still not ruled out, with the anomaly still being there. Future measurements might shed light on the origin of the LSND/MiniBooNE anomaly, but for now there is no definite answer.

There are more anomalies in the fields of particle physics and cosmology than the ones listed above, too many to all be treated in detail here. These anomalies include e.g. an underabundance of cosmological ^{7}Li [131], a discrepancy between different measurements of the Hubble constant [132, 133], a deviation from the expected signal in nuclear transitions of ^{8}Be and ^{4}He [134, 135], an excess of cosmic rays [136–139], and a difference in the CP asymmetry between the decay $B^+ \to K^+\pi^0$ and $B^- \to K^+\pi^-$ [140].

Gauge unification

As discussed in Sec. 2.2.2, there are reasons to believe that the gauge group of the SM $SU(3)_c \times SU(2)_L \times U(1)_Y$ comes from the breaking of some larger gauge group at a very high energy, often through some intermediate extended symmetry. In this case, the fundamental forces of the SM could be unified into a single force, in what is known as a Grand Unified Theory (GUT) [141–143]. If such a breaking does occur, the fermions of the SM could be explained as being different incarnations of a small number or even a single type of fermion. The coupling constants of the SM would no longer be free parameters, but rather they would depend on the coupling constant of the GUT gauge group, as well as running effects. However, according to Goldstone's theorem, there is a massless Goldstone boson for each broken generator of the GUT gauge group, and depending on the model these can be quite many. In order to explain the experimental non-appearance of such degrees of freedom, they are often assumed to be eaten by new massive gauge bosons via a Higgs-like mechanisms, and these gauge bosons are assumed to be too massive to have been detected. Many GUT models also lead to proton decay, which is constrained by the stringent limit on the proton lifetime of $\tau > 2.4 \times 10^{34}$ years for the $p \to e^+\pi^0$ mode, set by the Super-Kamiokande collaboration [144]. There are several

different candidate gauge groups which can achieve unification of the SM forces. Examples of these are $SU(3)_c \times SU(2)_L \times SU(2)_R \times U(1)_{B-L}$ [145–147], $SU(4) \times SU(2)_L \times SU(2)_R$ [148], $SU(4) \times SU(2)_L \times U(1)_R$ [149–151], $SU(5)$ [152], $SO(10)$ [153], E_6 [154], and many more.

Hierarchy problem

One of the historically most firmly believed signs for the need of BSM physics is a theoretical problem known as the *Hierarchy problem*[51] [155–157]. This problem is connected to the quantum corrections to the Higgs mass, which depend on the momentum as well as the masses and couplings of all fields that the Higgs boson couples to. The momentum-dependent quantum corrections appear as loop-level diagrams, where any field that the Higgs couples to can contribute in a loop, and therefore provide a correction to the Higgs mass[52]. Assuming that the SM is valid up to the high energy scale $M \sim 10^{15}$ GeV, corrections to the Higgs mass can only come from terms proportional to M^2. At the scale M, there are many contributions to the Higgs mass, including the classical mass as well as quantum corrections. Since we assumed M to be the cut-off of the SM, the parameter $m_h \sim 125$ GeV should arise even when the momentum scale in the quantum fluctuations is taken to be M. The problem here then lies in the large hierarchy between M and m_h, since quantum corrections with momentum M are expected to produce mass parameters of order M. In order for different contributions at the scale M to approximately cancel each other such that the mass scale m_h is produced, the physics at the scale M has to be extremely fine-tuned. In fact, different terms at M have to cancel up to 26 decimal places [158]. There is nothing inherently inconsistent with such a fine tuning, but it is believed by many that it is a sign that something is wrong with the current theory.

The Hierarchy problem is not unique to the Higgs boson, as can be seen in the following example, which is taken from Ref. [159]. Consider the pion π, which approximately obeys an $SU(2)$ symmetry containing a neutral and charged component π^0 and $\pi^\pm$, respectively, with masses $m_{\pi^0} = 135$ MeV and $m_{\pi^\pm} = 140$ MeV, such that $\pi = \exp(\sum_{i=0,\pm} \pi^i \sigma^i / f_\pi)$, where σ_i are the Pauli matrices and f_π is a structure constant. The $SU(2)$ symmetry is broken by the mass difference between π^0 and $\pi^\pm$, but it is approximately conserved. The mass term in the Lagrangian of this model respects the $SU(2)$ symmetry, and is given by

$$\mathcal{L} \supset \frac{1}{2} m_\pi^2 f_\pi^2 \operatorname{Tr} \pi = \frac{1}{2} m_\pi (\pi^0)^2 + \frac{1}{2} m_\pi \pi^+ \pi^- + \dots . \tag{2.118}$$

However, the charged pions have electromagnetic interactions while the neutral ones do not, as can be seen in the kinetic part of the Lagrangian

$$\mathcal{L} \supset \frac{1}{2} \left(\partial_\mu \pi_0\right)^2 + \left| \left(\partial_\mu + ieA_\mu\right) \pi^+ \right|^2 . \tag{2.119}$$

[51] *Hierarchy* here refers to a hierarchy of mass scales.

[52] Note that not all contributions appear with the same sign. In fact, bosons and fermions in the loop lead to different signs, such that if the contributions from one increases the mass, those from the other will reduce it. In the SM, the biggest quantum correction comes from the top quark.

It could be possible to account for the observed mass difference between π^0 and $\pi^\pm$ by the electromagnetic interaction of $\pi^\pm$. Using an Effective field theory[53] (EFT) description of the electromagnetic contribution, we can estimate its size as

$$\delta\mathcal{L} = \frac{e^2}{(4\pi)^2}\Lambda_\pi^2\pi^+\pi^-\,, \tag{2.120}$$

where Λ_π is the energy scale of the electromagnetic contribution. If $\Lambda_\pi \approx 750$ MeV, the term in Eq. (2.120) could precisely explain the observed mass difference between π^0 and $\pi^\pm$. However, if we had excluded the existence of any new particles below some very high scale $M \gg \Lambda_\pi$, and found no new particles around Λ_π, there would be nothing to mediate the electromagnetic interaction that we think explains the pion mass difference. Hypothetically, particles could still exists at scales similar to M, but the electromagnetic contribution from these particles would be huge, and we would then be in a tough situation to explain why their presence is not more clearly seen in the pion mass splitting. There is a way out if we assume that there is some *other* NP occurring at M, which contributes to the pion mass difference via

$$\delta\mathcal{L} = -\delta_m^2\pi^+\pi^-\,. \tag{2.121}$$

If $\delta_m^2 \approx M^2e^2/(4\pi)^2$, this term would almost cancel the term in Eq. (2.120). However, we then have a Hierarchy problem, since the involvement of physics at the scale M in a mass difference $\Delta m_\pi \ll M$ begs an explanation: why is the physics at the high scale M affecting the low-scale physics at δ_m? Luckily, there is the ρ meson, which comes in at $m_\rho = 775$ MeV [14]. This particle mediates the electromagnetic interaction, which explains the pion mass difference [160], and therefore we do not have a Hierarchy problem among the pions in the SM.

For the Higgs boson, the quantum correction to its mass coming from the top quark can be written as

$$\delta\mathcal{L} = 6\frac{\lambda_t^2}{(4\pi)^2}\Lambda_h|h|^2\,. \tag{2.122}$$

In order for the quantum correction to stay below the scale of EWSB, we would require $\Lambda_h \lesssim 500$ GeV. However, unlike in the pion example, no new particles that fit the criteria have been found at this scale. Finding a solution to the Hierarchy problem was one of the main motivations for Supersymmetry (SUSY) [161–164]. However, the non-observation of supersymmetric particles at the LHC has lead to its gradual decrease in popularity as a solution. Other solutions include extra dimensions [165,166] or the treatment of the Higgs as a Nambu-Goldstone boson of a broken global symmetry [167,168].

This concludes our list of some of the most commonly encountered motivations to go beyond the SM. In Sec. 2.3.2 we discuss the different fields that we consider as possible extensions to the SM in subsequent chapters, and in Sec. 2.3.3 we describe the effective field theory framework, in which SM extensions can be studied model-independently.

[53] See Sec. 2.3.3.

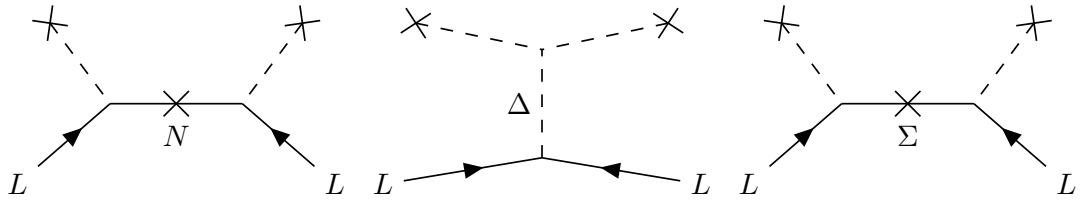

Figure 2.3.: Type I (left), Type II (centre), and Type III (right) seesaw diagrams.

2.3.2. Phenomenology of beyond-the-Standard-model particles

There is a wide range of models that incorporate BSM physics in order to explain different observed phenomena or to solve theoretical issues. Many such models involve new particles, which can be sought for experimentally. There are too many different kinds of BSM models to go through each of them here. Instead, this section deals with the BSM particles that are most relevant for the later chapters.

Many of these particles can play significant roles in cosmological evolution. Some of the scalar fields could potentially act as inflatons, and some particles could be dark matter candidates. Rather than focusing on such aspects, we are instead interested in lepton/baryon number violation and neutrino masses, and in terms of cosmology we mainly concentrate on the generation of a baryon asymmetry of the Universe. Notable examples of BSM phenomena that will not be mentioned further is the axion [169–171] and Kaluza-Klein states [172–174].

In Sec. 2.3.2 we list the different BSM fields that are considered in this thesis, most notably in Ch. 5. In Sec. 2.3.2 we discuss the three seesaw fields, after which we describe different BSM scalar-, fermion-, and vector fields in Secs. 2.3.2, 2.3.2, and 2.3.2, respectively.

Seesaw particles

As discussed in Sec. 2.3.1, there is experimental evidence for the existence of neutrino masses but the mechanism that generates them remains unknown. Neutrinos could acquire their mass though a Dirac term via an interaction with the Higgs boson,

$$\mathcal{L}_{\text{Dirac}} = -y^{\nu}_{ij} L^a_i \phi^a \bar{\nu}_{Rj} + \text{h.c.} \tag{2.123}$$

with ν_R being the right-handed neutrino, or through a Majorana mass term

$$\mathcal{L}_{\text{Majorana}} = -\frac{C_1^{(5)ij}}{\Lambda_1^{(5)}} L^a_i L^b_j \phi^a \phi^b + \text{h.c.}\,, \tag{2.124}$$

where the factor $C_1^{(5)ij}/\Lambda_1^{(5)}$ has mass dimension -1 and encodes effects of NP (see Sec. 2.3.3). In fact, Eq.(2.124) is not renormalisable, and in order to find a satisfactory theory for neutrino Majorana masses we need to add BSM fields, since the absence of NP would lead to $C_{ij}/\Lambda = 0$. One such NP scenario can be realised by adding to Eq. (2.123) a bare mass term[54] for the

[54] *Bare mass* here refers to a term with a coefficient M of mass dimension 1, such that $\mathcal{L} \supset -M\bar{\psi}^c\psi$. The mass is bare in the sense that it does not come from an interaction with any other particle. Only field bilinears that are

right-handed neutrino, which we now rename $\nu_R \to N$ to signify this modification[55], such that

$$\mathcal{L}_{\text{Type-i}} = -y_{ij}^{\nu N} L_i^a \phi^a N_j - \frac{1}{2} M_{ij} N_i N_j + \text{h.c.}\,, \tag{2.125}$$

where we have identified $N = \bar{N}^c$ and therefore written only N. In Eq. (2.125) we wrote the Lagrangian with an index *Type-i* in anticipation of realising a Majorana mass term in the spirit of Eq. (2.124) via the so-called Type-i seesaw mechanism [175]. Diagrammatically, the this mechanism can be understood as two instances of an interaction between the lepton doublet L and the Higgs doublet H, in-between which there is a right-handed neutrino N with a Majorana mass insertion, as illustrated in Fig. 2.3 (left). In this way the left-handed neutrino mixes with the right-handed one to produce an effective left-handed neutrino mass. We can then redefine the fields ν_L and N in order to obtain fields with definite masses that do not mix. To see this, we first observe that Eq. (2.125) can be written in matrix form,

$$\mathcal{L}_{\text{Type-i}} = -\frac{1}{2} \begin{pmatrix} \nu_L^T & N^T \end{pmatrix} \begin{pmatrix} m_L & m_D^T \\ m_D & m_R \end{pmatrix} C^{-1} \begin{pmatrix} \nu_L \\ N \end{pmatrix} + \text{h.c.}\,. \tag{2.126}$$

where C is the charge conjugation matrix. Note that Eq. (2.126) is written after EWSB, and that the fields ν_L and N are written as vectors in flavour space. This promotes the masses from Eq. (2.125) to matrices such that

$$(m_D)_{ij} = y_{ij}\langle\phi\rangle, \qquad (m_R)_{ij} = M_{ij}\,. \tag{2.127}$$

For completeness we have also introduced m_L as a Majorana mass matrix for ν_L that could arise in different models. We now wish to redefine the fields $\nu_L \to \nu_L'$ and $N \to N'$ according to

$$\begin{pmatrix} \nu_L \\ N \end{pmatrix} = W \begin{pmatrix} \nu_L' \\ N' \end{pmatrix}\,, \tag{2.128}$$

where W is defined such that the mass matrix is diagonalised,

$$W^T \begin{pmatrix} m_L & m_D^T \\ m_D & m_R \end{pmatrix} W = \begin{pmatrix} m_L' & 0 \\ 0 & m_R' \end{pmatrix}\,. \tag{2.129}$$

This leads to ν_L' and N' being separate mass eigenstates that do not mix. For W we now use the ansatz of a rotation matrix[56]

$$W = \begin{pmatrix} \sqrt{1-\sin^2\theta} & \sin\theta \\ -\sin\theta & \sqrt{1-\sin^2\theta}\,, \end{pmatrix} \tag{2.130}$$

complete singlets under the gauge group of the model under consideration can have bare mass terms, since such a term would otherwise violate the gauge symmetry.

[55] Though it is a convention not strictly subscribed to by some, the notation ν_R is often reserved for light right-handed neutrinos in the literature, and N is instead used for higher mass neutrinos.

[56] Note that in Eq. (2.130) each entry should be thought of as being multiplied by an identity matrix, though this is not shown explicitly. By writing Eq. (2.130) in this way we have assumed that the different generations of ν_L and N do not mix with each other. In general, we can promote the mixing angle to a matrix $\sin\theta \to B$, $\sin^2\theta \to B^\dagger B$ to treat also inter-generational mixing [176].

where for small angles θ we use the approximation

$$\sqrt{1-\sin^2\theta} \approx 1 - \frac{1}{2}\sin^2\theta. \tag{2.131}$$

Inserting Eq. (2.130) in Eq. (2.129) now gives the following set of equations:

$$m'_L = (1-\frac{1}{2}\sin^2\theta)\left(m_L(1-\frac{1}{2}\sin^2\theta) - m_D^T\sin\theta\right) - \sin\theta\left(m_D(1-\frac{1}{2}\sin^2\theta) - m_R\sin\theta\right), \tag{2.132}$$

$$0 = (1-\frac{1}{2}\sin^2\theta)\left(m_D^T(1-\frac{1}{2}\sin^2\theta) + m_L\sin\theta\right) - \sin\theta\left(m_R(1-\frac{1}{2}\sin^2\theta) - m_D\sin\theta\right), \tag{2.133}$$

$$0 = (1-\frac{1}{2}\sin^2\theta)\left(m_D(1-\frac{1}{2}\sin^2\theta) - m_R\sin\theta\right) + \sin\theta\left(m_L(1-\frac{1}{2}\sin^2\theta) - m_D^T\sin\theta\right), \tag{2.134}$$

$$m'_R = (1-\frac{1}{2}\sin^2\theta)\left(m_R(1-\frac{1}{2}\sin^2\theta) + m_D\sin\theta\right) + \sin\theta\left(m_D^T(1-\frac{1}{2}\sin^2\theta) + m_L\sin\theta\right), \tag{2.135}$$

which, assuming $m_L \ll m_R$ and $m_L \ll m_D$, gives us[57] $m_D = m_R\sin\theta$ and subsequently

$$m'_L \approx m_L - m_D^T m_R^{-1} m_D, \tag{2.136}$$

$$m'_R \approx m_R\,. \tag{2.137}$$

Note that the second term comes with an inverse power of m_R. This tells us that the heavier N is, the lighter ν_L will be[58].

A similar analysis can be performed for the Type-iii seesaw mechanism [177,178], which is illustrated in Fig. 2.3 (right), and for which the Lagrangian is given by

$$\mathcal{L}_{\text{Type-iii}} = -y_{ij}^{\nu\Sigma} L_i^a \phi^b \Sigma_j^{ab} - \frac{1}{2} M_{ij} \Sigma_i^{ab} \Sigma_j^{ab} + \text{h.c.}\,. \tag{2.138}$$

The main difference between the Type-i and Type-iii seesaw mechanisms is that the latter is mediated by an $SU(2)_L$-triplet fermion Σ rather than a right-handed neutrino N as in the former case. Below EWSB the tree-level neutrino mass Lagrangian is identical between these two seesaw types, if the neutral component of Σ is substituted for N. The remaining seesaw mechanism, Type-ii [179–181], is illustrated in Fig. 2.3 (centre) and its Lagrangian is given by

$$\mathcal{L}_{\text{Type-ii}} = -y_{ij}^{\Delta\nu} L_i^a L_j^b \Delta^{ab} - \mu\tilde{\phi}^a\tilde{\phi}^b\Delta^{ab} + \text{h.c.}\,. \tag{2.139}$$

For Type-ii seesaw there is no additional fermion for the neutrino to mix with. Instead, neutrinos get their mass from the m_L-entry in Eq. (2.129).

[57] Note that since we assumed there to not be any mixing between the generations, m_D and m_D^T are the same matrix (m_D is diagonal).

[58] This effect is what gives the name to the seesaw mechanism. When one side of a seesaw goes up the other goes down, and when one neutrino goes massive the other goes light.

Field	Representation
N	$F(1,1,0)(0)$
Δ	$S(1,3,1)(0)$
Σ	$F(1,3,0)(0)$

Table 2.4.: The three seesaw fields N, Δ, and Σ, along with their representation under the SM gauge group. Here $X(a,b,c)(3B)$, where B is the baryon number, should be read as $X \in \{S,F,V\}$ denoting whether the field is a scalar (S), fermion (F), or vector (V), and (a,b,c) denoting the representation of the field under the SM gauge group $G_{\rm SM} = SU(3)_c \times SU(2)_L \times U(1)_Y$, such that the field is an a-plet under $SU(3)_c$, b-plet under $SU(2)_L$, and carries a hypercharge c.

There is no other possibility to generate a tree-level neutrino Majorana mass with only two mass insertions and one mediator. Therefore, the three seesaw types constitute the simplest realisations of neutrino Majorana masses, relying only on the addition of a single BSM field each. These fields are listed in Tab. 2.4 along with their representation under the SM gauge group.

Extended scalar sector

The scalar potential[59] $V_{\rm SM}(\phi)$ of the broken SM consists only of the physical Higgs field, and contains two self-interaction terms and a mass term

$$V_{\rm SM}(\phi) = \frac{1}{2} m_h^2 h^2 + \lambda_3 h^3 + \lambda_4 h^4 \,. \tag{2.140}$$

The Higgs vev v and the mass m_h of the physical Higgs field are related to the couplings λ_3 and λ_4 in the SM according to the relations

$$\lambda_3 = \frac{m_h^2}{2v}, \qquad \lambda_4 = \frac{m_h^2}{8v^2} \,. \tag{2.141}$$

The value for the mass $m_h = 125.25 \pm 0.17$ GeV at 95% CL is obtained experimentally at the LHC [14], and the value of the vev is related to the Fermi constant G_F via $v = (2G_F)^{-1/2} = 173.35$ GeV, where G_F in turn is measured from the lifetime of the muon [182]. Therefore, values for the Higgs self-couplings are obtained indirectly as $\lambda_3 \approx 45$ GeV and $\lambda_4 \approx 0065$. Direct measurements of these couplings could be possible [183], notably so in future colliders such as FCC-hh [184], FCC-ee [185], ILC [186], CLIC [187], and CEPC [188]. Such measurements could shed light on possible BSM scenarios, since these couplings can have different values with the introduction of new particles, or with modifications of the Higgs boson as e.g. in composite Higgs models [189–191].

Modifications of the potential $V_{\rm SM}(\phi) \to V_{\rm BSM}(\phi, \dots)$ can include a number of different scalar fields depending on the model. They may be charged under any SM subgroup (colour,

[59] Technically $V_{\rm SM}(\phi)$ is a potential density in three dimensions and not a potential.

Field	Representation
$\mathcal{S}$	$S(1,1,0)(0)$
ξ	$S(1,1,0)(6)$
Ξ	$S(1,3,0)(0)$
h'	$S(1,1,1)(0)$
φ	$S(1,2,1/2)(0)$
Θ_1	$S(1,4,1/2)(0)$
Θ_3	$S(1,4,3/2)(0)$
S_1	$S(\bar{3},1,1/3)(-1)$
$\tilde{R}_2$	$S(3,2,1/6)(1)$
S_3	$S(\bar{3},3,1/3)(-1)$
X_{dd}	$S(3,1,2/3)(-2/3)$
X_{uu}	$S(3,1,-4/3)(-2/3)$
X_{ud}	$S(3,1,-1/3)(-2/3)$

Table 2.5.: A list of non-seesaw BSM scalar fields that are used in subsequent chapters, along with their representation under the SM gauge group. Here $X(a,b,c)(3B)$, where B is the baryon number, should be read as $X \in \{S,F,V\}$ denoting whether the field is a scalar (S), fermion (F), or vector (V), and (a,b,c) denoting the representation of the field under the SM gauge group $G_{\text{SM}} = SU(3)_c \times SU(2)_L \times U(1)_Y$, such that the field is an a-plet under $SU(3)_c$, b-plet under $SU(2)_L$, and carries a hypercharge c.

electroweak, or hypercharge) and could carry a non-zero lepton/baryon number. Some of these fields (the ones that are also used in subsequent chapters) are listed in Tab. 2.5, but note that this is by no means a complete list of possible BSM scalar fields. Scalar extensions of the SM are relatively harmless as compared to fermionic or vector extensions, since no anomaly cancellation is needed (as with chiral fermions), and no higher gauge symmetry is needed in order to motivate their existence (as some argue is the case for massive vector fields).

Vector-like fermions

As seen in Sec. 2.1.5, chiral fermions require anomaly cancellation in order for the theory to be consistent. If the anomalies cancel, there has to be a delicate balance between the charge assignments of the different chiral fermions under each gauge group considered in the theory. In the SM, which contains chiral fermions, the different charges of $SU(3)_c$, $SU(2)_L$, and $U(1)_Y$ distributed among the fermions lead to cancellations in each scenario separately, leading to a cancellation of anomalies. Suppose now that we want to extend the SM by a chiral fermion that is charged under any of the SM gauge groups. We would then disrupt the balance in at least one anomalous diagram, and to make up for it we could have to add more chiral fermions with particular charge assignments until the theory becomes consistent again, which is not an easy task given how many different anomalous diagrams exist. It would be far easier

Field	Representation
Σ_1	$F(1,3,-1)(0)$
Δ_1	$F(1,2,-1/2)(0)$
Δ_3	$F(1,2,-3/2)(0)$
F_4	$F(1,4,1/2)(0)$
U	$F(3,1,2/3)(1)$
Q_5	$F(3,2,-5/6)(1)$
Q_7	$F(3,2,7/6)(1)$
T_1	$F(3,3,-1/3)(1)$
T_2	$F(3,3,2/3)(1)$

Table 2.6.: A list of non-seesaw BSM fermion fields that are used in subsequent chapters, along with their representation under the SM gauge group. Here $X(a,b,c)(3B)$, where B is the baryon number, should be read as $X \in \{S,F,V\}$ denoting whether the field is a scalar (S), fermion (F), or vector (V), and (a,b,c) denoting the representation of the field under the SM gauge group $G_{\text{SM}} = SU(3)_c \times SU(2)_L \times U(1)_Y$, such that the field is an a-plet under $SU(3)_c$, b-plet under $SU(2)_L$, and carries a hypercharge c.

to accommodate additional fermions if they were *vector-like*[60], since they would then simply cancel their own contributions to the chiral anomalies[61]. Many BSM models that include new fermions therefore consider them to be vector-like. Some such fermions that are commonly considered are listed in Tab. 2.6.

New heavy vector bosons

As seen in Sec. 2.2.2 and Sec. 2.3.1, there are reasons to believe that the SM gauge group is not the final symmetry of our Universe. Instead, it is possible that another symmetry is found at higher energy scales, which subsequently breaks into the SM. If this is the case, there would be associated gauge bosons and massless Goldstone bosons that appear as a consequence of the symmetry breaking. If the process of going from the higher symmetry to the SM is similar to the electroweak phase transition, the new gauge bosons would eat the Goldstone modes and become very massive[62], which would explain their non-appearance in experimental searches. Consider e.g. the Georgi-Glashow model [152], in which the symmetry group $SU(5)$ is used to unify the forces of the SM. Following Ref. [20] we see that one generation of SM

[60] Vector-like here means that the left-and right-handed components of the fermion are equally charged under all gauge groups. Note that in this way, if the field that we add is a non-singlet of $SU(2)_L$, this must also be true for the right-handed component, even though the L supposedly stands for *left*.

[61] Note however that if we have a chiral fermion that is uncharged under $U(1)_Y$ it does not contribute to any anomalous diagram (c.f. Sec. 2.1.5). As a consequence of this, one can simply add fermions such as Σ and N from Tab. 2.4 and let them be chiral without disturbing the consistency of the model.

[62] The mass of the new gauge bosons is usually considered to be around the scale at which the symmetry breaks, which is true unless the mixing angle between them takes some peculiar value.

Field	Representation
W_1'	$V(1,1,1)(0)$
V_3	$V(1,2,3/2)(0)$
U_1	$V(3,1,2/3)(1)$
$\tilde{V}_2$	$V(\overline{3},2,-1/6)(-1)$
U_3	$V(3,3,2/3)(1)$
Z_1'	$V(1,1,0)(0)$

Table 2.7.: A list of BSM vector fields that are used in subsequent chapters, along with their representation under the SM gauge group. Here $X(a,b,c)(3B)$, where B is the baryon number, should be read as $X \in \{S,F,V\}$ denoting whether the field is a scalar (S), fermion (F), or vector (V), and (a,b,c) denoting the representation of the field under the SM gauge group $G_{\text{SM}} = SU(3)_c \times SU(2)_L \times U(1)_Y$, such that the field is an a-plet under $SU(3)_c$, b-plet under $SU(2)_L$, and carries a hypercharge c.

fermions appear[63] from the 10 and $\overline{5}$ of $SU(5)$ according to[64]

$$\begin{aligned} 10 &\to \left(\overline{3},1,-\tfrac{2}{3}\right) \oplus \left(3,2,\tfrac{1}{6}\right) \oplus (1,1,1) \ , \\ \overline{5} &\to \left(\overline{3},1,\tfrac{1}{3}\right) \oplus \left(1,2,-\tfrac{1}{2}\right) \ . \end{aligned} \tag{2.142}$$

The gauge bosons are appropriately found in the adjoint 24 which breaks as

$$24 \to (8,1,0) \oplus (1,3,0) \oplus (1,1,0) \oplus \left(3,2,-\tfrac{5}{6}\right) \oplus \left(\overline{3},2,\tfrac{5}{6}\right) \ . \tag{2.143}$$

In addition to the SM gauge bosons, we here find two new fields under the $\left(3,2,-\frac{5}{6}\right)$ and $\left(\overline{3},2,\frac{5}{6}\right)$ representations, which both acquire masses in the $SU(5)$ breaking. These representations are associated with the vector leptoquark[65] V_2, which has a number of phenomenological detection prospects. Perhaps most notably, it can lead to rapid proton decay in the channel $p^+ \to \pi^0 e^+$, which has so far avoided detection up to a half time of $\tau_{p^+ \to \pi^0 e^+} > 2.4 \times 10^{34}$ years [144]. In GUT models, the mass of new heavy gauge bosons is typically assumed to lie around the unification scale M_{GUT}, which is usually taken to be $M_{\text{GUT}} \gtrsim 10^{14}$ GeV. Therefore, if the V_2 leptoquark is found at the LHC close to current limits ($\sim \mathcal{O}(\text{few})$ TeV [193]), it is unlikely to come from $SU(5)$, but it could come from a similar symmetry breaking involving another gauge group. In this way, heavy vector bosons are theoretically motivated since their origin is similar to that of the SM gauge bosons. However, a Lagrangian can very well contain both kinetic and interaction terms involving a heavy vector field without requiring that this field is part of the covariant derivative or has an

[63] Note that right-handed neutrinos can be found in the singlet $1 \to (1,1,0)$.

[64] Comparing to other sources, e.g. [192], there is a mismatch in the $U(1)$ charge of the SM representation in Eq. (2.142). This is due to a different normalisation convention of the $SU(5)$ coupling constant g_5, which is here matched to the $U(1)_Y$ coupling constant as $g_5 = \sqrt{\frac{5}{3}} g_1$ at the breaking scale.

[65] Though we here refer to them as leptoquarks in order to tie them into a broader picture of BSM phenomenology, these $SU(5)$ gauge bosons are often referred to as the X and Y bosons.

associated gauge symmetry. In this agnostic approach, the origin of the vector field from a theoretical perspective is of secondary interest, while its phenomenology is primary. In subsequent chapters this philosophy is employed, and the vector fields considered are those shown in Tab. 2.7.

This concludes our (partial) list of BSM fields that could serve as extensions to the SM. In Sec. 2.3.3 we describe a framework in which the effects of these fields can be studied in an effective and model-independent way.

2.3.3. Effective field theory

A separation of scales in physical systems often leads to an isolation of macroscopic from microscopic phenomena, in the sense that the physics at short distances does not significantly affect relatively large structures. This holds true also in particle physics [194, 195]. For example, the gravitational interaction between two protons is neglected at colliders such as the LHC, where the beam energy per proton is much less than that needed to resolve structure at scales short enough for gravity to be important[66]. Less extremely, the gauge bosons $W^\pm$ of the SM are much more massive than any other energy scale involved in β-decays of nuclei, such that predictions for the rate of this process can be made without needing to know the dynamics of $W^\pm$. In the first example, the small-scale interaction (gravitation) is weak enough to not affect the collision process at all, and it can be safely ignored. In the second example however, the $W^\pm$ boson is what actually mediates the β-decay, which would not be possible without it. We can therefore not ignore the $W^\pm$ boson, but what we can do is ignore its dynamics, and instead treat the interaction as being point-like. In fact, this is how β-decay was first successfully described in 1933 [196], long before the discovery of the $W^\pm$ boson in 1983 [197]. Rather than using the kinetic terms from the SM Lagrangian,

$$\mathcal{L}_{\text{SM}} \supset -\frac{1}{2} g \bar{Q} \gamma_\mu \left(W_1^\mu \sigma_1 + W_2^\mu \sigma_2 \right) Q - \frac{1}{2} g \bar{L} \gamma_\mu \left(W_1^\mu \sigma_1 + W_2^\mu \sigma_2 \right) L \,, \tag{2.144}$$

we write an effective interaction

$$\mathcal{L}_{\text{eff}} = -\frac{4 G_F}{\sqrt{2}} \left(\bar{e} \gamma_\mu P_L \nu_e \right) \left(\bar{u} \gamma^\mu P_L d \right) \,, \tag{2.145}$$

where $G_F = \sqrt{2} g^2 / 8 m_W^2$ is the Fermi constant. In fact, Eq. (2.145), as well as the fully leptonic analogue, is often referred to as the Fermi interaction. In going from Eq. (2.144) to Eq. (2.145), we expand the $W^\pm$-mediator in terms of its momentum p divided by its mass m_W, and keep

[66] Note that in the wave-particle duality of quantum excitations, a high energy corresponds to short wavelengths $\lambda \ll \ell_0$, which in turn can resolve structures at smaller scales ℓ_0. Longer wavelength particles $\lambda \gg \ell_0$ are blind to the details of structures at short distances. This is why in e.g. medical physics electron spectroscopy is used where X-rays cannot reveal enough detail, and neutron spectroscopy is used where even electrons fail. The increasing typical energy of the particle $E_\gamma < E_e < E_n$ associated with the mass hierarchy $m_\gamma < m_e < m_n$ leads to a shorter wavelength $\lambda \propto 1/m$.

only the zeroth order term,

$$\frac{-i\left(\eta_{\mu\nu}-\frac{p_\mu p_\nu}{m_W^2}\right)}{p^2-m_W^2}=\frac{i}{m_W^2}\frac{\eta_{\mu\nu}-\hat{p}_\mu\hat{p}_\nu\frac{p^2}{m_W^2}}{1-\frac{p^2}{m_W^2}}\approx\frac{i\eta_{\mu\nu}}{m_W^2}\,. \tag{2.146}$$

This was done under the assumption that the momentum is small, $p^2 \ll m_W^2$, which is indeed the case in β-decay[67]. This way of treating the $W^\pm$-mediated process as an effective point interaction does lead to accurate predictions, and it is our first example of an effective field theory (EFT). One drawback of this treatment is that the effective Lagrangian in Eq. (2.145) is not renormalisable, and therefore it does not lead to a consistent theory on its own. This can be seen by noting that the operator in Eq. (2.145) has mass dimension[68] 6 in order to match the dimension of the Lagrangian density of the LHS, since G_F has dimension -2 ($[G_F] = -2$). A full UV-complete[69] Lagrangian is needed in order to have a consistent theory, but an effective Lagrangian can still be used to connect models to experiment. Furthermore, the EFT formalism is only valid so long as the energy scales involved in a given process are below the mass of the particle of which the dynamics are neglected. This is the case in β-decay, where the observable energy scale involved in the process $|\vec{p}_e|$ is much less than the mass scale of the heavy physics m_W. If this were not the case the whole formalism would have been invalid, since we could not expand in powers of p^2/m_W^2 in Eq. (2.146). It is also not enough that the interaction strength is weak, such that e.g. G_F is small in Eq. (2.145). Since G_F depends on both the coupling g^2 and the mass m_W^2, it could be small as a consequence of small couplings rather than a large mass, but the consistency condition with regards to the expansion of the mediator depends only on the mass and momentum, not on the coupling.

Standard model effective field theory

There are many different EFTs used in different branches of particle physics. For example, in chiral perturbation theory (ChPT or χPT) the dynamics above Λ_{QCD} are neglected. This EFT assumes a chiral $SU(3)_L \times SU(3)_R$ symmetry among the u-, d-, and s-quarks, and is used in the physics of light hadrons. Another example is low-energy effective field theory (LEFT), in which the broken SM symmetry $SU(3)_c \times U(1)_{\text{em}}$ is used and the dynamics of the weak gauge bosons $W^\pm$ and Z are neglected[70]. In subsequent chapters, one EFT that is reoccurring is Standard Model effective field theory (SMEFT) [198–201]. In this EFT it is assumed that the SM gauge symmetry $G_{\text{SM}} = SU(3)_c \times SU(2)_L \times U(1)_Y$ is obeyed, and the fields for which the dynamics is neglected are those that are heavier that the EWSB scale.

[67] This can be seen by noting that the kinetic energy available in the decay is roughly equal to the mass difference between the neutron and proton $\sqrt{p^2} \sim |m_n - m_p| \sim \mathcal{O}(1\text{ MeV})$, while the $W^\pm$ mass $m_W \approx 80.4$ GeV is much greater.

[68] The term *mass dimension* is often simply abbreviated as *dimension* in the EFT literature. Note however that this has nothing to do with spacetime dimensions.

[69] The term *UV-complete* means that a theory is not effective, no new fields or interactions need to be introduced at ultraviolet (UV) energy scales.

[70] The Fermi interaction in Eq. (2.145) is therefore an example of LEFT.

This means that all SM particles are fully taken into consideration, while it is assumed that some heavy BSM fields could mediate interactions that would not be present in the SM alone, as long as each interaction is Lorentz invariant and obeys the gauge symmetry G_{SM}. All possible combinations of fields can then be clumped together in operators similar to the Fermi interaction operator in Eq. (2.145). These operators $\mathcal{O}_i$ are usually sorted by mass dimension, and since the SM already contains every possible 4-dimensional term that can be constructed out of the SM fields, the SMEFT operators all have mass dimensions $D \geq 5$. In fact, at dimension-5 there is only a single SMEFT operator $\mathcal{O}_1^{(5)}$ that can be constructed, the *Weinberg operator* given in Eq. (2.124). At higher dimensions there are significantly more operators, where as a rule of thumb their number increases with increasing dimension. The full SMEFT Lagrangian may then be written as a sum,

$$\mathcal{L}_{\text{SMEFT}} = \mathcal{L}_{\text{SM}} + \sum_{D=5}^{\infty} \sum_{i}^{N_D} \frac{C_i^{(D)}}{\Lambda_i^{D-4}} \mathcal{O}_i^{(D)} \,. \tag{2.147}$$

Here D is the dimension of the operators $\mathcal{O}_i$ for $i \in \{1, \ldots, N_D\}$, where N_D is the number of operators at dimension D, $C_i^{(D)}$ is a dimensionless coefficient called the *Wilson coefficient*[71], and Λ_i is the energy scale at which the BSM mediators lie. The dimensions of $\Lambda^{-(D-4)}$ and $\mathcal{O}_i^{(D)}$ perfectly balance, since we have $[\Lambda_i] = 1$, $[C_i^{(D)}] = 0$, and $[\mathcal{O}_i] = D$. The dimension of an operator reveals what combinations of fields and derivatives it could possibly contain, via the relations[72]

$$[\psi] = \tfrac{3}{2}, \qquad [\phi] = 1, \qquad [V^\mu] = 1, \qquad [D^\mu] = 1, \qquad [X^{\mu\nu}] = 2 \,. \tag{2.148}$$

Here ψ is a fermion, ϕ is a scalar, V^μ is a vector, D^μ is a covariant derivative, and $X^{\mu\nu}$ is a field strength. As a rule of thumb, the higher the dimension of an operator the less stringent any experimental constraints on the scale of NP Λ_i will be. This can be seen by noting that experimental constraints are generally put on observable quantities such as cross sections σ, where

$$\sigma \propto |\mathcal{M}|^2 \propto |\langle \text{out}| \mathcal{O}_i |\text{in}\rangle|^2 \propto \Lambda^{-(2D-8)} \,. \tag{2.149}$$

An experimental limit on the cross section $\sigma < X$ then translates into a limit $\Lambda < X^{2D-8}$. For larger D, this limit increases, resulting in less stringent limits on Λ. The sum over dimensions in Eq. (2.147) should therefore be truncated at a certain dimension depending on the accuracy sought. Using EFTs such as SMEFT therefore allows for a systematic treatment of BSM physics without being primarily concerned with models. It leads to a model-independent way of connecting experiment to theory, where different models lead to different operators, which in turn have distinct experimental signatures.

[71] Sometimes $C_i^{(D)}/\Lambda_i^{D-4}$ is simply written as C_i, in which case C_i is sometimes also called the Wilson coefficient, with mass dimension $[C_i] = 4 - D$.

[72] By using these relations we can now confirm that the operators in Eqs. (2.124) and (2.145) are dimension 5 and 6 respectively.

3. The baryon asymmetry of the Universe

All SM particles behaved as radiation right after the Big Bang, since they were ultra-relativistic, and the number density n_f of a given thermalised fermion f was close to that of photons γ. Today the story is very different, the ratio $\eta_B = n_B/n_\gamma$ of baryon to photon number densities is[1] [55]

$$\eta_B = (6.20 \pm 0.15) \times 10^{-10} \qquad 68\%\ \text{C.L}\,, \tag{3.1}$$

showing that light-particles are much more abundant than matter[2]. What happened was that the fermions and antifermions that both existed very numerously in the early Universe annihilated each other almost completely, such that only one part in a billion remained one trillionth of a second after the Big Bang. This small excess in fermions over antifermions that survives to this day is the reason that the baryon to photon ratio in Eq. (3.1) is not zero. It's entirely possible that this asymmetry between matter and antimatter was there from the very beginning, such that it was an initial condition for the big bang. However, due to the rapid expansion of space during inflation, this primordial asymmetry would have largely been erased by the time of reheating. If the baryon asymmetry was primordial, then $n_{\Delta B} = (N_B - N_{\bar{B}})/x^3$ decreases significantly during inflation when space x^3 expands. When the inflaton decays into a SM thermal bath the n_γ increases[3], such that the relative baryon number density η_B decreases. We see then in a multi-pronged way how an initial baryon asymmetry would be eradicated. However, this argument relies on the fact that we have inflation, which is not guaranteed. As discussed in Sec. 2.2, inflation is the leading theory to explain how the structure of our Universe could arise the way it is from an initial singularity, but it is not the only theory, and there are arguments as to why it might not be the true one [202, 203]. There is also another argument against the primordial asymmetry, coming from potential washout[4] sources in NP models. In Sec. 2.3.1 we saw that the SM needs to be extended in order to fit the experimental data. Many such extensions involve violation of lepton number or baryon number. If such models are realised, the additional BSM processes would be active also in the early Universe, where they would largely erase the asymmetry between baryons and antibaryons. Therefore, extensions of the SM that even modestly violate

[1] Here we write η_B as a measure of the normalised baryon number density while in the early Universe we are interested in the difference between baryons and antibaryons $\eta_{\Delta B} = \eta_B - \eta_{\bar{B}}$. At present time, the antibaryon number density $n_{\bar{B}} \approx 10^{-4} n_B$ [37], due to cosmic rays, falls within the error bars of the measured value of η_B, so we might treat them as the same.

[2] In terms of number density, photons are much more abundant than baryonic matter, but in terms of energy density baryons make up a much larger part of our Universe.

[3] The entropy density s and photon number density n_γ are related in the early Universe via $s \approx 1.8 g_* n_\gamma$, where g_* is the number of degrees of freedom of the Universe.

[4] *Washout* is explained in more detail in Sec. 3.3.

lepton- or baryon number would lead to any initial baryon asymmetry being removed. But this argument again hinges on the existence of NP of a certain kind, which is not guaranteed to be there either. Therefore a primordial baryon asymmetry remains a viable option[5], but we do not pursue this hypothesis further here. Instead, in subsequent chapters we assume that the baryon asymmetry was created dynamically. A dynamical mechanism that generates a baryon asymmetry is called *baryogenesis*. If baryogenesis occurs via lepton number violation coupled to sphalerons, the mechanism is instead called *leptogenesis*.

In this section we give a phenomenological overview of baryogenesis. In Sec. 3.1 we discuss different observational evidence for the presence of a baryon asymmetry in our Universe, and in Secs. 3.2 to 3.4 review the conditions needed for successful baryogenesis. Finally, in Secs. 3.5 and 3.6 we discuss different baryogenesis models from a phenomenological point of view.

3.1. Evidence of a matter-antimatter asymmetry

Here we review the three main reasons why it is believed that there is an asymmetry between the number densities of baryons and antibaryons, or equally between matter and antimatter[6], in our Universe.

The existence of structure

Just like Descartes, we can be certain that there is matter in the Universe because we are made of it. Matter is all around us, but for antimatter we have to look very hard. Between the stars lies the interstellar medium, and between the galaxies similarly lies the intergalactic

[5]One common argument that speaks for a primordial asymmetry comes from the possibility that our Universe is a black hole in some larger universe. When black holes form from the collapse of massive stars, the matter that goes into it is that which the star is made of, which in our Universe would be baryons, and not antibaryons. If black holes are other universes, they could then potentially be seeded with an initial baryon number. If our Universe was similarly created in the universe above, it too could have received such a seed.

[6]The technical difference between an *matter-antimatter asymmetry* and a *baryon asymmetry* lies in the leptons. Firstly, in Sec. 2.2.2 we saw that neutrinos decouple from the rest of matter at some point in the early history of the Universe. Efforts have been made to investigate how this background can be probed [204–208], but so far the Cosmic Neutrino Background (CNB) has never been detected. It is therefore not known whether the CNB consists of only neutrinos or antineutrinos, or if it is a mixture of them, and because of this the total lepton number density of the Universe is not known, though hints of a large lepton asymmetry can come from ^{4}He measurements of distant galaxies [209]. Some baryogenesis models conserve $B - L$, the difference between baryon number and lepton number, while other models violate either B or L separately. Measuring the CNB could help in scrutinising between these two classes of models. Secondly, the mass of leptons is much smaller than that of protons and neutrons. If we go by energy density, practically all matter content of the Universe lies in the baryons, and it is therefore appropriate to refer to matter simply as baryons. In the very early Universe, what is relevant is $B - L$, since this is what is conserved by the sphaleron. Because neutrinos decoupled from matter after the sphaleron became inactive, it could be expected that there is an asymmetry between neutrinos and antineutrinos in the CNB that together with the charged leptons perfectly cancel the baryon number, such that the total B and total L are the same in our Universe, but this is not guaranteed, partially because there could also be processes that are active after the sphalerons shut off that could disrupt such a balance.

medium, both made up of ordinary atoms. If there should be also some antimatter around, it would annihilate on contact with this medium, producing x-rays that have not been seen [210]. Potentially there could also be macroscopic antimatter objects such as antistars, but they have not been observed either [211]. Our visible Universe is full of matter, and without any antimatter around we can rest assured that there is an asymmetry between the two. This argument however does not lead to any quantifiable number density of baryons, it is merely illustrative of our need for a theory that can explain the origin of such an asymmetry.

CMB

The *Cosmic Microwave Background* (CMB) is a remnant from the time at which our Universe was filled completely with plasma. When the temperature dropped and electrons were bound to nuclei in an event called *recombination* (see Sec. 2.2.2), light no longer scattered like it used to when there were charged particles around. This light has then travelled all the way to us, creating a background beyond which light cannot reach us. Although extremely homogeneous, there are small temperature variations in the CMB that reveal how patches of over- and underdensities were distributed in the plasma back then, which reveals a lot about the matter content of the Universe at that time. Since protons are charged they repel each other, which inhibits structure formation. Protons also have mass, so they do attract each other slightly through gravity, but forming prominent structures requires particles that interact almost exclusively through gravitation. We have just such a candidate particle, namely dark matter. The more dark matter we have in the early Universe, the more structure we can naively expect. Baryons then fall into these structures until they repel each other too much via their electromagnetic interactions. The story then goes as follows: dark matter forms clumps due to its gravitational interaction, which attracts the baryons. When the baryons fall very deep into the gravitational well, their density becomes too large and they repel each other, flying out of the well again. When they are sufficiently far out they are no longer affected by the electromagnetic repelling and they can again fall into the well. This goes on and on. Both the amount of baryons and that of dark matter determines how this formation of over- and underdensities in the plasma proceeds. The density fluctuations lead to pressure fluctuations in the plasma and therefore temperature fluctuations in the CMB. Based on the amplitude of the CMB temperature fluctuations, it is therefore possible to infer the baryon density at the time of recombination [212].

BBN

Protons and neutrons fuse to form stable nuclei at sufficiently high temperatures. This happened in the early Universe in a process called *Big Bang Nucleosynthesis* (BBN). The final abundance of different elements is sensitive to the density of baryons, as can be seen below, following Ref. [53]. The number density n_i of a nuclear species i is given by

$$n_i = g_i e^{\mu_i/T} \left(\frac{m_i T}{2\pi}\right)^{3/2} e^{-m_i/T}, \tag{3.2}$$

where g_i is the number of degrees of freedom, T is the temperature, m_i is the mass, and

$$\mu_i = Z_i \mu_p + (A_i - Z_i)\, \mu_n \tag{3.3}$$

is the chemical potential, where p and n denote the proton and neutron, and where i consists of Z_i protons and A_i nucleons. Next we normalise the number density in Eq. (3.2) to that of nucleons,

$$X_i \equiv \frac{n_i}{n_{\text{Nucleons}}}\,, \tag{3.4}$$

where we have $n_{\text{Nucleons}} \approx n_B$ in the approximation $X_p \approx X_n \approx 1$. We now want to find the temperature where $X_i \approx 1/A_i$, i.e. where most nucleons are bound. To do this we define the binding energy

$$B_i = Z_i m_p + (A_i - Z_i)\, m_n - m_i \tag{3.5}$$

and write the normalised number density as

$$X_i = \frac{g_i}{2} X_p^{Z_i} X_n^{A_i - Z_i} A_i^{3/2} \left(\frac{1}{2} n_N (2\pi)^{3/2} (m_N T)^{-3/2}\right)^{A_i - 1} e^{B_i/T}\,. \tag{3.6}$$

Now using $n_B = \eta_B n_\gamma$, where the photon number density is given by

$$n_\gamma = 2\frac{\zeta(3)}{\pi^2} T^3\,, \tag{3.7}$$

we find[7]

$$T_i^{\text{NUC}} \sim \frac{B_i/(A_i - 1)}{\ln\left(\eta_B^{-1}\right) + 1.5 \ln\left(m_N / T_i^{\text{NUC}}\right)}\,. \tag{3.8}$$

Here T_i^{NUC} is the nucleation temperature of i, which corresponds to the temperature at which the nuclei forms. We see that this temperature depends on the baryon number density η_B, and as a consequence the final abundance of a given element also depends on η_B. The role of the binding energy B_i in Eq. (3.8) is highlighted if we acknowledge that we have so far assumed that nuclei always follow their equilibrium number densities, which is not necessarily true.

Deuterium ^{2}H has a very low binding energy compared to other low-mass nuclei, and therefore it forms quite late in the thermal history. Larger nuclei such as ^{3}He or ^{4}He cannot form without deuterium, and due to the late onset of deuterium production, their abundances are lower than what would be expected from equilibrium calculations alone, being instead largely determined by the rate of Deuterium production. This effect is often referred to as the *deuterium bottleneck*.

By measuring the densities of different elements in primordial gas clouds, where very little stellar nucleosynthesis has taken place, it is possible to match the observed number

[7] Note that here we used the approximation

$$\frac{g}{2} A^{5/2} \left(\frac{\zeta(3)}{\pi^2} (2\pi)^{3/2}\right)^{A-1} \sim 1$$

which indicates that our result in Eq. (3.8) is not to be taken as an exact relation.

densities of different nuclei with a certain value of η_B [213,214]. Such observations agree with CMB measurements of η_B [215]. There is however an anomaly in the BBN prediction for the abundance of ^{7}Li, which is found to be a factor $\mathcal{O}(\text{few})$ below the SM prediction, leading to the so-called *Lithium problem* [131].

The combination of CMB and BBN leads to a well established value for $\eta_B = (6.20 \pm 0.15) \times 10^{-10}$ at 68% C.L [55]. Having a high certainty regarding the value of this non-trivial parameter leads to only one problem remaining: how it came to be.

3.2. Sakharov conditions

Dynamical baryon asymmetry generation can only occur via mechanisms that fulfil the three Sakharov conditions [216]. It is not enough that the three conditions are fulfilled in different parts of the model, they have to be connected to the same mechanism: being once out of equilibrium and then violating CP conservation in a totally disconnected sector does not yield any baryon asymmetry. Below, we outline the three Sakharov conditions and present classes of models in which they are typically present.

3.2.1. Baryon number violation

The first Sakharov condition is violation of baryon number B. To generate an asymmetry between baryons and antibaryons, it is paramount that baryon number is not a fundamental symmetry, and that the conservation of B is violated. This is perhaps the most obvious of the Sakharov conditions, since a totally B-conserving model cannot change the initial B charge of the Universe, which we are assuming to be zero.

In the SM, sphalerons are expected to be highly active above the EWSB scale. Since sphalerons violate B conservation we are already given this condition for free, but to make use of it we need a model in which the out-of-equilibrium condition as well as C and CP violation are directly connected to them. What sphalerons do not violate is $B - L$, where L is the lepton number, rather they violate the sum $B + L$. Therefore, if a new source of B violation is added to the SM which also violates $B - L$, the sphaleron can redistribute the $B - L$ charge also to the lepton sector. The reverse mechanism also works: L violation can lead to an asymmetry in B. This latter effect is crucial in leptogenesis models (see Sec. 3.5), where the three Sakharov conditions are all fulfilled in the lepton sector.

3.2.2. C and CP violation

The second Sakharov condition is violation of charge conjugation (C) symmetry and[8] charge-parity conjugation (CP) symmetry. Acting with the operator C on a particle takes it to its antiparticle, and therefore if C symmetry is conserved in a given process the cross section

[8]Technically it can be argued that these are two separate conditions: one being the violation of C and the other that of CP. However, they are so similar that they are usually considered together. In fact, many model-building theorists worry only about having sufficient CP violation, and assume that the C violation follows along, or that it comes from the C violation in the SM.

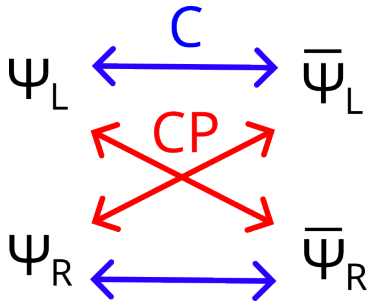

Figure 3.1.: Illustration of why both C and CP violation are needed in order to generate a baryon asymmetry in a particle Ψ. If there is no C violation, there will be equal numbers of particles and antiparticles. If there is no CP violation, there will be equal amounts of left-handed particles and right-handed antiparticles, and vice versa.

is equal for particles and antiparticles. A parity transformation P flips one spatial axis: it is what happens to you when you look in the mirror. A left-handed field will look like a right-handed field after P has been applied, and a CP transformation then takes a particle into its parity conjugated antiparticle. As illustrated in Fig. 3.1, both C and CP are needed in order to create an asymmetry between the total amount of particles $\sum_i \Psi_i = \Psi_L + \Psi_R$ and antiparticles $\sum_i \bar{\Psi}_i = \bar{\Psi}_L + \bar{\Psi}_R$. If C is conserved but CP is violated, we have the conditions $N_{\Psi_L} = N_{\bar{\Psi}_L}$ and $N_{\Psi_R} = N_{\bar{\Psi}_R}$, where N_i is the number of particles i. This leads of course to the sums also being conserved, $\sum_i N_{\Psi_i} = \sum_i N_{\bar{\Psi}_i}$. If CP is conserved but C is violated, we instead have the conditions $N_{\Psi_L} = N_{\bar{\Psi}_R}$ and $N_{\bar{\Psi}_L} = N_{\Psi_R}$, again leading to $\sum_i N_{\Psi_i} = \sum_i N_{\bar{\Psi}_i}$. Only if both C and CP are violated can we have $\sum_i N_{\Psi_i} \neq \sum_i N_{\bar{\Psi}_i}$. However, in the SM all fermions are chiral. For chiral fermions, $\Psi_{L/R}$ and $\bar{\Psi}_{L/R}$ are completely different fields, such that they may not take part in the same interactions, and there is no worry in creating equal amounts of $\Psi_{L/R}$ and $\bar{\Psi}_{L/R}$. Therefore, only CP violation is relevant for baryogenesis processes in which the asymmetry is generated in chiral fields such as the SM fermions. One can say that C is already explicitly violated in the SM.

One common source of CP violation is the interference between tree- and loop-level decay diagrams. Consider a decay process described by the sum of the tree- and one-loop level complex matrix elements $\mathcal{M}_0$ and $\mathcal{M}_1$ such that

$$\mathcal{M} = \mathcal{M}_0 e^{i\phi_0} + \mathcal{M}_1 e^{i\phi_1}\,, \tag{3.9}$$

where the CP conjugate matrix element is given by

$$\overline{\mathcal{M}} = \mathcal{M}_0 e^{-i\phi_0} + \mathcal{M}_1 e^{-i\phi_1}\,. \tag{3.10}$$

Squaring Eq. (3.9) we have

$$\begin{aligned}|\mathcal{M}|^2 &= \left(\mathcal{M}_0 e^{i(\phi_0)} + \mathcal{M}_1 e^{i(\phi_1)}\right)\left(\mathcal{M}_0 e^{i(\phi_0)} + \mathcal{M}_1 e^{i(\phi_1)}\right)^* \\ &= |\mathcal{M}_0|^2 + |\mathcal{M}_1|^2 + \mathcal{M}_0\mathcal{M}_1^* e^{i(\phi_0-\phi_1)} + \mathcal{M}_0^*\mathcal{M}_1 e^{i(\phi_1-\phi_0)} \\ &= |\mathcal{M}_0|^2 + |\mathcal{M}_1|^2 + 2\,\mathrm{Re}\left(\mathcal{M}_0\mathcal{M}_1^* e^{i(\phi_0-\phi_1)}\right),\end{aligned} \tag{3.11}$$

and similarly the CP conjugate matrix element in Eq. (3.10) gives

$$|\overline{\mathcal{M}}|^2 = |\mathcal{M}_0|^2 + |\mathcal{M}_1|^2 + 2\,\mathrm{Re}\left(\mathcal{M}_0\mathcal{M}_1^* e^{i(\phi_1-\phi_0)}\right), \tag{3.12}$$

such that

$$|\mathcal{M}|^2 - |\overline{\mathcal{M}}|^2 = 4\,\mathrm{Im}\left(\mathcal{M}_0\mathcal{M}_1^*\right)\sin\left(\phi_0-\phi_1\right). \tag{3.13}$$

we see that the difference between the squared decay matrix element and its CP conjugate is proportional to the imaginary part of the product of the tree-level matrix element $\mathcal{M}_0$ and the loop-level matrix element $\mathcal{M}_1$. This source of CP violation is common in many different types of baryogenesis models.

Another source of CP violation that is commonly used in baryogenesis mechanisms comes from the quark sector of the SM. In Sec. 2.1.3 we saw that the mass and flavour bases of the quarks can be transformed via the CKM matrix V, which is given by

$$V = \begin{pmatrix} V_{ud} & V_{us} & V_{ub} \\ V_{cd} & V_{cs} & V_{cb} \\ V_{td} & V_{ts} & V_{tb} \end{pmatrix}. \tag{3.14}$$

Some constraints on the CKM matrix are weak universality

$$\sum_k |V_{ik}|^2 = \sum_k |V_{ki}^2| = 1 \tag{3.15}$$

for any i, and universality

$$\sum_k V_{ik} V_{jk}^* = 0 \tag{3.16}$$

for any $i \neq j$. These constraints let us write the CKM matrix as a product of three rotation matrices, such that we can parametrise it as

$$V = \begin{pmatrix} c_{12}c_{13} & s_{12}c_{13} & s_{13}e^{-i\delta} \\ -s_{12}c_{23} - c_{12}s_{23}s_{13}e^{i\delta} & c_{12}c_{23} - s_{12}s_{23}s_{13}e^{i\delta} & s_{23}c_{13} \\ s_{12}s_{23} - c_{12}c_{23}s_{13}e^{i\delta} & -c_{12}s_{23} - s_{12}c_{23}s_{13}e^{i\delta} & c_{23}c_{13} \end{pmatrix}. \tag{3.17}$$

Here δ is a CP-violating phase, and we have defined $s_{12} \equiv \sin\theta_{12}$, $c_{23} \equiv \cos\theta_{23}$, and so on, where θ_{12} and θ_{23} are mixing angles. Now writing the CKM matrix as $V = V_{dL}V_{uL}^\dagger$, we can diagonalise the quark mass matrices as

$$V_{uL}M_u V_{uL}^\dagger = \begin{pmatrix} m_u & 0 & 0 \\ 0 & m_c & 0 \\ 0 & 0 & m_t \end{pmatrix}, \qquad V_{dL}M_d V_{dL}^\dagger = \begin{pmatrix} m_d & 0 & 0 \\ 0 & m_s & 0 \\ 0 & 0 & m_b \end{pmatrix}. \tag{3.18}$$

If we now take the commutator of the undiagonalised mass matrices

$$[M_u, M_d] = iC\,, \tag{3.19}$$

and subsequently take the determinant of C, we get

$$\begin{aligned}\det C = &-2(m_t - m_c)(m_t - m_u)(m_c - m_u)(m_b - m_s)(m_b - m_d)(m_s - m_d) \\ &\times c_{12}c_{13}^2 c_{23}s_{12}s_{13}s_{23}\sin\delta\,.\end{aligned} \tag{3.20}$$

What we have ended up with in Eq. (3.20) is the *Jarlskog determinant*. It is a measure of how much CP violation there is in the quark sector of the SM[9]. If $\det C$ vanishes there is no CP violation, while if $\det C$ is non-zero there definitely is [217]. Often the masses are omitted when considering the CP violation of the quarks, and one instead considers the *Jarlskog invariant* J, which is given by[10]

$$J \equiv c_{12}c_{13}^2 c_{23}s_{12}s_{13}s_{23}\sin\delta = \mathrm{Im}(V_{ud}V_{cs}V_{us}^*V_{cd}^*)\,. \tag{3.21}$$

For only two generations of quarks, there would be no CP violation since the corresponding determinant would vanish. The CP violating kaons as mentioned in Sec. 2.1.4 could then be considered a hint for a third generation of quarks, even though they only consist of the first and second generation.

3.2.3. Out-of-equilibrium dynamics

The third Sakharov condition is that the baryogenesis mechanism has to occur out of thermal equilibrium. Since all particle reactions can happen in reverse, there is a process that creates an antibaryon overabundance for each process that can create a baryon overabundance. If all particles involved in a reaction are in thermal equilibrium, the process and its reverse occur at equal rates, thereby not creating any asymmetry. There is a distinction between *thermal*[11] and *chemical* equilibrium. A particle i that is in thermal but not chemical equilibrium has a temperature-dependent number density n_i^{eq} given by

$$n_i = \int_0^\infty \frac{dp_i^3}{(2\pi)^3}\frac{g_i}{e^{(E_i-\mu_i)/T}\pm 1}\,, \tag{3.22}$$

where p_i is the momentum, g_i the number of degrees of freedom, E_i the energy, and μ_i the chemical potential of i, and T is the temperature. If $\mu_i = 0$, the particle is also in chemical equilibrium. The chemical potential μ_i can only be defined for particles which have a number density that follows Eq. (3.22), i.e. particles that are in thermal equilibrium. In order to generate a baryon asymmetry, a departure from thermal equilibrium is needed. Being out

[9] One can similarly construct a Jarlskog invariant for the lepton sector.

[10] Note that due to the unitarity of the CKM matrix, the specific combination of CKM matrix elements that appears on the RHS of Eq. (3.21) is not unique. One could similarly have written $J = \mathrm{Im}(V_{ij}V_{k\ell}V_{kj}^*V_{i\ell}^*)$ for any i, j, k, ℓ, where no Einstein summation is implied.

[11] Also known as *kinetic* equilibrium.

of chemical equilibrium simply means having a difference between the number density of a particle i and its antiparticle $\bar{i}$, as can be seen from the relation

$$\mu_i = -\mu_{\bar{i}}\,. \tag{3.23}$$

Generating such an asymmetry in particles that have baryon number is precisely the point of baryogenesis. For a baryon asymmetry to arise from an out-of-equilibrium state would then be equivalent to it being primordial, unless some dynamical mechanism generated the chemical non-equilibrium, i.e. baryogenesis.

One can also see this by noting that the baryon number B of a particle is opposite to that of its antiparticle, and is also spacetime translation invariant. This means that B is odd under charge conjugation C and positive under parity transformation P and time reversal T. Along with the fact that the Hamiltonian H of any theory must be invariant under CPT transformations, we find

$$\begin{aligned}\langle B\rangle &= \mathrm{Tr}\left(e^{-H/T}B\right) = \mathrm{Tr}\left((CPT)(CPT)^{-1}e^{-H/T}B\right)\\ &= \mathrm{Tr}\left(e^{-H/T}(CPT)^{-1}B(CPT)\right) = -\,\mathrm{Tr}\left(e^{-H/T}B\right)\,,\end{aligned} \tag{3.24}$$

where he have used $[H, CPT] = 0$ and $\mathrm{Tr}\,(AB) = \mathrm{Tr}\,(BA)$, and where Eq. (3.24) is only applicable in a thermal distribution of B. Since $\langle B\rangle = \mathrm{Tr}\left(e^{-H/T}B\right) = -\,\mathrm{Tr}\left(e^{-H/T}B\right)$, the only solution is $\langle B\rangle = 0$, and we see that the average of the baryon number charge is zero for states in thermal equilibrium.

3.2.4. Toy model example

Here, following Ref. [32], we give an illustrative example of how the three Sakharov conditions can all be simultaneously satisfied in one mechanism. Consider the interaction Lagrangian

$$\mathcal{L}_{\text{int}} = g_1 X f_2^\dagger f_1 + g_2 X f_4^\dagger f_3 + g_3 Y f_1^\dagger f_3 + g_4 Y f_2^\dagger f_4 + \text{h.c.}\,, \tag{3.25}$$

where the scalar fields X and Y are much more massive than the fermions f_i for $i \in \{1,2,3,4\}$. The field X can then decay into fermions $\bar{f}_1$ and f_2 via the the tree- and loop-level diagrams in Fig 3.2. Including both tree- and loop-level contributions, the decay widths of X and $\bar{X}$ can be written as

$$\begin{aligned}\Gamma\left(X \to \bar{f}_1 + f_2\right) &= g_1 g_2^* g_3 g_4^* I_X + \text{c.c.}\,,\\ \Gamma\left(\bar{X} \to f_1 + \bar{f}_2\right) &= g_1^* g_2 g_3^* g_4 I_X + \text{c.c.}\,,\end{aligned} \tag{3.26}$$

where I_X is a complex-valued integral over phase space and *c.c.* stands for *complex conjugate*. A non-vanishing difference between the X and $\bar{X}$ decay widths, given by

$$\Delta\Gamma\left(X \to \bar{f}_1 + f_2\right) = \Gamma\left(X \to \bar{f}_1 + f_2\right) - \Gamma\left(\bar{X} \to f_1 + \bar{f}_2\right) = 4\,\mathrm{Im}\,(I_X)\,\mathrm{Im}(g_1^* g_2 g_3^* g_4)\,, \tag{3.27}$$

is a consequence of CP violation in the theory. The field X can also decay into $\bar{f}_3$, and f_4, for which we find the decay width difference to be

$$\Delta\Gamma\left(X \to \bar{f}_3 + f_4\right) = \Gamma\left(X \to \bar{f}_3 + f_4\right) - \Gamma\left(\bar{X} \to f_3 + \bar{f}_4\right) = -4\,\mathrm{Im}\,(I_X)\,\mathrm{Im}(g_1^* g_2 g_3^* g_4)\,, \tag{3.28}$$

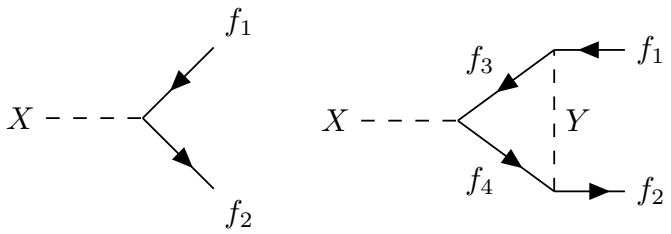

Figure 3.2.: Tree-level (left) and loop-level (right) decay of the scalar field X into fermions $\bar{f}_1$ and f_2 in the toy model described by Eq. (3.25).

perfectly cancelling the one in Eq. (3.27) if we add them up[12]. The total asymmetry created in the decay of X is then given by

$$\epsilon_X = \sum_a \frac{\Delta B(a)\Delta\Gamma_X(a)}{\Gamma_{\text{tot}}}\,, \tag{3.29}$$

where $a \in \{X \to \bar{f}_1 + f_2, X \to \bar{f}_3 + f_4\}$ denotes a decay mode, and $\Delta B(a)$ is the difference in baryon number that is generated in the decay. If we assign to X a vanishing baryon number, while giving f_i a baryon number B_i, we then have

$$\epsilon_X = \frac{(B_1 - B_2)\Delta\Gamma\left(X \to \bar{f}_1 + f_2\right) + (B_3 - B_4)\Delta\Gamma\left(X \to \bar{f}_3 + f_4\right)}{\Gamma_{\text{tot}}}\,. \tag{3.30}$$

Therefore we see that we need CP violation as well as baryon number violation in order to generate an asymmetry, since without CP violation we have $\Delta\Gamma\left(X \to \bar{f}_1 + f_2\right) = \Delta\Gamma\left(X \to \bar{f}_3 + f_4\right) = 0$ and without baryon number violation we would have $B_1 = B_2$ and $B_3 = B_4$, leading to $\epsilon_X = 0$. Yet if decays $X \to \cdots$ happen at equal rates to inverse decays $\cdots \to X$, any asymmetry created according to Eq. (3.30) is destroyed. An out-of-equilibrium condition that ensures that decays happen more frequently than inverse decays can come from the expansion and subsequent cooling of the Universe. As the temperature drops below roughly the mass of X, the average energy of a pair of fermions is not sufficient to create a particle X, and the inverse decay is suppressed. Any X particles that are still around are then out of thermal equilibrium, and they decay without there being an equal rate of inverse decays. This effect is not visible in Eq. (3.30) alone.

3.3. Washout

With the three Sakharov conditions out of the way, we can move on to developing specific frameworks in which to explicitly evaluate the time-evolution of the baryon asymmetry. But before we do that, let us first discuss one more ingredient in baryogenesis models, namely the *washout*.

[12]This is necessary in order for the decay to conserve CPT, since otherwise the total width of X would not equal that of $\bar{X}$.

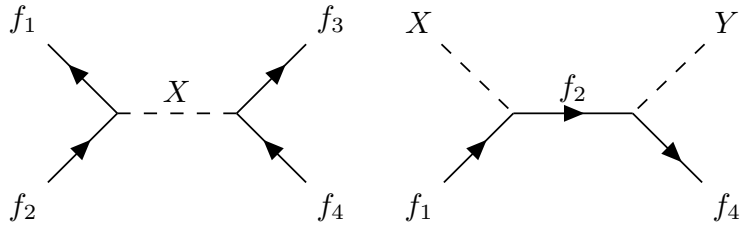

Figure 3.3.: Left: Washout process $\bar{f}_1 + f_2 \to X \to \bar{f}_3 + f_4$ in the toy model for baryogenesis described by the Lagrangian in Eq. (3.25). **Right:** washout process $X + f_1 \to f_2 \to Y + f_4$ in the same model.

A washout is a process that reduces the baryon asymmetry of the Universe. During and after baryogenesis, washout processes can be active, and their presence brings some particle number densities closer to their equilibrium. The inverse of an asymmetry generating process is a washout, and the reason baryogenesis has to occur out of equilibrium is to overcome this washout process. Washout processes are necessarily there in most models, because the conditions needed to realise them, B violation and out-of-equilibrium dynamics, are already satisfied automatically by the Sakharov conditions. No CP violation is necessary since we do not need to create a difference between particles and antiparticles, all that is needed is to go towards equilibrium for the baryon-number carrying particles. Any given baryogenesis model already contains B violation, and the baryon asymmetry itself is in a state of being out of equilibrium if it is non-zero. Therefore, washouts can, and often will, be present in most baryogenesis models.

Let us consider the toy model is Sec. 3.2.4. If we for simplicity assume that $B_3 = B_4 = 0$ and $B_1 \neq B_2$, the baryon asymmetry generation is driven by the decay $X \to \bar{f}_1 + f_2$. The reverse process $\bar{f}_1 + f_2 \to X$ is also allowed, provided that the fermion pair has enough centre-of-mass energy to produce an X particle. This *inverse decay* is a washout process as it reduces the baryon asymmetry that is generated by the decay. Both processes violate baryon number by the same amount but with different sign. If the decay and inverse decay occur at equal rates no asymmetry is generated, but if the Universe has an overabundance of X particles they decay more rapidly than the inverse decay can occur, thereby leading to a baryon asymmetry. In the same toy model, there are other washout processes as well. The scattering $\bar{f}_1 + f_2 \to X \to \bar{f}_3 + f_4$, as illustrated in Fig. 3.3 (left), violates baryon number and can be mediated by an off-shell X particle, such that it could still be active at temperatures that are too low for the inverse decay of X to occur. In Fig. 3.3 (right) we have another scattering washout $X + f_1 \to f_2 \to Y + f_4$, which similarly violates baryon number, but is only active at high temperatures where the number density of X and Y have not significantly dropped due to decays. There are many more scattering diagrams that are possible, so long as they violate baryon number and are allowed by the model they lead to washout. If the participating fields are charged under the SM gauge group also gauge fields can be involved as mediators or external particles. If the washout processes are weak enough a baryon asymmetry can still arise, but if they are strong they can completely remove any asymmetry that was around

before they got active[13].

In the next section we show how the different processes that are involved in a baryogenesis mechanism can interact dynamically.

3.4. Boltzmann equations

Here we show how the equations governing baryogenesis can be obtained using classical mechanics and the FLRW metric, following Refs. [53,218,219]. These classical equations do not take quantum effects into account, and are not applicable in all baryogenesis scenarios. Another approach is to use the *closed time-path formalism* [220–222] (see e.g. Ref. [223] for a review).

Solutions to the classical time evolution of particle distributions can be found using the Boltzmann equation, which is given by

$$L[f] = C[f], \tag{3.31}$$

where L is the Liouville operator, f is a time-dependent particle distribution, and C is a collision operator. In classical mechanics the Liouville operator is given by

$$L[f] = \frac{d}{dt}f + \vec{p}/m \cdot \vec{\nabla}_x f + \vec{F} \cdot \vec{\nabla}_p f\,, \tag{3.32}$$

where $\vec{p}$ is the momentum of a particle, $\vec{F}$ the force that the particle is subjugated to, m its mass, and $\vec{\nabla}_i = \left(\partial/\partial i_x, \partial/\partial i_y, \partial/\partial i_z\right)$ is the derivative vector, where $i \in \{x, p\}$ and where $\vec{x}$ is the position vector. The relativistic version of the Liouville operator is given by

$$L[f] = p^\alpha \frac{\partial}{\partial x^\alpha} f - \Gamma^\alpha_{\beta\gamma} \frac{\partial}{\partial p^\alpha} f\,, \tag{3.33}$$

where $\Gamma^\alpha_{\beta\gamma}$ is the Christoffel symbol, and in a universe that is described by the FLRW metric we then have

$$L[f] = E\frac{\partial}{\partial t}f - Hp^2\frac{\partial}{\partial E}f\,, \tag{3.34}$$

where E is the energy and H is the Hubble rate. Using Eq. (3.34) we can rewrite Eq. (3.31) in terms of the number density[14]

$$n = 4\pi g \int dp p^2 f\,, \tag{3.35}$$

where g is the number of degrees of freedom, such that

$$4\pi g \int dp p^2 \frac{L[f]}{E} = \frac{dn}{dt} - 4\pi H g \int dp \frac{p^4}{E}\frac{\partial f}{\partial E} = \frac{dn}{dt} + 4\pi H g \int dp \frac{\partial p^3}{\partial p} = \frac{dn}{dt} + 3Hn\,, \tag{3.36}$$

[13] This is one of the arguments against a primordial baryon asymmetry, as discussed in the beginning of this chapter.

[14] Note that we are here assuming isotropy, which is a valid assumption since we are using the FLRW metric.

where in the second step we used integration by parts as well as the assumption that $p^2 \gg m^2$ such that $E^2 \approx p^2$. Our Boltzmann equation now looks like[15]

$$\frac{dn}{dt} + 3Hn = \frac{g}{(2\pi)^3}\int \frac{d^3p}{E} C[f]\,. \tag{3.37}$$

To evaluate the collision term, we now denote the particle for which we want to evaluate the number density by ψ, such that in Eq. (3.37) we have $n \to n_\psi$, $g \to g_\psi$, on so on. For a general interaction $\psi + a + b + \cdots \leftrightarrow i + j + \cdots$ we can write the RHS of Eq. (3.37) as

$$\begin{aligned}\frac{g_\psi}{(2\pi)^3}\int \frac{d^3p_\psi}{E_\psi} C[f_\psi] = &-\int d\Pi_\psi d\Pi_a d\Pi_b \cdots d\Pi_i d\Pi_j \cdots \\ &\times (2\pi)^4 \delta^4\left(p_\psi + p_a + p_b \cdots - p_i - p_j \cdots\right) \\ &\times \Big(|\mathcal{M}|^2_{\psi+a+b+\cdots\to i+j+\cdots} f_\psi f_a f_b \cdots (1 \pm f_i)(1 \pm f_j) \cdots \\ &- |\mathcal{M}|^2_{i+j+\cdots\to\psi+a+b+\cdots} f_i f_j \cdots (1 \pm f_\psi)(1 \pm f_a)(1 \pm f_b) \cdots \Big)\,.\end{aligned} \tag{3.38}$$

Here p are four-momenta, $\mathcal{M}$ are matrix elements, f are the phase space distributions, where a $+$ $(-)$ sign should be used for bosons (fermions), and the integrands are given by

$$d\Pi = \frac{g}{(2\pi)^3}\frac{d^3p}{2E}\,. \tag{3.39}$$

Assuming that we can neglect the effects of Pauli blocking and Bose condensation we can write $1 \pm f \approx 1$. For each particle we now insert a factor $f^{\rm eq}/f^{\rm eq}$ and integrate $f/f^{\rm eq}$ over the phase space to obtain a factor $n/n^{\rm eq}$, leaving a factor $f^{\rm eq}$ inside the integral instead of f. Assuming a Maxwell-Boltzmann distribution we have $f^{\rm eq} = e^{-E/T}$, which gives us

$$\begin{aligned}\frac{g_\psi}{(2\pi)^3}\int \frac{d^3p_\psi}{E_\psi} C[f_\psi] = &-\frac{n_\psi n_a n_b \cdots}{n^{\rm eq}_\psi n^{\rm eq}_a n^{\rm eq}_b \cdots}\int d\Pi_\psi d\Pi_a d\Pi_b \cdots \\ &\times (2\pi)^4 \delta^4\left(p_\psi + p_a + p_b \cdots - p_i - p_j \cdots\right) \\ &\times |\mathcal{M}|^2_{\psi+a+b+\cdots\to i+j+\cdots} e^{-E_\psi/T} e^{-E_a/T} e^{-E_B/t} \cdots \\ &+ \frac{n_i n_j \cdots}{n^{\rm eq}_i n^{\rm eq}_j \cdots}\int d\Pi_i d\Pi_j \cdots \\ &\times (2\pi)^4 \delta^4\left(p_\psi + p_a + p_b \cdots - p_i - p_j \cdots\right) \\ &\times |\mathcal{M}|^2_{i+j+\cdots\to\psi+a+b+\cdots} e^{-E_i/T} e^{-E_j/T} \cdots\,.\end{aligned} \tag{3.40}$$

From here on we define the equilibrium reaction rate density $\gamma^{\rm eq}$ as

$$\begin{aligned}\gamma^{\rm eq}(\psi\, a\, b \cdots \to i\, j \cdots) = &\int d\Pi_\psi d\Pi_a d\Pi_b \cdots \\ &\times (2\pi)^4 \delta^4\left(p_\psi + p_a + p_b \cdots - p_i - p_j \cdots\right) \\ &\times |\mathcal{M}|^2_{\psi+a+b+\cdots\to i+j+\cdots} e^{-E_\psi/T} e^{-E_a/T} e^{-E_B/t} \cdots\,.\end{aligned} \tag{3.41}$$

[15] Note that in the RHS of Eq. (3.37) we have not yet assumed isotropy in the collisions.

Finally, we adapt the notation from Ref. [224] using the brackets

$$\begin{aligned}[\psi ab\cdots \to ij\cdots] \equiv \frac{n_\psi n_a n_b \cdots}{n_\psi^{\rm eq} n_a^{\rm eq} n_b^{\rm eq} \cdots}\gamma^{\rm eq}(\psi + a + b + \cdots \to i\, j \cdots) \\ - \frac{n_i n_j \cdots}{n_i^{\rm eq} n_j^{\rm eq} \cdots}\gamma^{\rm eq}(i + j + \cdots \to \psi + a + b + \cdots)\,.\end{aligned} \tag{3.42}$$

Assuming that the particle ψ partakes in many different interactions, we must sum over all the collision terms that affect the number density of ψ. The final expression for the Boltzmann equation for a general particle ψ that we end up with is then given by

$$\frac{dn_\psi}{dt} + 3Hn_\psi = -\sum_{a,b,i,j,\ldots}[\psi ab\cdots \to ij\cdots]\,. \tag{3.43}$$

In Appendix E we further evaluate Eq. (3.43) by writing it in terms of the normalised number density η_ψ as well as giving general expressions for the brackets on the RHS depending on the number of particles involved in an interaction. In the remainder of this chapter we go through different models for generating a baryon asymmetry.

3.5. Models of leptogenesis and baryogenesis

The class of models where a matter-antimatter asymmetry is first generated in the leptonic sector and then translated into the baryons via sphaleron processes is called leptogenesis [225]. Many such models include a right-handed neutrino N, which is a natural candidate for a Majorana particle realised in nature. Since it is a complete SM singlet, $N \in \{1, 1, 0\}$, there is nothing forbidding a term

$$\mathcal{L} \supset -\frac{1}{2}M_{ij}\bar{N}^c{}_i N_j\,, \tag{3.44}$$

which would violate lepton number conservation. This is of course only true provided that N carries a lepton number charge, but in case we do not assign it one, the Yukawa term $\mathcal{L} \supset -y_{ij}L_i\phi N_j + \text{h.c.}$ would violate it instead. Violation of lepton number L coupled to sphalerons leads to baryon number violation, which is one of the three Sakharov conditions. The way in which the other two are fulfilled varies between the different leptogenesis models.

3.5.1. Standard leptogenesis

Leptogenesis via the L- and CP-violating out-of-equilibrium decay of heavy right-handed neutrinos N_1 is one of the most studied baryogenesis models [226–230]. It is often referred to as *Standard leptogenesis* or *Vanilla leptogenesis* (see e.g. Refs. [32, 47, 224, 231–233] for reviews). This model follows naturally from the Type-i seesaw mechanism: the right-handed neutrino has to be sufficiently heavy such that it generates a tiny left-handed neutrino mass, which means that it should fall out of equilibrium quite early in the thermal history of the Universe, precisely what is needed in order to create a sizeable asymmetry. If the mass of N_1 is too low, not enough asymmetry is generated, since the out-of-equilibrium decay of N_1 occurs at

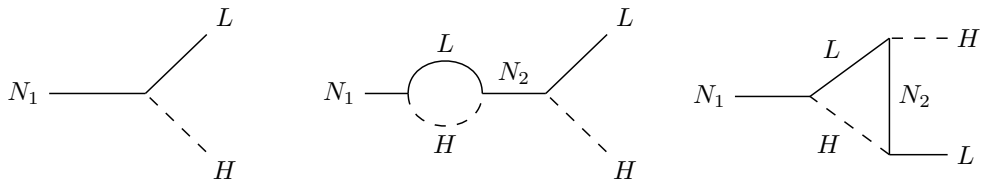

Figure 3.4.: Decay diagrams for a right-handed neutrino N_1 into a lepton- and Higgs doublet in the standard leptogenesis scenario.

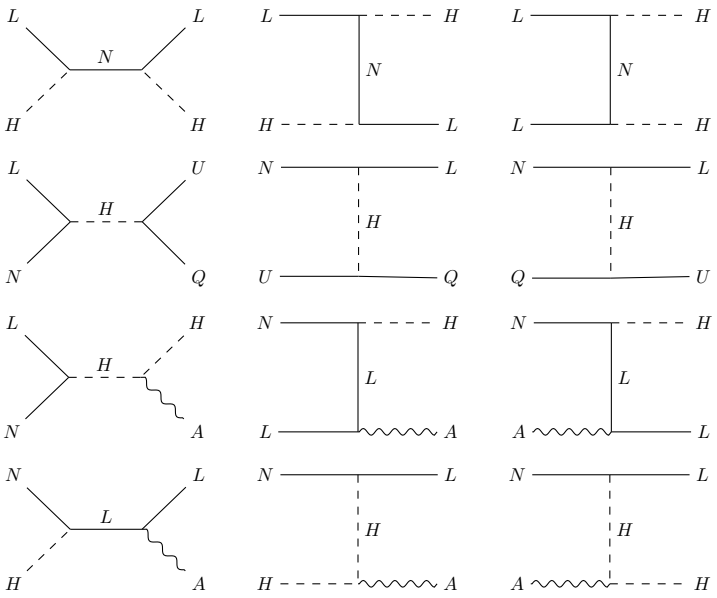

Figure 3.5.: Scattering diagrams involving N_1 (here denoted as N) that are relevant in standard leptogenesis.

relatively late times when the Universe has expanded enough to dilute the N_1 number density. Violation of CP occurs via the interference of tree- and loop-level decay diagrams, which are illustrated in Fig. 3.4. A second generation of the right-handed neutrino N_2, where the first generation is denoted by N_1, is needed in order for the interference to be CP-violating. If N_1 and N_2 are degenerate there may be resonant enhancement of the CP-violating decay, which effectively lowers the mass of N_1 needed for successful leptogenesis [234, 235]. A typical scale for N_1 in standard leptogenesis is $m_{N_1} \sim 10^{14}$ GeV, while in *resonant leptogenesis* it can be as low as $m_{N_1} \sim \mathcal{O}$TeV [234].

To illustrate an application of the Boltzmann equation formalism in Eq. (3.43), we now derive equations governing the evolution of a matter-antimatter asymmetry in the standard leptogenesis model, using some results taken from Appendix E. Our first step is to identify N_1, which we now denote simply as N, as the particle being responsible for generating an asymmetry, and it is therefore the particle for which we wish to evaluate the Boltzmann equation. We also note that the asymmetry is generated in the number density of L, so we

also want to solve for the difference in number density between L and $\bar{L}$. The second step is then to identify the interactions of N that are relevant for leptogenesis, i.e. which diagrams we can draw that would affect the time-evolution of the number density of either N itself or the lepton asymmetry. Apart from the decay diagrams in Fig. 3.4, we also have the scattering diagrams shown in Fig. 3.5. Here A denotes a gauge boson, either W_a^μ or B^μ, and we have only included the up-type quark singlet since we anticipate that we can discard any SM Yukawa interaction apart from that of the top quark, which is dominant. To shorten the notation we can group together interactions of the type $L + N \to X + Y$ for any X and Y that lead to allowed scattering diagrams according to Fig. 3.5, and similarly for interactions $N + X \to \bar{L} + Y$, and give the other interactions shorter names, such that

$$\begin{aligned}
\gamma_{\to}^{D} &\equiv \gamma^{\text{eq}}(N \to L + H) \\
\gamma_{\to}^{S_S} &\equiv \gamma_s^{\text{eq}}(NL \to u\bar{Q}) + \gamma_s^{\text{eq}}(NL \to H^\dagger A) + \gamma_s^{\text{eq}}(NH \to \bar{L}A) \\
\gamma_{\to}^{S_T} &\equiv \gamma_t^{\text{eq}}(N\bar{u}^c \to \bar{L}Q) + \gamma_t^{\text{eq}}(NQ^c \to \bar{L}u^c) + \gamma_t^{\text{eq}}(NL \to H^\dagger A) \\
&\quad + \gamma_t^{\text{eq}}(NA \to \bar{L}H^\dagger) + \gamma_t^{\text{eq}}(NH \to \bar{L}A) \\
\gamma_{\to}^{X_S} &\equiv \gamma_s^{\text{eq}}(LH \to \bar{L}H^\dagger) \\
\gamma_{\to}^{X_T} &\equiv \gamma_t^{\text{eq}}(LH \to \bar{L}H^\dagger) + \gamma_t^{\text{eq}}(LL \to H^\dagger H^\dagger)\,.
\end{aligned} \tag{3.45}$$

Here the arrow denotes the flow of the process, where an arrow in the opposite direction would indicate the reverse reaction, such that

$$\gamma_{\to} \equiv \gamma^{\text{eq}}\left(\psi\, a\, b \cdots \to i\, j \cdots\right) \quad \Rightarrow \quad \gamma_{\leftarrow} \equiv \gamma^{\text{eq}}\left(i\, j \cdots \to \psi\, a\, b \cdots\right)\,, \tag{3.46}$$

such that $\gamma_{\leftarrow}^{D} \equiv \gamma^{\text{eq}}(L + H \to N)$ and $\gamma_{\leftarrow}^{S_S} \equiv \gamma^{\text{eq}}(u\bar{Q} \to NL) + \gamma^{\text{eq}}(H^\dagger A \to NL)$ and so on. A subscript s and t in Eq. (3.45) denotes that the scattering is mediated in the s- or t-channel respectively, such that e.g. the first term in the last row in Eq. (3.45) corresponds to the top-centre diagram in Fig. 3.5, while the term in the second-to-last row corresponds to the top-left diagram. We now let a bar denote the corresponding process for the antiparticles, such that

$$\overline{\gamma^{\text{eq}}}\left(\psi\, a\, b \cdots \to i\, j \cdots\right) \equiv \gamma^{\text{eq}}\left(\bar{\psi}\, \bar{a}\, \bar{b} \cdots \to \bar{i}\, \bar{j} \cdots\right)\,. \tag{3.47}$$

Assuming that all SM particles are in chemical equilibrium[16], we obtain from Eq. (3.43) and Appendix E the following Boltzmann equation for N:

$$\begin{aligned}
zHn_\gamma\eta_N = &-\frac{\eta_N}{\eta_N^{\text{eq}}}\gamma_{\to}^{D} + \frac{\eta_L}{\eta_L^{\text{eq}}}\gamma_{\leftarrow}^{D} - \frac{\eta_{\bar{N}}}{\eta_N^{\text{eq}}}\overline{\gamma}_{\to}^{D} + \frac{\eta_{\bar{L}}}{\eta_L^{\text{eq}}}\overline{\gamma}_{\leftarrow}^{D} \\
&- \frac{\eta_N\eta_L}{\eta_N^{\text{eq}}\eta_L^{\text{eq}}}\gamma_{\to}^{S_S} + \gamma_{\leftarrow}^{S_S} - \frac{\eta_{\bar{N}}\eta_{\bar{L}}}{\eta_N^{\text{eq}}\eta_L^{\text{eq}}}\overline{\gamma}_{\to}^{S_S} + \overline{\gamma}_{\leftarrow}^{S_S} \\
&- 2\frac{\eta_N}{\eta_N^{\text{eq}}}\gamma_{\to}^{S_T} + 2\frac{\eta_{\bar{L}}}{\eta_L^{\text{eq}}}\gamma_{\leftarrow}^{S_T} - 2\frac{\eta_{\bar{N}}}{\eta_N^{\text{eq}}}\overline{\gamma}_{\to}^{S_T} + 2\frac{\eta_L}{\eta_L^{\text{eq}}}\overline{\gamma}_{\leftarrow}^{S_T}\,.
\end{aligned} \tag{3.48}$$

Here η_x denotes the number density of x normalised to the photon number density, such that $\eta_x \equiv n_x/n_\gamma$, H is the Hubble rate and $z \equiv T/m_N$ is a time-parameter, where m_N is the

[16] More on this in Appendix D.

mass of N and T is the temperature. The additional factor 2 in the last row accounts for the u-channel scatterings which are also present for any of the t-channel diagrams in Fig. 3.5. Using η rather than n lets us rewrite the LHS of the Boltzmann equation as a single term rather than two (c.f. Eq. (3.43) with Eq. (3.48), see Appendix E for details). We have used the fact that the equilibrium number densities of particles and antiparticles are the same, such that $\eta_x^{\text{eq}} = \eta_{\bar{x}}^{\text{eq}}$. We can now simplify Eq. (3.48) by making several assumptions. First, we note that N is a Majorana particle, such that $N = \bar{N}^c$, and we therefore have $\eta_N = \eta_{\bar{N}}$. Secondly we assume that the sum of the lepton and antilepton doublet number densities is conserved, such that $\eta_L + \eta_{\bar{L}} = 2\eta_L^{\text{eq}}$. This assumption is motivated from the fact that L and $\bar{L}$ are in thermal equilibrium, for details see Appendix D. Next, we note that from CPT-invariance we have

$$\mathcal{M}(\psi\, a\, b \cdots \to i\, j \cdots) \overset{CPT}{=} \mathcal{M}(\bar{i}\, \bar{j} \cdots \to \bar{\psi}\, \bar{a}\, \bar{b} \cdots)\,, \tag{3.49}$$

and for any CP-conserving process we also have

$$\mathcal{M}(\psi\, a\, b \cdots \to i\, j \cdots) \overset{CP}{=} \mathcal{M}(\bar{\psi}\, \bar{a}\, \bar{b} \cdots \to \bar{i}\, \bar{j} \cdots) \overset{CP}{=} \mathcal{M}(i\, j \cdots \to \psi\, a\, b \cdots)\,. \tag{3.50}$$

Assuming that the interaction $N \to L + H$ is the only CP-violating vertex that we have, we obtain the relations

$$\begin{aligned} \gamma_{\to}^{S_S} = \gamma_{\leftarrow}^{S_S} = \overline{\gamma}_{\to}^{S_S} = \overline{\gamma}_{\leftarrow}^{S_S} \equiv \gamma_{S_S} \\ \gamma_{\to}^{S_T} = \gamma_{\leftarrow}^{S_T} = \overline{\gamma}_{\to}^{S_T} = \overline{\gamma}_{\leftarrow}^{S_T} \equiv \gamma_{S_T}\,. \end{aligned} \tag{3.51}$$

For the decay we can parametrise the CP-violation in terms of the parameter ϵ, such that

$$\begin{aligned} \gamma_{\to}^{D} = \overline{\gamma}_{\leftarrow}^{D} \equiv \frac{1}{2}\gamma_D(1+\epsilon) \\ \gamma_{\leftarrow}^{D} = \overline{\gamma}_{\to}^{D} \equiv \frac{1}{2}\gamma_D(1-\epsilon)\,. \end{aligned} \tag{3.52}$$

With these assumptions, we can rewrite Eq. (3.48) as

$$\begin{aligned} zHn_\gamma\eta_N = &-\frac{\eta_N}{\eta_N^{\text{eq}}}\frac{1}{2}(1+\epsilon)\gamma_D + \frac{\eta_L}{\eta_L^{\text{eq}}}\frac{1}{2}(1-\epsilon)\gamma_D \\ &- \frac{\eta_N}{\eta_N^{\text{eq}}}\frac{1}{2}(1-\epsilon)\gamma_D + \frac{\eta_L}{\eta_L^{\text{eq}}}\frac{1}{2}(1+\epsilon)\gamma_D \\ &- 2\frac{\eta_N}{\eta_N^{\text{eq}}}\gamma_{S_S} + 2\gamma_{S_S} - 4\frac{\eta_N}{\eta_N^{\text{eq}}}\gamma_{S_T} + 4\gamma_{S_T}\,, \end{aligned} \tag{3.53}$$

which finally gives us

$$zHn_\gamma\eta_N = -\left(\frac{\eta_N}{\eta_N^{\text{eq}}} - 1\right)\left(\gamma_D + 2\gamma_{S_S} + 4\gamma_{S_T}\right)\,. \tag{3.54}$$

Next, we wish to find an equation for $\eta_{\Delta L} \equiv \eta_L - \eta_{\bar{L}}$, and to do that we first need equations

for both η_L and $\eta_{\bar{L}}$. For η_L we have

$$\begin{aligned} zHn_\gamma\eta_L = &-\frac{\eta_L}{\eta_L^{\rm eq}}\frac{1}{2}(1-\epsilon)\gamma_D + \frac{\eta_N}{\eta_N^{\rm eq}}\frac{1}{2}(1+\epsilon)\gamma_D \\ &- \frac{\eta_L}{\eta_L^{\rm eq}}\gamma_{X_S}^{\rm sub} + \frac{\eta_{\bar{L}}}{\eta_L^{\rm eq}}\gamma_{X_S}^{\rm sub} - 2\frac{\eta_L^2}{(\eta_L^{\rm eq})^2}\gamma_{X_T} + 2\gamma_{X_T} \\ &- \frac{\eta_N\eta_L}{\eta_N^{\rm eq}\eta_L^{\rm eq}}\gamma_{S_S} + \gamma_{S_S} - 2\frac{\eta_L}{\eta_L^{\rm eq}}\gamma_{S_T} + 2\frac{\eta_N}{\eta_N^{\rm eq}}\gamma_{S_T}\,, \end{aligned} \tag{3.55}$$

and similarly for $\eta_{\bar{L}}$ we have

$$\begin{aligned} zHn_\gamma\eta_{\bar{L}} = &-\frac{\eta_{\bar{L}}}{\eta_L^{\rm eq}}\frac{1}{2}(1+\epsilon)\gamma_D + \frac{\eta_N}{\eta_N^{\rm eq}}\frac{1}{2}(1-\epsilon)\gamma_D \\ &- \frac{\eta_{\bar{L}}}{\eta_L^{\rm eq}}\gamma_{X_S}^{\rm sub} + \frac{\eta_L}{\eta_L^{\rm eq}}\gamma_{X_S}^{\rm sub} - 2\frac{\eta_{\bar{L}}^2}{(\eta_L^{\rm eq})^2}\gamma_{X_T} + 2\gamma_{X_T} \\ &- \frac{\eta_N\eta_{\bar{L}}}{\eta_N^{\rm eq}\eta_L^{\rm eq}}\gamma_{S_S} + \gamma_{S_S} - 2\frac{\eta_{\bar{L}}}{\eta_L^{\rm eq}}\gamma_{S_T} + 2\frac{\eta_N}{\eta_N^{\rm eq}}\gamma_{S_T}\,. \end{aligned} \tag{3.56}$$

The superscript *sub* in Eqs. (3.55) and (3.56) denotes that the on-shell part of γ_{S_S} has to be subtracted, as otherwise it would be double counted, since it is the same contribution as the decay and inverse decay described by γ_D (see Appendix E). This subtraction can be achieved by writing [224]

$$\begin{aligned} \gamma_{X_S}^{\rm sub} &= \gamma_{X_S} - (1-\epsilon)^2\frac{1}{4}\gamma_D\,. \\ \overline{\gamma}_{X_S}^{\rm sub} &= \gamma_{X_S} - (1+\epsilon)^2\frac{1}{4}\gamma_D\,. \end{aligned} \tag{3.57}$$

Here the CP-violating parameter ϵ again appears since the γ_{X_S} interaction involves the CP-violating vertex between N, L, and H. With this treatment we properly subtract the CP-violating on-shell contribution of γ_{X_S}, while neglecting any CP-violation in the off-shell part since these only appear at loop-order[17]. In terms of $\eta_{\Delta L}$ we can combine Eqs. (3.55) and (3.56) to get

$$\begin{aligned} zHn_\gamma\eta_{\Delta L} = &-\frac{\eta_{\Delta L}}{\eta_L^{\rm eq}}\frac{1}{2}\gamma_D + \epsilon\gamma_D + \frac{\eta_N}{\eta_N^{\rm eq}}\epsilon\gamma_D - 2\frac{\eta_L}{\eta_L^{\rm eq}}\gamma_{X_S}^{\rm sub} + 2\frac{\eta_{\bar{L}}}{\eta_L^{\rm eq}}\gamma_{X_S}^{\rm sub} \\ &- 2\frac{\eta_{\Delta L}}{\eta_L^{\rm eq}}\gamma_{X_T} - \frac{\eta_N\eta_{\Delta L}}{\eta_N^{\rm eq}\eta_L^{\rm eq}}\gamma_{S_S} - 2\frac{\eta_{\Delta L}}{\eta_L^{\rm eq}}\gamma_{S_T}\,. \end{aligned} \tag{3.58}$$

Finally using the relations in Eq. (3.57) we have

$$zHn_\gamma\eta_{\Delta L} = \epsilon\gamma_D\left(\frac{\eta_N}{\eta_N^{\rm eq}} - 1\right) - \frac{\eta_{\Delta L}}{\eta_L^{\rm eq}}\left(2\gamma_{X_S} - 2\gamma_{X_T} - \frac{\eta_N}{\eta_N^{\rm eq}}\gamma_{S_S} - 2\gamma_{S_T}\right)\,. \tag{3.59}$$

[17] This treatment is indeed consistent since we are only concerned with CP-violation when it comes to the generation of a baryon asymmetry. For washouts, like the one we get from γ_{X_S}, the CP-violating effects do not significantly affect the final result in most baryogenesis models.

Here we neglected terms of $\mathcal{O}(\epsilon^2)$, and used the relation $\eta_L^2 - \eta_{\bar{L}}^2 = \eta_{\Delta L}\eta_L^{\text{eq}}$. Eqs. (3.54) and (3.59) together describe the dynamical generation of a matter-antimatter asymmetry in the lepton sector, where Eq. (3.54) describes the number density evolution of N, and Eq. (3.59) the number density evolution of ΔL, which depends non-trivially on the density of N. These equations are usually called the *first* and *second* Boltzmann equations respectively. Note however that the result from Eq. (3.59) is given in terms of a lepton asymmetry, while the relevant experimentally measured quantity is the baryon asymmetry. The conversion between these two is explained in Sec. 2.1.6 and Appendix D. On a similar note, the result obtained from Eq. (3.59) is typically valid within a few orders of magnitude around the temperature T_* where the asymmetry is generated, usually near the mass scale of N. Again, the observed quantity is the baryon asymmetry at the time of recombination[18], when the temperature is T_0. To convert between these two temperatures, we assume that the Universe evolves adiabatically, such that the entropy

$$s \times V = \frac{2\pi^2}{45} g_s(T) T^3 \times V \,, \tag{3.60}$$

where V is the volume, remains constant. To account for the change in photon number density $n_\gamma \propto T^3$, we can convert the normalised number density according to

$$\eta_{\Delta B}(T_0) = \frac{g_s(T_*)}{g_s(T_0)} \eta_{\Delta B}(T_*) \equiv d_{\text{dil}} \eta_{\Delta B}(T_*) \,. \tag{3.61}$$

Assuming that all SM species were relativistic at T_*, and that photons as well as three neutrino generations were relativistic at T_0, we have[19] [53]

$$d_{\text{dil}} = \frac{g_s(T_*)}{g_s(T_0)} = \frac{103.75}{2 + \frac{7}{8} \times 2 \times 3 \times \frac{4}{11}} \approx \frac{1}{27} \,. \tag{3.62}$$

The general scheme of things is often quite similar between the different models of baryogenesis/leptogenesis. The rest of this chapter deals with some of the most popular and historically most relevant such models.

3.5.2. Electroweak baryogenesis

The SM already contains a mechanism for baryogenesis that successfully incorporates all three Sakharov conditions, namely *electroweak baryogenesis* [45] (for reviews see e.g. Ref. [236–238]). In this mechanism, a baryon asymmetry is generated quite dramatically as the Universe departs from its electroweak symmetry [239–243]. The only problem with it is that the resulting asymmetry is too small, since the Higgs field is not sufficiently light (the requirement is $m_h \lesssim 70$ GeV) [244, 245]. Electroweak baryogenesis requires that the phase transition is strongly first order, but with the Higgs mass $m_h \approx 125$ GeV [246, 247] it instead appears that

[18] Assuming that CMB data is used to observe the value of $\eta_{\Delta B}$.

[19] Note that the factor $7/8$ in Eq. (3.62) accounts for fermion statistics as opposed to boson statistics, and the factor $4/11$ comes from the temperature difference between neutrinos and photons, see e.g. Refs. [53, 83].

the electroweak phase transition was second order. However, in some BSM extensions, e.g. modifications to the Higgs potential, electroweak baryogenesis is still viable.

During the electroweak phase transition the Universe went from being symmetric under the SM gauge group $SU(3)_c \times SU(2)_L \times U(1)_Y$ to being symmetric only under the subgroup $SU(3)_c \times U(1)_{\text{em}}$. This transition occurred as the temperature dropped low enough for the neutral component of the Higgs field ϕ_0 to settle into the minimum of its potential $\langle \phi_0 \rangle = v$ (see Sec. 2.1.7). Due to temperature fluctuations, the transition happened slightly earlier in some places than in others, forming local pockets of broken phase called *bubbles*, which were separated from the rest of the Universe in the sense that some particles may be kinematically forbidden to enter the bubbles[20]. The border between the bubble and the rest of the universe is called a *domain wall*, and it's mainly the CP-violating interaction between the domain walls and top quarks which can drive the baryon asymmetry generation in this scenario, though the resulting amount of CP-violation from this source may not be enough [248, 249]. The baryon number violation comes from the sphalerons, which are active at the domain wall, but not inside the bubble, and the out-of-equilibrium condition is fulfilled by the additional energy coming from the domain wall sweeping through the Universe.

The SM scalar potential itself is not enough to create the strongly first order phase transition that is needed for successful baryogenesis, but with modifications to the scalar sector, this picture can change [250–255]. Electroweak baryogenesis therefore motivates the search for scalar particles other than the Higgs, as well as careful experimental determination of the different Higgs couplings to SM particles.

If the electroweak phase transition was strongly first order, gravitational waves from collisions of expanding bubbles could be seen at the future LISA mission [256–258].

3.5.3. Leptogenesis via oscillations

There are other possible sources of CP-violation than interference of tree- and loop-level decay diagrams as in standard leptogenesis. In Sec. 3.2.2 we saw that there is a non-zero CP-violating parameter associated with the weak interaction of quarks, due to there being three generations. A similar effect is present in the lepton sector, but due to the convention of having the charged lepton weak interactions flavour diagonal, this CP-violation appears in the oscillations of the neutrinos, as can be seen if we pick up from where we left off in Sec. 2.3.1. We can use the following identity for complex numbers z_i, $i \in \{1, 2, 3\}$:

$$|z_1 + z_2 + z_3|^2 = |z_1|^2 + |z_2|^2 + |z_3|^2 + 2\,\text{Re}(z_1 z_2^* + z_1 z_3^* + z_2 z_3^*)\,, \tag{3.63}$$

[20] Note that it's the non-zero vev of the Higgs field which gives a zero-temperature mass to the SM fermions. If say a massless top-quark has too little momentum to enter the broken phase bubble and become massive without violating conservation of energy, it would bounce off and for a time be trapped in the symmetric universe (until it gains enough momentum by bouncing off bubbles).

such that we can write the oscillation probability $P(\nu_e \to \nu_\mu)$ from Eq. (2.113) as

$$\begin{aligned} P(\nu_e \to \nu_\mu) = &|U_{e1}^* U_{\mu 1}|^2 + |U_{e2}^* U_{\mu 2}|^2 + |U_{e3}^* U_{\mu 3}|^2 \\ &+ 2\,\mathrm{Re}\left(U_{e1}^* U_{\mu 1} U_{e2} U_{\mu 2}^* e^{-i(\phi_1 - \phi_2)}\right) \\ &+ 2\,\mathrm{Re}\left(U_{e1}^* U_{\mu 1} U_{e3} U_{\mu 3}^* e^{-i(\phi_1 - \phi_3)}\right) \\ &+ 2\,\mathrm{Re}\left(U_{e2}^* U_{\mu 2} U_{e3} U_{\mu 3}^* e^{-i(\phi_2 - \phi_3)}\right) . \end{aligned} \tag{3.64}$$

Now using the unitarity of the PMNS matrix

$$U_{e1}^* U_{\mu 1} + U_{e2}^* U_{\mu 2} + U_{e3}^* U_{\mu 3} = 0\,, \tag{3.65}$$

we obtain

$$P(\nu_e \to \nu_\mu) = -4 \sum_{i<j} \mathrm{Re}\left(U_{ei}^* U_{\mu i} U_{ej} U_{\mu j}^*\right) \sin^2 \Delta_{ij} + 2 \sum_{i<j} \mathrm{Im}\left(U_{ei}^* U_{\mu i} U_{ej} U_{\mu j}^*\right) \sin 2\Delta_{ij}\,. \tag{3.66}$$

Here we have also used the identity $\cos(2\theta) = \cos^2(\theta) - \sin^2(\theta)$ as well as having defined

$$\Delta_{ij} \equiv \frac{\phi_i - \phi_j}{2} = \frac{(m_j^2 - m_i^2)L}{4E_\nu}\,. \tag{3.67}$$

Again using the unitarity condition, but this time in the form of

$$\mathrm{Im}\left(U_{e3} U_{\mu 3}^* \left(U_{e1}^* U_{\mu 1} + U_{e2}^* U_{\mu 2} + U_{e3}^* U_{\mu 3}\right)\right) = 0\,, \tag{3.68}$$

we can define the CP-violating parameter J as

$$J \equiv -\,\mathrm{Im}\left(U_{e1}^* U_{\mu 1} U_{e3} U_{\mu 3}^*\right) = \mathrm{Im}\left(U_{e2}^* U_{\mu 2} U_{e3} U_{\mu 3}^*\right) = \mathrm{Im}\left(U_{e1}^* U_{\mu 1} U_{e2} U_{\mu 2}^*\right) . \tag{3.69}$$

Now using the identity $\Delta_{12} + \Delta_{23} = \Delta_{13}$ as well as

$$\sin\alpha + \sin\beta - \sin(\alpha+\beta) = 4 \sin\left(\tfrac{\alpha}{2}\right) \sin\left(\tfrac{\beta}{2}\right) \sin\left(\tfrac{\alpha+\beta}{2}\right) \tag{3.70}$$

we can write

$$P(\nu_e \to \nu_\mu) = -4 \sum_{i<j} \mathrm{Re}\left(U_{ei}^* U_{\mu i} U_{ej} U_{\mu j}^*\right) \sin \Delta_{ij} + 8J \sin\Delta_{12} \sin\Delta_{13} \sin\Delta_{23}\,. \tag{3.71}$$

Finally, CPT-invariance tells us that

$$P(\nu_e \to \nu_\mu) = P(\bar{\nu}_\mu \to \bar{\nu}_e)\,. \tag{3.72}$$

We can use this fact to get an expression for $P(\bar{\nu}_e \to \bar{\nu}_\mu)$ by changing $e \leftrightarrow \mu$ in Eq. (3.71). We then get an expression for the difference between an oscillation $\nu_e \to \nu_\mu$ and its CP-conjugated process as

$$P(\nu_e \to \nu_\mu) - P(\bar{\nu}_e \to \bar{\nu}_\mu) = 16J \sin\Delta_{12} \sin\Delta_{13} \sin\Delta_{23}\,. \tag{3.73}$$

This shows that there is a non-vanishing CP-violating contribution to the SM neutrino oscillations. The amount of CP-violation depends on the mass splitting between the neutrinos, as well as the specific structure of the PMNS matrix as parametrised by J in Eq. (3.69). Assuming that we also have three generations of heavy right-handed neutrinos N_i, $i \in \{1, 2, 3\}$, a similar mechanism could exist for them as for the SM neutrinos. Oscillations between the flavour-eigenstates of N then provide a possible source of CP-violation, fulfilling one of the Sakharov conditions and therefore possibly being able to lead to leptogenesis. This kind of mechanism is often appropriately referred to as *leptogenesis via oscillations*, or *ARS leptogenesis* after the authors of the original paper [259] (see e.g. Ref. [260] for a review).

In leptogenesis via oscillations, three right-handed neutrinos are introduced with a CP-violating oscillation. They start out with vanishing number densities, and are slowly brought into thermal equilibrium through a coupling to the SM Higgs and Lepton doublets. While coming into equilibrium, the neutrinos are oscillating between the three flavour eigenstates, where the τ flavour has the strongest coupling to the SM and e the weakest. The τ-flavoured N then reaches equilibrium before the μ and e flavours, since its coupling to the SM is stronger. Because the oscillation is CP-violating, the anti-τ right-handed neutrino does not come into equilibrium at the same time as the τ-flavoured right-handed neutrino, while still being earlier than the anti-μ and anti-e ones. Since any N in equilibrium changes the chemical potential of the lepton doublet L it couples to via the Higgs, this difference in the time at which the τ- and anti-τ-flavoured N comes into equilibrium leads to a lepton number asymmetry in the τ-flavoured sector, which can spread to the other flavours via the Higgs coupling to the lepton singlets and via the electroweak sphaleron, the latter also spreading the asymmetry to the baryon sector. Since CPT is conserved, the total strength of the τ-, μ-, and e-flavoured couplings of the right-handed neutrinos has to be equal to the total strength of the anti-τ, anti-μ, and anti-e. Therefore, any asymmetry generated via oscillations is then removed by the time the e- and anti-e-flavoured right-handed neutrinos come into equilibrium. However, if the electroweak sphaleron shuts off before that happens, i.e. if the e-flavoured N comes into equilibrium after EWSB, an asymmetry remains in the baryon sector, being unable to be converted into the lepton sector any more. This remaining asymmetry would in this case survive until today, leading to successful baryogenesis.

3.5.4. Affleck-Dine Baryogenesis

Supersymmetry is a symmetry for which the corresponding transformation takes a fermion to a boson and vice versa [161, 163] (for reviews see e.g. Refs. [164, 261, 262]). According to supersymmetry, there is a corresponding scalar superpartner for every fermion, and similarly there is a fermionic partner for each boson. In supersymmetric models, such superpartners are used to solve theoretical issues or explain experimental observations. Since we do not observe it today, if supersymmetry is realised in nature it has to have been broken at some point during the cosmological evolution of the Universe [263–267].

One implementation of supersymmetry is a mechanism in which the baryon asymmetry of the Universe can be generated, namely via Affleck-Dine baryogenesis [268] (see Ref. [269] for a review). Since all quantum numbers of a given field and its superpartner are the same except

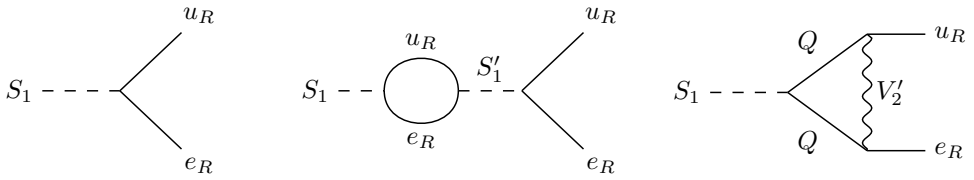

Figure 3.6.: Decay diagrams of S_1 in $SU(5)$ that violate both B and CP.

for the spin, even in minimal supersymmetric models there would exist scalar fields with baryon- or lepton number, namely the superpartners of quarks and leptons[21]. A condensate $\langle\chi\rangle \neq 0$ of a colourless and electrically neutral combination of such fields is able survive inflation [270, 271], and when $\langle\chi\rangle$ subsequently decays it can lead to the generation of a baryon asymmetry [272, 273].

An attractive feature of this type of model is that it does not rely on high-scale reheating. It may turn out from cosmological observations that a low reheating temperature is preferable, and in such a scenario any high-scale baryogenesis mechanism would be effectively ruled out, possibly favouring models such as Affleck-Dine.

3.5.5. GUT baryogenesis

Many theories of BSM physics incorporate a unification of the SM forces into a higher framework (see also Sec. 2.3.1), which leads to the possibility of generating a baryon asymmetry via the GUT degrees of freedom [36, 274–280]. In many such models, though not all, the conservation of the difference between baryon number and lepton number, $B - L$, is explicitly broken at some high scale. This difference is what is conserved by the sphaleron, such that in combination with a GUT model, B and L can be both independently broken. By combining leptons and quarks in the same multiplet under the GUT symmetry[22], coloured gauge bosons[23] arise that can transform them to each other while conserving $B - L$. Breaking the GUT symmetry in this way therefore also breaks the $B - L$ symmetry, fulfilling the first Sakharov condition. Various GUT baryogenesis mechanisms fulfil the second and third conditions in different ways, but commonly they involve the CP-violating out-of-equilibrium decay of heavy particles similar to standard leptogenesis[24] (see Sec. 3.5).

In the example of $SU(5)$ from Sec. 2.3.2, the simplest representation that could contain a scalar Higgs field is the 5 [152, 281]. The component of 5 that does not become the Higgs

[21] These scalar fields are called *squarks* and *sleptons*. The naming convention for superpartners of fermionic fields is to put an *s-* in front, as in e.g. *stop squark* and *selectron*. For bosons, the convention is instead to put an *-ino* at the end of the superpartner's name, as in e.g. *higgsino* and *gluino*. Note however that the neutrino is not the superpartner of any SM field.

[22] Such a combination often occurs in GUT models since one of the main points is to unify the SM forces (colour, electroweak, and hypercharge) into a single force, thereby making colour no longer a separate interaction.

[23] Since these gauge bosons interact with leptons and quarks in a single vertex, they fall under the category of vector leptoquarks.

[24] In fact, many GUT models contain a singlet fermion N which can be identified as the right-handed neutrino. Vanilla leptogenesis can in this sense also be embedded in a GUT framework.

field is the S_1 leptoquark, which has the representation $(3, 1, -\frac{1}{3})$ under the SM gauge group. This field has baryon number violating interactions with the SM quarks and leptons, and could potentially drive the baryogenesis mechanism via its decays if it is sufficiently heavy[25]. However, with only one copy of S_1, it is not possible to have CP-violating decays via the interactions of the tree- and loop-level diagrams shown in Fig 3.6 [37, 282, 283]. In order to have baryogenesis via the decay of S_1 in $SU(5)$, additional fields can be introduced, the easiest solution perhaps being to add another 5 giving a second leptoquark S_1' or to simply use the $SU(5)$ gauge boson $V_2 \in (3, 2, -\frac{5}{6})$. In this case, a non-vanishing CP-violating contribution to the decay is possible. Similar baryogenesis mechanisms via decays of heavy particles can be embedded in many different GUT models.

3.5.6. Asymmetric dark matter

In terms of the densities Ω_i from Sec. 2.2, it is remarkable that the two matter components of the Universe, dark matter (DM) and baryonic matter (B), are so close in their energy densities

$$\Omega_{\mathrm{DM}} \approx 5 \times \Omega_{\mathrm{B}} \,. \tag{3.74}$$

Since the two densities are of the same order of magnitude, they might have a common origin, such that a single mechanism could have created both a baryon asymmetry and a dark matter abundance [97, 98, 284–287]. Models that attempt to explain this possible common origin go by many names, as there are several different kinds of models, one being *asymmetric dark matter* [100, 288, 289] and another[26] *WIMPy baryogenesis* [290–293]. In many models, baryons and dark matter particles are both the decay product of some other particle, but it is also possible that the asymmetry is created via scatterings [294, 295].

As an example, consider a modification of the standard leptogenesis scenario where N decays into L and ϕ', and where N and ϕ' are now charged under a global $\mathbb{Z}_2$ symmetry [296–304]. If there is no additional lighter particle with a $\mathbb{Z}_2$ charge, ϕ' is stable and therefore a dark matter candidate[27], as long as it is massive or weakly-interacting enough to avoid experimental constraints. In the CP-violating decay of N we now generate both a baryon asymmetry and a dark matter abundance.

3.5.7. Other models

There are more models of baryogenesis than can be discussed in detail here. In this section we have covered some of the more popular ones, and we here lastly mention a few others. For in-depth reviews of different baryogenesis mechanisms, see e.g. Refs. [305–309].

[25] Having S_1 sufficiently heavy while keeping the SM Higgs field at its observed mass would require significant fine-tuning, in the absence of additional modifications to the model [20]

[26] WIMP stands for Weakly Interacting Massive Particle, which is a popular class of dark matter candidates with masses around the electroweak scale and interaction strengths similar to the weak interaction.

[27] Note that if $N \in (1, 1, 0)$ is the right-handed neutrino, ϕ' has to have the quantum numbers $(1, 2, \frac{1}{2})$, similar to the SM Higgs field. It may look strange that we have a dark matter particle with an electric charge, but keep in mind that after EWSB ϕ' is split into its charged and neutral components, where the neutral component is the dark matter particle.

- **B-ball baryogenesis** If the condensate $\langle\chi\rangle$ in Affleck-Dine leptogenesis (described above) decays mainly into Q-balls [310], which are extended objects that in this case are principally made up of squarks that carry a non-zero baryon number B, the Q-balls[28] could decay after EWSB into neutralinos and quarks, creating a baryon asymmetry and a dark matter[29] abundance at the same time [311,312].

- **Baryogenesis via low-scale gravity** Quantum gravity is often assumed to be unimportant at scales below the Planck mass $m_{\rm Pl}$. However, some models lead to gravity effects at much lower scales, which could have implications for baryogenesis e.g. via the gravity-mediated decay of heavy particles [313–315].

- **Black hole capture** It could be possible that black holes absorb particles in the presence of a process that violates CP and B, creating a baryon asymmetry by sucking up all the antibaryons [316–319].

- **Black hole evaporation** Black holes emit particles via Hawking radiation [320]. In some models of baryogenesis, Hawking radiation in the early Universe can violate CP and B to create a baryon asymmetry (the event horizon already fulfils the out-of-equilibrium condition) [321–326].

- **Cosmic string decay** Local topological defects can form during different kinds of phase transitions. In the early Universe, this could lead to magnetic monopoles or cosmic strings being created in the transition from some higher symmetry into e.g. the SM. Cosmic strings may then decay into particles [327–330], possibly creating an over-abundance of e.g. right-handed neutrinos N, which could decay and generate a baryon asymmetry according to standard leptogenesis.

- **Dirac leptogenesis** It could be possible that a small Dirac mass for the right-handed neutrino could lead to a baryon asymmetry being generated via the electroweak sphaleron [331,332].

- **Exotic sphalerons** In some models with additional symmetries, new exotic sphalerons such as dark sphalerons [333] or right-handed $SU(2)_R$ sphalerons [334] could lead to a baryon asymmetry.

- **Gravitational baryogenesis** Some BSM Lagrangians include couplings between massive fields and either the Ricci scalar R or Ricci tensor $R_{\mu\nu}$. In such models, it may be possible to generate a baryon asymmetry, if these terms also violate $B-L$ [335–340].

- **Inflationary baryogenesis** In a wide class of models, baryogenesis has been considered to occur either during inflation or in the decay of the inflaton [341–351].

[28] Q-balls that carry baryon number are sometimes referred to as *B-balls*.

[29] Dark matter is here made up of the neutralinos (an electrically neutral fermionic composition of the superpartners of the Higgs, W^a_μ, and B_μ bosons), which in this case is the Lightest Supersymmetric Particle (LSP), and therefore stable unless R-parity is broken (R-parity is a hypothetical $\mathbb{Z}_2$-symmetry under which all supersymmetric partners but no SM particles are charged).

- **Mesogenesis** The baryon asymmetry and dark matter could both be generated in the oscillation and decay of B-mesons, in a mechanism called *Mesogenesis* [352, 353]. This mechanism can be tested at B-factories such as LHCb [354] and Belle-II [355].

- **Post-sphaleron baryogenesis** The baryon asymmetry of the Universe is often considered to be generated at a high scale where the sphalerons are active. In post-sphaleron models, the baryon asymmetry can be generated after EWSB via high-dimensional operators, leading to observable experimental predictions [356, 357].

- **Spontaneous baryogenesis** Promoting baryon number B to a broken global $U(1)_B$ symmetry, it could be possible that the pseudo-Goldstone boson from the $U(1)_B$ breaking obtains random space-dependent initial values $\theta_0(x)$, and subsequently relaxes to the ground state $\theta = 0$. In this process of relaxing, a baryon asymmetry may be generated locally depending on the value of θ_0 [358–361], and during inflation this local asymmetry is stretched out to a large volume, while keeping the total baryon number of the Universe zero due to the existence of antimatter domains (see e.g. [362, 363]).

- **Types ii and iii seesaw** Not only the right-handed neutrino N can generate a baryon asymmetry via its decays. The other two tree-level realisations of the Weinberg operator $\mathcal{O}_1$ can similarly lead to baryogenesis, via the out-of-equilibrium decay of the mediator of the Type-ii [364–371] or Type-iii [371–374] seesaw mechanisms (for a review, see Ref. [375]).

3.6. Phenomenology of baryogenesis models

The great variety between the different baryogenesis and leptogenesis models makes them difficult to probe in a model-independent way. Instead, more specific approaches can be used for the different models, e.g. searching for extra scalar fields in order to probe the validity of a strong first order phase transition in electroweak baryogenesis, or searching for supersymmetric partners in order to probe Affleck-Dine leptogenesis. However, since any model that explains the existence of a baryon asymmetry has to fulfil the three Sakharov conditions, we know that an experimental signature of baryon- or lepton number violation[30] is inevitably tied to baryogenesis. Since the SM alone cannot lead to a baryon asymmetry, searches for NP also constrain baryogenesis models. Having the possibility of being Majorana, the nature of neutrino masses could hold the key to knowing which mechanism generated the baryon asymmetry of the Universe. The rest of this thesis addresses different probes of NP and lepton/baryon number violation, and how to connect these probes to baryogenesis and neutrino masses using simplified models and effective field theory.

[30] The other two Sakharov conditions can also be probed in the lab, but perhaps the most straight-forward one is baryon number violation, since it can more readily be studied in a model-independent way.

4. Phenomenology of LNV in SMEFT

As discussed in Sec. 2.3.3, the EFT approach is a powerful tool to study BSM physics. Specifically, Standard Model EFT (SMEFT) is a general framework that is used extensively to describe NP effects generated at mass scales higher than the scale of EWSB. In this chapter we discuss in detail how LNV can be studied phenomenologically in SMEFT, by connecting $\Delta L = 2$ operators to different experimental probes.

We put special emphasis on dimension-7 operators. One of the main motivations for this choice is the wide applicability these operators have in terms of experimental searches for LNV, while still being generated at a relatively low dimension. Seven is the second-lowest dimension at which $\Delta L = 2$ operators can be realised, and dimension-7 $\Delta L = 2$ operators therefore offer the second-simplest possible solution to describe LNV processes. The only lower-dimension operator is the one found at dimension-5. However, this operator does not couple to the same range of SM fields as the dimension-7 operators, and therefore its connection to some LNV observables may be less direct. Furthermore, dimension-7 LNV offers a broader range of possible underlying tree-level UV-completions than dimension-5.

The phenomenology of dimension-5 LNV has been well studied in the literature, including loop corrections [376–378]. LNV at dimension-7 has been explored in terms of specific neutrino mass models [379, 380], operator classification, matching, and renormalisation group evolution [381–384], extensions using right-handed neutrinos [385, 386], different LNV observables [387, 388], and model-independent neutrino mass classifications [389–391]. We seek to continue this work here, especially that of Ref. [391], in which constraints on LNV neutrino-mass operators were compared with constraints on the different NP fields that generate them. In this chapter, as well as in Ch. 5, we extend the work of Ref. [391] by considering a different set of LNV probes, and by performing an analysis in terms of simplified models containing pairs of NP fields rather than one NP field at a time. In Sec. 4.1 we describe SMEFT and its connection to low-energy probes in different bases. In Secs. 4.2 and 4.3 we give a broad overview of different low-scale LNV probes, and in Sec. 4.4 we derive new collider limits that are subject for publication in Ref. [4]. In Secs. 4.5 to 4.7 we discuss various other aspects of $\Delta L = 2$ operators, after which we finally combine the different analyses in Sec. 4.8. As a complement to our EFT-based description in this chapter, we categorise all tree-level UV-completions of dimension-7 $\Delta L = 2$ operators in Ch. 5.

4.1. LNV SMEFT operators

SMEFT contains all fields of the unbroken SM, and describes all interactions that are Lorentz invariant as well as invariant under the SM gauge group $SU(3)_c \times SU(2)_L \times U(1)_Y$ [392].

Starting at low mass dimension, the first operator that appears is the dimension-5 Weinberg operator [198]

$$\mathcal{O}_1^{(5)} = L^\alpha L^\beta H^\rho H^\sigma \epsilon_{\alpha\rho}\epsilon_{\beta\sigma}\,, \tag{4.1}$$

where Greek letters denote $SU(2)_L$ indices. LNV operators can generally only appear at odd mass dimension [393,394], such that the $\Delta L = 2$ interaction Lagrangian can be written as

$$\mathcal{L} = \mathcal{L}_{\text{SM}} + \frac{\mathcal{C}_1^{(5)}}{\Lambda_1}\mathcal{O}_1^{(5)} + \sum_i \frac{\mathcal{C}_i^{(7)}}{\Lambda_i^3}\mathcal{O}_i^{(7)} + \sum_i \frac{\mathcal{C}_i^{(9)}}{\Lambda_i^5}\mathcal{O}_i^{(9)} + \cdots\,, \tag{4.2}$$

where $\mathcal{O}_i^{(D)}$ corresponds to a SMEFT operator at dimension $D \geq 5$, where i denotes an individual operator, and where D only takes odd values. Note however that D can take on even values for lepton number conserving operators. Furthermore, $\mathcal{C}$ denotes a dimensionless Wilson coefficient, and Λ_i represents the scale at which the given operator is generated. The product of a given operator and its Wilson coefficient always yield a mass-dimension four object.

The fields that are used in SMEFT operators are all the SM fermions and bosons,

$$L = \begin{pmatrix}\nu_L \\ e_L\end{pmatrix},\ Q = \begin{pmatrix}u_L \\ d_L\end{pmatrix},\ H = \begin{pmatrix}h^+ \\ h^0\end{pmatrix},\ e^c,\ u^c,\ d^c,\ W_\mu^I,\ B_\mu\,, \tag{4.3}$$

where B_μ is the SM $U(1)_Y$ gauge boson, $I \in \{1,2,3\}$ numbers the different $SU(2)_L$ gauge bosons W_μ^I, and the fields L, Q, and H are $SU(2)_L$ doublets. All fermion fields that appear in Eq. (4.3) are left-handed two-component Weyl spinors, and a superscript c denotes that the field is charge-conjugated. For the purposes of studying LNV, we assume in this chapter that the neutrino is a Majorana particle, such that we can construct it as a four-component spinor $\nu = \nu_L + \nu_L^c$. If any of the $\Delta L = 2$ SMEFT operators is realised in nature, it could indeed induce a Majorana mass for the neutrino.

Note that we have not included the gluon field in Eq. (4.3) since it is not relevant for any of the operators that enter into our analysis. Gluons do however appear in lepton-number conserving (LNC) SMEFT operators and at higher dimension in the case of LNV. Note also that the fields in Eq. (4.3) are only defined at energies above the electroweak scale, where the SM gauge group is a valid symmetry. Any NP fields that generate the SMEFT operators also have to have masses above this scale, since otherwise there would be an inconsistency in terms of which fields are considered heavy and which are considered light. Before discussing the different SMEFT bases we use, a few remarks on the notation are warranted:

- A Wilson coefficient written in calligraphy $\mathcal{C}_i^{ijkn}$ is dimensionless.
- A Wilson coefficient written without calligraphy C_i^{ijkn} has the dimension $4 - D$, where D is the dimension of the associated operator.
- A scale written with flavour indices, Λ_{ijkn}, has absorbed the associated dimensionless Wilson coefficient, such that $1/(\Lambda_{ijkn})^{D-4} = \mathcal{C}_i^{ijkn}/\Lambda^{D-4} = C_i^{ijkn}$.

- A *short range* interaction is one where no external vertices are needed to mediate the process, while a *long range* interaction uses external vertices. A concrete example of this distinction is given in Sec. 4.3.2.

All LNV operators up to $D = 11$ have been classified in the literature [393–395], except those that include covariant derivatives. Such operators may be more difficult to include in UV-complete models, but are interesting from a phenomenological point of view. In Tab. 4.1 we list some of the dimension-5, -7, and -9 operators that are used for the analysis in this chapter. These operators are written in the basis introduced in Ref. [395], which we here refer to as the Babu-Leung basis. Another basis that is used in this thesis, given for dimension-7 in Sec. 4.3, is the one introduced in Ref. [381] and modified in Ref. [382], which we call the Lehman basis. In the LNV literature, the Babu-Leung basis has often been used for large surveys of operators up to dimension 11 [393,394], while the Lehman basis has often been used to study LNV at dimension-7 [383,384,388,396]. In order to match with existing literature, we switch between these bases depending on the context. In Sec. 4.2, we use the Babu-Leung basis for the discussion of effective neutrino masses, rare kaon decays, and fully leptonic meson decays. In Sec. 4.3 we introduce the Lehman basis, which we then use for the remaining chapters.

4.2. Low scale probes of LNV in the Babu-Leung basis

Various experimental searches have been used to study the phenomenology of LNV. In this section, we go through three observables in detail and comment on the flavour aspect. We use the Babu-Leung basis in order to match with the most relevant literature [1,393,394]. At the end of this section we make a connection to the Lehman basis, which will be used from Sec. 4.3 onwards.

A list of relevant dimension-5, -7 and -9 operators is given in Tab. 4.1 in the Babu-Leung basis, where the naming convention follows Ref. [395]. These LNV operators are the ones with dimension lower than $D = 11$ that trigger either rare kaon decays or fully leptonic LNV meson decays. In the Babu-Leung basis, spinor contractions are not written explicitly. When applying the operators to observables, we use the convention that each operator is defined as having the spinor contractions relevant for the probe in question. Furthermore, a superscript H^2 indicates contraction with $\bar{H}^\eta H_\eta$, and a superscript y_d contraction with $\bar{Q}^\eta H_\eta \bar{d}^c$.

In Sec. 4.2.1 we describe a method of estimating the neutrino mass contribution from each operator in Tab. 4.1, and derive constraints on the scale of LNV assuming a neutrino Majorana mass $m_\nu = 0.1$ eV. In Secs. 4.2.2 and 4.2.3 we constrain LNV scales using experimental limits on the branching ratio of rare kaon decays and fully leptonic LNV meson decays, respectively. The analysis presented in these three sections led to the publication in Ref. [1].

4.2.1. Absolute neutrino mass

i	$\mathcal{O}_i$
1	$L^\alpha L^\beta H^\rho H^\sigma \epsilon_{\alpha\rho}\epsilon_{\beta\sigma}$
1^{y_d}	$L^\alpha L^\beta H^\rho H^\sigma \bar{Q}^\eta H_\eta \bar{d}^c \epsilon_{\alpha\rho}\epsilon_{\beta\sigma}$
$3a$	$L^\alpha L^\beta Q^\rho d^c H^\sigma \epsilon_{\alpha\beta}\epsilon_{\rho\sigma}$
$3a^{H^2}$	$L^\alpha L^\beta Q^\rho d^c H^\sigma \bar{H}^\eta H_\eta \epsilon_{\alpha\beta}\epsilon_{\rho\sigma}$
$3b$	$L^\alpha L^\beta Q^\rho d^c H^\sigma \epsilon_{\alpha\rho}\epsilon_{\beta\sigma}$
$3b^{H^2}$	$L^\alpha L^\beta Q^\rho d^c H^\sigma \bar{H}^\eta H_\eta \epsilon_{\alpha\rho}\epsilon_{\beta\sigma}$
$4a$	$L^\alpha L^\beta \bar{Q}_\alpha \bar{u}^c H^\rho \epsilon_{\beta\rho}$
$4a^{H^2}$	$L^\alpha L^\beta \bar{Q}_\alpha \bar{u}^c H^\rho \bar{H}^\sigma H_\sigma \epsilon_{\beta\rho}$
$4b^\dagger$	$L^\alpha L^\beta \bar{Q}_\rho \bar{u}^c H^\rho \epsilon_{\alpha\beta}$
$4b^{\dagger H^2}$	$L^\alpha L^\beta \bar{Q}_\rho \bar{u}^c H^\rho \bar{H}^\sigma H_\sigma \epsilon_{\alpha\beta}$
5	$L^\alpha L^\beta Q^\rho d^c H^\sigma H^\eta \bar{H}_\alpha \epsilon_{\beta\sigma}\epsilon_{\rho\eta}$
6	$L^\alpha L^\beta \bar{Q}_\rho \bar{u}^c H^\sigma H^\rho \bar{H}_\alpha \epsilon_{\beta\sigma}$
7	$L^\alpha Q^\beta \bar{e}^c \bar{Q}^\rho H_\rho H^\sigma H^\eta \epsilon_{\alpha\sigma}\epsilon_{\beta\eta}$
8	$L^\alpha \bar{e}^c \bar{u}^c d^c H^\beta \epsilon_{\alpha\beta}$
8^{H^2}	$L^\alpha \bar{e}^c \bar{u}^c d^c H^\beta \bar{H}^\rho H_\rho \epsilon_{\alpha\beta}$
10	$L^\alpha L^\beta L^\rho e^c Q^\sigma d^c \epsilon_{\alpha\beta}\epsilon_{\rho\sigma}$
$11a$	$L^\alpha L^\beta Q^\rho d^c Q^\sigma d^c \epsilon_{\alpha\beta}\epsilon_{\rho\sigma}$
$11b$	$L^\alpha L^\beta Q^\rho d^c Q^\sigma d^c \epsilon_{\alpha\rho}\epsilon_{\beta\sigma}$
$12a$	$L^\alpha L^\beta \bar{Q}_\alpha \bar{u}^c \bar{Q}_\beta \bar{u}^c$
$12b^*$	$L^\alpha L^\beta \bar{Q}^\rho \bar{u}^c \bar{Q}^\sigma \bar{u}^c \epsilon_{\alpha\beta}\epsilon_{\rho\sigma}$
13	$L^\alpha L^\beta \bar{Q}_\alpha \bar{u}^c L^\rho \bar{e}^c \epsilon_{\beta\rho}$
$14a$	$L^\alpha L^\beta \bar{Q}_\rho \bar{u}^c Q^\rho d^c \epsilon_{\alpha\beta}$
$14b$	$L^\alpha L^\beta \bar{Q}_\alpha \bar{u}^c Q^\rho d^c \epsilon_{\beta\rho}$
16	$L^\alpha L^\beta e^c d^c \bar{e}^c \bar{u}^c \epsilon_{\alpha\beta}$
19	$L^\alpha Q^\beta d^c d^c \bar{e}^c \bar{u}^c \epsilon_{\alpha\beta}$
20	$L^\alpha \bar{Q}_\alpha d^c \bar{u}^c \bar{e}^c \bar{u}^c$
66	$L^\alpha L^\beta H^\rho H^\sigma Q^\eta \bar{H}_\eta d^c \epsilon_{\alpha\rho}\epsilon_{\beta\sigma}$

Table 4.1.: List of relevant dimension-5, 7 and 9 $\Delta L = 2$ SMEFT operators in the Babu-Leung basis [395] that we consider in our analysis. The superscript † indicates that $\mathcal{O}_{4_b}$ is Fierz-related to $\mathcal{O}_{4_a}$.

Neutrinos are by far the lightest known fundamental fermions. From direct measurements of the tritium beta decay electron kinematic spectrum endpoint at the KATRIN experiment [397,398], the electron-flavoured row of the neutrino mass matrix $m_\nu^2 \equiv \sum_i |U_{ei}|^2 m_i^2$ is constrained to $m_\nu < 0.8$ eV at 90% C.L [399,400], where U_{ij} are the PMNS matrix elements (see Sec. 2.3.1). From neutrino oscillation data the largest squared mass difference between any two neutrino mass eigenstates is $\Delta m^2_{31} = (2.510 \pm 0.027) \times 10^{-3}$ eV^2 for normal ordering (NO) and $\Delta m^2_{32} = -(2.490^{+0.026}_{-0.028}) \times 10^{-3}$ eV^2 for inverted ordering[1] (IO), where the error ranges are given at 1σ significance [401]. Since the lightest neutrino may in principle be massless, the maximum neutrino mass splitting sets a lower limit on the most massive neutrino $m_3 \gtrsim 0.05$ eV. Lastly, the Planck collaboration has set a cosmological bound on the sum of neutrino masses $\sum m_\nu < 0.12$ eV at 95% CL [55].

Assuming a generic value for the neutrino mass that is allowed by experimental constraints, e.g. $m_\nu = 0.1$ eV, an estimated limit on the scale of LNV can be derived corresponding to a given SMEFT operator. Adapting the formalism in Refs. [393,394], we use the following recipe to obtain the diagrams that generate a neutrino mass given a single $\Delta L = 2$ SMEFT operator in the Babu-Leung basis from Tab. 4.1:

1. Draw the operator with all its external legs.

[1] Note that, per definition, the largest mass splitting is between the first and third mass eigenstates in normal ordering, but between the third and second in inverted ordering, therefore the largest squared mass splitting is denoted as Δm^2_{31} and Δm^2_{32} in normal and inverted ordering, respectively.

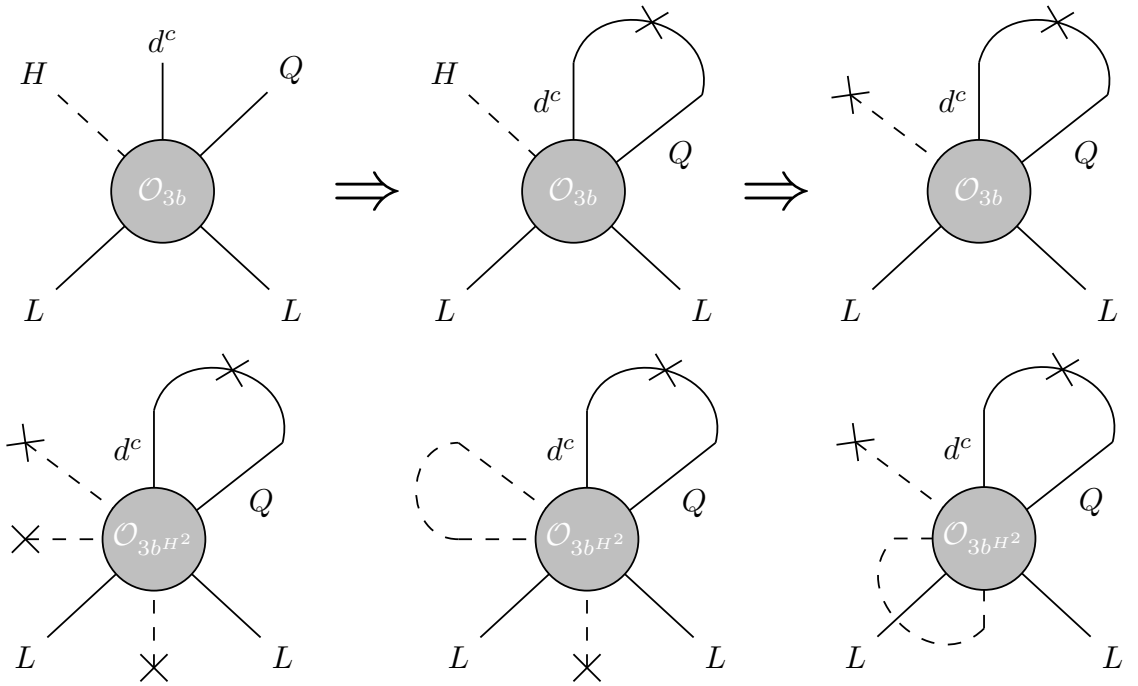

Figure 4.1.: Top row: Process of estimating the neutrino mass given the $\Delta L = 2$ SMEFT operator $\mathcal{O}_{3b}$. First the quark legs are closed into a loop, after which the Higgs field is substituted for a mass insertion.**Bottom row:** Different diagrams that contribute to the neutrino mass via operator $\mathcal{O}_{3bH^2}$.

2. Pair up the external fermion legs in all possible ways that they can be closed into loops via mass insertions, while leaving only two neutral components of lepton doublet fields left unclosed. If such neutral components are not available, use charged components or electron singlets instead.

3. For each unclosed lepton leg that is a right-handed singlet field e^c, turn it into the neutrino component of a lepton doublet field L by having it interact with the charged component of a Higgs doublet $\phi^{\pm}$ that comes either from the operator itself or from one of the other external fields or loops.

4. For each unclosed lepton leg that is a charged component of the left-handed lepton doublet, turn it into a neutrino by having it interact with a W boson that either comes from the operator itself or from another external leg or loop.

5. Close any left-over vector boson or charged components of Higgs fields into loops.

6. For each neutral component of a Higgs field, allow for both possibilities of closing it into a loop and having it give a mass insertion to the operator.

Now the appropriate diagrams should have been drawn. The following steps show how these diagrams lead to an expression for the neutrino mass:

7. Begin with the quantity $\frac{1}{\Lambda^{D-4}}$ where D is the dimension of the operator.

8. Multiply by v^m where v is the SM Higgs vev and m is the number of mass insertions from Higgs fields to the operator.

9. Multiply by vy_f^i for each fermion loop closed with a mass insertion, where y_f^i is the Yukawa coupling corresponding to SM Dirac fermion f of generation i that goes in the loop. For a flavour-specific Wilson coefficient, choose the corresponding specific index i, while for a flavour-general Wilson coefficient sum over all indices i.

10. Multiply by $\frac{1}{16\pi^2}$ for each loop, including coupling constants g for each weak interaction and y_{ij}^f for each Yukawa interaction.

11. Multiply by Λ^{2x}, where x is the number of loops in which the operator directly participates. This leads to a factor $f(\Lambda) = \left(\frac{2}{16\pi^2} + \frac{v^2}{\Lambda^2}\right)$ for each self-contracted Higgs-anti-Higgs pair $\bar{H}^\eta H_\eta$. Note that Λ^{2x} here comes as a cut-off scale that regulates the loops connected to the operator. This is not strictly allowed in a pure EFT formalism, rather it is here assumed that there is some UV-complete theory underlying the operator for which Λ is an appropriate scale [393, 394]. Therefore, the expression for the neutrino mass that we obtain in the end does not come from pure EFT, but rather from a middle ground between EFT and simplified models. In order to separate it from other methods of estimating the neutrino mass, we still call the neutrino mass obtained using the steps in this list as the *EFT-based* neutrino mass.

12. For each step where multiple choices were allowed, sum over all contributions, and finally write the whole expression as equal to the neutrino mass m_ν.

An example of this procedure is illustrated for operator $\mathcal{O}_{3b}$ in Fig. 4.1 (top row), and the different diagrams that should be summed up for operator $\mathcal{O}_{3b^{H^2}}$ are shown in Fig. 4.1 (bottom row). Due to the smallness of the neutrino mass, the procedure outlined above can put severe constraints on the scale of LNV corresponding to a given operator, for some dimension-7 operators it can be as high as $\Lambda_{\text{LNV}} \gtrsim 10^7$ GeV [1]. However, as is discussed in Sec. 5.3, these constraints depend highly on the UV-completion of the operator. Only in certain specific scenarios is this EFT mass limit applicable, and depending on the internal mass hierarchy between different heavy degrees of freedom the actual limit on the scale of LNV can be lower by several orders of magnitude [4].

The resulting LNV scales corresponding to $m_\nu = 0.1$ eV are shown in Tab. 4.2 for dimension-7 and -9 LNV operators in the Babu-Leung basis, using first generation Yukawa couplings. We see that the LNV scales vary greatly depending on the operator, ranging from 7.4×10^{-9} TeV for $\mathcal{O}_{16}$ to 5.2×10^4 TeV for $\mathcal{O}_{3b}$. Some of the scales in Tab. 4.2 would increase further if second or third generation Yukawa couplings are considered, for e.g. operator $\mathcal{O}_{4a}$ the scale corresponding to a top-quark in the loop is given by $\frac{y_t}{y_u} \times (2.4 \times 10^4)$ TeV $= 1.9 \times 10^9$ TeV. In Secs. 4.2.2 and 4.2.3 we will compare these neutrino mass scales to LNV meson decay limits.

$\mathcal{O}$	m_ν	Λ^{m_ν} [TeV]
1^{y_d}	$\frac{y_d}{16\pi^2}\frac{v^4}{\Lambda^3}$	11.6
$3a$	$\frac{y_d g^2}{(16\pi^2)^2}\frac{v^2}{\Lambda}$	69
$3a^{H^2}$	$\frac{y_d g^2}{(16\pi^2)^2}\frac{v^2}{\Lambda}f(\Lambda)$	0.4
$3b$	$\frac{y_d}{16\pi^2}\frac{v^2}{\Lambda}$	5.2×10^4
$3b^{H^2}$	$\frac{y_d}{16\pi^2}\frac{v^2}{\Lambda}f(\Lambda)$	330
$4a$	$\frac{y_u}{16\pi^2}\frac{v^2}{\Lambda}$	2.4×10^4
$4a^{H^2}$	$\frac{y_u}{16\pi^2}\frac{v^2}{\Lambda}f(\Lambda)$	150
$4b^{\dagger}$	$\frac{y_u g^2}{(16\pi^2)^2}\frac{v^2}{\Lambda}$	33
$4b^{\dagger H^2}$	$\frac{y_u g^2}{(16\pi^2)^3}\frac{v^2}{\Lambda}$	0.2
5	$\frac{y_d}{(16\pi^2)^2}\frac{v^2}{\Lambda}$	330
6	$\frac{y_u}{(16\pi^2)^2}\frac{v^2}{\Lambda}$	150
7	$\frac{y_e g^2}{(16\pi^2)^2}\frac{v^2}{\Lambda}f(\Lambda)$	0.6
8	$\frac{y_e y_d y_u g^2}{(16\pi^2)^2}\frac{v^4}{\Lambda^3}$	4.3×10^{-4}

$\mathcal{O}$	m_ν	Λ^{m_ν} [TeV]
8^{H^2}	$\frac{y_e y_d y_u g^2}{(16\pi^2)^2}\frac{v^4}{\Lambda^3}f(\Lambda)$	7.9×10^{-5}
10	$\frac{y_e y_d}{(16\pi^2)^2}\frac{v^2}{\Lambda}$	9.6×10^{-4}
$11a$	$\frac{y_d^2 g^2}{(16\pi^2)^3}\frac{v^2}{\Lambda}$	1.2×10^{-5}
$11b$	$\frac{y_d^2}{(16\pi^2)^2}\frac{v^2}{\Lambda}$	8.9×10^{-3}
$12a$	$\frac{y_u^2}{(16\pi^2)^2}\frac{v^2}{\Lambda}$	1.9×10^{-3}
$12b^*$	$\frac{y_u^2 g^2}{(16\pi^2)^3}\frac{v^2}{\Lambda}$	2.6×10^{-6}
13	$\frac{y_e y_u}{(16\pi^2)^2}\frac{v^2}{\Lambda}$	4.5×10^{-4}
$14a$	$\frac{y_u y_d g^2}{(16\pi^2)^3}\frac{v^2}{\Lambda}$	5.6×10^{-6}
$14b$	$\frac{y_d y_u}{(16\pi^2)^2}\frac{v^2}{\Lambda}$	4.1×10^{-3}
16	$\frac{y_d y_u g^4}{(16\pi^2)^4}\frac{v^2}{\Lambda}$	7.4×10^{-9}
19	$\frac{y_e y_u y_d^2 g^2}{(16\pi^2)^3}\frac{v^4}{\Lambda^3}$	2.4×10^{-6}
20	$\frac{y_e y_u^2 y_d g^2}{(16\pi^2)^3}\frac{v^4}{\Lambda^3}$	1.8×10^{-6}
66	$\frac{y_d}{16\pi^2}\frac{v^2}{\Lambda}f(\Lambda)$	330

Table 4.2.: LNV scales Λ^{m_ν} that generate a neutrino mass $m_\nu = 0.1$ eV for dimension-7 and -9 operators in the Babu-Leung basis, calculated according to the expressions in the second column of each respective table. First generation SM Yukawa couplings were used, as well as a a diagonal CKM matrix. The function $f(\Lambda)$ is given by $f(\Lambda) = \left(\frac{2}{16\pi^2} + \frac{v^2}{\Lambda^2}\right)$.

$\mathcal{O}$	$K \to \pi\nu\nu$	$\sum_i \Lambda^{\text{E949}}_{iisd}$ [TeV]
1^{y_d}	$\frac{v^3}{\Lambda^5}$	2.4
$3b$	$\frac{v}{\Lambda^3}$	11.5
$3b^{H^2}$	$f(\Lambda)\frac{v}{\Lambda^3}$	5.7
5	$\frac{1}{16\pi^2}\frac{v}{\Lambda^3}$	2.6
10	$\frac{1}{16\pi^2}\frac{y_e v}{\Lambda^3}$	0.8
$11b$	$\frac{1}{16\pi^2}\frac{y_d v}{\Lambda^3}$	0.8
$14b$	$\frac{1}{16\pi^2}\frac{y_u v}{\Lambda^3}$	2.9
66	$f(\Lambda)\frac{v}{\Lambda^3}$	5.1

Table 4.3.: List of effective dimension-6 coefficients that contribute to the rare kaon decay $K \to \pi\nu\nu$ and come from dimension-7 and -9 $\Delta L = 2$ SMEFT operators in the Babu-Leung basis. Here y_f are the Yukawa couplings of the SM fermions and Λ is the scale of NP corresponding to a single operator. The constraints in the last column are calculated using the E949 limit in Eq. (4.10).

4.2.2. Rare kaon decay

As is also discussed in Ch. 6, rare kaon decays are processes in which a kaon decays into a pion and a pair of neutrinos. This process can be LNV in case the two final state neutrinos carry the same lepton number. At dimension-7 there is only one operator in the Babu-Leung basis that can trigger this decay at short range, namely $\mathcal{O}_{3b}$. Here we focus mainly on this operator, since the 9-dimensional ones are expected to give less stringent constraints.

Contracting the $SU(2)_L$-indices of operator $\mathcal{O}_{3b}$ in a way that is relevant for rare kaon decays gives

$$\mathcal{O}_{3b} = L_i^\alpha L_j^\beta Q_a^\rho d_b^c H^\sigma \epsilon_{\alpha\rho}\epsilon_{\beta\sigma} \to h^0 d_a^c d_{L_b} \nu_{L_i} \nu_{L_j} \,. \tag{4.4}$$

In this broken phase there are two possible spinor index contractions

$$C_3^{ijab} b h^0 d_a^c d_{L_b} \nu_{L_i} \nu_{L_j} \to C_1^{ijab} h^0 \left(d_a^c d_{L_b}\right) \left(\nu_{L_i} \nu_{L_j}\right) + C_2^{ijab} h^0 \left(d_a^c \nu_{L_i}\right) \left(\nu_{L_j} d_{L_b}\right) \,, \tag{4.5}$$

and these contractions can be related via Fierz transformations [402] (c.f. Appendix B)

$$\begin{aligned} &C_1^{ijab} h^0 \left(d_a^c d_{L_b}\right) \left(\nu_{L_i} \nu_{L_j}\right) + C_2^{ijab} h^0 \left(d_a^c \nu_{L_i}\right) \left(\nu_{L_j} d_{L_b}\right) = \\ &\left(C_1^{ijab} - \frac{C_2^{ijab}}{2}\right) h^0 \left(d_a^c d_{L_b}\right) \left(\nu_{L_i} \nu_{L_j}\right) - \frac{C_2^{ijab}}{2} h^0 \left(d_a^c \sigma^{\mu\nu} d_{L_b}\right) \left(\nu_{L_j} \sigma_{\mu\nu} \nu_{L_i}\right) \,. \end{aligned} \tag{4.6}$$

The last term on the RHS of Eq. (4.7) contains a tensor interaction that vanishes for identical neutrino flavours. For the rest of this section we consider identical neutrino flavours only, such that this last term vanishes. Considering also the Hermitian conjugate of $\mathcal{O}_{3b}$ while assuming

$c_{1,2} = c_{1,2}^*$ now lets us rewrite the expression in terms of the Dirac spinors $d = (d_L, \bar{d}^c)^T$ and $\nu = (\nu_L, \bar{\nu}_L)^T$ such that

$$C_{\mathcal{O}_{3b}}^{ijab}\left(\mathcal{O}_{3b} + \mathcal{O}_{3b}^\dagger\right) = \left(C_1^{ijab} - \frac{C_2^{ijab}}{2}\right) h^0 \left[\left(\bar{d}_a d_b\right)\left(\bar{\nu}_i \nu_j\right) + \left(\bar{d}_a \gamma_5 d_b\right)\left(\bar{\nu}_i \gamma_5 \nu_j\right)\right] , \tag{4.7}$$

where only the first term contributes to the rare kaon decay due to conservation of angular momentum. From here on we absorb the two Wilson coefficients into a single LNV scale such that

$$C_1^{ijab} - \frac{C_2^{ijab}}{2} \to \frac{1}{\Lambda_{ijab}^3} . \tag{4.8}$$

As is discussed in Ch. 6, this LNV scale can be related to the branching ratio of rare kaon decays, and experimental constraints on rare kaon decays can then be used to set limits on the scale of LNV. Using the expression for the LNV rare kaon decay branching ratio from Ch. 6, the expected total number of LNC and LNV rare kaon decay events can be expressed as

$$N(K \to \pi\nu\nu) = \Big(\mathrm{BR}(K \to \pi\nu\bar{\nu})_{\mathrm{SM}} A_{\mathrm{SM}} + \mathrm{BR}(K \to \pi\nu\nu)_{\mathrm{LNV}} A_{\mathrm{LNV}}\Big) N_K , \tag{4.9}$$

where N_K is the number of kaons, and A_{SM} and A_{LNV} are the fraction of SM and LNV events that are accepted in the experiment, respectively. Using $A_{\mathrm{LNV}}/A_{\mathrm{SM}} = 0.41$ [1], constraints on the scale of LNV can be found from the expression [403]

$$\mathrm{BR}(K \to \pi\nu\bar{\nu})_{\mathrm{SM}} + \left(\frac{A_{\mathrm{LNV}}}{A_{\mathrm{SM}}}\right) \times \sum_{i\leq j=1}^{3} \mathrm{BR}(K \to \pi\nu_i\nu_j)_{\mathrm{LNV}} < 3.35 \times 10^{-10} , \tag{4.10}$$

where the experimental constraint comes from the E949 experiment [403], and where we have used $\sum_{i\leq j=1}^{3} \mathrm{BR}(K \to \pi\nu_i\nu_j)_{\mathrm{LNV}} = 3 \times \mathrm{BR}(K \to \pi\nu_1\nu_1)_{\mathrm{LNV}}$, assuming identical neutrino flavours as well as flavour universality. The constraints on LNV scales in dimension-7 and -9 operators coming from this expression can be found in Tab. 4.3. Here we see that the most stringent constraint comes from the dimension-7 operator $\mathcal{O}_{3b}$. All other operators appearing in Tab. 4.3 are 9-dimensional, and therefore we may expect their corresponding constraints to be less stringent. In the second column we also show the general expression with which the LNV scale enters into the rare kaon decay matrix element. These expressions may be compared to the estimates of the scale of LNV coming from a neutrino mass of $m_\nu = 0.1$ eV, as given in Sec. 4.2.1. We see that for most operators, though not all, the neutrino mass provides a more stringent constraint than rare kaon decays. Note however that the neutrino mass constraint should only be taken as indicative, as the true value of the neutrino mass depends on the details of the UV-completion of a given LNV operator.

The NA62 experiment provides a more stringent limit than the E949 experiment on the branching ratio of rare kaon decays $K^+ \to \pi^+\nu\bar{\nu}$, given by $\mathrm{BR}(K^+ \to \pi^+\nu\bar{\nu})_{\mathrm{NA62}} < 1.78 \times 10^{-10}$ [404]. Furthermore, for the neutral mode $K_L \to \pi^0\nu\bar{\nu}$, the KOTO experiment provides a limit $\mathrm{BR}(K_L \to \pi^0\nu\bar{\nu})_{\mathrm{KOTO}} < 3.0 \times 10^{-9}$ [405]. However, for these experiments there are no dedicated limits on the current that mediates the LNV mode, while such a limit

does exits for the E949 experiment. As is discussed in Ch. 6, both the NA62 and KOTO experiments have different relative acceptance rates for LNV and LNC currents, given by $A_{\rm LNV}/A_{\rm SM} = 0.23/0.15$ for NA62 and $A_{\rm LNV}/A_{\rm SM} = 0.64/0.30$ for KOTO [1]. Using this fact, we approximate the limit on the LNV scale for operator $\mathcal{O}_{3b}$ as $\sum_i \Lambda_{iisd} > 17.2$ TeV for $K^+ \to \pi^+\nu\nu$ at the NA62 experiment, and $\sum_i \Lambda_{iisd} > 12.3$ TeV for $K_L \to \pi^0\nu\nu$ at the KOTO experiment.

In Sec. 4.8 we compare the constraint on the dimension-7 operator $\mathcal{O}_{3b}$ with other probes of LNV. This comparison is done in the Lehman basis, for which the $\mathcal{O}_{3b}$-constraint coming from NA62 is translated into a constraint on the operator $\mathcal{O}_{\bar{d}LQLH1}$ of

$$\Lambda_{\bar{d}LQLH1} > 21.8 \text{ TeV} \tag{4.11}$$

for the charged mode $K^+ \to \pi^+\nu\nu$ and

$$\Lambda_{\bar{d}LQLH1} > 21.6 \text{ TeV} \tag{4.12}$$

for the neutral mode $K_L \to \pi^0\nu\nu$.

4.2.3. Fully leptonic kaon and pion decay

The fully leptonic decays $\pi^+ \to \mu^+\bar{\nu}_e$ and $K^+ \to \mu^+\bar{\nu}_e$ [406] could be triggered by a variety of dimension-7 operators at short range. The hadronic matrix element in fully leptonic decays of pseudoscalar mesons consists of a parity-odd current, since the initial meson is parity-odd while the vacuum is parity even[2] [407,408]. The form factors for such decays can be obtained from the vector and axial vector current form factors as

$$\begin{aligned} \langle 0|\, \bar{q}_2\gamma^\mu q_1\, |M(p)\rangle &= 0 \\ \langle 0|\, \bar{q}_2\gamma^\mu\gamma_5 q_1\, |M(p)\rangle &= -if_M p_\mu\,, \end{aligned} \tag{4.13}$$

where $M(p)$ is a meson with momentum p and decay constant f_M, consisting of the quarks q_1 and q_2. Using the equation of motion

$$i\partial_\mu\left(\bar{q}_2\gamma^\mu\gamma_5 q_1\right) = -\left(m_{q_1} + m_{q_2}\right)\bar{q}_2\gamma_5 q_1\,, \tag{4.14}$$

the scalar and pseudoscalar form factors are obtained as

$$\begin{aligned} \langle 0|\, \bar{q}_2 q_1\, |M(p)\rangle &= 0\,, \\ \langle 0|\, \bar{q}_2\gamma_5 q_1\, |M(p)\rangle &= i\frac{m_M^2}{m_{q_1} + m_{q_2}} f_M\,. \end{aligned} \tag{4.15}$$

Taking $\mathcal{O}_{3b}$ as an example, the matrix element for the process $M \to \mu^+\bar{\nu}_e$ ($M = K^+, \pi^+$) can be expressed as [1]

$$i\mathcal{M} = i\frac{v}{\Lambda^3_{ijkl}}\left(m_M^2 - m_\mu^2\right)\frac{m_M^2}{m_{q_k} + m_{q_n}} f_M\,. \tag{4.16}$$

[2]The hadronic part of fully leptonic meson decays consists of a meson decaying into vacuum, since the final state leptons are not part of any hadron.

$\mathcal{O}$	$M^+ \to \ell_i^+ \bar{\nu}_j$	$\Lambda_{e\mu us}$ [TeV]	$\Lambda_{e\mu ud}$ [TeV]
$3a$	$\frac{v}{\Lambda^3}$	2.2	1.7
$3a^{H^2}$	$f(\Lambda)\frac{v}{\Lambda^3}$	1.3	1.1
$4a$	$\frac{v}{\Lambda^3}$	2.2	1.7
$4a^{H^2}$	$f(\Lambda)\frac{v}{\Lambda^3}$	1.3	1.1
$4b^{\dagger}$	$\frac{v}{\Lambda^3}$	2.2	1.7
$4b^{\dagger H^2}$	$f(\Lambda)\frac{v}{\Lambda^3}$	1.3	1.1
6	$f(\Lambda)\frac{v}{\Lambda^3}$	1.3	1.1
7	$\frac{v^3}{\Lambda^5}$	0.8	0.7
8	$\frac{v}{\Lambda^3}$	2.2	1.7
8^{H^2}	$f(\Lambda)\frac{v}{\Lambda^3}$	1.3	1.1
$11a$	$\frac{1}{16\pi^2}\frac{y_d v}{\Lambda^3}$	0.2	0.1
$12a$	$\frac{1}{16\pi^2}\frac{y_u v}{\Lambda^3}$	0.6	0.5
$12b^*$	$\frac{1}{16\pi^2}\frac{y_u v}{\Lambda^3}$	0.7	0.6
13	$\frac{1}{16\pi^2}\frac{y_e v}{\Lambda^3}$	0.2	0.2
$14a$	$\frac{1}{16\pi^2}\frac{(y_u+y_d)v}{\Lambda^3}$	0.6	0.5
16	$\frac{1}{16\pi^2}\frac{y_e v}{\Lambda^3}$	0.1	0.1
19	$\frac{1}{16\pi^2}\frac{y_d v}{\Lambda^3}$	0.1	0.1
20	$\frac{1}{16\pi^2}\frac{y_u v}{\Lambda^3}$	0.5	0.4

Table 4.4.: List of the effective contributions to dimension-6 interactions mediating the fully leptonic LNV charged pion and kaon decays for the relevant dimension-7 and -9 $\Delta L = 2$ operators in the Babu-Leung basis. Here y_f are the Yukawa couplings of the SM fermions, Λ is the scale scale of NP corresponding to a single operator, and g is the weak coupling constant. Only operators that do not lead to the rare kaon decay $K \to \pi\nu\nu$ are listed, since those limits are expected to be stronger.

Using this matrix element to obtain the LNV decay width as a function of the LNV scale Λ_{ijkl}, the corresponding branching ratios [1]

$$\begin{aligned} \text{BR}\left(K^+ \to \mu^+ \bar{\nu}_e\right) &= 10^{-3} \left(\frac{2.9 \text{ TeV}}{\Lambda_{e\mu us}}\right)^6 , \\ \text{BR}\left(\pi^+ \to \mu^+ \bar{\nu}_e\right) &= 10^{-3} \left(\frac{2.0 \text{ TeV}}{\Lambda_{e\mu ud}}\right)^6 . \end{aligned} \tag{4.17}$$

can be compared to the 90% CL experimental constraints [406]

$$\begin{aligned} \text{BR}\left(K^+ \to \mu^+ \bar{\nu}_e\right) &< 3.3 \times 10^{-3} , \\ \text{BR}\left(\pi^+ \to \mu^+ \bar{\nu}_e\right) &< 1.5 \times 10^{-3} \end{aligned} \tag{4.18}$$

to obtain limits on the scale of LNV, as shown in Tab. 4.4. Here we show limits both for fully leptonic kaon (flavour content $e\mu us$) and pion ($e\mu ud$) decays. These constraints are generally lower than the constraint on $\mathcal{O}_{3b}$ coming from rare kaon decays. Furthermore, similar to the rare kaon decays, we see that the dimension-7 operators in Tab. 4.4 generally lead to more stringent constraints than the dimension-9 operators. In the second column of Tab. 4.4 we show the general form in which the LNV scale enters into the fully leptonic meson decay matrix element, c.f. Eq. (4.16). We only show SMEFT operators that do not trigger the rare kaon decays discussed in Sec. 4.2.2, since the constraints from those decays are more stringent.

Considering the neutrino mass constraints from Sec. 4.2.1, we see that for many operators they are more stringent than the constraints put by fully leptonic LNV decays. However, LNV scale constraints obtained from the absolute value of neutrino masses are not as strict as direct experimental constraints, since the neutrino mass can depend on the details of the UV-completion of the operator [4], as discussed in Sec. 4.2.1.

In the Lehman basis, fully leptonic LNV meson decays lead to constraints on operators $\mathcal{O}_{\bar{d}LQLH1}$, $\mathcal{O}_{\bar{d}LQLH2}$, $\mathcal{O}_{\bar{Q}uLLH}$, and $\mathcal{O}_{\bar{d}LueH}$. The analysis of these constraints are subject for future work and will not be discussed in the comparison of different LNV probes in Sec. 4.8.

4.3. Low scale probes of LNV in the Lehman basis

In this section we discuss the remaining LNV probes that are considered in this chapter, including new limits from collider searches that are subject for future publication in Ref. [4]. From here on we work in the Lehman basis, for which the dimension-7 $\Delta L = 2$ SMEFT operators are given in Tab. 4.5. An advantage of this basis is that the spinor contractions are well defined, such that the basis is not overcomplete. In Tab. 4.5 the spinor contractions are written in terms of parentheses, such that e.g. $(\psi_1\psi_2) = \psi_1^\alpha \psi_{2\alpha}$. In Sec. 4.3.1 we discuss the connection of this dimension-7 SMEFT basis to dimension-6 LEFT operators, after which we discuss different low-scale LNV probes in Secs. 4.3.2 to 4.3.8 and high-scale LHC searches in Sec. 4.4.

Type	$\mathcal{O}$	Operator
Ψ^2H^4	$\mathcal{O}^{pr}_{LH}$	$\epsilon_{ij}\epsilon_{mn}(\overline{L_p^c}^i L_r^m)H^jH^n(H^\dagger H)$
Ψ^2H^3D	$\mathcal{O}^{pr}_{LeHD}$	$\epsilon_{ij}\epsilon_{mn}(\overline{L_p^c}^i \gamma_\mu e_r)H^j(H^m iD^\mu H^n)$
$\Psi^2H^2D^2$	$\mathcal{O}^{pr}_{LHD1}$	$\epsilon_{ij}\epsilon_{mn}(\overline{L_p^c}^i D_\mu L_r^j)(H^m D^\mu H^n)$
	$\mathcal{O}^{pr}_{LHD2}$	$\epsilon_{im}\epsilon_{jn}(\overline{L_p^c}^i D_\mu L_r^j)(H^m D^\mu H^n)$
Ψ^2H^2X	$\mathcal{O}^{pr}_{LHB}$	$g\epsilon_{ij}\epsilon_{mn}(\overline{L_p^c}^i \sigma_{\mu\nu} L_r^m)H^jH^nB^{\mu\nu}$
	$\mathcal{O}^{pr}_{LHW}$	$g'\epsilon_{ij}(\epsilon\tau^I)_{mn}(\overline{L_p^c}^i \sigma_{\mu\nu} L_r^m)H^jH^nW^{I\mu\nu}$
Ψ^4D	$\mathcal{O}^{prst}_{\bar{d}uLLD}$	$\epsilon_{ij}(\overline{d_p}\gamma_\mu u_r)(\overline{L_s^c}^i iD^\mu L_t^j)$
Ψ^4H	$\mathcal{O}^{prst}_{\bar{e}LLLH}$	$\epsilon_{ij}\epsilon_{mn}(\overline{e_p}L_r^i)(\overline{L_s^c}^j L_t^m)H^n$
	$\mathcal{O}^{prst}_{\bar{d}LueH}$	$\epsilon_{ij}(\overline{d_p}L_r^i)(\overline{u_s^c}e_t)H^j$
	$\mathcal{O}^{prst}_{\bar{d}LQLH1}$	$\epsilon_{ij}\epsilon_{mn}(\overline{d_p}L_r^i)(\overline{Q_s^c}^j L_t^m)H^n$
	$\mathcal{O}^{prst}_{\bar{d}LQLH2}$	$\epsilon_{im}\epsilon_{jn}(\overline{d_p}L_r^i)(\overline{Q_s^c}^j L_t^m)H^n$
	$\mathcal{O}^{prst}_{\bar{Q}uLLH}$	$\epsilon_{ij}(\overline{Q_p}u_r)(\overline{L_s^c}L_t^i)H^j$

Table 4.5.: List of all dimension 7 $\Delta L = 2$ SMEFT operators in the Lehman basis [381, 382].

4.3.1. Connection to LEFT

Many of the LNV observables that are discussed in Sec. 4.2 involve momentum scales that are lower than the scale of EWSB $\Lambda_{\text{EW}} \approx 100$ GeV. For these probes SMEFT is not a suitable framework, since it involves fields which are only defined above Λ_{EW}, and respects the full SM gauge symmetry group unlike the physics at lower scales. Therefore it is appropriate to introduce a basis of Low energy effective field theory (LEFT) operators that can be used at low scales, and match the corresponding operators onto SMEFT at the electroweak scale in order to compare high- and low-scale observables. In Tab. 4.6 we give the complete list of dimension-6 $\Delta L = 2$ LEFT operators, and show how they match with dimension-7 SMEFT operators[3].

4.3.2. Neutrinoless double beta decay

One of the most well-studied probes of LNV is neutrinoless double beta ($0\nu\beta\beta$) decay. As opposed to ordinary beta decay, in which a neutron turns into a proton by emitting one

[3]Note that dimension-7 SMEFT operators can generally match onto LEFT operators with other mass dimensions than 6. When going from SMEFT to LEFT, the Higgs doublet is no longer an external field and can instead be written as a vev v, changing value of the Wilson coefficient and reducing the dimension of the operator by one. We find that the operators obtained in this way are often the ones most constrained by LNV observables, therefore we choose dimension-6 LEFT operators as our main focus for analysing low-scale experimental constraints.

$\mathcal{O}$	Operator	Matching
$\mathcal{O}^{S,prst}_{ev1} = \mathcal{O}^{S,prst}_{ev;LL}$	$(\overline{e_{Rp}}e_{Lr})(\overline{\nu_s^c}\nu_t)$	$C^{S,prst}_{ev1} = -\frac{v}{4}\left(2C^{prst}_{\bar{e}LLLH} + C^{psrt}_{\bar{e}LLLH} + s \leftrightarrow t\right)$
$\mathcal{O}^{S,prst}_{ev2} = \mathcal{O}^{S,prst}_{ev;RL}$	$(\overline{e_{Lp}}e_{Rr})(\overline{\nu_s^c}\nu_t)$	$C^{S,prst}_{ev2} = -v\left(C^{sr}_{LeHD}\delta^{tp} + C^{tr}_{LeHD}\delta^{sp}\right)$
$\mathcal{O}^{T,prst}_{ev} = \mathcal{O}^{T,prst}_{ev;LL}$	$(\overline{e_{Rp}}\sigma_{\mu\nu}e_{Lr})(\overline{\nu_s^c}\sigma^{\mu\nu}\nu_t)$	$C^{T,prst}_{ev} = +\frac{v}{16}\left(C^{psrt}_{\bar{e}LLLH} - C^{ptrs}_{\bar{e}LLLH}\right)$
$\mathcal{O}^{S,prst}_{dv} = \mathcal{O}^{S,prst}_{dv;LL}$	$(\overline{d_{Rp}}d_{Lr})(\overline{\nu_s^c}\nu_t)$	$C^{S,prst}_{dv} = -\frac{v}{4}(C^{psrt}_{\bar{d}LQLH1} + C^{ptrs}_{\bar{d}LQLH1})$
$\mathcal{O}^{T,prst}_{dv} = \mathcal{O}^{T,prst}_{dv;LL}$	$(\overline{d_{Rp}}\sigma_{\mu\nu}d_{Lr})(\overline{\nu_s^c}\sigma^{\mu\nu}\nu_t)$	$C^{T,prst}_{dv} = -\frac{v}{4}(C^{psrt}_{\bar{d}LQLH1} - C^{ptrs}_{\bar{d}LQLH1})$
$\mathcal{O}^{S,prst}_{uv} = \mathcal{O}^{S,prst}_{uv;RL}$	$(\overline{u_{Lp}}u_{Rr})(\overline{\nu_s^c}\nu_t)$	$C^{S,prst}_{uv} = +\frac{v}{2}\left(C^{prst}_{\bar{Q}uLLH} + C^{prts}_{\bar{Q}uLLH}\right)$
$\mathcal{O}^{S,prst}_{duve1} = \mathcal{O}^{S,prst}_{duve;LL}$	$(\overline{d_{Rp}}u_{Lr})(\overline{\nu_s^c}e_{Lt})$	$C^{S,prst}_{duve1} = -\frac{v}{2}(C^{psrt}_{\bar{d}LQLH1} - C^{ptrs}_{\bar{d}LQLH1} - C^{ptrs}_{\bar{d}LQLH2})$
$\mathcal{O}^{S,prst}_{duve2} = \mathcal{O}^{S,prst}_{duve;RL}$	$(\overline{d_{Lp}}u_{Rr})(\overline{\nu_s^c}e_{Lt})$	$C^{S,prst}_{duve2} = +vV^*_{xp}C^{xrts}_{\bar{Q}uLLH}$
$\mathcal{O}^{T,prst}_{duve} = \mathcal{O}^{T,prst}_{duve;LL}$	$(\overline{d_{Rp}}\sigma_{\mu\nu}u_{Lr})(\overline{\nu_s^c}\sigma^{\mu\nu}e_{Lt})$	$C^{T,prst}_{duve} = -\frac{v}{2}(C^{psrt}_{\bar{d}LQLH1} + C^{ptrs}_{\bar{d}LQLH1} - C^{ptrs}_{\bar{d}LQLH2})$
$\mathcal{O}^{V,prst}_{duve1} = \mathcal{O}^{V,prst}_{duve;LR}$	$(\overline{d_{Lp}}\gamma_\mu u_{Lr})(\overline{\nu_s^c}\gamma^\mu e_{Rt})$	$C^{V,prst}_{duve1} = +vV^*_{rp}C^{st}_{LeHD}$
$\mathcal{O}^{V,prst}_{duve2} = \mathcal{O}^{V,prst}_{duve;RR}$	$(\overline{d_{Rp}}\gamma_\mu u_{Rr})(\overline{\nu_s^c}\gamma^\mu e_{Rt})$	$C^{V,prst}_{duve2} = +\frac{v}{2}C^{psrt}_{\bar{d}LueH}$
$\mathcal{O}^{S,prst}_{dv;RL}$	$(\overline{d_{Lp}}d_{Rr})(\overline{\nu_s^c}\nu_t)$	no matching at dim 7 in SMEFT
$\mathcal{O}^{S,prst}_{uv;LL}$	$(\overline{u_{Rp}}u_{Lr})(\overline{\nu_s^c}\nu_t)$	
$\mathcal{O}^{T,prst}_{uv;LL}$	$(\overline{u_{Rp}}\sigma_{\mu\nu}u_{Lr})(\overline{\nu_s^c}\sigma^{\mu\nu}\nu_t)$	

Table 4.6.: List of the dimension-6 $\Delta L = 2$ LEFT operators that match onto dimension-7 SMEFT operators, along with the matching relations.

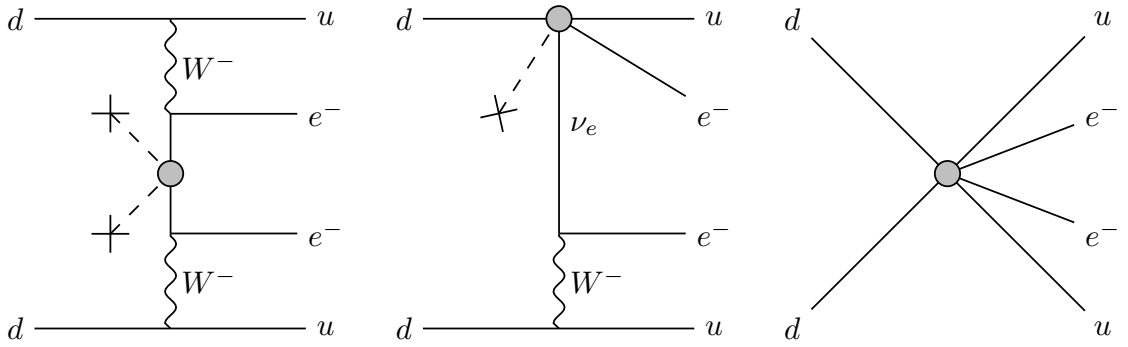

Figure 4.2.: Examples of diagrams corresponding to $0\nu\beta\beta$ decay induced by a dimension-5 (left), dimension-7 (centre), and dimension-9 (right) operator, respectively.

electron and one electron-flavoured antineutrino, $0\nu\beta\beta$ decay is a process where two neutrons beta-decay simultaneously without emitting any neutrinos or antineutrinos. The initial state consists of two neutrons, and the final state of two protons and two electrons. Baryon number is conserved, but the difference in initial and final lepton number $\Delta L = 2$ is two units, and the process is therefore LNV. Typically, a light neutrino exchange between the neutrons is assumed to trigger the double decay, in which case the process would be suppressed by a light Majorana neutrino mass insertion induced by the dimension-5 LNV operator, see Fig. 4.2 (left). However, $0\nu\beta\beta$ can also be induced by a variety of other BSM processes, such as higher dimensional LNV operators [387, 393, 394, 409–419]. At dimension-7, such operators lead to long-range contributions, meaning that the LNV process can be thought of as occurring in one nucleus rather than in the propagation of the exchanged neutrino, as shown in Fig. 4.2 (centre). For dimension-9 operators, the interaction can instead be short-range, meaning that quarks from both nuclei are present in the NP interaction, see Fig. 4.2 (right).

In the experimental search for $0\nu\beta\beta$ decay, the most stringent limits come from the Xenon isotope ${}^{136}_{54}\mathrm{Xe}$, leading to the constraint [420]

$$T_{1/2}^{\mathrm{Xe}} \equiv T_{1/2}\left({}^{136}_{54}\mathrm{Xe} \to {}^{136}_{56}\mathrm{Ba} + e^- e^-\right) > 2.3 \times 10^{26}\ \mathrm{y} \tag{4.19}$$

on the decay half life $T_{1/2}$. For $0\nu\beta\beta$ decay induced by the dimension-5 LNV operator, the decay rate can be estimated on dimensional grounds as $\Gamma^{0\nu\beta\beta}_{m_\nu} \sim m_\nu^2 G_F^4 m_F^2 Q_{\beta\beta}^5 \sim (m_\nu/0.1\ \mathrm{eV})^2 (10^{26}\ \mathrm{y})^{-1}$. Here $m_F \approx 100$ MeV is the typical energy scale involved in $0\nu\beta\beta$ decay, G_F is the Fermi constant, and the final state phase space that is available to the two electrons is proportional to $Q_{\beta\beta}^5$, where for a typical double beta decay we have $Q_{\beta\beta} = \mathcal{O}(1\ \mathrm{MeV})$. For a dimension-5 LNV operator the neutrino mass m_ν can be estimated as $m_\nu \approx v^2/\Lambda^{(5)}_{\mathrm{LNV}}$, where v is the SM Higgs vev, such that $m_\nu \approx 0.1$ eV leads to LNV scales as high as $\Lambda^{(5)}_{\mathrm{LNV}} \approx 3 \times 10^{14}$ GeV. For dimension-7, the long-range rate can be estimated as $\Gamma^{0\nu\beta\beta}_{\mathrm{LR}} \sim v^2 (\Lambda^{(7)}_{\mathrm{LNV}})^{-6} G_F^2 m_F^4 Q_{\beta\beta}^5 \sim (10^5\ \mathrm{GeV}/\Lambda^{(7)}_{\mathrm{LNV}})^6 (10^{26}\ \mathrm{y})^{-1}$. Finally, dimension-9 operators lead to the short-range rate $\Gamma^{0\nu\beta\beta}_{\mathrm{SR}} \sim (\Lambda^{(9)}_{\mathrm{LNV}})^{-8} m_F^4 Q_{\beta\beta}^5 \sim (10^5\ \mathrm{GeV}/\Lambda^{(9)}_{\mathrm{LNV}})^8 (10^{26}\ \mathrm{y})^{-1}$. Incidentally, dimension-7 and -9 operators probe similar LNV scales in $0\nu\beta\beta$ experiments.

Following Ref. [387], we write the $0\nu\beta\beta$ decay Lagrangian coming from dimension-7 SMEFT operators in the LEFT basis as

$$\begin{aligned}\mathcal{L}^{(6)}_{\Delta L=2} = \frac{2G_F}{\sqrt{2}}\Big[&C^{(6)}_{\mathrm{VL}}\ (\overline{u_L}\gamma^\mu d_L)\ (\overline{e_R}\gamma_\mu \nu^c_L) + C^{(6)}_{\mathrm{VR}}\ (\overline{u_R}\gamma^\mu d_R)\ (\overline{e_R}\gamma_\mu \nu^c_L)\\ &+C^{(6)}_{\mathrm{SL}}\ (\overline{u_R} d_L)\ (\overline{e_L}\nu^c_L) + C^{(6)}_{\mathrm{SR}}\ (\overline{u_L} d_R)\ (\overline{e_L}\nu^c_L)\\ &+C^{(6)}_{\mathrm{T}}\ (\overline{u_L}\sigma^{\mu\nu} d_R)\ (\overline{e_L}\sigma_{\mu\nu}\nu^c_L)\Big] + \text{h.c.}\end{aligned} \tag{4.20}$$

for dimension-6 LEFT operators. For a single higher dimensional operator leading to the $0\nu\beta\beta$ matrix element $M_{0\nu}$, the inverse decay half life can be written as

$$T^{-1}_{1/2} = |\epsilon|^2 G_{0\nu} |M_{0\nu}|^2\,, \tag{4.21}$$

where $G_{0\nu}$ is a phase space factor corresponding to the leptonic current and ϵ is a NP effective coupling. By connecting the dimension-7 SMEFT operators from Tab. 4.5 to the LEFT Lagrangians in Eqs. (4.20) and (**??**) according to the formalism in Sec. 4.3.1, the constraints on the scale of dimension-7 LNV operators can be calculated using the formalism in Ref. [387]. Limits on the scales of the dimension-7 operators are given by [383]

$$\begin{aligned}&\Lambda_{LeHD} > 171\ \text{TeV}\,, && \Lambda_{LHD1} > 27.9\ \text{TeV}\,,\\ &\Lambda_{LHW} > 43.7\ \text{TeV}\,, && \Lambda_{\bar{d}uLLD} > 19.6\ \text{TeV}\,,\\ &\Lambda_{\bar{d}LQLH1} > 113\ \text{TeV}\,, && \Lambda_{\bar{d}LQLH2} > 149\ \text{TeV}\,,\\ &\Lambda_{\bar{d}LueH} > 23.6\ \text{TeV}\,, && \Lambda_{\bar{Q}uLLH} > 136\ \text{TeV}.\end{aligned} \tag{4.22}$$

4.3.3. Same-sign charged lepton kaon decay

As we saw in Sec. 2.1.4, kaons are mesons consisting of one strange and one first generation quark, where one of the constituent fermions is an antiquark such that the kaon is colourless. In the decay of kaons, there are several different LNV modes that are allowed kinematically, such that they could be induced by LNV SMEFT operators. One such mode is $K^+ \to \pi^-\ell^+\ell^+$ [421–423], where $\ell \in \{e, \mu\}$. This decay cannot be mediated by dimension-7 operators at short range, and therefore dimension-9 operators are often considered instead [396, 424]. Effective long-range contributions from dimension-7 SMEFT operators can however lead to $K^+ \to \pi^-\ell^+\ell^+$ decays [388]. Such operators can be matched onto dimension-9 LEFT operators to derive constraints on the scale of LNV from experimental bounds. However, the constraints obtained in this way are generally low, for $\Lambda = 1$ TeV the predicted LNV branching ratios lie several orders of magnitude below experimental bounds [396]. We therefore do not consider experimental constraints coming from $K^+ \to \pi^-\ell^+\ell^+$ decays further.

4.3.4. Rare B-meson decay

Mesons containing one b-quark are appropriately called B-mesons. Similarly to kaons, B-mesons can potentially decay via LNV modes if e.g. dimension-7 LNV operators are realised

in nature. One well-studied scenario is the rare decay of B-mesons into an (excited) kaon and two neutrinos, $B \to K^{(*)}\nu\nu$. This mode is LNV since there are two neutrinos in the final state, rather than a neutrino and an antineutrino as in the SM decay $B \to K^{(*)}\nu\bar{\nu}$, where this latter mode is predicted by the SM but has never been observed[4]. Since the final state neutrinos in such decays are not detected directly, the LNV nature can only be observed indirectly, via an excess in the number of events as compared to the SM or in the distribution of the final state kaon. In the LEFT basis, the Lagrangian corresponding to the LNC $b \to s\nu\bar{\nu}$ transition is given by [425,426]

$$\mathcal{L} = \sum_{X=L,R} C^V_{d\nu;XL}\mathcal{O}^V_{d\nu;XL}\,, \tag{4.23}$$

while the Lagrangian corresponding to the LNV transition $b \to s\nu\nu$ is given by [425,426]

$$\mathcal{L} = \sum_{X=L,R} C^S_{d\nu;XL}\mathcal{O}^S_{d\nu;XL} + C^T_{d\nu;LL}\mathcal{O}^T_{d\nu;LL} + \text{h.c.}\,, \tag{4.24}$$

where the different operators are defined in Sec. 4.3.1. For the SM mode $b \to s\nu_\alpha\bar{\nu}_\alpha$, the only Wilson coefficient that has a sizeable contribution is given by the left-chiral vector interaction [427]

$$C^{V,sb\alpha\alpha,\text{SM}}_{d\nu;LL} = -\frac{4G_F}{\sqrt{2}}\frac{\alpha}{2\pi}V^*_{ts}V_{tb}\left(\frac{X}{\sin^2\theta_W}\right)\,, \tag{4.25}$$

where $X = 6.402\sin^2\theta_W$ comes from electroweak corrections [428], V_{ij} are the CKM matrix elements, α is the fine-structure constant, and θ_W is the weak mixing angle. The LEFT operators most relevant for LNV rare B-meson decays that can be induced by dimension-7 SMEFT operators are $\mathcal{O}^S_{d\nu;LL}$ and $\mathcal{O}^T_{d\nu;LL}$. Due to the small mass of B-mesons in comparison to the SMEFT scale Λ_{EW}, there can be a large difference in the values of the Wilson coefficients between these scales. The RG running effects from QCD between the hadronic scale of the B-meson $\Lambda_H = 4.8$ GeV and the electroweak scale Λ_{EW} can be numerically expressed as [429]

$$C^S_{d\nu;LL}(4.8\text{GeV}) = 1.4\,C^S_{d\nu;LL}(\Lambda_{\text{EW}})\,,\quad C^T_{d\nu;LL}(4.8\text{GeV}) = 0.9\,C^T_{d\nu;LL}(\Lambda_{\text{EW}})\,. \tag{4.26}$$

Experimental searches for rare B-meson decays have been performed at the BaBar [430] and Belle [431,432] experiments, both reaching sensitivities in the branching ratio a factor $\mathcal{O}$(few) above that predicted by the SM, while the future Belle II experiment is predicted to probe values as low as 10% of the SM value [433]. The predicted SM values for different $b \to s\nu\bar{\nu}$ decay branching ratios based on light-cone sum rules (LCSR) and lattice QCD [434,435] are given by [428,429]

$$\begin{aligned} &\text{BR}(B^0 \to K^0\nu\bar{\nu}) = (4.1 \pm 0.5)\times 10^{-6} && \text{BR}(B^+ \to K^+\nu\bar{\nu}) = (4.4 \pm 0.7)\times 10^{-6} \\ &\text{BR}(B^0 \to K^{*0}\nu\bar{\nu}) = (11.6 \pm 1.1)\times 10^{-6} && \text{BR}(B^+ \to K^{*+}\nu\bar{\nu}) = (12.4 \pm 1.2)\times 10^{-6}\,, \end{aligned} \tag{4.27}$$

[4]Decays with final state neutrino pairs $\nu\bar{\nu}$ or $\nu\nu$ generally have very small branching ratios, which is why we denote them as *rare*.

leading to the experimental constraints at 90% CL [430–432]

$$\begin{aligned} &\mathrm{BR}(B^0 \to K^0 \nu\bar{\nu}) < 2.6 \times 10^{-5} \qquad &&\mathrm{BR}(B^+ \to K^+ \nu\bar{\nu}) < 1.6 \times 10^{-5} \\ &\mathrm{BR}(B^0 \to K^{*0} \nu\bar{\nu}) < 1.8 \times 10^{-5} \qquad &&\mathrm{BR}(B^+ \to K^{*+} \nu\bar{\nu}) < 4.0 \times 10^{-5}\,. \end{aligned} \tag{4.28}$$

Assuming that a single LEFT operator dominates, these experimental limits lead to constraints on the LNV scale given by

$$\Lambda_{\mathcal{O}^S_{dv;LL}} > 10 \text{ TeV}, \qquad \Lambda_{\mathcal{O}^T_{dv;LL}} > 25 \text{ TeV}\,. \tag{4.29}$$

Using the matching relations in Tab. 4.6 this leads to a SMEFT constraint on the $\Delta L = 2$ SMEFT operator $\mathcal{O}_{\bar{d}LQLH1}$ given by

$$\Lambda_{\bar{d}LQLH1} > 1.9 \text{ TeV}. \tag{4.30}$$

4.3.5. Invisible kaon decay

Neutral mesons have the possibility to decay invisibly, meaning that the final state consists only of neutrinos. For LNC modes one of the final state particles is a neutrino and the other is an antineutrino, while decay modes triggered by dimension-7 LNV operators would consist of two neutrinos or two antineutrinos in the final state. For invisible LNV kaon decays $K_L \to \nu\nu$ we can express the Lagrangian in terms of LEFT Wilson coefficients as [424]

$$\mathcal{L}_{K_L \to \nu\nu} = \frac{iBF_0}{2}\Big[(C^{S,sd\alpha\beta}_{dv;LL} + C^{S,ds\alpha\beta}_{dv;LL})(\overline{\nu^C_\alpha}\nu_\beta) - (C^{S,ds\alpha\beta*}_{dv;LL} + C^{S,sd\alpha\beta*}_{dv;LL})(\overline{\nu_\alpha}\nu^C_\beta)\Big]K_L\,, \tag{4.31}$$

and similarly for K_S we have

$$\mathcal{L}_{K_S \to \nu\nu} = \frac{iBF_0}{2}\Big[(C^{S,sd\alpha\beta}_{dv;LL} - C^{S,ds\alpha\beta}_{dv;LL})(\overline{\nu^C_\alpha}\nu_\beta) - (C^{S,ds\alpha\beta*}_{dv;LL} - C^{S,sd\alpha\beta*}_{dv;LL})(\overline{\nu_\alpha}\nu^C_\beta)\Big]K_S\,. \tag{4.32}$$

Since kaons are pseudoscalar particles, a helicity-flip in one of the neutrinos is needed in order to conserve angular momentum. This makes contributions to invisible kaon decays from LNC operators suppressed by the smallness of the neutrino mass.

There is only one LEFT operator contributing to LNV invisible kaon decays that matches to a dimension-7 SMEFT operator at tree-level, namely $\mathcal{O}^S_{dv1}$, which is triggered by the SMEFT operator $\mathcal{O}_{\bar{d}LQLH1}$. From QCD running the Wilson coefficient of this operator at the scale of EWSB can be expressed in terms of its value at the chiral symmetry breaking scale Λ_χ via [424]

$$C^S_{dv1}(\Lambda_\chi) = 1.656\; C^S_{dv1}(\Lambda_{\mathrm{EW}})\,. \tag{4.33}$$

The invisible kaon decay branching ratio can then be expressed as [424]

$$\mathrm{BR}\,(K_L \to \nu\nu) = 0.014\,\frac{m_{K_L}}{\Gamma^{\mathrm{Exp}}_{K_L}}\left|\frac{BF_0}{\sqrt{G_F}}\,C_{\bar{d}LQLH1}\right|^2\,, \tag{4.34}$$

where $B = -\langle\bar{q}q\rangle_0/(3F_0^2) \simeq 2.8$ GeV [387] and $F_0 = 87$ MeV [436] are parameters related to the quark condensate. By summing up all the observed kaon branching ratios in the PDG [14] we get a limit on BR $(K_L \to \text{visible})$, which in turn can be translated into a constraint on the invisible mode as [437]

$$\text{BR}\,(K_L \to \text{invisible}) \quad < \quad 6.3 \times 10^{-4}\ (95\%\ \text{CL})\,. \tag{4.35}$$

This constraint is less stringent than that of rare kaon decays, and the subsequent constraint on the scale of LNV

$$\Lambda_{\bar{d}LQLH1} > 12.8\ \text{TeV} \tag{4.36}$$

is therefore not expected to be competitive.

4.3.6. τ decay

The only lepton that is massive enough to have hadronic decay modes is the τ. Semileptonic LNV τ decays $\tau^\pm \to \ell_\alpha^\mp P_i^\pm P_j^\pm$ with $P_{i,j}^\pm = \pi^\pm$, $K^\pm$ can potentially lead to constraints on the scale of dimension-7 SMEFT operators, with the unique feature that the constraints are specifically put on the τ-flavoured part of the Wilson coefficient. Experimental sensitivities on the branching ratios for LNV τ decays are however lower than for other observables. From the Belle experiment we have the constraints [438]

$$\begin{aligned}
&\text{BR}(\tau^- \to e^+\pi^-\pi^-) < 2.0 \times 10^{-8}\,, \quad \text{BR}(\tau^- \to \mu^+\pi^-\pi^-) < 3.9 \times 10^{-8}\,,\\
&\text{BR}(\tau^- \to e^+K^-K^-) < 3.3 \times 10^{-8}\,, \quad \text{BR}(\tau^- \to \mu^+K^-K^-) < 4.7 \times 10^{-8}\,,\\
&\text{BR}(\tau^- \to e^+K^-\pi^-) < 3.2 \times 10^{-8}\,, \quad \text{BR}(\tau^- \to \mu^+K^-\pi^-) < 4.8 \times 10^{-8}\,.
\end{aligned} \tag{4.37}$$

These limits are expected to be improved by the Belle-II experiment, giving the future limits [355, 439]

$$\begin{aligned}
&\text{BR}(\tau^- \to e^+\pi^-\pi^-) < 3 \times 10^{-10}\,, \quad \text{BR}(\tau^- \to \mu^+\pi^-\pi^-) < 7 \times 10^{-10}\,,\\
&\text{BR}(\tau^- \to e^+K^-K^-) < 6 \times 10^{-10}\,, \quad \text{BR}(\tau^- \to \mu^+K^-K^-) < 9 \times 10^{-10}\,,\\
&\text{BR}(\tau^- \to e^+K^-\pi^-) < 6 \times 10^{-10}\,, \quad \text{BR}(\tau^- \to \mu^+K^-\pi^-) < 9 \times 10^{-10}\,.
\end{aligned} \tag{4.38}$$

Even with these improvements, the future experimental limits are at least three orders of magnitude away from probing dimension-7 LNV scales of $\mathcal{O}(\Lambda_{\text{EW}})$ [440]. Therefore, LNV τ decays are not competitive probes of LNV[5].

4.3.7. μ decay

The only SM fermions that muons can decay into are electrons and neutrinos[6]. Therefore, tree-level LNV muon decays can only be induced by a single dimension-7 SMEFT operator at

[5] This picture could however change with the introduction of additional light sterile states [441–444].

[6] Note that muons are kinematically allowed to also decay into photons, as in e.g. $\mu \to e\gamma$. This mode can be used to set very stringent constraints on violation of charged lepton flavour conservation, but it is not LNV.

tree-level, namely $\mathcal{O}_{\bar{e}LLLH}$. It is worth noting that this operator does not lead to $0\nu\beta\beta$ decay at tree-level, and therefore LNV muon decays can potentially be the most sensitive probe of its corresponding scale. Below EWSB, the Lagrangian for LNV muon decays can be written as [387]

$$\begin{aligned}\mathcal{L} &= -\frac{4G_F}{\sqrt{2}}\Big\{C_{\mathrm{S}}^{\mu e}\,\bar{\mu}_R e_L\,\nu_{L,e}^T C\nu_{L,\mu} + C_{\mathrm{S}}^{e\mu}\,\bar{e}_R\mu_L\,\nu_{L,e}^T C\nu_{L,\mu} \\ &\quad + \frac{1}{4}C_{\mathrm{T}}^{\mu e}\,\bar{\mu}_R\sigma^{\mu\nu}e_L\,\nu_{L,e}^T C\sigma_{\mu\nu}\nu_{L,\mu} + \frac{1}{4}C_{\mathrm{T}}^{e\mu}\,\bar{e}_R\sigma^{\mu\nu}\mu_L\,\nu_{L,e}^T C\sigma_{\mu\nu}\nu_{L,\mu}\Big\} + \text{h.c.}\,, \end{aligned} \tag{4.39}$$

where $C_{\mathrm{S,T}}^{\mu e}$ ($C_{\mathrm{S,T}}^{\mu e*}$) mediates the LNV decay $\mu^+ \to e^+\bar{\nu}_e\bar{\nu}_\mu$ ($\mu^- \to e^-\nu_e\nu_\mu$). These Wilson coefficients can be matched onto the SMEFT Wilson coefficient of $\mathcal{O}_{\bar{e}LLLH}$ via [4]

$$\begin{aligned} C_{\mathrm{S}}^{\mu e} &= \frac{v^3}{4\sqrt{2}}\left(\mathcal{C}_{\bar{e}LLLH}^{\mu\mu\,ee} + 2\mathcal{C}_{\bar{e}LLLH}^{\mu e\,\mu e} + 3\mathcal{C}_{\bar{e}LLLH}^{\mu e\,e\mu}\right), \quad C_{\mathrm{T}}^{\mu e} = \frac{v^3}{4\sqrt{2}}\left(\mathcal{C}_{\bar{e}LLLH}^{\mu\mu\,ee} - \mathcal{C}_{\bar{e}LLLH}^{\mu e\,e\mu}\right), \\ C_{\mathrm{S}}^{e\mu} &= \frac{v^3}{4\sqrt{2}}\left(\mathcal{C}_{\bar{e}LLLH}^{ee\,\mu\mu} + 2\mathcal{C}_{\bar{e}LLLH}^{e\mu\,e\mu} + 3\mathcal{C}_{\bar{e}LLLH}^{e\mu\,\mu e}\right), \quad C_{\mathrm{T}}^{e\mu} = -\frac{v^3}{4\sqrt{2}}\left(\mathcal{C}_{\bar{e}LLLH}^{ee\,\mu\mu} - \mathcal{C}_{\bar{e}LLLH}^{e\mu\,\mu e}\right). \end{aligned} \tag{4.40}$$

The KARMEN experiment [445] has set constraints on LNV muon decay modes by searching for $\bar{\nu}_e$ neutrinos via the capture process $p\bar{\nu}_e \to e^+ n$. Since the muon-flavoured neutrino is not detected, the ability of this experiment to set constraints on the LNV mode relies on the assumption that there are no LNC flavour violating modes such as $\mu^+ \to e^+\bar{\nu}_e\nu_\mu$. Provided that this assumption holds, the branching ratio of LNV muon decays can be expressed in terms of the Wilson coefficients as [387]

$$\mathrm{BR}\left(\mu^+ \to e^+\bar{\nu}_e\bar{\nu}_\mu\right) = \frac{\Gamma\left(\mu^+ \to e^+\bar{\nu}_e\bar{\nu}_\mu\right)}{\Gamma\left(\mu^+ \to e^+\nu_e\bar{\nu}_\mu\right)} = \frac{1}{4}\left|C_{\mathrm{S}}^{\mu e}\right|^2 + \frac{3}{4}\left|C_{\mathrm{T}}^{\mu e}\right|^2, \tag{4.41}$$

and the experimental limits on the branching ratio at 90% CL are then given by [445]

$$\mathrm{BR}\left(\mu^+ \to e^+\bar{\nu}_e\bar{\nu}_\mu, \tilde{\rho} = 0.75\right) < 0.9\cdot 10^{-3}, \qquad \mathrm{BR}\left(\mu^+ \to e^+\bar{\nu}_e\bar{\nu}_\mu, \tilde{\rho} = 0.25\right) < 1.3\cdot 10^{-3}, \tag{4.42}$$

where $\tilde{\rho}$ is the Michel parameter [446], which determines how strongly the decay rate depends on the energy of $\bar{\nu}_e$. Relating the experimental limits to the Wilson coefficients leads to the constraints $|C_{\mathrm{S}}^{\mu e}| < 0.06$ and $|C_{\mathrm{T}}^{\mu e}| < 0.04$ [387]. The corresponding constraint on the scale of LNV is given by

$$\Lambda_{\bar{e}LLLH} > 0.64 \text{ TeV}. \tag{4.43}$$

4.3.8. μ^- to e^+ conversion

Experiments that search for charged lepton flavour violation in the conversion $\mu^- \to e^-$ in nuclei can potentially also be sensitive to the LNV $\mu^- \to e^+$ conversion [447, 448]. The currently most stringent limit on the LNV mode comes from conversion in Ti nuclei at the SINDRUM II experiment [449] given by

$$R_{\mu^-e^+}^{\mathrm{Ti}} \equiv \frac{\Gamma(\mu^- + \mathrm{Ti} \to e^+ + \mathrm{Ca})}{\Gamma(\mu^- + \mathrm{Ti} \to \nu_\mu + \mathrm{Sc})} < 1.7\times 10^{-12}\ (\,90\%\ \mathrm{CL})\,. \tag{4.44}$$

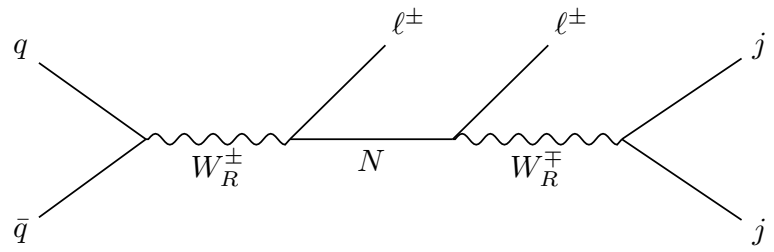

Figure 4.3.: Keung-Senjanovic diagram leading to $pp \to \ell^{\pm}\ell^{\pm}$ at colliders.

Near-future experiments such as Mu2e [447] and COMET [450] are expected to significantly improve the constraints on the LNC mode, with the projected limits

$$\begin{aligned} \text{Mu2e:} \quad & R^{\text{Al}}_{\mu^- e^-} > 6.6 \times 10^{-17} \text{ (90\% CL)}, \\ \text{COMET Phase-I:} \quad & R^{\text{Al}}_{\mu^- e^-} > 7.2 \times 10^{-15} \text{ (90\% CL)}. \end{aligned}$$

Both of these experiments will be sensitive to the charge of the outgoing lepton, and therefore they can also possibly set constraints on μ^- to e^+ conversion. This latter mode can be used to set constraints on the scale of LNV in the context of $\Delta L = 2$ SMEFT operators [451]. However, both current and future experimental sensitivities in μ^- to e^+ conversion are not stringent enough to probe dimension-7 LNV scales of $\mathcal{O}(\Lambda_{\text{EW}})$, and therefore these modes are not competitive with other experimental searches[7].

4.4. LHC

LNV can be studied at high-energy colliders via dijet plus same-sign dilepton final states without missing energy. At the LHC, such a signal can be obtained from the process

$$pp \to \ell^{\pm}\ell^{\pm} jj + X\,, \tag{4.45}$$

where $\ell \in \{e, \mu, \tau\}$, and where X stands for possible hadronic or electromagnetic fields that accompany the signal. Concretely, we use $X \in \{\text{nothing}, j, a\}$, where j is a jet and a is a photon, and keep the kinematic cuts for these additional particles to their default values. Other possible final state particles such as a physical Higgs boson h or a Z boson do not contribute significantly to the cross section. A jet pair $X = jj$ does contribute with a factor $\mathcal{O}(\text{few})$ less than a single jet $X = j$. However, an additional jet pair $X = jj$ increases the computation time significantly, and we therefore omit it in the following analysis. In models with a $SU(2)_R \times SU(2)_L$ symmetry that contain massive Majorana fermion fields N and heavy right-handed gauge bosons W_R, the interaction in Eq. (4.45) can be transmitted via the Keung-Senjanovic diagram [452] shown in Fig. 4.3, in which a W_R boson is produced in a collision between protons, after which it decays to two same-sign leptons and two jets via

[7] Note that μ^- to e^+ conversion can only occur at long range for dimension-7 operators. Similar to $0\nu\beta\beta$ decay, short-range μ^- to e^+ conversion requires at least dimension-9 operators.

an intermediate right-handed neutrino N and an additional W_R. Similar topologies can also arise in models that contain Majorana fermions as well as additional heavy scalar fields [453]. Collider signatures of UV-completions to the LNV dimension-7 operators $\mathcal{O}_{LH}$ and $\mathcal{O}_{LeHD}$ are discussed in detail in Ref. [389] and Ref. [415], respectively. For other considerations of LNV at the LHC see e.g. Refs. [454–456].

From a model-agnostic perspective, the scale of LNV in dimension-7 operators can be constrained using the non-observation of same-sign dilepton signals at LHC searches. It is also possible to put severe constraints on high-scale leptogenesis given a potential LNV signal [457], since the process that mediates the LNV interaction at the LHC should also contribute to effective washout at relatively low scales.

In Ref. [458], the collider signatures of the dimension-5 LNV operator $\ell^\pm\ell'^\pm W^\mp W^\mp$, which can be matched to the dimension-7 SMEFT operator $\mathcal{O}_{LDH1}$, were discussed in the context of neutrino masses. At the SMEFT level, possible muon-channel collider signatures of LNV vector boson fusion processes using the dimension-5 Weinberg operator $\mathcal{O}_{LH}^{(5)} = \epsilon_{ij}\epsilon_{mn}(\overline{L^c}^i L^m)H^j H^n$ were studied in Refs. [459, 460].

Collider limits on the scale of LNV in all dimension-7 $\Delta L = 2$ SMEFT operators are presented in this section, where the results are subject for publication in Ref. [4]. The operators were implemented using FeynRules [461], where a corresponding model file containing each dimension-7 operator we consider is given in Appendix F. The LO cross sections calculated using MadGraph5_aMC@NLO [462] using the commands

```
generate p p > e+ e+ j j QED=2 QCD=0
add process p p > e- e- j j QED=2 QCD=0
add process p p > e+ e+ j j j QED=2 QCD=2
add process p p > e- e- j j j QED=2 QCD=2
add process p p > e+ e+ j j a QED=3 QCD=0
add process p p > e- e- j j a QED=3 QCD=0
```

for a final state same-sign electron pair, with the kinematic cuts shown in Tab. 4.7. For a muon pair, the `e` is simply swapped for `mu`. These cuts are identical to the ones used by the ATLAS collaboration in Ref. [463], which allows for effective data comparison based on the non-observation of LNV events. For the PDFs the set NNPDF30 was used, which was provided by LHAPDF6 [464], while hadronisation was handled by Pythia8 [465] and detector simulation by Delphes3 [466].

With this set-up we get a similar but not identical result as Ref. [459] for a LHC vector-boson-fusion cross section with the dimension-5 LNV SMEFT operator. Comparing the benchmark scenario $m_N = 0.3$ GeV and $\Lambda_{\text{LNV}} = 200$ TeV, we obtain the LO cross-section 0.107 ab while in Ref. [459] the NLO cross section 0.361 ab is reported. This difference could e.g. come from a different treatment of the additional final states represented by X, the fact that their cross section is at NLO while we evaluate it at LO, or the different treatment of jet clustering, where in Ref. [459] the authors use the package Fastjet [467], while we do not.

Similarly comparing the LNV vector boson fusion via a $\ell^\pm\ell^\pm W^\mp W^\mp$ operator, we obtain a cross section 4.1 pb for $\Lambda_{\text{LNV}} = 1$ TeV while in Ref. [458] a cross section of 4.5 pb is reported.

Cuts for $pp \to \ell^\pm\ell^\pm jj$ at $\sqrt{s} = 13$ TeV	
$p_T^{\ell^{1(2)}} > 30$ GeV	$p_T^{j^{1(2)}} > 100$ GeV
$H_T > 400$ GeV	$\eta^{j^{1(2)}} < 2.0$
$\eta^{e^{1(2)}} < 2.47$	$\eta^{\mu^{1(2)}} < 2.5$
$m_{\ell^1\ell^2} > 400$ GeV	$m_{j^1j^2} > 110$ GeV
Changes for $\sqrt{s} = 100$ TeV	
$\eta^{\ell^{1(2)}} < 4.5$	$\eta^{j^{1(2)}} < 4.0$
$m_{\ell^1\ell^2} > 700$ GeV	$m_{j^1j^2} > 200$ GeV

Cuts for $pp \to \ell^\pm\ell^\pm tb$ at $\sqrt{s} = 13$ TeV	
$p_T^{\ell^{1(2)}} > 30$ GeV	$p_T^b > 100$ GeV
$\eta^b < 2.0$	$\eta^{e^{1(2)}} < 2.47$
$\eta^{\mu^{1(2)}} < 2.5$	$m_{\ell^1\ell^2} > 400$ GeV
Changes for $\sqrt{s} = 100$ TeV	
$\eta^{\ell^{1(2)}} < 4.5$	$\eta^b < 4.0$
$m_{\ell^1\ell^2} > 700$ GeV	

Table 4.7.: The cuts used in the evaluation of $\sigma(pp \to jj\ell^\pm\ell^\pm)$ (left) and $\sigma(pp \to tb\ell^\pm\ell^\pm)$ (right) at collider experiments. Here the final state tb corresponds to $\bar{t}b$ for a positively charged lepton pair $\ell^+\ell^+$ and $t\bar{b}$ for a negatively charged pair $\ell^-\ell^-$. In the dijet final state process the cuts are reproduced from Ref. [463] such that the LNV scale can be constrained using the data therein. The cuts used in the tb final state process are constructed to be as similar as possible to the cuts for the dijet final state process for better comparison between the two. The scaling of the cuts for the FCC process in rapidity and invariant mass account for the increased centre-of-mass energy.

This discrepancy could come from a difference in the implementation of the $\ell^\pm\ell^\pm W^\mp W^\mp$ operator. In order to have a consistency check with our subsequent implementation of dimension-7 SMEFT operators, we started with the dimension-9 operator $\overline{\ell_R^c}\ell_R\left(\tilde{\phi}^\dagger D_\mu\phi\right)^2$ and broke it to the $SU(3)_c \times U(1)_{em}$ symmetric level, while in Ref. [458] the starting point could have been the already broken phase. It is possible that partial cancellations occur from different broken-phase operators corresponding to the dimension-9 SMEFT operator in our case. Furthermore, it is not clear in Ref. [458] which PDF set is used, and a difference in the PDFs could cause further discrepancies.

The cuts in Tab. 4.7 are given in terms of the pseudorapidity $\eta^a \equiv -\ln\left(\tan\frac{\theta^a}{2}\right)$, where θ^a is the angle between the momentum of particle a and the beam axis, transverse momentum $p_T^a = |\vec{p}_a \cdot (\hat{y} + \hat{x})|$, and invariant mass $m_{ab} = \sqrt{2p_T^a p_T^b\left[\cosh(\eta_a - \eta_b) - \cos(\phi_a - \phi_v)\right]}$, where ϕ is the azimuthal angle with respect to the beam. The quantity $H_T \equiv \sum_i p_T^{j^i}$ is the sum of the transverse momenta of the final state jets.

In Tab. 4.8, the cross sections for the process $pp \to \ell^\pm\ell'^\pm jj + X$ corresponding to all 7-dimensional $\Delta L = 2$ LNV operators are presented for both the FCC-hh with $\sqrt{s} = 100$ TeV and the LHC with $\sqrt{s} = 13$ TeV. These cross sections were calculated for two quark generations under the assumption that $\mathcal{C}^{1/3}/\Lambda = 1$ TeV^{-1}. The scaling of the cross sections with respect

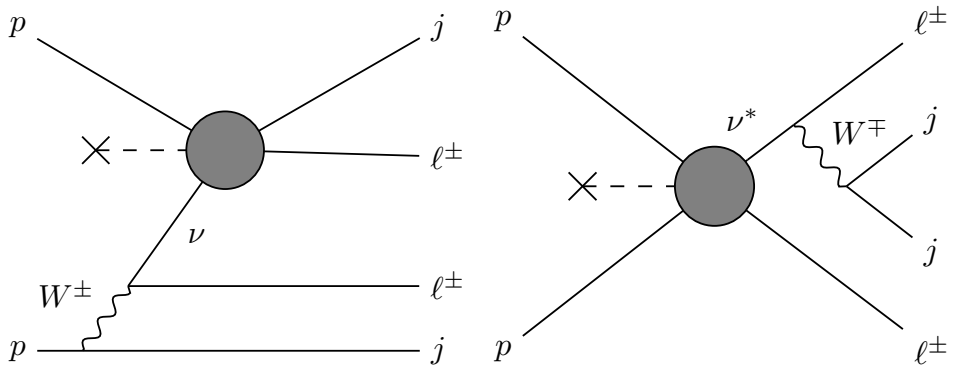

Figure 4.4.: Diagrams that correspond to same-sign dilepton plus dijet production at colliders via $\Delta L = 2$ dimension-7 operators that contain four fermions.

to Λ for all operators is found to follow the relation

$$\sigma(pp \to \ell^\pm \ell^\pm jj + X) = \sigma_0 \times \Lambda^{-1/6}\,, \tag{4.46}$$

as is shown in Fig. 4.6, where σ_0 corresponds to the cross section found using $\mathcal{C}^{1/3}/\Lambda = 1\ \text{TeV}^{-1}$. Exclusion limits on the scale of LNV corresponding to the different operators can be found using the asymptotic formula [468]

$$Z_0 = \sqrt{2\left(s - b\ln\left(\frac{s+b}{b}\right)\right)}\,, \tag{4.47}$$

where $s = \mathcal{L} \times \sigma(pp \to \ell^\pm \ell^\pm jj + X)$ is the number of signal events that is expected for a given luminosity $\mathcal{L}$, b is the number of background events, and Z_0 is the statistical significance. The expected number of background events for an integrated luminosity of $\mathcal{L}_0 = 36.1\ \text{fb}^{-1}$ is given by the ATLAS collaboration as $b = 11.2$. Following Ref. [469] we assume that b scales linearly with the luminosity and therefore use $b = 11.2 \times \mathcal{L}/(36.1\text{fb}^{-1})$. By solving Eq. (4.47) for $Z_0 = 1.96$ we find the 95% CL limits on the scale Λ_{LNV} for the different dimension-7 operators, as shown in Tab. 4.8. Assuming that a similar number of background events is expected at FCC-hh [184] per integrated luminosity, projected future 95% CL limits assuming a search for $pp \to \ell^\pm \ell^\pm jj$ at FCC-hh are also shown in Tab. 4.8 with the modified 100 TeV-cuts from Tab. 4.7, using an integrated luminosity of 30 ab^{-1}.

The cross sections corresponding to the LNV process $pp \to \ell^\pm \ell^\pm tb + X$ for the dimension-7 operators are also shown in Tab. 4.8, where t and b represent top- and bottom-quarks, respectively. The pair tb in the final state denotes $\bar{t}b$ for a positive lepton pair $\ell^+\ell^+$ and $t\bar{b}$ for a negative lepton pair $\ell^-\ell^-$. These processes containing third generation quarks are interesting as a complementary search to the dijet final state due to the difference in topologies. In the Feynman gauge we can have final state charged Goldstone bosons that decay into a pair of quarks and antiquarks, where the decay width is greatest for third generation fermions. As is shown in Fig. 4.5 (left), this kind of topology involves two charged leptons of the same sign entering the dimension-7 operator directly. This effectively reduces the number of mediators

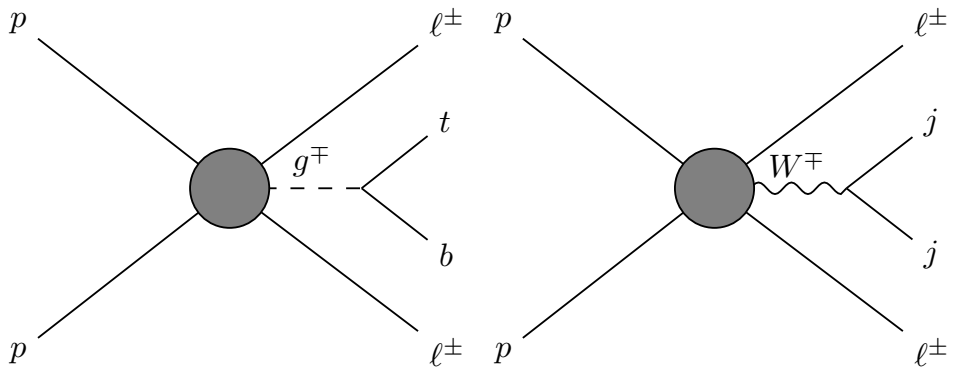

Figure 4.5.: Left: Diagram corresponding to the production of same-sign dilepton plus a third generation quark-antiquark pair at colliders for LNV dimension-7 operators that contain four fermions. **Right:** Diagram corresponding to same-sign dilepton plus dijet production for operator $\mathcal{O}_{\bar{d}uLLD}$.

from two to one compared with the W boson-mediated diagrams (c.f. Fig. 4.4 left and right), and removes the need of an additional mass insertion. For third generation final states, the cross section of the Goldstone boson-mediated process is therefore greater than that of the W boson-mediated one. However, no limits on the LNV scale can be drawn using this mode since there have been no specifically dedicated searches for it (to the knowledge of the author).

As seen in Tab. 4.8, the operators of type $\Psi^4 H$ all have similar cross sections for the same-sign dilepton process. There are still minor differences between the different cross sections, which come from a variety of effects.

For the given the $SU(2)_L$ structure of an operator, there are usually many different diagrams corresponding to $pp \to jj\ell^\pm\ell^\pm$ that can be drawn. As an example, we note that $\mathcal{O}_{\bar{d}LQLH2}$ leads to a greater number of diagrams than $\mathcal{O}_{\bar{d}LQLH1}$ since the structure of $SU(2)_L$ indices features a contraction of the two lepton doublets with each other in the former, but the quark- and Higgs doublets in the latter, leading to a factor two difference in the number of possibilities to generate diagrams of the topology shown in Fig. 4.4 (left). For $\mathcal{O}_{\bar{d}LQLH2}$ there is an ambiguity in which lepton doublet should correspond to the neutrino and which to the charged lepton, while for $\mathcal{O}_{\bar{d}LQLH1}$ there is no such ambiguity. Note however that these two $SU(2)_L$ contractions of $\mathcal{O}_{\bar{d}LQLH2}$ come with a different sign, due to the structure of the Levi-Civita tensor, which effectively leads to a reduction of the cross section in diagrams where both leptons are in the final state, i.e. diagrams with the topology shown in Fig. 4.4 (right). Such diagrams are relatively more dominant at higher collision energies, which is why the cross sections coming from $\mathcal{O}_{\bar{d}LQLH1}$ and $\mathcal{O}_{\bar{d}LQLH2}$ compare differently at the LHC and FCC.

Another effect that changes the cross section in operators with four fermions comes from the number of up-type quarks it can contain. In protons the prevalence of up-type quarks is greater than that of down-type quarks, and therefore a greater number of up-type quarks in an operator generally leads to higher cross sections. This is the reason that the cross section

Operator	$\sigma(pp \to \ell^\pm\ell^\pm jj + X)$ (pb)		$\sigma(pp \to \ell^\pm\ell^\pm tb + X)$ (pb)		Λ_{LNV}	$\Lambda_{\text{LNV}}^{\text{future}}$
	LHC	FCC	LHC	FCC		
$\mathcal{O}_{\bar{d}LueH}$	2.9×10^{-5}	0.12	1.8×10^{-4}	3.9	0.72	5.1
$\mathcal{O}_{\bar{d}LQLH1}$	2.8×10^{-5}	0.081	2.3×10^{-4}	4.8	0.71	4.8
$\mathcal{O}_{\bar{d}LQLH2}$	2.8×10^{-5}	0.030	7.6×10^{-7}	2.8×10^{-3}	0.71	4.1
$\mathcal{O}_{\bar{Q}uLLH}$	8.2×10^{-5}	0.29	8.3×10^{-4}	22	0.85	6.0
$\mathcal{O}_{LDH1}$	8.7×10^{-7}	6.8×10^{-3}	1.8×10^{-8}	0.015	0.40	3.2
$\mathcal{O}_{LDH2}$	2.1×10^{-8}	2.1×10^{-5}	1.9×10^{-8}	2.4×10^{-3}	0.22	1.2
$\mathcal{O}_{LeHD}$	1.3×10^{-9}	1.1×10^{-7}	5.7×10^{-9}	3.1×10^{-6}	0.13	0.51
$\mathcal{O}_{\bar{d}uLLD}$	0.023	2.9×10^{3}	1.0×10^{-4}	390	2.2	28
$\mathcal{O}_{LH}$	1.3×10^{-8}	3.6×10^{-6}	6.2×10^{-9}	1.2×10^{-6}	0.20	0.91

Table 4.8.: Cross sections and constraints on the scale of LNV corresponding to same-sign dilepton searches at both the LHC and FCC, using the cuts from Tab. 4.7. The cross sections for the collider processes $pp \to \ell^\pm\ell^\pm jj + X$ and $pp \to \ell^\pm\ell^\pm tb + X$ are given in the second to fifth columns, where X denotes additional hadronic or electromagnetic contributions. All cross sections presented here are calculated under the assumption that the scale of LNV is realised at 1 TeV such that $\mathcal{C}^{1/3}/\Lambda = 1\ \text{TeV}^{-1}$. The limits on the scale of LNV shown in the last and second-to-last columns are given at 95% CL in units of TeV. The exclusion limits Λ_{LNV} are derived using the non-observation of same-sign dilepton events at the ATLAS experiment [463], while $\Lambda_{\text{LNV}}^{\text{future}}$ is the scale which could potentially be excluded at 95% CL by searches at FCC-hh [184] for an integrated luminosity of 30 ab^{-1}. Both limits on the scale of LNV correspond to same-sign dilepton plus dijet searches.

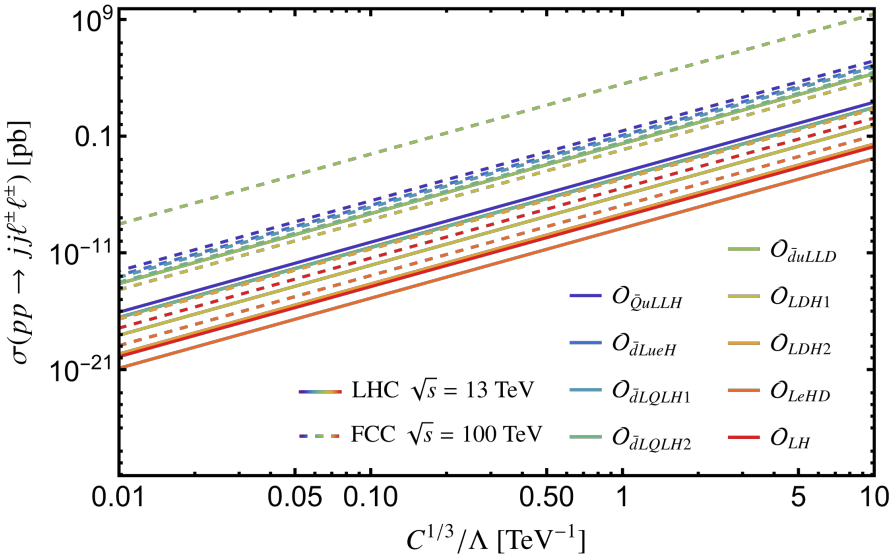

Figure 4.6.: Cross sections corresponding to the process $pp \to jj\ell^\pm\ell^\pm$ at the LHC (solid lines) and FCC-hh (dashed lines) as a function of the LNV scale, evaluated using the cuts given in Tab. 4.7.

corresponding to $\mathcal{O}_{\bar{Q}uLLH}$ is higher than that of the other four-fermion operators.

One cross section that sticks out in Tab. 4.8 is the one that corresponds to $\mathcal{O}_{\bar{d}uLLH}$. This cross section is significantly higher than the others, and the reason for this is that $\mathcal{O}_{\bar{d}uLLH}$ leads to a unique topology that involves a final state W boson, as shown in Fig. 4.5 (right). For this diagram there is only a single external mediator, yet still there is no need to have a Goldstone boson, such that the final state quarks may also be of the first or second generation.

Out of the twelve $\Delta L = 2$ dimension-7 operators, three do not lead to the process $pp \to \ell^\pm\ell^\pm jj$ at tree-level, namely $\mathcal{O}_{\bar{e}LLLH}$, $\mathcal{O}_{LHB}$ and $\mathcal{O}_{LHW}$. The operators $\mathcal{O}_{LHB}$ and $\mathcal{O}_{LHW}$ are both antisymmetric in flavour indices. Searches involving these operators must therefore include a differently flavoured same-sign lepton pair $\ell^\pm\ell'^\pm$ in the final state, where $\ell \neq \ell'$. Additionally, operator $\mathcal{O}_{LHB}$ involves only neutral gauge bosons, which means that the electromagnetic charge must be compensated for by a charged Goldstone boson for each charged lepton in the operator. This leads to a very strong suppression with respect to $\mathcal{O}_{LHW}$ for processes with a charged dilepton final state.

The operator $\mathcal{O}_{\bar{e}LLLH}$ leads to processes $pp \to \ell^\pm\ell^\pm\ell'^\pm\ell''^\mp jj + X$ at tree-level, where $\ell', \ell'' \in \{e, \mu\}$ with no constraint on identical flavour, while $\mathcal{O}_{LHB}$ and $\mathcal{O}_{LHW}$ both lead to $pp \to \ell^\pm\ell'^\pm jj + X$ where $\ell \neq \ell'$. The cross sections corresponding to these processes are shown in Tab. 4.9, where the cuts from Tab. 4.7 have been used. For the $pp \to \ell^\pm\ell^\pm\ell'^\pm\ell''^\mp jj + X$ process, the lepton cuts apply to all leptons. We see that with four leptons in the final state the cross section is very small, and it may therefore be doubtful whether or not $\mathcal{O}_{\bar{e}LLLH}$ can possibly lead to LNV signals at the LHC. The cross sections with $\ell^\pm\ell'^\pm$ in the final state,

Operator	LHC	FCC	LHC	FCC
	$\sigma(pp \to \ell^\pm\ell^\pm\ell'^\pm\ell''^\mp jj + X)$ (pb)		$\sigma(pp \to \ell^\pm\ell^\pm\ell'^\pm\ell''^\mp tb + X)$ (pb)	
$\mathcal{O}_{\bar{e}LLLH}$	3.6×10^{-16}	7.9×10^{-21}	3.1×10^{-23}	1.1×10^{-18}
	$\sigma(pp \to \ell^\pm\ell'^\pm jj + X)$ (fb)		$\sigma(pp \to \ell^\pm\ell'^\pm tb + X)$ (fb)	
$\mathcal{O}_{LHB}$	2.21×10^{-10}	3.6×10^{-6}	7.3×10^{-12}	9.6×10^{-9}
$\mathcal{O}_{LHW}$	1.382×10^{-6}	2.0×10^{-4}	2.0×10^{-8}	6.2×10^{-6}

Table 4.9.: Cross sections corresponding to same-sign dilepton processes $pp \to \ell^\pm\ell^\pm\ell'^\pm\ell''^\mp(jj/tb) + X$ with $\ell, \ell', \ell'' \in \{e, \mu\}$ for operator $\mathcal{O}_{\bar{e}LLLH}$ and the non-flavour diagonal process $pp \to \ell^\pm\ell'^\pm jj + X$ with $\ell \neq \ell'$ for operators $\mathcal{O}_{LHB}$ and $\mathcal{O}_{LHW}$, evaluated using the cuts in Tab. 4.7 under the assumption of a LNV scale at 1 TeV such that $\mathcal{C}^{1/3}/\Lambda = 1\ \text{TeV}^{-1}$.

corresponding to operators $\mathcal{O}_{LHB}$ and $\mathcal{O}_{LHW}$, are comparable to the same-flavour dilepton pair cross sections in Tab. 4.8. A dedicated collider search for $pp \to \ell^\pm\ell'^\pm jj$ may therefore be of interest, as it could potentially lead to constraints on LNV scales of $\mathcal{O}(1\ \text{TeV})$. Such searches have been made, c.f. e.g. Ref. [470], and the analysis of this mode with respect to dimension-7 LNV is reserved for future work.

4.5. Limitations on the applicability of the EFT formalism

As discussed in Sec. 2.3.3, the momentum scales involved in a given process must be sufficiently small for EFT to be an accurate description. The EFT expansion of a mediator that contains a particle of mass M_{med} is given by

$$\frac{1}{Q^2 - M_{\text{med}}^2} = -\frac{1}{M_{\text{med}}^2}\left(1 + \frac{Q^2}{M_{\text{med}}^2} + \mathcal{O}\left(\frac{Q^4}{M_{\text{med}}^4}\right)\right), \tag{4.48}$$

where Q^2 is the square of the momentum exchanged by the mediator. If Q^2 is large compared to the squared mediator mass M_{med}^2, this expansion is invalid, and the EFT method becomes a bad tool to describe the given process. A requirement in order for the EFT to be valid is therefore that the condition $M_{\text{med}}^2 > Q^2$ holds. For observables in which only small momentum scales are involved, such as e.g. $0\nu\beta\beta$ decay, this condition poses no problem since the NP scales being probed are presumably high enough to validate the expansion in Eq. (4.48). For high-energy observables however, such as e.g. the LHC where Q^2 can be quite large, it is important to take the limitations of the EFT framework into account, such that it is not used it beyond its validity [471–473].

Following Ref. [472], a lower limit on the mass M_{med} can be found by taking the average of the transferred momentum in proton-proton collisions at the parton level. Since there may be

many different topologies that enter into the LHC processes, there is no way to calculate a general averaged momentum transfer which is applicable to all diagrams directly. To obtain a useful limit on M_{med} we therefore take the most extreme topology where the transferred momentum is expected to be the highest, in which the partons directly enter into the LNV operator, as illustrated in Fig. 4.4 (right). Such diagrams lead to the most stringent constraints, and the limits obtained therefrom should therefore be viewed as conservative.

In the collision of two partons q_1 and $\bar{q}_2$, with parton distribution functions (PDFs) f_{q_1} and $f_{\bar{q}_2}$, respectively, the squared transferred momentum Q^2 is given by

$$Q^2 = (x_1 + x_2)^2 \frac{s}{4}, \tag{4.49}$$

where x_1 and x_2 are the momentum fractions[8] carried by the two partons, respectively. Assuming that protons contain four quark flavours[9], the average $\langle Q^2 \rangle$ of the squared momentum transfer for the topology shown in Fig. 4.4 (right) can then be estimated as

$$\langle Q^2 \rangle = \frac{\sum_{q_1=u,c} \sum_{q_2=d,s} \int dx_1 dx_2 \left(f_{q_1}(x_1) f_{\bar{q}_2}(x_2) + f_{q_1}(x_2) f_{\bar{q}_2}(x_1) \right) \Theta(Q - Q_0) Q^2}{\sum_{q_1=u,c} \sum_{q_2=d,s} \int dx_1 dx_2 \left(f_{q_1}(x_1) f_{\bar{q}_2}(x_2) + f_{q_1}(x_2) f_{\bar{q}_2}(x_1) \right) \Theta(Q - Q_0)}. \tag{4.50}$$

Here Θ is the Heaviside function and Q_0 is the minimum transferred momentum, which can be estimated as the sum of the lower limits on the invariant masses of the lepton and jet pairs that are used in the cuts (c.f. Tab. 4.7) such that we have $Q_0 = 510$ GeV. Using the PDF set NNPDF30 [464] and setting Q_0 to be the renormalisation scale for the PDFs, the average momentum transfer $\langle Q^2 \rangle^{1/2} \approx 1200$ GeV can be obtained using the centre-of-mass energy $\sqrt{s} = 13$ TeV [4].

The mediator in Eq. (4.48) couples to two vertices in a given decay or scattering diagram, and we choose to denote the corresponding coupling constants by λ_1 and λ_2. If we assume that only a single mediator mass scale is involved in the different dimension-seven $\Delta L = 2$ operators, this leads to a lower limit on the scale of LNV given by

$$\Lambda_{\text{LNV}} = M_{\text{med}} / (\lambda_1 \lambda_2)^{1/3}. \tag{4.51}$$

For a constraint on the coupling we can take the perturbative limit[10] $\lambda_1, \lambda_2 < 4\pi$, such that the lower limit on the scale of LNV for a given mediator mass is given by $\Lambda_{\text{LNV}} > (4\pi)^{-2/3} M_{\text{med}} \approx 0.185 \times M_{\text{med}}$. Combining this with the constraint $\langle Q^2 \rangle^{1/2} \gtrsim 1200$ GeV coming from the momentum transfer, the limit on LNV scales of dimension-7 operators that can be probed at the LHC is given by $\Lambda_{\text{LNV}} \gtrsim 220$ GeV. However, this lowest scale only applies to coupling constants that are very close to the perturbative limit, if they are smaller the limit on the scale of LNV should be higher, with a scaling behaviour described by Eq. (4.51) .

[8] These momentum fractions represent how much of the total momentum of the proton is carried by the partons in question. Typically, in proton-proton collisions with a centre-of-mass energy $\sqrt{s} = 13$ TeV, a single proton has an energy of 6.5 TeV, and a parton with $x = 0.5$ therefore has the energy of 3.25 TeV.

[9] Protons contain not just two up-type quarks and one down-type quark, but in fact a whole sea of quark-antiquark pairs, as discussed in Sec. 2.1.4.

[10] Another way to limit the couplings is by using the unitarity of the S-matrix rather than the requirement that the interaction is perturbative, see e.g. Ref. [474].

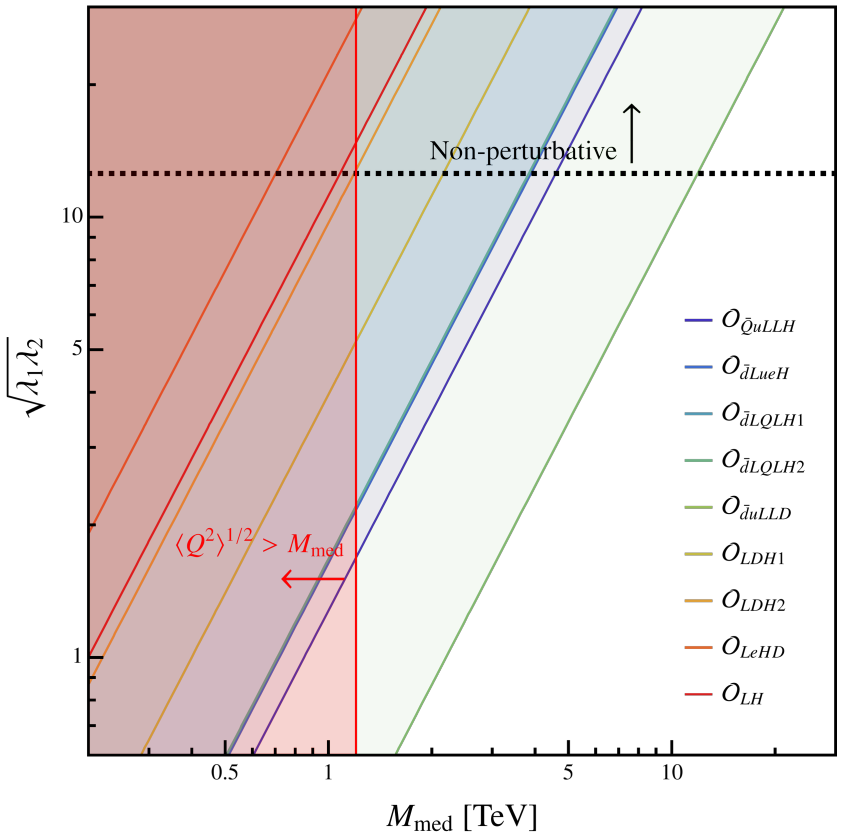

Figure 4.7.: LHC constraints on the LNV scale corresponding to dimension-7 $\Delta L = 2$ operators as a function of the effective mediator mass $M_{\rm med}$ and coupling $\sqrt{\lambda_1\lambda_2}$. The red-shaded area in the low-$M_{\rm med}$ side of the plot shows where the EFT approach is invalid due to the fact that the average momentum scales involved are larger than the effective mediator mass $M_{\rm med}$. The various other coloured regions are excluded by LHC same-sign dilepton searches at 95% CL for the different dimension-7 operators, and the black dashed line indicates the perturbative limit $\sqrt{\lambda_1\lambda_2} = 4\pi$.

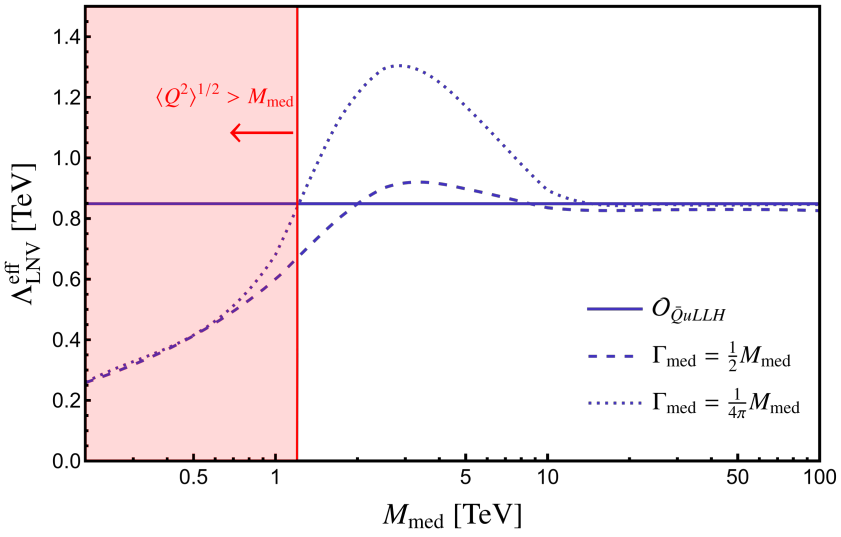

Figure 4.8.: Limits on the scale of LNV $\Lambda^{\rm eff}_{\rm LNV}$ at 95% CL as a function of the effective mediator mass $M_{\rm med}$ for the operator $\mathcal{O}_{\bar{Q}uLLH}$ (solid), as well as a UV-completion described by Eq. (4.52) where the mediator has a width $\Gamma_{\rm med} = \frac{1}{2} M_{\rm med}$ (dashed) and $\Gamma_{\rm med} = \frac{1}{4\pi} M_{\rm med}$ (dotted).

Fig. 4.7 shows the constraints corresponding to different dimension-7 $\Delta L = 2$ operators as a function of the effective mediator mass $M_{\rm med}$ and coupling $\sqrt{\lambda_1 \lambda_2}$. We here make the simplifying assumption that only a single mediator mass scale is involved in the process, whereby we use Eq. (4.51) to relate $M_{\rm med}$ to the LNV scale. This assumption can be regarded as being valid for tree-level processes at the LHC that are realised by UV-completions of dimension-7 operators where mixing occurs between the two heavy BSM fields. Such UV-completions do exist for all dimension-7 $\Delta L = 2$ operators that we consider here, as can be seen in Ch. 5. For operators $\mathcal{O}_{LH}$, $\mathcal{O}_{LeHD}$, and $\mathcal{O}_{LDH2}$, no part of the excluded region overlaps with the region where the underlying UV-completion can be perturbative. The other operators do have such regions, ranging up to ~ 12 TeV in the mediator mass $M_{\rm med}$ for $\mathcal{O}_{\bar{d}uLLD}$, which is the most stringently constrained dimension-7 operator at the LHC.

In order to study the level of agreement between LNV EFT operators and simplified-model extensions for same-sign dilepton searches at colliders, let us now take operator $\mathcal{O}_{\bar{Q}uLLH}$ as an example and compare different effective limits on the scale of LNV using both the operator itself as well as a generic UV-completion. In the mass basis, the simplified model example we consider includes a scalar field χ with couplings to both quark- and lepton bilinears. The Lagrangian is given by

$$\mathcal{L} \supset \lambda_1 \bar{d}_L u_R \chi^* + \lambda_2 \bar{e}^c_L \nu_L \chi + \text{h.c.}\,, \tag{4.52}$$

where the field χ can be realised as one component of the admixture of the fields $\varphi \in (1, 2, \frac{1}{2})$

and $\Delta \in (1,3,1)$. Now relating the couplings and masses as

$$\frac{\lambda_1 \lambda_2}{M_{\text{med}}^2} = \frac{v}{(\Lambda_{\text{LNV}}^{\text{eff}})^3}\,, \tag{4.53}$$

where $\Lambda_{\text{LNV}}^{\text{eff}}$ is an effective LNV scale corresponding to the scenario where the heavy field χ with mass M_{med} is integrated out, we can compare the LHC constraints coming from the simplified model and operator $\mathcal{O}_{\bar{Q}uLLH}$, where the latter is given in Tab. 4.8. In Fig. 4.8 the 95% CL constraints on the effective scale $\Lambda_{\text{LNV}}^{\text{eff}}$ are shown for both approaches. The constraints coming from the simplified model were obtained using MadGraph5_aMC@NLO [462] with the same procedure and cuts as for the operator (c.f. Sec. 4.4). The red-shaded low-M_{med} region of the plot shows where the EFT formalism breaks down due to the average momentum scales being greater than the mediator mass. The operator limit is shown in solid blue (c.f. Tab. 4.8), and the blue dotted and dashed lines correspond to the model in Eq. (4.52) for the mediator widths $\Gamma_{\text{med}} = \frac{1}{4\pi} M_{\text{med}}$ and $\Gamma_{\text{med}} = \frac{1}{2} M_{\text{med}}$, respectively. The former width is found using $\lambda_1 = 1$ while assuming large scales $v M_{\text{med}}^2 \ll (\Lambda_{\text{LNV}}^{\text{eff}})^3$, which leads to $\lambda_2 \ll 1$. The latter, larger width allows for additional decay modes of the mediator, such that couplings of χ can go beyond those given in Eq. (4.53).

A smaller width in Fig. 4.8 leads to an increase in $\Lambda_{\text{LNV}}^{\text{eff}}$ for some mediator masses. This increase comes from resonant enhancement in s-channel χ-mediators, which is greater for smaller widths. This effect is not seen in the EFT approach, where all contributions are assumed to be off-shell. For somewhat small mediator masses $\mathcal{O}(1)$ TeV $\lesssim M_{\text{med}} \lesssim$ $\mathcal{O}(10)$ TeV, the EFT approach therefore leads to an underestimation of the constraint on Λ_{LNV}. The simplified-model limits on $\Lambda_{\text{LNV}}^{\text{eff}}$ are lower than the operator limit in the regions of parameter space where the EFT-approach breaks down due to the fact that the kinematic cuts remove a larger part of the phase space for small mediator masses, leading to an overestimation of the limit on the LNV scale for $M_{\text{med}} \lesssim \mathcal{O}(1)$ TeV. In this region of parameter space we do not consider the EFT-based limits to be meaningful. For large mediator masses $M_{\text{med}} \gtrsim \mathcal{O}(1)$ TeV, there is a high level of agreement between the EFT- and simplified-model approaches, as expected. For such masses the simplified-model limits lie only slightly below the ones coming from the operator, where the small difference is due to the fact that the non-zero decay width modifies the s-channel mediators, which leads to a slight reduction in the cross section.

In Sec. 5.4.2 we compare neutrino masses with different constraints on the scale of LNV in the context of simplified-model UV-completions of the four-fermion dimension-7 $\Delta L = 2$ operators. Due to the large number of parameters present, some simplifying assumptions are made, one being our choice of setting all couplings to unity. With these couplings the LHC constraints on the scale of LNV all approximately fall within the region of non-validity, and therefore we neglect LHC constraints on the operator scales in Sec. 5.4.2.

This concludes our list of LNV observables. Other experimental methods that could potentially lead to constraints include LNV CEνNS and neutrino oscillations. The analysis of these probes is reserved for future work [4]. In Secs. 4.6 and 4.7 we cover two additional aspects of LNV operators, before giving a combined overview of the different experimental constraints in Sec. 4.8.

4.6. Washout from SMEFT operators

Realisations of LNV operators in nature would not only have implications for Majorana neutrino masses, but also for the mechanism behind the generation of the baryon asymmetry of the Universe. In order to generate a baryon asymmetry, the three Sakharov conditions [216] have to be fulfilled, as discussed in Ch. 3. However, the asymmetry can only survive to this day in the absence of strong additional washout processes. If such washouts are there, a pre-existing asymmetry could be removed, and even though it was initially generated, no baryon asymmetry would be left to leave the imprint in BBN and the CMB that we observe. The $\Delta L = 2$ SMEFT operators that we have considered in this chapter could lead to such washouts [394,475,476]. If these operators are indeed realised at a relatively low scale, any asymmetry generated at a high scale would be effectively removed, due to the LNV operators being active at a later time. Therefore, in case LNV is observed using one of the probes in Secs. 4.2.1 to 4.2.3 or Secs. 4.3.2 to 4.3.8, and it is due to heavy NP, the corresponding heavy scale Λ_{LNV} can lead to an effective scale $\hat{\lambda}$ where the washout stops being effective [394], as is discussed below. First, we note that the Boltzmann equation (c.f. Sec. 3.4 and Appendix E)

$$HTn_\gamma \frac{d\eta_L}{dT} = -\left(\frac{n_L n_i \dots}{n_L^{\text{eq}} n_i^{\text{eq}} \dots} - \frac{n_j n_k \dots}{n_j^{\text{eq}} n_k^{\text{eq}} \dots}\right) \gamma^{\text{eq}} \left(Li \cdots \to jk \dots\right) + \text{permutations}. \tag{4.54}$$

can lead to an effective equation relating the lepton asymmetry to the scale Λ of LNV corresponding to a SMEFT operator, given by [1,394]

$$\frac{d\eta_{\Delta L}}{dz} = -\frac{\eta_{\Delta L}}{z} c'_D \frac{\Lambda_{\text{Pl}}}{\Lambda} \left(\frac{T}{\Lambda}\right)^{2D-9}, \tag{4.55}$$

where c'_D is a numerical coefficient that can be obtained using chemical potential relations (c.f. Appendix D) and D is the dimension of the operator. The form given in Eq. (4.55) comes from an approximation of the equilibrium reaction rate density γ^{eq} that is given towards the end of Appendix E, which is useful for complicated phase spaces. Assuming a large initial asymmetry $\eta_{\Delta L} \approx 1$ at some high temperature, the washout from the LNV operator is active at a lower temperature T in the range

$$\hat{\lambda} \lesssim T \lesssim \Lambda\,. \tag{4.56}$$

Here the upper limit Λ comes from the fact that our LNV operator is not defined above this scale, and the lower limit $\hat{\lambda}$ is given by [394]

$$\hat{\lambda} = \left[(2D-9) \ln\left(\frac{10^{-2}}{\eta_B^{\text{obs}}}\right) \lambda^{2D-9} + v^{2D-9}\right]^{1/(2D-9)}. \tag{4.57}$$

with $\lambda = \Lambda(\Lambda/(c'_D \Lambda_{\text{Pl}}))^{1/(2D-9)}$. The precise form of Eq. (4.57) comes from considering the dilution of baryon asymmetry between the high scale and the time of recombination (assuming that the observed value of the baryon asymmetry η_B^{obs} is based on CMB measurements). The

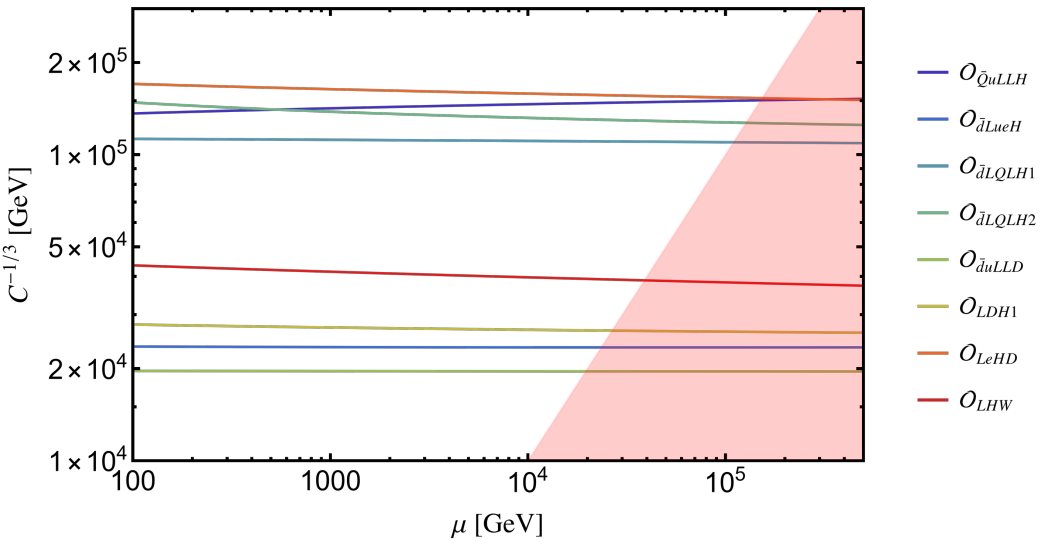

Figure 4.9.: Running of the dimension-7 $\Delta L = 2$ operators that are relevant for $0\nu\beta\beta$ decay. The EFT formalism is not valid in the red region under the assumption of unitary couplings in the underlying UV-theory.

details of this calculation, as well as a specific example of how the chemical potential relations can be applied to obtain the final form of the Boltzmann equation, are given in Sec. 8.2. Effectively, any asymmetry generated above the scale $\hat{\lambda}$ should be washed out completely. This means that if LNV is experimentally observed, severe constraints can be put on high scale baryogenesis/leptogenesis, since the baryon asymmetry of the Universe should then have been generated below $\hat{\lambda}$.

4.7. RG-running of dimension-7 SMEFT operators

The Wilson coefficients of the dimension-7 operators in Tab. 4.5 run with respect the the energy scale μ at which they are evaluated. The running of the subset of Wilson coefficients relevant for $0\nu\beta\beta$ decay is described in Ref. [383] for first generation quark- and lepton flavour indices. Below we give the running relations for general indices:

$$\frac{d}{d\mu}C^{pr\dagger}_{LHD1} = -\frac{1}{4\pi}\Big\{(\alpha_1 - 2\alpha_2 - 6\alpha_t)C^{pr\dagger}_{LHD1} + \frac{1}{2}(\alpha_1 - 7\alpha_2)C^{rp\dagger}_{LHD1} + \frac{1}{4}(7\alpha_1 + 11\alpha_2 + 8\alpha_\lambda)C^{pr\dagger}_{LHD2} + (\alpha_1 + 2\alpha_2)C^{rp\dagger}_{LHD2}\Big\} \tag{4.58}$$

$$\frac{d}{d\mu}C^{pr\dagger}_{LHD2} = -\frac{1}{4\pi}\Bigg\{7\alpha_2 C^{pr\dagger}_{LHD1} + \alpha_2 C^{rp\dagger}_{LHD1} - \frac{1}{2}(5\alpha_1 - \alpha_2 + 8\alpha_\lambda + 12\alpha_t)C^{pr\dagger}_{LHD2} - \frac{1}{2}(3\alpha_1 + 7\alpha_2)C^{rp\dagger}_{LHD2}\Bigg\} \tag{4.59}$$

$$\frac{d}{d\mu}C^{prst\dagger}_{\bar{d}uLLD} = -\frac{1}{4\pi}\Bigg\{ -\frac{1}{6}(5\alpha_1 + 3\alpha_2 + 6\alpha_t\delta^{r3})C^{prst\dagger}_{\bar{d}uLLD} + \frac{1}{3}(\alpha_1 + 3\alpha_2)C^{prts\dagger}_{\bar{d}uLLD}\Bigg\} \tag{4.60}$$

$$\frac{d}{d\mu}C^{pr\dagger}_{LeHD} = -\frac{1}{4\pi}\Bigg\{\frac{1}{2}(3\alpha_1 - 12\alpha_\lambda - 18\alpha_t)C^{pr\dagger}_{LeHD}\Bigg\} \tag{4.61}$$

$$\frac{d}{d\mu}C^{prst\dagger}_{\bar{d}LueH} = -\frac{1}{4\pi}\Bigg\{\frac{1}{4}(23\alpha_1 + 9\alpha_2 - 12\alpha_t(1 + \delta^{s3}))C^{prst\dagger}_{\bar{d}LueH}\Bigg\} \tag{4.62}$$

$$\frac{d}{d\mu}C^{prst\dagger}_{\bar{Q}uLLH} = -\frac{1}{4\pi}\Bigg\{ -\frac{1}{12}(\alpha_1 - 45\alpha_2 - 96\alpha_3 + 6\alpha_t(6 + 5\delta^{p3} + 6\delta^{r3} + 12\delta^{p3}\delta^{r3}))C^{prst\dagger}_{\bar{Q}uLLH} - 3\alpha_2 C^{prts\dagger}_{\bar{Q}uLLH} - \sqrt{\alpha_t}\frac{\sqrt{\pi}}{2}(4\alpha_1 - 3\alpha_2)\delta^{p3}\delta^{r3}(C^{ts\dagger}_{LHD1} - C^{st\dagger}_{LHD1}) - \sqrt{\alpha_t}\sqrt{\pi}(\alpha_1 + 3\alpha_2)\delta^{p3}\delta^{r3}(C^{ts\dagger}_{LHD2} - C^{st\dagger}_{LHD2})\Bigg\} \tag{4.63}$$

$$\frac{d}{d\mu}C^{prst\dagger}_{\bar{d}LQLH1} = -\frac{1}{4\pi}\Bigg\{\frac{1}{36}(41\alpha_1 + 63\alpha_2 + 96\alpha_3 - 18\alpha_t(6 + \delta^{s3}))C^{prst\dagger}_{\bar{d}LQLH1} - \frac{1}{9}(20\alpha_1 + 36\alpha_2 - 48\alpha_3)C^{ptsr\dagger}_{\bar{d}LQLH1} - 4\alpha_2 C^{prst\dagger}_{\bar{d}LQLH2} - 2\alpha_2 C^{ptsr\dagger}_{\bar{d}LQLH2}\Bigg\} \tag{4.64}$$

$$\frac{d}{d\mu}C^{prst\dagger}_{\bar{d}LQLH2} = -\frac{1}{4\pi}\Bigg\{\frac{1}{9}(20\alpha_1 + 18\alpha_2 - 47\alpha_3)C^{ptsr\dagger}_{\bar{d}LQLH1} - (2\alpha_2 + \alpha_t\delta^{s3})C^{prst\dagger}_{\bar{d}LQLH1} + \frac{1}{36}(41\alpha_1 + 207\alpha_2 + 96\alpha_3 - 18\alpha_t(6 + 5\delta^{s3}))C^{prst\dagger}_{\bar{d}LQLH2} + \frac{1}{3}(10\alpha_1 - 9\alpha_2 - 24\alpha_3)C^{ptsr\dagger}_{\bar{d}LQLH2}\Bigg\} \tag{4.65}$$

$$\frac{d}{d\mu}C^{pr\dagger}_{LHW} = -\frac{1}{4\pi}\Bigg\{ -\frac{7}{8}\alpha_2 C^{pr\dagger}_{LHD1} + \frac{1}{4}\alpha_2 C^{rp\dagger}_{LHD1} + \frac{1}{16}(3\alpha_1 - 7\alpha_2)C^{pr\dagger}_{LHD2} \\ - \frac{1}{4}\alpha_2 C^{rp\dagger}_{LHD2} - 3\alpha_1 C^{pr\dagger}_{LHB} - \frac{17}{4}\alpha_2 C^{rp\dagger}_{LHW} \\ + \frac{1}{4}(8\alpha_1 - 9\alpha_2 - 16\alpha_\lambda - 24\alpha_t)C^{pr\dagger}_{LHW}\Bigg\} \tag{4.66}$$

$$\frac{d}{d\mu}C^{pr\dagger}_{LH} = -\frac{1}{4\pi}\Bigg\{\frac{1}{2}(3\alpha_1 + 15\alpha_2 - 80\alpha_\lambda - 24\alpha_t)C^{pr\dagger}_{LH} \\ + \frac{3\pi}{2}(2\alpha_2^2 - \alpha_\lambda\alpha_2)(C^{pr\dagger}_{LHD1} + C^{rp\dagger}_{LHD1}) \\ + \frac{3\pi}{8}\Big(4\alpha_1^2 + 8\alpha_1\alpha_2 + 12\alpha_2^2 - \alpha_\lambda\alpha_2\Big)(C^{pr\dagger}_{LHD2} + C^{rp\dagger}_{LHD2}) \\ + 6\pi\alpha_2^2(C^{pr\dagger}_{LHW} + C^{rp\dagger}_{LHW}) \\ - 12\sqrt{\pi}(\alpha_\lambda\sqrt{\alpha_t} - \alpha_t^{3/2})\delta^{s3}\delta^{t3}(C^{stpr\dagger}_{\bar{Q}uLLH} + C^{strp\dagger}_{\bar{Q}uLLH})\Bigg\} \tag{4.67}$$

$$\frac{d}{d\mu}C^{prst\dagger}_{\bar{e}LLLH} = -\frac{1}{4\pi}\Bigg\{\frac{1}{4}(9\alpha_1 + 7\alpha_2 - 12\alpha_t)C^{prst\dagger}_{\bar{e}LLLH} - 2\alpha_2 C^{prts\dagger}_{\bar{e}LLLH} \\ + 2\alpha_2 C^{pstr\dagger}_{\bar{e}LLLH} - 4\alpha_2 C^{ptsr\dagger}_{\bar{e}LLLH}\Bigg\} \tag{4.68}$$

$$\frac{d}{d\mu}C^{pr\dagger}_{LHB} = -\frac{1}{4\pi}\Bigg\{ -\frac{9}{32}\alpha_2(C^{pr\dagger}_{LHD1} - C^{rp\dagger}_{LHD1}) + \frac{6}{128}(\alpha_1 - \alpha_2)(C^{pr\dagger}_{LHD2} - C^{rp\dagger}_{LHD2}) \\ + \frac{1}{2}(\alpha_1 + 10\alpha_2 - 8\alpha_\lambda - 12\alpha_t)C^{pr\dagger}_{LHB} - \frac{3}{8}\alpha_2(C^{pr\dagger}_{LHW} - C^{rp\dagger}_{LHW})\Bigg\}, \tag{4.69}$$

where α_i, $i \in \{1, 2, 3, \lambda\}$ is the coupling constant corresponding to the $U(1)_Y$, $SU(2)_L$, $SU(3)_c$ gauge interactions and quartic Higgs interaction, respectively, and δ^{ij} is the Dirac delta function. As can be seen from the relations above, the operators mix in the running. In Fig. 4.9 the running is shown for a given initial value at $\mu = m_W$ corresponding to the exclusion limits from $0\nu\beta\beta$ experiments (c.f. Sec. 4.3.2), where m_W is the mass of the W-boson. We see that the running has a minor effect on the Wilson coefficients, and we therefore neglect RG-running effects of dimension-7 $\Delta L = 2$ SMEFT operators in subsequent chapters. Note however that other forms of RG running, in particular due to QCD, can play an important role (c.f. e.g. Sec. 8.1.2).

Operator	$0\nu\beta\beta$	Meson decays	LHC	μ^+ decays
$\mathcal{O}_{LH}$	-	-	0.20	-
$\mathcal{O}_{LeHD}$	171	-	0.13	-
$\mathcal{O}_{LHD1}$	27.9	-	0.40	-
$\mathcal{O}_{LHD2}$	-	-	0.22	-
$\mathcal{O}_{LHW}$	43.7	-	-	-
$\mathcal{O}_{\bar{d}uLLD}$	19.6	-	2.2	-
$\mathcal{O}_{\bar{e}LLLH}$	-	-	-	0.64
$\mathcal{O}_{\bar{d}LQLH1}$	113	21.8	0.71	-
$\mathcal{O}_{\bar{d}LQLH2}$	149	-	0.71	-
$\mathcal{O}_{\bar{d}LueH}$	23.6	-	0.72	-
$\mathcal{O}_{\bar{Q}uLLH}$	136	-	0.86	-

Table 4.10.: Experimental constraints on the scale of LNV in 7-dimensional $\Delta L = 2$ SMEFT operators, in units of TeV.

4.8. Combined analysis of different observables at dimension-7

In Figs. 4.10 and 4.11 the different constraints arising from the LNV observables listed in Sec. 4.2 are compiled, where the numerical values corresponding to the different bars are presented in Tab. 4.10. We see in Fig. 4.10 that $0\nu\beta\beta$ decay is generally the most constraining probe of LNV. However, as mentioned previously in this chapter, $0\nu\beta\beta$ only probes the electron-flavour components of the different LNV operators. To constrain also other flavours, a wider set of observables is needed. For the muon flavour, LHC is the most stringent probe for the operators that lead to the $pp \to \ell^\pm\ell^\pm jj$ process. Operator $\mathcal{O}_{\bar{e}LLLH}$ does not trigger this mode, and is instead constrained by LNV muon decays. Rare meson decays constrain all flavours universally since the flavour-content is undetermined in the final state neutrinos. However, only one operator triggers such decays, namely $\mathcal{O}_{\bar{d}LQLH1}$. A comparison of different LNV meson decay modes is shown in Fig. 4.11, where we see that the rare kaon decay $K^+ \to \pi^+\nu\nu$ leads to the most stringent limits. Note that operator $\mathcal{O}_{LHB}$ is absent from Figs. 4.10, 4.11 and Tab. 4.10. This operator is in general poorly constrained by experimental searches for LNV.

If a signal is seen in one of the LNV observables, a next step would be to find out what kind of NP generates the process. To this end, it is interesting to see whether the different LNV operators can be disentangled. Given a signal in one of the next-generation $0\nu\beta\beta$ experiments, we can expect the scale of LNV to be sufficiently high such that it is out of reach of near-future collider searches. However, as is seen in Ch. 5, the details of the UV-complete model underlying the LNV operator could still lead to collider signatures. Rare kaon decays might additionally offer insights in case the process favours μ- or τ-neutrinos, thereby enhancing the expected signal for this observable. If signals are seen in both $0\nu\beta\beta$ decay and rare kaon decays, we may suspect that the processes are mediated by operator $\mathcal{O}_{\bar{d}LQLH1}$.

In this section we have not included neutrino masses as a probe of the scale of LNV in

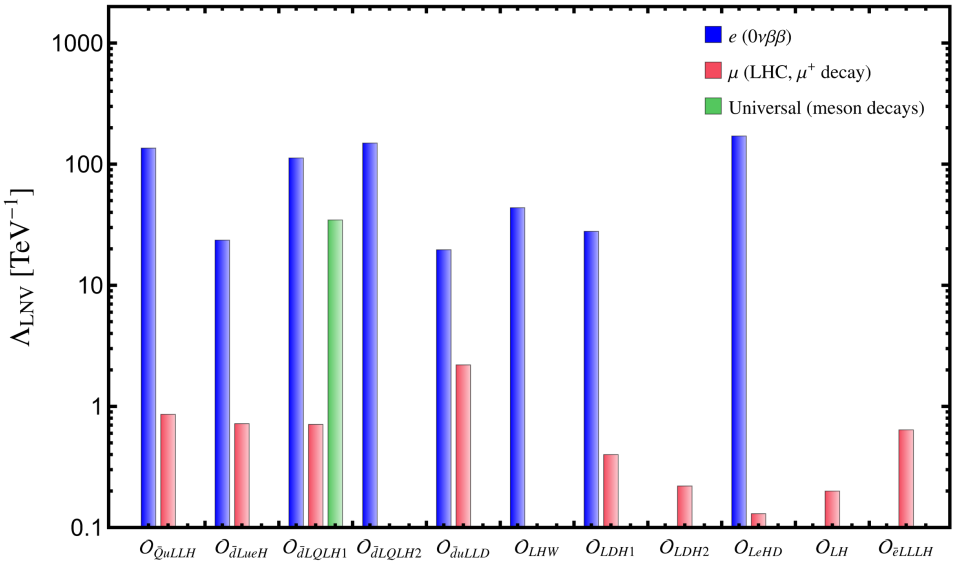

Figure 4.10.: Constraints on the scale of LNV corresponding to different dimension-7 operators. Here the blue bars indicate the limits coming from $0\nu\beta\beta$ decay (electron flavour), and the green bars correspond to constraints coming from LNV meson decays (flavour universal). The red bars indicate limits on the muon-flavour Wilson coefficients, where these limits come from the LHC in all cases except for operator $\mathcal{O}_{\bar{e}LLLH}$, where they come from LNV μ^+ decays.

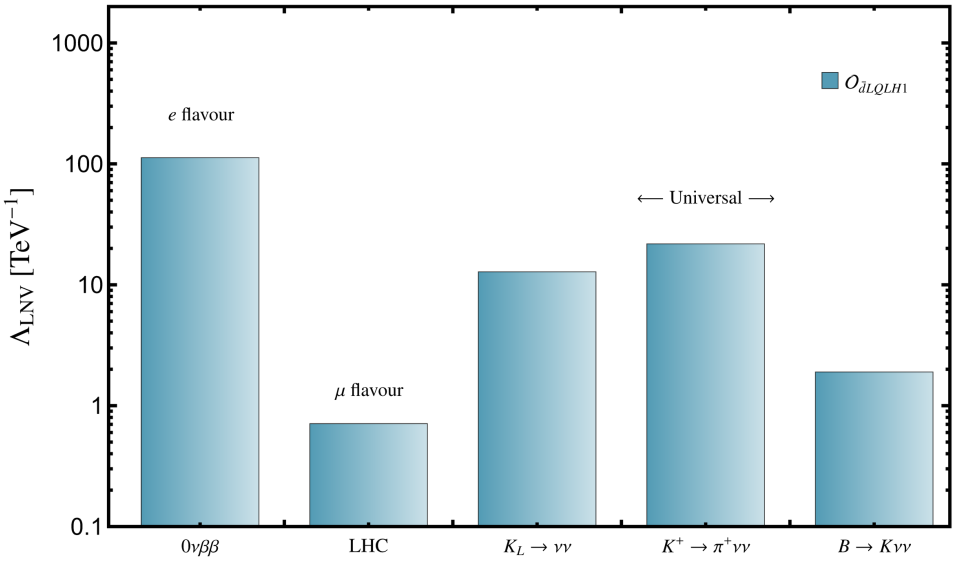

Figure 4.11.: Constraints on the scale of LNV in dimension-7 operator $\mathcal{O}_{\bar{d}LQLH1}$. Here the different meson decay observables are shown, where the rare kaon decay limits constitute the most stringent constraints.

dimension-7 operators. The reason for this is that such constraints depend highly on the details of the UV-completion that realises the operator in question, a feature not in common with the other probes of LNV. The conventional method of generating neutrino mass-based constraints on LNV scales, described in Sec. 4.2.1, is ill-equipped to capture the influence of such model-specific details. In Ch. 5 we describe a novel way of estimating the constraints on LNV operators coming from neutrino masses.

Conclusion to Chapter 4

In this section we have discussed how different observables of LNV can be analysed in effective field theories, in particular SMEFT. This connects the NP scenarios discussed in Sec. 2.3 with the possible baryogenesis mechanisms from Ch. 3, and highlights the benefits of model-independent experimental searches. We have reviewed the most constraining LNV probes in terms of dimension-7 LNV operators, including $0\nu\beta\beta$ decay, different LNV meson and lepton decays, and μ^- to e^+ conversion. New limits were derived for rare kaon decays $K^+ \to \pi^+\nu\nu$ and fully leptonic meson decays $K^+/\pi^+ \to \ell^+\bar{\nu}$, as well as the LHC. The meson-decay results were published in Ref. [1], and the LHC results are subject for future publication [4]. This analysis is useful for Ch. 5, where all tree-level UV-completions of dimension-7 LNV operators are systematically analysed.

The EFT formalism is applicable to NP that is realised at high scales, which is a well motivated in scenario terms of e.g. baryogenesis, gauge unification, and neutrino masses. However, there are limitations to EFTs that make it worthwhile to also look for other tools. We discussed one such limitation in an analysis subject for future publication [4] that was presented in Sec. 4.5. There it was noted that the parameter space available to EFT studies at the LHC was limited due to the breakdown of the underlying assumptions that validate an EFT framework, namely the smallness of momentum scales with respect to the scale of NP. Another limitation comes from the fact that there is only a single EFT scale involved in a given operator. For NP scenarios that contain multiple scales, any effects coming from a hierarchy in the internal degrees of freedom is missed by an EFT.

In Ch. 5 we continue the analysis presented in this chapter by considering tree-level UV-completions of dimension-7 LNV operators in the context of neutrino masses and hierarchies in the heavy scales.

5. Beyond SMEFT: LNV simplified models at dimension-7

In Ch. 4 we discussed the SMEFT formalism with a particular focus on the dimension-7 $\Delta L = 2$ operators shown in Tab. 4.5. From a phenomenological perspective, these operators were found to be constrained by a range of different experimental searches, including $0\nu\beta\beta$ decay, rare kaon decays, LNV muon decays, and proton-proton collisions at the LHC. In this chapter we continue our investigation of dimension-7 operators by systematically analysing and categorising all tree-level UV-completions in a bottom-up approach[1]. In Sec. 5.1 we review the covariant-derivative-expansion framework, which lays the foundation for our categorisation of UV-completions in Sec. 5.2. We connect the UV-completions to neutrino masses in Sec. 5.3. In Sec. 5.4 we derive constraints on the UV-completions in terms of LNV searches and neutrino mass limits, and present a new analysis in terms of an internal hierarchy in the degrees of freedom, that is subject for publication in Ref. [4].

One of our motivations to study LNV at dimension-7 is its relative simplicity. Only a single scenario can be thought of as simpler, namely LNV realised by the dimension-5 operator, which can be generated at tree-level in three different ways: the three seesaw types. However, if neither of the seesaw fields are realised in nature at a heavy scale, it could be the case that LNV is first generated at dimension-7.

Rather than a single operator leading to three possible UV-completions, at dimension-7 we have 12 operators leading to 26 different NP fields that combine in 56 pairs. This sharp increase in complexity highlights the rich phenomenology of higher dimensional operators [390, 391, 477–486], where e.g. neutrino Majorana mass generation could be connected to a wide range of different models [487,488]. In this chapter, we systematically categorise each UV-completion that is found at tree-level corresponding to the dimension-7 LNV operators, and compare experimental constraints to neutrino mass realisations in the context of a varying internal hierarchy in the heavy degrees of freedom. We call these UV-completions *simplified models* to differentiate them from models that are constructed in order to solve a specific problem, e.g. gauge coupling unification or generating a dark matter candidate. Simplified models constitute extensions to the SM by $\mathcal{O}(\text{few})$ heavy fields, and they could potentially fit into the framework of a more complete model. However, in this chapter we are mostly concerned with models given at the simplified level.

Note that we are here focusing on tree-level UV-completions. It is entirely possible that the LNV operators we consider are instead realised at loop-level, in which case the analysis we perform here must be modified. Loop-level UV-completions do not offer the same kind of absoluteness in terms of classifying the different BSM fields that could participate: as soon as

[1] For a top-down approach see Ref. [391].

there is a loop consisting of purely BSM fields the $U(1)_Y$ charges could in principle take on any value. The same goes for any additional symmetry group $U(1)_X$ or $\mathbb{Z}_i$ for $i \in \mathbb{N}$ that could be imposed on the BSM fields. There is no handle on such charges since for loop-level UV-completions they can be conserved internally, while at tree-level each BSM field has to talk to the SM fields, even if indirectly[2]. We therefore choose to limit ourselves to tree-level UV-completions.

5.1. Covariant derivative expansion

Following the method used in Ref. [489], the operators in Tab. 4.5 can be expanded to find all NP field combinations that generate them at tree-level. To do this, we first systematically integrate out heavy fields from a simplified-model Lagrangian to find all SM-invariant operators (see also Refs. [490–495]). After this we identify the operators we obtain with those from dimension-7 $\Delta L = 2$ SMEFT, and compare with our simplified model starting point to identify the quantum numbers of the UV-fields.

We start with a simplified generic extension to the SM

$$\mathcal{L}_{\mathrm{S}} = \sum_{ij} \left(\mathcal{L}_{\pi_i} + \mathcal{L}^{\mathrm{int}}_{\Pi_j} + \mathcal{L}^{\mathrm{kin}}_{\Pi_j} \right) , \tag{5.1}$$

where π_i is a light field, Π_j is a heavy field, and the whole Lagrangian $\mathcal{L}_{\mathrm{S}}$ corresponds to one simplified model (S). We first write $\mathcal{L}_S$ only in terms of light fields, by creating non-renormalisable terms where heavy scalar, vector, or fermion fields are integrated out. These non-renormalisable terms are then identified as EFT operators. The integrating-out procedure can then be repeated until there are no more heavy fields in the Lagrangian. All operators are then written only in terms of light fields. In the case of SMEFT, all light fields belong to the SM, and after identifying the light fields as such we deconstruct the operators to find all possible simplified model UV-completions. Below we first show how fields of different Lorentz structures can be integrated out, after which we systematically deconstruct the dimension-7 $\Delta L = 2$ operators. The scalar- and fermion field deconstructions in Secs. 5.1.1 and 5.1.1, respectively, are given in Ref. [201], while the vector field deconstruction in Sec. 5.1.3 is given here for the first time (to the knowledge of the author). Many of the identities used in this section are presented in Appendix B.

5.1.1. Scalar field

The first type of effective Lagrangian that we consider is the one we obtain by integrating out a heavy scalar field $\Pi_j \to \Phi$. Using covariant derivative expansion (CDE) [201], the terms

[2] As an example of this we may look at an extension of the type-i seesaw. For the regular diagram we know that N has to be uncharged under $U(1)_Y$ in order to preserve this symmetry. However, if we now imagine that one of the L-H vertices is a triangle loop, all the fields in the loop could carry a $U(1)_Y$-charge of $x \in \mathbb{R}$. The symmetry would still be preserved, but we have no systematic way of identifying all particles classified in terms of their hypercharge. This complicates the problem in comparison to tree-level UV-completions.

that involve both light fields π_i and a heavy complex scalar field Φ can be written as

$$\mathcal{L}_S \supset \mathcal{L}_\Phi^{\text{int}} + \mathcal{L}_\Phi^{\text{kin}} = \left(\Phi \frac{\partial \mathcal{L}_\Phi^{\text{int}}}{\partial \Phi} + \text{h.c.}\right) + \Phi^* \left(-D^2 - m_\Phi^2\right) \Phi + \mathcal{O}(\Phi^3)\,, \tag{5.2}$$

where D is a covariant derivative. In Eq. (5.2) we have ignored quadratic terms in Φ, such that

$$\mathcal{L}_S \not\supset \Phi^* \frac{\partial^2 \mathcal{L}_\Phi^{\text{int}}}{\partial \Phi^* \partial \Phi} \Phi\,. \tag{5.3}$$

Such terms do not lead to new fields in the explosion procedure that would not also have been found from the terms in Eq. (5.1), since any quadratic vertex can also be drawn as two trilinear vertices, with identical legs. Evaluating the equations of motion (EOM) for Φ we have

$$\left(-D^2 - m_\Phi^2\right) \Phi = -\frac{\partial \mathcal{L}_\Phi^{\text{int}}}{\partial \Phi^*} + \mathcal{O}(\Phi^2)\,. \tag{5.4}$$

We can solve the linearised EOM using the classical field

$$\Phi_{\text{cl}} = \frac{1}{D^2 + m_\Phi^2} \frac{\partial \mathcal{L}_\Phi^{\text{int}}}{\partial \Phi^*}\,, \tag{5.5}$$

which can be expanded in D^2/m_Φ^2 as a power series, giving us

$$\Phi_{\text{cl}} = \frac{1}{m_\Phi^2} \left(1 + \frac{D^2}{m_\pi^2}\right)^{-1} \frac{\partial \mathcal{L}_\Phi^{\text{int}}}{\partial \Phi^*} = \left(\frac{1}{m_\Phi^2} - \frac{D^2}{m_\Phi^4} + \dots\right) \frac{\partial \mathcal{L}_\Phi^{\text{int}}}{\partial \Phi^*}\,. \tag{5.6}$$

If we substitute the classical field into the simplified model Lagrangian in Eq. (5.2) we get a series of interaction terms

$$\mathcal{L}_{\text{eff}} \supset \mathcal{L}_{\text{eff}}^\Phi = \frac{\partial \mathcal{L}_\Phi^{\text{int}}}{\partial \Phi} \left(\frac{1}{m_\Phi^2} - \frac{D^2}{m_\Phi^4} + \dots\right) \frac{\partial \mathcal{L}_\Phi^{\text{int}}}{\partial \Phi^*}\,. \tag{5.7}$$

Eq. (5.7) now contains an effective Lagrangian that does not feature the heavy scalar field Φ, but that does depend on its interactions with other possible heavy fields as well as the light fields π_i. Such interactions are contained in the derivatives $\partial \mathcal{L}_\Phi^{\text{int}} / \partial \Phi^{(*)}$. A general expression of this type of derivative is given below, but first we apply a similar procedure as the one outlined here to find an effective Lagrangian that encode the interactions of heavy fermion and vector fields.

5.1.2. Fermion field

A heavy Dirac fermion field $\Psi \equiv \left(\chi_\alpha\,,\, \eta^{\dagger\dot{\alpha}}\right)^T$ leads to the simplified Lagrangian

$$\begin{aligned} \mathcal{L}_S &\supset i\bar{\Psi} \not{D} \Psi - m_\Psi \bar{\Psi}\Psi + \left(\Psi \frac{\partial \mathcal{L}_\Psi^{\text{int}}}{\partial \Psi} + \text{h.c.}\right) \\ &= i\chi_{\dot{\alpha}}^\dagger D^{\dot{\alpha}\beta} \chi_\beta + i\eta^\alpha D_{\alpha\dot{\beta}} \eta^{\dagger\dot{\beta}} + \left(\chi_\alpha \frac{\partial \mathcal{L}_\Psi^{\text{int}}}{\partial \chi_\alpha} + \eta^\alpha \frac{\partial \mathcal{L}_\Psi^{\text{int}}}{\partial \eta^\alpha} - m_\Psi \eta^\alpha \chi_\alpha + \text{h.c.}\right)\,, \end{aligned} \tag{5.8}$$

where we have used the relations

$$D^{\dot{\alpha}\beta} \equiv D^{\mu}\bar{\sigma}_{\mu}^{\dot{\alpha}\beta}, \qquad D_{\alpha\dot{\beta}} \equiv D^{\mu}\sigma_{\mu\alpha\dot{\beta}}\,. \tag{5.9}$$

In Eq. (5.8), the second term can be written in the same form as the first term by using integration by parts (IBP), assuming that the total derivative vanishes,

$$i\eta^{\alpha}D_{\alpha\dot{\beta}}\eta^{\dagger\dot{\beta}} = -i(D^{\mu}\eta^{\alpha})\sigma_{\mu\alpha\dot{\beta}}\eta^{\dagger\dot{\beta}}\,, \tag{5.10}$$

after which we apply a Fierz transformation (see Appendix B)

$$-i(D^{\mu}\eta^{\alpha})\sigma_{\mu\alpha\dot{\beta}}\eta^{\dagger\dot{\beta}} = i\eta^{\dagger}_{\dot{\beta}}\bar{\sigma}_{\mu}^{\dot{\beta}\alpha}D^{\mu}\eta_{\alpha} = i\eta^{\dagger}_{\dot{\beta}}D^{\dot{\beta}\alpha}\eta_{\alpha}\,, \tag{5.11}$$

such that we can write the coupled EOM as

$$iD^{\dot{\alpha}\beta}\chi_{\beta} - m_{\Psi}\eta^{\dagger\dot{\alpha}} + \frac{\partial\mathcal{L}^{\text{int}}_{\Psi}}{\partial\chi^{\dagger}_{\dot{\alpha}}} = 0 \tag{5.12}$$

$$iD^{\dot{\alpha}\beta}\eta_{\beta} - m_{\Psi}\chi^{\dagger\dot{\alpha}} + \frac{\partial\mathcal{L}^{\text{int}}_{\Psi}}{\partial\eta^{\dagger}_{\dot{\alpha}}} = 0\,, \tag{5.13}$$

where Eq. (5.12) can be solved for $\eta^{\dagger}_{\dot{\beta}}$,

$$\eta^{\dagger}_{\dot{\beta}} = \frac{1}{m_{\Psi}}\epsilon_{\dot{\beta}\dot{\alpha}}\left(iD^{\dot{\alpha}\beta}\chi_{\beta} + \frac{\partial\mathcal{L}^{\text{int}}_{\Psi}}{\partial\chi^{\dagger}_{\dot{\alpha}}}\right) = i\frac{1}{m_{\Psi}}\epsilon_{\dot{\beta}\dot{\alpha}}D^{\dot{\alpha}\beta}\chi_{\beta} + \frac{1}{m_{\Psi}}\frac{\partial\mathcal{L}^{\text{int}}_{\Psi}}{\partial\chi^{\dagger\dot{\beta}}}\,. \tag{5.14}$$

Inserting this result into the complex conjugate of Eq. (5.13) now leads to

$$\frac{1}{m_{\Psi}}D^{\dot{\beta}\alpha}\epsilon_{\dot{\beta}\dot{\alpha}}D^{\dot{\alpha}\beta}\chi_{\beta} + i\frac{1}{m_{\Psi}}D^{\dot{\beta}\alpha}\frac{\partial\mathcal{L}^{\text{int}}_{\Psi}}{\partial\chi^{\dagger\dot{\beta}}} - m_{\Psi}\chi^{\alpha} + \frac{\partial\mathcal{L}^{\text{int}}_{\Psi}}{\partial\eta_{\alpha}} = 0\,. \tag{5.15}$$

We can express the first term in Eq. (5.15) in terms of the field strength

$$X_{\alpha}{}^{\beta} \equiv X^{\mu\nu}\sigma_{\nu\alpha\dot{\gamma}}\bar{\sigma}_{\mu}^{\dot{\gamma}\beta} = -i\left[D^{\mu},\, D^{\nu}\right]\sigma_{\nu\alpha\dot{\gamma}}\bar{\sigma}_{\mu}^{\dot{\gamma}\beta} \tag{5.16}$$

by using the relation

$$\begin{aligned} D^{\dot{\beta}\alpha}\epsilon_{\dot{\beta}\dot{\alpha}}D^{\dot{\alpha}\beta} &= D^{\mu}D^{\nu}\bar{\sigma}_{\mu}^{\dot{\alpha}\beta}\epsilon_{\dot{\beta}\dot{\alpha}}\bar{\sigma}_{\nu}^{\dot{\beta}\alpha} \\ &= D^{\mu}D^{\nu}\epsilon^{\beta\gamma}\sigma_{\mu\gamma\dot{\beta}}\bar{\sigma}_{\nu}^{\dot{\beta}\alpha} \\ &= D^{\mu}D^{\nu}\epsilon^{\beta\gamma}\left(\eta_{\mu\nu}\delta_{\gamma}{}^{\alpha} - 2i(\sigma_{\mu\nu})_{\gamma}{}^{\alpha}\right) \\ &= D^{2}\epsilon^{\beta\alpha} + \frac{i}{2}\epsilon^{\beta\gamma}X_{\gamma}{}^{\alpha}\,, \end{aligned} \tag{5.17}$$

where we have

$$(\sigma_{\mu\nu})_{\alpha}{}^{\beta} \equiv \frac{i}{4}\left(\sigma_{\mu\alpha\dot{\gamma}}\bar{\sigma}_{\nu}^{\dot{\gamma}\beta} - \sigma_{\nu\alpha\dot{\gamma}}\bar{\sigma}_{\mu}^{\dot{\gamma}\beta}\right)\,, \quad (\bar{\sigma}_{\mu\nu})^{\dot{\alpha}}{}_{\dot{\beta}} \equiv \frac{i}{4}\left(\bar{\sigma}_{\mu}^{\dot{\alpha}\gamma}\sigma_{\nu\gamma\dot{\beta}} - \bar{\sigma}_{\nu}^{\dot{\alpha}\gamma}\sigma_{\mu\gamma\dot{\beta}}\right)\,. \tag{5.18}$$

This then leads to the relation

$$m_\Psi^2\left(\frac{-D^2\epsilon^{\alpha\delta}-\frac{i}{2}X_\gamma{}^\alpha\epsilon^{\gamma\delta}}{m_\Psi^2}-\epsilon^{\alpha\delta}\right)\chi_\delta+iD^{\dot\beta\alpha}\frac{\partial\mathcal{L}_\Psi^{\rm int}}{\partial\chi^{\dagger\dot\beta}}+m_\Psi\frac{\partial\mathcal{L}_\Psi^{\rm int}}{\partial\eta_\alpha}=0\,, \tag{5.19}$$

which can solved by the classical fermion field

$$\begin{aligned}(\chi_{\rm cl})_\delta&=\frac{1}{m_\Psi^2}\left(\frac{-D^2\epsilon^{\alpha\delta}-\frac{i}{2}X_\gamma{}^\alpha\epsilon^{\gamma\delta}}{m_\Psi^2}-\epsilon^{\alpha\delta}\right)^{-1}\left(iD^{\dot\beta\alpha}\frac{\partial\mathcal{L}_\Psi^{\rm int}}{\partial\chi^{\dagger\dot\beta}}+m_\Psi\frac{\partial\mathcal{L}_\Psi^{\rm int}}{\partial\eta_\alpha}\right)\\&=\left(\frac{\epsilon_{\alpha\delta}}{m_\Psi^2}+\frac{D^2\epsilon_{\alpha\delta}+\frac{i}{2}X_\alpha{}^\gamma\epsilon_{\gamma\delta}}{m_\Psi^4}+\dots\right)\left(iD^{\dot\beta\alpha}\frac{\partial\mathcal{L}_\Psi^{\rm int}}{\partial\chi^{\dagger\dot\beta}}+m_\Psi\frac{\partial\mathcal{L}_\Psi^{\rm int}}{\partial\eta_\alpha}\right).\end{aligned} \tag{5.20}$$

The corresponding classical field $(\eta_{\rm cl})_\delta$ can be found in the same way. Now substituting the fields in the effective Lagrangian in Eq. (5.8) we get a series of interaction terms

$$\begin{aligned}\mathcal{L}_{\rm eff}\supset\mathcal{L}_{\rm eff}^\Psi&=\frac{\partial\mathcal{L}_\Psi^{\rm int}}{\partial\chi_\delta}\left(\frac{\epsilon_{\alpha\delta}}{m_\Psi^2}+\frac{D^2\epsilon_{\alpha\delta}+\frac{i}{2}X_\alpha{}^\gamma\epsilon_{\gamma\delta}}{m_\Psi^4}+\dots\right)\left(iD^{\dot\beta\alpha}\frac{\partial\mathcal{L}_\Psi^{\rm int}}{\partial\chi^{\dagger\dot\beta}}+m_\Psi\frac{\partial\mathcal{L}_\Psi^{\rm int}}{\partial\eta_\alpha}\right)\\&+\frac{\partial\mathcal{L}_\Psi^{\rm int}}{\partial\eta_\delta}\left(\frac{\epsilon_{\alpha\delta}}{m_\Psi^2}+\frac{D^2\epsilon_{\alpha\delta}+\frac{i}{2}X_\alpha{}^\gamma\epsilon_{\gamma\delta}}{m_\Psi^4}+\dots\right)\left(iD^{\dot\beta\alpha}\frac{\partial\mathcal{L}_\Psi^{\rm int}}{\partial\eta^{\dagger\dot\beta}}+m_\Psi\frac{\partial\mathcal{L}_\Psi^{\rm int}}{\partial\chi_\alpha}\right)+\text{h.c.}\\&=\frac{\partial\mathcal{L}_\Psi^{\rm int}}{\partial\bar\Psi}\left(\frac{1}{m_\Psi^2}+\frac{D^2+\frac{1}{2}X_{\mu\nu}\sigma^{\mu\nu}}{m_\Psi^4}+\dots\right)(i\not{D}+m_\Psi)\frac{\partial\mathcal{L}_\Psi^{\rm int}}{\partial\Psi}\,,\end{aligned} \tag{5.21}$$

where we have used the relation

$$\sigma^{\mu\nu}\equiv\frac{i}{2}\left[\gamma^\mu,\gamma^\nu\right]. \tag{5.22}$$

Extending this formalism to Majorana fields can be done via the replacement $\eta^\alpha\to\chi^\alpha$ and $m_\Psi\to\frac{1}{2}m_\Psi$.

5.1.3. Vector field

A massive vector field $\mathbf{V}^\mu$ leads to the simplified Lagrangian

$$\mathcal{L}_{\rm S}\supset-\frac{1}{4}\left(D_\mu\mathbf{V}_\nu^*-D_\nu\mathbf{V}_\mu^*\right)\left(D^\mu\mathbf{V}^\nu-D^\nu\mathbf{V}^\mu\right)+\frac{1}{2}m_{\mathbf{V}}^2\mathbf{V}_\mu^*\mathbf{V}^\mu-\frac{\partial\mathcal{L}_{\mathbf{V}}^{\rm int}}{\partial\mathbf{V}_\mu^*}\mathbf{V}_\mu^*\,, \tag{5.23}$$

where we have the field strength $X^{\mu\nu}=-i\left[D^\mu,D^\nu\right]$. From Eq. (5.23) we then obtain the EOM

$$D^2\mathbf{V}^\mu-D^\nu D_\mu\mathbf{V}^\nu+m_{\mathbf{V}}^2\mathbf{V}^\mu-\frac{\partial\mathcal{L}_{\mathbf{V}}^{\rm int}}{\partial\mathbf{V}_\mu^*}=0\,, \tag{5.24}$$

which can be solved by the classical vector field

$$\begin{aligned}(\mathbf{V}_{\rm cl})_\rho&=\left(D^2\eta^{\mu\rho}-D^\nu D^\mu\eta_{\nu\rho}+m_{\mathbf{V}}^2\eta^{\mu\rho}\right)^{-1}\frac{\partial\mathcal{L}_{\mathbf{V}}^{\rm int}}{\partial\mathbf{V}_\mu^*}\\&=\frac{1}{m_{\mathbf{V}}^2}\left(\eta_{\mu\rho}+\frac{D^2\eta_{\mu\rho}-D_\nu D_\mu\eta^{\nu\rho}}{m_{\mathbf{V}}^2}+\dots\right)\frac{\partial\mathcal{L}_{\mathbf{V}}^{\rm int}}{\partial\mathbf{V}_\mu^*}.\end{aligned} \tag{5.25}$$

In the effective Lagrangian this then leads to a series of interaction terms

$$\begin{aligned}\mathcal{L}_{\text{eff}} \supset \mathcal{L}^{\mathbf{V}}_{\text{eff}} &= \frac{\partial \mathcal{L}^{\text{int}}_{\mathbf{V}}}{\partial \mathbf{V}_\nu}\left(\frac{\eta_{\mu\nu}}{m^2_{\mathbf{V}}} + \frac{D^2\eta_{\mu\nu} - D_\nu D_\mu}{m^4_{\mathbf{V}}} + \dots\right)\frac{\partial \mathcal{L}^{\text{int}}_{\mathbf{V}}}{\partial \mathbf{V}^*_\mu} \\ &= \frac{1}{4}\frac{\partial \mathcal{L}^{\text{int}}_{\mathbf{V}}}{\partial \mathbf{V}_{\alpha\dot\beta}}\left(\frac{2\delta_\alpha{}^\delta\delta_{\dot\beta}{}^{\dot\gamma}}{m^2_{\mathbf{V}}} + \frac{2D^2\delta_\alpha{}^\delta\delta_{\dot\beta}{}^{\dot\gamma} - D_{\alpha\dot\beta}D^{\dot\gamma\delta}}{m^4_{\mathbf{V}}} + \dots\right)\frac{\partial \mathcal{L}^{\text{int}}_{\mathbf{V}}}{\partial \mathbf{V}^{*\dot\gamma\delta}}\,.\end{aligned} \tag{5.26}$$

This concludes our analysis of the different Lorentz structures in CDE. In the next section we apply this formalism to EFT operators to find their underlying UV-completions.

5.2. Operator expansion

The derivative of an interaction Lagrangian with respect to the heavy field Π_j can be written in terms of light scalar ϕ_i and fermion ψ_i fields, as well as heavy BSM fields Π_i, such that we have

$$\frac{\partial \mathcal{L}^{\text{int}}_\Phi}{\partial \Pi^\dagger_j} = \sum_{i,a,b,c}\left(1 + c_{\Pi_i}\frac{\partial \mathcal{L}^{\text{int}}_\Phi}{\partial \Pi^\dagger_i}\right)\left(c_\psi \psi^\alpha_a \psi_{b\alpha} + c_{\psi^\dagger}\psi^\dagger_{a\dot\alpha}\psi^{\dagger\dot\alpha}_b + c_\phi \phi_a\phi_b\phi_c + \mu_\phi\phi_a\phi_b\right)\,. \tag{5.27}$$

Here c_i are dimensionless coupling constants, and μ_i has mass dimension one. The derivative $\partial\mathcal{L}^{\text{int}}_\Phi/\partial\Pi^\dagger_i$ can subsequently be expanded again, and this procedure can be repeated until only light fields remain. Note that we do not include light vector fields because we want to match with the SM, where all vector bosons are gauge bosons that instead appear in the covariant derivative. In a given UV-complete simplified model, there can exist multiple heavy fields with different interactions terms and different Lorentz- and gauge structures. We therefore write the total effective Lagrangian as

$$\mathcal{L}_{\text{eff}} = \mathcal{L}_{\text{SM}} + \sum_i \sum_{a,b,\dots} \mathcal{L}^{\Pi_a,\Pi_b,\dots(i)}_{\text{eff}}\,. \tag{5.28}$$

Here the dimension of the light field bilinears that were obtained in the CDE is denoted by the superscript (i), where the smallest possible mass dimension is 5. Furthermore, Π_a denotes a heavy vector, scalar, or fermion field that leads to the given light-field bilinear when integrated out. We want to finally match with SMEFT, and therefore all terms in the effective Lagrangian must only contain light fields that are part of the SM. However, since in the CDE only one heavy field is integrated out at a time, the terms in the UV-complete simplified model Lagrangian that contain several heavy BSM fields $\Pi_a, \Pi_b, \dots$ must go through many iterations of the CDE procedure, leaving only SM fields in the end.

Eq. (5.28) can be matched to an EFT Lagrangian written in terms of a series of NP operators and Wilson coefficients,

$$\mathcal{L}_{\text{eff}} = \mathcal{L}_{\text{SM}} + \sum_i \sum_a C^{(i)}_a \mathcal{O}^{(i)}_a\,. \tag{5.29}$$

For each mass dimension i, the effective Lagrangian in Eq. (5.29) can be written using a full basis of SMEFT operators that contain SM fields, covariant derivatives, and field strengths.

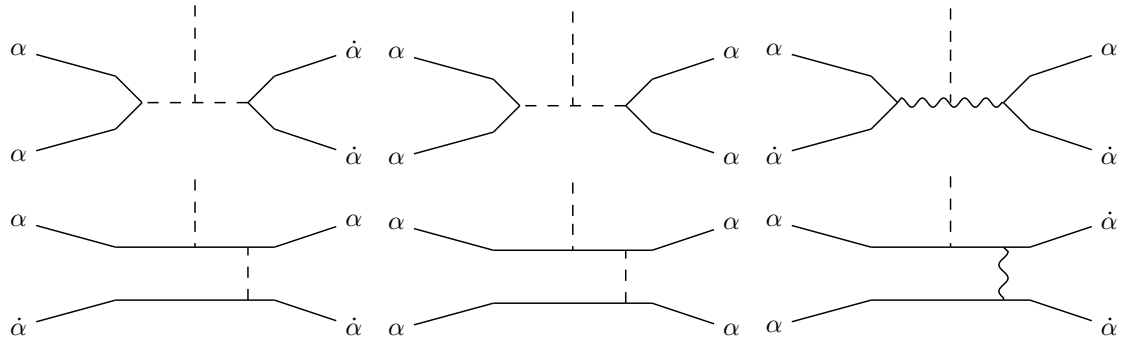

Figure 5.1.: Tree-level topologies that appear in UV-completions of dimension-7 $\Delta L = 2$ operators of type $\Psi^4 H$. Here α is a spinor index and $\dot{\alpha}$ is an antispinor index.

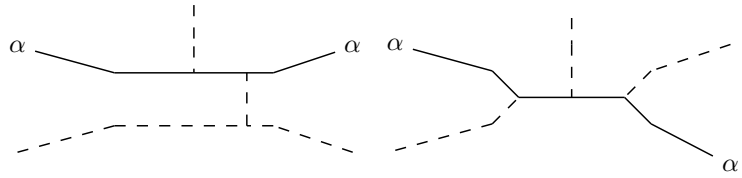

Figure 5.2.: Tree-level topologies that appear in UV-completions of dimension-7 $\Delta L = 2$ operators of type $\Psi^2 H^3 D$. Here α is a spinor index.

When matching this EFT Lagrangian to the expression in Eq. (5.28), the Wilson coefficients are expressed in terms of the masses and coupling constants corresponding to the heavy fields, and the SMEFT operators are obtained from derivatives of the heavy field interaction Lagrangians. By performing the CDE in reverse for a given SMEFT operator and all its Fierz transformed counterparts, in all ways that do not leave any free spinor- or Lorentz indices and does not produce any term that is charged under the SM gauge symmetry group $SU(3)_c \times SU(2)_L \times U(1)_Y$, we can obtain all possible combinations of heavy fields that lead to tree-level UV completions of the operator in question. We call this procedure *exploding* following Ref. [489], in which systematic decompositions of $\Delta L = 2$ operators in the Babu-Leung basis were made for scalar and fermionic UV-completions. We extend this work here using the Lehman basis by considering also heavy vector fields and by analysing the results in a novel way in terms of a hierarchy in the internal degrees of freedom.

In Tab. 4.5 we list all dimension-7 $\Delta L = 2$ SMEFT operators. From this list, the ones that will be the main focus in this chapter are those of type $\Psi^4 H$ ($\mathcal{O}_{\bar{e}LLLH}$, $\mathcal{O}_{\bar{d}LQLH1}$, $\mathcal{O}_{\bar{d}LQLH2}$, $\mathcal{O}_{\bar{d}LueH}$, and $\mathcal{O}_{\bar{Q}uLLH}$), type $\Psi^2 H^3 D$ ($\mathcal{O}_{LeHD}$), and type $\Psi^2 H^4$ ($\mathcal{O}_{LH}$). Exploding these operators results in the list of heavy BSM fields shown in Tab. 5.1. These are the only fields that can UV-complete the dimension-7 $\Delta L = 2$ SMEFT operators at tree-level. In the interaction basis, at least two fields from Tab. 5.1 are used per UV-completion, and for operator $\mathcal{O}_{LH}$ some UV-completions involve three heavy fields. We denote these types of UV-completions as *two-* and *three-field combinations*, respectively, where our main focus towards the end of this chapter will be on two-field combinations.

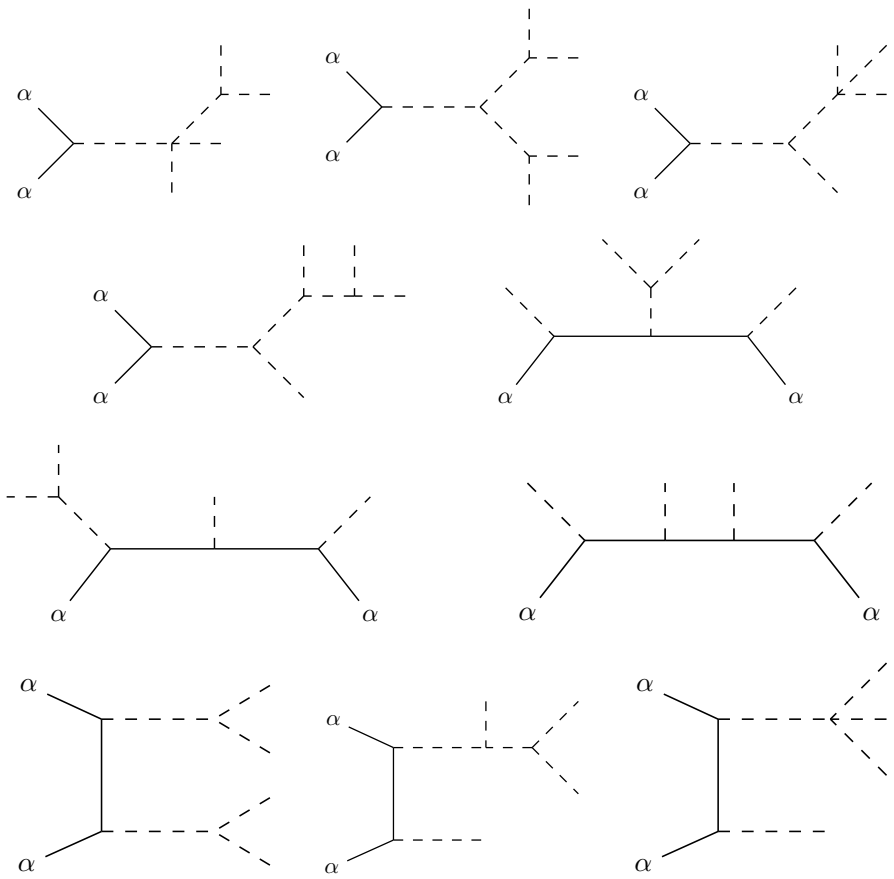

Figure 5.3.: Tree-level topologies that appear in UV-completions of dimension-7 $\Delta L = 2$ operators of type $\psi^2 H^4$. Here α is a spinor index.

Field	Rep	Coupling to SM fields (+h.c.)
$\mathcal{S}$	$S(1,1,0)(0)$	$\frac{1}{2}\kappa_{\mathcal{S}}\mathcal{S}H^\dagger H + \frac{1}{2}\lambda_{\mathcal{S}}\mathcal{S}\mathcal{S}H^\dagger H$
Ξ	$S(1,3,0)(0)$	$\frac{1}{2}\kappa_\Xi H^\dagger \Xi^a \sigma^a H + \frac{1}{2}\lambda_\Xi \left(\Xi\Xi\right)\left(H^\dagger H\right)$
h	$S(1,1,1)(0)$	$y_h h^\dagger \bar{L} i\sigma_2 L^c + \kappa_h h^\dagger \tilde{H}^\dagger H$
Δ	$S(1,3,1)(0)$	$\frac{1}{4}\lambda_\Delta \left(\Delta^\dagger\Delta\right)\left(H^\dagger H\right) + \frac{1}{4}\lambda'_\Delta f_{abc}\left(\Delta^{a\dagger}\Delta^b\right)\left(H^\dagger\sigma^c H\right)$ $+ y_\Delta \Delta^{a\dagger}\bar{L}\sigma^a i\sigma_2 L^c + \kappa_\Delta \Delta^{a\dagger}\left(\tilde{H}^\dagger\sigma^a H\right)$
φ	$S(1,2,1/2)(0)$	$\lambda_\varphi\left(\varphi^\dagger H\right)\left(H^\dagger H\right) + y^e_\varphi \varphi^\dagger \bar{e} L + y^d_\varphi \varphi^\dagger \bar{d} Q + y^u_\varphi \varphi^\dagger i\sigma_2 \bar{Q}^T u$
Θ_1	$S(1,4,1/2)(0)$	$\lambda_{\Theta_1}\left(H^\dagger\sigma^a H\right) C^I_{ab}\tilde{H}^b \epsilon_{IJ}\Theta^J_1$
Θ_3	$S(1,4,3/2)(0)$	$\lambda_{\Theta_3}\left(H^\dagger\sigma^a\tilde{H}\right) C^I_{ab}\tilde{H}^b \epsilon_{IJ}\Theta^J_3$
S_1	$S(\bar{3},1,1/3)(-1)$	$y^{ql}_{S_1} S_1 \bar{Q}^c i\sigma_2 L + y^{qq}_{S_1} S_1 \bar{Q} i\sigma_2 Q^c + y^{du}_{S_1} S_1 \bar{d} u^c + y^{eu}_{S_1} S_1 \bar{e}^c u$
$\tilde{R}_2$	$S(3,2,1/6)(1)$	$y_{\tilde{R}_2}\tilde{R}_2^\dagger i\sigma_2 \bar{L}^T d$
S_3	$S(\bar{3},3,1/3)(-1)$	$y^{ql}_{S_3} S^a_3 \bar{Q}^c i\sigma_2\sigma^a L + y^{qq}_{S_3} S^a_3 \bar{Q}\sigma^a i\sigma_2 Q^c$
N	$F(1,1,0)(0)$	$\lambda_N \bar{N}\tilde{\phi}^\dagger L$
Σ	$F(1,3,0)(0)$	$\frac{1}{2}\lambda_\Sigma \bar{\Sigma}^a \tilde{\phi}^\dagger \sigma^a L$
Σ_1	$F(1,3,-1)(0)$	$\frac{1}{2}\lambda_{\Sigma_1}\bar{\Sigma}^a_1 \phi^\dagger \sigma^a L$
Δ_1	$F(1,2,-1/2)(0)$	$\lambda_{\Delta_1}\bar{\Delta}_1 He$
Δ_3	$F(1,2,-3/2)(0)$	$\lambda_{\Delta_3}\bar{\Delta}_1 \tilde{H} e$
F_4	$F(1,4,1/2)(0)$	$-$
U	$F(3,1,2/3)(1)$	$\lambda_U \bar{U}\tilde{H}^\dagger Q$
Q_5	$F(3,2,-5/6)(1)$	$\lambda_{Q_5}\bar{Q}_5 \tilde{H} d$
Q_7	$F(3,2,7/6)(1)$	$\lambda_{Q_7}\bar{Q}_7 H u$
T_1	$F(3,3,-1/3)(1)$	$\frac{1}{2}\lambda_{T_1}\bar{T}^a_1 H^\dagger \sigma^a Q^b$
T_2	$F(3,3,2/3)(1)$	$\frac{1}{2}\lambda_{T_2}\bar{T}^a_2 \tilde{H}^\dagger \sigma^a Q^b$
W'_1	$V(1,1,1)(0)$	$\frac{1}{2} g^{du}_{W'_1} W'^{\mu\dagger}_1 \bar{d}\gamma_\mu u + g^H_{W'_1} W'^{\mu\dagger}_1 iD_\mu H^T i\sigma_2 H$
V_3	$V(1,2,3/2)(0)$	$V^\mu_3 \bar{e}^c \gamma_\mu L$
U_1	$V(3,1,2/3)(1)$	$g^{ed}_{U_1} U^{\mu\dagger}_1 \bar{e}\gamma_\mu d + g^{lq}_{U_1} U^{\mu\dagger}_1 \bar{L}\gamma_\mu Q$
$\bar{V}_2$	$V(\bar{3},2,-1/6)(-1)$	$g^{ul}_{\bar{V}_2}\bar{V}^\mu_2 \bar{u}^c\gamma_\mu L + g^\mu_{\bar{V}_2}\bar{d}\gamma_\mu i\sigma_2 Q^c$
U_3	$V(3,3,2/3)(1)$	$g_{U_3} U^{a\mu\dagger}_3 \bar{L}\gamma_\mu\sigma^a Q$

Table 5.1.: All heavy BSM fields that appear in the explosions of dimension-7 LNV operators, shown in the representation that has a positive hypercharge, as well as their allowed couplings to SM fields. The different naming conventions follow from Refs. [480, 484, 496–498]. The representation in the second column corresponds to the SM gauge group $SU(3)_c \times SU(2)_L \times U(1)_Y$, where the last parenthesis $(3B)$ shows the baryon number B multiplied by three, and the letter in front of the representation indicates whether the field is a scalar (S), fermion (F), or vector (V).

	$\mathcal{O}_{LH}$	$\mathcal{O}_{LeHD}$	$\mathcal{O}_{\bar{e}LLLH}$	$\mathcal{O}_{\bar{d}LueH}$	$\mathcal{O}_{\bar{d}LQLH1}$	$\mathcal{O}_{\bar{d}LQLH2}$	$\mathcal{O}_{\bar{Q}uLLH}$
$\mathcal{S}$	Δ, N, Σ						
Ξ	Δ, Σ						
h			$\varphi, N, \Delta_3^\dagger$			$\varphi, U, Q_5^\dagger$	
Δ	$\mathcal{S}, \Xi, \Delta, \varphi, \Theta_1, \Theta_3, \Sigma$	$\Sigma, \Delta_1^\dagger$	$\varphi, \Sigma, \Delta_3^\dagger$		$\varphi, S_3, Q_5^\dagger$		$\varphi, Q_7, T_1^\dagger$
φ	Δ, N, Σ		h, Δ, N, Σ		Δ, N, Σ	h, Σ	Δ, N, Σ
Θ_1	Δ, Σ						
Θ_3	$\Delta, \Sigma_1^\dagger$						
S_1				$\tilde{R}_2, N, Q_5^\dagger$	$\tilde{R}_2, N, Q_5^\dagger$		
$\tilde{R}_2$				$S_1, \Delta_1^\dagger, Q_7$	S_1, S_3, N, Σ, T_2	S_3, Σ, U	
S_3				$\Delta, \tilde{R}_2, \Sigma, Q_5^\dagger$	$\tilde{R}_2, \Sigma, Q_5^\dagger$	$\tilde{R}_2$	
N	$\mathcal{S}, \varphi, \Delta_1^\dagger$	$\Delta_1^\dagger$	h, φ	S_1, W_1', U_1	$\varphi, S_1, \tilde{R}_2$		$\varphi, U_1, \bar{V}_2^\dagger$
Σ	$\mathcal{S}, \Xi, \Delta, \varphi, \Theta_1, \Delta_1^\dagger, F_4$	$\Delta, \Delta_1^\dagger$	Δ, φ		$\varphi, \tilde{R}_2, S_3$	$\varphi, \tilde{R}_2, S_3$	$\varphi, \bar{V}_2^\dagger, U_3$
$\Sigma_1^\dagger$	Θ_3						

Table 5.2.: Part 1 of a list showing the combinations of heavy BSM fields that generate tree-level UV-completions of dimension-7 $\Delta L = 2$ operators. Here the operators at the top are generated by combining the fields in their respective columns with the corresponding field to the left in each row. There is one row for each field, and since we are considering two-field UV-completions, each UV-completion is listed exactly twice. For the representations of the different fields under the SM symmetry group, as well as their couplings to the SM fields, see Tab. 5.1.

	$\mathcal{O}_{LH}$	$\mathcal{O}_{LeHD}$	$\mathcal{O}_{\bar{e}LLLH}$	$\mathcal{O}_{\bar{d}LueH}$	$\mathcal{O}_{\bar{d}LQLH1}$	$\mathcal{O}_{\bar{d}LQLH2}$	$\mathcal{O}_{\bar{Q}uLLH}$
$\Delta_1^\dagger$	N, Σ	Δ, N, Σ		$\tilde{R}_2, W_1', \bar{V}_2^\dagger$			
$\Delta_3^\dagger$			h, Δ				
F_4	Σ						
U						$h, \tilde{R}_2$	
$Q_5^\dagger$				$S_1, V_3, \bar{V}_2^\dagger$	Δ, S_1, S_3	h, S_3	
Q_7				$\tilde{R}_2, V_3, U_1$			Δ, U_1, U_3
$T_1^\dagger$							$\Delta, \bar{V}_2^\dagger$
T_2					$\tilde{R}_2$		
W_1'				$N, \Delta_1^\dagger, V_3$			
V_3				$Q_5^\dagger, Q_7, W_1'$			
U_1				$N, Q_7, \bar{V}_2^\dagger$			$N, Q_7, \bar{V}_2^\dagger$
$\bar{V}_2^\dagger$				$\Delta_1^\dagger, Q_5^\dagger, U_1$			$N, \Sigma, T_1^\dagger, U_1, U_3$
U_3							$\Sigma, Q_7, \bar{V}_2^\dagger$

Table 5.3.: Part 2 of a list showing the combinations of heavy BSM fields that generate tree-level UV-completions of dimension-7 $\Delta L = 2$ operators. Here the operators at the top are generated by combining the fields in their respective columns with the corresponding field to the left in each row. There is one row for each field, and since we are considering two-field UV-completions, each UV-completion is listed exactly twice. For the representations of the different fields under the SM symmetry group, as well as their couplings to the SM fields, see Tab. 5.1.

In Fig. 5.1, 5.2, and 5.3 we show the different topologies corresponding to operators of types $\Psi^4 H$, $\Psi^2 H^3 D$, and $\Psi^4 H$, respectively. Here scalar and vector bosons are drawn with dashed and wavy lines, respectively, and fermions are drawn with solid lines, where spinor indices are indicated by α and antispinor indices by $\dot{\alpha}$. In Fig. 5.1 we see that different Lorentz structures appear in the contraction of fermions depending on whether they have spinor- or antispinor indices. Diagrams where all fermions have spinor indices lead only to UV-completions with scalar mediators, while if two fermions have antispinor indices also vector mediators can be generated. In Fig. 5.3 we see that many topologies coming from operator $\mathcal{O}_{LH}$ have three heavy mediators. However, in some of these three-field UV-completions, two out of the three fields are identical. In such cases, we classify the UV-completion as two-field.

In Tabs. 5.2 and 5.3, the specific two-field combinations of the fields that give rise to different operators are shown. This list is exhaustive: there are no other tree-level UV-completions of $\Delta L = 2$ dimension-7 SMEFT operators. We see that only two operators feature UV-completions with vector fields, namely $\mathcal{O}_{\bar{Q}uLLH}$ and $\mathcal{O}_{\bar{d}LueH}$. These are the only operators that contain fermions with spinor indices as well as fermions with antispinor indices, and therefore they are the only ones that can generate a vector mediator. There are many heavy fields that are unique to operator $\mathcal{O}_{LH}$, where three of these are $SU(2)_L$ quadruplets (Θ_1, Θ_3, and F_4). The heavy fields N and Σ both appear in six out of the seven operators, while Δ and φ both appear in five out of seven. These are the most commonly occurring fields in explosions of dimension-7 $\Delta L = 2$ operators. As discussed in Sec. 2.3.2, the fields N, Δ, and Σ are the ones that give rise to the three possible tree-level UV-completions of the dimension-5 operator. The field φ on the other hand has the same representation under the SM gauge symmetry group as the Higgs fields, which means that it can couple to a large variety of other SM fields.

As an example of how the explosion can be done, the method of obtaining the UV-completions for operator $\mathcal{O}_{\bar{Q}uLLH}$ is outlined below.

5.2.1. Example: $\mathcal{O}_{\bar{Q}uLLH}$

We now proceed to explode the operator $\mathcal{O}_{\bar{Q}uLLH} = \epsilon_{ij}(\overline{Q}u)(\overline{L^c}L^i)H^j$. Assuming that this operator has been obtained in the CDE by repeatedly integrating out heavy fields, we can reverse the process to find the underlying UV-completions. The goal of this explosion is to identify all ways in which a CDE method could have led to $\mathcal{O}_{\bar{Q}uLLH}$. We hope to find all minimal renormalisable simplified-model Lagrangians containing only SM fields as well as generic heavy vector-, fermion-, or scalar fields that could lead to some Fierz transformed version of $\mathcal{O}_{\bar{Q}uLLH}$. The first step is to disentangle the spinor contractions, such that we consider all of them, and randomly select one SM field that couples to the other SM fields one at a time,

$$\mathcal{O}_{\bar{Q}uLLH} = \epsilon_{ij}(\overline{Q}u)(\overline{L^c}L^i)H^j \quad \rightarrow \quad \epsilon_{ij}\overline{Q}^k u L^k L^i H^j \,. \tag{5.30}$$

The above equation should be read as follows: we consider the quark doublet $\overline{Q}^k$ to be part of

a renormalisable term in the full simplified-model Lagrangian along with one of the other SM fields from the operator, u, L^k, L^i, or H^j, as well as a new heavy field which we generically denote as χ_1, ψ_1, ϕ_1, or ω_1. The Lorentz structures and SM gauge group representations of the heavy fields can be read off from the combination of the SM fields it contracts with in the full simplified Lagrangian, using the fact that the whole term has to be a Lorentz-invariant SM singlet. We then repeat the procedure by coupling the remaining SM fields to the heavy field, one at a time, such that we have

$$\mathcal{O}_{\bar{Q}uLLH} \quad \to \quad \epsilon_{ij}\overset{\chi_3}{\overbrace{\chi_1{}^k L^k}}\underset{\chi_2}{\underbrace{L^i}}\overset{\chi_4}{\overbrace{H^j}} \;\Big/\; \epsilon_{ij}\overset{\psi_2}{\overbrace{\psi_1{}^k}}\overset{\psi_4}{\overbrace{u L^i}}\underset{\psi_3}{\underbrace{H^j}} \;\Big/\; \epsilon_{ij}\overset{\phi_2}{\overbrace{\phi_1{}^k}}\overset{\phi_4}{\overbrace{u L^k}}\underset{\phi_3}{\underbrace{H^j}} \;\Big/\; \epsilon_{ij}\overset{\omega_2}{\overbrace{\omega_1{}^k}}\overset{\omega_4}{\overbrace{u L^k}}\underset{\omega_3}{\underbrace{L^i}}\,. \tag{5.31}$$

Now all terms are renormalisable and the process comes to an end[3]. In our notation, the field χ_1 can be paired with χ_i, $i \in \{2,3,4\}$ to realise a tree-level UV-completion of the the operator $\mathcal{O}_{\bar{Q}uLLH}$. Similarly, we can pair ψ_1 with ψ_i, $i \in \{2,3,4\}$, and so on. There is however one remaining caveat: our initial choice of selecting the quark doublet $\overline{Q}^k$ to contract with the other fields was an arbitrary one. It is possible construct the operator $\mathcal{O}_{\bar{Q}uLLH}$ using renormalizable terms for which, in addition to the SM terms, $\overline{Q}^k$ only couples to heavy BSM fields. In this case there are no terms of the form given in Eq. (5.31), instead all terms involving $\overline{Q}^k$ can be written as $\overline{Q}^k\zeta_1\zeta_2$, where ζ_1 and ζ_2 are heavy fields. This leads to three possibilities, namely

$$\{\zeta_1,\zeta_2\} = \{\chi_2,\phi_4\},\ \{\chi_3,\psi_4\},\ \{\chi_4,\psi_3\}\,. \tag{5.32}$$

After this last consideration we have exhausted the possibilities to tree-level UV-complete the operator $\mathcal{O}_{\bar{Q}uLLH}$. The representations under the SM gauge group and Lorentz structures of the new fields can be deduced from the combination of SM fields that they couple to in the full Lagrangian. We then simply read off

$$\begin{array}{llll}
\chi_1 \sim S(1,2,1/2) & \psi_1 \sim V(\overline{3},1,-2/3) & \phi_1 \sim V(\overline{3},3,-2/3) & \omega_1 \sim F_L(\overline{3},3,1/3) \\
\chi_2 \sim F_R(1,1,0) & \psi_2 \sim F_R(1,1,0) & \phi_2 \sim F_R(1,3,0) & \omega_2 \sim S(1,3,1) \\
\chi_3 \sim F_R(1,3,0) & \psi_3 \sim F_L(\overline{3},2,-7/6) & \phi_3 \sim F_L(\overline{3},2,-7/6) & \omega_3 \sim V(\overline{3},2,-1/6) \\
\chi_4 \sim S(1,3,1) & \psi_4 \sim V(\overline{3},2,-1/6) & \phi_4 \sim V(\overline{3},2,-1/6) & \omega_4 \sim V(\overline{3},2,-1/6)\ .
\end{array} \tag{5.33}$$

Here S, V, F_L, and F_R denote scalar, vector, left-handed fermion, and right-handed fermion fields, respectively. Note however that due to anomaly cancellation (c.f. Sec. 2.1.5) we generally cannot introduce new heavy chiral fermions naively, and we therefore considerer all BSM fermions to be vector-like $F_L, F_R \to F$ from here on. Many fields have identical representations in Eq. (5.33), and this list is therefore overcomplete.

[3]Note that for some higher dimensional operators, e.g. dimension 9 or 11, as well as the dimension-7 operator $\mathcal{O}_{LH}$, we would have had to continue the procedure by repeating the second step until only renormalizable terms remain.

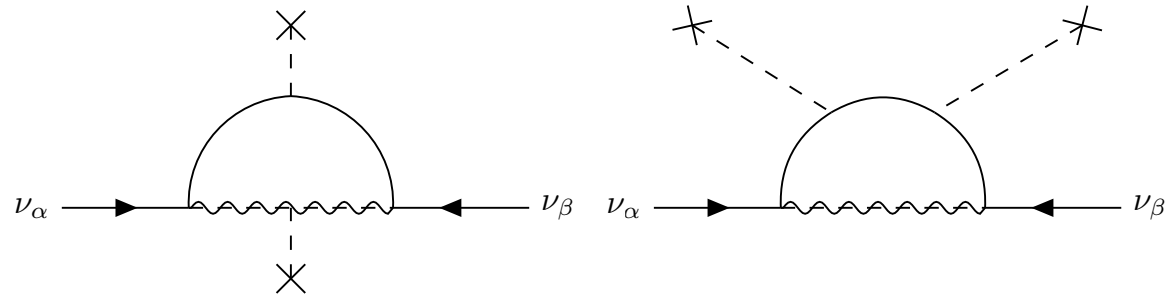

Figure 5.4.: Left: Topology I **Right:** Topology II.

This concludes our explosion of operator $\mathcal{O}_{\bar{Q}uLLH}$. In the next section, we will discuss the neutrino mass topologies that are generated by the different UV-completions underlying dimension-7 $\Delta L = 2$ operators.

5.3. Neutrino masses in UV-completions at dimension-7

In this section we will discuss the radiative neutrino mass topologies that can be generated in the simplified models found by applying the explosion procedure from Sec. 5.2 onto the dimension-7 $\Delta L = 2$ operators.

From the twelve operators in Tab. 4.5, seven lead to tree-level UV-completions that do not necessarily involve any of the seesaw fields. As can be seen in the CDE in Sec. 5.1, operators of types $\Psi^2H^2D^2$ and $\Psi^2H^2X^2$ appear as higher order corrections to UV-completions of the Weinberg operator at tree-level. Therefore, the underlying simplified model also induces the dimension-5 operator at tree-level in addition to the higher order dimension-7 operator. Furthermore, the operator of type Ψ^4D cannot lead to a tree-level UV-completion according to the CDE formalism, since the covariant derivative D should arise from a fermion mediator, however the four fermion legs of the operator cannot be contracted with a fermion mediator due to conservation of fermion number. The conclusion is then that this operator can only be realised at loop-level.

5.3.1. Neutrino mass topologies

Out of the seven explosive operators, one is of the form ΨH^4, one Ψ^2H^3D, and the rest Ψ^4H. In the following sections we construct all possible neutrino mass realisations beyond the three seesaw types using the UV-completions of these seven dimension-7 operators.

Ψ^4H

Operators of type Ψ^4H contain two distinct subtypes: those where all fermions carry spinor indices, and those where only two fermions have spinor indices while the other two have antispinor indices. The first subtype gives rise to radiative neutrino mass diagrams mediated via either scalar or vector bosons, while the second subtype only leads to scalar-mediated

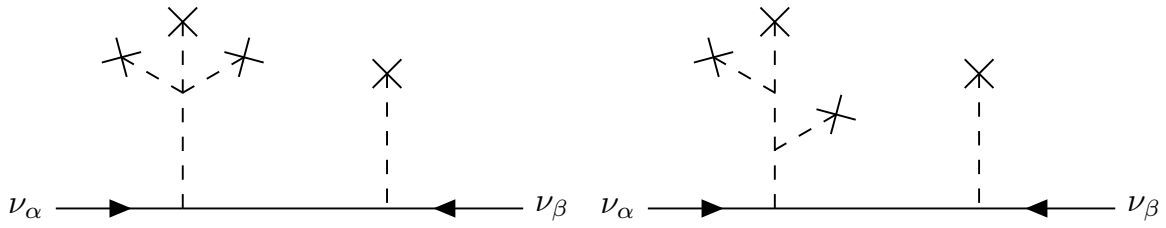

Figure 5.5.: Left: Topology III **Right:** Topology IV.

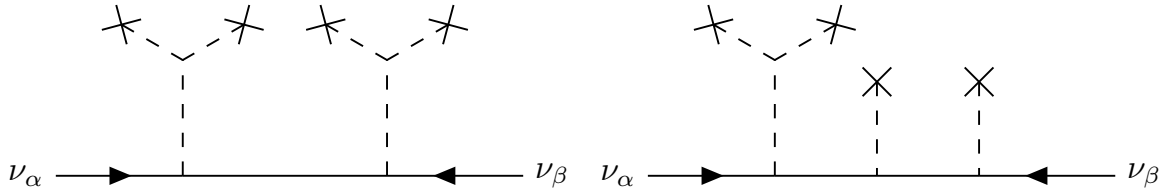

Figure 5.6.: Left: Topology V **Right:** Topology VI.

diagrams. There are two distinct topologies (which we denote as Topology I and Topology II) for this radiative mass, and both of them are shown in Fig. 5.4, where the bosonic mediator is either scalar or vector. For UV-completions that generate Topology II with a type-ii seesaw mediator boson Δ there is also an additional diagram where the seesaw field contracts directly with the two neutrinos.

Ψ^2H^3D

For type Ψ^2H^3D there is only one dimension-7 $\Delta L = 2$ operator, namely $\mathcal{O}_{LeHD}$. For this operator there is only one tree-level UV-completion that does not also lead to a tree-level UV-completion of the Weinberg operator: the combination of Δ and $\Delta_1^\dagger$. Rather than closing two fermion legs, as is how neutrino mass diagrams of Topology I can be generated from operators of type Ψ^4H, for this specific UV-completion of $\mathcal{O}_{LeHD}$ we can connect one of the Higgs fields to the lepton singlet leg, thereby closing them in a loop. This leads to an external L leg, as required in a neutrino mass diagram.

Ψ^2H^4

There is also only a single dimension-7 $\Delta L = 2$ operator for type Ψ^2H^4, namely $\mathcal{O}_{LH}$. This operator is of the same structure as the Weinberg operator, except that it has an additional Higgs-anti-Higgs pair with self-contracting $SU(2)_L$-indices. This simple modification to the dimension-5 operator leads to a plethora of UV-completions with many possible neutrino mass topologies, as shown in Figs. 5.5 to 5.7. However, for $\mathcal{O}_{LH}$ there is only one tree-level UV-completion that does not contain any of the seesaw fields. This UV-completion is realised by the combination of Θ_3 and $\Sigma_1^\dagger$, as can be seen in Tabs. 5.2 and 5.3. Due to the fact that $\mathcal{O}_{LH}$ contains six external legs rather than five, as is the case in Ψ^4H- and Ψ^2H^3D-type operators,

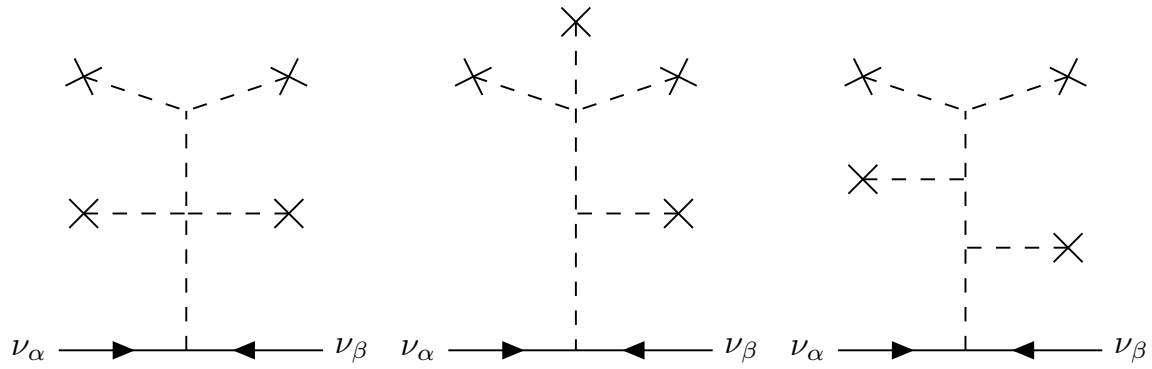

Figure 5.7.: Left: Topology VII **Centre:** Topology VIII **Right:** Topology IX.

tree-level UV-completions of $\mathcal{O}_{LH}$ can contain three different BSM fields rather than only two[4]. All such combinations of three fields are shown in Tabs. 5.11 to 5.13, where two of the fields are given in the row and column of each table, and the third is the seesaw field shown in the respective top-left corners. All UV-completions of $\mathcal{O}_{LH}$ with three fields contain at least one of the three seesaw fields. Entries in the diagonal of Tabs. 5.11 to 5.13 show the UV-completions that only require two heavy fields: the seesaw field in the top-left corner and the field in the corresponding row and column. The tree-level neutrino mass diagrams that appear for $\mathcal{O}_{LH}$ can be thought of as extended seesaw diagrams, such that they constitute the next-simplest neutrino Majorana mass diagrams at tree-level, where the three regular seesaw diagrams are the simplest.

Figs. 5.5 to 5.7 do not represent an exhaustive list of extended seesaw diagrams. However, the additional diagrams not shown there contain either the type-i or iii seesaw fields, which would lead to a tree-level UV-completion of the dimension-5 operator, as is discussed in Sec. 5.3.2. Note that extended seesaw diagrams with type-i or iii seesaw fields could still provide the most dominant contribution to neutrino masses depending on the hierarchy between Dirac and Majorana mass contributions (e.g. as in inverse seesaw [499–501]).

5.3.2. Simplified neutrino mass models

Here we summarise the results of the explosion procedure described in Sec. 5.2 applied to all dimension-7 $\Delta L = 2$ operators that lead to tree-level UV-completions, in the context of the radiative neutrino Majorana mass diagrams discussed in Sec. 5.3. These results are presented as tables corresponding to each individual operator that describe the specific neutrino mass topology (c.f. Sec. 5.3.1) that is generated for each combination of heavy BSM fields. We are mainly interested in radiative neutrino mass diagrams that do not contain couplings that inevitably also lead to a tree-level UV-completion of the dimension-5 operator. The reason for this is that the radiative diagram would be expected to be subdominant to the seesaw

[4]The maximum number of heavy NP mediators n needed to tree-level UV-complete a given operator that contains $m \geq 3$ external legs is $n = m - 3$. For operators with multiple boson legs this number can be smaller since four bosons can couple to the same vertex.

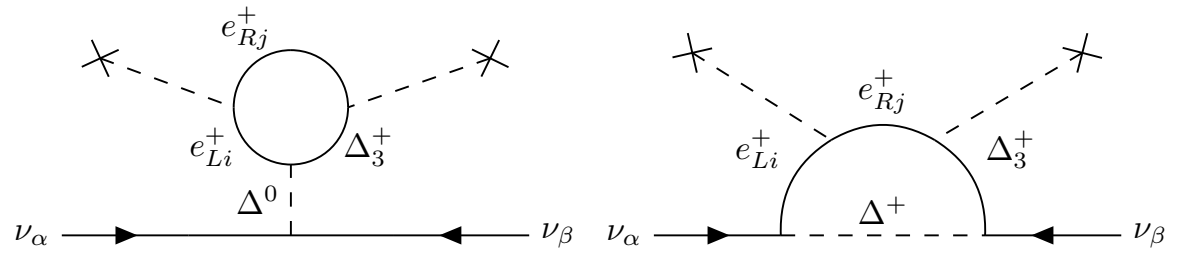

Figure 5.8.: Example of a scenario where a UV-completion leads to a neutrino mass diagram containing Δ in the absence of its coupling to the SM Higgs doublet, such that $\mathcal{L} \not\supset \mu H^i H^j \Delta^{*ij}$. These diagrams can come from a UV-completion of operator $\mathcal{O}_{\bar{e}LLLH}$ realised by Δ and $\Delta_3^\dagger$ (c.f. Tabs. 5.2 and 5.3).

diagram in such cases.

If a simplified model contains any one of the three heavy seesaw particles N, Δ, or Σ, it could lead to a tree-level UV-completion of the Weinberg operator. For seesaw types i and iii this occurs if there is a coupling between the heavy seesaw field, SM Higgs field, and SM lepton doublet via terms of the form $H^\alpha L_\alpha N$ or $H^\alpha L^\beta \Sigma_{\alpha\beta}$. Unless there is a significant hierarchy in the coupling constants of the seesaw fields, the Weinberg operator will most likely dominate in the contribution to the neutrino mass over any additionally generated dimension-7 operators. If the dimension-7 operator dominates over the dimension-5, there could be a still greater contribution coming from a dimension-9 operator. The reason for this can be seen by noting that any dimension-7 $\Delta L = 2$ SMEFT operator containing at least two lepton doublets L and a Higgs doublet H can be written in the form of $LH \times L(\text{dim-3})$, where (dim-3) denotes a dimension-3 object. As is shown in this section, operators with two lepton doublets L and one Higgs doublet H can lead to one-loop radiative neutrino Majorana masses [498,502,503]. If a given tree-level UV-completion contains a heavy type-i or iii seesaw field $F \in \{N, \Sigma\}$, this field couples to the combination LH. The two parts of the dimension-7 operator, LH and $L(\text{dim-3})$, are then connected via the heavy seesaw fermion F. Should the coupling LHF be stronger than the corresponding coupling $FL(\text{dim-3})$, two instances of LHF can be used to construct the Weinberg operator $LLHH$, which should have a bigger contribution than the dimension-7 operator to the neutrino mass. If instead the $FL(\text{dim-3})$ coupling dominates, it can be used twice to form the dimension-9 operator $LL(\text{dim-3})(\text{dim-3})$, which should constitute the leading contribution. There is therefore never a scenario in which the most dominant neutrino mass contribution comes from a dimension-7 $\Delta L = 2$ operator of this type[5].

For type-ii seesaw, there are two couplings involved in the generation of the dimension-5 operator, namely $H^\alpha H^\beta \Delta_{\alpha\beta}$ and $L^\alpha L^\beta \Delta_{\alpha\beta}$. Tree-level UV-completions of a given $\Delta L = 2$ dimension-7 operator containing the field Δ do not *a priori* induce the dimension-5 operator, since it could be that only one of the two couplings are part of the simplified model[6], see

[5] A similar argument can also be applied to operators containing a lepton singlet e^c.

[6] Note also that if a given UV-completion contains two copies Δ_1 and Δ_2, where one interacts with HH and the

$$\mathcal{O}_{\bar{Q}uLLH} = \epsilon_{ij}(\overline{Q_p}u_r)(\overline{L_s^c}L_t^i)H^j$$

	Δ	φ	N	Σ	Q_7	$T_1^\dagger$	U_1	$\bar{V}_2^\dagger$	U_3
Δ		I			II	II			
φ			○	○					
N							○	○	
Σ								○	○
Q_7							II		II
$T_1^\dagger$								II	
U_1								I	
$\bar{V}_2^\dagger$									I
U_3									

Table 5.4.: All combinations of fields that UV-complete $\mathcal{O}_{\bar{Q}uLLH}$ at tree-level. Here each entry indicates which neutrino mass topology (c.f. Fig. 5.4) is generated by combining the fields to the top and left that share the same column and row as the given entry, respectively. An empty entry indicates that no UV-completion is generated by this combination of fields, and a circle indicates that the dimension-5 operator is generated.

Fig. 5.8 for an example. This can be the case for operators of e.g. types Ψ^2H^3D, Ψ^4H, and Ψ^2H^4. For the latter type, many UV-completions contain Δ along with a factor LHF, leading to the generation of the Weinberg operator via F.

In Tabs. 5.4 to 5.8 all possible tree-level UV-completions are shown for all Ψ^4H-type dimension-7 $\Delta L = 2$ operators, where each table corresponds to a single operator. In these tables, the leftmost column and the top row indicate the heavy BSM fields that arise as a result of the operator explosion procedure discussed in Sec. 5.2. Entries that contain a Roman number (I to IX) indicates that the two fields that overlap, i.e. the corresponding fields to the left and top in the same row and column as the entry, lead to a radiative neutrino Majorana mass topology corresponding to the Roman number, as given in Figs. 5.4 to 5.7. Only the top-right parts of each table is used, since otherwise each entry would be double counted. An empty circle in a given entry indicates that this combination of fields inevitably generates a tree-level UV-completion of the Weinberg operator, in which case the dominant contribution to the neutrino Majorana mass generally either comes from the Weinberg operator itself or a corresponding dimension-9 operator, as discussed in Sec. 5.3. A filled circle represents the case where this combination of BSM fields indeed generate the operator in question, but that this UV-completion does not lead to any tree- or one-loop-level neutrino Majorana mass diagrams. The dominant contribution could instead come from a two-loop diagram, as e.g. realised for $\mathcal{O}_{\bar{d}LQLH2}$ via an additional W-loop or for $\mathcal{O}_{\bar{d}LueH}$ via an additional H-loop.

In Sec. 5.3.3 we give general expressions for the neutrino mass in Topologies I and II

other with LL, the Weinberg operator can be suppressed.

$$\mathcal{O}_{\bar{d}LQLH1} = \epsilon_{ij}\epsilon_{mn}(\overline{d_p}L_r^i)(\overline{Q_s^c}^j L_t^m)H^n$$

	Δ	φ	S_1	$\tilde{R}_2$	S_3	N	Σ	$Q_5^\dagger$	T_2
Δ		I			I			II	
φ						○	○		
S_1				I		○		II	
$\tilde{R}_2$					I	○	○		II
S_3							○	II	
N									
Σ									
$Q_5^\dagger$									
T_2									

Table 5.5.: All combinations of fields that UV-complete $\mathcal{O}_{\bar{d}LQLH1}$ at tree-level. Here each entry indicates which neutrino mass topology (c.f. Fig. 5.4) is generated by combining the fields to the top and left that share the same column and row as the given entry, respectively. An empty entry indicates that no UV-completion is generated by this combination of fields, and a circle indicates that the dimension-5 operator is generated.

$$\mathcal{O}_{\bar{d}LQLH2} = \epsilon_{im}\epsilon_{jn}(\overline{d_p}L_r^i)(\overline{Q_s^c}^j L_t^m)H^n$$

	h	φ	$\tilde{R}_2$	S_3	Σ	U	$Q_5^\dagger$
h		●				●	●
φ					○		
$\tilde{R}_2$				●	○	●	
S_3					○		●
Σ							
U							
$Q_5^\dagger$							

Table 5.6.: All combinations of fields that UV-complete $\mathcal{O}_{\bar{d}LQLH2}$ at tree-level. Here each entry indicates that a UV-completion is generated by combining the fields to the top and left that share the same column and row as the given entry, respectively. An empty entry indicates that no UV-completion is generated by this combination of fields, a filled circle denotes that this combination of fields leads to a two-loop radiative neutrino mass, and an empty circle indicates that the dimension-5 operator is generated.

$$\mathcal{O}_{\bar{e}LLLH} = \epsilon_{ij}\epsilon_{mn}(\overline{e_p}L_r^i)(\overline{L_s^c}^j L_t^m)H^n$$

	h	Δ	φ	N	Σ	$\Delta_3^\dagger$
h			I	○		II
Δ			I		○	II
φ				○	○	
N						
Σ						
$\Delta_3^\dagger$						

Table 5.7.: All combinations of fields that UV-complete $\mathcal{O}_{\bar{e}LLLH}$ at tree-level. Here each entry indicates which neutrino mass topology (c.f. Fig. 5.4) is generated by combining the fields to the top and left that share the same column and row as the given entry, respectively. An empty entry indicates that no UV-completion is generated by this combination of fields, and a circle indicates that the dimension-5 operator is generated.

$$\mathcal{O}_{\bar{d}LueH} = \epsilon_{ij}(\overline{d_p}L_r^i)(\overline{u_s^c}e_t)H^j$$

	S_1	$\tilde{R}_2$	N	$\Delta_1^\dagger$	$Q_5^\dagger$	Q_7	W_1'	V_3	U_1	$\bar{V}_2^\dagger$
S_1		●	○		●					
$\tilde{R}_2$				●		●				
N							○		○	
$\Delta_1^\dagger$							●			●
$Q_5^\dagger$								●		●
Q_7								●	●	
W_1'								●		
V_3										
U_1										●
$\bar{V}_2^\dagger$										

Table 5.8.: All combinations of fields that UV-complete $\mathcal{O}_{\bar{d}LueH}$ at tree-level. Here each entry indicates that a UV-completion is generated by combining the fields to the top and left that share the same column and row as the given entry, respectively. An empty entry indicates that no UV-completion is generated by this combination of fields, a filled circle denotes that this combination of fields leads to a two-loop radiative neutrino mass, and an empty circle indicates that the dimension-5 operator is generated.

$$\mathcal{O}_{LeHD} = \epsilon_{ij}\epsilon_{mn}(\overline{L_p^c}\gamma_\mu e_r)H^j(H^m iD^\mu H^n)$$

	Δ	N	Σ	$\Delta_1^\dagger$
Δ			○	I
N				○
Σ				○
$\Delta_1^\dagger$				

Table 5.9.: All combinations of fields that UV-complete $\mathcal{O}_{LeHD}$ at tree-level. Here each entry indicates which neutrino mass topology (c.f. Fig. 5.4) is generated by combining the fields to the top and left that share the same column and row as the given entry, respectively. An empty entry indicates that no UV-completion is generated by this combination of fields, and a circle indicates that the dimension-5 operator is generated.

$$\mathcal{O}_{LH} = \epsilon_{ij}\epsilon_{mn}(\overline{L_p^c}^i L_r^m)H^j H^n(H^\dagger H)$$

	Θ_3	$\Sigma_1^\dagger$
Θ_3		III
$\Sigma_1^\dagger$		

Table 5.10.: All combinations of fields that UV-complete $\mathcal{O}_{LH}$ at tree-level using only two fields. Here each entry indicates which neutrino mass topology (c.f. Fig. 5.5) is generated by combining the fields to the top and left that share the same column and row as the given entry, respectively. An empty entry indicates that no UV-completion is generated by this combination of fields, and a circle indicates that the dimension-5 operator is generated.

$$\mathcal{O}_{LH} = \epsilon_{ij}\epsilon_{mn}(\overline{L_p^c}^i L_r^m)H^j H^n (H^\dagger H)$$

N	$\mathcal{S}$	Ξ	Δ	φ	Σ	$\Sigma_1^\dagger$	$\Delta_1^\dagger$
$\mathcal{S}$	○			○			○
Ξ				○	○		○
Δ				○		○	○
φ				○			
Σ							○
$\Sigma_1^\dagger$							○
$\Delta_1^\dagger$							○

Table 5.11.: All combinations of fields that UV-complete $\mathcal{O}_{LH}$ at tree-level using three fields. Here each entry indicates that a UV-completion is generated by combining the fields to the top and left that share the same column and row as the given entry, respectively, as well as the third field N. An empty entry indicates that no UV-completion is generated by this combination of fields, and a circle indicates that the dimension-5 operator is generated.

$$\mathcal{O}_{LH} = \epsilon_{ij}\epsilon_{mn}(\overline{L_p^c}^i L_r^m)H^j H^n (H^\dagger H)$$

Δ	$\mathcal{S}$	Ξ	Δ	φ	Θ_1	Θ_3	$\Sigma_1^\dagger$	$\Delta_1^\dagger$	F_4
$\mathcal{S}$	VII			IX				V	
Ξ		VII		IX	IX			V	V
Δ			○						
φ				VIII					
Θ_1					VIII				
Θ_3						VIII	IV		
$\Sigma_1^\dagger$								VI	VI
$\Delta_1^\dagger$									
F_4									

Table 5.12.: All combinations of fields that UV-complete $\mathcal{O}_{LH}$ at tree-level using three fields. Here each entry indicates which neutrino mass topology (c.f. Figs. 5.5 to 5.7) is generated by combining the fields to the top and left that share the same column and row as the given entry, respectively, together with the third field Δ. An empty entry indicates that no UV-completion is generated by this combination of fields, and a circle indicates that the dimension-5 operator is generated.

$$\mathcal{O}_{LH} = \epsilon_{ij}\epsilon_{mn}(\overline{L_p^c}^i L_r^m) H^j H^n (H^\dagger H)$$

Σ	$\mathcal{S}$	Ξ	Δ	φ	Θ_1	$\Sigma_1^\dagger$	$\Delta_1^\dagger$	F_4
$\mathcal{S}$	○			○			○	
Ξ		○		○	○		○	○
Δ			○	○	○	○	○	○
φ				○				
Θ_1					○			
$\Sigma_1^\dagger$							○	○
$\Delta_1^\dagger$							○	
F_4								○

Table 5.13.: All combinations of fields that UV-complete $\mathcal{O}_{LH}$ at tree-level using three fields. Here each entry indicates that a UV-completion is generated by combining the fields to the top and left that share the same column and row as the given entry, respectively, as well as the third field Σ. An empty entry indicates that no UV-completion is generated by this combination of fields, and a circle indicates that the dimension-5 operator is generated.

applicable to all simplified models, before comparing these expressions with a concrete model example in Sec. 5.3.4.

5.3.3. Model-independent neutrino masses

In Sec. 5.3.2, we showed for each explosive $\Delta L = 2$ dimension-7 operator which radiative neutrino mass topologies it could generate (c.f. Sec. 5.3.1). In this section we derive simplified expressions for the neutrino mass in these topologies, and in Sec. 5.3.4 we compare this treatment to a specific simplified model featuring leptoquarks.

A simplified model containing the SM plus one heavy fermion Ψ and one heavy scalar Φ can be described by the Lagrangian

$$\mathcal{L} = \mathcal{L}_{\text{SM}} + \mathcal{L}_{\Psi}^{\text{kin}} + \mathcal{L}_{\Phi}^{\text{kin}} - \lambda_f f L \Phi^* - y_\Psi f \bar{\Psi} H \,, \tag{5.34}$$

where $\mathcal{L}_{\Psi}^{\text{kin}}$ and $\mathcal{L}_{\Phi}^{\text{kin}}$ contain the kinetic terms of the heavy fermion and scalar, respectively, and f is a SM fermion. Similarly, a simplified model with two heavy scalars Φ_1 and Φ_2 can be described by the Lagrangian

$$\mathcal{L} = \mathcal{L}_{\text{SM}} + \mathcal{L}_{\Phi_1}^{\text{kin}} + \mathcal{L}_{\Phi_2}^{\text{kin}} - \lambda_{\Phi_1} f L \Phi_1^* - \lambda_{\Phi_2} f L \Phi_2^* - \mu \Phi_1^* \Phi_2^* H \,. \tag{5.35}$$

To calculate the value of the radiative neutrino mass generated in a generic UV-completion, we use the following expression for Topology I (c.f. Fig. 5.4 right),

$$(m_\nu)_{ij} \approx \frac{1}{16\pi^2} \frac{v}{\max(m_\Phi^2, m_\Psi^2)} \left(\lambda_f M_f y_\Psi M_\Psi^T \lambda_\Psi^T + \lambda_\Psi M_\Psi y_\Psi^T M_f^T \lambda_f^T \right)_{ij} . \tag{5.36}$$

	$\mathcal{S}$	Ξ	h	Δ	φ	Θ_1	Θ_3	S_1	$\tilde{R}_2$	S_3	N	Σ	$\Sigma_1^\dagger$
$\mathcal{S}$				A							A	A	
Ξ				A								A	
h					CF						C		
Δ				WA	*	A	A			E		†	
φ											*	*F	
Θ_1												A	
Θ_3													A
S_1									ED		ED		
$\tilde{R}_2$										EF	E	EF	
S_3												EF	
N											W		
Σ												W	
$\Sigma_1^\dagger$													

Table 5.14.: Part 1 of a compilation of all one- and two-field UV-completions of dimension-7 operators. For each non-empty entry, the operator indicated by the corresponding letter(s) is generated by the field in the top row and leftmost column that share the same column and row as the given entry, respectively. The single-field UV-completions are correspondingly given along the diagonal. Here the letters refer to the operators as A $= \mathcal{O}_{LH}$, B $= \mathcal{O}_{LeHD}$, C $= \mathcal{O}_{\bar{e}LLLH}$, D $= \mathcal{O}_{\bar{d}LueH}$, E $= \mathcal{O}_{\bar{d}LQLH1}$, F $= \mathcal{O}_{\bar{d}LQLH2}$, and G $= \mathcal{O}_{\bar{Q}uLLH}$, where we use the shorthand notation * = ACEG and † = ABC. Along the diagonal, a W indicates that the Weinberg operator is generated by this field, and therefore the non-explosive dimension-7 operators $\mathcal{O}_{LHD1}$, $\mathcal{O}_{LHD2}$, $\mathcal{O}_{LHB}$, and $\mathcal{O}_{LHW}$ can be generated as well.

	$\Delta_1^\dagger$	$\Delta_3^\dagger$	F_4	U	$Q_5^\dagger$	Q_7	$T_1^\dagger$	T_2	W_1'	V_3	U_1	$\bar{V}_2^\dagger$	U_3
$\mathcal{S}$													
Ξ													
h		C		F	F								
Δ	B	C			E	G	G						
φ													
Θ_1													
Θ_3													
S_1					ED								
$\tilde{R}_2$	D			F		D		E					
S_3					EF								
N	AB								D		DG	G	
Σ	AB		A									G	G
$\Sigma_1^\dagger$													
$\Delta_1^\dagger$									D			D	
$\Delta_3^\dagger$													
F_4													
U													
$Q_5^\dagger$										D		D	
Q_7										D	DG		G
$T_1^\dagger$												G	
T_2													
W_1'										D			
V_3													
U_1												DG	
$\bar{V}_2^\dagger$													G
U_3													

Table 5.15.: Part 2 of a compilation of all one- and two-field UV-completions of dimension-7 operators. For each non-empty entry, the operator indicated by the corresponding letter(s) is generated by the field in the top row and leftmost column that share the same column and row as the given entry, respectively. The single-field UV-completions are correspondingly given along the diagonal. Here the letters refer to the operators as A $= \mathcal{O}_{LH}$, B $= \mathcal{O}_{LeHD}$, C $= \mathcal{O}_{\bar{e}LLLH}$, D $= \mathcal{O}_{\bar{d}LueH}$, E $= \mathcal{O}_{\bar{d}LQLH1}$, F $= \mathcal{O}_{\bar{d}LQLH2}$, and G $= \mathcal{O}_{\bar{Q}uLLH}$.

$\mathcal{O}$	Operator	EFT Neutrino mass	Key
$\mathcal{O}_{LH}^{pr}$	$\epsilon_{ij}\epsilon_{mn}(\overline{L_p^c}^i L_r^m)H^j H^n (H^\dagger H)$	$\left(\frac{1}{16\pi^2}+\frac{v^2}{\Lambda^2}\right)\frac{v^2}{\Lambda}$	A
$\mathcal{O}_{LeHD}^{pr}$	$\epsilon_{ij}\epsilon_{mn}(\overline{L_p^c}^i \gamma_\mu e_r)H^j (H^m i D^\mu H^n)$	$y_e^{ri}\frac{g'}{(16\pi^2)^2}\frac{v^2}{\Lambda}$	B
$\mathcal{O}_{\bar{e}LLLH}^{prst}$	$\epsilon_{ij}\epsilon_{mn}(\overline{e_p}L_r^i)(\overline{L_s^c}^j L_t^m)H^n$	$(y_e^{pr}+y_e^{ps}+y_e^{pt})\frac{1}{16\pi^2}\frac{v^2}{\Lambda}$	C
$\mathcal{O}_{\bar{d}LueH}^{prst}$	$\epsilon_{ij}(\overline{d_p}L_r^i)(\overline{u_s^c}e_t)H^j$	$\sum_{ij} y_u^{sj} y_d^{jp} y_e^{ti}\frac{1}{(16\pi^2)^2}\frac{v^2}{\Lambda}$	D
$\mathcal{O}_{\bar{d}LQLH1}^{prst}$	$\epsilon_{ij}\epsilon_{mn}(\overline{d_p}L_r^i)(\overline{Q_s^c}^j L_t^m)H^n$	$y_d^{ps}\frac{1}{16\pi^2}\frac{v^2}{\Lambda}$	E
$\mathcal{O}_{\bar{d}LQLH2}^{prst}$	$\epsilon_{im}\epsilon_{jn}(\overline{d_p}L_r^i)(\overline{Q_s^c}^j L_t^m)H^n$	$y_d^{ps}\frac{g^2}{(16\pi^2)^2}\frac{v^2}{\Lambda}$	F
$\mathcal{O}_{\bar{Q}uLLH}^{prst}$	$\epsilon_{ij}(\overline{Q_p}u_r)(\overline{L_s^c}L_t^i)H^j$	$y_u^{pr}\frac{1}{16\pi^2}\frac{v^2}{\Lambda}$	G

Table 5.16.: List of the seven dimension-7 $\Delta L = 2$ SMEFT operators that lead to successful explosions. The dimension-7 operators not listed here either only have tree-level UV-completions that inevitably lead to the dimension-5 operator, or have no tree-level UV-completions at all.

and the following for Topology II (c.f. Fig. 5.4 left),

$$(m_\nu)_{ij} \approx \frac{1}{16\pi^2}\frac{v\mu}{\max(m_{\Phi_1}^2, m_{\Phi_2}^2)}\left(\lambda_{\Phi_1} M_f \lambda_{\Phi_2}^T + \lambda_{\Phi_2} M_f^T \lambda_{\Phi_1}^T\right)_{ij}. \tag{5.37}$$

Here m_Ψ, m_Φ, m_{Φ_1}, and m_{Φ_2} are the masses corresponding to Ψ, Φ, Φ_1, and Φ_2, respectively. Furthermore, i and j are lepton flavour indices, and $M_f = \mathrm{diag}(m_{f_1}, m_{f_2}, m_{f_3})$ is a diagonal 3×3 mass matrix containing three generations of the SM fermion $f \in \{e, u, d\}$. For simplicity we consider the possibility for Φ, Φ_1, and Φ_2 to also be vector fields. In Eq. (5.36), M_Ψ is the mass matrix of Ψ; λ_f is the coupling matrix between the SM fermion f, an outer neutrino and Φ; λ_Ψ is the coupling matrix between Ψ, Φ and the other outer neutrino; and y_Ψ is the Yukawa coupling matrix between f, Ψ and the SM Higgs. In Eq. (5.37), λ_{Φ_1} (λ_{Φ_2}) is a coupling matrix between the outer neutrinos, SM loop fermions and the heavy boson Φ_1 (Φ_2); and μ is the dimensionful coupling between Φ_1, Φ_2 and the SM Higgs field.

For two-loop radiative neutrino mass diagrams, i.e. in the cases where an additional Higgs- or W-boson loop is present, loop factors including Yukawa- or weak gauge-coupling constants can be included in the expressions in Eqs. (5.36) and (5.37) according to Step 10 in Sec. 4.2.1.

Besides leading to radiative neutrino Majorana masses, the generic simplified models we consider here give rise to dimension-7 $\Delta L = 2$ operators via the Wilson coefficients

$$\frac{\mathcal{C}_{ij}}{\Lambda^3} = \frac{\left(\lambda_\Psi y_\Psi \lambda_f\right)_{ij}}{m_\Phi^2 m_\Psi} \tag{5.38}$$

for UV-completions with one fermion and one scalar (Topology I) and

$$\frac{\mathcal{C}_{ij}}{\Lambda^3} = \frac{\mu\left(\lambda_{\Phi_1}\lambda_{\Phi_2}\right)_{ij}}{m_{\Phi_1}^2 m_{\Phi_2}^2} \tag{5.39}$$

for two-boson UV-completions (Topology II).

In Sec. 5.3.4, we take one concrete simplified-model example, and compare the one- and two-loop Topology II radiative neutrino masses from a full Feynman-rules-based evaluation with the approximate expressions from Eqs. (5.36) and (5.37) as well as the EFT-based estimate from the corresponding dimension-7 operator in Tab. 5.16.

5.3.4. Model example: leptoquarks at one- and two-loop

In this section, which is based on work that led to the publication in Ref. [1], we use the leptoquark model described in Ref. [504]. As an example of how the neutrino mass in a simplified model compares to the general expression in Eqs. (5.36) and (5.37) and EFT-based estimates in Tab. 5.16, we here consider a model in which the SM is extended by the two leptoquarks S_1 and $\tilde{R}_2$, which constitute a possible UV-completion to the $\Psi^4 H$-type operators $\mathcal{O}_{\bar{d}LeuH}$ and $\mathcal{O}_{\bar{d}LQLH1}$ (c.f. Tab. 5.2). This model is of special interest since it leads to LNV rare kaon decays [1] (c.f. Sec. 4.2.2 and Ch. 6). Rare kaon decay is a leading probe of LNV in universal lepton flavours, as opposed to $0\nu\beta\beta$ which only probes first generation fermions. It is therefore interesting to see how a non-trivial flavour structure in the leptoquark sector could lead to observable rare kaon decays, as well as the appropriate neutrino mass, without triggering $0\nu\beta\beta$ decay. In this section we will give an example of such a flavour structure in a leptoquark-mediated two-loop radiative neutrino Majorana mass diagram. Furthermore, S_1 and $\tilde{R}_2$ along with the leptoquark $S_3 \in (\bar{3},\, 3,\, 1/3)$, have been suggested as related to a possible solution of the $R_{K^{(*)}}$ anomaly [504–508] (c.f. Sec. 2.3.1).

The representations of the leptoquarks S_1 and $\tilde{R}_2$ under the SM symmetry group are given by [496]

$$\begin{aligned} \tilde{R}_2 &\in (3,\, 2,\, 1/6)\ , \\ S_1 &\in (\bar{3},\, 1,\, 1/3)\ . \end{aligned} \tag{5.40}$$

The Lagrangian for this model given by [504]

$$\begin{aligned} \mathcal{L} = \mathcal{L}_{\text{SM}} &- \tilde{R}_2^{\dagger\alpha}(\Box + m^2_{\tilde{R}_2})\tilde{R}_{2\alpha} - S_1^*(\Box + m^2_{S_1})S_1 \\ &+ \mu S_1 H^{\dagger\alpha}\tilde{R}_{2\alpha} - g_1^{ik}\bar{L}_{i\alpha}i\sigma_2^{\alpha\beta}\tilde{R}^*_{2\beta}\overline{d}^c_k - g_2^{jn}Q^\alpha_n L^\beta_j \epsilon_{\alpha\beta}S_1 \\ &- g_3^{jn}\bar{u}^c_n e_j S_1 + \text{h.c.}\,, \end{aligned} \tag{5.41}$$

where $\Box = \eta^{\mu\nu}\partial_\mu\partial_\nu$ is the d'Alembert operator. Greek and Roman letters in Eq. (5.41) correspond to $SU(2)_L$- and flavour-indices, respectively, and σ_2 is the second Pauli matrix. Taking both S_1 and $\tilde{R}_1$ to carry lepton number[7] $L = -1$, all terms on Eq. (5.41) conserve lepton number except the first term on the second row: the interaction between the two leptoquarks and the SM Higgs field. The Lagrangian in Eq. (5.41) can also lead to LNC rare kaon decays via dimension-6 effective operators, which constitutes another probe of the model.

[7] Which lepton number charge to assign to the leptoquarks is somewhat arbitrary since the Lagrangian we consider here violates lepton number conservation, and it is therefore not a well-defined conserved charge. Our choice of assignment leads to the dimensionful tri-scalar coupling being the LNV vertex, which can be motivated as originating from a mass insertion by a $B - L$-breaking scalar field.

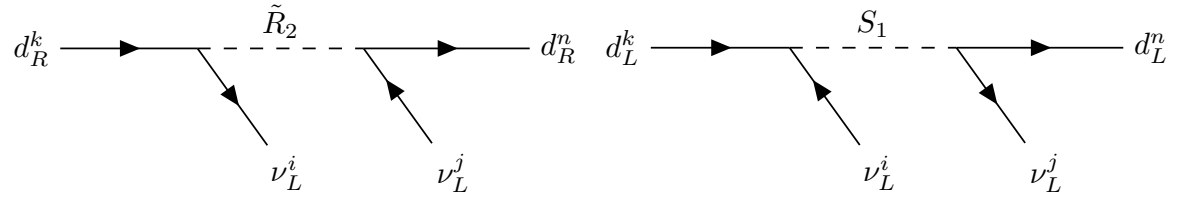

Figure 5.9.: Diagrams showing leptoquark-mediated LNC meson decays at dimension 6. The left diagram corresponds to the first term in Eq. (5.42) featuring $\tilde{R}_2$, while the right diagram corresponds to the second term featuring S_1.

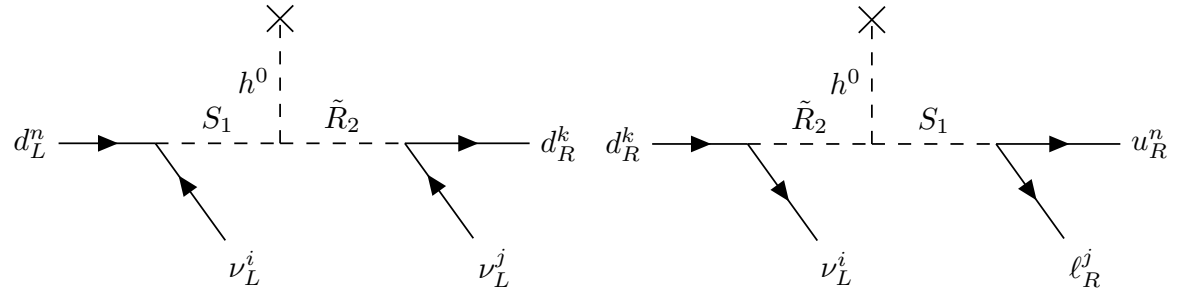

Figure 5.10.: Diagrams showing leptoquark-mediated LNV meson decays at dimension 7 with two-neutrino final state (left) corresponding to $\mathcal{O}_{\bar{d}LQLH1}$ or neutrino + charged lepton final states (right) corresponding to $\mathcal{O}_{\bar{d}LueH}$.

Integrating out the heavy leptoquarks, we first arrive at a dimension-6 effective Lagrangian [504]

$$\begin{aligned}\mathcal{L}_{6D} = &-\frac{g_1^{ik} g_1^{*jn}}{2m_{\tilde{R}_2}^2}\left(\bar{d}_n\gamma^\mu d_k\right)\left(\bar{L}_i^\alpha\gamma_\mu L_{j\alpha}\right) + \frac{g_2^{ik} g_2^{*jn}}{2m_{S_1}^2}\epsilon_{\alpha\beta}\epsilon_{\rho\sigma}(\bar{Q}_n^\alpha\gamma^\mu Q_k^\rho)(\bar{L}_i^\beta\gamma_\mu L_j^\sigma)\\ &+\frac{g_3^{ik} g_3^{*jn}}{2m_{S_1}^2}\left(\bar{u}_n\gamma^\mu u_k\right)\left(\bar{e}_i\gamma_\mu e_j\right) - \frac{g_2^{ik} g_3^{*jn}}{2m_{S_1}^2}\epsilon_{\alpha\beta}\left(\bar{u}_n Q_k^\alpha\right)\left(\bar{e}_i L_{j\beta}\right)\\ &+\frac{g_2^{ik} g_3^{*jn}}{8m_{S_1}^2}\epsilon_{\alpha\beta}(\bar{u}_n\sigma^{\mu\nu}Q_k^\alpha)(\bar{e}_i\sigma_{\mu\nu}L_j^\beta)\,,\end{aligned} \tag{5.42}$$

where $\sigma^{\mu\nu} = \frac{i}{2}\left[\gamma^\mu,\gamma^\nu\right]$. These LNC terms lead to the rare kaon decay diagrams shown in Fig. 5.9. At dimension-7 we obtain [504]

$$\begin{aligned}\mathcal{L}_{7D} = &-\frac{\mu g_1^{ik} g_2^{jn}}{2m_{\tilde{R}_2}^2 m_{S_1}^2}(d_k^c L_i^\nu)(Q_n^\mu L_j^\alpha)H^\beta\epsilon_{\alpha\beta}\epsilon_{\mu\nu} - \frac{\mu g_1^{ik} g_2^{jn}}{2m_{\tilde{R}_2}^2 m_{S_1}^2}(d_k^c\sigma^{\mu\nu} L_i^\nu)(Q_n^\mu\sigma_{\mu\nu} L_j^\alpha)H^\beta\epsilon_{\alpha\beta}\epsilon_{\mu\nu}\\ &+\frac{\mu g_1^{ik} g_3^{jn}}{m_{\tilde{R}_2}^2 m_{S_1}^2}(d_k^c L_i^\alpha)(u_n^c e_j^c)H^\beta\epsilon_{\alpha\beta}\,.\end{aligned} \tag{5.43}$$

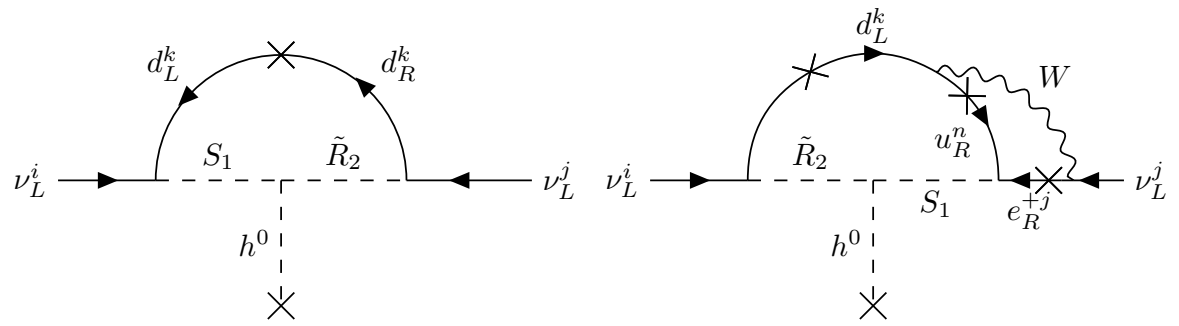

Figure 5.11.: One- and two-loop level radiative neutrino mass diagrams generated via leptoquarks, corresponding to the LNV dimension-7 operators $\mathcal{O}_{\bar{d}LQLH1}$ (left) and $\mathcal{O}_{\bar{d}LueH}$ (right).

We can identify the first term in Eq. (5.43) with the $\Delta L = 2$ dimension-7 operator $\mathcal{O}_{\bar{d}LQLH1}$ and the second term with $\mathcal{O}_{\bar{d}LueH}$. These operators lead to LNV rare kaon decays and fully leptonic LNV kaon decays, respectively (c.f. Secs. 4.2.3 and 4.2.2). The corresponding decay diagrams are shown in Fig. 5.10. Matching the model parameters to the flavour-specific LNV Wilson coefficient C^{ijkn} we find the relation

$$C^{ijkn}_{\bar{d}LQLH1\,(\bar{d}LueH)} = -\frac{\mu g_1^{ik} g_2 (-\frac{1}{2} g_3^{jn})}{2 m^2_{\tilde{R}_2} m^2_{S_1}}\,, \tag{5.44}$$

where g_2 corresponds to $\mathcal{O}_{\bar{d}LQLH1}$ and $-\frac{1}{2}g_3$ to $\mathcal{O}_{\bar{d}LueH}$, respectively. Since rare kaon decays are a more stringent probe of LNV than fully leptonic meson decays, we choose to focus specifically on $\mathcal{O}_{\bar{d}LQLH1}$. For this observable we would have the flavour indices $k = s/d$, $j = d/s$, and $i, n \in \{e, \mu, \tau\}$ in Eq. (5.44).

The couplings that generate the effective interactions in Eq. (5.43) also lead to corresponding one- and two-loop neutrino mass diagrams, as shown in Fig. 5.11. As is discussed below, the one-loop diagram is only the most dominant contributor to the neutrino mass under certain flavour-structures of the coupling matrices. It could be possible that a two-loop diagram dominates instead. The neutrino mass corresponding to the one-loop diagram in Fig. 5.11 (left) is given by [487]

$$(m_\nu)_i = \sum_{jk} \frac{3 \sin(2\theta)\, y^d_{kk} v \tilde{g}_1^{ik} \tilde{g}_2^{kj} U_{ji}}{32\pi^2} \log \frac{m^2_{\mathrm{LQ}_1}}{m^2_{\mathrm{LQ}_2}}\,, \tag{5.45}$$

where we do not use Einstein summation, such that the mass eigenstate index $i \in \{1, 2, 3\}$ is not summed over. Here several things need clarification. First of all, y^d_{ij} and v are the SM down-type quark Yukawa coupling matrix and Higgs vev, respectively, which come from closing the down-type quark loop with a mass insertion, as seen in Fig. 5.11. Secondly, we note that the leptoquarks in Eq. (5.41) were written in the interaction basis, where their mass

matrix is given by

$$M^2 = \begin{pmatrix} m^2_{\tilde{R}_2} & \mu v \\ \mu v & m^2_{S_1} \end{pmatrix} . \tag{5.46}$$

To generate the neutrino mass diagram, the upper $SU(2)_L$ index $\alpha = 1$ must be picked out in the lepton doublet from the second term in the second row of Eq. (5.41), which means that the lower index $\beta = 2$ is picked out from the leptoquark doublet

$$\tilde{R}_2 = \begin{pmatrix} \omega_1 \\ \omega_2 \end{pmatrix} , \tag{5.47}$$

where $m_{\omega_1} = m_{\omega_2} \equiv m_{\tilde{R}_2}$. The field ω_2 has the same $U(1)_Y$ hypercharge as S_1, and the two of them mix according to the matrix in Eq. (5.46), leading to the two mass eigenstates

$$\begin{aligned} \mathrm{LQ}_1 &= \cos\theta\omega_2 + \sin\theta S_1 \\ \mathrm{LQ}_2 &= -\sin\theta\omega_2 + \cos\theta S_1 . \end{aligned} \tag{5.48}$$

for which the squared masses are given by

$$m^2_{\mathrm{LQ}_{1,2}} = \frac{1}{2}\left(m^2_{\tilde{R}_2} + m^2_{S_1} \pm \sqrt{(m^2_{\tilde{R}_2} - m^2_{S_1})^2 + \mu^2 v^2} \right) . \tag{5.49}$$

for the mixing angle θ given by [509–511]

$$\tan(2\theta) = \frac{2\mu v}{m^2_{\tilde{R}_2} - m^2_{S_1}}. \tag{5.50}$$

Lastly, the couplings $\tilde{g}$ are written in the mass basis, such that

$$\tilde{g}_1^{ik} = \sum_\alpha g_1^{\alpha k} U^{i\alpha}, \quad \tilde{g}_2^{jn} = \sum_\alpha g_2^{j\alpha} V^{\alpha n} , \tag{5.51}$$

where U is the PMNS matrix and V the CKM matrix.

The expression in Eq. (5.45) represents the lowest loop-order radiative neutrino mass diagram that can be generated by the leptoquarks $\tilde{R}_2$ and S_1, however there is one remaining caveat. Out of necessity by the flavour conservation of the SM Yukawa interaction, the same quark-flavour index is picked out in the coupling constants $\tilde{g}_1$ and $\tilde{g}_2$. However, in rare kaon decays a different set of couplings are present, since the initial state consists of a strange quark while the final state consists of a down quark, c.f. the text below Eq. (5.44). It could then be possible that the structure of the leptoquark coupling matrix specifically favours rare kaon decays while suppressing the neutrino mass by having very small diagonal couplings. The most dominant contribution to the neutrino mass could then instead come from a two-loop diagram, where an additional W-boson loop is used to transform one flavour into the other.

Considering the scenario where the leptoquarks most favour the flavour structure present in rare kaon decays, the two-loop diagram giving the most dominant contribution, shown in

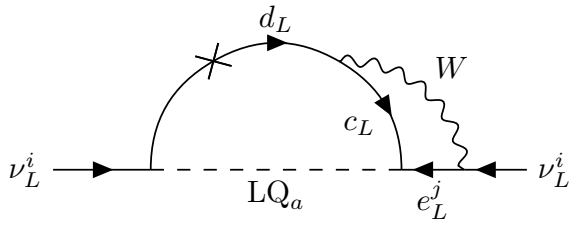

Figure 5.12.: Two-loop radiative neutrino mass with the leptoquark LQ_a being a mass eigenstate in the admixture of $\tilde{R}_2$ and S_1. Here the W-loop is needed in order to satisfy the flavour constraints coming from the leptoquark coupling matrices in the specific scenario where the most dominant couplings are those present in rare kaon decays.

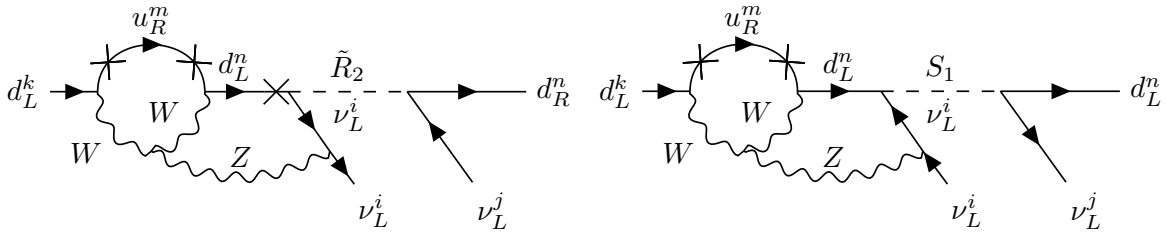

Figure 5.13.: Diagrams showing leptoquark-mediated two-loop LNC meson decays at dimension 6 in the specific scenario where the most dominant couplings are those present in rare kaon decays. The left diagram corresponds to the first term in Eq. (5.42) featuring $\tilde{R}_2$, while the right diagram corresponds to the second term featuring S_1.

Fig. 5.12, leads to the neutrino mass [1]

$$(m_\nu)_i = \sum_j \frac{3\sin(2\theta) g^2 V_{cd} \tilde{g}_1^{id} \tilde{g}_2^{jc} U_{ji}}{512\pi^4} m_d I(m^2_{\mathrm{LQ}_1}, m^2_{\mathrm{LQ}_2}, m^2_W)\,. \tag{5.52}$$

Considering the SM fermions to be massless, the loop function $I(m^2_{\mathrm{LQ}_1}, m^2_{\mathrm{LQ}_2}, m^2_W)$ is given by [510]

$$\begin{aligned} I(m^2_{\mathrm{LQ}_1}, m^2_{\mathrm{LQ}_2}, m^2_W) \approx \left(1 - \frac{m^2_{\mathrm{LQ}_1}}{m^2_{\mathrm{LQ}_2}}\right) \times \\ \left[1 + \frac{\pi^2}{3} + \frac{m^2_{\mathrm{LQ}_1} \log \frac{m^2_{\mathrm{LQ}_2}}{m^2_W} - m^2_{\mathrm{LQ}_2} \log \frac{m^2_{\mathrm{LQ}_1}}{m^2_W}}{m^2_{\mathrm{LQ}_2} - m^2_{\mathrm{LQ}_1}} + \right. \\ \left. \frac{1}{2} \frac{m^2_{\mathrm{LQ}_1} \left(\log \frac{m^2_{\mathrm{LQ}_2}}{m^2_W}\right)^2 - m^2_{\mathrm{LQ}_2} \left(\log \frac{m^2_{\mathrm{LQ}_1}}{m^2_W}\right)^2}{m^2_{\mathrm{LQ}_2} - m^2_{\mathrm{LQ}_1}} \right]. \end{aligned} \tag{5.53}$$

The LNV rare kaon decay for this set-up is by construction unaffected by the constraints we have put on the coupling constants between the leptoquarks and SM fermions. However, the LNC rare kaon decay from dimension-6 effective operators is suppressed similar to the neutrino mass, appearing first at two-loop order as seen in Fig. 5.13. Due to this suppression, we expect the LNV mode to dominate over the BSM LNC mode for these couplings.

We now consider the difference between neutrino masses evaluated in the leptoquark model, given by the one- and two-loop masses in from Eqs. (5.45) and (5.52), and the general simplified model expression for a diagram of the same topology in Eq. (5.37), as well as the EFT-based neutrino mass estimate given for $\mathcal{O}_{\bar{d}LQLH1}$ (c.f. Sec. 4.2.1) by

$$(m_\nu)_{ij} = \frac{y^d_{kn}}{16\pi^2} \frac{v^2}{\left(C^{ijkn}_{\bar{d}LQLH1}\right)^{-1/3}}\,, \tag{5.54}$$

with the LNV Wilson coefficient $C^{ijkn}_{\bar{d}LQLH1}$ related to the leptoquark masses via Eq. (5.44) using g_2.

In Fig. 5.14, we show how the trace of the neutrino mass matrix in the mass basis scales with respect to the hierarchy parameter

$$\xi \equiv \frac{\max\left(m_{\Phi_1}, m_{\Phi_1}\right)}{\min\left(m_{\Phi_1}, m_{\Phi_1}\right)} - 1\,, \tag{5.55}$$

when evaluated by the different one- and two-loop mass expressions. We here choose $m_{\Phi_1} = m_{\tilde{R}_2}$ and $m_{\Phi_2} = m_{S_1}$, with $m_{\tilde{R}_2} > m_{S_1}$, and keep a constant value of the product $m_{\tilde{R}_2} \times m_{S_1} = (20\text{ TeV})^2$. Furthermore, we use $\tilde{g}_1 = \tilde{g}_2 = \mathbb{1}$ in the one-loop case, and

$$\tilde{g}_1 = \begin{pmatrix} 1 & 0 & 0 \\ 1 & 0 & 0 \\ 1 & 0 & 0 \end{pmatrix}, \qquad \tilde{g}_2 = \begin{pmatrix} 0 & 1 & 0 \\ 0 & 1 & 0 \\ 0 & 1 & 0 \end{pmatrix} \tag{5.56}$$

in the two-loop case, and set the dimensionful coupling to $\mu = 20$ TeV. For the PMNS matrix elements we use the central values of the normal ordering neutrino mixing angles

$$\theta_{12} = 33.44^\circ, \qquad \theta_{13} = 8.57^\circ, \qquad \theta_{23} = 49.2^\circ, \qquad \delta_{CP} = 197^\circ\,, \tag{5.57}$$

as provided by the NuFit collaboration [512]. A similar analysis could be performed for inverse ordering as well, with very minor changes to the conclusion.

We see that for the one-loop mass, the three expressions agree well for small hierarchies $\xi \lesssim 1$. For large hierarchies $\xi \gtrsim 1$ the EFT-based estimate stays constant while the simplified- and leptoquark model expressions go down to lower masses, staying about an order of magnitude apart. We can conclude that the EFT-based expression does not capture the effect of an internal hierarchy of scales, something our simplified-model expression from Eq. (5.37) does quite well. This feature is important in Sec. 5.4.2 where we compare different constraints in the plane spanned by the two heavy BSM field masses of general simplified models.

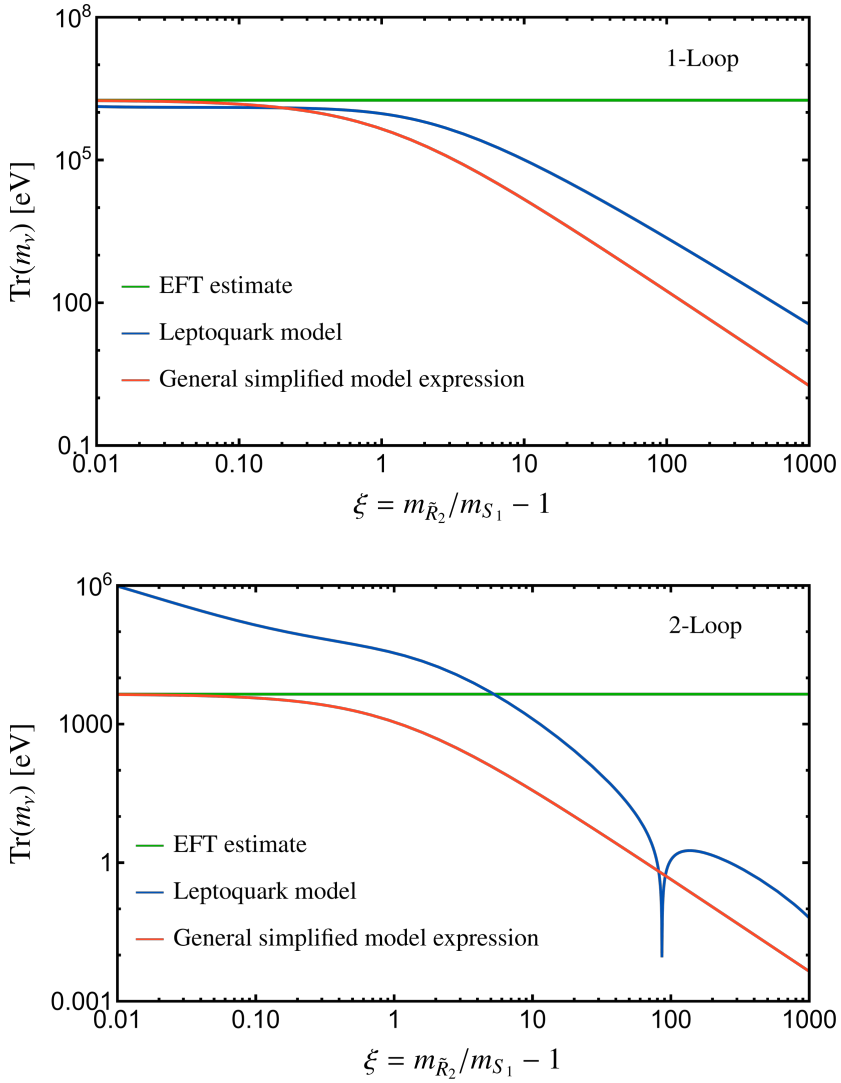

Figure 5.14.: The trace of the neutrino mass matrix as a function of the hierarchy parameter ξ, where a greater value of ξ corresponds to larger hierarchies. The neutrino mass here comes from a one- (top) and two-loop (bottom) radiative diagram involving two heavy leptoquarks and a down-type quark, where the mass is estimated using an EFT-based approximation (green), full radiative diagram (blue), and an approximate expression from a general simplified model (red).

For the two-loop mass, both the simplified model expression and EFT-based estimates underestimate the neutrino mass for small hierarchies $\xi \lesssim 10$. The effect of an increasing hierarchy is again well described by the simplified model expression, though it stays below the leptoquark model by roughly two orders of magnitude. The dip at $\xi \approx 85$ comes from the last two terms in the second parenthesis of Eq. (5.53) cancelling the first two. For vanishing hierarchies there is an enhancement of the two-loop mass that is not captured by either the simplified model expression or the EFT estimate.

For the parameters chosen in Fig. 5.14 we would get $\Lambda_{\text{LNV}} = 20$ TeV, which is excluded in the electron-flavour by $0\nu\beta\beta$ experiments, and at the limit of exclusion for rare kaon decay experiments.

5.4. Combined analysis of UV-completions at dimension-7

In Sec. 5.3.2 we discussed the different neutrino mass diagrams that appear in explosions of dimension-7 $\Delta L = 2$ operators. Neutrinos have a very small mass in comparison to the other known particles, which can set severe constraints on the different UV-completions of LNV dimension-7 operators. It could very well be possible that the generation of neutrino masses occurs via some UV-completion of a dimension-7 operator, and for this reason it is interesting to see if there are regions of parameter space that generate a plausible value for the neutrino mass while still not being excluded by other experimental searches.

The method outlined in Sec. 4.2.1 has been commonly used in the literature to estimate the size of neutrino masses being induced by EFT operators. However, as shown in the previous section, this method misses entirely the effect of a hierarchy in the internal degrees of freedom, something that can alter the neutrino mass by several orders of magnitude.

In Sec. 5.3.3 we proposed a new method to describe neutrino masses in higher-dimensional operators. This method does capture the effect of an internal hierarchy, as is shown in the model example in Sec. 5.3.4. In this section we investigate the parameter space of dimension-7 UV-completions in the context of neutrino masses calculated using the model-independent formalism in Sec. 5.3.3.

5.4.1. Global fit constraints on the relevant BSM particles

The dimension-7 LNV operators in Tab. 4.5 can lead to tree-level UV-completions that contain the fields listed in Tab. 5.1 via the assignment shown in Tabs. 5.2 and 5.3. Under the assumption that all operators are generated at tree-level, LHC constraints on the fields in Tab. 5.1 also lead to constraints the scale of the dimension-7 operators that they generate. If the dimension-7 $\Delta L = 2$ operators are generated at tree-level, the underlying UV-completions could also lead to LNC dimension-6 operators. The validity of the tree-level assumption can therefore be tested under different conditions, by comparing regions of parameter space excluded by searches for dimension-6 operators with constraints on the dimension-7 operators from LNV observables.

In Tab. 5.17 constraints on the mass of different heavy NP particles coming from global

Field	Rep	Coupling	Mass constraint 95% CL
$\mathcal{S}$	$S(1,1,0)(0)$	$\kappa_{\mathcal{S}} = 1$ TeV	$m_{\mathcal{S}} \geq 7.5$ TeV [513]
Ξ	$S(1,3,0)(0)$	$\kappa_{\Xi} = 1$ TeV	$m_{\Xi} \geq 3.0$ TeV [513]
h	$S(1,1,1)(0)$	$y_h = 1$	$m_h \geq 0.84$ TeV [513]
φ	$S(1,2,1/2)(0)$	$Z_6 \cos\beta = 1$	$m_{\varphi} \geq 1.0$ TeV [513]
S_1	$S(\bar{3},1,1/3)(-1)$	$y^{eu}_{S_1} = 1$	$m_{S_1} \geq 4.1$ TeV [514]
$\tilde{R}_2$	$S(3,2,1/6)(1)$	$y_{\tilde{R}_2} = 1$	$m_{\tilde{R}_2} \geq 3.9$ TeV [514]
S_3	$S(\bar{3},3,1/3)(-1)$	$y^{ql}_{S_3} = 1$	$m_{S_3} \geq 4.2$ TeV [514]
N	$F(1,1,0)(0)$	$\lambda_N = 1$	$m_N \geq 5.0$ TeV [513]
Σ	$F(1,3,0)(0)$	$\lambda_{\Sigma} = 1$	$m_{\Sigma} \geq 4.6$ TeV [513]
$\Sigma_1^{\dagger}$	$F(1,3,1)(0)$	$\lambda_{\Sigma_1} = 1$	$m_{\Sigma_1} \geq 6.1$ TeV [513]
$\Delta_1^{\dagger}$	$F(1,2,1/2)(0)$	$\lambda_{\Delta_1} = 1$	$m_{\Delta_1} \geq 7.6$ TeV [513]
$\Delta_3^{\dagger}$	$F(1,2,3/2)(0)$	$\lambda_{\Delta_3} = 1$	$m_{\Delta_3} \geq 5.9$ TeV [513]
U	$F(3,1,2/3)(1)$	$\lambda_U = 1$	$m_U \geq 3.6$ TeV [513]
$Q_5^{\dagger}$	$F(\bar{3},2,5/6)(-1)$	$\lambda_{Q_5} = 1$	$m_{Q_5} \geq 2.0$ TeV [513]
Q_7	$F(3,2,7/6)(1)$	$\lambda_{Q_7} = 1$	$m_{Q_7} \geq 2.6$ TeV [513]
$T_1^{\dagger}$	$F(\bar{3},3,1/3)(-1)$	$\lambda_{T_1} = 1$	$m_{T_1} \geq 2.1$ TeV [513]
T_2	$F(3,3,2/3)(1)$	$\lambda_{T_2} = 1$	$m_{T_2} \geq 3.1$ TeV [513]
W_1'	$V(1,1,1)(0)$	$g^{H}_{W_1'} = 1$	$m_{W_1'} \geq 11.7$ TeV [513]
U_1	$V(3,1,2/3)(1)$	$g^{lq}_{U_1} = 1$	$m_{U_1} \geq 5.6$ TeV [514]
$\tilde{V}_2^{\dagger}$	$V(3,2,1/6)(1)$	$g^{ul}_{\tilde{V}_2} = 1$	$m_{\tilde{V}_2} \geq 3.7$ TeV [514]
U_3	$V(3,3,2/3)(1)$	$g_{U_3} = 1$	$m_{U_3} \geq 9.9$ TeV [514]

Table 5.17.: BSM fields that appear in the explosions of dimension-7 $\Delta L = 2$ operators, as well as the constraints on the mass of the different fields (last column) coming from Refs. [514] and [513], provided that one specific coupling to the SM is set to unity (second column).

fits of LNC dimension-6 operators [513,514] are listed at 95% CL under the assumption that one coupling per particle is set to unity, where this coupling is given in the third column (c.f. Tabs. 5.2 and 5.3). For the constraints coming from Ref. [514] we have chosen for Tab. 5.17 to show the most stringent limits in the cases where more than one constraint is given per field. Note also that the limits given in Ref. [514] are applicable only to first generation leptoquarks. We compare these limits to other mass constraints under the assumption that the relevant NP couplings are all flavour-universal. Following Refs. [513,515], we use the coupling product $Z_6 \cos\beta$ for φ rather than one of the couplings given in Tab. 5.1. This follows a notation that is commonly used in Two-Higgs-doublet models, c.f. e.g. Ref. [516].

The couplings in Tab. 5.17 that are set to unity do not necessarily correspond to the couplings that appear in the CDE leading to the different dimension-7 operators. The mass limits from global fits should therefore not be directly compared to the LNV limits on the operator in question, but should rather be taken as indicative.

Under the assumption that the dimension-7 $\Delta L = 2$ operators that led to the fields in Tab. 5.17 are realised at tree-level only, constraints on the individual masses of the fields coming from global fits also constitute indirect constraints on the scale of LNV. Therefore, we consider global-fit constraints along with different LNV probes in Sec. 5.4.2, and compare them to neutrino masses coming from radiative diagrams containing the heavy BSM fields.

5.4.2. Comparison of neutrino masses with EFT constraints

The simplified-model based neutrino mass expressions in Eqs. (5.36) and (5.37) can be compared to the EFT-based estimate of the neutrino mass found using the formalism in Sec. 4.2.1 for the Wilson coefficients in Eqs. (5.38) and (5.39). In the third column of Tab. 5.16, the concrete expressions corresponding to the EFT neutrino mass is shown for each explosive dimension-7 operator under the assumption of a unitary dimensionless Wilson coefficient $C_{ij} \to 1$. In this section, comparisons between the EFT- and simplified-model-based neutrino mass expressions are made for generic UV-completions of all $\Psi^4 H$-type operators leading to radiative Majorana neutrino mass Topologies I and II, including different constraints on the scale of LNV from low-scale experiments as well as global-fit-constraints on the BSM fields.

To compare LNV constraints and the global-fit constraints from Refs. [513] and [514] with the neutrino masses in general simplified models that correspond to the exploded dimension-7 $\Delta L = 2$ $\Psi^4 H$-type operators we go to the plane spanned by the masses of the two heavy BSM fields. One reason for this choice of analysis is the dependence of the neutrino mass on the hierarchy of scales between the two internal degrees of freedom, as discussed in the model example in Sec. 5.3.4. Such a dependence can clearly be seen in a mass-mass plane, but is not visible in e.g. mass-coupling or coupling-coupling planes. We look only at $\Psi^4 H$-type operators as an example. Operator $\mathcal{O}_{LeHD}$ only leads to a single UV-completion that does not also generate the dimension-5 operator, and $\mathcal{O}_{LH}$ leads to too many different topologies to be studied systematically in a condensed manner. We therefore reserve the analysis of the exploded operators $\mathcal{O}_{LeHD}$ and $\mathcal{O}_{LH}$ for future work.

In Figs. 5.15 to 5.17 we compare EFT constraints with neutrino masses for dimension-7 $\Delta L = 2$ operators $\mathcal{O}_{\bar{Q}uLLH}$, $\mathcal{O}_{\bar{d}LueH}$, $\mathcal{O}_{\bar{d}LQLH1}$, $\mathcal{O}_{\bar{d}LQLH2}$, and $\mathcal{O}_{\bar{e}LLLH}$, respectively. Note that we

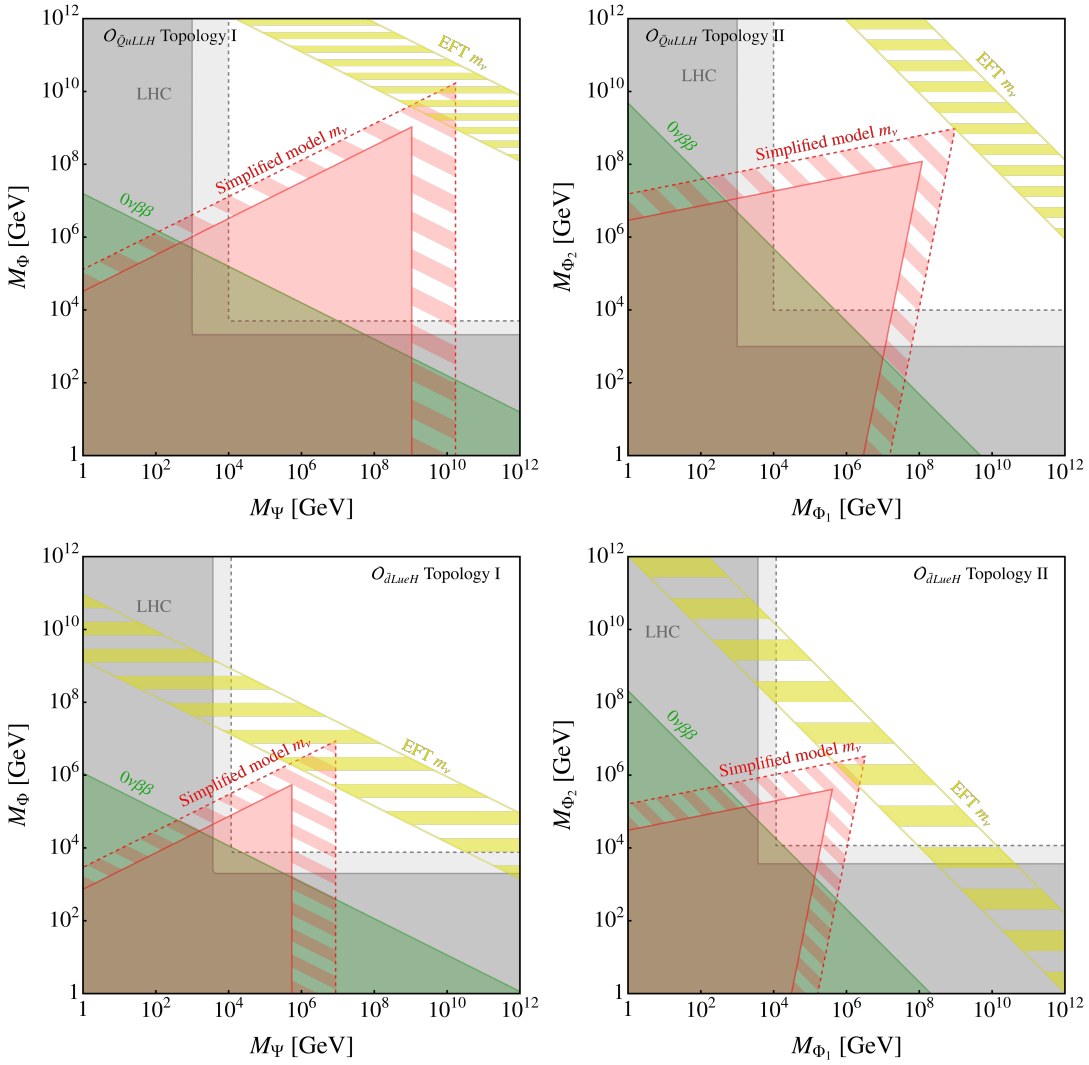

Figure 5.15.: Constraints on the masses of two BSM fields that combine to UV-complete the dimension-7 $\Delta L = 2$ operator $\mathcal{O}_{\bar{Q}uLLH}$ (top row) and $\mathcal{O}_{\bar{d}LueH}$ (bottom row) with the couplings $\lambda_\Psi = \lambda_f = 1$ and $y_\Psi = 0.1$ for Topology I (left column), and $\lambda_{\Phi_1} = \lambda_{\Phi_2} = 1$ and $\mu = (v m_{\Phi_1} m_{\Phi_2})^{1/3}$ for Topology II (right column). The grey areas correspond to the regions excluded by global fit constraints from Tab. 5.17, with the least (most) stringent limit being shown by a solid (dashed) line. The green area is excluded by $0\nu\beta\beta$ experiments, and the yellow striped area corresponds to the EFT-based estimate of the neutrino mass. The red striped area corresponds to the simplified-model-based neutrino mass expression from Eqs. (5.36) and (5.37) for Topologies I and II, respectively, where the filled red area is excluded due to the neutrino mass being too large.

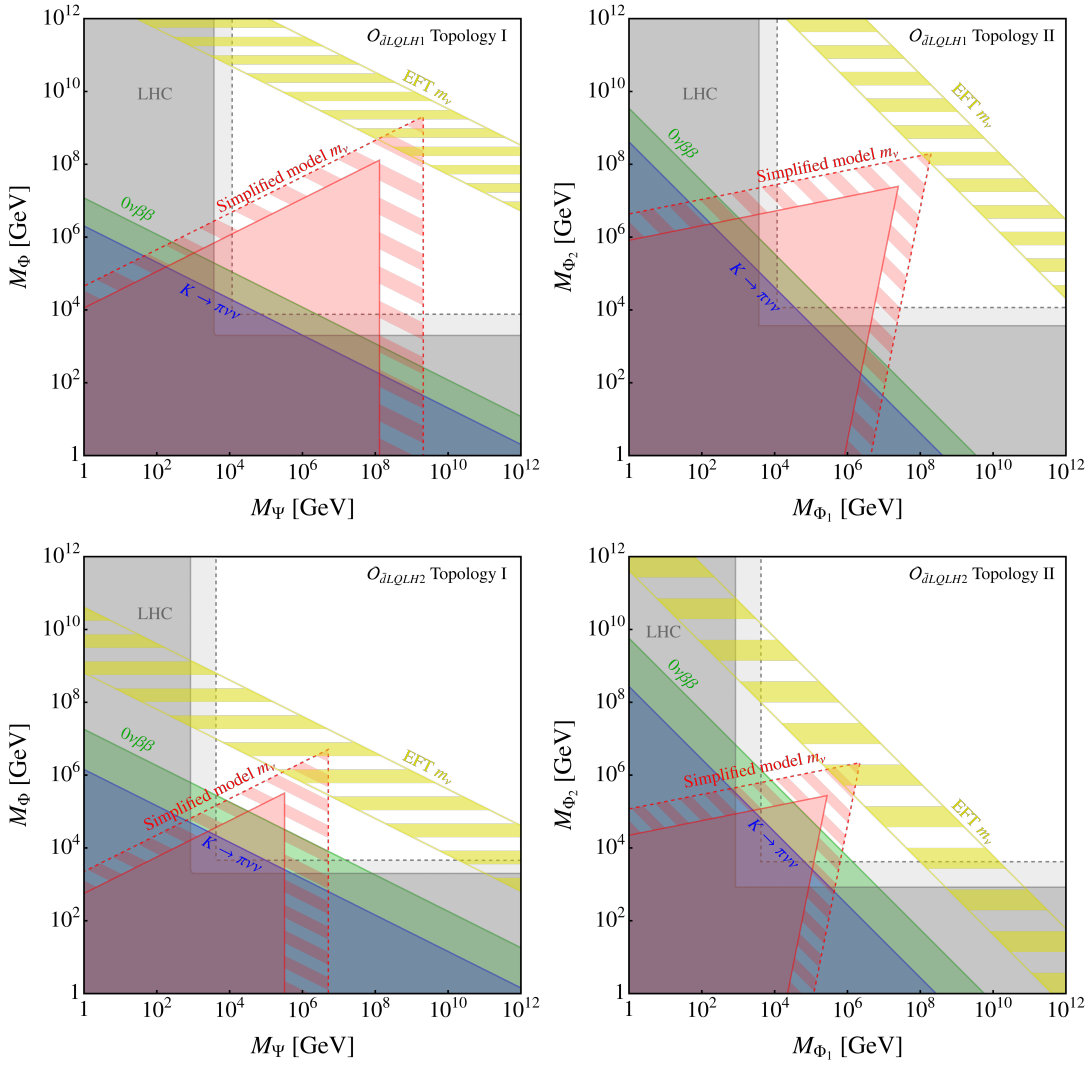

Figure 5.16.: Constraints on the masses of two BSM fields that combine to UV-complete the dimension-7 $\Delta L = 2$ operator $\mathcal{O}_{\bar{d}LQLH1}$ (top row) and $\mathcal{O}_{\bar{d}LQLH2}$ (bottom row) with the couplings $\lambda_\Psi = \lambda_f = 1$ and $y_\Psi = 0.1$ for Topology I (left column), and $\lambda_{\Phi_1} = \lambda_{\Phi_2} = 1$ and $\mu = (v m_{\Phi_1} m_{\Phi_2})^{1/3}$ for Topology II (right column). The grey areas correspond to the regions excluded by global fit constraints from Tab. 5.17, with the least (most) stringent limit being shown by a solid (dashed) line. The green area is excluded by $0\nu\beta\beta$ experiments, and the blue area is excluded by rare kaon decays. The red striped area corresponds to the simplified-model-based neutrino mass expression from Eqs. (5.36) and (5.37) for Topologies I and II, respectively, where the filled red area is excluded due to the neutrino mass being too large. The yellow striped area corresponds to the EFT-based estimate of the neutrino mass.

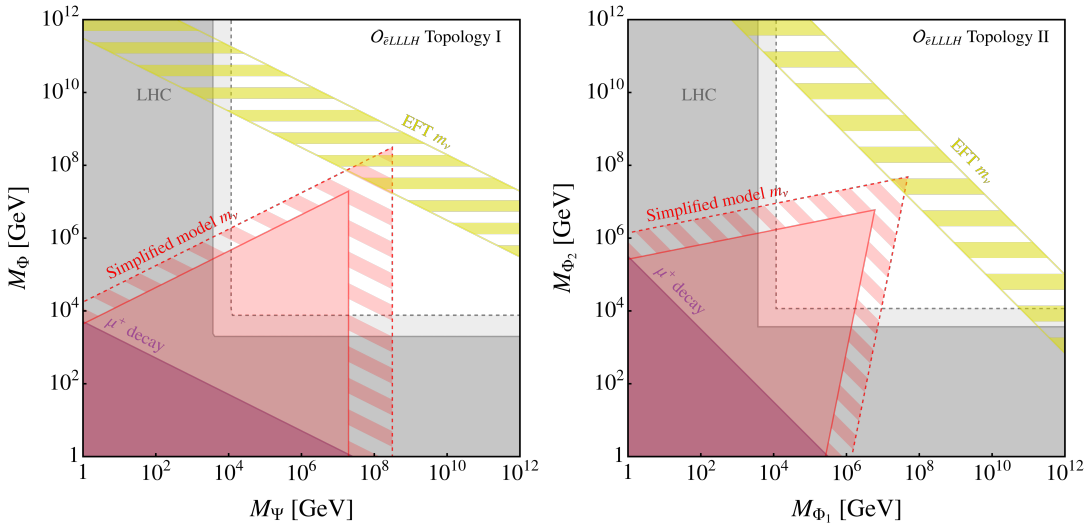

Figure 5.17.: Constraints on the masses of two BSM fields that combine to UV-complete the dimension-7 $\Delta L = 2$ operator $\mathcal{O}_{\bar{e}LLLH}$ with the couplings $\lambda_\Psi = \lambda_f = 1$ and $y_\Psi = 0.1$ for Topology I (left), and $\lambda_{\Phi_1} = \lambda_{\Phi_2} = 1$ and $\mu = (v m_{\Phi_1} m_{\Phi_2})^{1/3}$ for Topology II (right). The grey areas correspond to the regions excluded by global fit constraints from Tab. 5.17, with the least (most) stringent limit being shown by a solid (dashed) line. The purple area is excluded by LNV μ^+ decays, and the yellow striped area corresponds to the EFT-based estimate of the neutrino mass from the third column of Tab. 5.16, with the LNV scale related to the BSM field masses via Eqs. (5.38) and (5.39) for Topologies I and II, respectively. The red striped area corresponds to the simplified-model-based neutrino mass expression from Eqs. (5.36) and (5.37) for Topologies I and II, respectively, where the filled red area is excluded due to the neutrino mass being too large.

here extend the parameter space to masses below the EWSB scale $\Lambda_{\text{EW}} \approx 100$ GeV for better visibility in the plots, even though SMEFT is not a suitable framework in this region. The striped areas correspond to neutrino masses that fall within the region allowed by neutrino oscillation experiments based on the central value of the normal-ordering mass splitting $\Delta m^2_{13} = 2.514 \times 10^{-3}$ eV^2 coming from the NuFit collaboration [512], while simultaneously falling below the largest allowed value of $(m_\nu)_e = U_{ei}(m_\nu)_i < 0.8$ eV coming from the KATRIN experiment [400]. The filled red areas lead to neutrino masses that are too large, and they therefore constitute excluded regions. The yellow striped regions correspond to the allowed neutrino mass range when evaluated using the EFT-based estimate from Sec. 4.2.1. This means that the whole parameter space to the bottom-left of this region should be excluded due to the neutrino mass being too large. However, as seen in the model example in Sec. 5.3.4, this EFT-estimate is not accurate when considering the possibility of an internal hierarchy in the degrees of freedom, and we therefore choose to not paint almost the whole figures yellow to denote the regions excluded by this estimate. The dark- and light grey areas correspond to regions that are excluded by global-fit constraints based on the least and most stringently constrained BSM field that appears in the explosion of each given operator, respectively. Lastly, the green, blue, and purple regions are respectively excluded by $0\nu\beta\beta$ decay, rare kaon decay, and non-standard muon decay experiments. Note that we do not include constraints from LHC searches, since the corresponding limits are too low for the values of the couplings considered here to fall within the region in which the EFT formalism is valid (c.f. Sec. 4.5). A simplified-model-based LHC analysis would probably lead to quite stringent limits in the parameter space spanned by two heavy masses in a given model, e.g. the leptoquark model from Sec. 5.3.4. Such an analysis is reserved for future work.

For all contour plots in Figs. 5.15 to 5.17, the simplified-model-based neutrino mass (red) is lower than the EFT-based estimate of the neutrino mass (yellow), especially for large hierarchies, as expected from the analysis in Sec. 5.3.4. In the absence of hierarchy (i.e. at the tip of each red triangle), we see that the two neutrino mass expressions agree quite well. We see therefore that the previously considered neutrino-mass constraints (yellow) only hold under very specific conditions, namely the absence of a hierarchy in the internal degrees of freedom of an LNV operator. As we show in this chapter, a more accurate description involving general simplified models (red) reveals the fact that the neutrino mass depends significantly on such a hierarchy. This conclusion constitutes the main result of this chapter.

Considering the possibility of an internal hierarchy in the LNV operators, regions of parameter space that were previously considered to be excluded are opened up. For most operators, the exclusion limits coming from global fits, low-scale observables, and neutrino masses all overlap in roughly the same region of parameter space. This means that, should a signal be seen either at any of the collider searches that enter into the global fits or any of the low-scale LNV observables, Figs. 5.15 to 5.17 can be used along with Tabs. 5.4 to 5.8 to determine where to look for new particles that could potentially generate Majorana neutrino masses. If a new particle is discovered at collider experiments, Tabs. 5.4 to 5.8 show which additional particles it could be matched with to generate a radiative neutrino mass, and Figs. 5.15 to 5.17 show at which energy scale such additional particles are expected to be

found. For example, if a new particle that is consistent with a leptoquark S_3 with mass $m_{S_3} = 10$ TeV is discovered at the LHC, we know from Tabs. 5.5, 5.6 and 5.8 that it could lead to a one-loop radiative neutrino mass if we also find $\tilde{R}_2$, Δ or $Q_5^\dagger$. In Figs. 5.15 and 5.16 we know that either $m_{S_3} = M_\Phi$ or $m_{S_3} = M_{\Phi_1}$ is equal to 10 TeV, depending on whether the additional field is a fermion or scalar. If LNV is realised in operator $\mathcal{O}_{\bar{d}LueH}$ or $\mathcal{O}_{\bar{d}LQLH2}$, we see that the observed neutrino mass is generated for $m_{\tilde{R}_2}$, $m_\Delta \approx 10^5$ GeV or $m_{Q_5} \approx 10^6$ GeV, a possibility that is excluded by $0\nu\beta\beta$ decay for $\mathcal{O}_{\bar{d}LQLH2}$ but not for $\mathcal{O}_{\bar{d}LueH}$. In this way these two operators can be disentangled by combining high- and low-scale probes with neutrino mass generation, but only if we consider the possibility of having a hierarchy in the internal degrees of freedom. For $\mathcal{O}_{\bar{d}LQLH1}$ we instead have $m_{\tilde{R}_2}$, $m_\delta \approx 10^7$ GeV or $m_{Q_5} \approx 10^9$ GeV.

The neutrino mass for $\mathcal{O}_{\bar{Q}uLLH}$ is the largest out of all the operators, due to the up-type quark running in the loop having the largest Yukawa coupling out of the SM fermions. For operators $\mathcal{O}_{\bar{d}LQLH1}$ and $\mathcal{O}_{\bar{d}LQLH2}$ there are constraints from both $0\nu\beta\beta$ decay and rare kaon decays, where these two probes constrain different flavour aspects of the Wilson coefficients (electron flavour for $0\nu\beta\beta$ decay, while the rare kaon decay constraints are flavour-universal, see Sec. 4.8). For operators $\mathcal{O}_{\bar{d}LQLH2}$ and $\mathcal{O}_{\bar{d}LQLH1}$ the neutrino masses are comparatively small, since the corresponding diagrams are given at two-loop rather than one-loop. The four-lepton operator $\mathcal{O}_{\bar{e}LLLH}$ is unconstrained by $0\nu\beta\beta$ and we instead show the limit coming from $\mu^+ \to e^+\bar{\nu}_e\bar{\nu}_\mu$ decays.

Conclusion to Chapter 5

In this chapter we have discussed the UV-completions of all twelve dimension-7 $\Delta L = 2$ SMEFT operators, based on an analysis that is subject for future publication [4]. Four out of the twelve operators arise as higher-order corrections to the dimension-5 operator, and one is not realised by any tree-level UV-completion. For the remaining seven dimension-7 operators, we systematically list all possible tree-level UV-completions and classify them in terms of the neutrino mass topology. Focusing on four-fermion operators, we compare the neutrino masses in generic simplified models with LHC- and low-scale LNV constraints, and find that a hierarchy in the internal degrees of freedom of an LNV operator could severely relax the neutrino-mass constraints. This opens up regions of parameter space in which both LNV probes and collider searches constrain models that could lead to the observed neutrino mass.

In case a signal is seen in one of the LNV probes, the results in Sec. 5.4.2 can guide the collider search for BSM particles that lead to Majorana neutrino masses. Similarly, if a new particle is found, the results in Secs. 5.3.2 and 5.4.2 show which other particles would be needed in order to generate a Majorana neutrino mass, and at which scale they are expected to be found.

In Secs. 4.2.2, 4.3.4 and 4.3.5 we saw that processes in which neutrinos are the only leptons involved can be used to set limits on the scale of LNV. If an excess is seen experiments that search for such modes, the additional contribution could be due to LNV. However, there would be no *a priori* way of distinguishing it from a LNC contribution, since it is not known whether the final state particles are neutrinos or antineutrinos. In Ch. 6, we show how such a distinction can be made in rare kaon decays $K \to \pi\nu\nu$ based on the kinematics of the final

state pion, and in Ch. 7 we show a similar distinction based on the distribution of final state photons in radiative CEνNS events. These results were published in Ref. [1] and Ref. [3], respectively.

6. Disentangling LNV and LNC in rare kaon decays

Neutrinos are very elusive particles that are difficult to observe experimentally. This is perhaps the main reason why the nature of neutrino masses remains unknown, despite a long history of searches (see Sec. 4.2). Observing charged leptons on the other hand is comparatively easy, since they interact electromagnetically. Searches for LNV therefore often involve final states that consist of two leptons that have the same charge, in the absence of any missing energy that could have been carried away by neutrinos. One feature of such processes is the fact that they necessarily involve an exchange of two units of electromagnetic charge, $\Delta Q = 2$, between the lepton sector and another sector (e.g. the quark-sector). To produce two units of charge difference, many external fields have to be involved. In an EFT description this increases the dimension of the effective operator that mediates the process, leading to a decrease in experimental sensitivity (see Sec. 2.3.3).

Another search strategy for LNV is to look for processes with neutrinos or antineutrinos in the final state, and infer whether or not the interaction is LNV based on the kinematic distribution of other final state particles. An advantage of such searches is that the constraints are applicable for all flavour-indices of the Wilson coefficients, since the flavour states of the final state neutrinos are undetermined.

In this chapter we discuss the details about the possibility to observe LNV in rare kaon decays. We review the SM contributions in Secs. 6.1 and 6.2, after which we focus on the LNV BSM decay in Sec. 6.3 in order to compare the two modes in Sec. 6.4. LNV contributions to rare kaon decays were discussed in Ref. [424], and the potentially observable difference in the kinematic distributions between a LNV contribution and the SM mode is discussed here, based on work that led to the publication in Ref. [1]. This difference in distribution impacts the sensitivity of different experiments, both past and ongoing, which can possibly lead to more stringent constraints on the scale of LNV in the near future.

6.1. Rare kaon decay in the SM

The two golden modes of kaon decays, $K^+ \to \pi^+ \nu\bar{\nu}$ and $K_L \to \pi^0 \nu\bar{\nu}$, are the main focus of this section. The former mode is also discussed in Sec. 4.2.2. They proceed via electroweak penguin and box diagrams in the SM, as shown in Fig. 6.1. These modes have a very small branching ratio (BR) due to Glashow–Iliopoulos–Maiani (GIM) suppression[1] [517]. The

[1] GIM suppression states that flavour-changing neutral current (FCNC) loop diagrams are suppressed due to the requirement of two mass insertions. If these mass insertions were not there, the corresponding diagram would

up-type quark in each diagram is not directly involved in the decay process, but it is part of the initial- and final state meson, and we therefore call it a *spectator quark*. If we replace the spectator up quark by a down quark, we would instead have the decay $K^0 \to \pi^0 \nu\bar{\nu}$. As seen in Sec. 2.1.4, the kaons K^0 and $\bar{K}^0$ mix to form K_L, which is a mass eigenstate with a small CP-violating component ϵ of $\mathcal{O}(10^{-3})$, such that [518]

$$|K_L\rangle = \frac{1}{\sqrt{2+2|\epsilon|^2}} \left[(1+\epsilon)|K^0\rangle + (1-\epsilon)|\bar{K}^0\rangle\right] . \tag{6.1}$$

The BRs of $K^+ \to \pi^+ \nu\bar{\nu}$ and $K_L \to \pi^0 \nu\bar{\nu}$ can be parametrised in the SM as [519, 520]

$$\mathrm{BR}(K^+ \to \pi^+ \nu\bar{\nu}) = \tilde{\kappa}^+ \left[\left(\frac{\mathrm{Im}(V_{ts}^* V_{td} X_t)}{\lambda^5} \right)^2 + \left(\frac{\mathrm{Re}(V_{cs}^* V_{cd})}{\lambda} P_c + \frac{\mathrm{Re}(V_{ts}^* V_{td} X_t)}{\lambda^5} \right)^2 \right] , \tag{6.2}$$

$$\mathrm{BR}(K_L \to \pi^0 \nu\bar{\nu}) = \kappa_L \left(\frac{\mathrm{Im}(V_{ts}^* V_{td} X_t)}{\lambda^5} \right)^2 , \tag{6.3}$$

where $X_t = 1.48$ and $P_c = 0.404$ are dimensionless parameters that correspond to loop effects of top and charm quarks, respectively. Furthermore, $\lambda \approx 0.225$ is the Wolfenstein parameter and V_{ij} are the CKM matrix elements. The parameters $\tilde{\kappa}^+ = 0.517 \times 10^{-10}$ and $\kappa_L = 2.23 \times 10^{-10}$ are experimentally determined from the more common decay modes $K^+ \to \pi^0 e^+ \nu$ and $K_L \to \pi^- e^+ \nu$, respectively [521, 522]. These quantities include hadronic uncertainties in the decay, and the fact that they are measured to such a high accuracy leads to very good theoretical predictions [523]

$$\mathrm{BR}(K^+ \to \pi^+ \nu\bar{\nu})_{\mathrm{SM}} = (8.4 \pm 1.0) \times 10^{-11} , \tag{6.4}$$

$$\mathrm{BR}(K_L \to \pi^0 \nu\bar{\nu})_{\mathrm{SM}} = (3.4 \pm 0.6) \times 10^{-11} . \tag{6.5}$$

The main uncertainty in these predictions comes from the experimental determination of the CKM matrix elements. Because the rare kaon decays are so clean, meaning that their BRs can be theoretically predicted to a very high accuracy, they serve as excellent probes of NP [524].

Note that in Eq. (6.5), the BR of $K_L \to \pi^0 \nu\bar{\nu}$ is proportional only to the imaginary part of the CKM matrix elements, which means that this mode can only proceed if there is CP-violation in the SM. This is a consequence of flavour conservation in the lepton-sector weak interactions. The two neutrinos form a CP-odd state that together with the pion form a CP-even state, unlike the CP-odd K_L [525, 526]. A CP-conserving contribution to the decay only appears at two-loop level [527].

From Eqs. (6.4) and (6.5) we see that the BR of the K_L decay is smaller than that of the K^+ decay. This should hold true even if there are BSM contributions, as the branching ratios of the two decay modes are related via the Grossman-Nir bound [525]

$$\mathrm{BR}(K_L \to \pi^0 \nu\bar{\nu}) < 4.4 \times \mathrm{BR}(K^+ \to \pi^+ \nu\bar{\nu}) . \tag{6.6}$$

vanish due to the unitarity of the CKM matrix.

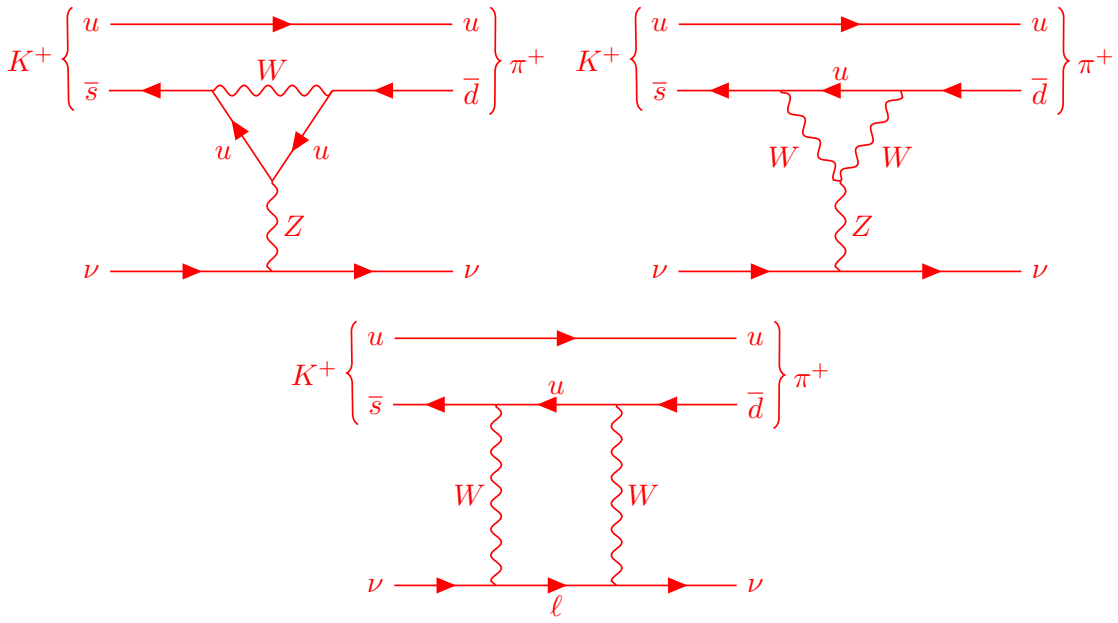

Figure 6.1.: Diagrams corresponding to the process to $K^+ \to \pi^+ \nu\bar{\nu}$ within the SM.

Experimentally, it is very difficult to probe this constraint since the outgoing neutrinos are difficult to measure[2]. The Grossman-Nir bound could therefore be broken in the presence of a modified final state, such as via $\Delta I = 3/2$ operators [531, 532] or dark particles in the final state [533–537].

6.2. Experimental searches for rare kaon decay

The most stringent experimental limits on the BRs of rare kaon decays come from the NA62 experiment [404, 538] for $K^+ \to \pi^+ \nu\bar{\nu}$ and from the KOTO experiment [528, 530] for $K_L \to \pi^0 \nu\bar{\nu}$. Still relevant is also the older E949 experiment [403], since they provide limits on the branching ratio for different Lorentz structures, as opposed to the modern experiments where the limit is only given for a vector current.

6.2.1. The E949 experiment

The E949 experiment was situated in Brookhaven National Laboratory, and searched for $K^+ \to \pi^+ + E_{\text{miss}}$ using stopped kaons, where E_{miss} is missing energy[3] [403]. With the vector current interpretation of their result, the E949 experiment yields the BR

$$\text{BR}(K^+ \to \pi^+ \nu\bar{\nu})_{\text{E949, vector}} = \left(1.73^{+1.15}_{-1.05}\right) \times 10^{-10}\,, \tag{6.7}$$

[2] As mentioned in Sec. 2.3.1, in 2019 there was a preliminary result from the KOTO experiment [528] which indicated a violation of the Grossman-Nir bound [106, 529, 530], but this anomaly later disappeared [107].

[3] Presumably the missing energy in such events consists of neutrinos.

with an upper limit

$$\mathrm{BR}(K^+ \to \pi^+ \nu\bar{\nu})_{\text{E949, vector}} < 3.35 \times 10^{-10}, \quad \text{at 90\% CL}\,. \tag{6.8}$$

This result is in agreement with the SM predicted value in Eq. (6.4). If the result is instead analysed in terms of a scalar current, the upper limit becomes

$$\mathrm{BR}(K^+ \to \pi^+ \nu\bar{\nu})_{\text{E949, scalar}} < 21 \times 10^{-10}\,, \quad \text{at 90\% CL.} \tag{6.9}$$

The E949 experiment collected data in two signal regions (SRs), called $\pi\nu\bar{\nu}(1)$ and $\pi\nu\bar{\nu}(2)$, which represent cuts in the momentum and kinetic energy of the final state pion. In the rest of this chapter, these SRs are approximated as corresponding only to momentum cuts, such that $\pi\nu\bar{\nu}(1)$ is defined as 211 MeV $< p_\pi <$ 229 MeV and $\pi\nu\bar{\nu}(2)$ is defined as 140 MeV $< p_\pi <$ 199 MeV.

6.2.2. The NA62 experiment

The NA62 experiment at CERN is currently ongoing and is searching for $K^+ \to \pi^+ + E_{\text{miss}}$ from kaons decaying in-flight [404,538]. Events are collected in SRs 1 and 2, which correspond to cuts in the pion momentum p_π and squared missing energy s. Both SRs have the pion momentum cut 15 GeV $< p_\pi <$ 35 GeV, while in terms of the missing energy SR 1 is defined as $0 < s < 0.01$ GeV^2 and SR 2 as 0.025 GeV^2 $< s <$ 0.068 GeV^2. The NA62 experiment is probing rare kaon decays at the SM sensitivity, and has found events in both signal regions, leading to the result [539]

$$\mathrm{BR}(K^+ \to \pi^+ \nu\bar{\nu})_{\text{NA62}} = \left(11.0^{+4.0}_{-3.5} \pm 0.3\right) \times 10^{-11} \qquad (3.5\sigma \text{ significance})\,. \tag{6.10}$$

The upper limit from NA62 that we consider is given by

$$\mathrm{BR}(K^+ \to \pi^+ \nu\bar{\nu})_{\text{NA62}} < 1.78 \times 10^{-10}\,, \quad \text{at 90 \% CL,} \tag{6.11}$$

which is in agreement with both the SM and E949. An even more stringent limit [540]

$$\mathrm{BR}(K^+ \to \pi^+ \nu\bar{\nu})_{\text{NA62}} = \left(10.6^{+4.0}_{-3.5} \pm 0.3\right) \times 10^{-11}\,, \quad \text{at 68 \% CL,} \tag{6.12}$$

has recently been reported. However, for consistency with the analysis in Ref. [1], we consider the limit given by Ref. [539] in this chapter. In the future, the NA62 experiment aims to reach 10% precision [541], which can be interpreted in terms of a BR as [1]

$$\mathrm{BR}(K^+ \to \pi^+ \nu\bar{\nu})^{\text{future}}_{\text{NA62}} \lesssim 1.11 \times 10^{-10}\,, \quad \text{at 90\% CL.} \tag{6.13}$$

6.2.3. The KOTO experiment

The KOTO experiment at J-PARC is also ongoing and is searching for $K_L \to \pi^0 + E_{\text{miss}}$ [528]. Similar to NA62, the KOTO experiment utilises kaons decaying in-flight. Since KOTO searches

for the neutral mode they have a π^0 in the final state, which rapidly decays into two photons[4]. Rather than measuring the final state pion, the KOTO experiment detects the two photons into which the pion decays, and based on measurements of the photons, the transverse momentum of the pion and decay location of the kaon are reconstructed. In the KOTO experiment there is a single SR which is defined in terms of the pion transverse momentum p_π^T and the location Z_{vtx} along the kaon beam at which the decay occurs. The upper limit on the transverse momentum is $p_\pi^T < 130$ MeV, while the lower limit depends on Z_{vtx}. The distribution of kaon momenta ranges from 0 GeV to 5 GeV, with a peak around 1.4 GeV [405]. The result from KOTO is an upper limit [528]

$$\text{BR}(K_L \to \pi^0 \nu\bar{\nu})_{\text{KOTO}} < 3.0 \times 10^{-9}\,, \quad \text{at 90\% CL}, \tag{6.14}$$

and a central value

$$\text{BR}(K_L \to \pi^0 \nu\bar{\nu})_{\text{KOTO}} = \left(2.1^{+4.1}_{-1.7}\right) \times 10^{-9}\,, \quad \text{at 95\% CL}. \tag{6.15}$$

Note that the central value of KOTO is in agreement with both the SM, c.f. Eq. (6.5), and the Grossman-Nir bound, c.f. Eqs. (6.6) and (6.4).

All experimental limits given above, except for the one in Eq. (6.9), are given under the assumption that the rare kaon decay proceeds via a vector current, i.e. the same Lorentz structure as that of the SM decay. Due to the fact that cuts are made in the phase space to define SRs in which signal events are accepted, the full phase space is not explored in any experiment. The fraction of the total phase space that an experiment can explore depends on the Lorentz structure of the interaction being studied. Since the three experiments mentioned above were/are mainly concerned with finding the SM mode (which is mediated by a vector current), their SRs are placed such that events from a vector current decay are mostly captured, which leaves as an unintended consequence the fact that events from a scalar current are less visible. In order to obtain proper limits on the scalar BR for NA62 and KOTO, statistical analyses would have to be performed to this end, which has not yet been done in the literature.

6.3. LNV in rare kaon decay

If LNV is realised in rare kaon decays $K \to \pi\nu\nu$, where the two final state neutrinos carry the same lepton number charge, it can be described in SMEFT at dimension 7 by the operator $\mathcal{O}_{\bar{d}LQLH1}$ from Tab. 4.5 [1,424]. The low-energy[5] matrix element corresponding to the scalar-current mediated decay $K \to \pi\nu_i\nu_j$ is given by

$$i\mathcal{M} = \frac{v}{\Lambda^3_{ijsd}} \left\langle \pi\nu_i\nu_j \right| \bar{d}s\overline{\nu}_i\nu_j \left| K \right\rangle \,. \tag{6.16}$$

[4]Decaying into two photons is by far the most dominant mode for neutral pions, with $\text{BR}(\pi^0 \to \gamma\gamma) = 98.823 \pm 0.034\%$ at 90% CL [14]. This decay is so rapid that it can be considered to occur inside the kaon beam at the KOTO experiment.

[5]Here we mean low energy with respect to the EWSB scale, such that we may use the fields of the broken SM. What is relevant in the frame of the kaon is the mass difference between kaons and pions, since this is the energy available to the final state. This energy is very far from the EWSB scale.

Here the fermions in the operator correspond to 4-component fields $d = (d_L, \bar{d}^c)^T$ and $\nu = (\nu_L, \bar{\nu}_L)^T$, where we assume that the SM neutrino is Majorana. From operator $\mathcal{O}_{\bar{d}LQLH1}$ there is also a tensor current contribution with non-identical neutrino flavours. We choose to consider identical flavours only, and we therefore do not consider the tensor current further. The matrix element in Eq. (6.16) corresponds to both the charged (K^+) and neutral (K_L) kaon decays, and the indices i and j indicate different neutrino flavours. We approximate the matrix element by separating the hadronic and leptonic parts,

$$i\mathcal{M} = \frac{v}{\Lambda^3_{ijsd}} \left\langle \pi(p') \right| \bar{d}s \left| K(p) \right\rangle \bar{\nu}_i(k)\nu_j(k') \,. \tag{6.17}$$

We can now replace the hadronic part with a form factor [542, 543]

$$\left\langle \pi(p') \right| \bar{d}s \left| K(p) \right\rangle = \frac{m_K^2 - m_\pi^2}{m_s - m_d} f_0^K(s) \,. \tag{6.18}$$

Here the form factor $f_0^K(s)$ is a function of $s = (p - p')^2 = (k + k')^2$, where p, p', k, and k' are the four-momenta of the kaon, pion, and neutrinos ν_i and ν_j, respectively. In solving Eq. (6.18) we here use the quark masses $m_s = 95$ MeV and $m_d = 4.7$ MeV, as well as the form factor [522, 543]

$$f_0^K(s) = f_+^K(0) \left(1 + \lambda_0 \frac{s}{m_\pi^2} \right) , \tag{6.19}$$

where $\lambda_0 = 13.38 \times 10^{-3}$, and where $f_+^K(0)$ is given by

$$f_+^{K^+}(0) = 0.9778, \quad f_+^{K_L}(0) = 0.9544 \,, \tag{6.20}$$

for the charged and neutral kaon decay, respectively. We can then write the squared matrix element as

$$|\mathcal{M}|^2 = \frac{v^2}{\Lambda^6_{ijsd}} \left(\frac{m_K^2 - m_\pi^2}{m_s - m_d} f_0^K(s) \right)^2 s \,. \tag{6.21}$$

The scalar form factor in Eq. (6.19) can be obtained from the vector form factor using equations of motion [544]. The pseudo-scalar part $\langle \pi | \bar{d}\gamma_5 s | K \rangle = 0$ of the matrix element vanishes since the decay is parity conserving. This type of current would instead lead to decays into vector mesons, which we do not consider here[6]. From Eq. (6.21) we can express a double differential decay width in terms of the variables s and $t = (k' + p')^2$ as

$$\begin{aligned} \frac{\Gamma\left(K \to \pi \nu_i \nu_j\right)}{ds\, dt} &= \frac{1}{1 + \delta_{ij}} \frac{1}{(2\pi)^3} \frac{1}{32 m_K^3} |\overline{\mathcal{M}}|^2 \,, \\ &= \frac{1}{1 + \delta_{ij}} \frac{1}{(2\pi)^3} \frac{1}{32 m_K^3} \frac{v^2}{\Lambda^6_{ijsd}} \left(\frac{m_K^2 - m_\pi^2}{m_s - m_d} \right)^2 |f_0^K(s)|^2 s \,, \end{aligned} \tag{6.22}$$

[6] In fact, the lightest vector meson, ρ, is too massive to be produced in the decays of kaons, and we would instead have had to consider B-meson decays such as $B \to \rho\nu\nu$. Rare decays of B-mesons into scalar mesons are however generally more constrained than decays into vector mesons (compare $\mathrm{BR}(B^+ \to \rho^+ \nu\nu) < 3.0 \times 10^{-5}$ at 95% CL [14] to $\mathrm{BR}(B^+ \to \pi^+ \nu\nu) < 1.4 \times 10^{-5}$ at 95% CL [14]).

where δ_{ij} takes care of the extra factor $1/2$ needed for identical final state neutrinos. The integration regions for t and s are $t \in [t^-, t^+]$ and $s \in [0, (m_K - m_\pi)^2]$, respectively, where

$$t^\pm = m_\pi^2 - \frac{1}{2}\left(s - (m_K^2 - m_\pi^2) \mp \sqrt{\lambda\left(s, m_K^2, m_\pi^2\right)}\right) , \tag{6.23}$$

and where

$$\lambda(a,b,c) \equiv a^2 + b^2 + c^2 - 2ab - 2ac - 2bc \tag{6.24}$$

is the Källén function. Using the total widths $\Gamma^{\text{tot}}_{K^+} = 5.32 \times 10^{-17}$ GeV and $\Gamma^{\text{tot}}_{K_L} = 1.29 \times 10^{-17}$ GeV for K^+ and K_L [14], respectively, we can express the LNV branching ratios as

$$\text{BR}_{\text{LNV}}(K^+ \to \pi^+ \nu_i \nu_j) = 10^{-10}\left(\frac{19.2\text{ TeV}}{\Lambda_{ijsd}}\right)^6 . \tag{6.25}$$

for K^+ and

$$\text{BR}_{\text{LNV}}(K_L \to \pi^0 \nu_i \nu_j) = 10^{-10}\left(\frac{24.9\text{ TeV}}{\Lambda_{ijsd}}\right)^6 , \tag{6.26}$$

for K_L, where Λ_{ijsd} is the re-parametrised flavour-specific NP scale $\Lambda^{-3}_{ijsd} = C_{ijsd}/\Lambda^3$. We have here assumed that the NP scale Λ_{ijsd} is real. Neglecting the small CP-violating parameter ϵ in neutral kaon mixing (c.f. Sec. 2.1.4), the matrix element of the rare K_L decay via a scalar current is proportional to the real part of the operator coefficient, as opposed to vector currents where it is proportional to the imaginary part. We can see this by noting the properties of the transformation between $\left|K^0\right\rangle$ and $\left|\bar{K}^0\right\rangle$ for different currents,

$$\begin{aligned} \left\langle \pi^0 \right| \bar{d}\,(1-\gamma_5)\, s \left|\bar{K}^0\right\rangle &= \quad \left\langle \pi^0 \right| \bar{s}\,(1-\gamma_5)\, d \left|K^0\right\rangle , \\ \left\langle \pi^0 \right| \bar{d}\gamma^\mu\,(1-\gamma_5)\, s \left|\bar{K}^0\right\rangle &= -\left\langle \pi^0 \right| \bar{s}\gamma^\mu\,(1-\gamma_5)\, d \left|K^0\right\rangle . \end{aligned} \tag{6.27}$$

Constructing a $|K_L\rangle$ matrix element from the states $\left|K^0\right\rangle$ and $\left|\bar{K}^0\right\rangle$ gives [545]

$$\begin{aligned} i\mathcal{M}\left(K_L \to \pi^0 \nu \overset{(-)}{\nu}\right) = \frac{1}{\sqrt{2+2|\epsilon|^2}}\Big(&F(1+\epsilon)\left\langle \pi^0 \right| C \left|K^0\right\rangle \\ &+F^*(1-\epsilon)\left\langle \pi^0 \right| C \left|\bar{K}^0\right\rangle \Big) \nu C \overset{(-)}{\nu} , \end{aligned} \tag{6.28}$$

where C is the current, which can take the form of $V-A$ or $S-P$, where V, A, S, and P stand for vector, axial-vector, scalar, and pseudo-scalar, respectively. The quantity F contains all the underlying parameters such as coupling constants. Neglecting ϵ we see that the imaginary part of F is picked out for a vector current, as in the SM, while the real part is picked out for scalar currents, as in the LNV case.

The SM contribution to the BR of the rare kaon decay can be parametrised as a dimension-6 EFT operator,

$$\mathcal{L}^{K\to\pi\nu\bar{\nu}}_{\text{SM}} = \frac{1}{\Lambda^2_{\text{SM}}} \sum_{i=1}^{3} \left(\bar{\nu}_i \gamma^\mu\,(1-\gamma_5)\,\nu_i\right)\left(\bar{d}\gamma_\mu\,(1-\gamma_5)\, s\right) , \tag{6.29}$$

where we have a single flavour index i rather than two as in the LNV case due to flavour conservation in the SM. The Lagrangian in Eq. (6.29) leads to the matrix element

$$i\mathcal{M} = \left\langle \pi(p')\nu_i(k)\bar{\nu}_i(k') \right| \mathcal{L}_{\text{SM}}^{K\to\pi\nu\bar{\nu}} \left| K(p) \right\rangle \,, \tag{6.30}$$

which in turn yields the squared matrix element

$$|\mathcal{M}|^2 = \frac{6}{\Lambda_{\text{SM}}^4} \left[m_K^2 \left(t - m_\pi^2\right) - t\left(s + t - m_\pi^2\right) \right] f_+^K(s)^2 \,. \tag{6.31}$$

Here the vector current form factor is given by

$$f_+^K(s) = f_+^K(0) \left(1 + \lambda'_+ \frac{s}{m_\pi^2} + \lambda''_+ \frac{s^2}{m_\pi^4} \right) \,, \tag{6.32}$$

where we have $\lambda'_+ = 24.82 \times 10^{-3}$ and $\lambda''_+ = 1.64 \times 10^{-3}$ [522]. Constructing a double differential decay width out of the SM matrix elements, we can integrate it over the phase space and match the operator coefficients to readily available expressions coming from loop-calculations. This yields the effective scales $|\Lambda_{\text{SM}}^{K^+}| = 8.5$ TeV and $\text{Im}(\Lambda_{\text{SM}}^{K_L}) = 15.46$ TeV. The BR of $K \to \pi\nu\overset{(-)}{\nu}$, where $\overset{(-)}{\nu}$ indicates either ν or $\bar{\nu}$, can then be written as

$$\text{BR}(K \to \pi\nu\overset{(-)}{\nu}) = \text{BR}_{\text{SM}}(K \to \pi\nu\bar{\nu}) + \sum_{i\leq j}^{3} \text{BR}_{\text{LNV}}(K \to \pi\nu_i\nu_j) \,. \tag{6.33}$$

Any interference between the SM and LNV contributions is suppressed by the smallness of the neutrino mass, and is therefore negligible.

6.4. Kinematic distributions in rare kaon decay

As discussed previously in this chapter, the SM rare kaon decay proceeds via a vector current, while possible BSM LNV contributions occur via scalar currents. The difference in current modifies the phase space distribution of final state particles, which is an experimental observable. Once enough data has been collected this can be used to distinguish between different types of BSM contributions to rare kaon decays, including those that are LNV, and can help to identify whether a possible excess is truly due to NP, as the deviation from a pure vector-current distribution would be a clear signal of BSM physics. An initial assumption about the phase space distribution would have to be made in order to set limits on the BR, as the different experiments only probe parts of the phase space. Any experimentally obtained limit on the BR of rare kaon decays would therefore have to correspond to a specific assumption about the current.

The double differential decay widths for both the SM and LNV contributions to rare kaon decays $K(p) \to \pi(p')\nu(k)\overset{(-)}{\nu}(k')$ were obtained in Sec. 6.3, in terms of the Lorentz invariant variables $s = (p - p')^2$ and $t = (k' + p')^2$. In Fig. 6.2 this double differential decay width is shown for charged rare kaon decays at the NA62 experiment in terms of the squared missing

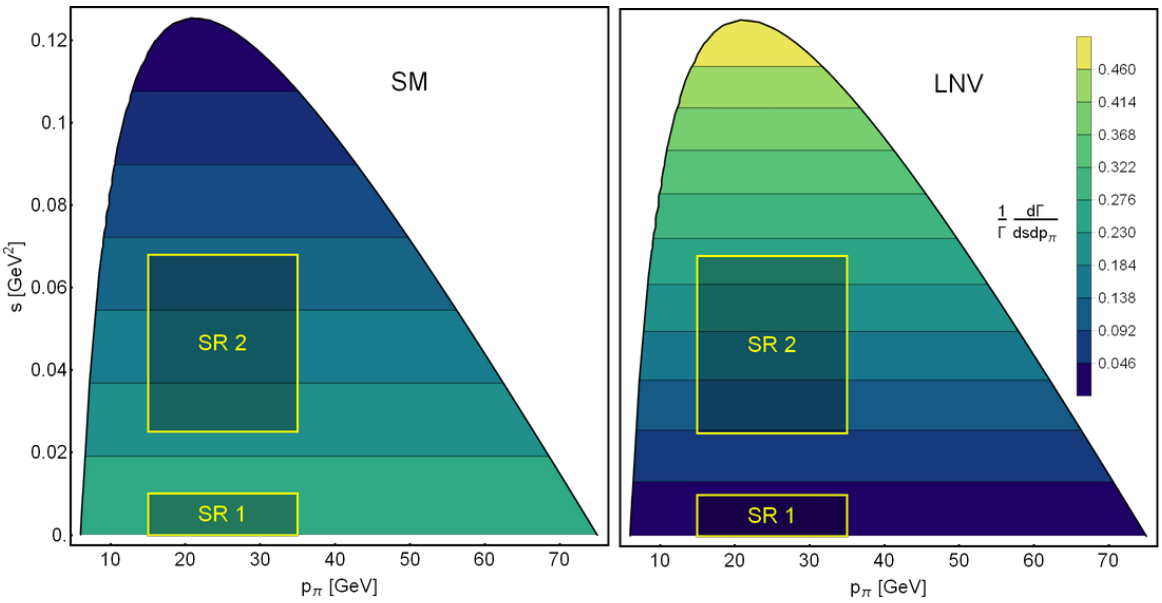

Figure 6.2.: Double differential decay width of the rare kaon decay process in terms of the squared missing energy s and pion momentum p_π, shown for both the SM decay $K^+ \to \pi^+ \nu\bar{\nu}$ (left) and the LNV decay $K^+ \to \pi^+ \nu\nu$ (right). The two signal regions of the NA62 experiment are shown as shaded areas. This figure is taken from Ref. [1].

energy s and the pion momentum $p_\pi \equiv \sqrt{p'^2 - m_\pi^2}$. The variable t can be transformed into a function of p_π and s using conservation of energy and momentum, given by the relation $p = p' + k + k'$. For both the SM (Fig. 6.2 left) and LNV (Fig. 6.2 right) modes, this distribution is shown in the lab frame in which the kaon has the initial momentum $p_{K^+} = \left(p^2 - m_{K^+}^2\right)^{1/2} = 75$ GeV. The upper edge of the distribution corresponds to the case where the direction of the pion is parallel to the initial direction of the kaon. Note that the range in pion momenta in Fig. 6.2 goes up to 75 GeV, which is the initial momentum of the kaon. The rightmost corners in the plots in this figure therefore corresponds to the case where the pion takes all the momentum of the kaon, which is allowed since the neutrinos are effectively massless. The lower limit on p_π in this frame is greater than zero since pions are not massless, there is no way to conserve both energy and momentum for $p_\pi = 0$. The two SRs of the NA62 experiment are also shown in Fig. 6.2 following their definition in Sec. 6.1. They are placed in a way such that the background is minimised.

From Fig. 6.2 it is apparent how the distribution in s varies significantly between the SM and LNV cases, while both distributions are constant in p_π when plotted with respect to[7] s.

[7]Note that this non-dependence of the distribution with respect to p_π is a consequence of the maximum s being a function of p_π, as can be seen by the fact that the location of the upper edge of the distribution in s varies with respect to p_π. If we integrate over s and plot the differential width with respect to p_π, the distribution will not be constant. The flat behaviour in Fig. 6.2 does therefore not lead to a non-dependence on p_π in terms of the number of events seen experimentally.

The SM distribution peaks at $s = 0$, and reaches its minimum at $s = s_{\max} = (m_K - m_\pi)^2$. For the LNV case the opposite is true, the distribution peaks at $s_{\max}$ while reaching its minimum at $s = 0$.

Angular momentum has to be conserved in the process, and this quantity is initially zero in the frame we are using. The missing energy s can be expressed in terms of the opening angle θ between the neutrinos as

$$s = (k + k')^2 = k^0 k'^0 - \cos\theta |\vec{k}||\vec{k}'| = k^0 k'^0 (1 - \cos\theta)\,, \tag{6.34}$$

where in the last step we considered the neutrinos to be massless. The pion is a pseudo-scalar particle, and the only angular momentum-carrying particles in the final state are therefore the neutrinos, since they have an intrinsic spin. The two neutrino spins have to cancel each other in order for angular momentum to be conserved, and this cancellation depends on the direction in which the neutrinos are going. Because both neutrinos in the final state of the LNV mode are left-handed, they cannot travel in the same direction (i.e the cross section for the limiting case $\theta \to 0$ should vanish). If they did there would be no way in which their spins could point in opposite directions such that the angular momentum vanishes, due to their common helicities. For increasing θ there is a larger phase space available in which the neutrino spins point oppositely, reaching a maximum at $\theta = \pi$ (in which case there is no possibility for the neutrino spins *not* to point oppositely). The spins of the two neutrinos in the LNV mode exactly cancel each other if they are travelling back-to-back. For the SM mode, we have one left-handed neutrino and one right-handed anti-neutrino in the final state. Similar arguments then apply as in the LNV case. For LNC decays, the neutrino spins have to again point in opposite directions in order to conserve angular momentum. However, for the SM mode this means that there is a larger phase space available if the neutrinos travel in the same direction. This is because one of them has positive helicity and the other negative, such that if they travel in the same direction their spins exactly cancel. In the SM mode the size of the available phase space is therefore maximum for $\theta = 0$ and vanishes for $\theta = \pi$.

In Fig. 6.3, the single differential decay width of $K^+ \to \pi^+ \nu \overset{(-)}{\nu}$, normalised to the total decay width, is shown in terms of s for the NA62 experiment[8]. The distribution is shown for both the SM (blue) and LNV (red modes), as well as some of the main background processes. The dotted blue and red lines correspond to the SM and LNV rare kaon decay distributions, respectively, after integrating only over the pion momentum range of the SRs (15 GeV $< p_\pi <$ 35 GeV), as opposed to integrating over the whole momentum range. For the LNV mode, the operator coefficient is set in such a way that the integrated branching fraction matches that of the SM mode, and the areas under the blue and red curves in Fig. 6.3 are therefore equal[9]. Furthermore, the widths of both the SM and LNV rare kaon decays have been multiplied by a factor 10^{10} for visibility, since their branching ratios are much smaller than the main background processes. Even with the strategic placement of the SRs

[8]Note that integrating over all distributions in Fig. 6.3 and summing them up does not lead to unity. This is because Γ_{tot} is evaluated in the rest frame of the kaon while $d\Gamma/ds$ is evaluated in the lab frame. All curves are therefore lowered by a factor $1/\gamma$ where $\gamma = E_{K^+}/m_{K^+}$ is the Lorentz factor.

[9]When naively comparing it however looks as if the area under the red curve is larger. This is simply a consequence of the y-axis being in logarithmic scale.

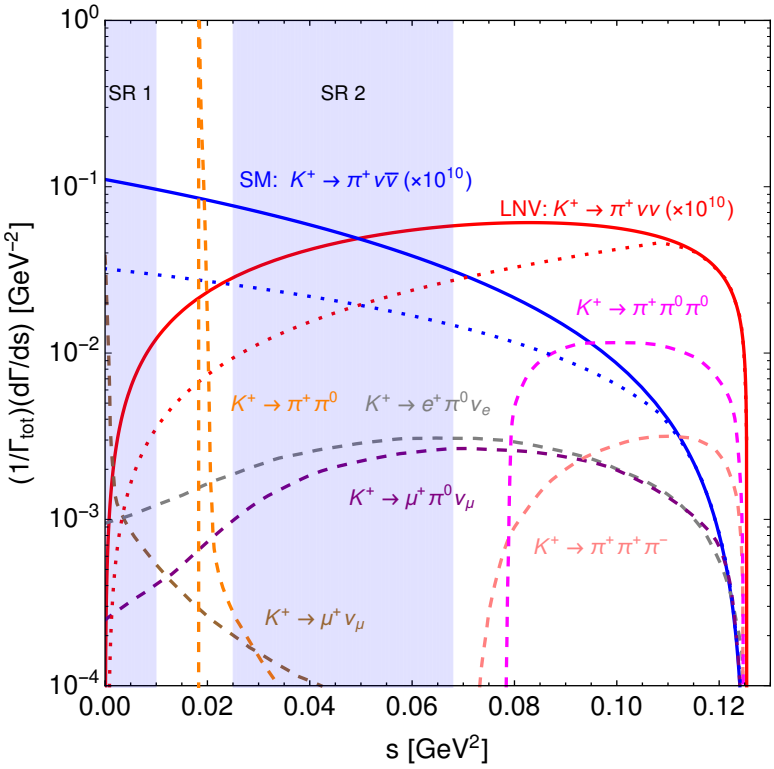

Figure 6.3.: Differential decay width of the rare kaon decay in terms of the squared missing energy s. The solid lines in red and blue correspond to the LNV decay $K^+ \to \pi^+ \nu\nu$ and SM decay $K^+ \to \pi^+ \nu\bar{\nu}$, respectively. The two rare kaon decay widths have been multiplied by a factor 10^{10} for visibility. The dotted red and blue lines show the rare kaon decay widths that correspond to the signal region constraint at NA62 in terms of the momentum of the pion. Differently coloured dashed lines show the distributions of the most relevant background processes at the NA62 experiment, and the two shaded blue areas correspond to the two signal regions. This figure is taken from Ref. [1].

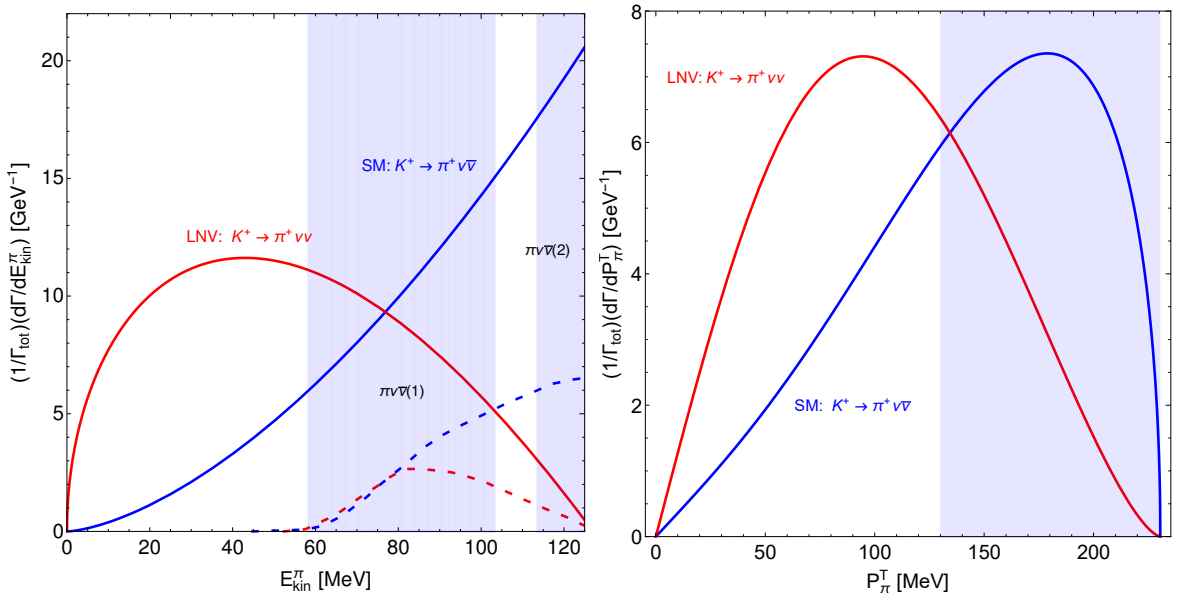

Figure 6.4.: Left: Differential decay width of rare kaon decays at the E949 experiment with respect to the kinetic energy of the pion in the centre of mass frame. Red and blue solid lines show the LNV decay $K^+ \to \pi^+ \nu\nu$ and SM decay $K^+ \to \pi^+ \nu\bar{\nu}$, respectively, while the dashed red and blue lines correspond to the decays after performing the kinematic cuts according to the signal region at the E949 experiment. The shaded areas indicate the signal regions. **Right:** Differential decay width of rare kaon decays at the KOTO experiment with respect to the pion transverse momentum. The shaded area indicates the signal region. This figure is taken from Ref. [1].

to avoid the main backgrounds, there is still a significant contribution from $K \to e^+\pi^0\nu_e$ and $K \to \mu^+\pi^0\nu_\mu$. Therefore, further selection criteria via particle identification and photon rejection have to be applied also inside the SRs [538].

Photon rejection is effective at eliminating backgrounds with a final state π^0, which rapidly decays into two photons. A final state μ^+ or e^+ could mimic a π^+, but would then appear to violate conservation of energy, since their masses are different, and π^+ can in this way be identified based on the final state kinematics.

Kinematic distributions of the pion are also shown for the E949 experiment in Fig. 6.4 (left), and the KOTO experiment in Fig. 6.4 (right). The y-axis shows the differential decay width normalised to the total decay width, and the x-axis shows the variable in which the SR is defined (pion kinetic energy E^{π}_{kin} for the E949 experiment and pion transverse momentum p^T_π for the KOTO experiment), where the blue shaded regions correspond to the SRs of the experiment. From the placement of the SRs it can be seen that the sensitivity to the SM mode is greater than that to the LNV mode in both the E949 and KOTO experiments.

In each rare kaon decay experiment it is the location of the SRs that determine the relative sensitivity to different currents. In Tab. 6.1 the fraction of phase space that falls within the

Experiment	SM (vector)	LNV (scalar)
NA62 SR 1	6%	0.3%
NA62 SR 2	17%	15%
E949 $\pi\nu\bar{\nu}(1)$	29%	2%
E949 $\pi\nu\bar{\nu}(2)$	45%	38%
KOTO	64%	30%

Table 6.1.: Differential partial rare kaon decay width percentages that fall within the signal regions of the NA62, E949, and KOTO experiments, for vector and scalar currents. This table is taken from Ref. [1].

different SRs are shown for the NA62, E949, and KOTO experiments [1]. These fractions can be obtained by expressing the phase space in terms of the relevant kinematic variables, integrating over the SR, and dividing by the width obtained by integrating over the whole phase space. The percentages in Tab. 6.1 serve as an indication of how sensitive each experiment is to the different currents. We see that the all experiments are more sensitive to vector currents than to scalar currents. For the NA62 experiment, most events are expected in SR 2, and the ratio of the percentage of available phase space between the SRs is SR 1 : SR 2 ≈ 0.02, while for vector currents the same ratio is SR 1 : SR 2 ≈ 0.35.

Conclusion to Chapter 6

Rare kaon decays offer a unique way to probe LNV with universal lepton-flavour content. Due to the difference in the kinematic distribution of the final state pion depending on the chiralities of the associated neutrinos, it is in principle possible to discern whether or not a potential excess in an experiment is due to a LNV interaction, if a significant number of events is observed. This highlights an important feature about some of the observables that involve final state neutrinos: even if the neutrinos themselves are not observed, their definite helicity can affect the kinematics of other final state particles [1].

In this chapter, we have seen how the distribution of pions in rare kaon decays at the NA62 experiment could lead to a distinction between LNC and LNV contributions. These results were published in Ref. [1]. In Ch. 7, we show another example of how LNV could potentially be probed using final state kinematics, namely via the electromagnetic interactions of neutrinos.

7. LNV in radiative CEνNS

Coherent elastic neutrino-nucleus scattering (CEνNS) [546] is a SM process that was first discovered by the COHERENT collaboration in 2017 [547]. Since its first observation, the goal in CEνNS experiments has shifted from confirming the existence of this mode to using it as a probe of SM parameters and to search for NP. In the future, CEνNS experiments will be able to detect extremely small momentum transfers of $\mathcal{O}$(eV), using very low nuclear recoil thresholds [548, 549]. One possible NP scenario that could potentially be observed in such experiments is the Primakoff upscattering of incoming neutrinos into heavy sterile neutrinos, e.g. via a transition magnetic dipole coupling, as illustrated in Fig. 7.1 (left). Such a dipole portal could simultaneously be a way to probe both the existence of sterile neutrinos as well as the NP that generates the magnetic moment coupling [3].

In this chapter we focus on a specific process involving dipole couplings at CEνNS experiments: the initial upscattering of a neutrino ν into a sterile neutrino N via a transition magnetic moment $\mu_{\nu N}$, and the subsequent decay of the sterile neutrino into a photon and an active neutrino, as shown in Fig. 7.1 (right). We call this process *radiative CEνNS*. Searches for it have been proposed for the DUNE [550], IceCube [551], Super-Kamiokande [552], and NUCLEUS [3] experiments. The latter experiment is the main focus of a large part of this chapter. First we discuss the details of neutrino transition magnetic moments (Sec. 7.1), how they are connected to neutrino masses (Sec. 7.2), and how they can be searched for in CEνNS experiments as well as how radiative CEνNS can be used to probe the possible existence of LNV and the nature of neutrino masses (Secs. 7.3 and 7.4). The work presented in this section led to the publication in Ref. [3].

7.1. Neutrino transition magnetic moments

To describe the transition magnetic moment coupling between an active neutrino $\nu_{\alpha L}$ of flavour $\alpha \in \{e, \mu, \tau\}$ and a sterile neutrino N we use the following Lagrangian:

$$\mathcal{L} \supset \mu^{\alpha}_{\nu N} \bar{\nu}_{\alpha L} \sigma_{\mu\nu} P_R N F^{\mu\nu} + \text{h.c.}\,, \tag{7.1}$$

where the electromagnetic field strength tensor is given by $F^{\mu\nu} = \partial^\mu A^\nu - \partial^\nu A^\mu$, and where $\mu^{\alpha}_{\nu N}$ are the transition magnetic dipole couplings. Note that Eq. (7.1) is only valid below the scale of EWSB since it is not invariant under the full SM gauge group. To obtain a Lagrangian which is valid at higher energies, Eq. (7.1) would need to be matched onto expressions given in terms of the SM doublets L_α and H as well as the $U(1)_Y$ and $SU(2)_L$ field strengths $B_{\mu\nu}$ and $W^a_{\mu\nu}$. The momentum scales involved in CEνNS are well below the scale of EWSB, and therefore Eq. (7.1) remains a valid description of this process. In order to have coherence in

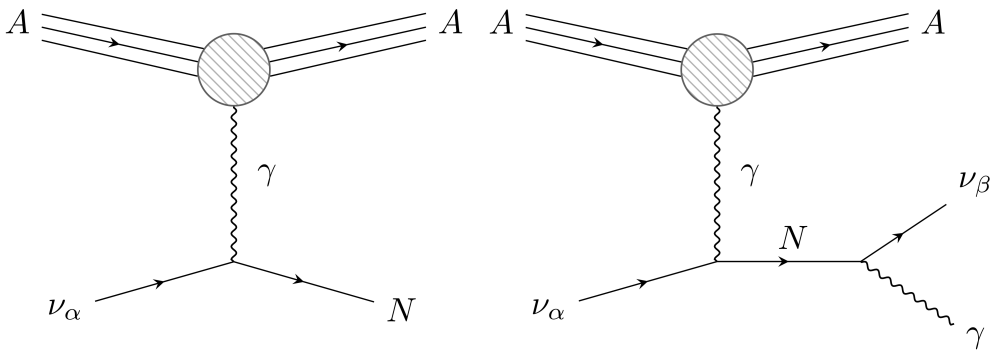

Figure 7.1.: Left: Primakoff upscattering of a light active neutrino ν_α into a heavy sterile neutrino N via a transition magnetic dipole moment interaction with nucleus A. **Right:** The same but with the additional decay of N into an active neutrino ν_β and a photon γ, i.e. the radiative CEνNS process.

the scattering, i.e. in order for the incoming neutrino to interact with the whole nucleus rather than individual nucleons, the energy of the neutrino has to be less than the inverse diameter of the nucleus, which for a nucleus of diameter 1 fm corresponds to an upper limit neutrino energy of about 0.2 GeV.

Both the active and sterile neutrinos could be of either Dirac or Majorana type. The active neutrinos $\nu_{\alpha L}$ are left-handed Weyl spinors that can be part of a Dirac ($\nu_\alpha = \nu_{\alpha L} + \nu_{\alpha R}$) or Majorana ($\nu_\alpha = \nu_{\alpha L} + \nu^c_{\alpha L}$) 4-component spinor. In the former case it is necessary to introduce yet another sterile field, namely $\nu_{\alpha R}$. The heavy sterile field N can similarly be decomposed into a left- and right-handed Weyl spinors according to whether it is a Dirac ($N = N_L + N_R$) or Majorana ($N = N_R + N^c_R$) field, where in the former case N_L has been additionally introduced. There are therefore four combinations of field types for the active and sterile neutrinos that can realise Eq. (7.1). However, for light active neutrino masses well below the momentum scales involved in the scattering $m_\nu \ll E_\nu$, the experimental resolution of the active neutrino mass type is very limited, and the differential scattering rates are approximately equal for Dirac and Majorana types. This is in agreement with the Dirac-Majorana confusion theorem [553, 554]. For the heavy sterile neutrino, the difference between Dirac or Majorana masses can be significant if m_N is close to E_ν.

The Lagrangian term in Eq. (7.1) leads to the Primakoff upscattering interaction $\nu_\alpha A \to NA$ [555, 556] depicted in Fig. 7.1 (left), where A is a nucleus. If the incoming neutrinos are relativistic, the distribution of the cross section in terms of the nuclear recoil energy E_R is identical for Dirac and Majorana N. Therefore, the current non-observation of any deviation from the expected SM distribution can lead to constraints on the size of the dipole coupling $\mu^\alpha_{\nu N}$ as a function of the sterile neutrino mass m_N, and these limits are then applicable to both Dirac and Majorana N. Such flavour-dependent constraints have been set by a range of different experiments [550].

Eq. (7.1) also leads to the radiative upscattering process $\nu_\alpha A \to \nu_\beta \gamma A$ [3] depicted in

Fig. 7.1 (right). The corresponding cross section is proportional to the factor $|\mu^{\alpha}_{\nu N}\mu^{\beta}_{\nu N}|^2$, which contains four powers of the transition magnetic moment coupling $\mu_{\nu N}$ as opposed to the two powers in ordinary Primakoff upscattering. This leads to a suppression of the rate of radiative upscattering in experiments. However, the final state photon provides an additional signal which can potentially be used to obtain more kinematical information about the process, which in turn could potentially be used to discriminate between Dirac and Majorana N, as can be seen below.

Note also that the final state neutrino ν_β remains undetected in CEνNS experiments. Therefore, additional decay channels of the sterile neutrino N that produces a photon could potentially also provide a signal. Introducing another sterile neutrino N' as an additional light state, such that $m_{N'} \ll m_N$, leads to the Lagrangian

$$\mathcal{L} \supset \mu^{\alpha}_{\nu N}\bar{\nu}_{\alpha L}\sigma_{\mu\nu}P_R N F^{\mu\nu} + \mu_{N'N}\bar{N'}\sigma_{\mu\nu}P_R N F^{\mu\nu} + \text{h.c.}\,. \tag{7.2}$$

From Eq. (7.2) we have the radiative upscattering process $\nu_\alpha A \to X_i A\gamma$, where $X_i \in \{\nu_\beta, N'\}$ is a light fermion. The corresponding cross section is then proportional to $|\mu^{\alpha}_{\nu N}\sum_i \mu_{X_i N}|^2$, which could lead to weaker experimental constraints as compared to the mode that only utilises the coupling between N and ν.

7.2. Neutrino masses from transition dipole couplings

In this section we consider the connections between transition neutrino magnetic dipole moments and active neutrino masses. If the radiative CEνNS interaction is realised in nature, and should the heavy sterile neutrino N that mediates the process be Majorana, the light active neutrinos must be Majorana as well. As illustrated in Fig. 7.2, the transition magnetic dipole moment coupling in combination with a Majorana mass insertion for the sterile neutrino inevitably leads to a one-loop radiative active neutrino Majorana mass diagram. While this contribution to the neutrino mass may in some instances not be the dominant one in the presence of a Dirac mass term with light right-handed sterile neutrinos ν_R, it does imply that the active left-handed neutrinos have a Majorana nature, which in turn implies LNV. For Dirac N, no direct conclusion about the nature of active neutrinos can be drawn.

A large neutrino transition magnetic dipole moment $\mu_{\nu N}$ in combination with small active neutrino masses could hint towards some underlying symmetry, e.g. related to the Voloshin mechanism [557] or inverse seesaw [499–501]. These mechanisms can be model-independently described in modified versions of SMEFT for both Dirac and Majorana neutrinos. The modification involves adding an additional light[1] Dirac or Majorana sterile neutrino[2] N. If the Weyl spinor component N_R couples to ν_L via an active-to-sterile transition magnetic moment, mass terms of the form

$$\mathcal{L} \supset m_{\nu N}\bar{\nu}_L N_R + \text{h.c.} \tag{7.3}$$

[1]Here we mean *light* with respect to the scale of EWSB. The light field in question, N, is often referred to as a *heavy* field in the text since it is heavy with respect to the light active neutrino mass.

[2]Such an EFT is often called νSMEFT in the literature.

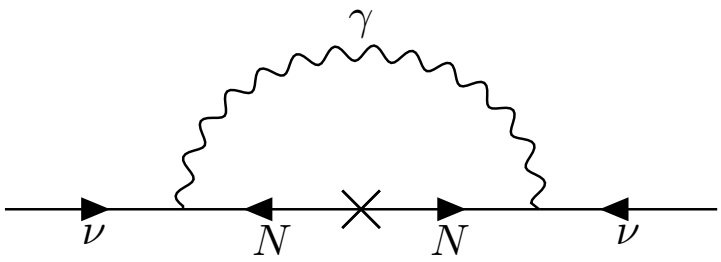

Figure 7.2.: Active neutrino radiative neutrino mass diagram induced my by the transition magnetic moment coupling $\mu_{\nu N}$ as well as a heavy sterile neutrino Majorana mass insertion. This figure is taken from Ref. [3].

can be generated in an EFT description [558]. We can construct an EFT Lagrangian as

$$\mathcal{L}_{\text{eff}} = \sum_{d,j} \frac{C_j^{(d)}(\mu)}{\Lambda^{d-4}} \, \mathcal{O}_j^{(d)}(\mu) \; + \; \text{h.c.}\,, \tag{7.4}$$

where j enumerates the different operators $\mathcal{O}_j^{(d)}$ and $C_j^{(d)}$ for a given dimension $d \geq 4$. Furthermore, Λ is the scale of NP, and μ is the renormalisation scale. In a SM invariant EFT formalism an effective active-to-sterile neutrino transition magnetic dipole moment involving Dirac sterile neutrinos can be generated at dimension $d = 6$ via operators that include couplings to the SM gauge field strengths $W^a_{\mu\nu}$ and $B_{\mu\nu}$. In the basis we consider here, going from the scale of EWSB to higher scales, these operators mix in renormalisation group running with another operator containing three copies of the Higgs field. The three operators in question are given by [558]

$$\begin{aligned} \mathcal{O}_1^{(6)} &= g' \bar{L} \tilde{H} \sigma_{\mu\nu} N_R B^{\mu\nu} \\ \mathcal{O}_2^{(6)} &= g \bar{L} \tau^a \tilde{H} \sigma_{\mu\nu} N_R W^{a\mu\nu} \\ \mathcal{O}_3^{(6)} &= \bar{L} \tilde{H} N_R \left(H^\dagger H \right) , \end{aligned} \tag{7.5}$$

where $\tau^a = \sigma^a/2$ are the generators of $SU(2)$. The operator $\mathcal{O}_3^{(6)}$ induces a Dirac neutrino mass term given in Eq. (7.3) after EWSB. Assuming that $\mathcal{O}_3^{(6)}$ vanishes at some high scale Λ such that $C_3^{(6)}(\mu = \Lambda) = 0$, non-zero values of $C_1^{(6)}(\mu = \Lambda)$ and $C_2^{(6)}(\mu = \Lambda)$ lead to a non-vanishing contribution to $\mathcal{O}_3^{(6)}$ at the EWSB scale v via mixing, such that $C_3^{(6)}(\mu = v) \neq 0$. In this way, Dirac active neutrino masses are generated from the magnetic moment operators $\mathcal{O}_1^{(6)}$ and $\mathcal{O}_2^{(6)}$. Below the scale of EWSB these two operators combine, giving the magnetic moment coefficient

$$\frac{\mu_{\nu N}}{\mu_B} = -16\sqrt{2} \left(\frac{m_e v}{\Lambda^2} \right) \left[C_1^{(6)}(v) + C_2^{(6)}(v) \right] , \tag{7.6}$$

where μ_B is the Bohr magneton, and $C_3^{(6)}$ leads to the Dirac mass contribution

$$\delta m_{\nu N} = -C_3^{(6)}(v)\frac{v^3}{2\sqrt{2}\Lambda^2}\,. \tag{7.7}$$

Eliminating Λ yields the relation

$$\delta m_{\nu N} = \frac{v^2}{16 m_e}\,\frac{C_3^{(6)}(v)}{C_1^{(6)}(v)+C_2^{(6)}(v)}\,\frac{\mu_{\nu N}}{\mu_B}\,. \tag{7.8}$$

Assuming now that we have $C_3^{(6)}(\mu=\Lambda)=0$ at $\Lambda = 1$ TeV, and that the mass constraint on light active neutrinos is $m_\nu \lesssim 1$ eV, the induced constraint on $\mu_{\nu N}$ is

$$\frac{|\mu_{\nu N}|}{\mu_B} \sim 10^{-15}\left(\frac{\delta m_{\nu N}}{1\text{ eV}}\right)\,. \tag{7.9}$$

However, in deriving Eq. (7.9) it was assumed that $C_1^{(6)}$ and $C_2^{(6)}$ have the same sign and contribute equally to the neutrino magnetic moment. In case there are partial cancellations between $C_1^{(6)}$ and $C_2^{(6)}$ the bound in Eq. (7.9) is no longer valid. Furthermore, there may be a cancellation between a radiatively induced neutrino mass and a tree-level Dirac mass term that is induced e.g. via a Yukawa coupling to some scalar with a non-zero vev. For the rest of this section we consider these types of cancellations to be possible.

In case there is a large mixing between active and sterile neutrinos, a transition magnetic moment can be induced via loop diagrams that involve charged leptons [559, 560]. This contribution is given by [555]

$$\frac{|\mu_{\nu N}|}{\mu_B} = \frac{3 m_{\nu N} m_e}{16\pi^2}\frac{G_F}{\sqrt{2}} \sim 10^{-13}\left(\frac{m_{\nu N}}{1\text{ MeV}}\right)\,. \tag{7.10}$$

For Majorana N, the loop diagram in Fig. 7.2 is induced in the presence of a transition magnetic moment. This contribution to the light active neutrino mass can be estimated as

$$m_\nu \sim \left(\frac{\mu_{\nu N}}{\mu_B}\right)^2 \frac{\alpha}{16\pi}\frac{m_N \Lambda^2}{m_e^2}\,, \tag{7.11}$$

where Λ is the scale of NP in the magnetic moment operator. For $\Lambda = 1$ TeV and $m_N = 1$ MeV, the mass constraint $m_\nu \lesssim 1$ eV leads to

$$\frac{|\mu_{\nu N}|}{\mu_B} \sim 10^{-8}\left(\frac{\delta m_{\nu N}}{1\text{ eV}}\right)\,. \tag{7.12}$$

Both Eqs. (7.10) and (7.11) depend on the Majorana mass of N, where the constraint on $\mu_{\nu N}$ grows weaker for large m_N due to reduced mixing, while the light active Majorana mass m_ν increases with increasing m_N. In e.g. the inverse seesaw mechanism [499–501], where light active neutrinos get their Majorana mass from a combination of m_{N_L} and the Yukawa couplings between ν_L, N_R and N_R, N_L, both constraints can simultaneously be satisfied by a set of parameters that keeps $m_{\nu N}$ small without having a large m_N, and that arises without fine-tuned cancellations.

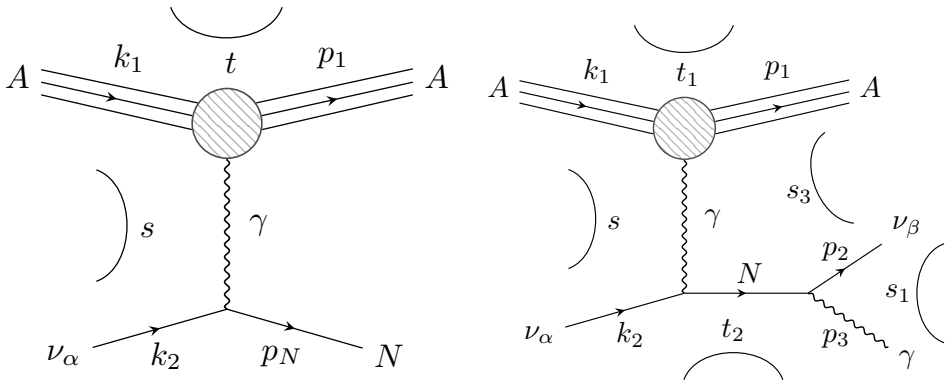

Figure 7.3.: Left: Primakoff upscattering of a light active neutrino ν_α into a heavy sterile neutrino N via a transition magnetic dipole moment interaction with a nucleus A, using the kinematic variables $s = (k_2 + k_1)^2$ and $t = (k_1 + p_1)^2$. **Right:** The same but with the additional decay of N into an active neutrino ν and a photon γ, i.e. the radiative upscattering process, with the kinematic variables $s = (k_2 + k_1)^2$, $t = (k_1 - p_1)^2$, $s_1 = (p_2 + p_3)^2$, $s_3 = (p_1 + p_2)^2$, and $t_2 = (k_2 - p_3)^2$. This figure is taken from Ref. [3].

7.3. Calculation of the radiative CEνNS process

In this section we calculate the cross section for both the Primakoff upscattering and radiative CEνNS processes given by the diagrams in Fig. 7.1 (left) and (right) respectively, and use the results to calculate event rates at the NUCLEUS experiment. The treatment of the kinematics in these calculations follow from Ref. [561].

7.3.1. Primakoff upscattering

First we consider the Primakoff upscattering of an incoming light active neutrino ν_α into a heavy sterile neutrino. In the flavour basis for ν_α and mass basis for N, this process can be described by the Lagrangian

$$\mathcal{L} \supset \mu^\alpha_{\nu N} \bar{\nu}_{\alpha L} \sigma_{\mu\nu} P_R N F^{\mu\nu} + (\mu^\alpha_{\nu N})^* \bar{N} \sigma_{\mu\nu} P_L \nu_{\alpha L} F^{\mu\nu} \,. \tag{7.13}$$

In case both ν_α and N are Majorana, we can simplify Eq. (7.13) as

$$\mathcal{L} \supset \mu^\alpha_{\nu N} \bar{\nu}_\alpha \left[\sigma_{\mu\nu} P_R - \mathcal{C} (\sigma_{\mu\nu} P_L)^\mathsf{T} \mathcal{C}^{-1} \right] N F^{\mu\nu} = \mu^\alpha_{\nu N} \bar{\nu}_\alpha \sigma_{\mu\nu} N F^{\mu\nu} \,, \tag{7.14}$$

where we have used the relations $(\mu^\alpha_{\nu N})^* = -\mu^\alpha_{\nu N}$, assuming CP-symmetry, and $\mathcal{C} P_L^\mathsf{T} \mathcal{C}^{-1} = P_L$. As shown in Fig. 7.3 (left), the momentum exchange between the neutrino and nucleus via the photon is $q = k_1 - p_1 = p_N - k_2$. For both Dirac and Majorana N, the process $\nu_\alpha A \to N A$ leads to the matrix element

$$i\mathcal{M}^{\mathrm{D(M)}}_{\nu_\alpha A \to N A} = \mu^\alpha_{\nu N} \left[\bar{u}_N \sigma_{\mu\rho} P_L q^\rho u_{\nu_\alpha} \right] \frac{(-i g^{\mu\sigma})}{q^2} J^A_\sigma \,, \tag{7.15}$$

while the process $\bar{\nu}_\alpha A \to \bar{N} A$ leads to

$$i\mathcal{M}^{\mathrm{D(M)}}_{\bar{\nu}_\alpha A\to \bar{N}A} = \mu^{\alpha}_{\nu N}\left[\bar{v}_{\nu_\alpha}\sigma_{\mu\rho}P_R q^\rho v_N\right]\frac{(-ig^{\mu\sigma})}{q^2}J^A_\sigma\,. \tag{7.16}$$

where the hadronic current is denoted by J^A_σ. We assume this current to take the form $J^A_\sigma = -ieZ(\bar{u}_A\gamma_\sigma u_A)\mathcal{F}(q^2)$, where $\mathcal{F}(q^2)$ is a nuclear form factor. In the case of Dirac N, the processes $\nu_\alpha A \to \bar{N}A$ and $\bar{\nu}_\alpha A \to NA$ are suppressed by a factor m_ν/k_2^0. For Majorana N these processes are not suppressed. Due to the relation $N = \bar{N}^c$ their corresponding matrix elements are again described by Eqs. (7.15) and (7.16), respectively. We work in the limit of vanishing active neutrino masses, for which the matrix element of the Primakoff upscattering process is same same for Dirac or Majorana N. In this limit there is also no such concept as Dirac or Majorana ν_α, since they are massless.

Using Eqs. (7.15) and (7.16) we can now find the differential cross section by taking the absolute square, averaging over incoming spins, and summing over outgoing spins. This differential cross section is given by [3]

$$d^2\sigma_{\nu_\alpha A\to NA} = \frac{1}{2(s-m_A^2)}\frac{1}{2}\sum_{\text{spins}}|\mathcal{M}^{\mathrm{D(M)}}_{\nu_\alpha A\to NA}|^2 d\Phi_2\,, \tag{7.17}$$

where m_A is the mass of the nucleus A and $d\Phi_2$ is a two-body phase space of the outgoing N and A (c.f. Appendix C), which is given by

$$d\Phi_2 = \frac{1}{(2\pi)^2}\frac{d^3\mathbf{p}_1}{2E_{\mathbf{p}_1}}\frac{d^3\mathbf{p}_N}{2E_{\mathbf{p}_N}}\delta^4(k_1+k_2-p_1-p_N)\,. \tag{7.18}$$

Integrating, we can eliminate the delta-function to obtain

$$\int \frac{1}{(2\pi)^2}\frac{d^3\mathbf{p}_1}{2E_{\mathbf{p}_1}}\frac{d^3\mathbf{p}_N}{2E_{\mathbf{p}_N}}\delta^4(k_1+k_2-p_1-p_N) = \int\frac{d\phi}{2\pi}\frac{dt}{8\pi(s-m_A^2)}\,. \tag{7.19}$$

Here we have expressed the phase space in terms of the azimuthal angle ϕ describing rotations in a plane perpendicular to the direction of the incoming neutrino, as well as the Mandelstam variable $t = q^2$. The integration limits for the phase space are given by the relation $\Delta_3 < 0$, where the 3×3 symmetric Gram determinant Δ_3 is given by

$$\Delta_3 = -\frac{1}{2}\begin{vmatrix} 0 & 0 & s & m_N^2 & 1\\ 0 & 0 & m_A^2 & t & 1\\ s & m_A^2 & 0 & m_A^2 & 1\\ m_N^2 & t & m_A^2 & 0 & 1\\ 1 & 1 & 1 & 1 & 0\end{vmatrix}\,. \tag{7.20}$$

The absolute squared matrix element summed over spins can be written as

$$\frac{1}{2}\sum_{\text{spins}}|\mathcal{M}_{\nu_\alpha A\to NA}|^2 = (\mu^{\alpha}_{\nu N})^2\frac{e^2Z^2\mathcal{F}^2(q^2)}{q^4}L_{\mu\nu}H^{\mu\nu}\,, \tag{7.21}$$

where Z is the number of nucleons, and the leptonic and hadronic tensors $L_{\mu\nu}$ and $H_{\mu\nu}$ are respectively given by

$$L_{\mu\nu} = \mathrm{Tr}[(\not{p}_N + m_N)\sigma_{\mu\rho}P_L \not{k}_2 \sigma_{\nu\lambda}]\, q^\rho q^\lambda \,, \tag{7.22}$$

$$H^{\mu\nu} = \frac{1}{2}\,\mathrm{Tr}[(\not{p}_1 + m_A)\gamma^\mu(\not{k}_1 + m_A)\gamma^\nu] \,. \tag{7.23}$$

There is no dependence on the azimuthal angle ϕ, and we can therefore integrate over it to obtain the single-differential cross section

$$\frac{d\sigma_{\nu_\alpha A\to NA}}{dt} = (\mu^\alpha_{\nu N})^2 \alpha Z^2 \mathcal{F}^2(t) \frac{F(s, m_N^2, t, m_A^2)}{2t^2(s - m_A^2)^2} \,, \tag{7.24}$$

where we have introduced

$$F(w,x,y,z) = 2y(w-z)^2 + 2y^2(w-z) - xy(2w+y) + x^2(2z+y) \,. \tag{7.25}$$

Converting Eq. (7.24) into an expression given in terms of variables that are defined in the lab frame, we can use the relations $k_1 = (m_A, \mathbf{0})$, $k_2 = (E_\nu, \mathbf{k}_2)$, $p_1 = (m_A + E_R, \mathbf{p}_1)$ and $p_N = (E_\nu - E_R, \mathbf{p}_N)$, where E_ν is the energy of the incoming neutrino and E_R is the nuclear recoil energy. The Mandelstam variables are now given by $s = m_A(m_A + 2E_\nu)$ and $t = -2m_A E_R$. Using the Jacobian $\mathcal{J}(E_R) = \frac{\partial t}{\partial E_R} = -2m_A$ gives us

$$\frac{d\sigma_{\nu_\alpha A\to NA}}{dE_R} = (\mu^\alpha_{\nu N})^2 \alpha Z^2 \mathcal{F}^2(E_R) \left[\frac{1}{E_R} - \frac{1}{E_\nu} - \frac{m_N^2}{4E_R E_\nu^2}\left(1 + \frac{2E_\nu - E_R}{m_A}\right) - \frac{m_N^4}{8m_A E_R^2 E_\nu^2}\left(1 - \frac{E_R}{m_A}\right)\right] . \tag{7.26}$$

We are going to be interested in the case where the momentum exchanged by the photon is much smaller than the mass of the nucleus, in which case we drop the terms in Eq. (7.26) that are proportional to E_ν^{-1} or m_ν^{-1}.

7.3.2. Radiative upscattering

We now compute the squared matrix element and differential cross section that corresponds to radiative upscattering $\nu_\alpha A \to \nu_\beta A\gamma$ [3]. This process can be thought of as a Primakoff upscattering $\nu_\alpha A \to NA$ followed by a sterile neutrino decay $N \to \nu_\beta\gamma$ that is induced by the magnetic moment coupling. For Dirac N the matrix element for the decay $N \to \nu_\beta\gamma$ is given by

$$i\mathcal{M}^{\mathrm{D}}_{N\to\nu_\beta\gamma} = \mu^\beta_{\nu N}[\bar{u}_{\nu_\beta}\sigma_{\mu\nu}P_R u_N] p_3^\mu \epsilon^{\nu *} \,. \tag{7.27}$$

Here p_3^μ and ϵ^ν are the momentum and polarisation of the final state photon, respectively, and $P_R = \frac{1}{2}(1+\gamma_5)$ is a right-handed projection operator. The matrix element for the conjugated process $\bar{N} \to \bar{\nu}_\beta\gamma$ can be obtained with the replacement $[\bar{u}_{\nu_\beta}\sigma_{\mu\nu}P_R u_N] \to [\bar{v}_N\sigma_{\mu\nu}P_L v_{\nu_\beta}]$. If N is

Majorana, the matrix element for N decaying via the transition magnetic moment coupling is given by the sum of the processes $N \to \nu_\beta \gamma$ and $\bar{N} \to \nu_\beta \gamma$. The matrix element is then given by

$$\begin{aligned} i\mathcal{M}^{\mathrm{M}}_{N\to\nu_\beta\gamma} &= \mu^{\beta}_{\nu N}\left[\bar{u}_{\nu_\beta}[\sigma_{\mu\nu}P_R - \mathcal{C}(\sigma_{\mu\nu}P_L)^{\mathsf{T}}\mathcal{C}^{-1}]u_N\right]p_3^{\mu}\epsilon^{\nu *} \\ &= \mu^{\beta}_{\nu N}[\bar{u}_{\nu_\beta}\sigma_{\mu\nu}(P_R+P_L)u_N]p_3^{\mu}\epsilon^{\nu *} = \mu^{\beta}_{\nu N}[\bar{u}_{\nu_\beta}\sigma_{\mu\nu}u_N]p_3^{\mu}\epsilon^{\nu *}\,. \end{aligned} \tag{7.28}$$

In order to obtain the differential decay width we must take the absolute squared of the matrix element and sum over spins and polarisations,

$$d^2\Gamma^{\mathrm{D(M)}}_{N\to\nu_\beta A} = \frac{1}{2m_N}\sum_{\text{spins, pols}}|\mathcal{M}^{\mathrm{D(M)}}_{N\to\nu_\beta\gamma}|^2 d\Phi_2\,. \tag{7.29}$$

Here we do not average over the spin of N, since in subsequent steps we take it to be an intermediate particle in the full radiative upscattering process. The squared and spin-summed matrix element is given by

$$\sum_{\text{spins, pols}}|\mathcal{M}^{\mathrm{M}}_{N\to\nu_\beta\gamma}|^2 = 2\sum_{\text{spins, pols}}|\mathcal{M}^{\mathrm{D}}_{N\to\nu_\beta\gamma}|^2 = 4(\mu^{\beta}_{\nu N})^2 m_N^4\,, \tag{7.30}$$

where the factor two difference between Dirac and Majorana N comes from the additional channel in the Majorana case. As seen in Appendix C, the two-body phase space can be expressed in terms of the angles θ and ϕ as

$$d\Phi_2 = \frac{1}{8\pi}\frac{d\phi}{2\pi}\frac{d\cos\theta}{2}, \tag{7.31}$$

and integrating then gives the decay width

$$\Gamma^{\mathrm{M}}_{N\to\nu_\beta\gamma} = 2\Gamma^{\mathrm{D}}_{N\to\nu_\beta\gamma} = \int d^2\Gamma^{\mathrm{D(M)}}_{N\to\nu_\beta A} = \frac{(\mu^{\beta}_{\nu N})^2 m_N^3}{4\pi}\,. \tag{7.32}$$

The relative factor two between Dirac and Majorana N that is seen in Eq. (7.32) also appears in vector neutral current decays [562, 563].

Now considering the full radiative upscattering process, we define the Lorentz invariant Mandelstam variables s, t, s_1, s_3, and t_2 as

$$s = (k_1+k_2)^2 = m_A(m_A+2E_\nu)\,, \tag{7.33}$$

$$t_1 = (k_1-p_1)^2 = -2m_A E_R\,, \tag{7.34}$$

$$s_1 = (p_2+p_3)^2 = -2m_A E_R - 2E_\nu(E_R - \sqrt{E_R(2m_A+E_R)}\cos\theta_R)\,, \tag{7.35}$$

$$s_3 = (p_1+p_2)^2 = m_A(m_A+2E_\nu-2E_\gamma) - 2E_\nu E_\gamma(1-\cos\theta_\gamma)\,, \tag{7.36}$$

$$t_2 = (k_2-p_3)^2 = -2E_\nu E_\gamma(1-\cos\theta_\gamma)\,, \tag{7.37}$$

where θ_γ and θ_R are the angles between the directions of the incoming neutrino and outgoing photon and nucleus, respectively, and E_γ is the photon energy. The Mandelstam variables

from Eq. (7.33) are illustrated in Fig. 7.3 (right) in terms of the associated momenta. For Dirac N we have the two possible processes $\nu_\alpha A \to NA \to \nu_\beta A\gamma$ and $\bar{\nu}_\alpha A \to \bar{N}A \to \bar{\nu}_\beta A\gamma$. The matrix elements for there processes are

$$i\mathcal{M}^{\mathrm{D}}_{\nu_\alpha A\to\nu_\beta A\gamma} = \mu^{\alpha}_{\nu N}\mu^{\beta}_{\nu N}\frac{i\left[\bar{u}_{\nu_\beta}\sigma_{\lambda\xi}P_R(\not{p}_N + m_N)\sigma_{\mu\rho}P_L u_{\nu_\alpha}\right]\epsilon^{\lambda *}p_3^{\xi}q^{\rho}}{p_N^2 - m_N^2 + im_N\Gamma_N}\frac{(-ig^{\mu\sigma})}{q^2}J^A_\sigma\,, \tag{7.38}$$

and

$$i\mathcal{M}^{\mathrm{D}}_{\bar{\nu}_\alpha A\to\bar{\nu}_\beta A\gamma} = \mu^{\alpha}_{\nu N}\mu^{\beta}_{\nu N}\frac{i\left[\bar{v}_{\nu_\alpha}\sigma_{\mu\rho}P_R(\not{p}_N + m_N)\sigma_{\lambda\xi}P_L v_{\nu_\beta}\right]\epsilon^{\lambda *}p_3^{\xi}q^{\rho}}{p_N^2 - m_N^2 + im_N\Gamma_N}\frac{(-ig^{\mu\sigma})}{q^2}J^A_\sigma\,, \tag{7.39}$$

respectively, where Γ_N is the total width of N and $p_N^\mu = (p_2 + p_3)^\mu$. For Majorana N, the additional processes $\nu_\alpha A \to \bar{\nu}_\beta A\gamma$ and $\bar{\nu}_\alpha A \to \nu_\beta A\gamma$ are allowed. The radiative upscattering matrix element is then given by

$$i\mathcal{M}^{\mathrm{M}}_{\nu_\alpha A\to\nu^{(c)}_\beta A\gamma} = \mu^{\alpha}_{\nu N}\mu^{\beta}_{\nu N}\frac{i\left[\bar{u}_{\nu_\beta}\sigma_{\lambda\xi}(\not{p}_N + m_N)\sigma_{\mu\rho}P_L u_{\nu_\alpha}\right]\epsilon^{\lambda *}p_3^{\xi}q^{\rho}}{p_N^2 - m_N^2 + im_N\Gamma_N}\frac{(-ig^{\mu\sigma})}{q^2}J^A_\sigma\,, \tag{7.40}$$

where the difference from the Dirac case is the absence of the projection operator P_R to the left of the N mediator, since the sum $P_L + P_R = 1$ is used for the two contributions in the Majorana case. Note that the final state neutrino $\nu^{(c)}_\beta$ may or may not be charge conjugated, depending on whether the process has a ν_β or $\bar{\nu}_\beta$ final state. This is strictly applicable to the Majorana N case, where ν is also Majorana. Assuming instead an incoming ν_α of predominantly positive helicity (corresponding to $\bar{\nu}_\alpha$ in the Dirac case) the replacement $\left[\bar{u}_{\nu_\beta}\sigma_{\lambda\xi}(\not{p}_N + m_N)\sigma_{\mu\rho}P_L u_{\nu_\alpha}\right] \to \left[\bar{v}_{\nu_\alpha}\sigma_{\lambda\xi}P_R(\not{p}_N + m_N)\sigma_{\mu\rho}v_{\nu_\beta}\right]$ should be made in Eq. (7.40).

The full differential cross section for the radiative CEνNS process can now be obtained by squaring the matrix element, summing over final state spins and polarisations, and averaging over the initial nucleus spin, [3]

$$d^5\sigma_{\nu_\alpha A\to\nu_\beta A\gamma} = \frac{1}{2(s - m_A^2)}\frac{1}{2}\sum_{\text{spins}}|\mathcal{M}^{\mathrm{D(M)}}_{\nu_\alpha A\to\nu_\beta A\gamma}|^2 d\Phi_3\,. \tag{7.41}$$

Here $d\Phi_3$ is the final state three-body phase space which is given by

$$\begin{aligned} d\Phi_3 &= \frac{1}{(2\pi)^5}\frac{d^3\mathbf{p}_1}{2E_{\mathbf{p}_1}}\frac{d^3\mathbf{p}_2}{2E_{\mathbf{p}_2}}\frac{d^3\mathbf{p}_3}{2E_{\mathbf{p}_3}}\delta^4(k_1 + k_2 - p_1 - p_2 - p_3) \\ &= \frac{d\phi}{2\pi}\frac{ds_1 dt_1 ds_3 dt_2}{256\pi^4(s - m_A^2)\sqrt{-\Delta_4}}\,. \end{aligned} \tag{7.42}$$

The physical phase space is defined as $\Delta_4 < 0$, where the 4×4 symmetric Gram determinant

Δ_4 is given by

$$\Delta_4 = -\frac{1}{16}\begin{vmatrix} 0 & 0 & s_3 & t_1 & m_A^2 & 1 \\ 0 & 0 & 0 & t_2 & s_1 & 1 \\ s_3 & 0 & 0 & 0 & s & 1 \\ t_1 & t_2 & 0 & 0 & m_A^2 & 1 \\ m_A^2 & s_1 & s & m_A^2 & 0 & 1 \\ 1 & 1 & 1 & 1 & 1 & 0 \end{vmatrix} . \tag{7.43}$$

The absolute squared and spin-summed matrix element can be written as

$$\frac{1}{2}\sum_{\text{spins, pols}} |\mathcal{M}^{\mathrm{D(M)}}_{\nu_\alpha A\to\nu_\beta A\gamma}|^2 = (\mu^\alpha_{\nu N}\mu^\beta_{\nu N})^2\,\frac{e^2Z^2\mathcal{F}^2(q^2)}{q^4}\,\frac{L^{\gamma,\mathrm{D(M)}}_{\mu\nu}H^{\mu\nu}}{(p_N^2-m_N^2)^2+m_N^2\Gamma_N^2}\,, \tag{7.44}$$

where the hadronic tensor $H^{\mu\nu}$ is the same as in in Eq. (7.23), and the leptonic tensors are given by

$$L^{\gamma,\mathrm{D}}_{\mu\nu} = \mathrm{Tr}[\not{p}_2\sigma_{\lambda\xi}\not{p}_N\sigma_{\mu\rho}\not{k}_2\sigma_{\nu\omega}P_R\not{p}_N\sigma_{\eta\zeta}]\,g^{\lambda\eta}p_3^\xi p_3^\zeta q^\rho q^\omega\,, \tag{7.45}$$

$$L^{\gamma,\mathrm{M}}_{\mu\nu} = \mathrm{Tr}[\not{p}_2\sigma_{\lambda\xi}(\not{p}_N+m_N)\sigma_{\mu\rho}\not{k}_2\sigma_{\nu\omega}P_R(\not{p}_N+m_N)\sigma_{\eta\zeta}]\,g^{\lambda\eta}p_3^\xi p_3^\zeta q^\rho q^\omega\,, \tag{7.46}$$

for Dirac and Majorana N, respectively. Integrating over the azimuthal angle ϕ we then obtain the Lorentz-invariant differential cross section

$$\frac{d^4\sigma^{\mathrm{D(M)}}_{\nu_\alpha A\to\nu_\beta A\gamma}}{ds_1dt_1ds_3dt_2} = (\mu^\alpha_{\nu N}\mu^\beta_{\nu N})^2\,\frac{\alpha Z^2\mathcal{F}^2(t_1)}{128\pi^3}\,\frac{L^{\gamma,\mathrm{D(M)}}_{\mu\nu}H^{\mu\nu}}{t_1^2(s-m_A^2)^2\left[(s_1-m_N^2)^2+m_N^2\Gamma_N^2\right]\sqrt{-\Delta_4}}\,. \tag{7.47}$$

7.3.3. Connection to experimental observables

Using the result in Eq. (7.47) we now connect the radiative CEνNS process to experimental observables in order to draw conclusions on the model parameters based on experimental results. In particular we are interested in the nuclear recoil energy E_R as well as the energy E_γ and outgoing angle θ_γ of the photon. In order to fully express Eq. (7.47) in terms of these variables we also need to use the nuclear recoil angle θ_R. The relation between the observables and the different Mandelstam variables can be found in Eq. (7.33). From these relations we see that s_3 and t_2 are both independent of E_R and θ_R. If we want to first express Eq. (7.47) in terms of the nuclear energy and angle we can then integrate over s_3 and t_2 such that

$$\frac{d^2\sigma^{\mathrm{D(M)}}_{\nu_\alpha A\to\nu_\beta A\gamma}}{ds_1dt_1} = \int_{t_2^-}^{t_2^+}dt_2\int_{s_3^-}^{s_3^+}ds_3\,\frac{d^4\sigma^{\mathrm{D(M)}}_{\nu_\alpha A\to\nu_\beta A\gamma}}{ds_1dt_1ds_3dt_2}\,. \tag{7.48}$$

Here the integration limits are found by solving $\Delta_4(s_3,t_2)=0$. Performing the integration for Dirac N we have

$$\frac{d^2\sigma^{\mathrm{D}}_{\nu_\alpha A\to\nu_\beta A\gamma}}{ds_1dt_1} = (\mu^\alpha_{\nu N}\mu^\beta_{\nu N})^2\,\frac{\alpha Z^2\mathcal{F}^2(t_1)}{16\pi^2}\,\frac{s_1^2F(s,s_1,t_1,m_A^2)}{t_1^2(s-m_A^2)^2\left[(s_1-m_N^2)^2+m_N^2\Gamma_N^2\right]}\,, \tag{7.49}$$

and for Majorana N we have

$$\frac{d^2\sigma^{\mathrm{M}}_{\nu_\alpha A\to\nu_\beta A\gamma}}{ds_1 dt_1} = (\mu^{\alpha}_{\nu N}\mu^{\beta}_{\nu N})^2\,\frac{\alpha Z^2\mathcal{F}^2(t_1)}{16\pi^2}\,\frac{s_1(s_1+m_N^2)F(s,s_1,t_1,m_A^2)}{t_1^2(s-m_A^2)^2\left[(s_1-m_N^2)^2+m_N^2\Gamma_N^2\right]}\,. \tag{7.50}$$

We see that these cross sections are quite similar. They vary by a factor $s_1/(s_1+m_N^2)$, as can be seen from the relation

$$\frac{d^2\sigma^{\mathrm{M}}_{\nu_\alpha A\to\nu_\beta A\gamma}}{ds_1 dt_1}\Bigg/\frac{d^2\sigma^{\mathrm{D}}_{\nu_\alpha A\to\nu_\beta A\gamma}}{ds_1 dt_1} = 1+\frac{m_N^2}{s_1}\,. \tag{7.51}$$

The second term in Eq. (7.51) corresponds to the additional channel that is present for Majorana N. To change variables into E_R and θ_R we now multiply the double differential cross sections with the Jacobian

$$\mathcal{J}(E_R,\theta_R) = \left|\frac{\partial(s_1,t_1)}{\partial(E_R,\theta_R)}\right| = -4E_\nu m_A\sqrt{E_R(2m_A+E_R)}\sin\theta_R\,, \tag{7.52}$$

such that

$$\frac{d^2\sigma^{\mathrm{D(M)}}_{\nu_\alpha A\to\nu_\beta A\gamma}}{dE_R d\theta_R} = \mathcal{J}(E_R,\theta_R)\,\frac{d^2\sigma^{\mathrm{D(M)}}_{\nu_\alpha A\to\nu_\beta A\gamma}}{ds_1 dt_1}\,. \tag{7.53}$$

Single differential cross sections can then be obtained by integrating over either the nuclear angle or the recoil energy, such that

$$\frac{d\sigma^{\mathrm{D(M)}}_{\nu_\alpha A\to\nu_\beta A\gamma}}{dE_R} = \int_0^{\theta_R^+} d\theta_R\,\frac{d^2\sigma^{\mathrm{D(M)}}_{\nu_\alpha A\to\nu_\beta A\gamma}}{dE_R d\theta_R}\,, \tag{7.54}$$

$$\frac{d\sigma^{\mathrm{D(M)}}_{\nu_\alpha A\to\nu_\beta A\gamma}}{d\theta_R} = \int_0^{E_R^+} dE_R\,\frac{d^2\sigma^{\mathrm{D(M)}}_{\nu_\alpha A\to\nu_\beta A\gamma}}{dE_R d\theta_R}\,, \tag{7.55}$$

where the integration limits are given by

$$\cos\theta_R^+ = \frac{E_R(m_A+E_\nu)}{E_\nu\sqrt{E_R(2m_A+E_R)}}\,, \tag{7.56}$$

$$E_R^+ = \frac{2m_A E_\nu^2\cos^2\theta_R}{m_A(m_A+2E_\nu)+E_\nu^2(1-\cos^2\theta_R)}\,. \tag{7.57}$$

In order to express the cross section in terms of the photon angle θ_γ and energy E_γ, we can integrate the differential cross section over s_1 and t_1 instead of s_3 and t_2. We then have

$$\frac{d^2\sigma^{\mathrm{D(M)}}_{\nu_\alpha A\to\nu_\beta A\gamma}}{ds_3 dt_2} = \int_{t_1^-}^{t_1^+} dt_1\int_{s_1^-}^{s_1^+} ds_1\,\frac{d^4\sigma^{\mathrm{D(M)}}_{\nu_\alpha A\to\nu_\beta A\gamma}}{ds_1 dt_1 ds_3 dt_2}\,, \tag{7.58}$$

where the integration limits can again be found by solving $\Delta_4(s_1,t_1)=0$. Both of the integrals in Eq. (7.58) are non-trivial since there is a s_1-dependence in the denominator of the squared

matrix element, and t_1 appears in the form factor $\mathcal{F}(t_1)$. After integrating we can change variables in the remaining double differential cross section into the photon angle and energy by using the Jacobian

$$\mathcal{J}(E_\gamma, \theta_\gamma) = \left| \frac{\partial(s_3, t_2)}{\partial(E_\gamma, \theta_\gamma)} \right| = 4 m_A E_\nu E_\gamma \sin\theta_\gamma \,. \tag{7.59}$$

The single differential cross sections can subsequently be obtained by integrating over the remaining variable such that

$$\frac{d\sigma^{\mathrm{D(M)}}_{\nu_\alpha A \to \nu_\beta A \gamma}}{dE_\gamma} = \int_0^\pi d\theta_\gamma \, \frac{d^2\sigma^{\mathrm{D(M)}}_{\nu_\alpha A \to \nu_\beta A \gamma}}{dE_\gamma d\theta_\gamma} \,, \tag{7.60}$$

$$\frac{d\sigma^{\mathrm{D(M)}}_{\nu_\alpha A \to \nu_\beta A \gamma}}{d\theta_\gamma} = \int_0^{E_\gamma^+} dE_\gamma \, \frac{d^2\sigma^{\mathrm{D(M)}}_{\nu_\alpha A \to \nu_\beta A \gamma}}{dE_\gamma d\theta_\gamma} \,, \tag{7.61}$$

where the integration limit on the photon energy is given by

$$E_\gamma^+ = \frac{m_A E_\nu}{m_A + E_\nu(1 - \cos\theta_\gamma)} \,. \tag{7.62}$$

To solve the integral in Eq. (7.58) we use the Narrow Width Approximation (NWA). This is implemented by making the replacement

$$\frac{1}{(s_1 - m_N^2)^2 + m_N^2 \Gamma_N^2} \to \frac{\pi}{m_N \Gamma_N} \delta(s_1 - m_N^2) \tag{7.63}$$

in the propagator. Now using the relation $s_1 = m_N^2$, which is given by the fact that N is on-shell in the NWA, we can relate the nuclear recoil energy and angle via

$$\cos\theta_R = \frac{m_N^2 + 2E_R(m_A + E_\nu)}{2E_\nu \sqrt{E_R(2m_A + E_R)}} \,. \tag{7.64}$$

Solving for E_R we instead have

$$E_R^\pm = \frac{2m_A E_\nu^2 c_R^2 - m_N^2(m_A + E_\nu) \pm E_\nu c_R \sqrt{4m_A^2 E_\nu^2 c_R^2 - 4m_A m_N^2 (m_A + E_\nu) + m_N^4}}{2m_A(m_A + 2E_\nu) + 2E_\nu^2(1 - c_R^2)} \,, \tag{7.65}$$

where $c_R = \cos\theta_R$. In the NWA formalism, the distance ℓ_0 that N travels in the lab frame before decaying is given by

$$l_0 = \frac{1}{\Gamma_N} \sqrt{\left(\frac{E_N}{m_N}\right)^2 - 1} = \frac{1}{\Gamma_N} \sqrt{\left(\frac{E_\nu - E_R}{m_N}\right)^2 - 1} \approx \frac{E_\nu}{m_N} \frac{1}{\Gamma_N} \,. \tag{7.66}$$

Here Eq. (7.66) is found by applying a boost factor $\beta\gamma = \sqrt{\gamma^2 - 1}$ to the time $\tau_N = \frac{1}{\Gamma_N}$ in the rest frame of N, where the assumption is made that N travels at (nearly) the speed of light.

We also assume that the nuclear recoil energy E_R is much smaller than the incoming neutrino energy E_ν. Using Eq. (7.66) we can then find the minimum decay width Γ_N that corresponds to a signal at an experiment of fixed length L_{det} between the CEνNS target and the photon detector.

The radiative upscattering cross section in the NWA is now given by [3]

$$\left.\frac{d\sigma^{\text{D(M)}}_{\nu_\alpha A\to\nu_\beta A\gamma}}{dE_R}\right|_{\text{NW}} = \frac{d\sigma_{\nu_\alpha A\to NA}}{dE_R}\frac{\Gamma^{\text{D(M)}}_{N\to\nu_\beta\gamma}}{\Gamma_N}\,. \tag{7.67}$$

From this cross section we can obtain the differential event rate for $\nu_\alpha A\to X$ where $X\in\{NA,\nu_\beta A\gamma\}$ at a given experiment as

$$\frac{dR^{\text{D(M)}}_{\nu_\alpha A\to X}}{dE_R} = \frac{1}{A\cdot m_p}\int_{E_\nu^{\min}(E_R)}^{E_\nu^{\max}} dE_\nu\,\frac{d\phi_{\nu_\alpha}}{dE_\nu}\,\frac{d\sigma^{\text{D(M)}}_{\nu_\alpha A\to X}}{dE_R}\,, \tag{7.68}$$

where

$$E_\nu^{\min}(E_R) = \left(\frac{E_R}{2}+\frac{m_N^2}{4m_A}\right)\left(1+\sqrt{1+\frac{2m_A}{E_R}}\right), \tag{7.69}$$

is the minimum energy of an incoming neutrino that can induce a recoil with energy E_R in the nucleus, and $\frac{d\phi_{\nu_\alpha}}{dE_\nu}$ is the incoming neutrino flux.

For radiative CEνNS cross sections that are differential in the photon energy E_γ and angle θ_γ, there is no analogue to the factorisation strategy used in Eq. (7.67) that works similarly well. Instead, we can write the double differential cross section as

$$\left.\frac{d^2\sigma^{\text{D(M)}}_{\nu_\alpha A\to\nu_\beta A\gamma}}{dE_\gamma d\theta_\gamma}\right|_{\text{NWA}} = |\mu^\alpha_{\nu N}\mu^\beta_{\nu N}|^2\frac{\alpha Z^2 E_\gamma\sin\theta_\gamma}{128\pi^2 m_A E_\nu m_N\Gamma_N}\int_{t_1^-}^{t_1^+}dt_1\,\left.\frac{L^{\gamma,\text{D(M)}}_{\mu\nu}H^{\mu\nu}\mathcal{F}^2(t_1)}{t_1^2\sqrt{-\Delta_4}}\right|_{s_1=m_N^2}, \tag{7.70}$$

where $t_1=q^2=-2m_AE_R$ is the momentum exchanged via the photon. Due to the presence of the nuclear form factor $\mathcal{F}(t_1)$, Eq. (7.70) cannot be solved analytically.

The differential event rate with respect to $X_\gamma\in\{E_\gamma,\theta_\gamma\}$ can be written as

$$\frac{dR^{\text{D(M)}}_{\nu_\alpha A\to\nu_\beta A\gamma}}{dX_\gamma} = \frac{1}{A\cdot m_p}\int_{E_\nu^{\min}(X_\gamma)}^{E_\nu^{\max}} dE_\nu\,\frac{d\phi_{\nu_\alpha}}{dE_\nu}\,\frac{d\sigma^{\text{D(M)}}_{\nu_\alpha A\to\nu_\beta A\gamma}}{dX_\gamma}\,, \tag{7.71}$$

where A is the number of nucleons, and where the value of the minimum incoming neutrino energy $E_\nu^{\min}(X_\gamma)$ depends on whether the distribution should be given in terms of E_γ or θ_γ. For E_γ we have

$$E_\nu^{\min}(E_\gamma) = E_\gamma+\frac{m_Am_N^2}{4m_AE_\gamma-2m_N^2}\,, \tag{7.72}$$

while for θ_γ we have

$$E_\nu^{\min}(\theta_\gamma) = \frac{m_N(2m_A-m_N)}{2(m_A-m_N)}\,. \tag{7.73}$$

These relations come from conservation of energy and momentum. Eq. (7.72) describes the minimum neutrino energy that can lead to the production of a photon with energy E_γ, and Eq. (7.73) describes the required neutrino energy that leads to an on-shell N. The latter relation follows from using $E_\gamma = m_N/2$ in the first, as this is the energy that the photon acquires from the decay of an on-shell N in its rest frame, assuming we have used the massless active neutrino approximation.

Apart from considerations of the event rate distribution, a difference between Dirac and Majorana N can potentially be seen in the polarisation of the final state photon [3]. For Dirac N ($\bar{N}$), the decay $N \to \nu_\beta \gamma$ ($\bar{N} \to \bar{\nu}_\beta \gamma$) leads to a left-polarised γ_- (right-polarised γ_+) photon in the final state. The other polarisation does not appear since such a process would violate conservation of angular momentum. A Majorana N can decay equally into a neutrino plus γ_+ or γ_-, where the distribution of events with $\gamma_\pm$ in the final state in terms of the photon angle θ_γ has the proportionality relation[3] $dR_{N\to\nu_\beta\gamma_\pm}/d\theta_\gamma \propto (1 \mp \cos\theta_\gamma)$. The total distribution for Majorana N is therefore isotropic in the rest frame of N while the same does not hold for Dirac N ($\bar{N}$), where small (large) angles θ_γ are preferred.

7.4. Experimental sensitivity to radiative CEνNS

In this section, we evaluate the potential experimental sensitivity to radiative CEνNS processes. Special focus is put on the future NUCLEUS experiment [548, 549] located 100 m from the Chooz nuclear reactor at a place called the Very Near Site (VNS), where it will receive an antineutrino flux $\phi_{\bar{\nu}_e} \sim 10^{12}\ \bar{\nu}_e\ \mathrm{cm}^{-2}\ \mathrm{s}^{-1}$. This experiment is designed to detect nuclear recoil energies as low as $\mathcal{O}(10)$ eV, making it an ideal environment to search for radiative CEνNS processes, where a large part of the incoming neutrino energy goes to the final state photon and neutrino rather than the nuclear recoil. In Phase I of the experiment a 10 g $Al_2O_3/CaWO_4$ target of diameter $L_{\mathrm{det}} \sim 5$ cm will be used. In the Phase II upgrade this will potentially be exchanged for a 1 kg ^{73}Ge target of diameter $L_{\mathrm{det}} \sim 25$ cm. A cryogenic outer veto that is used for background rejection in the NUCLEUS experiment could be sensitive to outgoing photons in radiative CEνNS events. These photons could potentially be detected in the energy range 1 keV to 10 MeV, where the high-energy end of this range could feature a resolution of $50 - 100$ keV [564]. It may be possible that the coincident signal of a nuclear recoil and a high-energy outgoing photon could lead to excellent background rejection in radiative CEνNS experiments. Therefore, when we consider radiative CEνNS events at NUCLEUS in this section, secondary background processes are neglected.

In Fig. 7.4 (left) the rate of both Primakoff upscattering events with $m_N = 1$ MeV and $\mu^e_{\nu N} = 10^{-10}\ \mu_B$, as well as ordinary CEνNS events, are shown for the NUCLEUS experiment, where the rates are calculated using the formalism from Sec. 7.3.3. Three different nuclear targets types are used: ^{73}Ge, Al_2O_3, and $CaWO_4$. The predicted nuclear recoil background is indicated by a horizontal black dotted line, and the region in which the nuclear recoil energy $E_R \gtrsim \mathcal{O}(10)$ eV is large enough to be detected by the NUCLEUS experiment is indicated in grey. In Fig. (7.4) (right), the event rate for the radiative CEνNS process is shown

[3]Note that this relation also holds for Dirac N ($\bar{N}$).

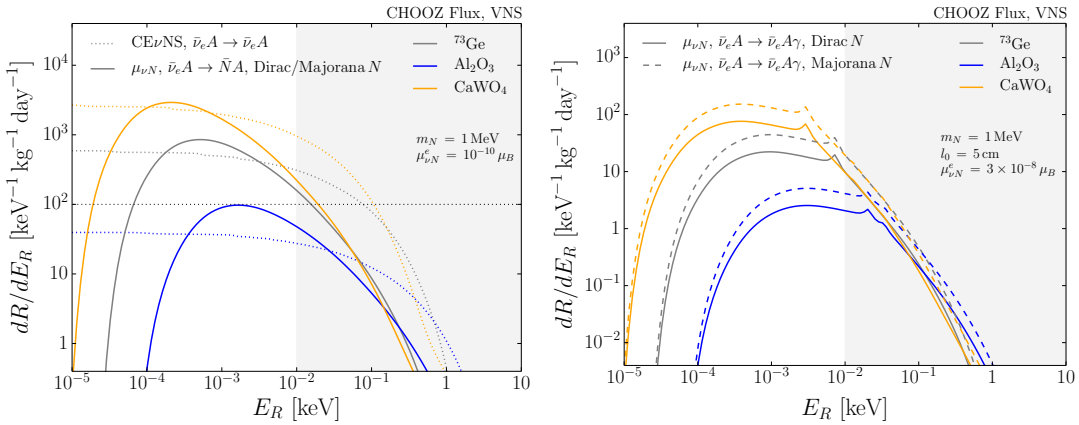

Figure 7.4.: Left: Differential event rates for Primakoff upscattering using three different target materials ^{73}Ge (grey), Al_2O_3 (blue) and $CaWO_4$ (orange) at the NUCLEUS experiment, with respect to the nuclear recoil energy E_R, where the values $m_N = 1$ MeV and $\mu^e_{\nu N} = 10^{-10}\ \mu_B$ have been used. The SM CEνNS rates are shown in dotted lines. **Right:** Differential event rates in terms of E_R for the radiative CEνNS process, using $m_N = 1$ MeV and $\mu^e_{\nu N} = 3 \times 10^{-8}\ \mu_B$, for both Dirac (solid lines) and Majorana (dashed) sterile neutrinos. This figure is taken from Ref. [3].

for the NUCLEUS experiment using the same three target materials for $m_N = 1$ MeV and $\mu^e_{\nu N} = 3 \times 10^{-8}\ \mu_B$, where the outgoing neutrino is assumed to be electron flavoured, for both Dirac (solid) and Majorana (dashed) N.

In Fig. 7.5 the double differential cross section for the radiative CEνNS interaction using a ^{73}Ge target, assuming $\mathcal{F}(t_1) = 1$ for simplicity, is shown in terms of E_γ and θ_γ for Dirac (left) and Majorana (right) N using benchmark values $E_\nu = 3$ MeV, $m_N = 1$ MeV, $\mu^\alpha_{\nu N} = 3 \times 10^{-8}\ \mu_B$, and $\Gamma_N = 10^{-11}$ MeV. The difference in the differential cross section between Dirac and Majorana N is clearly visible in the respective bottom-right corners of the two figures, where it can be seen that a significant rate of high-E_γ low-θ_γ events should be expected in a radiative CEνNS experiment if N is Majorana, but very few such events would be there for Dirac N.

In Fig. 7.6 the differential event rates for the radiative CEνNS process, obtained from Eq. (7.71), are shown for Dirac (solid lines) and Majorana (dashed lines) N, for the three different target materials ^{73}Ge, Al_2O_3, and $CaWO_4$ at the NUCLEUS experiment. A difference between Dirac and Majorana N can be seen in the distribution of events in terms of both E_γ and θ_γ. In Fig. 7.6 (left), we see that the distribution of events in terms of E_γ is symmetric around the peak at $E_\gamma = m_N/2$ for Majorana N, while for Dirac N smaller values of E_γ are preferred. Since we consider active neutrinos to be massless as well as using the NWA, the relation $E_\gamma = m_N/2$ holds in the rest frame of N. The distribution in Fig. 7.6 (left) appears when boosting to the lab frame. In Fig. 7.6 (right) the radiative CEνNS event distribution is shown in terms of the photon angle θ_γ. Here it can be seen that smaller angles are preferred for Majorana N relative to Dirac N.

Using the neutrino flux from the Chooz reactor, radiative CEνNS events have the largest

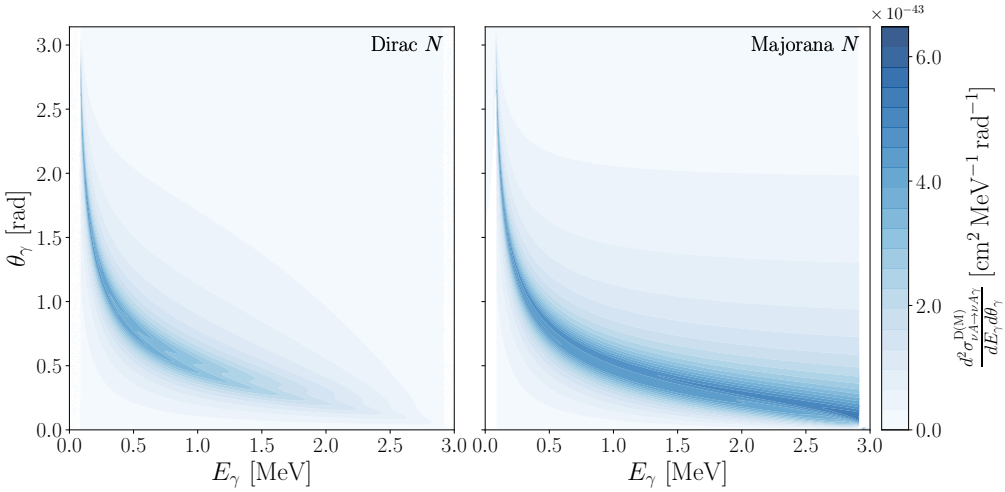

Figure 7.5.: Differential cross sections for the radiative process $\nu_\alpha A \to \nu_\alpha A\gamma$ in terms of the outgoing photon energy E_γ and photon angle θ_γ, where the incoming neutrino has an energy of $E_\nu = 3$ MeV and ^{73}Ge is used as a target material, assuming a sterile neutrino mass $m_N = 1$ MeV. The values $\mu^\alpha_{\nu N} = 3 \times 10^{-8}\ \mu_B$ and $\Gamma_N = 10^{-11}$ MeV are used, where these variables change the magnitude but not the shape of the contours. The left and right figures correspond to Dirac and Majorana sterile neutrinos, respectively. This figure is taken from Ref. [3].

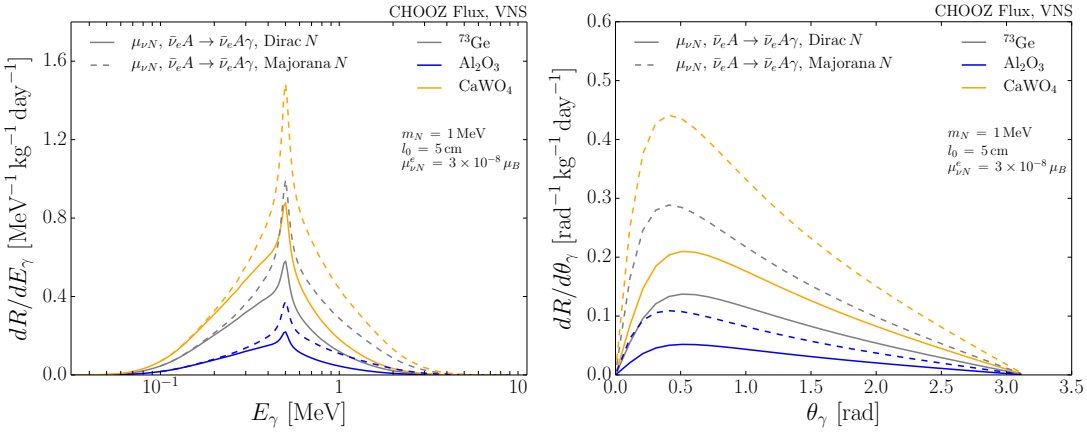

Figure 7.6.: Differential event rates in terms of the photon energy E_γ (left) and angle θ_γ (right) at the NUCLEUS experiment, for target materials ^{73}Ge (grey), Al_2O_3 (blue) and $CaWO_4$ (orange) and for Dirac (solid) and Majorana (dashed) sterile neutrinos, assuming a sterile neutrino mass $m_N = 1$ MeV and transition magnetic moment $\mu^e_{\nu N} = 3 \times 10^{-8}\ \mu_B$. This figure is taken from Ref. [3].

cross section for sterile neutrino masses in the range $m_N \sim 1 - 5$ MeV. For a given value of m_N, the radiative CEνNS cross section increases for higher incoming neutrino energies.

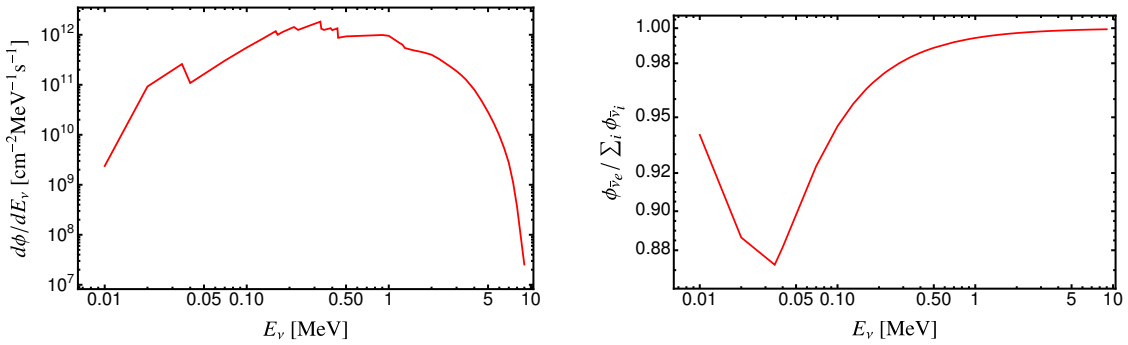

Figure 7.7.: Left: Flux of antineutrinos from the Chooz nuclear reactor at the VNS. **Right:** Fraction of neutrinos that arrive at the VNS from Chooz that are in the electron flavour, as a function of the neutrino energy, where $i \in \{e, \mu, \tau\}$.

In Fig. 7.7 (left) we see the flux of neutrinos at the VNS as a function of energy. Since the flux decreases for increasing E_ν, the total event rate will also fall off even though the cross section increases. In Fig. 7.7 (right) the fraction of the flux at the VNS that consists of electron flavoured antineutrinos is shown. This fraction deviates from unity due to neutrino oscillations, where the oscillation rate is calculated using the formalism in Sec. 2.3.1. Since this fraction is very high for most values of E_ν, we use the approximation that the entire flux consists of antineutrinos in the electron flavour.

In order to determine the experimental reach of the NUCLEUS experiment in probing the neutrino transition magnetic dipole moment parameter space, we need to consider both Primakoff upscattering as well as radiative CEνNS processes. Assuming that N_{obs} events are seen during the runtime T, the chi-squared can be constructed as

$$\chi^2 = (N_{\text{obs}} - N_{\text{exp}})^2 / N_{\text{exp}} \,. \tag{7.74}$$

Here $N_{\text{exp}} = N_{\text{bkg}} + N_{\nu A} + N_{NA}$ is the total number of expected events, where N_{bkg} is the expected number of background events, $N_{\nu A}$ is the expected number of SM CEνNS events, and N_{NA} the expected number of Primakoff upscattering events for a given set of parameters. The rate of background events is estimated by the NUCLEUS collaboration to be $dR_{\text{bkg}}/dE_R = 100$ day^{-1} keV^{-1} kg^{-1} [549], where the unit kg^{-1} refers to the mass of the detector. Assuming that there is no excess of events for a runtime T, i.e. that the observed number of events $N_{\text{exp}} = N_{\text{bkg}} + N_{\nu A}$ has no departure from that expected in the SM, we have $\chi^2 = N_{NA}^2/N_{\text{exp}}$. Neglecting systematic errors for simplicity, we then obtain 90% CL bounds on μ^e_{nuN} for a given m_N by solving $\chi^2 < 2.71$.

For radiative CEνNS the coincident photon plus nuclear recoil signal could lead to efficient background reduction. As a first approximation we therefore assume that background processes are negligible and take the expected number of events to be equal to the theoretical value $N^\gamma_{\text{exp}} = N_{\nu A\gamma}$, where $N_{\nu A\gamma}$ can be found using the formalism in Sec. 7.3.3. If no radiative CEνNS events are observed at NUCLEUS, the 90% CL bounds on $\mu^e_{\nu N}$ may be found by solving $\chi^2 < 2.30$.

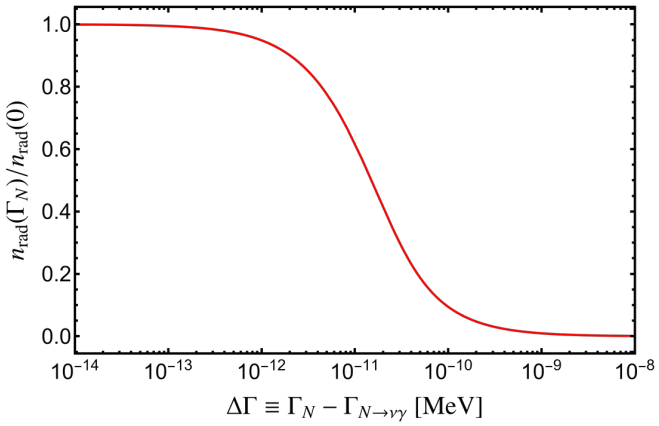

Figure 7.8.: Number of radiative decays that occur inside the detector with respect to $\Delta\Gamma_N \equiv \Gamma_N - \Gamma_{N\to\nu\gamma}$, normalised to the total number of decays, using $m_N = 1$ MeV, $l_0 = 5$ cm, $E_\nu = 3$ MeV, $\mu_{\nu N} = 10^{-7}\ \mu_B$.

In order for the experimental set up to be able to capture the final state photon, the radiative decay of N must occur inside the detector, otherwise the signal mimics that of a Primakoff upscattering. To capture this effect we multiply the radiative CEνNS cross section with the probability factor

$$P_N^{\rm det} = 1 - \exp(-L_{\rm det}\Gamma_N/\beta\gamma)\,, \tag{7.75}$$

which describes the probability that N decays inside the detector. Fixing the decay width Γ_N to a specific value, e.g $\Gamma_N \sim 10^{-11}$ MeV, does not lead to any limitations on the applicability of the calculations to different values of $\mu^e_{\nu N}$ or m_N. To see the effect of a changing value of Γ_N we consider the number of radiative decay events occurring inside the detector $n_{\rm rad}$, normalised to the total number of decays, which is given by

$$\frac{n_{\rm rad}\left(\Delta\Gamma_N\right)}{n_{\rm rad}\left(\Delta\Gamma_N = 0\right)} = \frac{\Gamma_{N\to\nu\gamma}}{\Gamma_N}\,\frac{1-\exp\left(-\frac{L_{\rm det}\Gamma_N}{\beta\gamma}\right)}{1-\exp\left(-\frac{L_{\rm det}\Gamma_{N\to\nu\gamma}}{\beta\gamma}\right)}\,. \tag{7.76}$$

Here $\Delta\Gamma_N \equiv \Gamma_N - \Gamma_{N\to\nu\gamma}$ is the difference in decay width between the sum of all decay modes and the radiative one. In Fig. 7.8 the fraction of radiative decay events that occur within the detector is shown as a function of $\Delta\Gamma_N$. For smaller differences $\Delta\Gamma_N$, the probability $P_N^{\rm det}$ that a decay should occur inside the detector is decreased, even though the branching ratio for $N \to \nu\gamma$ is greater. For larger differences $\Delta\Gamma_N$, the probability $P_N^{\rm det}$ increases while the branching ratio of $N \to \nu\gamma$ decreases, ending up in a reduction in the number of radiative CEνNS events. This demonstrates that by choosing e.g. $\Gamma_N \sim 10^{-11}$ MeV, there is no commitment to one specific scenario. As shown in Fig. 7.8, a decay width difference $\Delta\Gamma_N \approx \Gamma_N \sim 10^{-11}$ MeV corresponds to the case where $\sim 60\%$ of the N decays that occur inside the detector proceed via the radiative mode. A smaller difference $\Delta\Gamma_N$ would lead to

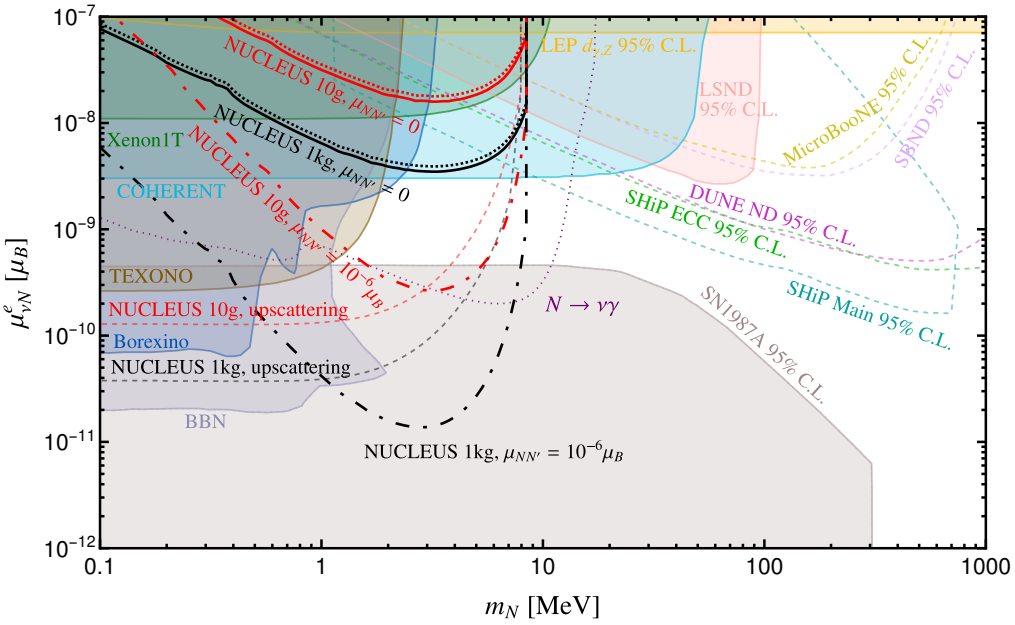

Figure 7.9.: Constraints and future sensitivities in the plane of the electron-flavoured transition dipole coupling $\mu^e_{\nu N}$ and sterile neutrino mass m_N, based on terrestrial experiments [3,550–552,555,565–570] and astrophysical observations [551,555,565]. Filled regions correspond to existing constraints, and unfilled regions to future projections. Solid red and black lines show the near- and far-future projected sensitivities of the NUCLEUS experiment for Majorana N, respectively, using the radiative CEνNS channel, where the dotted lines include additional invisible decay channels for N with a width $\Gamma_{\text{inv}} = \beta\gamma/L_{\text{det}}$ (c.f. Appendix C). Dot-dashed red and black lines show these projected sensitivities assuming an additional decay channel into a light sterile neutrino, $N \to N'\gamma$, via a coupling $\mu_{N'N} = 10^{-6}\ \mu_B$. Dashed red and black lines correspond to constraints from Primakoff upscattering processes at the NUCLEUS experiment. All future projections associated with the NUCLEUS experiment are shown assuming a run time of 2 years, and all projections are given at 90% CL unless otherwise is shown. This figure is taken from Ref. [3].

an increased number of signal events, and therefore also to a more stringent constraint on $\mu_{\nu N}$.

In Fig. 7.9 the current and future constraints on the electron flavoured neutrino transition magnetic dipole moment coupling $\mu^e_{\nu N}$ is shown as a function of the sterile neutrino mass m_N. Here many different terrestrial and astrophysical observations are considered. The limits from Primakoff upscattering processes at NUCLEUS are shown as blue and grey dashed lines for Phase I and II, respectively. The solid blue and grey lines correspond to the potential future NUCLEUS limits on the radiative CEνNS process for Phase I and II, respectively. Finally, the dot-dashed blue and grey lines correspond to the radiative upscattering process at NUCLEUS where an additional radiative decay channel $N \to N'\gamma$ is assumed, with the coupling $\mu_{N'N} = 10^{-6}\ \mu_B$ (c.f. Sec. 7.1). A run time of two years is assumed for all limits derived from the NUCLEUS experiment.

In the radiative CEνNS mode, an experimental signal would consist of a coincident nuclear recoil and outgoing photon. We have described a novel approach to search for such events, which led to the publication in Ref. [3], where the final state photons are searched for in a detector that is separated from the CEνNS target. Searching for Primakoff upscattering events, the NUCLEUS experiment would improve on existing limits and probe an area of parameter space for sterile neutrino masses $m_N \lesssim 10$ MeV that is either unconstrained or only constrained by astrophysical observables. If Primakoff upscattering is observed at Phase I of NUCLEUS, it would motivate the search for radiative CEνNS events in Phase II. Even without such an observation, the experimental reach in the search for radiative CEνNS events could be extended further if additional (light) sterile states, e.g. N', are considered, such that the radiative CEνNS cross section is proportional to $|\mu^e_{\nu N} \sum_X \mu_{XN}|^2$, where $X \in \{\nu, N', \dots\}$.

An advantage of using a reactor source is that the flux consists of only antineutrinos, such that the total lepton number of the initial state particles is known. LNV could then be deduced if the final state has a different total lepton number. If radiative CEνNS is observed with a significant number of events, the Dirac/Majorana nature of sterile neutrinos could be deduced based on the final state photon distribution, potentially providing an answer to whether or not $B - L$ is a conserved charge in nature. This would have implications for the origin of neutrino masses as well as the generation of the baryon asymmetry of the Universe.

Conclusion to Chapter 7

The nature of neutrino masses remains one of the big open questions in particle physics. Since neutrinos are massive, there must be some NP that generates the mass, and this NP could also lead to other neutrino properties such as transition magnetic dipole moments. In this chapter we have seen how CEνNS experiments can be used to search for transition magnetic moments via upscattering from a light active neutrino into a heavy sterile neutrino. We have also seen that, if the heavy neutrinos decay on detector lengthscales, an observation of the final state photon distribution potentially also lead to a distinction between Dirac and Majorana neutrinos. These results were published in Ref. [3].

In two examples, that of radiative CEνNS in this chapter, and rare kaon decays in Ch. 6, we have seen how the kinematics of final state particles that participate in interactions involving

neutrinos can vary depending on whether or not the process was LNV. Therefore, in case an excess is seen in either CEνNS or rare kaon decays, a dedicated experimental search program to determine the distribution of final state particles would be beneficial in the search for LNV. If the distribution is determined to a reasonably high accuracy, it is possible that LNV could be discovered.

In Chs. 4 to 7 we have discussed different aspects of $\Delta L = 2$ interactions, including neutrino mass generation and leptogenesis. Since $B + L$ is violated in the SM via sphaleron transitions, LNV inevitably leads to baryon number violation (BNV) in the early Universe, and vice versa. In Ch. 8, we discuss $\Delta B = 2$ interactions, and connect them to baryogenesis both in an EFT description and in a simplified model. The results of Ch. 8 were published in Ref. [2].

8. Beyond LNV: the case of $\Delta B = 2$

In Chs. 4 to 7 we discussed different theoretical and phenomenological aspects of $\Delta L = 2$ processes, most prominently Majorana neutrino masses and the generation of a baryon asymmetry via sphaleron transitions. However, both of these phenomena can also be realised via baryon number violation (BNV). For successful baryogenesis it is enough to violate conservation of baryon number B, an asymmetry can be generated without any $\Delta L = 2$ interactions. Furthermore, in the presence of both $\Delta B = -\Delta L = 1$ and $\Delta B = 2$ processes, a $\Delta L = 2$ process associated with a neutrino Majorana mass can be generated indirectly via the $\Delta B = -\Delta L = 3$ sphaleron [571], as can be shown in the naïve arithmetic

$$\Big[\Delta B = -\Delta L = 1\Big] + \Big[\Delta B = 2,\, \Delta L = 0\Big] - \Big[\Delta B = -\Delta L = 3\Big] = \Big[\Delta B = 0,\, \Delta L = 2\Big]\,. \tag{8.1}$$

However, in making this argument we have so far ignored the fact that sphalerons necessarily involve all different fermion flavours, while the flavour content of the $\Delta B = -\Delta L = 1$ and $\Delta B = 2$ processes are undetermined. Furthermore, there may be any number of additional BSM effects that need to be taken into account between the neutrino mass scale and the scale at which the different $\Delta B = 2$ and $\Delta B = -\Delta L = 1$ processes in Eq. (8.1) are generated. It is nevertheless interesting to note the intricate connection between BNV and LNV processes.

Due to the presence of sphaleron transitions we know that B and L are both violated individually in the early Universe, while their difference $B - L$ is conserved. Whether a certain mechanism is $\Delta B = 2$ or $\Delta L = 2$ is therefore of little importance with respect to the generation of a baryon asymmetry in the temperature range where sphalerons are active.

Processes that violate both baryon- and lepton number, e.g. dimension-6 $\Delta B = -\Delta L = 1$ operators, can lead to proton decay modes such as $p \to e^+\pi^0$. Experimental results lead to very stringent constraints on the operator scales, in some instances as high as $\mathcal{O}(10^{16})$ GeV [572]. These limits are not transferable to dimension-9 $\Delta B = 2$ operators[1], which are less constrained as they do not directly lead to proton decay [573]. Unlike $\Delta B = -\Delta L = 1$ operators, the $\Delta B = 2$ operators violate $B - L$, similar to the $\Delta L = 2$ operators. This means that $\Delta B = 2$ operators can affect the evolution of the total baryon number if they are present in the early Universe, while the effects of $\Delta B = -\Delta L = 1$ operators would be negated by the sphalerons.

Observables that constrain $\Delta B = 2$ operators include n-$\bar{n}$ oscillations and dinucleon decay e.g. via the mode $nn \to \pi^0\pi^0$. The main focus of this section is on the former mode, but we also revisit the latter for a comparison. Recent progress in lattice-QCD calculations have led

[1] Note that the lowest dimension at which a $\Delta B = 2$ SM invariant operator can be generated is dimension-9. This is because the only SM fields that carry baryon number are the quarks, which have $B = 1/3$. To make an operator violate B by two units, at least six quarks are needed, leading to dimension-9.

to an improvement in the accuracy of QCD matrix elements related to n-$\bar{n}$ oscillations [574], which allows for a greater theoretical accuracy in connecting different BSM scenarios that realise n-$\bar{n}$ operators to experiments. On the observational side, several upcoming experiments will put increasingly stringent constraints on the n-$\bar{n}$ oscillation time. Experimental searches can be divided into two categories: bound n-$\bar{n}$ oscillation, where neutrons reside within nuclei, and free n-$\bar{n}$ oscillation, where the neutrons are unbounded. Currently, the most stringent limit comes from bound n-$\bar{n}$ oscillations, for which the Super-Kamiokande experiment [575] provides a constraint $\tau^{\rm SK}_{n\text{-}\bar{n}} \geq 4.7 \times 10^8$ s. For free oscillations the most stringent constraint comes from the ILL experiment [576] $\tau^{\rm ILL}_{n\text{-}\bar{n}} \geq 0.86 \times 10^8$ s. For both bound and free oscillations the sensitivity is expected to be increased in the next generation of experiments. The bound oscillation limit is predicted to reach a sensitivity of $\tau^{\rm DUNE}_{n\text{-}\bar{n}} \geq 7 \times 10^8$ s at the DUNE experiment [577], and for free oscillations the NNBAR experiment [578] is expected to reach a sensitivity of $\tau^{\rm NNBAR}_{n\text{-}\bar{n}} \geq 3 \times 10^9$ s.

In this chapter we explore the connection between n-$\bar{n}$ oscillation and baryogenesis, as well as compare phenomenological realisations of n-$\bar{n}$ oscillation to other low-scale observables and collider searches. The work presented here led to the publication in Ref. [2]. We start with an EFT description in Secs. 8.1 and 8.2, and follow up with a UV-completion with connections to baryogenesis in Sec. 8.3. We discuss this UV-completion in terms of grand unification in Sec. 8.4, and in Sec. 8.5 we connect it to different experimental probes. Lastly, in Sec. 8.6 we explore the parameter space and identify regions that lead to successful baryogenesis.

8.1. Neutron-antineutron oscillation in effective field theory

Since n-$\bar{n}$ oscillation violates baryon number, if it does occur it must be induced by some NP beyond the SM. Such BSM physics can be model-independently described using an EFT, where the effects of heavy NP degrees of freedom are encoded in dimension-9 operators. Running down from a high scale to the scale relevant for n-$\bar{n}$ oscillation, the Wilson coefficients can be matched onto hadronic matrix elements obtained from lattice computations.

8.1.1. Operator basis

At the QCD scale, the 9-dimensional operators relevant for n-$\bar{n}$ oscillation consist of six quark fields that are described by the broken SM Lagrangian obeying a $SU(3)_c \times U(1)_{\rm em}$ symmetry. A complete basis[2] of these operators can be constructed as [579–583]:

$$\begin{aligned}
\mathcal{O}^1_{\chi_1\chi_2\chi_3} &= (u_i^T C P_{\chi_1} u_j)(d_k^T C P_{\chi_2} d_l)(d_m^T C P_{\chi_3} d_n) T^{\rm SSS}_{\{ij\}\{kl\}\{mn\}}\,, \\
\mathcal{O}^2_{\chi_1\chi_2\chi_3} &= (u_i^T C P_{\chi_1} d_j)(u_k^T C P_{\chi_2} d_l)(d_m^T C P_{\chi_3} d_n) T^{\rm SSS}_{\{ij\}\{kl\}\{mn\}}\,, \\
\mathcal{O}^3_{\chi_1\chi_2\chi_3} &= (u_i^T C P_{\chi_1} d_j)(u_k^T C P_{\chi_2} d_l)(d_m^T C P_{\chi_3} d_n) T^{\rm AAS}_{[ij][kl]\{mn\}}\,,
\end{aligned} \tag{8.2}$$

[2]Note that all operators in Eq. (8.2) are written with scalar currents. Performing Fierz transformations on a pair of spinor contractions yields also operators with vector or tensor currents.

where $\chi = \{L, R\}$ denotes chirality, $P_{L,R} = \frac{1}{2}(1 \mp \gamma_5)$ are projection operators, and C is the charge conjugation operator. The colour tensors T are defined as

$$\begin{aligned} T^{SSS}_{\{ij\}\{kl\}\{mn\}} &= \varepsilon_{ikm}\varepsilon_{jln} + \varepsilon_{jkm}\varepsilon_{iln} + \varepsilon_{ilm}\varepsilon_{jkn} + \varepsilon_{jlm}\varepsilon_{ikn}\,, \\ T^{AAS}_{[ij][kl]\{mn\}} &= \varepsilon_{ijm}\varepsilon_{kln} + \varepsilon_{ijn}\varepsilon_{klm}\,, \end{aligned} \tag{8.3}$$

where $[\ \ ]$ denotes index antisymmetrisation and $\{\ \}$ symmetrisation. Each operator in Eq. (8.2) leads to eight operators when the different chirality combinations are considered, yielding 24 operators in total. However, using the antisymmetrisation relations

$$\mathcal{O}^1_{\chi_1 LR} = \mathcal{O}^1_{\chi_1 RL}\,, \quad \mathcal{O}^{2,3}_{LR\chi_3} = \mathcal{O}^{2,3}_{RL\chi_3}\,, \tag{8.4}$$

along with the identity

$$\mathcal{O}^2_{\chi\chi\chi'} - \mathcal{O}^1_{\chi\chi\chi'} = 3\mathcal{O}^3_{\chi\chi\chi'}\,, \tag{8.5}$$

where $\chi, \chi' \in [L, R]$, leads to only 14 operators remaining. To match with the most recent lattice-QCD calculations, it is convenient to express these operators in a basis that preserves the chiral symmetry $SU(2)_L \times SU(2)_R$ [584]. A Lagrangian describing n-$\bar{n}$ oscillation may then be expressed as

$$\mathcal{L}^{\bar{n}\text{-}n}_{\text{eff}} = \sum_{i=1,2,3,5} \Big[C_i(\mu)\mathcal{O}_i(\mu) + C^P_i(\mu)\mathcal{O}^P_i(\mu) \Big] + \text{h.c.}\,, \tag{8.6}$$

where C_i are the Wilson coefficients corresponding to operators $\mathcal{O}_i$, and a superscript P denotes parity conjugation. In terms of the basis from Eq. (8.2), the operators in Eq. (8.6) can be expressed as [574]

$$\begin{aligned} \mathcal{O}_1 &= -4\mathcal{O}^3_{RRR} = (\psi C P_R i\tau^2 \psi)(\psi C P_R i\tau^2 \psi)(\psi C P_R i\tau^2 \tau^+ \psi) T^{AAS}\,, \\ \mathcal{O}_2 &= -4\mathcal{O}^3_{LRR} = (\psi C P_L i\tau^2 \psi)(\psi C P_R i\tau^2 \psi)(\psi C P_R i\tau^2 \tau^+ \psi) T^{AAS}\,, \\ \mathcal{O}_3 &= -4\mathcal{O}^3_{LLR} = (\psi C P_L i\tau^2 \psi)(\psi C P_L i\tau^2 \psi)(\psi C P_R i\tau^2 \tau^+ \psi) T^{AAS}\,, \\ \mathcal{O}_4 &= -\frac{4}{5}\mathcal{O}^1_{RRR} - \frac{16}{5}\mathcal{O}^2_{RRR} \\ &= \left[(\psi C P_R i\tau^2 \tau^3 \psi)(\psi C P_R i\tau^2 \tau^3 \psi) - \frac{1}{5}(\psi C P_R i\tau^2 \tau^a \psi)(\psi C P_R i\tau^2 \tau^a \psi) \right] (\psi C P_R i\tau^2 \tau^+ \psi) T^{SSS}\,, \\ \mathcal{O}_5 &= \mathcal{O}^1_{RLL} = (\psi C P_R i\tau^2 \tau^- \psi)(\psi C P_L i\tau^2 \tau^+ \psi)(\psi C P_L i\tau^2 \tau^+ \psi) T^{SSS}\,, \\ \mathcal{O}_6 &= -4\mathcal{O}^2_{RLL} = (\psi C P_R i\tau^2 \tau^3 \psi)(\psi C P_L i\tau^2 \tau^3 \psi)(\psi C P_L i\tau^2 \tau^+ \psi) T^{SSS}\,, \\ \mathcal{O}_7 &= -\frac{4}{3}\mathcal{O}^1_{LLR} - \frac{8}{3}\mathcal{O}^2_{LLR} \\ &= \left[(\psi C P_L i\tau^2 \tau^3 \psi)(\psi C P_L i\tau^2 \tau^3 \psi) - \frac{1}{3}(\psi C P_L i\tau^2 \tau^a \psi)(\psi C P_L i\tau^2 \tau^a \psi) \right] (\psi C P_R i\tau^2 \tau^+ \psi) T^{SSS}\,, \end{aligned} \tag{8.7}$$

where $\psi = (u, d)^T$ is an isospin doublet and τ^a are the Pauli matrices, with $\tau^\pm = \frac{1}{2}(\tau^1 \pm i\tau^2)$. Note that we have here suppressed colour indices for brevity. Together with their respective parity transformations, the seven operators in Eq. (8.7) lead to the total 14 operators that

remain after imposing the relations in Eqs. (8.4) and (8.5). In addition to the operators in Eq. (8.7), some NP models also generate the operators [584]

$$\begin{aligned}\tilde{\mathcal{O}}_1 &= -4/3(\mathcal{O}^2_{RRR} - \mathcal{O}^1_{RRR}) = (\psi C P_R i\tau^2\tau^a\psi)(\psi C P_R i\tau^2\tau^a\psi)(\psi C P_R i\tau^2\tau^+\psi)T^{SSS}\,,\\ \tilde{\mathcal{O}}_3 &= -4/3(\mathcal{O}^2_{LLR} - \mathcal{O}^1_{LLR}) = (\psi C P_L i\tau^2\tau^a\psi)(\psi C P_L i\tau^2\tau^a\psi)(\psi C P_R i\tau^2\tau^+\psi)T^{SSS}\,.\end{aligned} \tag{8.8}$$

These operators are not independent from the basis in Eq. (8.7). In fact, in $D = 4$ spacetime dimensions $\tilde{\mathcal{O}}_1$ and $\tilde{\mathcal{O}}_3$ are equal to $\mathcal{O}_1$ and $\mathcal{O}_3$, respectively. However, for arbitrary D, the operators in Eq. (8.8) could be needed for a full description of the n-$\bar{n}$ oscillation process.

In case isospin symmetry is imposed, the operators in Eq. (8.7) form an overcomplete basis, and the number of operators can be further reduced. The matrix element corresponding to $\mathcal{O}_4$ vanishes completely,

$$\langle\bar{n}|\mathcal{O}_4|n\rangle = 0\,, \tag{8.9}$$

while those of $\mathcal{O}_5$, $\mathcal{O}_6$, and $\mathcal{O}_7$ are related via

$$\langle\bar{n}|\mathcal{O}_5|n\rangle = \langle\bar{n}|\mathcal{O}_6|n\rangle = -\frac{3}{2}\langle\bar{n}|\mathcal{O}_7|n\rangle\,. \tag{8.10}$$

The n-$\bar{n}$ oscillation time $\tau_{n\text{-}\bar{n}}$ can be described by

$$\tau^{-1}_{n\text{-}\bar{n}} = \langle\bar{n}|\mathcal{L}^{\bar{n}\text{-}n}_{\text{eff}}|n\rangle = \Big|\sum_{i=1,2,3,5}(C_i(\mu)\mathcal{M}_i(\mu) + C^P_i(\mu)\mathcal{M}^P_i(\mu))\Big|\,, \tag{8.11}$$

where $\mathcal{M}_i(\mu) \equiv \langle\bar{n}|\mathcal{O}_i|n\rangle$ is the $n \to \bar{n}$ transition matrix element corresponding to $\mathcal{O}_i$, and μ is the scale at which the matrix elements are defined. We take the matrix elements of operators $\tilde{\mathcal{O}}_1$ and $\tilde{\mathcal{O}}_3$ to be equal to those of $\mathcal{O}_1$ and $\mathcal{O}_3$, respectively.

8.1.2. RG running effects

Numerical values corresponding to the matrix elements $\mathcal{M}_i(\mu)$ from Eq. (8.11) are available in the $\overline{\text{MS}}$ scheme at $\mu = 2$ GeV from lattice-QCD calculations [574]. We are interested in scales much higher than 2 GeV, and therefore it is appropriate to consider running effects. An operator defined at $\mu = \mu_0$ can run up to a higher scale μ_{NP} via the relation [584]

$$\mathcal{O}_i(\mu_{\text{NP}}) = U'_i(\mu_{NP},\mu_0)\mathcal{O}_i(\mu_0) \equiv U_i^{N_f=6}(\mu_{NP},m_t)U_i^{N_f=5}(m_t,m_b)U_i^{N_f=4}(m_b,\mu_0)\mathcal{O}_i(\mu_0)\,, \tag{8.12}$$

where we have assumed the inequalities $m_c < \mu_0 < m_b$ and $\mu_{\text{NP}} > m_t$ to hold. Up to $\mathcal{O}(\alpha_s^2)$, the running factors $U_i^{N_f}(q_1,q_2)$ are given by

$$U_i^{N_f}(q_1,q_2) = \left(\frac{\alpha_S(q_2)}{\alpha_S(q_1)}\right)^{-\gamma_i^0/8\pi\beta_0}\left[1 - \delta_{q_2,\mu_0}r_i^{(0)}\frac{\alpha_S(\mu_0)}{4\pi} + \left(\frac{\beta_1\gamma_i^{(0)}4\pi}{2\beta_0^2} - \frac{\gamma_i^{(1)}}{2\beta_0}\right)\frac{\alpha_S(q_2)-\alpha_S(q_1)}{16\pi^2}\right]\,, \tag{8.13}$$

where q_1 and q_2 are two energy scales obeying $q_1 > q_2$, and N_f is the number of quark generations with masses greater than q_2. The one- and two-loop $\overline{\text{MS}}$ anomalous dimensions $\gamma_i^{(0)}$ and $\gamma_i^{(1)}$, as well as the one-loop Landau gauge Regularisation-Independent-Momentum

$\mathcal{O}$	$\gamma_i^{(0)}$	$\gamma_i^{(1)}$	$r_i^{(0)}$	$\mathcal{M}(2\text{ GeV})$ [GeV^6]
$\mathcal{O}_1$	4	$335/3 - 34N_f/9$	$101/30 + 8/15\ln 2$	$-46(13)(2) \times 10^{-5}$
$\mathcal{O}_2$	-4	$91/3 - 26N_f/9$	$-31/6 + 88/15\ln 2$	$95(15)(7) \times 10^{-5}$
$\mathcal{O}_3$	0	$64 - 10N_f/3$	$-9/10 + 16/5\ln 2$	$-50(10)(6) \times 10^{-5}$
$\mathcal{O}_5$	24	$238 - 14N_f$	$49/10 - 24/5\ln 2$	$-1.06(45)(15) \times 10^{-5}$
$\tilde{\mathcal{O}}_1$	4	$797/3 - 118N_f/9$	$-109/30 + 8/15\ln 2$	-
$\tilde{\mathcal{O}}_3$	0	$218 - 38N_f/3$	$-79/10 + 16/5\ln 2$	-

Table 8.1.: Running factors $\gamma_i^{(0)}$ and $\gamma_i^{(1)}$ for one- and two-loop diagrams, respectively, as well as the one-loop matching factor $r_i^{(0)}$, corresponding to operators $\mathcal{O}_i$ for $i \in \{1,2,3,5\}$ and $\tilde{\mathcal{O}}_i$ for $i \in \{1,3\}$ [574,584].

matching factor $r_i^{(0)}$, are all given in Table 8.1. At four-loop order, the scale-dependent strong coupling constant $\alpha_S(q)$ is given by [585]

$$\begin{aligned}\alpha_S(q) = &\frac{1}{\beta_0 L} - \frac{1}{\beta_0^3 L^2}\beta_1 \ln L + \frac{1}{\beta_0^3 L^3}\left[\frac{\beta_1^2}{\beta_0^2}(\ln^2 L - \ln L - 1) + \frac{\beta_2}{\beta_0}\right] \\ &+ \frac{1}{\beta_0^4 L^4}\left[\frac{\beta_1^3}{\beta_0^3}\left(-\ln^3 L + \frac{5}{2}\ln^2 L + 2\ln L - \frac{1}{2}\right) - 3\frac{\beta_1\beta_2}{\beta_0^2}\ln L - \frac{\beta_3}{2\beta_0}\right],\end{aligned} \tag{8.14}$$

where

$$L \equiv \ln\left(\frac{q^2 e^{1/(\beta_0 \alpha_S(q_\alpha))}}{q_\alpha^2}\right), \tag{8.15}$$

and where q_α corresponds to a scale at which the value of α_S is known. The β-functions in Tab. 8.1 and Eq. (8.14) are given by

$$\begin{aligned}\beta_0 &= \frac{33 - 2N_f}{12\pi}, \\ \beta_1 &= \frac{153 - 19N_f}{24\pi^2}, \\ \beta_2 &= \frac{77139 - 15099N_f + 325N_f^2}{3456\pi^3}, \\ \beta_3 &\approx \frac{29243 - 6946.3N_f + 405.089N_f^2 + 1.49931N_f^3}{256\pi^4}.\end{aligned} \tag{8.16}$$

In Fig. 8.1 the running of the matrix elements relevant for n-$\bar{n}$ oscillation is shown between the low $\mathcal{O}(1\text{ GeV})$ and high $\mathcal{O}(10^{15}\text{ GeV})$ scales. The n-$\bar{n}$ oscillation time can now be expressed

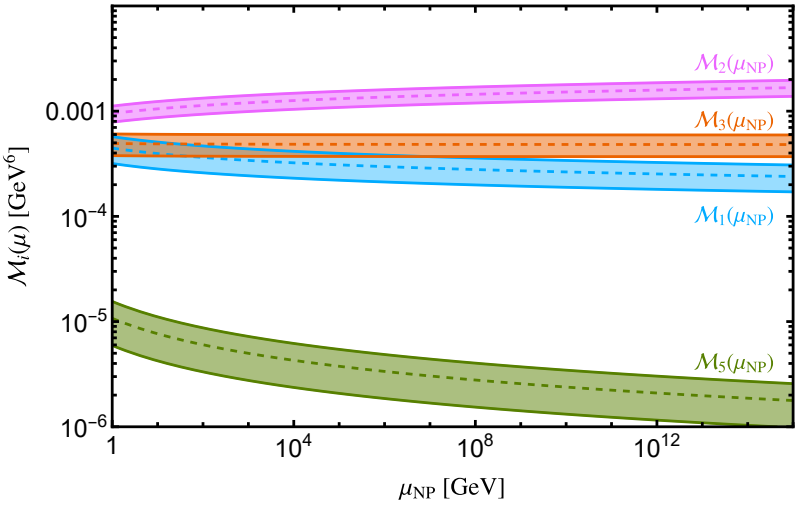

Figure 8.1.: Running of n-$\bar{n}$ matrix elements with regards to the scale $\mu_{\rm NP}$. Filled areas represent the errors, c.f. Tab. 8.1, and the dashed lines show the central values.

as

$$\begin{aligned}\tau_{n\text{-}\bar{n}}^{-1} &= 1.52\times10^{18}\left|\sum_{i=1,2,3,5}\frac{\mathcal{M}_i(\mu)}{(\text{GeV})^6}\left[\left(\frac{C_i(\mu)}{(\text{TeV})^{-5}}\right)-\left(\frac{C_i^P(\mu)}{(\text{TeV})^{-5}}\right)\right]\right|_{\mu=\mu_{\rm NP}}\times10^{-9}\ \text{s}^{-1} \qquad (8.17)\\ &= 1.52\times10^{18}\left|\sum_{i=1,2,3,5}U_i'(\mu,2\ \text{GeV})\frac{\mathcal{M}_i(2\ \text{GeV})}{(\text{GeV})^6}\left[\left(\frac{C_i(\mu)}{(\text{TeV})^{-5}}\right)-\left(\frac{C_i^P(\mu)}{(\text{TeV})^{-5}}\right)\right]\right|_{\mu=\mu_{\rm NP}}\times10^{-9}\ \text{s}^{-1},\end{aligned}$$

where the matrix elements at 2 GeV are given in Tab. 8.1. The Wilson coefficients can be computed at the high scale by integrating out the relevant heavy degrees of freedom. As a demonstrative example, we now consider $\mathcal{O}_1$ to generate n-$\bar{n}$ oscillations, and for simplicity write the Wilson coefficient as $C_1(\mu = \Lambda_1) = \Lambda_1^{-5}$, where Λ_1 is the scale of NP. Using the most stringent limits from the Super-Kamiokande experiment $\tau_{n\text{-}\bar{n}}^{\rm SK} \geq 4.7\times10^8$ s leads to a limit on the scale of NP given by $\Lambda_1 \geq 7.04\times10^5$ GeV [2].

8.2. Model-independent n-$\bar{n}$ oscillation and the baryon asymmetry

In this section we study the effects of a potential n-$\bar{n}$ oscillation signal on baryogenesis. First we develop a model-independent washout description based on the EFT formalism from Sec. 8.1, after which, in the following section, a thorough analysis of one class of simplified models is made.

A Boltzmann equation describing the time evolution of the number density of a particle X

has the generic form (see e.g. Refs. [224,586,587] as well as Ch. 3 and Appendix E)

$$zHn_\gamma \frac{d\eta_X}{dz} = -\sum_{a,i,j,\cdots} [Xa\cdots \leftrightarrow ij\cdots]\,, \tag{8.18}$$

where z is a time-variable that is related to the temperature T and X-mass m_X via $z \equiv m_X/T$. The square brackets denote a function of number densities and scattering rates given by

$$[Xa\cdots \leftrightarrow ij\cdots] = \frac{n_X n_a \cdots}{n_X^{\rm eq} n_a^{\rm eq}\cdots}\gamma^{\rm eq}(Xa\cdots \to ij\cdots) - \frac{n_i n_j \cdots}{n_i^{\rm eq} n_j^{\rm eq}\cdots}\gamma^{\rm eq}(ij\cdots \to Xa\cdots)\,, \tag{8.19}$$

where $\gamma^{\rm eq}$ is the equilibrium scattering rate density and $n_\alpha^{(\rm eq)}$ is the (equilibrium) number density of particle α. In the LHS of Eq. (8.18), the Hubble rate H is given by

$$H(T) = \frac{1.66\sqrt{g_*}}{m_{\rm Pl}}T^2\,, \tag{8.20}$$

with $g_* \sim 107$ being the effective number of degrees of freedom in the SM and $m_{\rm Pl}$ the Planck mass. The photon density is given by

$$n_\gamma^{\rm eq} = 2\frac{\zeta(3)}{\pi^2}T^3\,, \tag{8.21}$$

where $\zeta(3) \approx 1.20$. To describe the evolution of baryon number density over time we can make the replacement $X \to \Delta B$, where the baryon number density $\eta_{\Delta B}$ is given by [2]

$$\eta_{\Delta B} \;=\; \sum_{u,d}\frac{1}{3}[(\eta_{u_L} - \eta_{\bar{u}_L}) + (\eta_{d_L} - \eta_{\bar{d}_L}) + (\eta_{\bar{u^c}} - \eta_{u^c}) + (\eta_{\bar{d^c}} - \eta_{d^c})]\,. \tag{8.22}$$

Here the sum u, d goes over the quarks that are in thermal equilibrium, and the fields u_L, d_L, u^c, and d^c are the SM quarks as defined in Sec. 2.1. For quarks in thermal equilibrium, the number densities of particles and antiparticles are related via

$$n_q - n_{\bar{q}} = \frac{g_q \mu_q T^2}{6}\,, \tag{8.23}$$

where $g_q = 3$ is the number of degrees of freedom and μ_q is the chemical potential of quark q. If the sphaleron and SM Yukawa interactions are in chemical equilibrium, the chemical potentials of the Higgs doublet and SM fermions can be related to that of u_L via [588] (c.f. Appendix D),

$$\mu_H = \frac{4}{21}\mu = -\frac{12}{7}\mu_{u_L}\,, \quad \mu_{\bar{u^c}} = \frac{5}{63}\mu = -\frac{5}{7}\mu_{u_L}\,, \quad \mu_{\bar{d^c}} = -\frac{19}{63}\mu = \frac{19}{7}\mu_{u_L}\,, \tag{8.24}$$

where $\mu \equiv \sum_{e,\mu,\tau}\mu_{e_L}$. Assuming these equilibrium relations to hold, we then rewrite Eq. (8.22) as

$$\eta_{\Delta B} = \sum_{u,d}\frac{g_q T^2}{6n_\gamma}(\mu_{u_L} + \mu_{d_L} + \mu_{\bar{u^c}} + \mu_{\bar{d^c}}) = \frac{\pi^2}{\zeta(3)}\frac{\mu_{u_L}}{T}\,. \tag{8.25}$$

Choosing $\mathcal{O}_1$ from Eq. (8.7) as an example, we now study the washout effects coming from a n-$\bar{n}$ oscillation operator. The Boltzmann equation for $\eta_{\Delta B}$ can be obtained by taking the derivative of Eq. (8.22), such that

$$zHn_\gamma \frac{d\eta_{\Delta B}}{dz} = \frac{1}{3} zHn_\gamma \left[\frac{d\left(\eta_{\bar{d}^c} - \eta_{d^c}\right)}{dz} + \frac{d\left(\eta_{\bar{u}^c} - \eta_{u^c}\right)}{dz} + \frac{d\left(\eta_{u_L} - \eta_{\bar{u}_L}\right)}{dz} + \frac{d\left(\eta_{d_L} - \eta_{\bar{d}_L}\right)}{dz} \right] . \quad (8.26)$$

Given the presence of $\mathcal{O}_1$, the baryon-number-violating interactions of quarks leads to expressions describing the time evolution of the different quark number densities. Taking e.g. d^c we have [2]

$$\begin{aligned} zHn_\gamma \frac{d\,\eta_{\bar{d}^c}}{dz} &= -\left[\bar{u}^c\bar{d}^c\bar{d}^c \leftrightarrow u^c d^c d^c\right] + (\text{other possible permutations}) \\ &= -\left(\frac{n_{\bar{u}^c} n^2_{\bar{d}^c}}{n^{\rm eq}_{\bar{u}^c} (n^{\rm eq}_{\bar{d}^c})^2} - \frac{n_{u^c} n^2_{d^c}}{n^{\rm eq}_{u^c} (n^{\rm eq}_{d^c})^2} \right) \gamma^{\rm eq}(\bar{u}^c\bar{d}^c\bar{d}^c \to u^c d^c d^c) + \cdots \\ &= -\frac{66\,\mu_{u_L}}{7\,T}\gamma^{\rm eq}(\bar{u}^c\bar{d}^c\bar{d}^c \to u^c d^c d^c) + \cdots \\ &= -\frac{66\,\zeta(3)}{7\pi^2}\eta_{\Delta B}\gamma^{\rm eq}(\bar{u}^c\bar{d}^c\bar{d}^c \to u^c d^c d^c) + \cdots , \end{aligned} \quad (8.27)$$

where we assume three fermion generations. The dots in Eq. (8.27) denote other possible $3 \leftrightarrow 3$ and $2 \leftrightarrow 4$ processes that can be formed by permutations of the initial and final states, all of which are still generated by $\mathcal{O}_1$.

Similar equations as Eq. (8.27) can be written down for $\bar{d}^c$, u^c, and $\bar{u}^c$. For the left handed quarks however, the time evolution of the difference between particle and antiparticle may be assumed to be negligible, since $\mathcal{O}_1$ only interacts directly with the right-handed fields. We then write $\frac{d}{dz}(\eta_{u_L} - \eta_{\bar{u}_L}) \simeq 0$ and $\frac{d}{dz}(\eta_{d_L} - \eta_{\bar{d}_L}) \simeq 0$, such that the total time evolution of $\eta_{\Delta B}$ can be written as

$$\begin{aligned} zHn_\gamma \frac{d\,\eta_{\Delta B}}{dz} &= -\frac{4}{3}\left[\bar{u}^c\bar{d}^c\bar{d}^c \leftrightarrow u^c d^c d^c\right] + \cdots \\ &= -\frac{88\,\zeta(3)}{7\pi^2}\eta_{\Delta B}\gamma^{\rm eq}(\bar{u}^c\bar{d}^c\bar{d}^c \to u^c d^c d^c) + \cdots . \end{aligned} \quad (8.28)$$

Following Refs. [394, 476], we describe the washout of baryon asymmetry coming from the operator $\mathcal{O}_1$ by the relation

$$zHn_\gamma \frac{d\,\eta_{\Delta B}}{dz} = -\frac{5}{3}\frac{2200\zeta(3)\,T^{14}}{7\pi^{11}\Lambda^{10}}\eta_{\Delta B} \equiv -c\frac{T^{14}}{\Lambda^{10}}\eta_{\Delta B}\,, \quad (8.29)$$

where we have neglected $2 \leftrightarrow 4$ scatterings due to severe phase space suppression. From Eq. (8.29) we can infer the reaction rate

$$\Gamma_W^{\mathcal{O}_1} = \frac{c}{n_\gamma}\frac{T^{14}}{\Lambda^{10}}\,, \quad (8.30)$$

such that the interaction can be regarded as being in equilibrium if the condition

$$\frac{\Gamma_W^{\mathcal{O}_1}}{H} \equiv \frac{c}{n_\gamma H}\frac{T^{14}}{\Lambda^{10}} = c'\frac{\Lambda_{\rm Pl}}{\Lambda}\left(\frac{T}{\Lambda}\right)^9 \gtrsim 1 \quad (8.31)$$

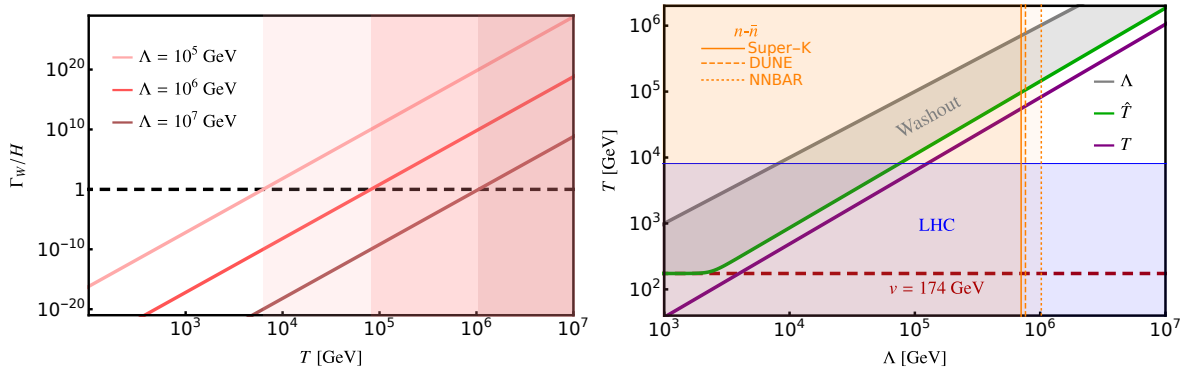

Figure 8.2.: Left: Ratio between the interaction width Γ_W corresponding to operator $\mathcal{O}_1$ and the Hubble rate H with respect to temperature T. Shaded areas indicate where this interaction is strong due to the ratio being greater than one. **Right:** Temperature as a function of the EFT scale Λ, where the purple line shows the temperature at which the ratio Γ_W/H falls below one, and the green line shows the temperature $\hat{T}$ from Eq. (8.33). Blue and orange shaded areas correspond to the regions excluded by the LHC and different n-$\bar{n}$ experiments, respectively. This figure is taken from Ref. [2].

is satisfied, where $c' = \pi^2 c/(\zeta(3)\, 3.3\sqrt{g_*}) \approx 0.3\, c$. The temperature T that solves Eq. (8.31),

$$T = \Lambda \left(\frac{1}{c'}\frac{\Lambda}{\Lambda_{\rm Pl}}\right)^{\frac{1}{9}}, \tag{8.32}$$

can be thought of as the limit where the washout stops. However, we find a more accurate expression for this temperature $T \to \hat{T}$ via the relation [2,394]

$$\hat{T} \simeq \left[9T^9 \ln\left(\frac{d_{\rm rec}}{\eta_B^{\rm obs}}\right) + v^9\right]^{\frac{1}{9}}, \tag{8.33}$$

where $d_{\rm rec} \approx 1/27$ is a dilution factor that accounts for the difference in entropy density between the temperature during which all SM fields were relativistic and the temperature of recombination $T = T_0$. The baryon number densities at these temperatures are related via $\eta_{\Delta B}(T_0) = g_s(T_0)/g_s(T_*)\, \eta_{\Delta B}(T_*) \simeq 1/27\, \eta_{\Delta B}(T_*)$, where g_s is the number of degrees of freedom, which is related to the entropy density s via $s = (2\pi^2/45) g_s T^3$.

In Fig. 8.2 (left) we see the washout parameter Γ_W/H as a function of the temperature T for different values of Λ. The point at which the lines cross $\Gamma_W/H = 1$ is where the washout effectively stops, such that the shaded areas to the right in the figure correspond to temperatures where no baryon asymmetry can survive, provided that the EFT prescription is accurate. In Fig. 8.2 (right) we see the temperature T as a function of the EFT scale Λ, where the purple and green lines denote the temperatures at which washout stops, according to the approximation methods in Eq. (8.32) and (8.33), respectively. The grey line shows $T = \Lambda$. The

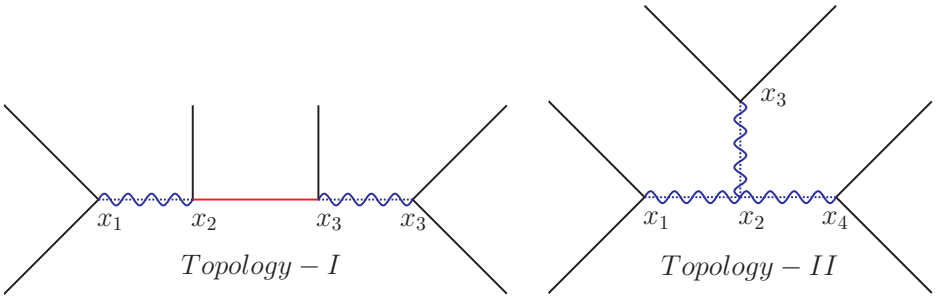

Figure 8.3.: The two possible tree-level n-$\bar{n}$ oscillation topologies, which we denote Topology I and Topology II in the text. This figure is taken from Ref. [2].

EFT breaks down above this line due to the momentum scales involved in the washout process (related to T) being greater than the integrated-out heavy mass scale (related to Λ). Washout is therefore effective between the grey and green lines. Furthermore, the orange shaded regions correspond to exclusion limits coming from n-$\bar{n}$ oscillation experiments [575,577,578], and the blue shaded region shows the approximate reach of the LHC for discovering heavy particles via resonant production with couplings of order unity. If n-$\bar{n}$ oscillations are discovered at the next-generation experiments (dotted orange line), and if the baryon asymmetry is generated at a high scale, we should expect colliders to see some NP between the blue line and the point at which the green line and dotted orange line overlap. This would motivate the search for NP at the scale $\sim$ 100 TeV, precisely the centre-of-mass energy at the proposed FCC collider [589].

In this section we have described the washout effects of a n-$\bar{n}$ oscillation operator, and discussed connections to the scale of baryogenesis. Using an EFT prescription we have been agnostic about the details of what NP generates the operator, and for this reason we have been limited to studying washouts, rather than baryon-asymmetry generation. In the next section, we study an example of a UV-completion of the n-$\bar{n}$ oscillation operator, and show how it can lead to baryogenesis.

8.3. A UV-complete baryogenesis model with n-$\bar{n}$ oscillation

In the previous section we connected n-$\bar{n}$ oscillation to baryogenesis via effective operators. Advantages of this method include its simplicity and applicability to other phenomena [590–592]. Drawbacks include missing the effects of e.g. 1) CP-violation (in the formalism we used here) and 2) a hierarchy in the internal degrees of freedom. The first point leads to the impossibility of describing baryon-asymmetry generation, since CP-violation is one of the three Sakharov conditions (c.f. Sec. 3.2). The second point limits the parameter space in which the description is valid. As we see towards the end of this chapter, covering the whole parameter space is crucial in order to find testable baryogenesis scenarios.

There are two possible topologies that generate the n-$\bar{n}$ oscillation operators at tree-level,

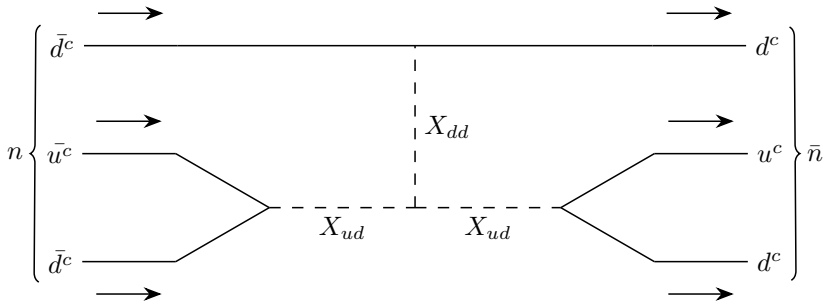

Figure 8.4.: Diagram corresponding to n-$\bar{n}$ oscillation using the model described by the Lagrangian in Eq. (8.34). This figure is taken from Ref. [2].

Field	$SU(3)_c$	$SU(2)_L$	$U(1)_Y$	$Q = T_{3L} + Y$	B
X_{dd}	$\overline{6}$ or 3	1	$+\frac{2}{3}$	$+\frac{2}{3}$	$-\frac{2}{3}$
X_{uu}	$\overline{6}$ or 3	1	$-\frac{4}{3}$	$-\frac{4}{3}$	$-\frac{2}{3}$
X_{ud}	$\overline{6}$ or 3	1	$-\frac{1}{3}$	$-\frac{1}{3}$	$-\frac{2}{3}$

Table 8.2.: Representations of the diquark fields from the Lagrangian in Eq. (8.34).

which we denote[3] Topology I and II, as shown in Fig. 8.3. In Topology I (Fig. 8.3 left) there are two heavy scalar/vector fields and one Majorana fermion mediator. This topology has been studied extensively in the context of specific models [500, 593–610] as well as baryogenesis from a more model-independent point of view in Ref. [611]. For Topology II (Fig. 8.3 right) there are three new heavy scalar/vector bosons, with a dimensionful trilinear coupling between them [612]. For this topology there is also an extensive list of specific models [356, 357, 573, 613–619], as well as possible scenarios leading to baryogenesis [2, 616, 617, 619].

In the rest of this chapter we consider in detail one specific scenario, in which provide a full baryogenesis description of a simplified model corresponding to Topology II, including detailed washout processes as well as different experimental constraints. This model serves as an example of how $\Delta B = 2$ processes at low scales can be related to baryogenesis mechanisms.

8.3.1. Diquark model

We consider the Lagrangian [2]

$$\begin{aligned}\mathcal{L}_{II} &= f_{ij}^{dd} X_{dd} \bar{d}_i^c \bar{d}_j^c + f_{ij}^{uu} X_{uu} \bar{u}_i^c \bar{u}_j^c + \frac{f_{ij}^{ud}}{\sqrt{2}} X_{ud} (\bar{u}_i^c \bar{d}_j^c + \bar{u}_j^c \bar{d}_i^c) \\ &\quad + \lambda \xi X_{dd} X_{ud} X_{ud} + \tilde{\lambda}\, \xi X_{uu} X_{dd} X_{dd} + \text{h.c.}\,, \end{aligned} \tag{8.34}$$

[3] Not to be confused with neutrino mass Topologies I and II from Sec. 5.3.2.

where X_{ud}, X_{dd}, and X_{uu} scalar diquark fields, with the charges under the SM gauge group shown in Tab. 8.2. Furthermore, ξ is a complex scalar field whose real part acquires a vev upon $B-L$-symmetry breaking such that we can replace it according to $\xi \to v' + \frac{1}{\sqrt{2}}(S + i\chi)$, with $v' \gg v$. Here χ is a Goldstone boson that we assume is eaten by a gauge field similar to the weak gauge bosons of the SM during EWSB. After $B-L$-symmetry breaking, the trilinear terms in the second row of Eq. (8.34) no longer conserve baryon number B. In fact, these terms now violate baryon number by two units, $\Delta B = 0$, as required by n-$\bar{n}$ oscillation. A diagram depicting n-$\bar{n}$ oscillation via X_{dd} and X_{ud} is shown in Fig. 8.4.

Some details are now worth mentioning. First, we note that the flavour structure of the couplings f_{ij} between diquarks and quarks is dependent on whether the diquarks are colour sextets or triplets. For sextets, the coupling matrices must be symmetric in flavour space, while for triplets they must be antisymmetric. Furthermore, in Eq. (8.34) the diquarks only couple to singlet quarks, while they could in principle also couple to the $SU(2)_L$ doublets Q. However, the presence of both left- and right-handed quark couplings for X_{ud} can lead to flavour-changing neutral current (FCNC) operators that induce large rates of meson oscillation and flavour-changing quark decays (e.g $b \to s\gamma$), processes which are stringently excluded by experiments. Therefore, as an example, we only consider the diquarks to have tree-level couplings to the quark singlets. Lastly, the diquarks in Tab. 8.2 can also have leptoquark couplings in case they are colour triplets. Without any symmetry forbidding such couplings, there would be no motivation to omit them, and their presence could lead to very rapid proton decay [620–622]. For the rest of this chapter, our main focus is on colour sextet diquarks.

Focusing on the diquarks X_{ud} and X_{dd}, and assuming a mass hierarchy $m_{X_{dd}} > m_{X_{ud}}$, we can write an effective Lagrangian as

$$\mathcal{L}^{\text{eff}} = \frac{f_{ij}^{dd}\lambda v'}{m^2_{X_{dd}}} X^*_{ud} X^*_{ud} \bar{d}^c_i \bar{d}^c_j + \frac{f_{ij}^{ud}}{\sqrt{2}} X_{ud} (\bar{u}^c_i \bar{d}^c_j + \bar{u}^c_j \bar{d}^c_i)\,. \tag{8.35}$$

Further integrating-out also the heavy field X_{dd}, we obtain a Lagrangian that can be expressed in terms of the $\Delta B = 2$ operator $\mathcal{O}^2_{RRR}$ from Eq. (8.2). Using different relations from Sec. 8.1.1 we then obtain [2]

$$\begin{aligned} \mathcal{L}^{\bar{n}\text{-}n}_{\text{eff}} = \frac{(f_{11}^{ud})^2 f_{11}^{dd}\lambda v'}{m^2_{X_{dd}} m^4_{X_{ud}}} \mathcal{O}^2_{RRR} &= \frac{(f_{11}^{ud})^2 f_{11}^{dd}\lambda v'}{4 m^2_{X_{dd}} m^4_{X_{ud}}} \left(\mathcal{O}_4 + \frac{3}{5}\tilde{\mathcal{O}}_1\right) \\ &\approx \frac{3\,(f_{11}^{ud})^2 f_{11}^{dd}\lambda v'}{20\, m^2_{X_{dd}} m^4_{X_{ud}}} \tilde{\mathcal{O}}_1\,. \end{aligned} \tag{8.36}$$

In comparing Eq. (8.36) with the formalism in Sec. 8.1.1 we have a relation between the simplified-model parameters (e.g. the masses and couplings of the diquarks) and Wilson coefficient describing the rate of n-$\bar{n}$ oscillation. In the next section, we derive a complete set of Boltzmann equations based on the interactions of X_{ud} and X_{dd}, in order to eventually see how the model parameters affect both n-$\bar{n}$ oscillation and the generation of a baryon asymmetry.

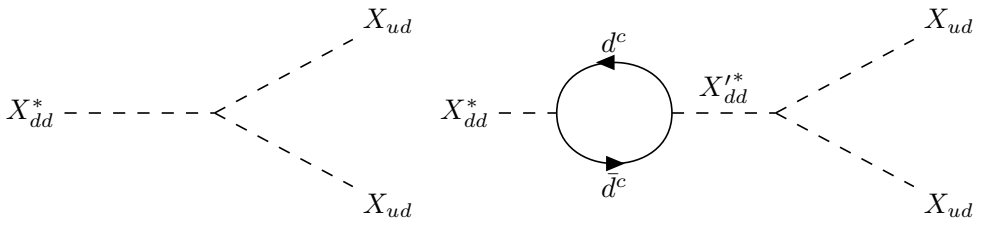

Figure 8.5.: Diagrams corresponding to tree- and loop-level decays of X_{dd}. This figure is taken from Ref. [2].

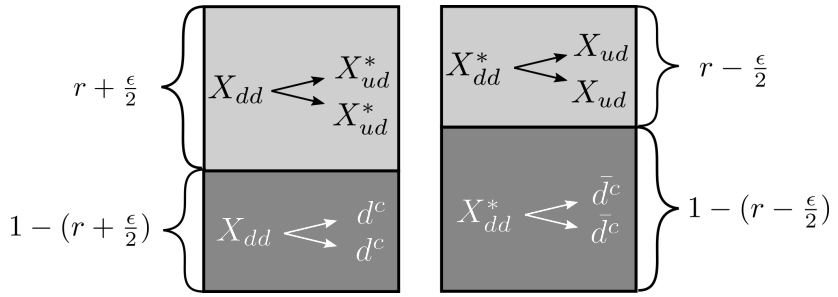

Figure 8.6.: Illustration comparing the branching ratios of the different X_{dd} decay modes. This figure is taken from Ref. [2].

8.3.2. Boltzmann equations in the diquark model

Assuming that the mass constraint $m_{X_{dd}} > 2m_{X_{ud}}$ holds, we consider the scenario where X_{dd} decays out-of-equilibrium into a pair of X_{ud} or a pair of quarks, where the decay violates conservation[4] of CP. Similar to type-i seesaw leptogenesis (c.f. Sec. 3.5.1), CP-violation can be realised in X_{dd} decays via the interference between tree- and loop-level decay diagrams, as seen in Fig. 8.5, where the loop involves a second copy of X_{dd} which we denote X'_{dd}, that has interactions with the quarks and other diquarks according to the Lagrangian

$$\mathcal{L}_{X'_{dd}} \;=\; f'^{dd}_{ij} X'_{dd} \bar{d}^c_i \bar{d}^c_j + \lambda' \xi X'_{dd} X_{ud} X_{ud} + \text{h.c.}\,. \tag{8.37}$$

The CP-violation parameter ϵ is given by [617]

$$\begin{aligned} \epsilon &\equiv \frac{\Gamma(X_{dd} \to X^*_{ud} X^*_{ud}) - \Gamma(X^*_{dd} \to X_{ud} X_{ud})}{\Gamma^{\text{tot}}(X_{dd})} \\ &= \frac{1}{\pi} \text{Im}\left[\frac{\text{Tr}\left[(f'^{dd})^\dagger f^{dd}\right](\lambda' v')^*(\lambda v')}{|\lambda v'|^2}\right]\left(\frac{x}{1-x}\right) r\,, \end{aligned} \tag{8.38}$$

[4]Note that the simplified model described by the Lagrangian in Eq. (8.34) can also lead to another mechanism for baryogenesis, namely the post-sphaleron decay of the real scalar S into six quarks $S \to \bar{u^c}\bar{d^c}\bar{u^c}\bar{d^c}\bar{d^c}\bar{d^c}$ as well as six antiquarks $S \to u^c d^c u^c d^c d^c d^c$ [356,357,615].

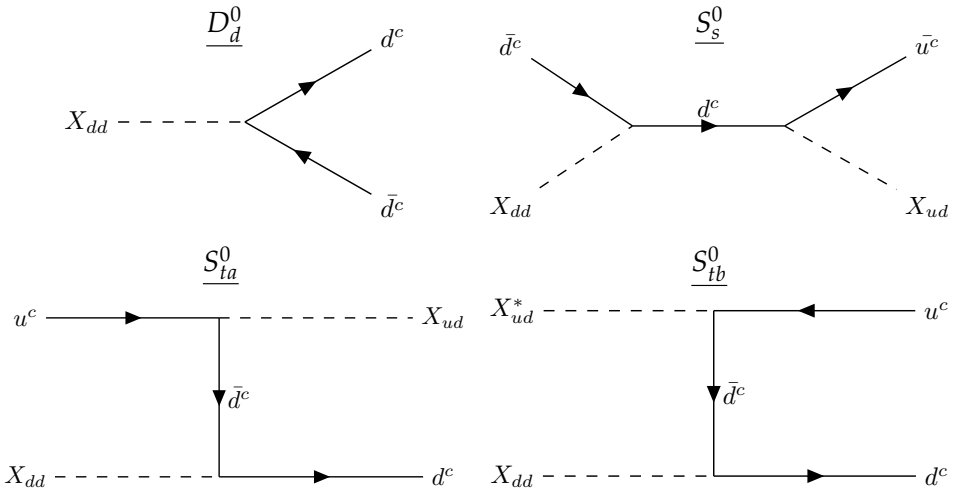

Figure 8.7.: Decay- and scattering diagrams involving the diquarks X_{ud} and X_{dd} where baryon number is conserved. Here the naming convention follows that of the Boltzmann equation formalism in the text.

where x is defined as $x \equiv m_{X_{dd}}^2/m_{X'_{dd}}^2$, and where $r \equiv \Gamma(X_{dd} \to X_{ud}^* X_{ud}^*)/\Gamma^{\text{tot}}(X_{dd})$ is the branching ratio of X_{dd} into diquarks. Since the total width of X_{dd} must be equal to that of its antiparticle X_{dd}^* in order for the decay to not violate CPT, CP-violating decays imply a difference between X_{dd} and X_{dd}^* in the two branching ratios, such that one field decays into quarks more often than the other. This effect is illustrated in Fig. 8.6.

Apart from the CP-violating decay of X_{dd}, the simplified model we consider also leads to a number of washout processes via scattering, as well as baryon-number conserving processes that modify the number density of X_{dd}. In Figs. 8.7 and 8.8 we collect all relevant diagrams for a full Boltzmann equation-based description of baryogenesis, and we denote

$$
\begin{aligned}
|\Delta B| = 0 \quad &: \quad D_d^0 = [X_{dd} \leftrightarrow d^c d^c] \\
&\quad S_s^0 = [X_{dd}\bar{d}^c \overset{d^c}{\underset{s}{\longleftrightarrow}} X_{ud}\bar{u}^c] \quad S_{t_a}^0 = [X_{dd}u^c \overset{d^c}{\underset{t}{\longleftrightarrow}} d^c X_{ud}] \quad S_{t_b}^0 = [X_{dd}X_{ud}^* \overset{d^c}{\underset{t}{\longleftrightarrow}} d^c\bar{u}^c] \\
|\Delta B| = 2 \quad &: \quad D_d = [X_{dd} \leftrightarrow X_{ud}^* X_{ud}^*] \\
&\quad X_s = [X_{ud}^* X_{ud}^* \overset{X_{dd}}{\underset{s}{\longleftrightarrow}} d^c d^c] \quad X_t = [X_{ud}^*\bar{d}^c \overset{X_{dd}}{\underset{t}{\longleftrightarrow}} X_{ud}d^c] \\
&\quad S_s = [X_{dd}X_{ud} \overset{X_{ud}^*}{\underset{s}{\longleftrightarrow}} \bar{d}^c\bar{u}^c] \quad S_{t_a} = [X_{dd}u^c \overset{X_{ud}^*}{\underset{t}{\longleftrightarrow}} X_{ud}^*\bar{d}^c] \quad S_{t_b} = [X_{dd}d^c \overset{X_{ud}^*}{\underset{t}{\longleftrightarrow}} X_{ud}^*\bar{u}^c]\,,
\end{aligned}
\tag{8.39}
$$

where the bracket-parentheses are defined in Eq. (8.19). The corresponding matrix elements are given by

$$
|\overline{\mathcal{M}}_{D_d^0}|^2 = 4f_{dd}^{ij2}\left(m_{X_{dd}}^2 - (m_{d_i} + m_{d_j})^2\right) \tag{8.40}
$$

$$
|\overline{\mathcal{M}}_{D_d}|^2 = \lambda^2 v'^2\,, \tag{8.41}
$$

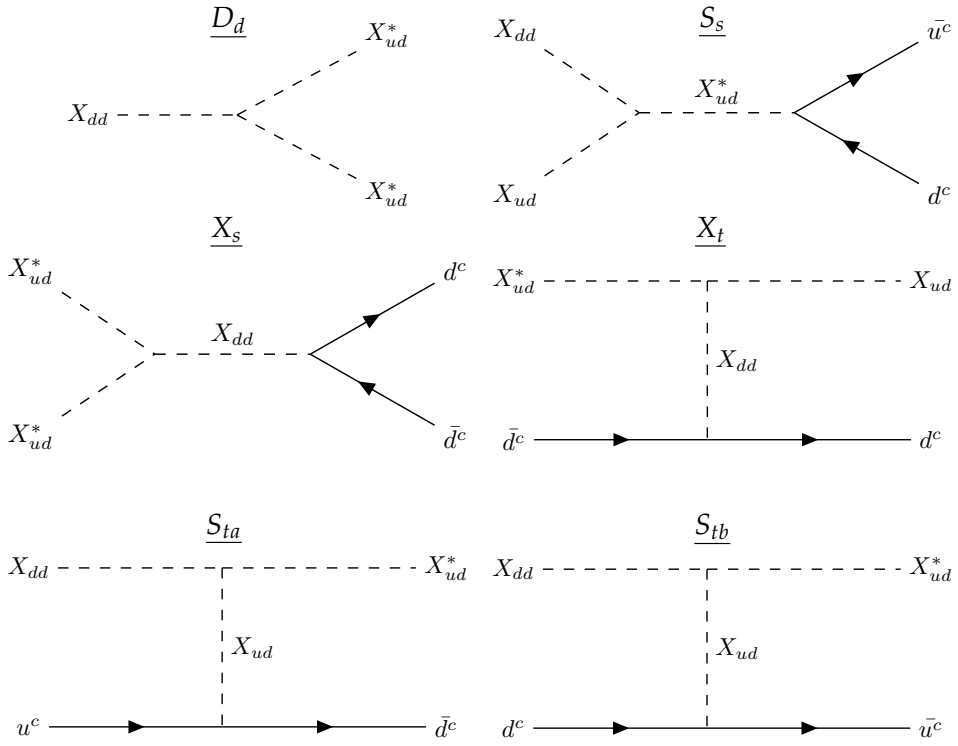

Figure 8.8.: Decay- and scattering diagrams involving the diquarks X_{ud} and X_{dd} where baryon number is violated. Here the naming convention follows that of the Boltzmann equation formalism in the text. This figure is taken from Ref. [2].

$$|\overline{\mathcal{M}}_{S_s}|^2 = \frac{2(\lambda v' f^{ij}_{ud})^2 \left(s - \left(m_{u_i} + m_{d_j}\right)^2\right)}{\left(s - m^2_{X_{ud}}\right)^2 + \Gamma^2_{X_{ud}} m^2_{X_{ud}}}, \tag{8.42}$$

$$|\overline{\mathcal{M}}_{S_t}|^2 = \frac{2(\lambda v' f^{ij}_{ud})^2 \left(t - \left(m_{u_i} + m_{d_j}\right)^2\right)}{\left(t - m^2_{X_{ud}}\right)^2}, \tag{8.43}$$

$$|\overline{\mathcal{M}}_{X_s}|^2 = \frac{2(\lambda v' f^{ij}_{dd})^2 \left(s - \left(m_{d_i} + m_{d_j}\right)^2\right)}{\left(s - m^2_{X_{dd}}\right)^2 + \Gamma^2_{X_{dd}} m^2_{X_{dd}}}, \tag{8.44}$$

$$|\overline{\mathcal{M}}_{X_t}|^2 = \frac{2(\lambda v' f^{ij}_{dd})^2 \left(t - \left(m_{d_i} + m_{d_j}\right)^2\right)}{\left(t - m^2_{X_{dd}}\right)^2}. \tag{8.45}$$

$$|\overline{\mathcal{M}}_{S_s^0}|^2 = \frac{(f_{dd}^{ik} f_{ud}^{kj})^2}{\left(s - m_{d_k}^2\right)^2} \Bigg\{ m_{X_{dd}}^2 \left(m_{X_{ud}}^2 - m_{u_j}(m_{u_j} + m_{d_k}) - s \right) + m_{d_i}^2 \left(m_{u_j}(m_{u_j} + m_{d_k}) - m_{X_{ud}}^2 \right) + m_{d_i} m_{d_k} \left(-m_{X_{ud}}^2 + m_{u_j}^2 + 2 m_{u_j} m_{d_k} + s \right) + s \left(-m_{X_{ud}}^2 + m_{u^j} m_{d^k} + s + t \right) \Bigg\}, \tag{8.46}$$

$$|\overline{\mathcal{M}}_{S_t^0}|^2 = \frac{(f_{dd}^{ik} f_{ud}^{kj})^2}{\left(t - m_{d_k}^2\right)^2} \Bigg\{ m_{X_{dd}}^2 \left(m_{d_i}(m_{d_k} - m_{d_i}) + m_{X_{ud}}^2 \right) + t \left(m_{d_i}^2 - m_{d_k}(m_{d_i} + m_{u_j}) + m_{u_j}^2 - s \right) + m_{u_j} \Big[m_{d_k} \left(m_{X_{ud}}^2 - m_{d_i}(m_{d_i} + m_{u_j}) \right) + m_{u_j}(m_{d_i} - m_{X_{ud}})(m_{d_i} + m_{X_{ud}}) + 2 m_{d_i} m_{d_k}^2 \Big] \Bigg\}. \tag{8.47}$$

Here m_{u_i} and m_{d_i} are the up- and down-type quark masses of the ith generation, corresponding to the quark that appears in a given diagram, and s and t are the Mandelstam variables.

Since the diquarks are coloured particles, they also interact with gluons. This means that we could have production of X_{dd} via gluon fusion channels $gg \to X_{dd} X_{dd}^*$ in the early Universe. As shown in Ref. [619] this production channel mainly dominates in early times, while around the time at which X_{dd} decays out-of-equilibrium it is highly suppressed. Therefore, the interactions between gluons and diquarks does not play a major role for baryogenesis[5], and we neglect them in the Boltzmann equations.

Using the interactions in Eq. (8.39), we can write the Boltzmann equation for $X_{dd}^{(*)} \equiv \frac{1}{2}(X_{dd} + X_{dd}^*)$ as

$$2zH(z)n_\gamma(z)\frac{d\eta_{X_{dd}^{(*)}}}{dz} = -D_d^0 - \overline{D_d^0} - D_d - \overline{D_d} - S_s^0 - \overline{S_s^0} - S_s - \overline{S_s} - S_t^0 - \overline{S_t^0} - S_t - \overline{S_t}\,, \tag{8.48}$$

where the factor two comes from the definition of $X^{(*)}$. Using Eq. (8.19) to rewrite Eq. (8.48) in terms of reaction rates we have

$$zH(z)n_\gamma(z)\frac{d\eta_{X_{dd}^{(*)}}}{dz} = -\left(\frac{\eta_{X_{dd}^{(*)}}}{\eta_{X_{dd}^{(*)}}^{\rm eq}} - 1\right)\left(\gamma_D^{X_{dd}^{(*)}} + \gamma_{S_s^0} + \gamma_{S_s} + \gamma_{S_{t_a}^0} + \gamma_{S_{t_a}} + \gamma_{S_{t_b}^0} + \gamma_{S_{t_b}}\right). \tag{8.49}$$

[5]Note that interactions between heavy scalars and gauge bosons can be important in some baryogenesis models, e.g. in type-ii seesaw leptogenesis where $W^a W^a \to \Delta\Delta^*$ plays a crucial role [370].

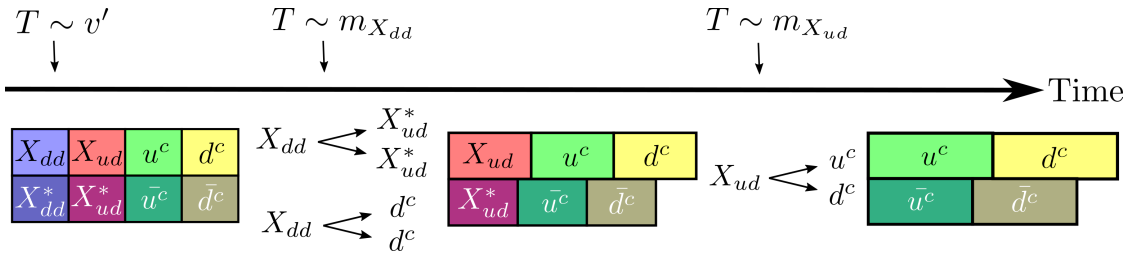

Figure 8.9.: Timeline illustrating the baryogenesis process described in the text. First X_{dd} falls out of equilibrium around $T \sim m_{X_{dd}}$ and a baryon asymmetry is generated via its decays to X_{ud} and d^c. Later, this asymmetry is completely transferred to the quark sector due to X_{ud} falling out of equilibrium and decaying to quark pairs. This figure is taken from Ref. [2].

If we assume that the number densities of X_{dd} and X^*_{dd} are initially identical[6], such that $\eta_{X_{dd}} = \eta_{X^*_{dd}} = \eta_{X^{(*)}_{dd}}$, a difference between the number densities of X_{dd} and X^*_{dd} can arise through interactions of $X^{(*)}_{dd}$ with e.g. X_{ud} and X^*_{ud}, provided that there is an asymmetry between these latter fields. However, such a back-reaction is proportional to $\eta_{\Delta B}$, which is small compared to the number density of X_{dd} during the time of baryogenesis. We therefore neglect effects coming from the difference in number density between X_{dd} and X^*_{dd}.

To obtain an equation describing the evolution of the baryon asymmetry, we first seek a consistent definition of the baryon-number number density in our framework. To this end, we first note that there are no couplings between diquarks and left-handed quarks in the simplified model we consider, and we therefore neglect any baryon number coming from the left-handed quarks in the generation of the baryon asymmetry[7] such that we have $\frac{d}{dz}(\eta_{u_L} - \eta_{\bar{u}_L}) = 0$ and $\frac{d}{dz}(\eta_{d_L} - \eta_{\bar{d}_L}) = 0$. Next, we also note that any asymmetry generated in X_{ud} and X^*_{ud} will be translated into an asymmetry in the quark sector once this diquark finally decays. These decays conserve baryon number, meaning that we may consider the asymmetry shared between the diquark- and quark sectors to be equal to the baryon asymmetry at late times. The timeline of this baryogenesis mechanism is illustrated in Fig. 8.9.

With all the considerations above, we define the baryon number density as

$$\eta_{\Delta B} \equiv \sum_{u,d}^{N} \frac{1}{3}\left[(\eta_{\bar{u}^c} - \eta_{u^c}) + (\eta_{\bar{d}^c} - \eta_{d^c}) + 2(\eta_{X^*_{ud}} - \eta_{X_{ud}})\right], \tag{8.50}$$

where N is the number of fermion generations[8]. Differentiating Eq. (8.50) with respect to z

[6] Note that this is a valid assumption since the previously mentioned $gg \to X_{dd}X^*_{dd}$ interactions quickly bring the diquarks into equilibrium before the onset of baryogenesis.

[7] Note however that the presence of left-handed quarks are accounted for in the chemical potential relations (c.f. Appendix D), as their presence does change the total baryon number.

[8] In the full SM we have $N = 3$. Note that we keep N as a free parameter due to the different times at which the different Yukawa interactions of the SM come into equilibrium [47, 623, 624]. This effectively reduces the

Process	Branching ratio
$X_{dd} \to X^*_{ud} X^*_{ud}$	$r + \frac{\epsilon}{2}$
$X_{dd} \to d^c d^c$	$1 - (r + \frac{\epsilon}{2})$
$X^*_{dd} \to X_{ud} X_{ud}$	$r - \frac{\epsilon}{2}$
$X^*_{dd} \to \bar{d}^c \bar{d}^c$	$1 - (r - \frac{\epsilon}{2})$

Table 8.3.: List of $X^{(*)}_{dd}$ decay modes as well as their corresponding branching ratios.

and multiplying by zHn_γ we subsequently obtain

$$zHn_\gamma \frac{d\eta_{\Delta B}}{dz} = \frac{1}{3} zHn_\gamma \left[N \frac{d\left(\eta_{\bar{d}^c} - \eta_{d^c}\right)}{dz} + N \frac{d\left(\eta_{\bar{u}^c} - \eta_{u^c}\right)}{dz} + 2 \frac{d\left(\eta_{X^*_{ud}} - \eta_{X_{ud}}\right)}{dz} \right] . \tag{8.51}$$

We now relate each term on the RHS of Eq. (8.51) to different interactions that the respective fields participate in,

$$\begin{aligned}
zH(z)n_\gamma(z)\frac{d\eta_{X^*_{ud}}}{dz} &= D_d - X_s - X_t - \overline{S_s} + S_t + \overline{S^0_s} + \overline{S^0_{t_a}} - S^0_{t_b} , && (8.52)\\
zH(z)n_\gamma(z)\frac{d\eta_{X_{ud}}}{dz} &= \overline{D_d} - \overline{X_s} + X_t - S_s + \overline{S_t} + S^0_s + S^0_{t_a} - \overline{S^0_{t_b}} , && (8.53)\\
zH(z)n_\gamma(z)\frac{d\eta_{\bar{d}^c}}{dz} &= \overline{D^0_d} + \overline{X_s} - X_t + S_s + S_{t_a} - \overline{S_{t_b}} - S^0_s + \overline{S^0_t} , && (8.54)\\
zH(z)n_\gamma(z)\frac{d\eta_{d^c}}{dz} &= D^0_d + X_s + X_t + \overline{S_s} + \overline{S_{t_a}} - S_{t_b} - \overline{S^0_s} + S^0_t , && (8.55)\\
zH(z)n_\gamma(z)\frac{d\eta_{\bar{u}^c}}{dz} &= S_s - \overline{S_{t_a}} + S_{t_b} + S^0_s - \overline{S^0_{t_a}} + S^0_{t_b} , && (8.56)\\
zH(z)n_\gamma(z)\frac{d\eta_{u^c}}{dz} &= \overline{S_s} - S_{t_a} + \overline{S_{t_b}} + \overline{S^0_s} - S^0_{t_a} + \overline{S^0_{t_b}} , && (8.57)
\end{aligned}$$

where we have defined $S^0_t \equiv S^0_{t_a} + S^0_{t_b}$ and $S_t \equiv S_{t_a} + S_{t_b}$. With the relations above we can rewrite Eq. (8.51) as

$$\begin{aligned}
3zHn_\gamma \frac{d\eta_{\Delta B}}{dz} &= 2(D_d - \overline{D_d}) + N(\overline{D^0_d} - D^0_d) - (N+2)\left[(X_s - \overline{X_s}) + 2X_t\right] \\
&\quad + 2(N+1)\left[(S_s - \overline{S_s}) + (S_t - \overline{S_t})\right] - 2\left[(S^0_s - \overline{S^0_s}) + (S^0_t - \overline{S^0_t})\right] . \quad (8.58)
\end{aligned}$$

Taking the CP-violating parameter ϵ into account, we can parametrise the branching ratios of the different X_{dd} (X^*_{dd}) decay modes as shown in Tab. 8.3, where again r is defined as $r \equiv \Gamma(X_{dd} \to X^*_{ud} X^*_{ud})/\Gamma^{\text{tot}}(X_{dd})$, which leads to the following expressions for the decay

number of generations that take part in certain interactions for some periods in the Universes history. To account for such effects we must be able to choose different values for N.

parameters:

$$\begin{aligned}
D_d &= \gamma_D^{X_{dd}} \left[\left(r + \frac{\epsilon}{2}\right) \frac{\eta_{X_{dd}}}{\eta^{\rm eq}_{X_{dd}}} - \left(r - \frac{\epsilon}{2}\right) \frac{\eta_{X^*_{ud}}{}^2}{\eta^{\rm eq\ 2}_{X_{ud}}} \right] , \\
D_d^0 &= \gamma_D^{X_{dd}} \left[\left(1 - r - \frac{\epsilon}{2}\right) \frac{\eta_{X_{dd}}}{\eta^{\rm eq}_{X_{dd}}} - \left(1 - r + \frac{\epsilon}{2}\right) \frac{\eta_{d^c}{}^2}{\eta^{\rm eq2}_{d^c}} \right] , \\
\overline{D_d} &= \gamma_D^{X^*_{dd}} \left[\left(r - \frac{\epsilon}{2}\right) \frac{\eta_{X_{dd}}}{\eta^{\rm eq}_{X_{dd}}} - \left(r + \frac{\epsilon}{2}\right) \frac{\eta_{X_{ud}}{}^2}{\eta^{\rm eq\ 2}_{X_{ud}}} \right] , \\
\overline{D_d^0} &= \gamma_D^{X^*_{dd}} \left[\left(1 - r + \frac{\epsilon}{2}\right) \frac{\eta_{X_{dd}}}{\eta^{\rm eq}_{X_{dd}}} - \left(1 - r - \frac{\epsilon}{2}\right) \frac{\eta_{\bar{d}^c}{}^2}{\eta^{\rm eq2}_{\bar{d}^c}} \right] . \qquad (8.59)
\end{aligned}$$

Now defining a total decay rate $\gamma_D^{\rm tot} \equiv 2\gamma_D^{X_{dd}} = 2\gamma_D^{X^*_{dd}}$ we can re-parametrise the relations in Eq. (8.59) as

$$\begin{aligned}
(D_d - \overline{D_d}) &= \frac{\gamma_D^{\rm tot}}{2} \left[\epsilon + \epsilon \frac{\eta_{X_{dd}}}{\eta^{\rm eq}_{X_{dd}}} - r \left(\frac{\eta_{X^*_{ud}}{}^2}{\eta^{\rm eq\ 2}_{X_{ud}}} - \frac{\eta_{X_{ud}}{}^2}{\eta^{\rm eq\ 2}_{X_{ud}}} \right) \right] , \\
(D_d^0 - \overline{D_d^0}) &= \frac{\gamma_D^{\rm tot}}{2} \left[-\epsilon - \epsilon \frac{\eta_{X_{dd}}}{\eta^{\rm eq}_{X_{dd}}} - (1 - r) \left(\frac{\eta_{\bar{d}^c}{}^2}{\eta^{\rm eq2}_{\bar{d}^c}} - \frac{\eta_{d^c}{}^2}{\eta^{\rm eq2}_{\bar{d}^c}} \right) \right] . \qquad (8.60)
\end{aligned}$$

Next we note that the s-channel scattering with a X_{dd} (X^*_{dd}) mediator must be on-shell-subtracted to avoid double-counting of the tree-level (inverse) X_{dd} decay. We therefore have

$$\begin{aligned}
X_s &= \left(\frac{\eta_{X^*_{ud}}}{\eta^{\rm eq}_{X_{ud}}} \right)^2 \left[\gamma_{X^*_{ud} X^*_{ud} \to d^c d^c} - \gamma^{\text{on-shell}}_{X^*_{ud} X^*_{ud} \to d^c d^c} \right] - \left(\frac{\eta_{d^c}}{\eta^{\rm eq}_{d^c}} \right)^2 \left[\gamma_{d^c d^c \to X^*_{ud} X^*_{ud}} - \gamma^{\text{on-shell}}_{d^c d^c \to X^*_{ud} X^*_{ud}} \right] , \\
\overline{X_s} &= \left(\frac{\eta_{X_{ud}}}{\eta^{\rm eq}_{X_{ud}}} \right)^2 \left[\gamma_{X_{ud} X_{ud} \to \bar{d}^c \bar{d}^c} - \gamma^{\text{on-shell}}_{X_{ud} X_{ud} \to \bar{d}^c \bar{d}^c} \right] - \left(\frac{\eta_{\bar{d}^c}}{\eta^{\rm eq}_{\bar{d}^c}} \right)^2 \left[\gamma_{\bar{d}^c \bar{d}^c \to X_{ud} X_{ud}} - \gamma^{\text{on-shell}}_{\bar{d}^c \bar{d}^c \to X_{ud} X_{ud}} \right] , \qquad (8.61)
\end{aligned}$$

with

$$\begin{aligned}
\gamma^{\text{on-shell}}_{X^*_{ud} X^*_{ud} \to d^c d^c} &= \gamma_{X^*_{ud} X^*_{ud} \to X_{dd}} \, \mathrm{BR}(X_{dd} \to d^c d^c) \simeq \left(r - r^2 - \frac{\epsilon}{2} \right) \frac{\gamma_D^{\rm tot}}{2} , \\
\gamma^{\text{on-shell}}_{d^c d^c \to X^*_{ud} X^*_{ud}} &= \gamma_{d^c d^c \to X_{dd}} \, \mathrm{BR}(X_{dd} \to X^*_{ud} X^*_{ud}) \simeq \left(r - r^2 + \frac{\epsilon}{2} \right) \frac{\gamma_D^{\rm tot}}{2} , \\
\gamma^{\text{on-shell}}_{X_{ud} X_{ud} \to \bar{d}^c \bar{d}^c} &= \gamma_{X_{ud} X_{ud} \to X^*_{dd}} \, \mathrm{BR}(X^*_{dd} \to \bar{d}^c \bar{d}^c) \simeq \left(r - r^2 + \frac{\epsilon}{2} \right) \frac{\gamma_D^{\rm tot}}{2} , \\
\gamma^{\text{on-shell}}_{\bar{d}^c \bar{d}^c \to X_{ud} X_{ud}} &= \gamma_{\bar{d}^c \bar{d}^c \to X^*_{dd}} \, \mathrm{BR}(X^*_{dd} \to X_{ud} X_{ud}) \simeq \left(r - r^2 - \frac{\epsilon}{2} \right) \frac{\gamma_D^{\rm tot}}{2} , \qquad (8.62)
\end{aligned}$$

where we have neglect terms of $\mathcal{O}(\epsilon^2)$. Using Eq. (8.62) we can take the difference between the two relations in Eq. (8.61) to obtain

$$X_s - \overline{X_s} = \epsilon\gamma_D^{\rm tot} + \left(\gamma_{X_s} - (r-r^2)\frac{\gamma_D^{\rm tot}}{2}\right)\left[\left(\frac{\eta_{X_{ud}^*}{}^2}{\eta_{X_{ud}}^{\rm eq\ 2}} - \frac{\eta_{X_{ud}}{}^2}{\eta_{X_{ud}}^{\rm eq\ 2}}\right) + \left(\frac{\eta_{\bar{d}^c}{}^2}{\eta_{\bar{d}^c}^{\rm eq2}} - \frac{\eta_{d^c}{}^2}{\eta_{\bar{d}^c}^{\rm eq2}}\right)\right] . \quad (8.63)$$

Similarly, for the t-channel mediated process we have

$$X_t = \gamma_{X_t}\left(\frac{\eta_{X_{ud}^*}}{\eta_{X_{ud}}^{\rm eq}}\frac{\eta_{\bar{d}^c}}{\eta_{\bar{d}^c}^{\rm eq}} - \frac{\eta_{X_{ud}}}{\eta_{X_{ud}}^{\rm eq}}\frac{\eta_{d^c}}{\eta_{\bar{d}^c}^{\rm eq}}\right) . \quad (8.64)$$

The diquark-mediated processes with external $X_{dd}^{(*)}$ field(s) lead to

$$\begin{aligned}
(S_s - \overline{S_s}) &= \gamma_{S_s}\left[\left(\frac{\eta_{X_{dd}}}{\eta_{X_{dd}}^{\rm eq}}\frac{\eta_{X_{ud}}}{\eta_{X_{ud}}^{\rm eq}} - \frac{\eta_{\bar{d}^c}}{\eta_{\bar{d}^c}^{\rm eq}}\frac{\eta_{\bar{u}^c}}{\eta_{\bar{u}^c}^{\rm eq}}\right) - \left(\frac{\eta_{X_{dd}}}{\eta_{X_{dd}}^{\rm eq}}\frac{\eta_{X_{ud}^*}}{\eta_{X_{ud}}^{\rm eq}} - \frac{\eta_{d^c}}{\eta_{\bar{d}^c}^{\rm eq}}\frac{\eta_{u^c}}{\eta_{\bar{u}^c}^{\rm eq}}\right)\right] , && (8.65)\\
(S_t - \overline{S_t}) &= (S_{t_a} - \overline{S}_{t_a}) + (S_{t_b} - \overline{S}_{t_b}) \\
&= \gamma_{S_{t_a}}\left[\left(\frac{\eta_{X_{dd}}}{\eta_{X_{dd}}^{\rm eq}}\frac{\eta_{u^c}}{\eta_{\bar{u}^c}^{\rm eq}} - \frac{\eta_{X_{ud}^*}}{\eta_{X_{ud}}^{\rm eq}}\frac{\eta_{\bar{d}^c}}{\eta_{\bar{d}^c}^{\rm eq}}\right) - \left(\frac{\eta_{X_{dd}}}{\eta_{X_{dd}}^{\rm eq}}\frac{\eta_{\bar{u}^c}}{\eta_{\bar{u}^c}^{\rm eq}} - \frac{\eta_{X_{ud}}}{\eta_{X_{ud}}^{\rm eq}}\frac{\eta_{d^c}}{\eta_{\bar{d}^c}^{\rm eq}}\right)\right] \\
&+ \gamma_{S_{t_b}}\left[\left(\frac{\eta_{X_{dd}}}{\eta_{X_{dd}}^{\rm eq}}\frac{\eta_{d^c}}{\eta_{\bar{d}^c}^{\rm eq}} - \frac{\eta_{X_{ud}^*}}{\eta_{X_{ud}}^{\rm eq}}\frac{\eta_{\bar{u}^c}}{\eta_{\bar{u}^c}^{\rm eq}}\right) - \left(\frac{\eta_{X_{dd}}}{\eta_{X_{dd}}^{\rm eq}}\frac{\eta_{\bar{d}^c}}{\eta_{\bar{d}^c}^{\rm eq}} - \frac{\eta_{X_{ud}}}{\eta_{X_{ud}}^{\rm eq}}\frac{\eta_{u^c}}{\eta_{\bar{u}^c}^{\rm eq}}\right)\right] , && (8.66)
\end{aligned}$$

and the quark-mediated scatterings to

$$\begin{aligned}
(S_s^0 - \overline{S}_s^0) &= \gamma_{S_s^0}\left[\left(\frac{\eta_{X_{dd}}}{\eta_{X_{dd}}^{\rm eq}}\frac{\eta_{\bar{d}^c}}{\eta_{\bar{d}^c}^{\rm eq}} - \frac{\eta_{X_{ud}}}{\eta_{X_{ud}}^{\rm eq}}\frac{\eta_{\bar{u}^c}}{\eta_{\bar{u}^c}^{\rm eq}}\right) - \left(\frac{\eta_{X_{dd}}}{\eta_{X_{dd}}^{\rm eq}}\frac{\eta_{d^c}}{\eta_{\bar{d}^c}^{\rm eq}} - \frac{\eta_{X_{ud}^*}}{\eta_{X_{ud}}^{\rm eq}}\frac{\eta_{u^c}}{\eta_{\bar{u}^c}^{\rm eq}}\right)\right] , && (8.67)\\
(S_t^0 - \overline{S}_t^0) &= (S_{t_a}^0 - \overline{S}_{t_a}^0) + (S_{t_b}^0 - \overline{S}_{t_b}^0) \\
&= \gamma_{S_{t_a}^0}\left[\frac{\eta_{X_{dd}}}{\eta_{X_{dd}}^{\rm eq}}\left(\frac{\eta_{u^c}}{\eta_{\bar{u}^c}^{\rm eq}} - \frac{\eta_{\bar{u}^c}}{\eta_{\bar{u}^c}^{\rm eq}}\right) + \left(\frac{\eta_{X_{ud}^*}}{\eta_{X_{ud}}^{\rm eq}}\frac{\eta_{\bar{d}^c}}{\eta_{\bar{d}^c}^{\rm eq}} - \frac{\eta_{X_{ud}}}{\eta_{X_{ud}}^{\rm eq}}\frac{\eta_{d^c}}{\eta_{\bar{d}^c}^{\rm eq}}\right)\right] \\
&+ \gamma_{S_{t_b}^0}\left[\frac{\eta_{X_{dd}}}{\eta_{X_{dd}}^{\rm eq}}\left(\frac{\eta_{X_{ud}^*}}{\eta_{X_{ud}}^{\rm eq}} - \frac{\eta_{X_{ud}}}{\eta_{X_{ud}}^{\rm eq}}\right) + \left(\frac{\eta_{\bar{d}^c}}{\eta_{\bar{d}^c}^{\rm eq}}\frac{\eta_{u^c}}{\eta_{\bar{u}^c}^{\rm eq}} - \frac{\eta_{d^c}}{\eta_{\bar{d}^c}^{\rm eq}}\frac{\eta_{\bar{u}^c}}{\eta_{\bar{u}^c}^{\rm eq}}\right)\right] . && (8.68)
\end{aligned}$$

In order to derive a Boltzmann equation for $\eta_{\Delta B}$, we need to relate the different number densities appearing in its definition to each other such that we can eliminate them in favour of only a single number density. Our strategy is based on the approximation $\eta_a/\eta_a^{\rm eq} \approx e^{\mu_a/T} \approx 1 + \frac{\mu_a}{T}$ where a is a particle species with chemical potential μ_a. This approximation is valid when the chemical potential is small with respect to the temperature T. For any particle a we can relate it to the number density of X_{ud}^* via

$$\mu_a = x_a \mu_{X_{ud}^*} , \quad (8.69)$$

where x_a can be found by relating different chemical potentials to each other, using the fact that some interactions are in chemical equilibrium (see also Appendix D). In order to

obtain a simple form of the Boltzmann equation describing the evolution of $\eta_{\Delta B}$, we make the assumption that the reaction $X^*_{ud} \leftrightarrow \bar{u^c} + \bar{d^c}$ is in equilibrium, leading to the relation

$$\mu_{X^*_{ud}} = \mu_{\bar{u^c}} + \mu_{\bar{d^c}} \,. \tag{8.70}$$

This assumption is well motivated in the scenario where X_{ud} is light compared to X_{dd} such that $m_{X_{dd}} \gg m_{X_{ud}}$, assuming the different couplings of the two diquarks are of similar strength. The total charge Q of the Universe can then be expressed as (c.f. Appendix D)

$$Q = 2N\left(\mu_Q + \mu_{\bar{u^c}}\right) - N\left(\mu_Q + \mu_{\bar{d^c}}\right) - N\left(\mu_L + \mu_{\bar{e^c}}\right) + 2\mu_H + 2\frac{C_{X^*_{ud}}}{3}\mu_{X^*_{ud}} \,, \tag{8.71}$$

where $C_{X^*_{ud}}$ is the colour-multiplicity of X^*_{ud}, such that $C_{X^*_{ud}} = 3$ for colour triplets and $C_{X^*_{ud}} = 6$ for sextets. Using Eq. (8.71) as well as the weak gauge- and N-generation Yukawa interactions from Appendix D we obtain the following relations for the chemical potentials of the quarks singlets:

$$x_{\bar{u^c}} = \frac{3 - 6N - 2C_{X^*_{ud}}}{12N + 6}, \quad x_{\bar{d^c}} = \frac{3 + 18N + 2C_{X^*_{ud}}}{12N + 6} \,. \tag{8.72}$$

This leads to the total baryon charge B being given by

$$B \equiv n_b - \bar{n}_b = \frac{T^2}{6}\left(N\mu_{\bar{d^c}} + N\mu_{\bar{u^c}} + 2N\mu_Q + \frac{4}{3}C_{X_{ud^*}}\mu_{X^*_{ud}}\right) = \frac{T^3}{6}\frac{6N + 4C_{X^*_{ud}}}{3}\frac{\mu_{X^*_{ud}}}{T} \,. \tag{8.73}$$

Furthermore, we can write the equilibrium number density corresponding to n_b as

$$n_b^{\mathrm{eq}} \equiv \frac{2}{3}C_{X^*_{ud}}n^{\mathrm{eq}}_{X^*_{ud}} + Nn^{\mathrm{eq}}_{\bar{d^c}} + Nn^{\mathrm{eq}}_{\bar{u^c}} + Nn^{\mathrm{eq}}_{u_L} + Nn^{\mathrm{eq}}_{d_L} = \frac{\zeta(3)T^3}{\pi^2}\frac{8C_{X^*_{ud}} + 36N}{12} \,, \tag{8.74}$$

where we have used the relations [2, 47, 53]

$$n_i^{\mathrm{eq}} = \frac{g_i T^3}{\pi^2} \times \begin{cases} \zeta(3) + \frac{\mu_i}{T}\zeta(2) + \ldots & (\text{bosons}) \\ \frac{3}{4}\zeta(3) + \frac{\mu_i}{T}\frac{\zeta(2)}{2} + \ldots & (\text{fermions}) \,, \end{cases} \tag{8.75}$$

where $\zeta(s)$ denotes the Riemann zeta function. The fraction between the number density of baryons and their equilibrium density, being what appears in the Boltzmann equation for $\eta_{\Delta B}$, is then given by

$$\frac{n_b - \bar{n}_b}{n_b^{\mathrm{eq}}} = \frac{\eta_b - \bar{\eta}_b}{\eta_b^{\mathrm{eq}}} = C_B\frac{\mu_{X^*_{ud}}}{T} \,, \tag{8.76}$$

where the constant C_B is defined as

$$C_B \equiv \frac{\pi^2}{3\zeta(3)}\frac{6N + 4C_{X^*_{ud}}}{18N + 4C_{X^*_{ud}}} \,. \tag{8.77}$$

Now taking colour sextet diquarks, we focus on the two scenarios $N = 1$ and $N = 3$,

$$C_B = \frac{\pi^2}{3\zeta(3)} \times \begin{cases} \frac{5}{7} & (N = 1) \\ \frac{7}{13} & (N = 3) \,. \end{cases} \tag{8.78}$$

The combination of decay terms that appear in the Boltzmann equation can then be expressed as

$$2(D_d - \overline{D_d}) + N(\overline{D_d^0} - D_d^0) = \frac{\gamma_D^{\rm tot}}{2}\left[(N+2)\epsilon\left(\frac{\eta_{X_{dd}}}{\eta_{X_{dd}}^{\rm eq}}+1\right) - \frac{4}{C_B}\left\{N(1-r)x_{\bar{d}^c}+2r\right\}\frac{\eta_{\Delta B}}{\eta_B^{\rm eq}}\right] \quad (8.79)$$

Similarly, the different combination of scattering terms lead to

$$X_s - \overline{X_s} = \epsilon\gamma_D^{\rm tot} + \frac{4}{C_B}(1+x_{\bar{d}^c})\left[\gamma_{X_s} - (r-r^2)\frac{\gamma_D^{\rm tot}}{2}\right]\frac{\eta_{\Delta B}}{\eta_B^{\rm eq}}\,, \quad (8.80)$$

$$X_t = \frac{2}{C_B}(1+x_{\bar{d}^c})\gamma_{X_t}\frac{\eta_{\Delta B}}{\eta_B^{\rm eq}}\,, \quad (8.81)$$

$$(S_s - \overline{S_s}) + (S_t - \overline{S_t}) = -\frac{2}{C_B}\frac{\eta_{\Delta B}}{\eta_B^{\rm eq}}\left[\tilde{\gamma}_{S_B} + \tilde{\gamma}_{S_X}\frac{\eta_{X_{dd}}}{\eta_{X_{dd}}^{\rm eq}}\right]\,, \quad (8.82)$$

$$(S_s^0 - \overline{S_s^0}) + (S_t^0 - \overline{S_t^0}) = \frac{2}{C_B}\frac{\eta_{\Delta B}}{\eta_B^{\rm eq}}\left[\tilde{\gamma}_{S_B^0} + \tilde{\gamma}_{S_X^0}\frac{\eta_{X_{dd}}}{\eta_{X_{dd}}^{\rm eq}}\right]\,, \quad (8.83)$$

where we have defined the reduced scattering rates

$$\tilde{\gamma}_{S_B} = (x_{\bar{d}^c}+x_{\bar{u}^c})\gamma_{S_s} + (x_{\bar{d}^c}+1)\gamma_{S_{t_a}} + (x_{\bar{u}^c}+1)\gamma_{S_{t_b}}\,, \quad (8.84)$$

$$\tilde{\gamma}_{S_X} = \gamma_{S_s} + x_{\bar{u}^c}\gamma_{S_{t_a}} + x_{\bar{d}^c}\gamma_{S_{t_b}}\,, \quad (8.85)$$

$$\tilde{\gamma}_{S_B^0} = (-x_{\bar{u}^c}+1)\gamma_{S_s^0} + (x_{\bar{d}^c}+1)\gamma_{S_{t_a}^0} + (x_{\bar{d}^c}-x_{\bar{u}^c})\gamma_{S_{t_b}^0}\,, \quad (8.86)$$

$$\tilde{\gamma}_{S_X^0} = x_{\bar{d}^c}\gamma_{S_s^0} - x_{\bar{u}^c}\gamma_{S_{t_a}^0} + \gamma_{S_{t_b}^0}\,. \quad (8.87)$$

Plugging the above results into Eq. (8.58) we obtain the final form

$$3zH(z)n_\gamma(z)\frac{d\eta_B}{dz} = \frac{\gamma_D^{\rm tot}}{2}\left[(N+2)\epsilon\left(\frac{\eta_{X_{dd}}}{\eta_{X_{dd}}^{\rm eq}}-1\right) - \frac{4}{C_B}\left\{N(1-r)x_{\bar{d}^c}+2r\right\}\frac{\eta_{\Delta B}}{\eta_B^{\rm eq}}\right] - \frac{4}{C_B}\frac{\eta_{\Delta B}}{\eta_B^{\rm eq}}$$
$$\times\left[(N+2)(1+x_{\bar{d}^c})\frac{\gamma_X^{\rm sub}}{2} + \left\{(N+1)\tilde{\gamma}_{S_B} + \tilde{\gamma}_{S_B^0}\right\} + \frac{\eta_{X_{dd}}}{\eta_{X_{dd}}^{\rm eq}}\left\{(N+1)\tilde{\gamma}_{S_X} + \tilde{\gamma}_{S_X^0}\right\}\right] \quad (8.88)$$

where

$$\gamma_X^{\rm sub} \equiv 2\gamma_{X_s} + 2\gamma_{X_t} - \left(r-r^2\right)\gamma_D^{\rm tot}\,. \quad (8.89)$$

Eqs. (8.49) and (8.88) now constitute a set of coupled Boltzmann equations that describe the time-evolution of baryon asymmetry in our simplified model. In a complete treatment, additional effects coming from the varying onset of different SM Yukawa interactions should be taken into account [86, 625, 626]. However, the impact on the final baryon asymmetry coming from these effects should be small, and we therefore neglect them.

Before we evaluate Eqs. (8.49) and (8.88) in Sec. 8.6 we complete our analysis of the simplified model described by Eq. (8.34) by considering its connection to grand unification in Sec. 8.4 and phenomenological constraints in Sec. 8.5.

$G_{\rm PS}$	$G_{\rm LR}$	$G_{\rm SM}$
$(2,1,4)$	$\left(3,2,1,\frac{1}{3}\right)$	$\left(3,2,\frac{1}{6}\right)$
	$(1,2,1,-1)$	$\left(1,2,-\frac{1}{2}\right)$
$\left(2,1,\overline{4}\right)$	$\left(\overline{3},1,2,-\frac{1}{3}\right)$	$\left(\overline{3},1,\frac{1}{3}\right) \oplus \left(\overline{3},1,-\frac{2}{3}\right)$
	$(1,1,2,1)$	$(1,1,1) \oplus (1,1,0)$

Table 8.4.: Decomposition of the $SO(10)$ representation 16 under $G_{\rm PS} \equiv SU(2)_L \times SU(2)_R \times SU(4)_c$, $G_{LR} \equiv SU(3)_c \times SU(2)_L \times SU(2)_R \times U(1)_{B-L}$ and $G_{\rm SM} \equiv SU(3)_c \times SU(2)_L \times U(1)_Y$.

8.4. Grand unification

In this section we connect the diquark-model to grand unification in order to connect it to a broader perspective. Diquarks naturally appear in many GUT gauge groups, e.g. in the Pati-Salam [148] group $G_{\rm PS} \equiv SU(2)_L \times SU(2)_R \times SU(4)_c$, E_6 [154], or $SO(10)$ [153]. In this section we mainly focus on $SO(10)$, which may break to the SM gauge group $G_{\rm SM} = SU(3)_c \times SU(2)_L \times U(1)_Y$ in a number of ways. Below we consider scenarios in which the breaking $SO(10) \to G_{\rm SM}$ goes via $G_{\rm PS}$ or the left-right symmetric gauge group $G_{LR} \equiv SU(3)_c \times SU(2)_L \times SU(2)_R \times U(1)_{B-L}$.

$G_{\rm PS}$	$G_{\rm LR}$	$G_{\rm SM}$
$(1,3,1)$	$(1,1,3,0)$	$(1,1,+1) \oplus (1,1,0) \oplus (1,1,-1)$
$(3,1,1)$	$(1,3,1,0)$	$(1,3,0)$
$(2,2,6)$	$\left(3,2,2,-\frac{2}{3}\right)$	$\left(3,2,+\frac{1}{6}\right) \oplus \left(3,2,-\frac{5}{6}\right)$
	$\left(\overline{3},2,2,+\frac{2}{3}\right)$	$\left(\overline{3},2,+\frac{5}{6}\right) \oplus \left(\overline{3},2,-\frac{1}{6}\right)$
$(1,1,15)$	$(1,1,1,0)$	$(1,1,0)$
	$\left(3,1,1,+\frac{4}{3}\right)$	$\left(3,1,+\frac{2}{3}\right)$
	$\left(\overline{3},1,1,-\frac{4}{3}\right)$	$\left(\overline{3},1,-\frac{2}{3}\right)$
	$(8,1,1,0)$	$(8,1,0)$

Table 8.5.: Decomposition of the $SO(10)$ representation 45 under $G_{\rm PS} \equiv SU(2)_L \times SU(2)_R \times SU(4)_c$, $G_{LR} \equiv SU(3)_c \times SU(2)_L \times SU(2)_R \times U(1)_{B-L}$ and $G_{\rm SM} \equiv SU(3)_c \times SU(2)_L \times U(1)_Y$.

G_{PS}	G_{LR}	G_{SM}
$(1,1,1)$	$(1,1,1,0)$	$(1,1,0)$
$(3,3,1)$	$(1,3,3,0)$	$(1,3,-1) \oplus (1,3,0) \oplus (1,3,+1)$
$(2,2,6)$	$\left(3,2,2,-\frac{2}{3}\right)$	$\left(3,2,+\frac{1}{6}\right) \oplus \left(3,2,-\frac{5}{6}\right)$
	$\left(\overline{3},2,2,+\frac{2}{3}\right)$	$\left(\overline{3},2,+\frac{5}{6}\right) \oplus \left(\overline{3},2,-\frac{1}{6}\right)$
$(1,1,20)$	$\left(6,1,1,+\frac{4}{3}\right)$	$\left(6,1,+\frac{2}{3}\right)$
	$\left(\overline{6},1,1,-\frac{4}{3}\right)$	$\left(\overline{6},1,-\frac{2}{3}\right)$
	$(8,1,1,0)$	$(8,1,0)$

Table 8.6.: Decomposition of the $SO(10)$ representation 54 under $G_{\mathrm{PS}} \equiv SU(2)_L \times SU(2)_R \times SU(4)_c$, $G_{LR} \equiv SU(3)_c \times SU(2)_L \times SU(2)_R \times U(1)_{B-L}$ and $G_{\mathrm{SM}} \equiv SU(3)_c \times SU(2)_L \times U(1)_Y$.

We now consider a limited set of $SO(10)$ multiplets, focusing on the ones that are relevant for this section. Their decomposition under G_{PS} is given by

$$\begin{aligned}
10 &= (2,2,1) + (1,1,6) \\
16 &= (2,1,4) + (1,2,\overline{4}) \\
45 &= (3,1,1) + (1,3,1) + (1,1,15) + (2,2,6) \\
54 &= (1,1,1) + (3,3,1) + (1,1,20) + (2,2,6) \\
120 &= (2,2,1) + (1,1,10) + (1,1,\overline{10}) + (3,1,6) + (1,3,6) + (2,2,15) \\
126 &= (1,1,6) + (3,1,10) + (1,3,\overline{10}) + (2,2,15) \\
210 &= (1,1,1) + (1,1,15) + (3,1,15) + (1,3,15) + (2,2,6) + (2,2,10) + (2,2,\overline{10})
\end{aligned} \tag{8.90}$$

The subsequent decomposition of the 10, 45, 54, and 126 of $SO(10)$ under G_{LR} and G_{SM} are shown in Tabs. 8.4, 8.6, 8.7, and 8.5, respectively. We see in Tab. 8.4 that all SM fermions can be accommodated in the 16 of $SO(10)$, where an additional neutral singlet appears that can be identified as a right-handed neutrino. Furthermore, the Higgs fields of the SM could come from e.g. a complex 126 of $SO(10)$ that couples to $16_i 16_j$, where the coupling is symmetric in flavour indices[9] i and j.

The breaking route from $SO(10)$ to G_{SM} is dictated by which $SO(10)$ multiplet breaks the symmetry. Using a real 210 or 54 along with the complex 126 that we identified with the SM Higgs leads to the intermediate symmetry[10] G_{PS}.

[9] The SM Higgs field could also come from the 10 or 120 of $SO(10)$. In the former case the flavour couplings would again be symmetric, while in the latter they would be antisymmetric.

[10] If we use a real 54, the gauge couplings of the partial symmetries $SU(2)_L$ and $SU(2)_R$ in G_{PS} are identical, $g_L = g_R$ [627], while if we use a 210 they are unequal, $g_L \neq g_R$.

G_{PS}	G_{LR}	G_{SM}
$(1,1,6)$	$\left(\overline{3},1,1,+\frac{2}{3}\right)$	$\left(\overline{3},1,+\frac{1}{3}\right)$
	$\left(3,1,1,-\frac{2}{3}\right)$	$\left(3,1,-\frac{1}{3}\right)$
$(3,1,10)$	$(1,3,1,-2)$	$(1,3,-1)$
	$\left(3,3,1,-\frac{2}{3}\right)$	$\left(3,3,-\frac{1}{3}\right)$
	$\left(6,3,1,+\frac{2}{3}\right)$	$\left(6,3,+\frac{1}{3}\right)$
$\left(1,3,\overline{10}\right)$	$(1,1,3,+2)$	$(1,1,0) \oplus (1,1,+1) \oplus (1,1,+2)$
	$\left(\overline{3},1,3,+\frac{2}{3}\right)$	$\left(\overline{3},1,-\frac{2}{3}\right) \oplus \left(\overline{3},1,+\frac{1}{3}\right) \oplus \left(\overline{3},1,+\frac{4}{3}\right)$
	$\left(\overline{6},1,3,-\frac{2}{3}\right)$	$\left(\overline{6},1,-\frac{4}{3}\right) \oplus \left(\overline{6},1,-\frac{1}{3}\right) \oplus \left(\overline{6},1,+\frac{2}{3}\right)$
$(2,2,15)$	$(1,2,2,0)$	$\left(1,2,-\frac{1}{2}\right) \oplus \left(1,2,+\frac{1}{2}\right)$
	$\left(\overline{3},2,2,-\frac{4}{3}\right)$	$\left(\overline{3},2,-\frac{7}{6}\right) \oplus \left(\overline{3},2,-\frac{1}{6}\right)$
	$\left(3,2,2,+\frac{4}{3}\right)$	$\left(3,2,+\frac{7}{6}\right) \oplus \left(3,2,+\frac{1}{6}\right)$
	$(8,2,2,0)$	$\left(8,2,-\frac{1}{2}\right) \oplus \left(8,2,+\frac{1}{2}\right)$

Table 8.7.: Decomposition of the $SO(10)$ representation 126 under $G_{\text{PS}} \equiv SU(2)_L \times SU(2)_R \times SU(4)_c$, $G_{LR} \equiv SU(3)_c \times SU(2)_L \times SU(2)_R \times U(1)_{B-L}$ and $G_{\text{SM}} \equiv SU(3)_c \times SU(2)_L \times U(1)_Y$.

The symmetry groups $SO(10)$, G_{PS}, and G_{SM} all explicitly conserve $B - L$, but G_{SM} does not. However, the field content of the SM does not lead to any $B - L$-breaking interactions, such that this charge is accidentally conserved by the lack of any $B - L$-violating terms in the SM Lagrangian. In the presence of new fields, such as the scalar diquarks $X_{uu} \in \left(\overline{6},1,-\frac{4}{3}\right)$, $X_{ud} \in \left(\overline{6},1,-\frac{1}{3}\right)$ and $X_{dd} \in \left(\overline{6},1,+\frac{2}{3}\right)$ from Sec. 8.3, $B - L$ can be broken explicitly at low scales. These diquarks do appear in the 126 of[11] $SO(10)$, as can be seen in the entry in Tab. 8.7 that corresponds to the $(1,3,\overline{10})$-representation of G_{PS}. In this entry there is also a complete SM singlet scalar field with the representation $(1,1,0)$, which we can identify as the $B - L$-breaking scalar ξ from the simplified-model Lagrangian in Eq. (8.34).

In the running of gauge couplings we assume that any intermediate symmetries between $SO(10)$ and G_{SM} are all broken around the GUT scale $m_{SO(10)}$. We therefore attempt unification of the three SM gauge couplings at this scale by including additional fields coming from the

[11] Note that the field $X_{dd} \in \left(\overline{6},1,+\frac{2}{3}\right)$ also appears in the 54 of $SO(10)$. This second copy of a $\left(\overline{6},1,+\frac{2}{3}\right)$-field can mix with the one from the 126 to form the two states X_{dd} and X'_{dd} needed for CP-violating decays as described in Sec. 8.3.2.

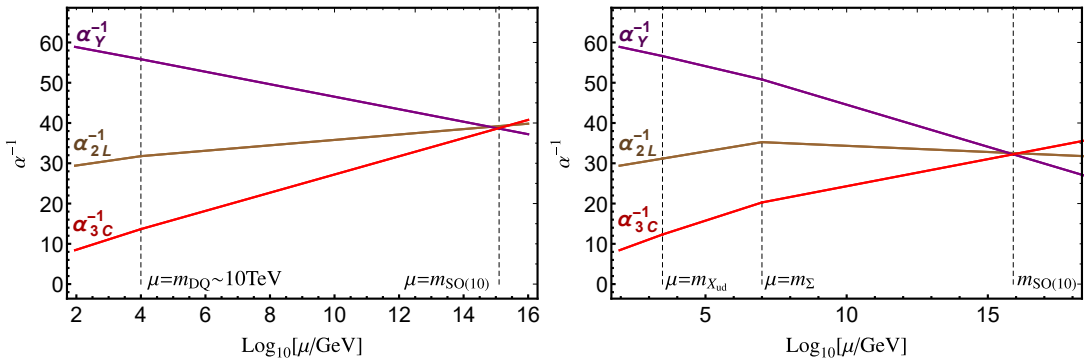

Figure 8.10.: Left: Running of SM gauge couplings α_1, α_2 and α_3 in the presence of a TeV-scale diquark X_{ud} and two copies of $\Delta \in (1,3,0)$, also at the TeV scale. **Right:** Running of SM gauge couplings α_1, α_2 and α_3 in the presence of a TeV-scale diquark X_{ud} and a $SU(2)_L$-triplet fermion $\Sigma \in \left(6,3,\frac{1}{3}\right)$, at an intermediate scale of 10^4 TeV. This figure is taken from Ref. [2].

$SO(10)$-multiplets in the one-loop renormalisation group equations (RGEs) given by

$$\mu \frac{\partial g_i}{\partial \mu} = \frac{b_i}{16\pi^2} g_i^3 \,, \tag{8.91}$$

or, equivalently,

$$\frac{1}{\alpha_i(\mu_2)} = \frac{1}{\alpha_i(\mu_1)} - \frac{b_i}{2\pi} \ln\left(\frac{\mu_2}{\mu_1}\right) \,, \tag{8.92}$$

for $\mu_2 > \mu_1$, where α_i is given by $\alpha_i = g_i^2/4\pi$, and where i denotes the SM gauge subgroups $SU(3)_c$, $SU(2)_L$, and $U(1)_Y$. The coefficients b_i are given at one-loop by [628]

$$b_i = -\frac{11}{3}\mathcal{C}_2(G) + \frac{2}{3}\sum_{R_f} T(R_f) \prod_{j\neq i} d_j(R_f) + \frac{1}{3}\sum_{R_s} T(R_s) \prod_{j\neq i} d_j(R_s) \,, \tag{8.93}$$

where $\mathcal{C}_2(G)$ is the quadratic Casimir operator in the adjoint representation, given by

$$\mathcal{C}_2(G) = \begin{cases} N & \text{if } SU(N) \,, \\ 0 & \text{if } \quad U(1) \,. \end{cases} \tag{8.94}$$

Furthermore, $d(R_{f,s})$ is the dimension of the representation $R_{f,s}$, and $T(R_f)$ ($T(R_s)$) is the Dynkin index of a fermion (scalar[12]) field, which is given by

$$T(R_{f,s}) = \begin{cases} \frac{1}{2} & \text{if } R_{f,s} \text{ is fundamental} \,, \\ N & \text{if } R_{f,s} \text{ is adjoint} \,, \\ 0 & \text{if } R_{f,s} \text{ is singlet} \,. \end{cases} \tag{8.95}$$

[12]Note that an additional factor $\frac{1}{2}$ should be included for $T(R_s)$ in case s is a real scalar field.

We now consider the special case[13] where X_{ud} is found at low scales while X_{uu} and X_{dd} lie at the GUT scale, such that $m_{X_{ud}} \sim \mathcal{O}(\text{TeV})$ and $m_{X_{uu}}, m_{X_{dd}} \sim m_{SO(10)}$. The presence of X_{ud} modifies the running of gauge couplings according to Eq. (8.93). However, no unification is found with X_{ud} alone. Instead, additional fields must be added in order for the three gauge couplings to unify at $m_{SO(10)}$, as can be seen in the two examples below.

In the first example, we add two copies of the scalar field $\Delta \in (1,3,0)$ around the same scale as X_{ud}, where Δ may come from the 45 or 54 of $SO(10)$ [617]. The running of gauge couplings for this scenario can be seen in Fig. 8.10 (left), where $m_{X_{ud}} = m_\Delta = 3$ TeV is used. Here we see that unification is achieved around $m_{SO(10)} \approx 10^{15}$ GeV. As a second example, we keep $m_{X_{ud}} = 3$ TeV and add a fermion field $\Sigma \in \left(6,3,\frac{1}{3}\right)$ at an intermediate scale $m_\Sigma = 10^4$ TeV, leading to unification at $m_{SO(10)} \approx 10^{16}$ GeV as can be seen in Fig. 8.10 (right).

8.5. Phenomenological constraints

Scalar diquarks are subject to a wide range of different phenomenological constraints, especially for masses below or around $\mathcal{O}(\text{TeV})$. In this section, we cover the most relevant ones[14], to finally compare the different limits with n-$\bar{n}$ oscillation searches and baryogenesis in Sec. 8.6.

8.5.1. LHC

Scalar diquarks can lead to distinct signals at collider experiments such as the LHC [616, 630–644]. They may be e.g. singly produced in resonant s-channel quark-quark collisions, or pair-produced in gluon-gluon fusion. For couplings greater than $\mathcal{O}(0.1)$ the former mode dominates, while the latter dominates for smaller couplings [629, 638]. Experimental results are only available up to masses of $\mathcal{O}(1\text{ TeV})$ in gluon fusion [645], while for resonant production the limits go up to $\mathcal{O}(10\text{ TeV})$ [646]. For these reasons, we choose to focus on resonant production here.

The different benchmark scenarios we consider in Sec. 8.6 all include X_{uu} masses at very high scales, while X_{ud} and X_{dd} may be at low scales. We therefore consider the LHC phenomenology of the latter two particles only.

For X_{ud}, the differential resonant production cross section with a top-quark in the final state is given by [2]

$$\frac{d\hat{\sigma}(u_i d_j \to X_{ud} \to t d_k)}{d\cos\theta^*} = \frac{|f_{ij}^{ud}|^2 |f_{3k}^{ud}|^2}{8\pi\hat{s}} \frac{(\hat{s} - m_t^2)^2}{(\hat{s} - m_{X_{ud}}^2)^2 + m_{X_{ud}}^2 \Gamma_{X_{ud}}^2}, \tag{8.96}$$

where all quarks except the top are considered to be massless, θ^* is the scattering angle, $\Gamma_{X_{ud}}$ is the total decay width of X_{ud}, and $\hat{s} \equiv x_1 x_2 s$ is the squared centre-of-mass energy in the

[13] This scenario is of interest for the evaluation of the baryon asymmetry, which is discussed in Sec. 8.6.

[14] Apart from the constraints that are covered in this section, we also note that additional constraints on the diquark couplings can come from the neutron electric dipole moment [629]. However, for the scenario we consider in Sec. 8.3.1, these constraints are not very stringent due to the absence of simultaneous left- and right-handed couplings as well as the presence of flavour-diagonal couplings [2].

parton system, for a proton-proton centre-of-mass energy $\sqrt{s}$ and momentum fractions x_1 and x_2. Changing $t \to u, c$ with $d_k \in \{d, s\}$ in Eq. (8.96) leads to a dijet final state. Note that in Eq. (8.96) we also need to take spin- and colour multiplicities for the initial and final states into account.

The different partial decay widths are given by

$$\begin{aligned} \Gamma(X_{ud} \to u_i d_j)|_{u_i \neq t} &= \frac{C_{X_{ud}}}{8\pi} |f_{ij}^{ud}|^2 \, m_{X_{ud}} \,, \\ \Gamma(X_{ud} \to t d_j) &= \frac{C_{X_{ud}}}{8\pi} |f_{3j}^{ud}|^2 \, m_{X_{ud}} \left(1 - \frac{m_t^2}{m_{X_{ud}}^2}\right)^2 \,, \end{aligned} \tag{8.97}$$

where $\Gamma_{X_{ud}} = \Gamma(X_{ud} \to u_i d_j)|_{u_i \neq t} + \Gamma(X_{ud} \to t d_j)$, and where $C_{X_{ud}}$ is the colour multiplicity. We can similarly express the differential cross section for resonant production of X_{dd} as [2]

$$\frac{d\hat{\sigma}(d_i d_j \to X_{dd} \to d_k d_l)}{d\cos\theta^*} = \frac{|f_{ij}^{dd}|^2 |f_{kl}^{dd}|^2}{16\pi} \frac{\hat{s}}{(\hat{s} - m_{X_{dd}}^2)^2 + m_{X_{dd}}^2 \Gamma_{X_{dd}}^2} \,, \tag{8.98}$$

where the width is given by

$$\Gamma_{X_{dd}} = \Gamma(X_{dd} \to d_i d_j) = \frac{C_{X_{ud}}}{16\pi} |f_{ij}^{dd}|^2 \, m_{X_{dd}} \,. \tag{8.99}$$

The parton-level differential cross sections in Eqs. (8.96) and (8.98) can be related to the measured hadronic cross section via

$$\sigma = \sum_{ij} \int dx_1 dx_2 f_i(x_1, \mu_F^2) f_j(x_2, \mu_F^2) \hat{\sigma}_{ij} \left(\alpha_s(\mu_R^2), \frac{Q^2}{\mu_F^2}, \frac{Q^2}{\mu_R^2}\right) , \tag{8.100}$$

where μ_F is the factorisation scale and Q is the characteristic energy scale of the interaction. We can write Eq. (8.100) in a more convenient form by introducing the parton luminosity factor [647]

$$\frac{dL_{ij}}{d\tau} = \int_0^1 \int_0^1 dx_1 dx_2 f_i(x_1) f_j(x_2) \delta(x_1 x_2 - \tau) \,, \tag{8.101}$$

where

$$\tau = x_1 x_2 = \frac{\hat{s}}{s}. \tag{8.102}$$

Next, we note that the rapidity $\bar{y} = 1/2 \ln(x_1/x_2)$ is a better integration variable than x_1 and x_2 for our purposes, since it allows us to take kinematic cuts into account. We therefore use the identity $dx_1 dx_2 = \frac{\partial(\tau, \bar{y})}{\partial x_1, x_2} d\tau d\bar{y} = d\tau d\bar{y}$ to re-express Eq. (8.101) as

$$\frac{dL_{ij}(\bar{y}_{\min}, \bar{y}_{\max})}{d\tau} = \int_{\bar{y}_{\min}}^{\bar{y}_{\max}} f_i\left(\sqrt{\tau} e^{\bar{y}}\right) f_j\left(\sqrt{\tau} e^{-\bar{y}}\right) d\bar{y} \,, \tag{8.103}$$

leading to the total hadronic cross section

$$\sigma_{\text{had}} = \sum_{i,j} \int \frac{d\tau}{\tau} \left[\frac{dL_{ij}}{d\hat{s}}\right] \left[\hat{s}\, \hat{\sigma}_{ij}\right] . \tag{8.104}$$

For efficient evaluation of the partonic cross section $\hat{\sigma}$ we use the Breit-Wigner form

$$\hat{\sigma}(m)\,(a+b\to X\to c+d) = 16\pi\times\mathcal{N}\times\frac{\Gamma(a+b\to X)\times\Gamma(X\to c+d)}{\left(m^2-m_X^2\right)^2+m_X^2\Gamma_X^2}\,, \tag{8.105}$$

where X is the resonance, $m\simeq\sqrt{\hat{s}}=\sqrt{\tau s}$ is the energy in the interaction, and $\mathcal{N}$ accounts for the different multiplicities such that

$$\mathcal{N}\equiv\frac{N_{S_X}}{N_{S_a}N_{S_b}}\frac{C_X}{C_aC_b}\,, \tag{8.106}$$

where N_{S_X} ($N_{S_{a,b}}$) and C_X ($C_{a,b}$) is the spin and colour multiplicity of the resonance (initial partons a and n), respectively. Note however that in Eq. (8.105) we have implicitly integrated over the whole range of the scattering angle θ^*. In practice, only certain values of θ^* are allowed due to kinematic cuts, and to take this into account we can further re-express Eq. (8.105) as

$$\hat{\sigma}(m) = \frac{16\pi\times\mathcal{N}\times\mathcal{A}\times\mathrm{BR}_{\mathrm{par}}\times\Gamma_X^2}{\left(m^2-m_X^2\right)^2+m_X^2\Gamma_X^2}\,, \tag{8.107}$$

where $\mathrm{BR}_{\mathrm{par}}$ is the branching ratio of X with respect to the partonic subprocess, and $\mathcal{A}$ is the experimental acceptance factor taking the limited range of θ^* into account. Lastly, applying also the NWA

$$\frac{1}{\left(m^2-m_X^2\right)^2+m_X^2\Gamma_X^2}\approx\frac{\pi}{m_X\Gamma_X}\delta(m^2-m_X^2)\,, \tag{8.108}$$

we arrive at the final hadronic cross section

$$\begin{aligned}\sigma_{\mathrm{had}}^{\mathrm{tot}}(m_X) &= 16\pi^2\times\mathcal{N}\times\mathcal{A}\times\sum_{ab}(1+\delta_{ab})\mathrm{BR}(X\to ab)\left[\frac{dL_{ab}(\bar{y}_{\min},\bar{y}_{\max})}{d\hat{s}}\right]_{\hat{s}=m_X^2}\\ &\quad\times\sum_{cd}\mathrm{BR}(X\to cd)\times\frac{\Gamma_X}{m_X}\,,\end{aligned} \tag{8.109}$$

where (a,b) and (c,d) denotes the different possible initial- and final state partons, respectively.

To numerically evaluate the cross section we use the acceptance factor $\mathcal{A}=\mathcal{A}_\Delta\mathcal{A}_\eta$, following Ref. [646], where $\mathcal{A}_\Delta=0.57$ and $\mathcal{A}_\eta\simeq 1$ account for the rapidity cuts $|\Delta\eta|<1.3$ and $|\eta|<2.5$, respectively. In Ref. [2], the hadronic cross sections were then calculated using the ManeParse package [648] with the PDF set CTEQ6L1 [649].

In Fig. 8.11 we show different exclusion limits on the X_{ud} (left column) and X_{dd} (right column) resonant production cross sections as a function of the diquark mass for the LHC (top and bottom rows) HE-LHC [589], and FCC-hh [651] (bottom row). Short dashed lines in Fig. 8.11 correspond to dijet final states, while long-dashed lines correspond to third generation quarks using top- and bottom tagging efficiencies ~ 0.3 and ~ 0.8, respectively, following Ref. [650].

For the LHC-specific cross sections, three different coupling constants $f=1$, 0.1, 0.01 are used. Comparing with the CMS data shown in black, we see that X_{ud} diquarks are excluded

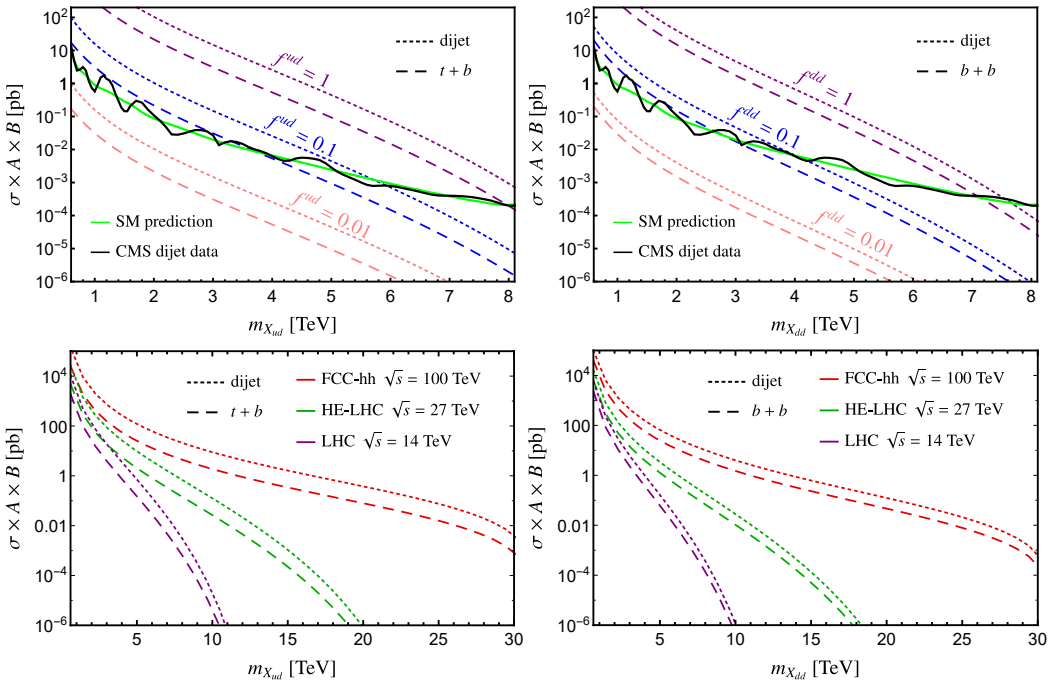

Figure 8.11.: Cross section for the diquark mediated s-channel scattering $u + d \to X_{ud} \to$ dijet $(t + \text{jet})$ (left column) and $d + d \to X_{dd} \to$ dijet $(b + b)$ (right column) as a function of the diquark mass, where experimental acceptance is accounted for by the factor $\mathcal{A}$. In the top row, the cross sections corresponding to searches at the LHC are shown for three different diquark couplings $f = 1.0$, 0.1, and 0.01, corresponding to purple, blue, and pink lines, respectively. Short-dashed lines correspond to dijet final states, while long-dashed lines correspond to third generation fermion final states. Black and green lines show CMS data for an integrated luminosity of 36 fb^{-1} [650] and the corresponding SM prediction for dijet searches, respectively. Projected cross sections for $f = 1$ at LHC, HE-LHC and FCC-hh are shown in the bottom row. This figure is taken from Ref. [2].

for $f_{ud} = 0.1$ up to $m_{X_{ud}} \sim \mathcal{O}(5\text{ TeV})$, while X_{dd} is excluded for $f_{dd} = 0.1$ up to $\mathcal{O}(3\text{ TeV})$. For couplings of order unity, $f = 1$, both diquarks are excluded up to $m \sim \mathcal{O}(8\text{ TeV})$. Comparing with the plots in the bottom row, where all cross sections are shown for $f = 1$, we see that future exclusions could in principle reach a lot higher in the diquark mass.

8.5.2. Meson oscillation

Neutral meson oscillations can severely constrain the masses and couplings of scalar diquarks [629]. Assuming X_{uu} to be very heavy[15], we here focus on meson oscillations induced by the diquarks X_{ud} and X_{dd}.

[15]Note however that if X_{uu} is light it can lead to $D^0 - \overline{D}^0$ oscillation [652].

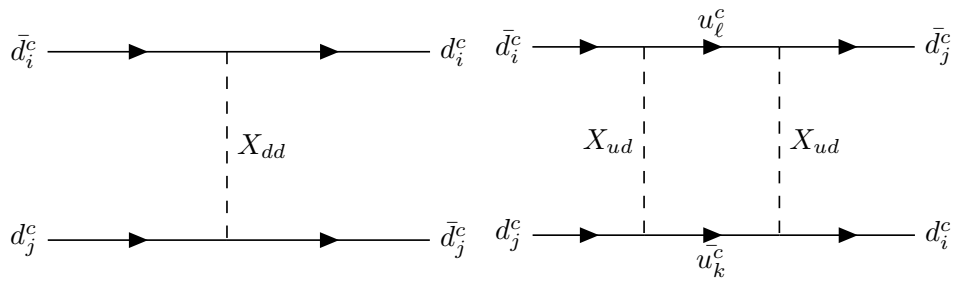

Figure 8.12.: Meson oscillation diagrams mediated by X_{dd} at tree-level (left) and X_{ud} at loop-level (right). This figure is taken from Ref. [2].

Mixing between the neutral mesons M and $\overline{M}$ can be described by the matrix element

$$\mathcal{M}_{M\overline{M}} = \langle M|H_{\text{eff}}|\overline{M}\rangle = \sum_j (C_j^{\text{SM}} + C_j^{\text{NP}})\langle M|\mathcal{O}_j|\overline{M}\rangle\,, \tag{8.110}$$

where $\mathcal{O}_j$ are four-quark operators with associated SM and NP Wilson coefficients C_j^{SM} and C_j^{NP}, respectively.

For B-meson oscillation $B_q - \overline{B_q}$, the SM contribution comes from the operator

$$\mathcal{O}_{V_L} = (\bar{q}\gamma_\mu P_L b)(\bar{q}\gamma^\mu P_L b)\,, \tag{8.111}$$

where the Wilson coefficient is given by [653]

$$C_{V_L}^{\text{SM}} = \frac{G_F^2}{4\pi^2} m_W^2 \hat{\eta}_B S_0(x_t)(V_{tb}V_{td(s)}^*)^2\,. \tag{8.112}$$

Here $\hat{\eta}_B = 0.8393$ comes from QCD-corrections, and $S_0(x_t) = 2.35$ with $x_t = \overline{m}_t^2/m_W^2$ is the Inami-Lim function corresponding to the SM top-quark box diagram. For kaon oscillations $K - \overline{K}$, the SM operator and Wilson coefficients are given by [653]

$$\mathcal{O}_{V_L} = (\bar{d}\gamma_\mu P_L s)(\bar{d}\gamma^\mu P_L s)\,, \tag{8.113}$$

and

$$C_{V_L}^{\text{SM}} = \frac{G_F^2}{4\pi^2} m_W^2 \Big(\eta_{tt} S_0(x_t)(V_{ts}V_{td}^*)^2 + \eta_{cc} S_0(x_c)(V_{cs}V_{cd}^*)^2 + 2\eta_{ct} S_0(x_c, x_t) V_{ts}V_{td}^* V_{cs}V_{cd}^*\Big)\,, \tag{8.114}$$

respectively, where $\eta_{tt} = 0.5765$, $\eta_{cc} = 1.39\ (1.29\,\text{GeV}/\overline{m}_c)^{1.1}$, and $\eta_{ct} = 0.47$ come from QCD-corrections, and $S_0(x_c) \approx x_c$, $S_0(x_c, x_t) \approx -x_c \log(x_c) + 0.56 x_c$ with $x_c = \overline{m}_c^2/m_W^2$ is the Inami-Lim function including the charm-quark box diagram.

The NP contribution to neutral meson oscillation coming from the diquarks X_{ud} or X_{dd} can be described by the operator [357]

$$\mathcal{O}_{V_R} = (\bar{d}_j\gamma_\mu P_R d_i)(\bar{d}_j\gamma^\mu P_R d_i)\,, \tag{8.115}$$

Observable	Diagram	Constraint
Δ_{B_s}	tree-level	$\left\|f^{dd}_{22}(f^{dd}_{33})^*\right\| \lesssim 3.1\times10^{-4}\ (m_{X_{dd}}/\text{TeV})^2$ [656]
	one-loop	$\left\|\sum_k \widehat{f}^{ud}_{k2}(\widehat{f}^{ud}_{k3})^*\right\| \lesssim 0.36\ (m_{X_{ud}}/\text{TeV})$ [656]
Δ_{B_d}	tree-level	$\left\|f^{dd}_{11}(f^{dd}_{33})^*\right\| \lesssim 1.5\times10^{-5}\ (m_{X_{dd}}/\text{TeV})^2$ [656]
	one-loop	$\left\|\sum_k \widehat{f}^{ud}_{k3}(\widehat{f}^{ud}_{k1})^*\right\| \lesssim 0.08\ (m_{X_{ud}}/\text{TeV})$ [656]
Δm_K	tree-level	$\left\|f^{dd}_{11}(f^{dd}_{22})^*\right\| \lesssim 2.2\times10^{-6}\ (m_{X_{dd}}/\text{TeV})^2$ [657]
	one-loop	$\left\|\sum_k \widehat{f}^{ud}_{k2}(\widehat{f}^{ud}_{k1})^*\right\| \lesssim 0.03\ (m_{X_{ud}}/\text{TeV})$ [657]

Table 8.8.: Constraints at 95% CL on the mass and coupling of diquarks X_{ud} and X_{dd} coming from $B^0_s - \overline{B^0_s}$, $B^0_d - \overline{B^0_d}$, and $K^0 - \overline{K^0}$.

where the quarks d_i and d_j should be taken as $(d_i, d_j) = (s,b)$, (d,b), (d,s) for B_s, B_d, and K oscillation, respectively. Diagrams corresponding to these oscillations are shown in Fig. 8.12, where X_{dd} only gives rise to tree-level diagrams for flavour-diagonal couplings f_{dd}, while X_{ud} only leads to loop-level diagrams due to its coupling to both up- and down-type quarks rather than two quarks of the same type [654,655]. For X_{dd}, this tree-level exchange leads to the Wilson coefficient

$$C^{\text{NP}}_{V_R} = -\frac{1}{2}\frac{f^{dd}_{ii}(f^{dd}_{jj})^*}{m^2_{X_{dd}}}\,, \tag{8.116}$$

while the box-diagram involving X_{ud} exchange, assuming a flavour-symmetric coupling matrix f_{ud}, leads to [357]

$$C^{\text{NP}}_{V_R} = \frac{3}{256\pi^2}\frac{1}{m^2_{X_{ud}}}\left[\widehat{f}^{ud}_{ki}(\widehat{f}^{ud}_{kj})^*\right]^2\,, \tag{8.117}$$

where $\widehat{f}^{ud}_{ij} = (V_R)_{ik} f^{ud}_{kj}$, with V_R being the matrix that diagonalises the right-handed quark charged current.

Following Refs. [653,656–658] we now consider the ratio between the total and SM-mediated meson oscillation contributions,

$$\Delta_M = \frac{\langle M|H_{\text{eff}}|\overline{M}\rangle}{\langle M|H^{\text{SM}}_{\text{eff}}|\overline{M}\rangle} = 1 + \frac{C^{\text{NP}}}{C^{\text{SM}}}\,, \tag{8.118}$$

where the complex parameter Δ_M is experimentally constrained at 95% CL to $\Delta_{B_{s(d)}} = 1.11^{+0.96}_{-0.48}$ $(1.05^{+1.0}_{-0.52})$ for B-mesons and $\text{Re}(\Delta_K) = 0.93^{+1.14}_{-0.43}$, $\text{Im}(\Delta_K) = 0.92^{+0.39}_{-0.26}$ for kaons [656, 657]. These constraints can be translated into limits on the masses and couplings of the diquarks,

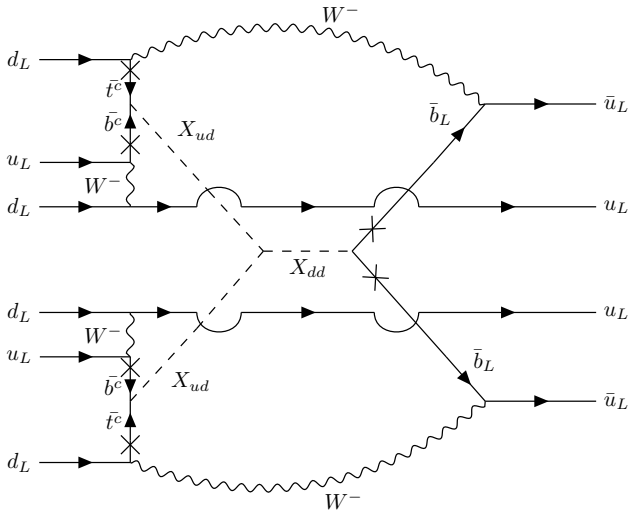

Figure 8.13.: A diagram showing the dinucleon decay $nn \to \pi^0\pi^0$ at two-loop level with third-generation diquark couplings. This figure is taken from Ref. [2].

as shown in Tab. 8.8. Here we see that kaon oscillations provide the most stringent limits, especially on the mass and coupling of X_{dd}.

Apart from meson oscillations, diquarks can lead to other flavour-changing neutral current (FCNC) processes such as non-leptonic rare meson decays [357, 629]. However, such constraints are generally weaker than those coming from meson oscillations.

8.5.3. Dinucleon decay

A $\Delta B = 2$ process that can be induced by scalar diquarks, apart from n-$\bar{n}$ oscillations, is dinucleon decay, e.g. $nn \to \pi^0\pi^0$. This decay mode involves couplings between diquarks and first-generation quarks, effectively constraining the same parameters as n-$\bar{n}$ oscillation. Due to large uncertainties in the dinucleon decay matrix elements, n-$\bar{n}$ oscillation leads to more reliable constraints for these parameters. However, dinucleon decay could still be a leading probe of $\Delta B = 2$ interactions in the special case where the diquarks most dominantly couple to third generation quarks. In such a scenario, the leading contribution to n-$\bar{n}$ oscillation would be found at 3-loop order, while two loops are sufficient to mediate $nn \to \pi^0\pi^0$ decays, as illustrated in[16] Fig. 8.13. This reduced number of loops could potentially lead to stronger limits coming from dinucleon decay than n-$\bar{n}$ oscillation.

[16]Note that the mass insertions in Fig. 8.13 are needed in order to flip the helicities of the quarks, since W-bosons only interact with left-handed quarks while for the model we considered in Sec. 8.3.1 the diquarks only interact with right-handed quarks. We ignore these mass insertions for the subsequent analysis of this section in the interest of simplification. The resulting uncertainty in the final result coming from this simplification is overshadowed by the uncertainty in the nuclear matrix elements corresponding to dinucleon decay.

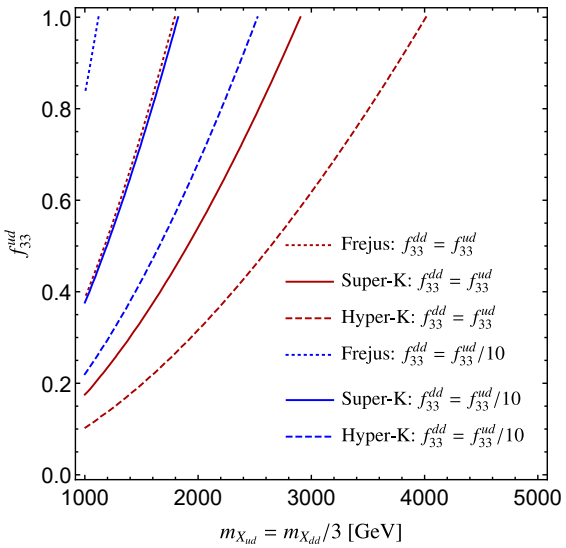

Figure 8.14.: Exclusion limits in the coupling-mass plane from different dinucleon decay experiments, assuming the two-loop diquark-mediated dinucleon decay mode to be the most dominant. Red lines correspond to equal couplings $f^{dd} = f^{ud}$, and blue lines to a coupling hierarchy $f^{ud} = 10 f^{dd}$. This figure is taken from Ref. [2].

The two-loop dinucleon decay rate is given by [596]

$$\Gamma \simeq \frac{9}{32\pi} \frac{|\mathcal{C}_{\rm DN}|^2}{m_n^2} |\langle \pi^0 \pi^0 | \mathcal{O}_{\rm DN}^{15} | nn \rangle|^2 \rho_n \,, \tag{8.119}$$

where m_n is the mass of the neutron, and $\rho_n \simeq 0.25\,\mathrm{fm}^{-3}$ is the nuclear density. The nuclear matrix element $|\langle \pi^0 \pi^0 | \mathcal{O}_{\rm DN}^{15} | nn \rangle|$ corresponding to a 15-dimensional operator has mass dimension eleven, such that $|\langle \pi^0 \pi^0 | \mathcal{O}_{\rm DN}^{15} | nn \rangle| \sim \Lambda^{11}$. In the absence of accurate nuclear matrix element calculations, we assume that Λ lies somewhere between $\Lambda_{\rm QCD}$ and m_n, and in the interest of deriving conservative limits we chose $\Lambda = m_n$ in the subsequent analysis. Here we omit some steps in the calculation of the dinucleon decay rate. The interested reader is referred to Ref. [2].

The most stringent experimental limit on the $nn \to \pi^0\pi^0$ decay mode of $\tau > 4.04 \times 10^{32}$ years comes from the Super-Kamiokande experiment [659], where τ is the partial lifetime. This limit can be compared with an earlier limit $\tau > 3.4 \times 10^{30}$ years from the Frejus experiment [660]. In the future, the Hyper-Kamiokande experiment is expected to set constraints that improve over existing bounds by an order of magnitude [661].

In Fig. 8.14 we show the past, current, and future experimental limits in the diquark mass-coupling plane, where the masses are related via $m_{X_{dd}} = 3 m_{X_{ud}}$, and the couplings are related via $f_{ud} = f_{ud}$ (red lines) and $f_{ud} = 10 f_{ud}$ (blue lines).

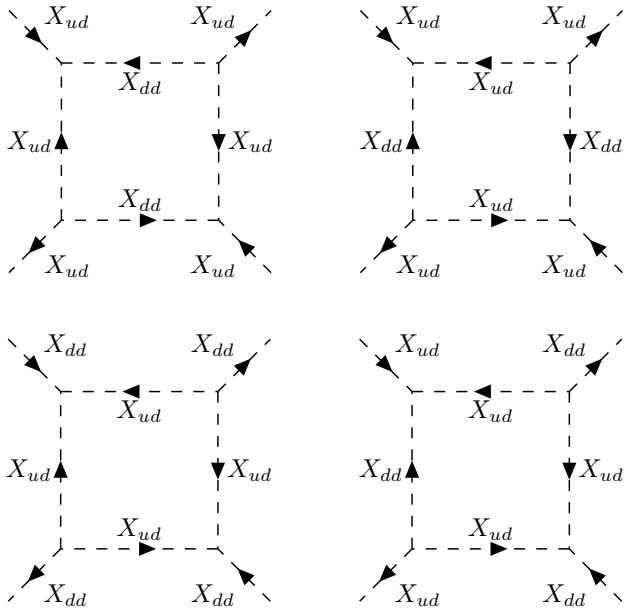

Figure 8.15.: Diagrams involving only the trilinear coupling $\mu X_{dd} X_{ud} X_{ud}$ that give rise to effective quartic interaction terms. This figure is taken from Ref. [2].

8.5.4. Colour-preserving vacuum

The trilinear diquark coupling $\mathcal{L} \supset \mu X_{dd} X_{ud} X_{ud}$, where the dimensionful coupling $\mu = \lambda v'$ arises from the vev v' of ξ (c.f. Sec. 8.3.1), can be constrained by the requirement that the vacuum should preserve colour charge. As illustrated in Fig. 8.15, combining multiple instances of this term can lead to effective quartic interactions according to the Lagrangian

$$-\mathcal{L}_{\text{eff}} = \lambda_{\text{eff}} (X_{ud})^2 (X_{ud}^\dagger)^2 \; + \; \lambda'_{\text{eff}} (X_{dd})^2 (X_{dd}^\dagger)^2 \; + \; \lambda''_{\text{eff}} (X_{ud} X_{ud}^\dagger)(X_{dd} X_{dd}^\dagger) \,, \tag{8.120}$$

where the effective coupling constants are given by [662]

$$\lambda_{\text{eff}} \;\sim\; -\frac{1}{2\pi^2} \frac{\mu^4}{(m^2_{X_{dd}} - m^2_{X_{ud}})^2} \left[\frac{m^2_{X_{dd}} + m^2_{X_{ud}}}{m^2_{X_{dd}} - m^2_{X_{ud}}} \log\left(\frac{m^2_{X_{dd}}}{m^2_{X_{ud}}} \right) \; - \; 2 \right] , \tag{8.121}$$

$$\lambda'_{\text{eff}} \;\sim\; -\frac{1}{4\pi^2} \frac{\mu^4}{6 m^4_{X_{ud}}} , \tag{8.122}$$

$$\lambda''_{\text{eff}} \;\sim\; -\frac{1}{\pi^2} \frac{\mu^4 m^2_{X_{dd}}}{2(m^2_{X_{dd}} - m^2_{X_{ud}})^3} \left[\frac{m^2_{X_{dd}}}{m^2_{X_{ud}}} - \frac{m^2_{X_{ud}}}{m^2_{X_{dd}}} - 2\log\left(\frac{m^2_{X_{dd}}}{m^2_{X_{ud}}} \right) \right] . \tag{8.123}$$

For the case where the two masses are of the same scale, $m_{X_{ud}} \approx m_{X_{dd}}$, we have the relation [2]

$$2\lambda_{\text{eff}} \;\approx\; \lambda''_{\text{eff}} \;\approx\; 4\lambda'_{\text{eff}} \;=\; -\frac{1}{\pi^2} \frac{\mu^4}{6 m^4_{X_{ud}}} . \tag{8.124}$$

The fact that the couplings in Eq. (8.124) are negative leads to a colour non-preserving vacuum, which is inconsistent with the SM. To account for this discrepancy, either additional positive quartic couplings or new colour-charged scalar fields must be added to the model.

In order for the effective quartic couplings to lead to a perturbative theory, we have the requirement $\lambda_{\text{eff}}, \lambda'_{\text{eff}}, \lambda''_{\text{eff}} < 4\pi$, which leads to constraints on the dimensionful coupling μ given by

$$\mu \;<\; \begin{cases} m_{X_{ud}} \times (24\pi^3)^{1/4} & \text{for } m_{X_{dd}} \sim m_{X_{ud}}\,, \\ m_{X_{ud}} \times (96\pi^3)^{1/4} & \text{for } m_{X_{dd}} > m_{X_{ud}}\,. \end{cases} \tag{8.125}$$

For the numerical study in Sec. 8.6, we choose $\mu = \lambda v' \approx m_{X_{dd}}$ for the scenarios where there is a small mass hierarchy between X_{ud} and X_{dd}, in order to preserve perturbativity. For large hierarchies, e.g. when $m_{X_{dd}}$ is of $\mathcal{O}(m_{\text{GUT}})$ while X_{ud} is of $\mathcal{O}(1\text{ TeV})$, we can integrate out X_{dd} from the effective quartic interactions to find the perturbativity constraint $\lambda_{\text{eff}} < 4\pi$ satisfied by the condition

$$\mu \sim \mathcal{O}\left(m_{X_{dd}}\right) \quad \text{for} \quad m_{X_{dd}} \gg T > m_{X_{ud}}\,. \tag{8.126}$$

Additionally considering the effects coming from X_{uu} with $m_{X_{uu}} \sim \mathcal{O}(m_{\text{GUT}})$ can lead to λ'_{eff} and λ''_{eff} not exceeding the values of the corresponding tree-level terms [617].

8.6. Probing baryogenesis with neutron-antineutron oscillation

It this section, we wish to explore the parameter space of the model described in Sec. 8.3.1 including n-$\bar{n}$ oscillation constraints, as well as the other probes described in Sec. 8.5. We are particularly interested in the final baryon asymmetry generated via the mechanism described in Sec. 8.3.2. Our central question is: can successful baryogenesis be achieved in the diquark model using parameters that are not excluded, but that could potentially be probed in upcoming experiments, in particular by next-generation n-$\bar{n}$ oscillation searches?

Based on the different considerations outlined in Sec. 8.5, we identify two benchmark scenarios that are of special interest, which we denote as the high- and low-scale scenarios:

High-scale scenario: In the high-scale scenario, we set the mass of X_{dd}, as well as the trilinear coupling constant $\lambda v'$, close to the GUT scale, while keeping X_{ud} within experimental reach of collider experiments. We then have $m_{X_{dd}} \approx \lambda v' \sim \mathcal{O}(10^{13} - 10^{14}\text{ GeV})$ and $m_{X_{ud}} \sim \mathcal{O}(10^3 - 10^4\text{ GeV})$, for couplings f_{ud}, $f_{dd} \sim 10^{-3} - 1$.
Low-scale scenario: In the low-scale scenario, we keep a tight hierarchy between X_{dd} and X_{ud}, such that their masses are approximately the same while still satisfying the condition $m_{X_{dd}} > 2m_{X_{ud}}$ needed for baryogenesis. Specifically we choose $m_{X_{dd}} = 3m_{X_{ud}}$, and for the trilinear coupling we further choose $\lambda v' = 1.2 m_{X_{dd}}$. As in the high-scale scenario, the quark-diquark couplings are kept in the range f_{ud}, $f_{dd} \sim 10^{-3} - 1$.

T(GeV)	Process	High-scale	Low-scale
$\gg 10^{13}$	Gauge interactions + t Yukawa	✓	✓
$> 10^{13}$	QCD sphaleron	✓	✓
$\sim 10^{13}$	EW sphaleron + b Yukawa	✓	✓
$\sim 10^{12}$	τ Yukawa	✓	✓
$\sim 10^{12}$	c Yukawa	✗	✓
$\sim 10^{10}$	μ, s Yukawa	✗	✓
$\ll 10^{8}$	u, d, e Yukawa	✗	✓

Table 8.9.: Temperatures at which various SM processes are expected to come into equilibrium [86]. Ticks indicate that the processes is assumed to be in equilibrium in the corresponding benchmark scenario shown in the top row, and crosses indicate that this assumption is not made.

Assuming that baryogenesis occurs via out-of-equilibrium decay of X_{dd} in the model described in Sec. 8.3.2, we evaluate the Boltzmann equations from Sec. 8.3.2 to find the value of the final baryon asymmetry. For both benchmark scenarios we define the CP-violation parameter ϵ under the simplifying assumption that the couplings of X_{dd} and X'_{dd} are related via $f'_{dd} = i f_{dd}$ and $\lambda' = \lambda$, where $f_{dd} \in \mathbb{R}$, such that

$$\epsilon = \frac{1}{\pi} \mathrm{Tr}\left[(f_{dd})^\dagger f_{dd}\right] \left(\frac{x}{1-x}\right) r\,. \tag{8.127}$$

Here we have further defined $x \equiv (m_{X_{dd}}/m'_{X_{dd}})^2$ and use $r = \mathrm{BR}\left(X_{dd} \to X^*_{ud} X^*_{ud}\right)$. The maximum value of ϵ is $\epsilon_{\mathrm{Max}} = 2r$, which can be compared to the value obtained from Eq. (8.127) in different benchmark scenarios. Below we denote these values for ϵ as the *maximum* and *loop-induced* values, respectively. Unless otherwise stated, we use $x = 0.2$ as an example case for the loop-induced ϵ.

For both the high- and low-scale scenarios we assume flavour-universal and flavour-diagonal couplings, such that f_{dd}, $f_{ud} \propto \mathbb{1}$. However, in the high-scale scenario we only consider the couplings to third generation quarks to affect the baryogenesis mechanism, due to the late onset of the other Yukawa couplings with respect to the scale of X_{dd}.

In the early Universe, different SM process come into equilibrium at different times, as discussed in Sec. 2.2.2. In Tab. 8.9, we show the approximate temperatures at which the gauge- and Yukawa interactions, as well as the two sphaleron processes, reach chemical equilibrium. In the last and second-to-last columns we denote which interactions are assumed to be in

equilibrium for the two benchmark scenarios, respectively.

In the next two sections, we show the results in the high- and low-scale scenarios respectively, by comparing the parameter space leading to successful baryogenesis with the regions excluded by different experimental searches.

8.6.1. High-scale scenario

Apart from n-$\bar{n}$ oscillation and baryogenesis, the high-scale scenario offers a connection to both grand unification and collider searches. In Sec. 8.4 we saw that a $\mathcal{O}(1\text{ TeV})$ scale X_{ud} can lead to gauge coupling unification at $m_{X_{dd}} \approx m_{\text{GUT}}$ in the presence of minor additional adjustments to the model. Furthermore, being at such low scales, the diquark X_{ud} can potentially be found in future collider searches at the LHC, HE-LHC, or FCC-hh, as was discussed in Sec. 8.5.1.

In Fig. 8.16, we show the evolution of $\eta_{X_{dd}}$ and $\eta_{\Delta B}$ with respect to the time-variable $z = m_{X_{dd}}/T$, as evaluated using Eqs. (8.49) and (8.49) from Sec. 8.3.2 in the high-scale scenario with $m_{X_{dd}} = 10^{14}$ GeV (left column) and $m_{X_{dd}} = 10^{13}$ GeV (right column), where the rest of the parameters are chosen as $f_{ud} = f_{dd} = 0.05$, $\lambda v' = 1.5 m_{X_{dd}}$, and $m_{X_{ud}} = 5$ TeV. Here the blue line shows the number density of X_{dd}, and the dashed green line is its equilibrium value. The orange line corresponds to the baryon asymmetry $\eta_{\Delta B}$ for the maximum value of the CP-violating parameter $\epsilon = \epsilon_{\text{Max}} = 2r$, while the red line shows $\eta_{\Delta B}$ for the loop-induced $\epsilon \approx 4 \times 10^{-4}$ as evaluated using Eq. (8.127) for $x = 0.2$.

In the top row of Fig. 8.16, the evaluation is performed assuming that X_{dd} is initially in equilibrium, while for the bottom row the condition $\eta_{X_{dd}}(z \to 0) = 0$ is used[17]. The fact that identical final asymmetries are found using both initial conditions motivates the simplification of neglecting $gg \to X_{dd} X_{dd}^*$ interactions in the derivation of Eq. (8.49). Such production processes would rapidly bring X_{dd} into equilibrium at low z, however we see in Fig. 8.16 that this has no effect on the final baryon asymmetry.

For the parameters used in Fig. 8.16, we see that the baryon asymmetry is about two orders of magnitude too large as compared to the observed value for the loop-induced ϵ, and six orders of magnitude too large for the maximum ϵ. Fig. 8.16 highlights the fact that large asymmetries can be generated in the high-scale scenario, a lower final baryon asymmetry can easily be accommodated using smaller couplings or a greater X'_{dd}-mass.

In Fig. 8.17 we show the final baryon asymmetry in the $m_{X_{ud}}$-f_{ud}-plane for $f_{ud} = f_{dd}$ and $\lambda v' = 1.5 m_{X_{dd}}$. The top row is evaluated for loop-induced ϵ, and in the bottom row the maximum value is taken. For the left column we use $m_{X_{dd}} = 10^{14}$ GeV and the right $m_{X_{dd}} = 10^{13}$ GeV. The yellower a region, the greater the final baryon asymmetry, with the observed value $\eta_B^{\text{obs}} = 6.2 \times 10^{-10}$ being represented by a red line. Stars show the benchmark scenarios used in Fig. 8.16, and the black and (solid, dashed) blue lines show exclusion limits from LHC- and (current, future) n-$\bar{n}$ oscillation searches, respectively.

There is no dependence on the mass of X_{ud} for the final baryon asymmetry, as can be

[17] Note that the dip in $\eta_{\Delta B}$ around $z = 0.1 - 1$ in Fig. 8.16 comes from the fact that $\eta_{\Delta B}$ flips sign as X_{dd} goes from being under- to overabundant (i.e. when $\eta_{X_{dd}}/\eta_{X_{dd}}^{\text{eq}}$ becomes greater than one).

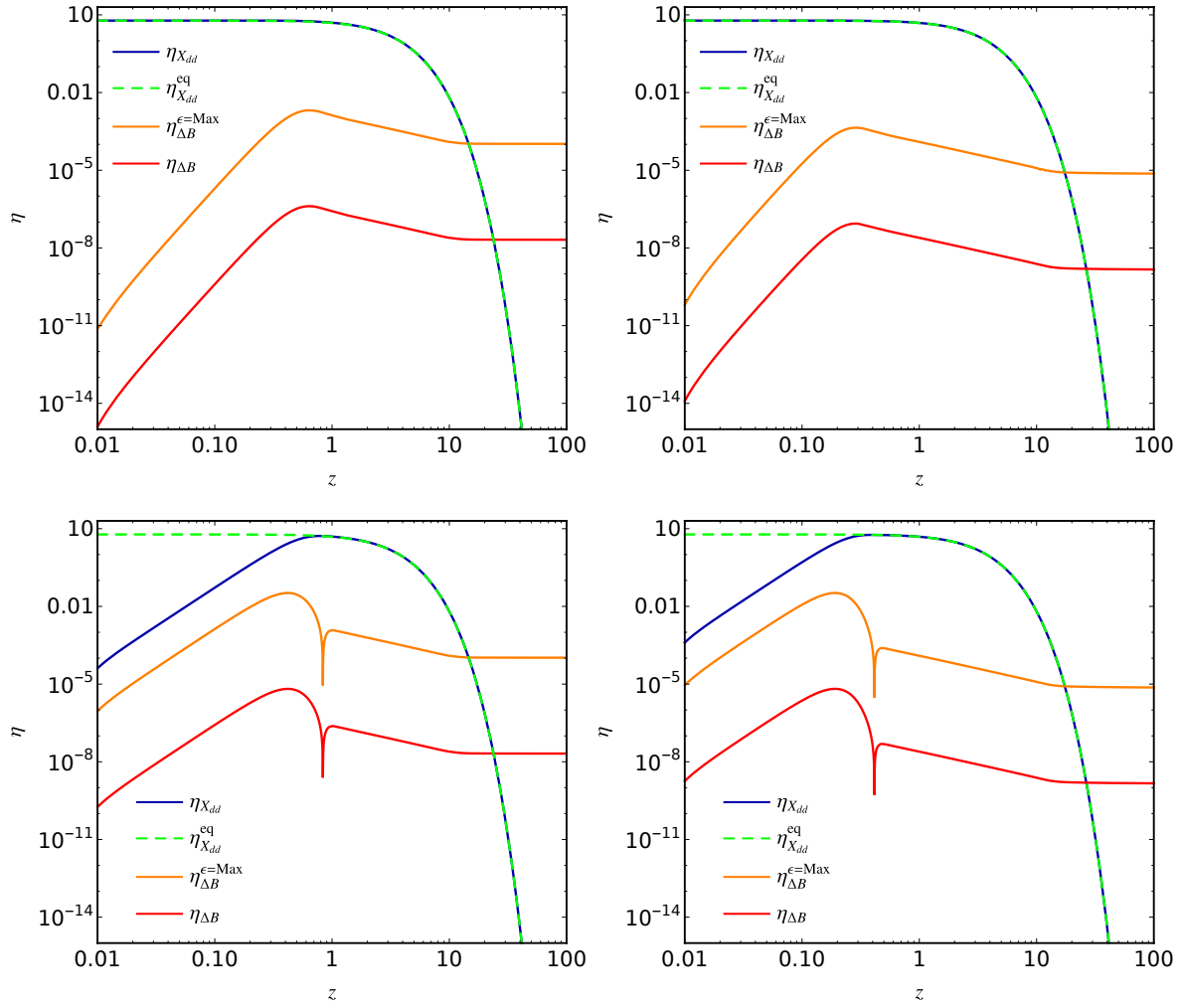

Figure 8.16.: Evolution of the baryon asymmetry $\eta_{\Delta B}$ and X_{dd} number density $\eta_{X_{dd}}$ with respect to $z = m_{X_{dd}}/T$ in the high-scale scenario, with $m_{X_{dd}} = 10^{14}$ GeV (left column) and $m_{X_{dd}} = 10^{13}$ GeV (right column). Here the different parameters are given by $f_{ud} = f_{dd} = 0.05$, $\lambda v' = 1.5 m_{X_{dd}}$, and $m_{X_{ud}} = 5$ TeV. The baryon asymmetry is evaluated for both maximum CP-violation (orange lines) and loop-induced CP-violation (red lines), for X_{dd} being initially in equilibrium (top row) or having a vanishing initial abundance (bottom row). This figure is taken from Ref. [2].

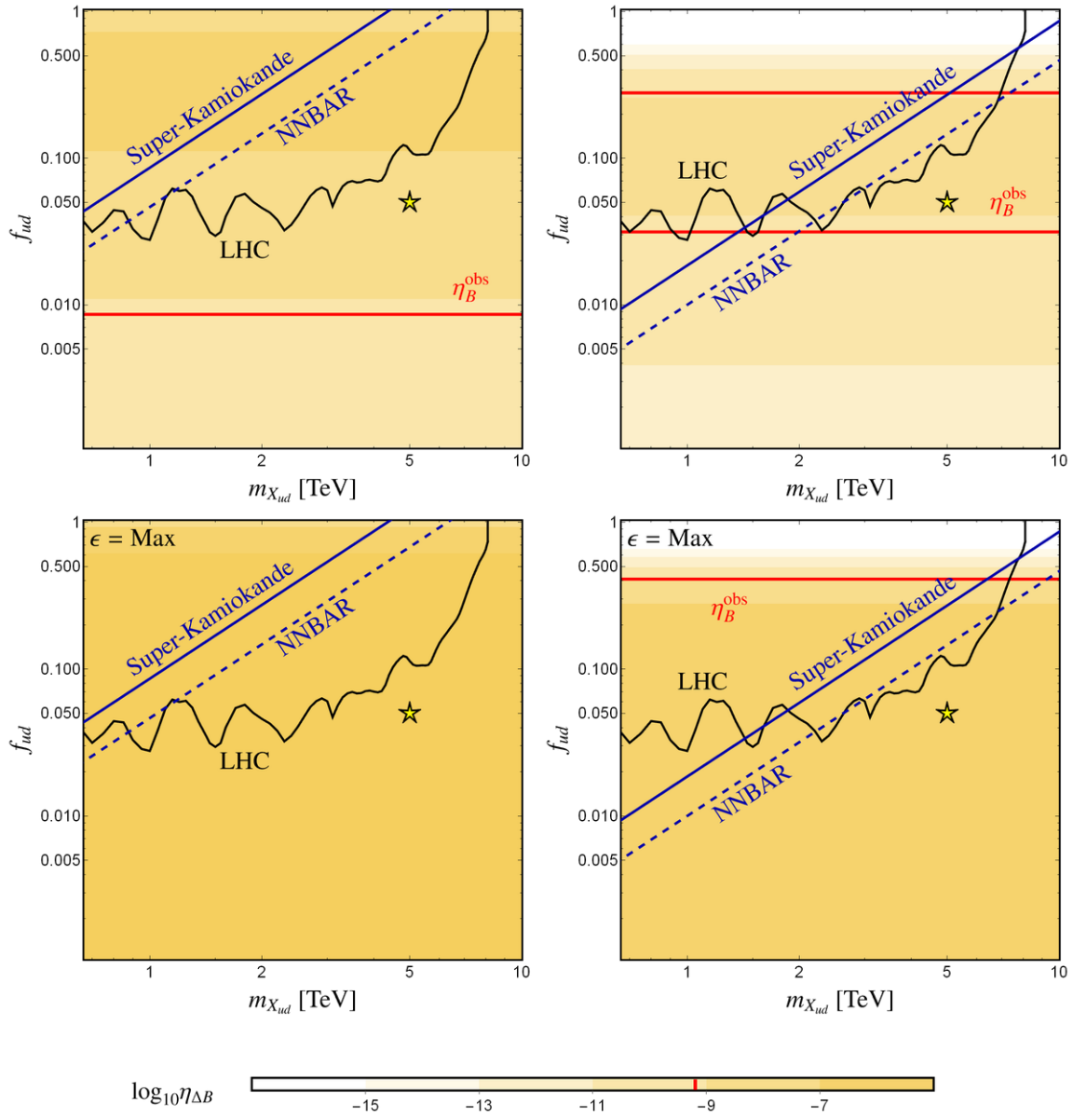

Figure 8.17.: Final baryon asymmetry in the $m_{X_{ud}}$-f_{ud}-plane for the high-scale scenario, with $m_{X_{dd}} = 10^{14}$ GeV (left column) and $m_{X_{dd}} = 10^{13}$ GeV (right column), for both loop-induced (top row) and maximum (bottom row) CP-violation, using the couplings $\lambda v' = 1.5 m_{X_{dd}}$ and $f_{dd} = f_{ud}$. Here the black and blue (solid, dashed) lines correspond to exclusion limits from the LHC and (current, future) n-$\bar{n}$ oscillation searches. This figure is taken from Ref. [2].

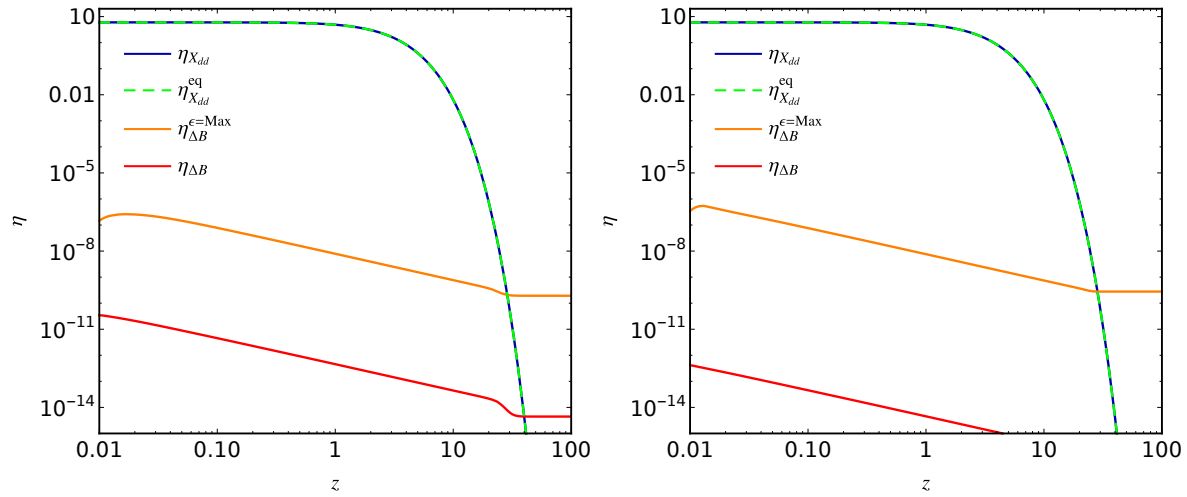

Figure 8.18.: Evolution of the baryon asymmetry $\eta_{\Delta B}$ and X_{dd} number density $\eta_{X_{dd}}$ with respect to $z = m_{X_{dd}}/T$ in the low-scale scenario, with $f_{ud} = f_{dd} = 0.05$ (left) and $f_{ud=}10 f_{dd} = 0.05$ (right). Here the different parameters are given by $m_{X_{dd}} = 3 \times 10^8$ GeV, $m_{X_{ud}} = 10^8$ GeV, and $\lambda v' = 1.2 m_{X_{dd}}$. The baryon asymmetry is evaluated for both maximum CP-violation (orange lines) and loop-induced CP-violation (red lines). This figure is taken from Ref. [2].

expected from the fact that baryogenesis occurs at very high scales $T \sim m_{X_{dd}} \gg m_{X_{ud}}$, where X_{ud} is effectively massless. For large couplings f_{ud} the final asymmetry is smaller, due to increased washout from X_{dd}-mediated scattering processes. For the loop-induced ϵ, a smaller asymmetry is also found for lower values of f_{ud}, due to reduced CP-violation (c.f. Eq. (8.127) keeping in mind that we here use $f_{ud} = f_{dd}$).

We see in Fig. 8.17 that LHC constraints are competitive with n-$\bar{n}$ oscillation searches for large parts of the parameter space in the high-scale scenario. Interestingly, these regions are also compatible with a large baryon asymmetry. We then conclude that the baryogenesis mechanism described in Sec. 8.3.2 can lead to the observed baryon asymmetry for parameters that could lead to signals in future n-$\bar{n}$ oscillation experiments as well as collider searches.

8.6.2. Low-scale scenario

The low-scale scenario offers a good comparison of the diquark model with the EFT-description of n-$\bar{n}$ oscillation and baryogenesis described in Secs. 8.1 and 8.2. Due to a small hierarchy in the internal degrees of freedom, many processes in the low-scale scenario are well described by only a single heavy scale $\Lambda \sim m_{X_{dd}} \sim m_{X_{ud}}$.

In Fig. 8.18 we show the evolution of the baryon asymmetry and X_{dd} number density in the low-scale scenario, for both maximum (orange lines) and loop-induced (red lines)

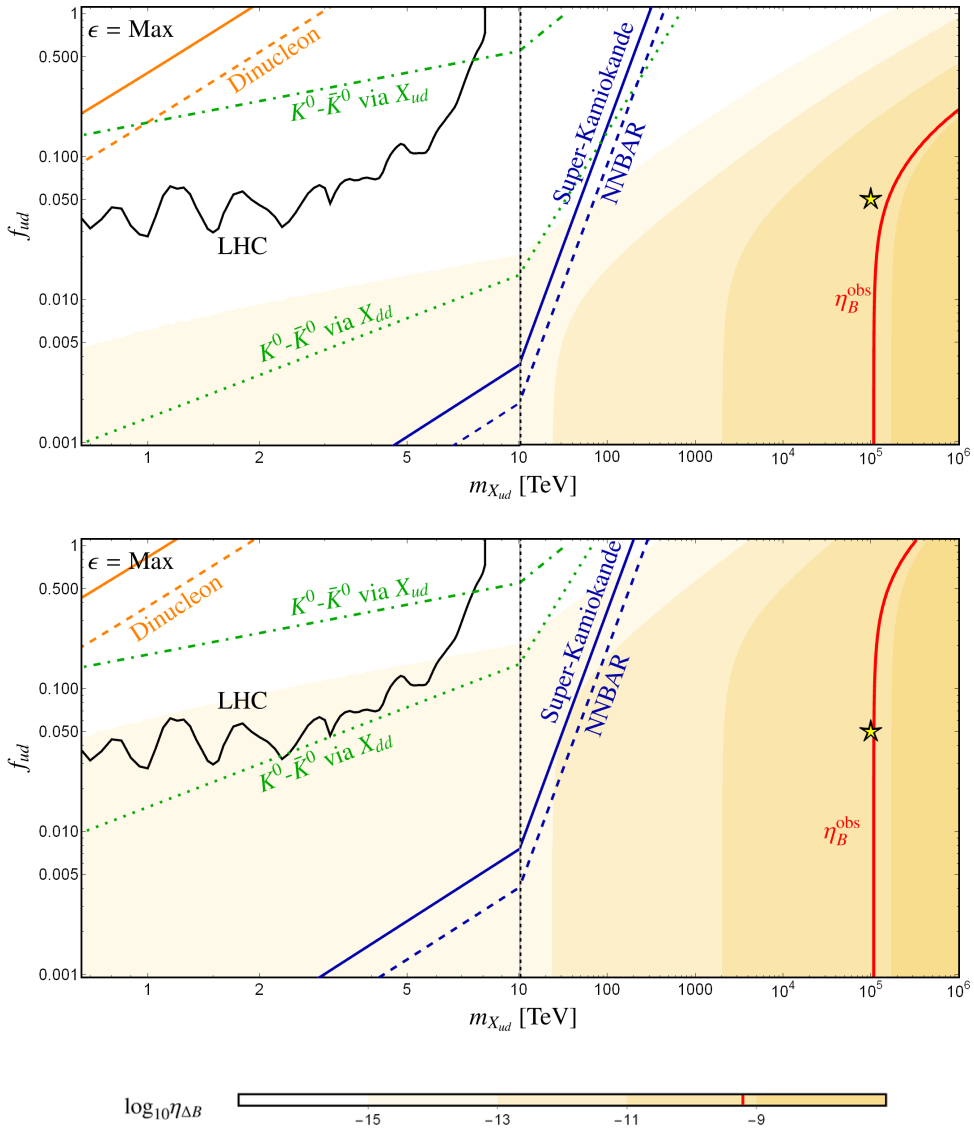

Figure 8.19.: Final baryon asymmetry in the $m_{X_{ud}}$-f_{ud}-plane for the low-scale scenario, with $f_{ud} = f_{dd} = 0.05$ (top) and $f_{ud} = 10 f_{dd} = 0.05$ (bottom), for maximum CP-violation only, using the trilinear coupling $\lambda v' = 1.2 m_{X_{dd}}$ and mass hierarchy $m_{X_{dd}} = 3 m_{X_{ud}}$. Here the orange (solid, dashed), green, black, and blue (solid, dashed) lines correspond to exclusion limits from (current, future) dinucleon decay searches, meson oscillations, the LHC, and (current, future) n-$\bar{n}$ oscillation searches.

ϵ. We here use the parameters $m_{X_{ud}} = \frac{1}{3} m_{X_{dd}} = 10^8$ GeV, $\lambda v' = 1.2 m_{X_{dd}}$, and the couplings $f_{ud} = f_{dd} = 0.05$ (Fig. 8.18 left) and $f_{ud} = 10 f_{dd} = 0.05$ (right).

The final baryon asymmetry for these parameters is significantly lower than our example in the high-scale scenario (c.f. Fig. 8.16), due mainly to the difference in scale at which baryogenesis occurs[18]. In Fig. 8.18 (left) there is a sudden drop in $\eta_{\Delta B}$ (red line) around $z \sim 20$ followed by a freeze-out around $z \sim 30$. The drop comes from X_{dd}-mediated washout starting to dominate due to the reduction in X_{dd} decay-rates, which reduces the asymmetry. However, due to the small hierarchy between X_{dd} and X_{ud}, the washout is only effective for a short period of time until the temperature drops too low to generate an on-shell pair of X_{ud}, and the $\eta_{\Delta B}$ therefore freezes out. For a large coupling hierarchy $f_{ud} = 10 f_{dd}$ (Fig. 8.18 right) the final asymmetry generated using the maximum value of ϵ (orange line) is greater than the corresponding value for a vanishing hierarchy $f_{ud} = f_{dd}$ (c.f. orange line in Fig. 8.18 left), due to reduced washout. However, for the loop-induced ϵ (red lines in Fig 8.18 left and right), the final baryon asymmetry is smaller for $f_{ud} = 10 f_{dd}$ than for $f_{ud} = f_{dd}$. The reason for this is that a hierarchy $f_{ud} = 10 f_{dd}$ implies a smaller CP-violation parameter $\epsilon \approx 4 \times 10^{-5}$ as compared to $\epsilon \approx 4 \times 10^{-3}$ for $f_{ud} = f_{dd}$, leading to a smaller asymmetry even though the washout is reduced.

In Fig. 8.19 we see the final baryon asymmetry for the low-scale scenario in the $m_{X_{ud}}$-f_{ud}-plane, evaluated using the formalism in Sec. 8.3.2. Yellow shades indicate the value of $\eta_{\Delta B}$, where the red line shows the observed value $\eta_B^{\text{obs}} = 6.2 \times 10^{-10}$ and the stars indicate the benchmark scenarios in Fig. 8.18. Orange, green, black, and blue lines correspond to experimental constraints coming from dinucleon decay, meson oscillation, LHC, and n-$\bar{n}$ oscillation, respectively. For dinucleon decay and n-$\bar{n}$ oscillation, solid lines correspond to current constraints while dashed lines show future projections. We see that the regions of parameter space that lead to successful baryogenesis lies far outside the reach of any current or near-future experimental reach. This result mimics the EFT-based-baryogenesis analysis in Sec. 8.2, where washout was found to be strong down to relatively low scales, leading to a vanishing baryon asymmetry. Therefore, the low-scale scenario is of small phenomenological impact as a mechanism for baryon-asymmetry generation, but still interesting with respect to excluding various high-scale baryogenesis mechanisms in case of a n-$\bar{n}$ signal in future experiments [2].

In Fig. 8.20 we show how the different reaction rates compare in the high- and low-scale scenarios for the two benchmarks shown in Figs. 8.16 (left column) and 8.18 (left), respectively. In both cases, the most dominant washout comes from X_{dd}-mediated scatterings, shown in green as the sum of $\gamma_{X_s}^{\text{eq}}$ and $\gamma_{X_t}^{\text{eq}}$ (c.f. Sec. 8.3.2).

In the high-scale scenario, the washout processes start to dominate over the decay rate γ_D^{eq} around the same time as $\eta_{\Delta B}$ freezes out, leading to a very small washout. For higher values of the coupling $f_{ud} = f_{dd}$, the washout starts slightly earlier, which can effectively remove the entire asymmetry (c.f. the top regions of each plot in Fig. 8.17).

[18] Higher baryogenesis scales generally lead to greater asymmetries since the Hubble rate $H \propto T^2$ is smaller at higher temperatures, leading to smaller reaction rates Γ being needed to satisfy the condition $\Gamma/H > 1$, which in turn determines whether Γ has an effect on the baryon asymmetry.

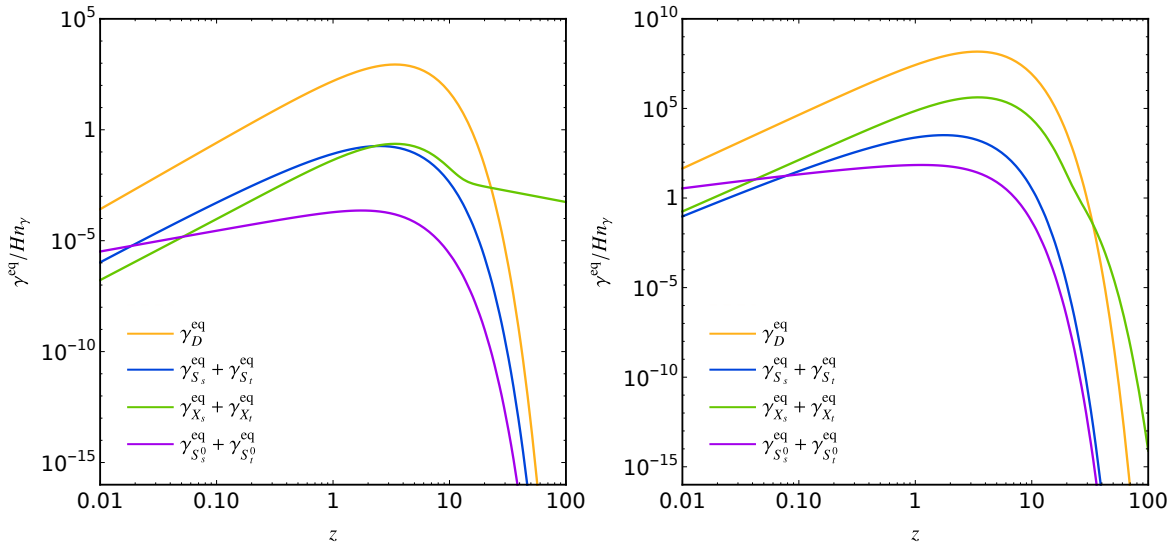

Figure 8.20.: Equilibrium decay and scattering rates in the high- (left) and low- (right) scale scenarios, with respect to $z = m_{X_{dd}}/T$, using the parameters described in the figure texts in Figs. 8.16 and 8.18 for the high- and low-scale scenarios, respectively. This figure is taken from Ref. [2].

In the low-scale scenario, a similar overlap of washout dominance and $\eta_{\Delta B}$ freeze out can be seen. Similar to the high-scale scenario, larger couplings $f_{ud} = f_{dd}$ would lead to a greater washout, as can be seen from the reduced asymmetry in the high-f_{ud} regions in Fig. 8.19. The non-trivial $m_{X_{ud}}$-scaling in Fig. 8.19 when compared to Fig. 8.17 comes mainly from the $m_{X_{ud}}$-dependence of $m_{X_{dd}}$ in the low-scale scenario, where a change in $m_{X_{ud}}$ therefore also changes the scale of baryogenesis, unlike in the high-scale scenario where $m_{X_{dd}}$ is independent of $m_{X_{ud}}$.

Conclusion to Chapter 8

In this chapter we have seen how $\Delta B = 2$ interactions that lead to n-$\bar{n}$ oscillation can explain the origin of the baryon asymmetry of the Universe. As an example scenario, we discussed a UV-completion of the n-$\bar{n}$ oscillation operator featuring scalar diquarks, and showed how successful baryogenesis can be achieved in two benchmark scenarios. These results were published in Ref. [2].

If a n-$\bar{n}$ oscillation signal is seen in the next-generation experiments, the underlying mechanism could be related to either the generation of a baryon asymmetry or its washout. Since a non-zero baryon asymmetry is observed, the latter must mean that there is some other NP at relatively low scales that would lead to baryogenesis. If the former is true, collider searches can be used to distinguish between different scenarios, an example of which being the diquark model discussed in this section.

This chapter concludes the main body of the thesis. In Ch. 9 we summarise Chs. 2 to 8, and discuss further directions into which the results presented here could lead.

9. Conclusion and outlook

The origin of the baryon asymmetry is one of the big open questions in particle physics. It holds one of the keys to discovering what lies beyond our current framework of understanding, and it is intricately connected to various other open questions, such as the unification of forces, the nature of dark matter, and the origin of neutrino masses. The different extensions that can accommodate such an asymmetry share a few common features, such as the violation of $B - L$. Another open question is the nature of neutrinos. If they are Majorana fermions, neutrinos and antineutrinos constitute the same field, meaning that lepton number is violated by two units, $\Delta L = 2$. Whatever mechanism generates the neutrino mass could then be active in the early Universe, possibly leading to baryogenesis. Constraining various models that lead to $B - L$-violation is crucial for our understanding of what could lie beyond the SM.

In this thesis we have shown how probes of LNV and BNV can lead to constraints on both neutrino masses and baryogenesis models. Using the full set of dimension-7 $\Delta L = 2$ SMEFT operators we have derived constraints on the scale of LNV using a wide range of different observables. In a collider-based analysis we presented new limits on the muon-component of many of the LNV Wilson coefficients, which represent the currently most stringent limits for this flavour. The results show how collider searches can be used to constrain LNV operators, and lays a foundation for future work regarding LNV at high-scale observables. By systematically studying tree-level UV-completions of $\Delta L = 2$ operators, we present a full list of simplified models leading to dimension-7 LNV. These results are useful for model-building purposes, as the possible Majorana neutrino mass topologies are shown explicitly for a wide range of BSM fields. They are also useful as a tool for discriminating between different models in case of a signal at collider experiments or in any of the LNV observables. Furthermore, we show how the extensively used EFT-estimate of the neutrino mass contribution coming from different LNV operators completely misses the effect of a hierarchy in the internal degrees of freedom. This result leads to wide ranges of parameter space that was previously considered excluded being opened up. We show how the internal hierarchy can be studied model-independently, and demonstrate how simplified models can capture the effect of its variation. This work lays a foundation for future studies of LNV and Majorana neutrino masses in simplified models and EFT. We also present a novel search strategy for constraining LNV interactions in neutrino-based observables. Rather than observing leptons directly, as is the conventional method, we show how LNV can be indirectly inferred using the kinematics of the other particles involved in the process. The results show that LNV may be differentiated from LNC in rare kaon decays as well as radiative CEνNS based on the energy spectrum of the final state particles. Finally, by deriving a new set of Boltzmann equations, we show how successful baryogenesis can be achieved in a model leading to neutron-antineutron oscillation. This work can be used to derive Boltzmann equations in other models, and

the results demonstrate how LHC searches may complement low-scale observables such as neutron-antineutron oscillation to possibly discover the mechanism behind baryogenesis.

In Chs. 4 and 5 we presented work that is subject for future publication in Ref. [4], in which $\Delta L = 2$ interactions were studied both at the effective level and in an exhaustive list of simplified models. We compared a wide range of LNV observables, including new limits derived from LHC searches. The results show that there are many different models leading to $\Delta L = 2$ interactions that could explain the origin of neutrino masses while also being detectable in various experiments. In Chs. 6 and 7, we showed how kinematic distributions in interactions that involve neutrinos could potentially reveal their Dirac/Majorana nature. These chapters were based on work that led to the publications in Refs. [1] and [3], respectively. In the former chapter, it was shown how the pion distribution in $K \to \pi\nu\nu$ decays can be used to differentiate between a neutrino pair ($\nu\nu$) and a neutrino-antineutrino pair ($\nu\bar{\nu}$) in the final state, leading to a probe of $B - L$-violation. In the latter we presented a novel search mode in which photons are searched for in CEνNS interactions, where the photon distribution again leads to a differentiation between $B - L$-conserving and -violating processes. In Ch. 8 we presented work that led to the publication in Ref. [2], in which baryogenesis was studied in the context of $\Delta B = 2$ interactions. New equations were derived that describe the time-evolution of a baryon asymmetry within the framework of a UV-complete model. The results show that successful baryogenesis can be achieved for model parameters that also lead to possible signals in neutron-antineutron oscillation experiments as well as collider searches.

The work presented above has led to new conclusions being drawn with respect to $B - L$-violation, neutrino masses, and baryogenesis, but also to new questions. With regards to the $\Delta L = 2$ operators in Chs. 4 and 5, it would be interesting to see how the story changes if another effective-field-theory framework is used, e.g. one containing light sterile neutrinos. One might also ask how the collider limits on the scale of LNV changes for different mass hierarchies in a simplified model, and whether this would have any consequence for neutrino masses. Chs. 6 and 7 may lead to the question of whether there are other processes in which particle distributions could be connected to $B - L$-violation. The analysis regarding $K \to \pi\nu\nu$ decays could be extended to tensor currents, and the new CEνNS mode could be applied to other experiments than the one presented here. For Ch. 8 other models could be studied in a similar framework as the one derived, and it would be interesting to see whether there are possible connections to proton decay.

Discovering the mechanism behind baryogenesis is an immense task. In this thesis we have presented some new directions of investigation, but there could potentially be a long road ahead before we know the answer to what the origin of matter in our Universe is. Until then, all we can do is wait for signals indicative of a baryogenesis mechanism, and hope that they come before long.

Acknowledgments

First of all I would like to thank my supervisor Dr. Julia Harz for all the help, guidance, and many rewarding physics discussions along the way. I would also like to thank Dr. Chandan Hati for always taking the time to discuss different topics with me and for helping me tackle different problems. Other than the two above I also want to thank my other research collaborators during this time: Dr. Mathias Becker, Dr. Patrick Bolton, Prof. Dr. Frank Deppisch, Dr. Lukáš Gráf, Florian Heger, Dr. Suchita Kulkarni, and Martin Mojahed.

I want to thank the entire Emmy Noether Group: Dr. Mathias Becker, Emanuele Copello, Dr. Julia Harz, Dr. Chandan Hati, Oliver Hein, Jonas Lang, Martin Mojahed, Martin Napetschnig, and Mohamed Younes Sassi, with the addition of Dr. Carlos Tamarit. It has been great fun working with all of you. Special thanks to Dr. Julia Harz, Dr. Chandan Hati, and Dr. Mathias Becker for giving me comments on this thesis and for helping me with translations. Thanks to Prof. Dr. Björn Garbrecht for acting as my mentor and for helping me find teaching duties. I would also like to extend a thank you to Prof. Dr. Riccardo Catena and Prof. Dr. Bengt E.W. Nilsson for all the support during my time in Gothenburg, and for encouraging me to go for a PhD.

Thank you to all my friends in Munich who made this time special: Juan, Giovanni, Wenyuan, Peter, Petter, Seb, Amy, Mathias, Chandan, Vassi, Emanuele, Sobeen, Felix, Zara, Santiago, Martin, Martin, and everyone else. Thanks also to everyone who went on hikes with me during this time, especially Vassi, Seb, and Keri. It has truly been a lot of fun.

I would also like to thank my friends and family in Sweden for showing so much encouragement: Maria, Erik, Maria, Ann-Marie, Lena, Hasse, Oskar, Astrid, Ylva, Björn, Alexander, Andreas, Madeleine, Noelle, Leopold, Carl-Johan, Svante, Jonathan, and everyone else. I especially want to thank my mom Maria and my dad Erik for all the support you have given me.

Lastly I want to thank Vassi for incredible amounts of patience, inspiration, and gumption. It's been great having you by my side during the writing of this thesis and as the different projects were developing. I am very grateful to have shared this experience with you.

A. Notation and Numerical values

Here we summarise the conventions used in this thesis, and explicitly give the numerical values for tabulated constants and quantities that are used in the calculations.

Unless otherwise stated, we work in units where

$$\hbar = c = k_B = 1. \tag{A.1}$$

Here $\hbar$ is the reduced Planck constant, c is the speed of light, and k_B is the Boltzmann constant. In these units, length and time have the dimensions of inverse energy, and energy in turn has the same dimension as mass. Therefore, we often refer simply to the mass dimension of an object. Furthermore, the relationship between the Planck mass m_{Pl} and the gravitational constant G is given by $m_{\mathrm{Pl}} = G^{-1/2}$. We use the *Mostly minus/West coast* convention for the metric:

$$\eta^{\mu\nu} = \eta_{\mu\nu} = \begin{pmatrix} 1 & 0 & 0 & 0 \\ 0 & -1 & 0 & 0 \\ 0 & 0 & -1 & 0 \\ 0 & 0 & 0 & -1 \end{pmatrix}. \tag{A.2}$$

An arrow indicates a 3-vector,

$$\vec{p}_a = \left(p_a^1,\, p_a^2,\, p_a^3\right), \tag{A.3}$$

where p_a^i here is the momentum of particle a in the direction i of a Cartesian coordinate system, and the absence of an arrow will, if the object in question is understood to be a vector, generally denote a four-vector

$$p_a = \left(p_a^0, p_a^1,\, p_a^2,\, p_a^3\right) = (E_a, \vec{p}\,), \tag{A.4}$$

where $p_a^0 = E_a = \sqrt{m_a^2 + |\vec{p}_a|^2}$ is the energy of particle a, with m_a being its mass. Indices of three-vectors are denoted by Roman letters, and that of four-vectors by Greek letters. We use Einstein summation convention such that

$$p_a \cdot p_b = p_a^\mu p_{b\mu} = p_a^\mu p_b^\nu \eta_{\mu\nu} = p_a^0 p_b^0 - \vec{p}_a \cdot \vec{p}_b = p_a^0 p_b^0 - \sum_i p_a^i p_b^i. \tag{A.5}$$

Unless otherwise stated, multiple repeated indices are also always summed, such that e.g.

$$-\frac{1}{4} W_{a\mu\nu} W_a^{\mu\nu} = -\frac{1}{4} \sum_a \sum_\mu \sum_\nu W_{a\mu\nu} W_a^{\mu\nu} \tag{A.6}$$

and

$$-y_{ij}\bar{Q}_i d_j \phi = -\sum_i \sum_j y_{ij}\bar{Q}_i d_j \phi. \tag{A.7}$$

For spacetime derivatives, we use the short-hand notation

$$\partial_\mu = \frac{\partial}{\partial x^\mu} = \left(\frac{\partial}{\partial t}, \vec{\nabla}\right). \tag{A.8}$$

Here we have used the spacetime four-vector

$$x^\mu = (t, \vec{x}), \tag{A.9}$$

where t is time and $\vec{x}$ denote space in Cartesian coordinates. A Lagrangian L is the difference between kinetic and potential energy, and the Lagrangian density $\mathcal{L}$, related to the Lagrangian via

$$L = \int d^3x \mathcal{L}, \tag{A.10}$$

is often referred to simply as the *Lagrangian*. A similar relation holds the Hermitian H (which is the sum of kinetic and potential energy) and the Hermitian density $\mathcal{H}$. In field theory, one purpose of the Lagrangian is to describe the action $\mathcal{S}[\varphi]$ of a field φ via[1]

$$\mathcal{S}[\varphi] = \int [L][\varphi, x^\mu, \dots] d^4x, \tag{A.11}$$

where the dots represent derivatives of φ with respect to x^μ. Equations of motion can be derived from the action via $\frac{\delta S[\varphi]}{\delta \varphi}$, where δ is a small variation. A slashed object denotes contraction with the gamma matrices such that

$$\not{a} = \gamma_\mu a^\mu. \tag{A.12}$$

A quantum field ψ is said to belong to a certain representation of a symmetry group

$$G_{\text{tot}} = G_1 \times G_2 \times \cdots \times G_N \tag{A.13}$$

by writing

$$\psi \in (R_1, R_2, \dots, R_N), \tag{A.14}$$

where R_1 is the representation of G_1 in which ψ resides, etc. If no symmetry group is given, and a field is written as belonging to a representation of a product of three groups, such that $N = 3$ in Eq. (A.13), it is meant that the symmetry group in question is the Standard model group[2]

$$G_{\text{SM}} = SU(3)_c \times SU(2)_L \times U(1)_Y. \tag{A.15}$$

[1] Note that the integral in Eq. (A.11) is the origin of the phrase *integrate out* in the EFT literature. If a field is sufficiently heavy we can neglect its dependence on the integrand d^4x, and move it to the left of the integral sign.

[2] See Sec. 2.1.

Scalar fields written with a tilde denote complex conjugation and contraction with a Levi-Civita symbol, such that

$$\tilde{\eta}^a = \epsilon_{ab}\eta^{*b} \tag{A.16}$$

Field strengths written with a tilde denote multiplication by $\frac{1}{2}$ and contraction with a Levi-Civita symbol with four indices,

$$\tilde{F}^{\mu\nu} = \frac{1}{2}\epsilon^{\mu\nu\rho\sigma}F_{\rho\sigma}\,. \tag{A.17}$$

An O written in calligraphy, $\mathcal{O}$, is used to both denote an order of magnitude and an operator. Which of the two uses is meant will be clear from the context in which the $\mathcal{O}$ is used. Unless otherwise stated, a dot $\dot{x}(t)$ represents a derivative with respect to time t, and a prime $x'(t)$ represents a derivative with respect to whatever quantity x is said to be a function of, such that $x'(t) = \partial x/\partial t = \dot{x}(t)$, and $x'(\phi) = \partial x/\partial\phi \neq \dot{x}(\phi)$. We often mix between denoting couplings as matrices and scalar numbers, such that even if e.g. the coupling f_{ud} is a matrix in flavour space, we write relations such as $f_{ud} = 0.3$ and so on. What is meant then is that the relevant entries in f_{ud} have the value 0.3.

In Tab. A.1 we tabulate the numerical values for constants and measured observables taken from the Particle Data Group (PDG) booklet [14] that are used in the calculations in subsequent chapters.

Quantity	**Symbol**	**Value**
Higgs vacuum expectation value	v	174 GeV
Fermi constant	G_F	1.66×10^{-5} GeV^{-2}
Bohr magneton	μ_B	0.296 MeV^{-1}
Elementary charge	e	0.303
Gravitational constant	G	6.71×10^{-39} GeV^{-2}
Strong coupling constant	$\alpha_s(m_Z)$	0.118
Electroweak coupling constant	α	1/137
Weinberg angle	$\sin^2\theta_W(m_Z)$	0.231
Higgs boson mass	m_h	125 GeV
$W^\pm$ boson mass	m_W	80.4 GeV
Z boson mass	m_Z	91.2 GeV
Electron mass	m_e	0.511 MeV
Muon mass	m_μ	106 MeV
τ mass	m_τ	1.78 GeV
u-quark mass	m_u	2.2 MeV
d-quark mass	m_d	4.7 MeV
s-quark mass	m_s	95 MeV
c-quark mass	m_c	1.28 GeV
b-quark mass	m_b	4.18 GeV
t-quark mass	m_t	173 GeV

Table A.1.: The values of constants and measured quantities taken from Ref. [14] that are used in this thesis. All coupling constants are given at the mass of the Z boson.

B. Particle algebra

Here we give a few useful identities relating to two-component spinor manipulation, for more information see Ref. [402].

Spinors ψ transform under hermitian conjugation according to

$$\psi^\dagger_{\dot\alpha} \equiv (\psi_\alpha)^\dagger, \qquad \psi^{\dagger\,\dot\alpha} \equiv (\psi^\alpha)^\dagger\,, \tag{B.1}$$

where α is a spinor index and $\dot\alpha$ is an antispinor index. These indices are lowered and raised according to

$$\psi_\alpha = \epsilon_{\alpha\beta}\psi^\beta\,, \qquad \psi^\alpha = \epsilon^{\alpha\beta}\psi_\beta\,, \qquad \psi^\dagger_{\dot\alpha} = \epsilon_{\dot\alpha\dot\beta}\psi^{\dagger\dot\beta}\,, \qquad \psi^{\dagger\dot\alpha} = \epsilon^{\dot\alpha\dot\beta}\psi^\dagger_{\dot\beta} \tag{B.2}$$

for spinors, and

$$A^{\gamma\delta} = \epsilon^{\gamma\alpha}\epsilon^{\delta\beta}A_{\alpha\beta}\,, \qquad\qquad A_{\gamma\delta} = \epsilon_{\gamma\alpha}\epsilon_{\delta\beta}A^{\alpha\beta} \tag{B.3}$$

for objects with two spinor indices. They also obey the Shouten identities

$$\epsilon_{\alpha\beta}\epsilon_{\gamma\delta} + \epsilon_{\alpha\gamma}\epsilon_{\delta\beta} + \epsilon_{\alpha\delta}\epsilon_{\beta\gamma} = 0\,, \qquad\qquad \epsilon_{\dot\alpha\dot\beta}\epsilon_{\dot\gamma\dot\delta} + \epsilon_{\dot\alpha\dot\gamma}\epsilon_{\dot\delta\dot\beta} + \epsilon_{\dot\alpha\dot\delta}\epsilon_{\dot\beta\dot\gamma} = 0\,. \tag{B.4}$$

Objects with a Lorentz index can be written with one spinor- and one antispinor index such that

$$V^\mu \equiv \frac{1}{2}\bar\sigma^{\mu\dot\beta\alpha}V_{\alpha\dot\beta}\,, \qquad\qquad V_{\alpha\dot\beta} = V^\mu\sigma_{\mu\alpha\dot\beta}\,, \tag{B.5}$$

where $\sigma^\mu \equiv (\mathbb{1},\, \sigma^1\,,\, \sigma^2\,,\, \sigma^3)$ and $\bar\sigma^\mu \equiv (\mathbb{1},\, -\sigma^1\,,\, -\sigma^2\,,\, -\sigma^3)$ are four-vectors containing the Pauli matrices. These two vectors are related via

$$\sigma^\mu_{\alpha\dot\alpha} = \epsilon_{\alpha\beta}\epsilon_{\dot\alpha\dot\beta}\bar\sigma^{\mu\,\dot\beta\beta}\,, \qquad \bar\sigma^{\mu\,\dot\alpha\alpha} = \epsilon^{\alpha\beta}\epsilon^{\dot\alpha\dot\beta}\sigma^\mu_{\beta\dot\beta}\,. \tag{B.6}$$

Spinor indices are often dropped for brevity in this thesis, in which case the following definitions are used for spinors ξ and η:

$$\xi\eta \equiv \xi^\alpha\eta_\alpha, \tag{B.7}$$

$$\xi^\dagger\eta^\dagger \equiv \xi^\dagger_{\dot\alpha}\eta^{\dagger\dot\alpha}, \tag{B.8}$$

$$\xi^\dagger\bar\sigma^\mu\eta \equiv \xi^\dagger_{\dot\alpha}\bar\sigma^{\mu\dot\alpha\beta}\eta_\beta, \tag{B.9}$$

$$\xi\sigma^\mu\eta^\dagger \equiv \xi^\alpha\sigma^\mu_{\alpha\dot\beta}\eta^{\dagger\dot\beta} \tag{B.10}$$

$$\xi\sigma^{\mu\nu}\eta \equiv \xi^\alpha(\sigma^{\mu\nu})_\alpha{}^\beta\eta_\beta\,, \tag{B.11}$$

$$\xi^\dagger\bar\sigma^{\mu\nu}\eta^\dagger \equiv \xi^\dagger{}_{\dot\alpha}(\bar\sigma^{\mu\nu})^{\dot\alpha}{}_{\dot\beta}\eta^{\dagger\dot\beta}\,, \tag{B.12}$$

where we have used the tensors

$$(\sigma^{\mu\nu})_\alpha{}^\beta \equiv \frac{i}{4}\left(\sigma^\mu_{\alpha\dot\gamma}\bar\sigma^{\nu\dot\gamma\beta} - \sigma^\nu_{\alpha\dot\gamma}\bar\sigma^{\mu\dot\gamma\beta}\right), \tag{B.13}$$

$$(\bar\sigma^{\mu\nu})^{\dot\alpha}{}_{\dot\beta} \equiv \frac{i}{4}\left(\bar\sigma^{\mu\dot\alpha\gamma}\sigma^\nu_{\gamma\dot\beta} - \bar\sigma^{\nu\dot\alpha\gamma}\sigma^\mu_{\gamma\dot\beta}\right). \tag{B.14}$$

The Hermitian conjugation relations are given by

$$(\xi\eta)^\dagger = \eta^\dagger\xi^\dagger, \tag{B.15}$$

$$(\xi\sigma^\mu\eta^\dagger)^\dagger = \eta\sigma^\mu\xi^\dagger, \tag{B.16}$$

$$(\xi\sigma^{\mu\nu}\eta)^\dagger = \eta^\dagger\bar\sigma^{\mu\nu}\xi^\dagger, \tag{B.17}$$

and for spinors z_i the commutation relations are given by

$$z_1 z_2 = -(-1)^A z_2 z_1, \tag{B.18}$$

$$z_1^\dagger z_2^\dagger = -(-1)^A z_2^\dagger z_1^\dagger, \tag{B.19}$$

$$z_1\sigma^\mu z_2^\dagger = (-1)^A z_2^\dagger\bar\sigma^\mu z_1, \tag{B.20}$$

$$z_1\sigma^{\mu\nu} z_2 = (-1)^A z_2\sigma^{\mu\nu} z_1, \tag{B.21}$$

$$z_1^\dagger\bar\sigma^{\mu\nu} z_2^\dagger = (-1)^A z_2^\dagger\bar\sigma^{\mu\nu} z_1^\dagger, \tag{B.22}$$

where we have

$$A \equiv \begin{cases} -1, & \text{commuting spinors,} \\ \\ +1, & \text{anticommuting spinors.} \end{cases} \tag{B.23}$$

The Shouten identity in Eq. (B.4) leads to

$$(z_1 z_2)(z_3 z_4) = -(z_1 z_3)(z_4 z_2) - (z_1 z_4)(z_2 z_3), \tag{B.24}$$

$$(z_1^\dagger z_2^\dagger)(z_3^\dagger z_4^\dagger) = -(z_1^\dagger z_3^\dagger)(z_4^\dagger z_2^\dagger) - (z_1^\dagger z_4^\dagger)(z_2^\dagger z_3^\dagger). \tag{B.25}$$

Using the relations above we have the Fierz identities

$$(z_1\sigma^\mu z_2^\dagger)(z_3^\dagger\bar\sigma_\mu z_4) = -2(z_1 z_4)(z_2^\dagger z_3^\dagger), \tag{B.26}$$

$$(z_1^\dagger\bar\sigma^\mu z_2)(z_3^\dagger\bar\sigma_\mu z_4) = -2(z_1^\dagger z_3^\dagger)(z_4 z_2), \tag{B.27}$$

$$(z_1\sigma^\mu z_2^\dagger)(z_3\sigma_\mu z_4^\dagger) = -2(z_1 z_3)(z_4^\dagger z_2^\dagger), \tag{B.28}$$

$$(z_1\sigma^{\mu\nu} z_2)(z_3\sigma_{\mu\nu} z_4) = -2(z_1 z_4)(z_2 z_3) - (z_1 z_2)(z_3 z_4), \tag{B.29}$$

$$(z_1^\dagger\bar\sigma^{\mu\nu} z_2^\dagger)(z_3^\dagger\bar\sigma_{\mu\nu} z_4^\dagger) = -2(z_1^\dagger z_4^\dagger)(z_2^\dagger z_3^\dagger) - (z_1^\dagger z_2^\dagger)(z_3^\dagger z_4^\dagger), \tag{B.30}$$

$$(z_1\sigma^{\mu\nu} z_2)(z_3^\dagger\bar\sigma_{\mu\nu} z_4^\dagger) = 0. \tag{B.31}$$

For four-component spinors, the Fierz relations are given by Tab. B.1, where S, V, T, A, and P denote scalar-, vector-, tensor-, axial vector-, and pseudoscalar currents, respectively.

	S	V	T	A	P
$S \times S$	1/4	1/4	-1/4	-1/4	1/4
$V \times V$	1	-1/2	0	-1/2	-1
$T \times T$	-3/2	0	-1/2	0	-3/2
$A \times A$	-1	-1/2	0	-1/2	1
$P \times P$	1/4	-1/4	-1/4	1/4	1/4

Table B.1.: Fierz transformations for four-component spinors.

The current structure in the leftmost column leads to a sum of currents given by the entries in the table after swapping the second and fourth components in a bilinear, such that e.g.

$$\begin{aligned}(\psi_1\psi_2)(\psi_3\psi_4) = &\frac{1}{4}(\psi_1\psi_4)(\psi_3\psi_2) + \frac{1}{4}(\psi_1\gamma_\mu\psi_4)(\psi_3\gamma^\mu\psi_2) \\ &- \frac{1}{4}(\psi_1\sigma_{\mu\nu}\psi_4)(\psi_3\sigma^{\mu\nu}\psi_2) + \frac{1}{4}(\psi_1\gamma_5\gamma_\mu\psi_4)(\psi_3\gamma_5\gamma^\mu\psi_2) \\ &+ \frac{1}{4}(\psi_1\gamma_5\psi_4)(\psi_3\gamma_5\psi_2)\,,\end{aligned} \tag{B.32}$$

as can be seen from the row containing $S \times S$ in Tab. B.1.

C. Particle kinematics

Here we give some general relations that are useful when calculating particle scattering- and decay rates.

C.1. Formulae

In the scattering of two particles into any number of particles, $A + B \to \cdots$, a measure of the strength of the interaction is given by the cross section $\sigma\left(a + b \to \cdots\right)$, which has the dimension of mass squared, and is obtained by the formula [21]

$$\begin{aligned} d\sigma\left(a + b \to \cdots\right) = & \frac{1}{4E_A E_B |v_A - v_B|} \prod_f^m \frac{d^3\vec{p}_f}{2E_f(2\pi)^3} \\ & \times \left|\mathcal{M}\left(a + b \to \cdots\right)\right|^2 (2\pi)^4 \delta^{(4)}\left(p_A + p_B - \sum_f p_f\right) . \end{aligned} \tag{C.1}$$

Here v_α is the velocity of particle α, and $|\mathcal{M}|^2$ is the squared matrix element, which is obtained from the scattering via drawing the diagram and using the appropriate Feynman rules, and then summing or averaging over all relevant quantum numbers. For a decay $a \to \cdots$, the decay width $\Gamma\left(A \to \cdots\right)$ is obtained from the formula [21]

$$d\Gamma\left(a \to \cdots\right) = \frac{1}{2m_a} \prod_f^m \frac{d^3\vec{p}_f}{2E_f(2\pi)^3} \left|\mathcal{M}\left(a \to \cdots\right)\right|^2 (2\pi)^4 \delta^{(4)}\left(p_A - \sum_f p_f\right) \tag{C.2}$$

Often, the four-momenta that are involved in particle interactions are parametrised in terms of the Lorentz invariant Mandelstam variables s, t, and u, which in a scattering $a + b \to i + j$ are given by

$$\begin{aligned} s &= (p_a + p_b)^2 = (p_i + p_j)^2, \\ t &= (p_a - p_i)^2 = (p_j - p_b)^2, \\ u &= (p_a - p_j)^2 = (p_i - p_b)^2 . \end{aligned} \tag{C.3}$$

From the relativistic expression of the energy

$$E_\alpha^2 = m_\alpha^2 + |\vec{p}_\alpha|^2 \tag{C.4}$$

and from conservation of four-momentum

$$p_a + p_b = p_i + p_j , \tag{C.5}$$

we then have

$$s + t + u = m_a^2 + m_b^2 + m_i^2 + m_j^2 \,. \tag{C.6}$$

Often the above relation is used to eliminate the u variable in a two-to-two scattering. In the center-of-mass (CMS) frame, where $\vec{p}_a = -\vec{p}_b$ and $\vec{p}_i = -\vec{p}_j$, the variable s can be expressed in terms of only energies,

$$s = (E_a + E_b)^2 = (E_i + E_j)^2 \,. \tag{C.7}$$

We can then find expressions for all energies and momenta in the CMS frame using only s and the different masses,

$$E_a = \frac{s + m_a^2 - m_b^2}{2\sqrt{s}}, \quad E_b = \frac{s + m_b^2 - m_a^2}{2\sqrt{s}}, \quad |\vec{p}_a| = \frac{\lambda^{1/2}(s, m_a^2, m_b^2)}{2\sqrt{s}}, \quad |\vec{p}_b| = |\vec{p}_a| \tag{C.8}$$

where

$$\lambda(a, b, c) = a^2 + b^2 + c^2 - 2ab - 2ac - 2bc \tag{C.9}$$

is the Källén function, and where the final state energies and momenta can be obtained by exchanging $a \leftrightarrow i$ and $b \leftrightarrow j$ in Eq. (C.8). For a decay $a \to i + j$ in the CMS frame, we have $|\vec{p}_a| = 0$ and $\sqrt{s} = m_a$. The formulae for the final state energies and momenta can then be obtained by performing this substitution in Eq. (C.8) after exchanging the particles as in the two-to-two scattering case.

The phase space element for m particles in the final state is given by

$$R_m \equiv \int \prod_f^m \frac{d^3\vec{p}_f}{2E_f(2\pi)^3} (2\pi)^4 \delta^{(4)} \left(P - \sum_f^m p_f \right) . \tag{C.10}$$

Here $P \equiv \sum_i^n p_i$ is the sum of the four-momenta of all n initial particles. Our goal in this section and the following is to turn this expression into something connected to observable variables, such as angles and energies, or Lorentz invariant variables, such as the Mandelstam variables.

C.2. Two-body phase space

For two particles in the final state, the phase space element is explicitly given by

$$R_2 = \int \frac{d^3\vec{p}_i}{2E_i(2\pi)^3} \frac{d^3\vec{p}_j}{2E_j(2\pi)^3} (2\pi)^4 \delta^{(4)}(P - p_i - p_j) \,. \tag{C.11}$$

The integrand of the particle j can be expressed in terms of its four-momentum,

$$\int \frac{d^3\vec{p}_j}{2E_j(2\pi)^3} = \int \frac{d^4 p_j}{(2\pi)^3} \delta(p_j^2 - m_j^2) \Theta(E_j) \tag{C.12}$$

where we have used

$$\delta(g(x)) = \frac{\delta(x - x_0)}{|g'(x_0)|} \,, \tag{C.13}$$

such that

$$\delta(p_j^2 - m_j^2) = \frac{\delta(p_j^0 - E_j)}{2E_j}\,, \tag{C.14}$$

and where the Heaviside function Θ ensures that the energy is positive. Substituting Eq. (C.12) in Eq. (C.11) and performing the d^4p_j integral, we have

$$R_2 = \int \frac{d^3\vec{p}_i}{2E_i(2\pi)^3}(2\pi)\delta((P-p_i)^2 - m_j^2)\,. \tag{C.15}$$

Changing to spherical coordinates, such that $d^3\vec{p}_i = |\vec{p}_i|^2 d|\vec{p}_i| d\cos\theta d\phi$, and further changing variables from momentum to energy via $|\vec{p}_i|d|\vec{p}_i| = E_i dE_i$, we have

$$R_2 = \int \frac{|\vec{p}_i|}{2(2\pi)^2} dE_i d\cos\theta d\phi \delta((P-p_i)^2 - m_j^2)\,. \tag{C.16}$$

Finally, in the CMS frame we can express $P = \sqrt{s}$, such that the delta function in Eq. (C.16) becomes

$$\delta((P-p_i)^2 - m_j^2) = \delta(s - 2\sqrt{s}E_i + m_i^2 - m_j^2)\,. \tag{C.17}$$

Using $\delta(\alpha x) = \delta(x)/|\alpha|$ for α a constant and performing the dE_i integral, the two-body phase space element is finally obtained as

$$R_2 = \frac{1}{16\pi^2}\frac{\lambda^{1/2}(s, m_i^2, m_j^2)}{2s}\int d\cos\theta d\phi\,. \tag{C.18}$$

For a two-body decay $a \to i + j$, this result leads to the simplified formula

$$\Gamma\left(a \to i + j\right) = \frac{1}{16\pi}\frac{\lambda^{1/2}(m_a^2, m_i^2, m_j^2)}{m_a^2}|\mathcal{M}\left(a \to i + j\right)|^2\,. \tag{C.19}$$

For a scattering cross section, the matrix element may depend non-trivially on the angles θ and ϕ. However, assuming that the matrix element does not depend on the angle ϕ, we may express the phase space element of a two-to-two scattering $a + b \to i + j$ in terms of the Mandelstam variable t via

$$t = m_a^2 + m_i^2 - \frac{(s + m_a^2 - m_b^2)(s + m_i^2 - m_j^2)}{2s} + \frac{\lambda^{1/2}(s, m_a^2, m_b^2)\lambda^{1/2}(s, m_i^2, m_j^2)}{2s}\cos\theta\,, \tag{C.20}$$

such that we can perform the change of variables

$$d\cos\theta = \frac{2s}{\lambda^{1/2}(s, m_a^2, m_b^2)\lambda^{1/2}(s, m_i^2, m_j^2)}dt\,. \tag{C.21}$$

Rewriting the relative velocity

$$E_a E_b|v_a - v_b| = |E_b p_a - E_a p_b| = \sqrt{(p_a \cdot p_b)^2 - m_a^2 m_b^2} = \tfrac{1}{2}\lambda^{1/2}(s, m_a^2, m_b^2)\,, \tag{C.22}$$

we obtain the two-to-two scattering cross section

$$\sigma\left(a + b \to i + j\right) = \frac{1}{16\pi\lambda^{1/2}(s, m_a^2, m_b^2)}\int dt|\mathcal{M}\left(a + b \to i + j\right)|\,. \tag{C.23}$$

The integration limits of t can be obtained by putting $\cos\theta = \pm 1$ in Eq. (C.20).

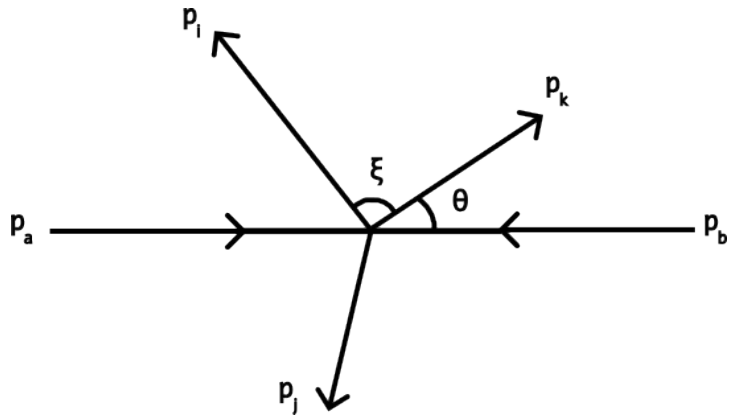

Figure C.1.: Coordinate system used for the evaluation of the three-body phase space element for a scattering $a + b \to i + j + k$. Note that p_i and p_j have components that point in or out of the page, such that the angle ξ does not necessarily lie in the same plane as the angle θ.

C.3. Three-body phase space

For three particles in the final state, the phase space element is

$$R_3 = \int \frac{d^3\vec{p}_i}{2E_i(2\pi)^3}\frac{d^3\vec{p}_j}{2E_j(2\pi)^3}\frac{d^3\vec{p}_k}{2E_k(2\pi)^3}(2\pi)^4\delta^{(4)}(P - p_i - p_j - p_k)\,. \tag{C.24}$$

Often the coordinate system of a scattering is fixed by the initial particles[1], and we are not free to define a new coordinate system for the final state particles, such as fixing one of them to go along a specific axis, without also relating it to the initial coordinate system. We define the z-axis of our coordinate system[2] to be the direction of momentum of the particle a, and define the angle between $\vec{p}_i$ and $\vec{p}_k$ as ξ, as well as between $\vec{p}_k$ and the z-axis as θ, as can be seen in Fig. C.1. The x-axis is defined such that $\vec{p}_k$ lies in the x-z-plane, while a third angle ϕ rotates the final state momenta around the z-axis. A fourth angle is then needed to completely describe the geometry of the final state, and we use the angle ψ between the x-y-plane and the plane spanned by p_i and p_j, such that

$$\cos\psi \equiv \frac{(\vec{p}_a \times \vec{p}_k)\cdot(\vec{p}_k \times \vec{p}_i)}{|\vec{p}_a||\vec{p}_i||\vec{p}_k|^2}\,. \tag{C.25}$$

Our first step is to re-write the integrands in Eq. (C.24) in terms of the four-momenta, such that

$$R_3 = \int \frac{1}{(2\pi)^5}d^4p_i d^4p_j d^4p_k \delta(p_i^2 - m_i^2)\delta(p_j^2 - m_j^2)\delta(p_k^2 - m_k^2)\delta^{(4)}(P - p_i - p_j - p_k)\,. \tag{C.26}$$

[1] In scattering experiments the direction of incoming particles is often known, and defines a coordinate system to which the final state phase space must be related.

[2] Note that this coordinate system can also be used for a three-body decay, and that our treatment of R_3 is completely general with respect to the initial state of the problem.

We can subsequently get rid of the delta function $\delta^{(4)}(P - p_i - p_j - p_k)$ by integrating over d^4p_j, such that

$$R_3 = \int \frac{1}{(2\pi)^5} d^4p_i d^4p_j d^4p_k \delta(p_i^2 - m_i^2)\delta(p_k^2 - m_k^2)\delta\left((P - p_i - p_k)^2 - m_j^2\right) . \tag{C.27}$$

Next, we convert the integrand d^4p_i into an integrand over energy and angle,

$$\int d^4p\delta(p_i^2 - m_i^2) = \int |\vec{p}_i|^2 d|\vec{p}_i| dE_i d\Omega_i \delta(E_i^2 - |\vec{p}_i|^2 - m_i^2) = \tfrac{1}{2}|\vec{p}_i| \int dE_i d\Omega_i \,, \tag{C.28}$$

where Ω_i denotes the angle of $\vec{p}_i$, and similarly for d^4p_k, such that

$$R_3 = \frac{1}{4}\frac{|\vec{p}_i||\vec{p}_k|}{(2\pi)^5} \int dE_i d\Omega_i dE_k d\Omega_k \delta\left((P - p_i - p_k)^2 - m_j^2\right) . \tag{C.29}$$

We can now identify $d\Omega_i = d\cos\xi d\psi$ and $d\Omega_k = d\cos\theta d\phi$.

C.4. Boosts

A boost in particle physics represents a change of reference frame from an initial frame F to a final frame F' with a non-zero velocity relative to F. We now assume that F' is moving in the z-direction relative to F with a velocity β given by

$$\beta = \frac{|\vec{p}_a|}{E_a} \,, \tag{C.30}$$

where $\vec{p}_a$ and E_a is the momentum and energy of a, respectively. The transformation relation between the energy and momentum of a particle a in the two frames is then given by

$$\begin{pmatrix} E_a' \\ p_z^{a\prime} \end{pmatrix} = \begin{pmatrix} \gamma & -\gamma\beta \\ -\gamma\beta & \gamma \end{pmatrix} \begin{pmatrix} E_a \\ p_z^a \end{pmatrix} , \quad \vec{p_T}' = \vec{p_T} \tag{C.31}$$

where p_z^a is the z-component of the momentum, and $\vec{p}_T$ is the transverse component. Here the Lorentz factor γ is given by

$$\gamma = \frac{1}{\sqrt{1 - \beta^2}} \,. \tag{C.32}$$

Applying Eq. (C.31) we can then shift between any frames F and F'. This shift is often used in order to e.g. change between rest- and lab frames in the analysis of a particle experiment.

D. Chemical potentials

Here we will go through some of the details relating to chemical potentials in the early Universe. When a particle a is thermal equilibrium but not chemical equilibrium, its chemical potential μ_a vanishes. The number density of a in and out of chemical equilibrium are therefore given by the expressions

$$n_a^{\rm eq} = \int_0^\infty \frac{dp_a^3}{(2\pi)^3} \frac{g_a}{e^{E_a/T} \pm 1}, \qquad n_a = \int_0^\infty \frac{dp_a^3}{(2\pi)^3} \frac{g_\alpha}{e^{(E_a - \mu_a)/T} \pm 1}, \tag{D.1}$$

respectively, where a superscript eq denotes equilibrium. Here $n_a^{\rm eq}$ is the (equilibrium) number density, p_a the momentum, g_a the degrees of freedom, and E_a the energy. Neglecting angular dependencies we write the number density n_a in Eq. (D.1) as

$$n_\alpha = \frac{1}{2\pi^2} \int_0^\infty dE_\alpha E_\alpha \sqrt{E_\alpha - m_\alpha} \frac{g_\alpha}{e^{(E_\alpha - \mu_\alpha)/T} \pm 1}, \tag{D.2}$$

which leads to [588]

$$\text{Bosons: } n_a - \bar{n}_a = \frac{g_a}{3} \mu_a T^2, \qquad \text{Fermions: } n_a - \bar{n}_a = \frac{g_a}{6} \mu_a T^2. \tag{D.3}$$

Ignoring relativistic effects and assuming a small chemical potential compared to the temperature, we treat fermions and bosons the same, and write the fraction of number density to equilibrium number density as

$$\frac{n_a}{n_a^{\rm eq}} = e^{\mu_a/T} \approx 1 + \frac{\mu_a}{T}, \tag{D.4}$$

where the only difference between the number density n_a of particle a and the number density $\bar{n}_a$ of its antiparticle $\bar{a}$ is a sign flip of the chemical potential, according to the relation

$$\mu_a = -\mu_a. \tag{D.5}$$

If e.g. a reaction $a + b \leftrightarrow c + d$ is in chemical equilibrium it leads to the relation $\mu_a + \mu_b = \mu_c + \mu_d$.

Eq. (D.4) turns out to be very useful when evaluating Boltzmann equations. To see this we first note that a number of reactions in the SM are in chemical equilibrium during the early Universe. First we note that the interactions involving $W^\pm$-bosons are all be chemical equilibrium, leading to the relations

$$\mu_{W^-} - \mu_{\phi^-} - \mu_{\phi^0} = 0, \tag{D.6}$$

$$\mu_{d_L} - \mu_{u_L} - \mu_{W^-} = 0, \tag{D.7}$$

$$\mu_{e_{Li}} - \mu_{\nu_{Li}} - \mu_{W^-} = 0, \tag{D.8}$$

where we also have $\mu_{W^-} = \mu_{W^+} = 0$ since the $SU(2)_L$-symmetry is unbroken in the early Universe. Using the above relations we now define $\mu_{d_{Li}} = \mu_{u_{Li}} \equiv \mu_{q_i}$, $\mu_{e_{Li}} \equiv \mu_{\ell_i}$, and $\mu_H \equiv \mu_{\phi^0}$. This subsequently leads to the following relations coming from Yukawa interactions, assuming that the ith generation Yukawa interactions of the SM are all in full equilibrium,

$$\mu_{q_i} - \mu_{u_i} + \mu_H = 0\,, \tag{D.9}$$

$$\mu_{q_i} - \mu_{d_i} - \mu_H = 0\,, \tag{D.10}$$

$$\mu_{\ell_i} - \mu_{e_i} - \mu_H = 0\,. \tag{D.11}$$

Finally, we also have the EW sphaleron leading to

$$\sum_i^N \left(3\mu_{q_i} + \mu_{\ell_i}\right) = 0\,, \tag{D.12}$$

where N is the number of fermion generations[1], as well as the QCD sphaleron leading to

$$\sum_i^N 2\mu_{Q_i} - \mu_{\bar{u}^c{}_i} - \mu_{\bar{d}^c{}_i} = 0\,. \tag{D.13}$$

Interestingly, the same constraint that is given by the QCD sphaleron is also fulfilled by the Yukawa interactions if all SM quark generations are in equilibrium.

Often it is also assumed that the total hypercharge of the Universe vanishes, in which case we would obtain the relation

$$\sum_i^N \left(\mu_{q_i} + 2\mu_{u_i} - \mu_{d_i} - \mu_{\ell_i} - \mu_{e_i} + \frac{2}{N_f}\mu_H\right) = 0\,. \tag{D.14}$$

This relation lets us express the lepton L and baryon B number charges of the Universe

$$B = \sum_i^N \left(2\mu_{q_i} + \mu_{u_i} + \mu_{d_i}\right)\,, \tag{D.15}$$

$$L = \sum_i^N \left(2\mu_{\ell_i} + \mu_{e_i}\right)\,, \tag{D.16}$$

only in terms of the single chemical potential $\mu_\ell \equiv \sum_i^N \mu_{\ell_i}$, such that

$$\begin{aligned} B &= -\frac{4}{3}N\mu_\ell\,, \\ L &= -\frac{14N^2 + 9N}{6N + 3}\mu_\ell\,. \end{aligned} \tag{D.17}$$

Relating B and L to each other we then have

$$B = c_s\left(B - L\right)\,, \tag{D.18}$$

$$L = \left(c_s - 1\right)\left(B - L\right)\,, \tag{D.19}$$

where c_s is given by

$$c_s = \frac{8N + 4}{22N + 13}\,. \tag{D.20}$$

[1]Note that $N = 3$ in the SM.

E. Boltzmann Equations

In the early Universe, the abundances of any number of particle species i can be dynamically described by a set of Boltzmann equations [224]. In this Appendix, which serves as a complement to Sec. 3.4, we go through some of the detail regarding the Boltzmann equation formalism.

E.1. The LHS of a general Boltzmann equation

For a general particle X, the Boltzmann equation reads

$$\frac{dn_X}{dt} + 3n_X H = -\sum_{i,j,\ldots} [X\, a \cdots \leftrightarrow i\, j \cdots]\,. \tag{E.1}$$

Here t is time, n_α is the number density of particle α, and

$$H = \frac{1}{a}\frac{da}{dt} = \frac{1.66\sqrt{g_*}}{m_{\rm Pl}} T^2 \tag{E.2}$$

is the Hubble rate, where T is the temperature, $a \propto 1/T$ is the scale factor, g_* is the number of degrees of freedom[1], and $m_{\rm Pl} = 1.2 \times 10^{12}$ GeV is the Planck mass. We can express the number density as a phase space integral

$$n_\alpha = \int_0^\infty \frac{dp_\alpha^3}{(2\pi)^3} \frac{g_\alpha}{e^{(E_\alpha - \mu_\alpha)/T} \pm 1}\,, \tag{E.3}$$

where a $+$ is used for fermions and a $-$ for bosons. Furthermore, p_α is the momentum, E_α the energy, g_α the number of degrees of freedom, and μ_α the chemical potential of particle α. Assuming $e^{E_\alpha/T} \gg \pm 1$, we can rewrite the number density for the case where α is in chemical equilibrium,

$$n_\alpha^{\rm eq} = \frac{g_\alpha}{2\pi^2}\int_0^\infty dp_\alpha p_\alpha^2 e^{-E_\alpha/T} = \frac{g_\alpha}{2\pi^2} T^3 \int_z^\infty dx x\sqrt{x^2 - z^2} e^{-x}\,, \tag{E.4}$$

where $x = E_\alpha/T$ and $z = m_\alpha/T$ for a mass m_α and temperature T. We can further express the RHS in terms of modified Bessel functions of the second kind [663]

$$K_\nu(z) = \frac{\sqrt{\pi}}{(n - \frac{1}{2})!}\left(\frac{1}{2}z\right)^\nu \int_1^\infty dx e^{-zx}(x^2 - 1)^{\nu - \frac{1}{2}} \tag{E.5}$$

[1] In the early Universe, the number of degrees of freedom decrease with time as more and more particles become non-relativistic and go out of equilibrium.

where, explicitly,

$$K_2(z) = \frac{1}{3\sqrt{z}} \int_z^\infty dx (x^2 - z^2)^{3/2} e^{-x} = \int_z^\infty dx z^{-2} x (x^2 - z^2)^{1/2} e^{-x} \,. \tag{E.6}$$

Here we used IBP in the last step assuming that the boundary term vanishes. We then arrive at the following expression for the equilibrium number density of particle α,

$$n_\alpha^{\rm eq} = \frac{g_\alpha}{2\pi^2} T m_X^2 K_2 \left(\frac{m_\alpha}{T} \right) \,. \tag{E.7}$$

For massless bosons such as the photon, the number density is instead evaluated as

$$n_\gamma = \frac{g_\gamma}{2\pi^2} \int_0^\infty dp_\gamma p_\gamma^2 \frac{1}{e^{E_\gamma/T} - 1} = \frac{g_\gamma}{2\pi^2} T^3 \int_0^\infty dx x^2 \frac{1}{e^x - 1} = \frac{g_\gamma}{\pi^2} \zeta(3) T^3 \,, \tag{E.8}$$

where $\zeta(3) = 1.202\ldots$ is the Riemann zeta function $\zeta(z)$ at $z = 3$. Here we have dropped the superscript *eq* since photons are always in chemical equilibrium in the early Universe due to photon number non-conserving processes such as $e^- \leftrightarrow e^- + \gamma$ being in equilibrium. When evaluating the Boltzmann equation, the number densities of particles will in general either be treated as variables, or taken to be the equilibrium densities. This is a simplification, a complete treatment of all particle number densities should include as many coupled Boltzmann equations as there are particle species involved. However, solving coupled differential equations over many orders of magnitude can be computationally challenging, and by reducing the number of particle species being out of equilibrium to only a few, as is most often done, it is possible to capture the relevant physics without making the problem essentially unsolvable.

Using the results above, the LHS of Eq. (E.1) can be rewritten by normalising the particle number density n_X to the photon number density[2] n_γ,

$$\frac{dn_X}{dt} + 3n_X H = n_\gamma \frac{d}{dt} \eta_X - n_\gamma^2 \eta_X \frac{d}{dt} \frac{1}{n_\gamma} + 3 n_\gamma \eta_X H \,, \tag{E.9}$$

where $\eta_\alpha \equiv n_\alpha / n_\gamma$. Assuming that the number of photons per co-moving volume is constant $d(n_\gamma R^3)/dt = 0$, where $R = R_0 a$ and[3] $R_0 \equiv n_\gamma^{-1/3} a^{-1}$, the second term on the RHS of Eq. (E.9) can be re-written as

$$n_\gamma^2 \eta_X \frac{d}{dt} \frac{1}{n_\gamma} = n_\gamma^2 \eta_X \frac{d}{dt} \frac{R^3}{a^3 n_\gamma} = n_\gamma^2 \eta_X \frac{d}{dt} R^3 = 3 n_\gamma^2 \eta_X R^2 \frac{d}{dt} R = 3 n_\gamma^2 \eta_X R^3 H = 3 n_\gamma \eta_X H \,. \tag{E.10}$$

[2] Another convention is to normalise the particle number density to the entropy density

$$s(T) = \frac{2 g_* \pi^2}{45} T^3 .$$

[3] Here R_0 has the dimension of length, and is constant under the assumption that the number of photons per co-moving volume does not change. Its product with a corresponds to the length of one side of a cube containing a single photon.

We see that the second and third term in the LHS of Eq. (E.9) cancel. The first term in the LHS of Eq. (E.9) can further be written in terms of $z = m_X/T \propto a$, where m_X is the mass of X, such that

$$n_\gamma \frac{d}{dt}\eta_X = n_\gamma \frac{dz}{dt}\frac{d}{dz}\eta_X = zHn_\gamma \frac{d}{dz}\eta_X \tag{E.11}$$

The Boltzmann equation can then be re-written as

$$zHn_\gamma \frac{d\eta_X}{dz} = -\sum_{i,j,\ldots}[X\cdots \leftrightarrow ij\cdots]\,. \tag{E.12}$$

E.2. The RHS of a general Boltzmann equation

The square brackets on the RHS of Eq. (E.12) are given by

$$[Xa\cdots \leftrightarrow ij\cdots] = \frac{\eta_X\eta_a\cdots}{\eta_X^{\rm eq}\eta_a^{\rm eq}\cdots}\gamma^{\rm eq}(Xa\cdots \to ij\cdots) - \frac{\eta_i\eta_j\cdots}{\eta_i^{\rm eq}\eta_j^{\rm eq}\cdots}\gamma^{\rm eq}(ij\cdots \to Xa\cdots)\,. \tag{E.13}$$

Here the dots $\cdots$ denote that any additional number of particles can be included, and the sum over $i, j, \ldots$ in Eq. (E.12) goes over all[4] combinations of initial and final particles that are involved in interactions with X. Furthermore, $\eta_\alpha^{\rm eq}$ is the thermal equilibrium number density of particle α, normalised to the photon number density, and $\gamma^{\rm eq}(Xa\cdots \to ij\cdots)$ is the equilibrium reaction rate density of the process[5] $Xa\cdots \to ij\cdots$, which is given by

$$\begin{aligned}\gamma^{\rm eq}(Xa\cdots \to ij\cdots) = \int \prod_i^n \frac{d^3p_i}{2E_i(2\pi)^3}e^{-E_i/T}\prod_f^m \frac{d^3p_f}{2E_f(2\pi)^3} \\ \times (2\pi)^4\delta^{(4)}\left(\sum_i^n p_i - \sum_f^m p_f\right)|\mathcal{M}(Xa\cdots \to ij\cdots)|^2\,.\end{aligned} \tag{E.14}$$

E.2.1. Reaction rates for two-body decays

For a two-body decay $X \to ij\cdots$ we have [664]

$$\begin{aligned}\gamma^{\rm eq}(X\to ij\cdots) &= \int \frac{d^3p_X}{2E_X(2\pi)^3}e^{-E_X/T}\prod_f^2\frac{d^3p_f}{2E_f(2\pi)^3}(2\pi)^4\delta^{(4)}\left(p_X - \sum_f^2 p_f\right)|\mathcal{M}(X\to ij)|^2 \\ &= \frac{1}{2m_X}n_X\left\langle\frac{1}{\gamma}\right\rangle\int\frac{d^3p_f}{2E_f(2\pi)^3}(2\pi)^4\delta^{(4)}\left(p_X - \sum_f^2 p_f\right)|\mathcal{M}(X\to ij)|^2 \\ &= n_X^{\rm eq}\left\langle\frac{1}{\gamma}\right\rangle\Gamma(X\to ij)\,.\end{aligned} \tag{E.15}$$

[4]The particles a and j do not both necessarily need to be included in Eq. (E.13). The minimum number of particles in the reaction rate density is three, and the summation in Eq. (E.12) should accordingly include all such processes as well.

[5]Note that, if CP-violating effects are absent, the equilibrium reaction rate $\gamma^{\rm eq}(Xa\cdots \to ij\cdots)$ is identical to that of the reverse process, $\gamma^{\rm eq}(\bar{i}\bar{j}\cdots \to \bar{X}\bar{a}\cdots)$.

Here we substituted the integration over initial momenta with the equilibrium number density of X, taking the average energy per degree of freedom to be the equal to the average special-relativistic mass of X such that

$$\langle E_X \rangle / g_X = \langle \gamma m_X \rangle = m_X \langle \gamma \rangle \,, \tag{E.16}$$

where

$$\gamma = \frac{1}{\sqrt{1 - v_X^2}} = \sqrt{1 + \frac{p_X^2}{m_X^2}} = \frac{m_X}{E_X} \tag{E.17}$$

is the Lorentz factor. The ensemble average of the inverse Lorentz factor can be expressed in terms of integrals over phase space using $z = m_X/T$ and $x = E_X/T$,

$$\left\langle \frac{1}{\gamma} \right\rangle = \frac{\int_0^\infty \frac{d^3 p_X}{(2\pi)^3} \frac{m_X}{E_X} e^{-E_X/T}}{\int_0^\infty \frac{d^3 p_X}{(2\pi)^3} e^{-E_X/T}} = \frac{\int_0^\infty dp_X p_X^2 \frac{m_X}{E_X} e^{-E_X/T}}{\int_0^\infty dp_X p_X^2 e^{-E_X/T}} = \frac{\int_z^\infty dx z \sqrt{x^2 - z^2} e^{-x}}{\int_z^\infty dx x \sqrt{x^2 - z^2} e^{-x}} \,. \tag{E.18}$$

Using the Bessel function

$$K_1(z) = \int_z^\infty dx z^{-1} (x^2 - z^2)^{1/2} e^{-x} \,, \tag{E.19}$$

the reaction rate density is obtained as

$$\gamma^{\rm eq}(X \to i\,j \cdots) = \gamma^{\rm eq}(\bar{i}\,\bar{j} \cdots \to \bar{X}) = n_X^{\rm eq} \frac{K_1(z)}{K_2(z)} \Gamma\left(X \to i\,j \cdots\right) \,. \tag{E.20}$$

Here $\Gamma\left(X \to i\,j \cdots\right)$ is the width of the decay $X \to ij \cdots$. For a two-body decay, the width is given by

$$\Gamma\left(X \to i\,j\right) = \frac{1}{1 + \delta_{ij}} \frac{m_X^2 - m_i^2 - m_j^2}{16\pi m_X^3} |\mathcal{M}\left(X \to i\,j\right)|^2 \,, \tag{E.21}$$

where δ_{ij} is the Kronecker delta, and $\mathcal{M}\left(X \to i\,j\right)$ is the matrix element of the decay.

E.2.2. Reaction rates for two-to-two scatterings

For a two-to-two scattering $Xa \to ij$, the reaction rate can be obtained, following Ref. [224], by multiplying Eq. (E.14) with $1 = \int d^4P \delta^4 \left(P - \sum_{\alpha=1}^2 p_\alpha\right)$ such that we have

$$\begin{aligned} \gamma^{\rm eq}\left(X\,a \to i\,j\right) = \int d^4P \prod_i^2 \frac{d^3 p_i}{2E_i (2\pi)^3} e^{-E_i/T} \prod_f^2 \frac{d^3 p_f}{2E_f (2\pi)^3} \delta^{(4)} \left(P - \sum_{\alpha=1}^2 p_i\right) \\ \times (2\pi)^4 \delta^{(4)} \left(\sum_i^2 p_i - \sum_f^2 p_f\right) |\mathcal{M}(X\,a \to i\,j)|^2 \,. \end{aligned} \tag{E.22}$$

Now we can evaluate the integral over the initial state momenta,

$$\begin{aligned}
&\int \prod_i^2 \frac{d^3\vec{p}_i}{2E_i(2\pi)^3} e^{-E_i/T} \delta^4\left(P - \sum_i^2 p_i\right) \\
&= \int \frac{d^3\vec{p}_X}{2E_X(2\pi)^3} \frac{d^3\vec{p}_a}{2E_a(2\pi)^3} e^{-(E_X+E_a)/T} \delta^{(4)}(P - p_X - p_a) \\
&= \int \frac{d^3\vec{p}_X}{2E_X(2\pi)^3} \frac{d^4 p_a}{2E_a(2\pi)^3} \delta(p_a^0 - E_a) e^{-(E_X+E_a)/T} \delta^4(P - p_X - p_a)\,.
\end{aligned} \tag{E.23}$$

In the last step we rewrote the integrand $d^3\vec{p}_a \to d^4 p_a$ by inserting an additional Dirac delta function $\delta(p_a^0 - E_a)$. We can now use the relation

$$\delta(p_a^2 - m_a^2) = \frac{\delta(p_a^0 - E_a)}{2E_a} \tag{E.24}$$

to perform the integral over $d^4 p_a$, such that

$$\begin{aligned}
&\frac{1}{(2\pi)^3} \int \frac{d^3\vec{p}_X}{2E_X(2\pi)^3} d^4 p_a \delta(p_a^2 - m_a^2) e^{-(E_X+E_a)/T} \delta^{(4)}(P - p_X - p_a) \\
&\qquad = \frac{1}{(2\pi)^3} \int \frac{d^3\vec{p}_X}{2E_X(2\pi)^3} \delta((P - p_X)^2 - m_a^2) e^{-P^0/T}\,.
\end{aligned} \tag{E.25}$$

Next we rewrite the Dirac delta function $\delta((P - p_X)^2 - m_X^2)$ in the centre-of-mass frame,

$$\delta((P - p_a X)^2 - m_a^2) = \delta(s - 2\sqrt{s}E_X + m_X^2 - m_a^2)\,, \tag{E.26}$$

where we have identified $s = P^2$. We can now integrate over E_X by rewriting the integrand $d^3 p_X = |\vec{p}_X|^2 d|\vec{p}_X| d\Omega = |\vec{p}_X| E_X dE_X d\Omega$, such that

$$\begin{aligned}
&\frac{1}{(2\pi)^6} \int \frac{|\vec{p}_X|}{2} dE_X d\Omega \delta(s - 2\sqrt{s}E_X + m_X^2 - m_a^2) e^{-P^0/T} \\
&\qquad = \frac{1}{(2\pi)^5} \frac{|\vec{p}_X|}{2\sqrt{s}} e^{-P^0/T}\,,
\end{aligned} \tag{E.27}$$

where we have assumed spherical symmetry. Further using $\sqrt{s} = E_X + E_a$ along with the centre-of-mass frame relations

$$E_X = \frac{s + m_X^2 - m_a^2}{2\sqrt{s}}, \quad E_a = \frac{s + m_a^2 - m_X^2}{2\sqrt{s}}\,, \tag{E.28}$$

we can rewrite the result in Eq. (E.27) as

$$\frac{1}{(2\pi)^5} \frac{|\vec{p}_X|}{2\sqrt{s}} e^{-P^0/T} = \frac{1}{(2\pi)^5} \frac{\lambda^{1/2}(s, m_X^2, m_a^2)}{4s} e^{-P^0/T}\,, \tag{E.29}$$

where $\lambda(a,b,c) = a^2 + b^2 + c^2 - 2ab - 2ac - 2bc$ is the Källén function. Inserting our result back into Eq. (E.22) we have

$$\begin{aligned}\gamma^{\mathrm{eq}}(X\,a \to i\,j) =& \frac{1}{(2\pi)^5}\int d^4P \prod_f^2 \frac{d^3p_f}{2E_f(2\pi)^3}\frac{\lambda^{1/2}(s,m_X^2,m_a^2)}{4s}e^{-P^0/T} \\ &\times (2\pi)^4\delta^{(4)}\left(\sum_i^2 p_i - \sum_f^2 p_f\right)|\mathcal{M}(X\,a \to i\,j)|^2\,,\end{aligned} \tag{E.30}$$

where we can identify the cross section [21]

$$\begin{aligned}&\sigma(X\,a \to i\,j) = \\ &\frac{1}{2\lambda^{1/2}(s,m_X^2,m_a^2)}\int\prod_f^2\frac{d^3p_f}{2E_f(2\pi)^3}(2\pi)^4\delta^4\left(\sum_i^2 p_i - \sum_f^2 p_f\right)|\mathcal{M}(X\,a \to i\,j)|^2\,,\end{aligned} \tag{E.31}$$

such that

$$\gamma^{\mathrm{eq}}(X\,a \to i\,j) = \frac{1}{8\pi}\int\frac{d^4P}{(2\pi)^4}e^{-P^0/T}\hat{\sigma}(X\,a \to i\,j)\,. \tag{E.32}$$

Here we have introduced the reduced cross section

$$\hat{\sigma}(X\,a \to i\,j) = \frac{2\lambda(s,m_X^2,m_a^2)}{s}\sigma(X\,a \to i\,j)\,. \tag{E.33}$$

Performing the same manipulation of the final state momenta as with the initial state momenta, the cross section in Eq. (E.31) can be re-written as

$$\sigma(X\,a \to i\,j) = \frac{1}{16\pi s}\frac{\lambda^{1/2}(s,m_i^2,m_j^2)}{\lambda^{1/2}(s,m_X^2,m_a^2)}\int d\Omega|\mathcal{M}(X\,a \to i\,j)|^2\,. \tag{E.34}$$

The angular integrand $d\Omega$ can, in the centre-of-mass frame, be written in terms of the Mandelstam variable

$$t = (p_X - p_i)^2 = \cdots + \frac{1}{2s}\lambda^{1/2}(s,m_X^2,m_a^2)\lambda^{1/2}(s,m_i^2,m_j^2)\cos\theta \tag{E.35}$$

such that

$$d\Omega = 2\pi d\cos\theta = \frac{4\pi s}{\lambda^{1/2}(s,m_X^2,m_a^2)\lambda^{1/2}(s,m_i^2,m_j^2)}dt\,, \tag{E.36}$$

which lets us re-write the reduced cross section from Eq. (E.33) as

$$\hat{\sigma}(X\,a \to i\,j) = \frac{1}{8\pi s}\int_{t_+}^{t_-} dt|\mathcal{M}(X\,a \to i\,j)|^2\,, \tag{E.37}$$

with the integration limits

$$\begin{aligned}t^{\pm} =& \frac{(m_X^2 - m_a^2 - m_i^2 + m_j^2)^2}{4s} \\ &- \left(\sqrt{\frac{(s + m_X^2 - m_a^2)^2}{4s} - m_X^2} \pm \sqrt{\frac{(s + m_i^2 - m_j^2)^2}{4s} - m_i^2}\right)^2\,.\end{aligned} \tag{E.38}$$

Lastly, we can further re-write the scattering rate density from Eq. (E.32) in terms of the modified Bessel function resulting in

$$\gamma^{\rm eq}(X\,a \to i\,j) = \frac{T}{64\pi^4}\int_{s_{\rm min}}^{\infty} ds\sqrt{s}\hat{\sigma}(X\,a \to i\,j)K_1\left(\frac{\sqrt{s}}{T}\right)\,, \tag{E.39}$$

where $s_{\rm min} = \max\left((m_X + m_a)^2, (m_i + m_j)^2\right)$.

E.2.3. Reaction rates for EFT operators

For processes with n particles in the initial state and m in the final state, we again insert

$$\begin{aligned} 1 &= \int d^4P\delta^{(4)}\left(P - \sum_{i=1}^{n} p_i\right) \\ &= \int dsdP_0d\Omega\frac{1}{2}\sqrt{P_0^2 - s}\delta^{(4)}\left(P - \sum_{i=1}^{n} p_i\right) \end{aligned} \tag{E.40}$$

in Eq. (E.14), where $s = P^2$, to obtain [394]

$$\begin{aligned} \gamma^{\rm eq}\left(X\,a\cdots \to i\,j\cdots\right) = \frac{1}{2}\int dsd\Omega dP_0 e^{-P_0/T}\sqrt{P_0^2 - s} \\ \times \int\prod_i^n \frac{d^3p_i}{2E_i(2\pi)^3}\prod_f^m \frac{d^3p_f}{2E_f(2\pi)^3}\delta^{(4)}\left(P - \sum_{i=1}^{n} p_i\right) \\ \times (2\pi)^4\delta^{(4)}\left(\sum_i^n p_i - \sum_f^m p_f\right)|\mathcal{M}(X\,a\cdots \to i\,j\cdots)|^2\,. \end{aligned} \tag{E.41}$$

Assuming that the matrix element does not depend on the distribution of initial or final momenta, we can express the n-body phase space element in the limit $\sqrt{s} \gg m_1, m_2, \ldots, m_n$ as [665]

$$R_n = \frac{1}{2(4\pi)^{2n-3}}\frac{s^{n-2}}{\Gamma(n)\Gamma(n-1)}\,, \tag{E.42}$$

where R_n is defined in Appendix C. We now rewrite the P_0 integral in terms of a Bessel function,

$$\int_{\sqrt{s}}^{\infty} dP_0 e^{-P_0/T}\sqrt{P_0^2 - s} = \frac{\sqrt{s}}{T}\int_{\sqrt{s}/T}^{\infty} d\left(\frac{P_0}{T}\right)\left(\frac{T}{\sqrt{s}}\right)\sqrt{\frac{P_0^2}{T^2} - \frac{s}{T^2}}e^{-P_0/T} = T\sqrt{s}K_1\left(\frac{\sqrt{s}}{T}\right)\,, \tag{E.43}$$

where we have used the lower limit $P_0^{\rm min} = \sqrt{s}$ which corresponds to $|\vec{P}| = 0$. Also performing the $d\Omega$ integral assuming no angle-dependence, we arrive at the expression

$$\begin{aligned} \gamma^{\rm eq}\left(X\,a\cdots \to i\,j\cdots\right) = \frac{2T}{(4\pi)^{2n+2m-3}}\int ds\sqrt{s}K_1\left(\frac{\sqrt{s}}{T}\right) \\ \times \frac{s^{n+m-4}}{\Gamma(n)\Gamma(n-1)\Gamma(m)\Gamma(m-1)}|\mathcal{M}(X\,a\cdots \to i\,j\cdots)|^2\,. \end{aligned} \tag{E.44}$$

We now turn to the integral [663]

$$\int_0^\infty dx K_1(ax) x^\mu = 2^{\mu-1} a^{-\mu-1} \Gamma\left(\frac{2+\mu}{2}\right) \Gamma\left(\frac{\mu}{2}\right) , \tag{E.45}$$

which is applicable for $x \to \sqrt{s}$ in the massless limit that we have already employed, assuming no dependence on s in the matrix element. We then obtain

$$\gamma^{\text{eq}}(X\,a\cdots \to i\,j\cdots) = \frac{1}{4} \frac{T^{2n+2m-4}}{(2\pi)^{2n+2m-3}} \frac{\Gamma(n+m-2)\Gamma(n+m-3)}{\Gamma(n)\Gamma(n-1)\Gamma(m)\Gamma(m-1)} |\mathcal{M}(X\,a\cdots \to i\,j\cdots)|^2 . \tag{E.46}$$

This expression does not contain any integrals, but the s-dependence of the matrix element is lost. For calculations where this approximation is not valid, Eq. (E.44) should be used instead.

F. FeynRules model file

Below we give the code corresponding to a model file that includes all the dimension-7 $\Delta L = 2$ SMEFT operators used in Sec. 4.4.

```
(* ************************* *)
(* *****  Information   ***** *)
(* ************************* *)
M$ModelName = "dimsevenLNV";

M$Information = {
Authors      -> {"K. Fridell"},
Institutions -> {"Technical University of Munich"},
Emails       -> {"kare.fridell@tum.de"}
};

FeynmanGauge = True;

M$InteractionOrderHierarchy = {
{QCD, 1},
{QED, 2},
{NP, 2}
};

(* ************************* *)
(* *****  Change  log   ***** *)
(* ************************* *)
(* v1.0: First build *)

(* ************************* *)
(* *****   Parameters   ***** *)
(* ************************* *)
M$Parameters = {
(* External Parameters *)
CbLambda == {
ParameterType -> External,
BlockName -> NUPHYSICS,
OrderBlock -> 1,
```

```
Value -> (1000000^2/1000^3),
InteractionOrder -> {NP,1},
ComplexParameter -> False,
TeX -> C/\[CapitalLambda]^3,
Description -> "EFT cutoff scale [GeV]"
},
CbLambdaR == {
ParameterType -> External,
BlockName -> NUPHYSICS,
OrderBlock -> 1,
Value -> (1/1000^3),
InteractionOrder -> {NP,1},
ComplexParameter -> False,
TeX -> C/\[CapitalLambda]^3,
Description -> "EFT cutoff scale [GeV]"
},
CbLambdaAS == {
ParameterType -> External,
Indices          -> {Index[Generation], Index[Generation]},
BlockName -> NUPHYSICS,
Value -> {CbLambda[1,1] -> 0.0, CbLambda[1,2] -> (1/1000^3),
CbLambda[1,3] -> (1/1000^3), CbLambda[2,1] -> (-1/1000^3),
CbLambda[2,2] -> 0.0, CbLambda[2,3] -> (1/1000^3),
CbLambda[3,1] -> (-1/1000^3), CbLambda[3,2] -> (-1/1000^3),
CbLambda[3,3] -> 0.0},
InteractionOrder -> {NP,1},
ComplexParameter -> False,
TeX -> C/\[CapitalLambda]^3,
Description -> "EFT cutoff scale [GeV]"
}
};

(* ************************** *)
(* **** Particle classes **** *)
(* ************************** *)

M$ClassesDescription = {

(* Fake scalars *)

S[110] == {
ClassName       -> SF1,
```

```
SelfConjugate   -> False,
Mass            -> {MSF1,1000000},
Width           -> {WSF1,0},
QuantumNumbers   -> {Q -> 2/3},
Indices          -> {Index[Colour]},
PropagatorLabel -> "SF1",
ParticleName    -> "SF1",
AntiParticleName    -> "SF1~",
FullName        -> "Scalar Fake One"
},
S[111] == {
ClassName       -> SF0,
SelfConjugate   -> False,
Mass            -> {MSF0,1000000},
Width           -> {WSF0,0},
QuantumNumbers   -> {Q -> -1/3},
Indices          -> {Index[Colour]},
PropagatorLabel -> "SF0",
ParticleName    -> "SF0",
AntiParticleName    -> "SF0~",
FullName        -> "Scalar Fake Zero"
},
S[112] == {
ClassName      -> SF,
Unphysical     -> True,
Indices        -> {Index[SU2D], Index[Colour]},
FlavorIndex    -> SU2D,
SelfConjugate  -> False,
QuantumNumbers -> {Y -> 1/6},
Definitions    -> { SF[1,cc_] -> SF1[cc], SF[2,cc_] -> SF0[cc]  }
},
SE[110] == {
ClassName       -> SEF1,
SelfConjugate   -> False,
Mass            -> {MSEF1,1000000},
Width           -> {WSEF1,0},
QuantumNumbers   -> {Q -> 1},
PropagatorLabel -> "SEF1",
ParticleName    -> "SEF1",
AntiParticleName    -> "SEF1~",
FullName        -> "Scalar E Fake One"
},
```

```
SE[111] == {
ClassName       -> SEF0,
SelfConjugate   -> False,
Mass            -> {MSEF0,1000000},
Width           -> {WSEF0,0},
PropagatorLabel -> "SEF0",
ParticleName    -> "SEF0",
AntiParticleName    -> "SEF0~",
FullName        -> "Scalar E Fake Zero"
},
SE[112] == {
ClassName      -> SEF,
Unphysical     -> True,
Indices        -> {Index[SU2D]},
FlavorIndex    -> SU2D,
SelfConjugate  -> False,
QuantumNumbers -> {Y -> 1/2},
Definitions    -> { SEF[1] -> SEF1, SEF[2] -> SEF0  }
},

(* Fake vector *)

V[110] == {
ClassName       -> VF,
SelfConjugate   -> False,
Mass            -> {MVF1,1000000},
Width           -> {WVF1,0},
QuantumNumbers   -> {Q -> -1},
PropagatorLabel -> "VF",
ParticleName    -> "VF",
AntiParticleName    -> "VF~",
FullName        -> "Vector Fake"
}};

(* ************************* *)
(* *****   Lagrangian   ***** *)
(* ************************* *)

LdLQLH1 :=
Block[{sp1,sp2,ii,jj,kk,ll,ff1,ff2,ff3,ff4,cc,feynmangaugerules},
feynmangaugerules = If[Not[FeynmanGauge], {G0|GP|GPbar ->0}, {}];
```

```
ExpandIndices[
(CbLambda)^(1/2) * Eps[ii,jj] dRbar[sp1,ff1,cc].LL[sp1,ii,ff2] SF[jj,cc]
+ (CbLambda)^(1/2) * Eps[kk,ll] SFbar[jj,cc]
CC[QLbar[sp2,jj,ff3,cc]].LL[sp2,kk,ff4] Phi[ll],
FlavorExpand -> SU2D]/.feynmangaugerules
];

LdLQLH2 :=
Block[{sp1,sp2,ii,jj,kk,ll,ff1,ff2,ff3,ff4,cc,feynmangaugerules},
feynmangaugerules = If[Not[FeynmanGauge], {G0|GP|GPbar ->0}, {}];

ExpandIndices[
(CbLambda)^(1/2) * Eps[ii,kk] dRbar[sp1,ff1,cc].LL[sp1,ii,ff2] SF[kk,cc]
+ (CbLambda)^(1/2) * Eps[jj,ll] SFbar[kk,cc]
CC[QLbar[sp2,jj,ff3,cc]].LL[sp2,kk,ff4] Phi[ll],
FlavorExpand -> SU2D]/.feynmangaugerules
];

LdLueH :=
Block[{sp1,sp2,ii,jj,ff1,ff2,ff3,ff4,cc,feynmangaugerules},
feynmangaugerules = If[Not[FeynmanGauge], {G0|GP|GPbar ->0}, {}];

ExpandIndices[
(CbLambda)^(1/2) * Eps[ii,jj] dRbar[sp1,ff1,cc].LL[sp1,ii,ff2] SF[jj,cc]
+ (CbLambda)^(1/2) * SFbar[jj,cc] CC[uRbar[sp2,ff3,cc]].lR[sp2,ff4]
Phi[jj], FlavorExpand -> SU2D]/.feynmangaugerules
];

LduLLH :=
Block[{sp1,sp2,sp3,ii,jj,ff1,ff2,ff3,ff4,cc,mu,lagu,feynmangaugerules},
feynmangaugerules = If[Not[FeynmanGauge], {G0|GP|GPbar ->0}, {}];

ExpandIndices[
I * (CbLambda)^(1/2) * dRbar[sp1,ff1,cc].Ga[mu,sp1,sp2].uR[sp2,ff2,cc]
VF[mu] +  I * (CbLambda)^(1/2) * Eps[ii,jj] VFbar[mu]
CC[LLbar[sp3,ii,ff3]].DC[LL[sp3,jj,ff4],mu],
FlavorExpand -> SU2D]/.feynmangaugerules
];

LLHB :=
Block[{sp1,ii,jj,kk,ll,ff1,ff2,mu,nu,feynmangaugerules},
feynmangaugerules = If[Not[FeynmanGauge], {G0|GP|GPbar ->0}, {}];
```

```
ExpandIndices[
I/2 * CbLambdaAS[ff1,ff2] * g1 (Ga[mu,sp1,sp3] Ga[nu,sp3,sp2] -
Ga[nu,sp1,sp3] Ga[mu,sp3,sp2] )
Eps[jj,mm] Eps[ii,kk]
CC[LLbar[sp1,jj,ff1]].LL[sp2,ii,ff2]
Phi[mm] Phi[kk] FS[B,mu,nu],
FlavorExpand->SU2D]/.feynmangaugerules
];

LeLLLH :=
Block[{sp1,sp2,ii,jj,kk,ll,ff1,ff2,ff3,ff4,feynmangaugerules},
feynmangaugerules = If[Not[FeynmanGauge], {G0|GP|GPbar ->0}, {}];

ExpandIndices[
(CbLambda)^(1/2) * lRbar[sp1,ff1].LL[sp1,ii,ff2] SEFbar[ii]
+ (CbLambda)^(1/2) * Eps[ii,jj] Eps[kk,ll] SEF[ii]
CC[LLbar[sp2,jj,ff3]].LL[sp2,kk,ff4] Phi[ll],
FlavorExpand -> SU2D]/.feynmangaugerules
];

LLeHD :=
Block[{sp1,sp2,ii,jj,kk,ll,ff1,ff2,mu,feynmangaugerules},
feynmangaugerules = If[Not[FeynmanGauge], {G0|GP|GPbar ->0}, {}];

ExpandIndices[
CbLambdaR * I * Eps[ii,jj] Eps[kk,ll]
CC[LLbar[sp1,ii,ff1]].Ga[mu,sp1,sp2].lR[sp2,ff2]
Phi[jj] Phi[kk] DC[Phi[ll],mu],
FlavorExpand -> SU2D]/.feynmangaugerules
];

LLHD1 :=
Block[{sp1,ii,jj,kk,ll,ff1,ff2,feynmangaugerules},
feynmangaugerules = If[Not[FeynmanGauge], {G0|GP|GPbar ->0}, {}];

ExpandIndices[
CbLambdaR * Eps[ii,jj] Eps[kk,ll]
CC[LLbar[sp1,ii,ff1]].DC[LL[sp1,jj,ff2],mu] Phi[kk]
DC[Phi[ll],mu], FlavorExpand -> SU2D]/.feynmangaugerules
];
```

```
LLHD2 :=
Block[{sp1,ii,jj,kk,ll,mu,ff1,ff2,feynmangaugerules},
feynmangaugerules = If[Not[FeynmanGauge], {G0|GP|GPbar ->0}, {}];

ExpandIndices[
CbLambdaR * Eps[ii,jj] Eps[kk,ll]
CC[LLbar[sp1,ii,ff1]].DC[LL[sp1,jj,ff2],mu]
Phi[kk] DC[Phi[ll],mu]
+ CbLambda * Eps[ii,ll] Eps[jj,kk]
CC[LLbar[sp1,ii,ff1]].DC[LL[sp1,jj,ff2],mu]
Phi[kk] DC[Phi[ll],mu],
FlavorExpand -> SU2D]/.feynmangaugerules
];

LLHW :=
Block[{sp1,sp2,ii,jj,ll,mm,nn,kk,A,ff1,ff2,mu,nu,feynmangaugerules},
feynmangaugerules = If[Not[FeynmanGauge], {G0|GP|GPbar ->0}, {}];

ExpandIndices[
I/2 * CbLambdaAS[ff1,ff2] * gw * Eps[mm,ll] Eps[ii,jj]
2*Ta[A,ll,nn] FS[Wi,mu,nu,A] (Ga[mu,sp1,sp3] Ga[nu,sp3,sp2]
- Ga[nu,sp1,sp3] Ga[mu,sp3,sp2] )
CC[LLbar[sp1,ii,ff1]].LL[sp2,mm,ff2] Phi[nn] Phi[jj],
FlavorExpand -> {SU2D,SU2W}]/.feynmangaugerules
];

LQuLLH :=
Block[{sp1,sp2,ii,jj,kk,ll,ff1,ff2,ff3,ff4,cc,feynmangaugerules},
feynmangaugerules = If[Not[FeynmanGauge], {G0|GP|GPbar ->0}, {}];

ExpandIndices[
(CbLambda)^(1/2) * Eps[ii,ll] QLbar[sp1,ii,ff1,cc].uR[sp1,ff2,cc]
SEFbar[ll] + (CbLambda)^(1/2) * Eps[ii,ll] SEF[ll]
Eps[kk, jj].CC[LLbar[sp2,ii,ff3]].LL[sp2,kk,ff4] Phi[jj],
FlavorExpand -> SU2D]/.feynmangaugerules
];

LLH :=
Block[{sp1,ii,jj,kk,ll,mm,ff1,ff2,feynmangaugerules},
feynmangaugerules = If[Not[FeynmanGauge], {G0|GP|GPbar ->0}, {}];

ExpandIndices[
```

```
CbLambdaR * Eps[ii,jj] Eps[kk,ll]
CC[LLbar[sp1,ii,ff1]].LL[sp1,kk,ff2]
Phi[jj] Phi[ll] Phibar[mm] Phi[mm],
FlavorExpand -> SU2D]/.feynmangaugerules
];

(* Combine dimension-7 Lagrangian *)
LD7 := LdLQLH1 + HC[LdLQLH1] + LdLQLH2 + HC[LdLQLH2]
+ LdLueH + HC[LdLueH] + LduLLH + HC[LduLLH]
+ LeLLLH + HC[LeLLLH] + LLeHD + HC[LLeHD]
+ LLHB + HC[LLHB] + LLHD1 + HC[LLHD1]
+ LLHD2 + HC[LLHD2] + LLHW + HC[LLHW]
+ LQuLLH + HC[LQuLLH]  + LLH + HC[LLH];

(* Combine full Lagrangian *)
LFull := LSM + LD7;
```

Bibliography

[1] F. F. Deppisch, K. Fridell and J. Harz, *Constraining lepton number violating interactions in rare kaon decays*, *JHEP* **12** (2020) 186, [2009.04494].

[2] K. Fridell, J. Harz and C. Hati, *Probing baryogenesis with neutron-antineutron oscillations*, *JHEP* **11** (2021) 185, [2105.06487].

[3] P. D. Bolton, F. F. Deppisch, K. Fridell, J. Harz, C. Hati and S. Kulkarni, *Probing active-sterile neutrino transition magnetic moments with photon emission from CEνNS*, *Phys. Rev. D* **106** (2022) 035036, [2110.02233].

[4] K. Fridell, L. Graf, J. Harz and C. Hati, in preparation.

[5] F. F. Deppisch, K. Fridell and J. Harz, *Implications of Rare Kaon Decays on Lepton Number Violating Interactions*, *PoS* **ICHEP2020** (2021) 130, [2012.14825].

[6] K. Fridell, J. Harz and C. Hati, *Neutron-antineutron oscillations as a probe of baryogenesis*, *J. Phys. Conf. Ser.* **2156** (2021) 012015.

[7] P. D. Bolton, F. F. Deppisch, K. Fridell, J. Harz, C. Hati and S. Kulkarni, *Transition neutrino magnetic moments in CEνNS*, *J. Phys. Conf. Ser.* **2156** (2021) 012218.

[8] K. Fridell, J. Harz and C. Hati, *Probing Baryogenesis using Neutron-Anti-Neutron Oscillation*, *PoS* **ICHEP2020** (2021) 243.

[9] C. Hati, P. Bolton, F. F. Deppisch, K. Fridell, J. Harz and S. Kulkarni, *Distinguishing Dirac vs Majorana Neutrinos at CEνNS experiments*, *PoS* **EPS-HEP2021** (2022) 225.

[10] S. Weinberg, *A Model of Leptons*, *Phys. Rev. Lett.* **19** (1967) 1264–1266.

[11] S. L. Glashow, *Partial Symmetries of Weak Interactions*, *Nucl. Phys.* **22** (1961) 579–588.

[12] A. Salam, *Weak and Electromagnetic Interactions*, *Conf. Proc. C* **680519** (1968) 367–377.

[13] T. Chupp, P. Fierlinger, M. Ramsey-Musolf and J. Singh, *Electric dipole moments of atoms, molecules, nuclei, and particles*, *Rev. Mod. Phys.* **91** (2019) 015001, [1710.02504].

[14] Particle Data Group collaboration, P. A. Zyla et al., *Review of Particle Physics*, *PTEP* **2020** (2020) 083C01.

[15] ATLAS collaboration, G. Aad et al., *Observation of a new particle in the search for the Standard Model Higgs boson with the ATLAS detector at the LHC*, *Phys. Lett. B* **716** (2012) 1–29, [1207.7214].

[16] CMS collaboration, S. Chatrchyan et al., *Observation of a New Boson at a Mass of 125 GeV with the CMS Experiment at the LHC*, *Phys. Lett. B* **716** (2012) 30–61, [1207.7235].

[17] Y. Grossman and Y. Nir, *The Standard Model*. Unpublished.

[18] S. Hossenfelder, *Das hässliche Universum: Warum unsere Suche nach Schönheit die Physik in die Sackgasse führt*. S. FISCHER, 2018.

[19] D. Griffiths, *Introduction to Elementary Particles*. Wiley, 1987.

[20] M. Srednicki, *Quantum Field Theory*. Cambridge University Press, 2007.

[21] M. E. Peskin and D. V. Schroeder, *An Introduction to Quantum Field Theory*. Westview Press, 1995.

[22] N. Cabibbo, *Unitary Symmetry and Leptonic Decays*, *Phys. Rev. Lett.* **10** (1963) 531–533.

[23] M. Kobayashi and T. Maskawa, *CP Violation in the Renormalizable Theory of Weak Interaction*, *Prog. Theor. Phys.* **49** (1973) 652–657.

[24] Y. Grossman and P. Tanedo, *Just a Taste: Lectures on Flavor Physics*, in *Theoretical Advanced Study Institute in Elementary Particle Physics: Anticipating the Next Discoveries in Particle Physics*, pp. 109–295, 2018. 1711.03624. DOI.

[25] D. Halzen and Martin, A. D., *Quarks and Leptons: An Introductory Course in Modern Particle Physics*. Wiley, 1991.

[26] W. Greiner and Müller, B., *Quantum Mechanics: Symmetries*. Springer, 1997.

[27] N. Lohitsiri, *Anomalies and the Standard Model of Particle Physics*. PhD thesis, Cambridge U., DAMTP, 2020. 10.17863/CAM.60191.

[28] C. Bouchiat, J. Iliopoulos and P. Meyer, *An Anomaly Free Version of Weinberg's Model*, *Phys. Lett. B* **38** (1972) 519–523.

[29] T. Eguchi, P. B. Gilkey and A. J. Hanson, *Gravitation, Gauge Theories and Differential Geometry*, *Phys. Rept.* **66** (1980) 213.

[30] J. Frohlich and B. Pedrini, *New applications of the chiral anomaly*, hep-th/0002195.

[31] A. M. Polyakov, *Gauge Fields and Strings*. CRC Press, 1987.

[32] M.-C. Chen, *TASI 2006 Lectures on Leptogenesis*, in *Theoretical Advanced Study Institute in Elementary Particle Physics: Exploring New Frontiers Using Colliders and Neutrinos*, pp. 123–176, 3, 2007. hep-ph/0703087.

[33] T. Cheng and L. Li, *Gauge Theory of elementary particle physics*. Oxford University Press, 1988.

[34] S. L. Adler, *Axial vector vertex in spinor electrodynamics*, *Phys. Rev.* **177** (1969) 2426–2438.

[35] J. S. Bell and R. Jackiw, *A PCAC puzzle: $\pi^0 \to \gamma\gamma$ in the σ model*, *Nuovo Cim. A* **60** (1969) 47–61.

[36] S. Dimopoulos and L. Susskind, *On the Baryon Number of the Universe*, *Phys. Rev. D* **18** (1978) 4500–4509.

[37] J. M. Cline, *Baryogenesis*, in *Les Houches Summer School - Session 86: Particle Physics and Cosmology: The Fabric of Spacetime*, 9, 2006. hep-ph/0609145.

[38] A. A. Belavin, A. M. Polyakov, A. S. Schwartz and Y. S. Tyupkin, *Pseudoparticle Solutions of the Yang-Mills Equations*, *Phys. Lett. B* **59** (1975) 85–87.

[39] G. 't Hooft, *Computation of the Quantum Effects Due to a Four-Dimensional Pseudoparticle*, *Phys. Rev. D* **14** (1976) 3432–3450.

[40] C. G. Callan, Jr., R. F. Dashen and D. J. Gross, *The Structure of the Gauge Theory Vacuum*, *Phys. Lett. B* **63** (1976) 334–340.

[41] N. S. Manton, *Topology in the Weinberg-Salam Theory*, *Phys. Rev. D* **28** (1983) 2019.

[42] F. R. Klinkhamer and N. S. Manton, *A Saddle Point Solution in the Weinberg-Salam Theory*, *Phys. Rev. D* **30** (1984) 2212.

[43] G. 't Hooft, *Symmetry Breaking Through Bell-Jackiw Anomalies*, *Phys. Rev. Lett.* **37** (1976) 8–11.

[44] L. D. McLerran, *Lectures on B+L violation at high temperature in electroweak theory*, in *Trieste Summer School on High-energy Physics and Cosmology (Part 1 (15 Jun - 3 Jul) includes Workshop on Superstrings and Related Topics, 2-3 Jul 1992) Part 2 will be held 6-31 Jul (Note: change of dates from 15 Jun-14 Aug)*, pp. 523–565, 11, 1992.

[45] V. A. Kuzmin, V. A. Rubakov and M. E. Shaposhnikov, *On the Anomalous Electroweak Baryon Number Nonconservation in the Early Universe*, *Phys. Lett. B* **155** (1985) 36.

[46] S. Y. Khlebnikov and M. E. Shaposhnikov, *The Statistical Theory of Anomalous Fermion Number Nonconservation*, *Nucl. Phys. B* **308** (1988) 885–912.

[47] S. Davidson, E. Nardi and Y. Nir, *Leptogenesis*, *Phys. Rept.* **466** (2008) 105–177, [0802.2962].

[48] P. B. Arnold, D. Son and L. G. Yaffe, *The Hot baryon violation rate is O (alpha-w**5 T**4)*, *Phys. Rev. D* **55** (1997) 6264–6273, [hep-ph/9609481].

[49] L. D. McLerran, E. Mottola and M. E. Shaposhnikov, *Sphalerons and Axion Dynamics in High Temperature QCD*, *Phys. Rev. D* **43** (1991) 2027–2035.

[50] G. F. Giudice and M. E. Shaposhnikov, *Strong sphalerons and electroweak baryogenesis*, *Phys. Lett. B* **326** (1994) 118–124, [hep-ph/9311367].

[51] G. D. Moore, *Computing the strong sphaleron rate*, *Phys. Lett. B* **412** (1997) 359–370, [hep-ph/9705248].

[52] L. Dolan and R. Jackiw, *Symmetry Behavior at Finite Temperature*, *Phys. Rev. D* **9** (1974) 3320–3341.

[53] E. Kolb and M. Turner, *The Early Universe*. CRC Press, 1994.

[54] A. Einstein, *The Foundation of the General Theory of Relativity*, *Annalen Phys.* **49** (1916) 769–822.

[55] Planck collaboration, N. Aghanim et al., *Planck 2018 results. VI. Cosmological parameters*, *Astron. Astrophys.* **641** (2020) A6, [1807.06209].

[56] Supernova Search Team collaboration, A. G. Riess et al., *Observational evidence from supernovae for an accelerating universe and a cosmological constant*, *Astron. J.* **116** (1998) 1009–1038, [astro-ph/9805201].

[57] Supernova Cosmology Project collaboration, S. Perlmutter et al., *Measurements of* Ω *and* Λ *from 42 high redshift supernovae*, *Astrophys. J.* **517** (1999) 565–586, [astro-ph/9812133].

[58] D. Saadeh, S. M. Feeney, A. Pontzen, H. V. Peiris and J. D. McEwen, *How isotropic is the Universe?*, *Phys. Rev. Lett.* **117** (2016) 131302, [1605.07178].

[59] D. Camarena, V. Marra, Z. Sakr and C. Clarkson, *The Copernican principle in light of the latest cosmological data*, 2107.02296.

[60] C. Bengaly, *A null test of the Cosmological Principle with BAO measurements*, 2111.06869.

[61] R. G. Clowes, L. E. Campusano, M. J. Graham and I. K. Soechting, *Two close Large Quasar Groups of size ~ 350 Mpc at z ~ 1.2*, *Mon. Not. Roy. Astron. Soc.* **419** (2012) 556, [1108.6221].

[62] R. G. Clowes, K. A. Harris, S. Raghunathan, L. E. Campusano, I. K. Soechting and M. J. Graham, *A structure in the early universe at z ~ 1.3 that exceeds the homogeneity scale of the R-W concordance cosmology*, *Mon. Not. Roy. Astron. Soc.* **429** (2013) 2910–2916, [1211.6256].

[63] I. Horvath, J. Hakkila and Z. Bagoly, *Possible structure in the GRB sky distribution at redshift two*, *Astron. Astrophys.* **561** (2014) L12, [1401.0533].

[64] eBOSS collaboration, S. Alam et al., *Completed SDSS-IV extended Baryon Oscillation Spectroscopic Survey: Cosmological implications from two decades of spectroscopic surveys at the Apache Point Observatory*, *Phys. Rev. D* **103** (2021) 083533, [2007.08991].

[65] A. Friedman, *On the Curvature of space*, *Z. Phys.* **10** (1922) 377–386.

[66] G. Lemaitre, *A homogeneous universe of constant mass and increasing radius accounting for the radial velocity of extra-galactic nebulae*, *Mon. Not. Roy. Astron. Soc.* **91** (1931) 483–490.

[67] H. P. Robertson, *Kinematics and World-Structure*, *Astrophys. J.* **82** (1935) 284–301.

[68] A. G. Walker, *On Milne's Theory of World-Structure*, *Proceedings of the London Mathematical Society* **42** (1937) 90–127.

[69] G. Lemaitre, *The expanding universe*, *Annales Soc. Sci. Bruxelles A* **53** (1933) 51–85.

[70] R. C. Tolman, *Effect of imhomogeneity on cosmological models*, *Proc. Nat. Acad. Sci.* **20** (1934) 169–176.

[71] H. Bondi, *Spherically symmetrical models in general relativity*, *Mon. Not. Roy. Astron. Soc.* **107** (1947) 410–425.

[72] A. Friedmann, *On the Possibility of a world with constant negative curvature of space*, *Z. Phys.* **21** (1924) 326–332.

[73] W. Handley, *Curvature tension: evidence for a closed universe*, *Phys. Rev. D* **103** (2021) L041301, [1908.09139].

[74] E. Di Valentino, A. Melchiorri and J. Silk, *Planck evidence for a closed Universe and a possible crisis for cosmology*, *Nature Astron.* **4** (2019) 196–203, [1911.02087].

[75] G. Efstathiou and S. Gratton, *The evidence for a spatially flat Universe*, *Mon. Not. Roy. Astron. Soc.* **496** (2020) L91–L95, [2002.06892].

[76] S. Vagnozzi, E. Di Valentino, S. Gariazzo, A. Melchiorri, O. Mena and J. Silk, *The galaxy power spectrum take on spatial curvature and cosmic concordance*, *Phys. Dark Univ.* **33** (2021) 100851, [2010.02230].

[77] S. Vagnozzi, A. Loeb and M. Moresco, *Eppur è piatto? The Cosmic Chronometers Take on Spatial Curvature and Cosmic Concordance*, *Astrophys. J.* **908** (2021) 84, [2011.11645].

[78] V. M. Slipher, *The radial velocity of the Andromeda Nebula*, *Lowell Observatory Bulletin* **1** (Jan., 1913) 56–57.

[79] E. Hubble, *A relation between distance and radial velocity among extra-galactic nebulae*, *Proc. Nat. Acad. Sci.* **15** (1929) 168–173.

[80] A. H. Guth, *The Inflationary Universe: A Possible Solution to the Horizon and Flatness Problems*, *Phys. Rev. D* **23** (1981) 347–356.

[81] A. D. Linde, *A New Inflationary Universe Scenario: A Possible Solution of the Horizon, Flatness, Homogeneity, Isotropy and Primordial Monopole Problems*, *Phys. Lett. B* **108** (1982) 389–393.

[82] L. Perivolaropoulos and F. Skara, *Challenges for ΛCDM: An update*, 2105.05208.

[83] S. Weinberg, *Cosmology*. Oxford University Press, 2008.

[84] S. Weinberg, *Gravitation and Cosmology*. John Wiley & Sons, Inc., 1972.

[85] M. Le Bellac, *Thermal Field Theory*. Cambridge University Press, 2000.

[86] B. Garbrecht and P. Schwaller, *Spectator Effects during Leptogenesis in the Strong Washout Regime*, *JCAP* **10** (2014) 012, [1404.2915].

[87] M. N. Saha, *On a Physical Theory of Stellar Spectra*, *Proceedings of the Royal Society of London Series A* **99** (May, 1921) 135–153.

[88] Super-Kamiokande collaboration, Y. Fukuda et al., *Evidence for oscillation of atmospheric neutrinos*, *Phys. Rev. Lett.* **81** (1998) 1562–1567, [hep-ex/9807003].

[89] SNO collaboration, Q. R. Ahmad et al., *Measurement of the rate of $\nu_e + d \to p + p + e^-$ interactions produced by ^8B solar neutrinos at the Sudbury Neutrino Observatory*, *Phys. Rev. Lett.* **87** (2001) 071301, [nucl-ex/0106015].

[90] B. Pontecorvo, *Inverse beta processes and nonconservation of lepton charge*, *Zh. Eksp. Teor. Fiz.* **34** (1957) 247.

[91] Z. Maki, M. Nakagawa and S. Sakata, *Remarks on the unified model of elementary particles*, *Prog. Theor. Phys.* **28** (1962) 870–880.

[92] G. Bertone and D. Hooper, *History of dark matter*, *Rev. Mod. Phys.* **90** (2018) 045002, [1605.04909].

[93] G. F. Chapline, *Cosmological effects of primordial black holes*, *Nature* **253** (1975) 251–252.

[94] B. Carr, F. Kuhnel and M. Sandstad, *Primordial Black Holes as Dark Matter*, *Phys. Rev. D* **94** (2016) 083504, [1607.06077].

[95] M. Milgrom, *A Modification of the Newtonian dynamics as a possible alternative to the hidden mass hypothesis*, *Astrophys. J.* **270** (1983) 365–370.

[96] M. Milgrom, *A Modification of the Newtonian dynamics: Implications for galaxies*, *Astrophys. J.* **270** (1983) 371–383.

[97] S. Nussinov, *TECHNOCOSMOLOGY: COULD A TECHNIBARYON EXCESS PROVIDE A 'NATURAL' MISSING MASS CANDIDATE?*, *Phys. Lett. B* **165** (1985) 55–58.

[98] D. B. Kaplan, *A Single explanation for both the baryon and dark matter densities*, *Phys. Rev. Lett.* **68** (1992) 741–743.

[99] M. Fujii and T. Yanagida, *A Solution to the coincidence puzzle of Omega(B) and Omega (DM)*, *Phys. Lett. B* **542** (2002) 80–88, [hep-ph/0206066].

[100] D. E. Kaplan, M. A. Luty and K. M. Zurek, *Asymmetric Dark Matter*, *Phys. Rev. D* **79** (2009) 115016, [0901.4117].

[101] E. Ma, *Verifiable radiative seesaw mechanism of neutrino mass and dark matter*, *Phys. Rev. D* **73** (2006) 077301, [hep-ph/0601225].

[102] *Search for resonances decaying to photon pairs in 3.2 fb^{-1} of pp collisions at $\sqrt{s}$ = 13 TeV with the ATLAS detector*, .

[103] CMS collaboration, *Search for new physics in high mass diphoton events in proton-proton collisions at 13TeV*, .

[104] ATLAS collaboration, *Search for resonances decaying to photon pairs in 139 fb^{-1} of pp collisions at $\sqrt{s}$ = 13 TeV with the ATLAS detector*, .

[105] CMS collaboration, A. M. Sirunyan et al., *Search for physics beyond the standard model in high-mass diphoton events from proton-proton collisions at $\sqrt{s} = 13$ TeV*, *Phys. Rev. D* **98** (2018) 092001, [1809.00327].

[106] KOTO collaboration, S. Shinohara, *Search for the rare decay $K_L \to \pi^0 \nu\bar{\nu}$ at J-PARC KOTO experiment*, *J. Phys. Conf. Ser.* **1526** (2020) 012002.

[107] KOTO collaboration, J. K. Ahn et al., *Study of the $K_L \to \pi^0 \nu\bar{\nu}$ Decay at the J-PARC KOTO Experiment*, *Phys. Rev. Lett.* **126** (2021) 121801, [2012.07571].

[108] HFLAV collaboration, Y. Amhis et al., *Averages of b-hadron, c-hadron, and τ-lepton properties as of summer 2016*, *Eur. Phys. J. C* **77** (2017) 895, [1612.07233].

[109] D. London and J. Matias, *B Flavour Anomalies: 2021 Theoretical Status Report*, 2110.13270.

[110] BaBar collaboration, J. P. Lees et al., *Evidence for an excess of $\bar{B} \to D^{(*)}\tau^-\bar{\nu}_\tau$ decays*, *Phys. Rev. Lett.* **109** (2012) 101802, [1205.5442].

[111] LHCb collaboration, R. Aaij et al., *Test of lepton universality using $B^+ \to K^+\ell^+\ell^-$ decays*, *Phys. Rev. Lett.* **113** (2014) 151601, [1406.6482].

[112] Belle collaboration, A. Abdesselam et al., *Measurement of $\mathcal{R}(D)$ and $\mathcal{R}(D^*)$ with a semileptonic tagging method*, 1904.08794.

[113] LHCb collaboration, R. Aaij et al., *Test of lepton universality in beauty-quark decays*, 2103.11769.

[114] LHCb collaboration, R. Aaij et al., *Search for lepton-universality violation in $B^+ \to K^+\ell^+\ell^-$ decays*, *Phys. Rev. Lett.* **122** (2019) 191801, [1903.09252].

[115] M. Bordone, G. Isidori and A. Pattori, *On the Standard Model predictions for R_K and R_{K^*}*, *Eur. Phys. J. C* **76** (2016) 440, [1605.07633].

[116] G. Isidori, S. Nabeebaccus and R. Zwicky, *QED corrections in $\overline{B} \to \overline{K}\ell^+\ell^-$ at the double-differential level*, *JHEP* **12** (2020) 104, [2009.00929].

[117] Muon g-2 collaboration, G. W. Bennett et al., *Final Report of the Muon E821 Anomalous Magnetic Moment Measurement at BNL*, *Phys. Rev. D* **73** (2006) 072003, [hep-ex/0602035].

[118] T. Aoyama et al., *The anomalous magnetic moment of the muon in the Standard Model*, *Phys. Rept.* **887** (2020) 1–166, [2006.04822].

[119] Muon g-2 collaboration, B. Abi et al., *Measurement of the Positive Muon Anomalous Magnetic Moment to 0.46 ppm*, *Phys. Rev. Lett.* **126** (2021) 141801, [2104.03281].

[120] S. Borsanyi et al., *Leading hadronic contribution to the muon magnetic moment from lattice QCD*, *Nature* **593** (2021) 51–55, [2002.12347].

[121] LSND collaboration, A. Aguilar-Arevalo et al., *Evidence for neutrino oscillations from the observation of $\bar{\nu}_e$ appearance in a $\bar{\nu}_\mu$ beam*, *Phys. Rev. D* **64** (2001) 112007, [hep-ex/0104049].

[122] M. Maltoni, T. Schwetz, M. A. Tortola and J. W. F. Valle, *Status of global fits to neutrino oscillations*, *New J. Phys.* **6** (2004) 122, [hep-ph/0405172].

[123] MiniBooNE collaboration, A. A. Aguilar-Arevalo et al., *Significant Excess of ElectronLike Events in the MiniBooNE Short-Baseline Neutrino Experiment*, *Phys. Rev. Lett.* **121** (2018) 221801, [1805.12028].

[124] MiniBooNE collaboration, A. A. Aguilar-Arevalo et al., *Updated MiniBooNE neutrino oscillation results with increased data and new background studies*, *Phys. Rev. D* **103** (2021) 052002, [2006.16883].

[125] A. Diaz, C. A. Argüelles, G. H. Collin, J. M. Conrad and M. H. Shaevitz, *Where Are We With Light Sterile Neutrinos?*, *Phys. Rept.* **884** (2020) 1–59, [1906.00045].

[126] C. A. Argüelles, I. Esteban, M. Hostert, K. J. Kelly, J. Kopp, P. A. N. Machado et al., *MicroBooNE and the ν_e Interpretation of the MiniBooNE Low-Energy Excess*, 2111.10359.

[127] MicroBooNE collaboration, P. Abratenko et al., *Search for Neutrino-Induced Neutral Current Δ Radiative Decay in MicroBooNE and a First Test of the MiniBooNE Low Energy Excess Under a Single-Photon Hypothesis*, 2110.00409.

[128] J. T. Peltoniemi, D. Tommasini and J. W. F. Valle, *Reconciling dark matter and solar neutrinos*, *Phys. Lett. B* **298** (1993) 383–390.

[129] J. T. Peltoniemi and J. W. F. Valle, *Reconciling dark matter, solar and atmospheric neutrinos*, *Nucl. Phys. B* **406** (1993) 409–422, [hep-ph/9302316].

[130] D. O. Caldwell and R. N. Mohapatra, *Neutrino mass explanations of solar and atmospheric neutrino deficits and hot dark matter*, *Phys. Rev. D* **48** (1993) 3259–3263.

[131] B. D. Fields, *The primordial lithium problem*, *Ann. Rev. Nucl. Part. Sci.* **61** (2011) 47–68, [1203.3551].

[132] E. Di Valentino et al., *Snowmass2021 - Letter of interest cosmology intertwined II: The hubble constant tension*, *Astropart. Phys.* **131** (2021) 102605, [2008.11284].

[133] A. G. Riess et al., *A Comprehensive Measurement of the Local Value of the Hubble Constant with 1 km/s/Mpc Uncertainty from the Hubble Space Telescope and the SH0ES Team*, 2112.04510.

[134] A. J. Krasznahorkay et al., *Observation of Anomalous Internal Pair Creation in Be8 : A Possible Indication of a Light, Neutral Boson*, *Phys. Rev. Lett.* **116** (2016) 042501, [1504.01527].

[135] A. J. Krasznahorkay et al., *New evidence supporting the existence of the hypothetic X17 particle*, 1910.10459.

[136] J. Chang et al., *An excess of cosmic ray electrons at energies of 300-800 GeV*, *Nature* **456** (2008) 362–365.

[137] PAMELA collaboration, O. Adriani et al., *An anomalous positron abundance in cosmic rays with energies 1.5-100 GeV*, *Nature* **458** (2009) 607–609, [0810.4995].

[138] Fermi-LAT collaboration, A. A. Abdo et al., *Measurement of the Cosmic Ray e+ plus e- spectrum from 20 GeV to 1 TeV with the Fermi Large Area Telescope*, *Phys. Rev. Lett.* **102** (2009) 181101, [0905.0025].

[139] AMS collaboration, M. Aguilar et al., *The Alpha Magnetic Spectrometer (AMS) on the international space station: Part II — Results from the first seven years*, *Phys. Rept.* **894** (2021) 1–116.

[140] LHCb collaboration, R. Aaij et al., *Measurement of CP Violation in the Decay $B^+ \to K^+\pi^0$*, *Phys. Rev. Lett.* **126** (2021) 091802, [2012.12789].

[141] M. Gell-Mann, P. Ramond and R. Slansky, *Complex Spinors and Unified Theories*, *Conf. Proc. C* **790927** (1979) 315–321, [1306.4669].

[142] T. Yanagida, *Horizontal gauge symmetry and masses of neutrinos*, *Conf. Proc. C* **7902131** (1979) 95–99.

[143] P. Langacker, *Grand Unified Theories and Proton Decay*, *Phys. Rept.* **72** (1981) 185.

[144] Super-Kamiokande collaboration, A. Takenaka et al., *Search for proton decay via $p \to e^+\pi^0$ and $p \to \mu^+\pi^0$ with an enlarged fiducial volume in Super-Kamiokande I-IV*, *Phys. Rev. D* **102** (2020) 112011, [2010.16098].

[145] R. N. Mohapatra and J. C. Pati, *Left-Right Gauge Symmetry and an Isoconjugate Model of CP Violation*, *Phys. Rev. D* **11** (1975) 566–571.

[146] R. N. Mohapatra and J. C. Pati, *A Natural Left-Right Symmetry*, *Phys. Rev. D* **11** (1975) 2558.

[147] G. Senjanovic and R. N. Mohapatra, *Exact Left-Right Symmetry and Spontaneous Violation of Parity*, *Phys. Rev. D* **12** (1975) 1502.

[148] J. C. Pati and A. Salam, *Lepton Number as the Fourth Color*, *Phys. Rev. D* **10** (1974) 275–289.

[149] A. D. Smirnov, *The Minimal quark - lepton symmetry model and the limit on Z-prime mass*, *Phys. Lett. B* **346** (1995) 297–302, [hep-ph/9503239].

[150] P. Fileviez Perez and M. B. Wise, *Low Scale Quark-Lepton Unification*, *Phys. Rev. D* **88** (2013) 057703, [1307.6213].

[151] B. Fornal, A. Rajaraman and T. M. P. Tait, *Baryon Number as the Fourth Color*, *Phys. Rev. D* **92** (2015) 055022, [1506.06131].

[152] H. Georgi and S. L. Glashow, *Unity of All Elementary Particle Forces*, *Phys. Rev. Lett.* **32** (1974) 438–441.

[153] H. Fritzsch and P. Minkowski, *Unified Interactions of Leptons and Hadrons*, *Annals Phys.* **93** (1975) 193–266.

[154] F. Gursey, P. Ramond and P. Sikivie, *A Universal Gauge Theory Model Based on E6*, *Phys. Lett. B* **60** (1976) 177–180.

[155] S. Weinberg, *Implications of Dynamical Symmetry Breaking*, *Phys. Rev. D* **13** (1976) 974–996.

[156] E. Gildener, *Gauge Symmetry Hierarchies*, *Phys. Rev. D* **14** (1976) 1667.

[157] L. Susskind, *Dynamics of Spontaneous Symmetry Breaking in the Weinberg-Salam Theory*, *Phys. Rev. D* **20** (1979) 2619–2625.

[158] L. Susskind, *THE GAUGE HIERARCHY PROBLEM, TECHNICOLOR, SUPERSYMMETRY, AND ALL THAT.*, *Phys. Rept.* **104** (1984) 181–193.

[159] M. McCullough, *Lectures on Physics Beyond the Standard Model.*, in *6th Tri-Institute Summer School on Elementary Particles*, 2018.

[160] T. Das, G. S. Guralnik, V. S. Mathur, F. E. Low and J. E. Young, *Electromagnetic mass difference of pions*, *Phys. Rev. Lett.* **18** (1967) 759–761.

[161] Y. A. Golfand and E. P. Likhtman, *Extension of the Algebra of Poincare Group Generators and Violation of p Invariance*, *JETP Lett.* **13** (1971) 323–326.

[162] D. V. Volkov and V. P. Akulov, *Is the Neutrino a Goldstone Particle?*, *Phys. Lett. B* **46** (1973) 109–110.

[163] J. Wess and B. Zumino, *Supergauge Transformations in Four-Dimensions*, *Nucl. Phys. B* **70** (1974) 39–50.

[164] S. P. Martin, *A Supersymmetry primer*, *Adv. Ser. Direct. High Energy Phys.* **18** (1998) 1–98, [hep-ph/9709356].

[165] N. Arkani-Hamed, S. Dimopoulos and G. R. Dvali, *The Hierarchy problem and new dimensions at a millimeter*, *Phys. Lett. B* **429** (1998) 263–272, [hep-ph/9803315].

[166] I. Antoniadis, N. Arkani-Hamed, S. Dimopoulos and G. R. Dvali, *New dimensions at a millimeter to a Fermi and superstrings at a TeV*, *Phys. Lett. B* **436** (1998) 257–263, [hep-ph/9804398].

[167] M. Schmaltz and D. Tucker-Smith, *Little Higgs review*, *Ann. Rev. Nucl. Part. Sci.* **55** (2005) 229–270, [hep-ph/0502182].

[168] R. Contino, *The Higgs as a Composite Nambu-Goldstone Boson*, in *Theoretical Advanced Study Institute in Elementary Particle Physics: Physics of the Large and the Small*, pp. 235–306, 2011. 1005.4269. DOI.

[169] R. D. Peccei and H. R. Quinn, *CP Conservation in the Presence of Instantons*, *Phys. Rev. Lett.* **38** (1977) 1440–1443.

[170] S. Weinberg, *A New Light Boson?*, *Phys. Rev. Lett.* **40** (1978) 223–226.

[171] F. Wilczek, *Problem of Strong P and T Invariance in the Presence of Instantons*, *Phys. Rev. Lett.* **40** (1978) 279–282.

[172] T. Kaluza, *Zum Unitätsproblem der Physik*, *Sitzungsberichte der Königlich Preußischen Akademie der Wissenschaften (Berlin* (Jan., 1921) 966–972.

[173] O. Klein, *The Atomicity of Electricity as a Quantum Theory Law*, *Nature* **118** (1926) 516.

[174] M. J. Duff, B. E. W. Nilsson and C. N. Pope, *Kaluza-Klein Supergravity*, *Phys. Rept.* **130** (1986) 1–142.

[175] P. Minkowski, $\mu \to e\gamma$ *at a Rate of One Out of* 10^9 *Muon Decays?*, *Phys. Lett. B* **67** (1977) 421–428.

[176] W. Grimus and L. Lavoura, *The Seesaw mechanism at arbitrary order: Disentangling the small scale from the large scale*, *JHEP* **11** (2000) 042, [hep-ph/0008179].

[177] R. N. Mohapatra and G. Senjanovic, *Neutrino Masses and Mixings in Gauge Models with Spontaneous Parity Violation*, *Phys. Rev. D* **23** (1981) 165.

[178] R. Foot, H. Lew, X. G. He and G. C. Joshi, *Seesaw Neutrino Masses Induced by a Triplet of Leptons*, *Z. Phys. C* **44** (1989) 441.

[179] R. N. Mohapatra and G. Senjanovic, *Neutrino Mass and Spontaneous Parity Nonconservation*, *Phys. Rev. Lett.* **44** (1980) 912.

[180] J. Schechter and J. W. F. Valle, *Neutrino Masses in SU(2) x U(1) Theories*, *Phys. Rev. D* **22** (1980) 2227.

[181] M. Magg and C. Wetterich, *Neutrino Mass Problem and Gauge Hierarchy*, *Phys. Lett. B* **94** (1980) 61–64.

[182] MuLan collaboration, D. M. Webber et al., *Measurement of the Positive Muon Lifetime and Determination of the Fermi Constant to Part-per-Million Precision*, *Phys. Rev. Lett.* **106** (2011) 041803, [1010.0991].

[183] T. Plehn and M. Rauch, *The quartic higgs coupling at hadron colliders*, *Phys. Rev. D* **72** (2005) 053008, [hep-ph/0507321].

[184] FCC collaboration, A. Abada et al., *FCC-hh: The Hadron Collider: Future Circular Collider Conceptual Design Report Volume 3*, *Eur. Phys. J. ST* **228** (2019) 755–1107.

[185] FCC collaboration, A. Abada et al., *FCC-ee: The Lepton Collider: Future Circular Collider Conceptual Design Report Volume 2*, *Eur. Phys. J. ST* **228** (2019) 261–623.

[186] T. Barklow, J. Brau, K. Fujii, J. Gao, J. List, N. Walker et al., *ILC Operating Scenarios*, 1506.07830.

[187] CLICdp, CLIC collaboration, T. K. Charles et al., *The Compact Linear Collider (CLIC) - 2018 Summary Report*, 1812.06018.

[188] CEPC Study Group collaboration, *CEPC Conceptual Design Report: Volume 1 - Accelerator*, 1809.00285.

[189] R. Contino, Y. Nomura and A. Pomarol, *Higgs as a holographic pseudoGoldstone boson*, *Nucl. Phys. B* **671** (2003) 148–174, [hep-ph/0306259].

[190] K. Agashe, R. Contino and A. Pomarol, *The Minimal composite Higgs model*, *Nucl. Phys. B* **719** (2005) 165–187, [hep-ph/0412089].

[191] R. Contino, L. Da Rold and A. Pomarol, *Light custodians in natural composite Higgs models*, *Phys. Rev. D* **75** (2007) 055014, [hep-ph/0612048].

[192] R. Feger, T. W. Kephart and R. J. Saskowski, *LieART 2.0 – A Mathematica application for Lie Algebras and Representation Theory*, *Comput. Phys. Commun.* **257** (2020) 107490, [1912.10969].

[193] A. Crivellin, D. Müller and L. Schnell, *Combined constraints on first generation leptoquarks*, *Phys. Rev. D* **103** (2021) 115023, [2104.06417].

[194] T. Appelquist and J. Carazzone, *Infrared Singularities and Massive Fields*, *Phys. Rev. D* **11** (1975) 2856.

[195] M. B. Einhorn and J. Wudka, *The Bases of Effective Field Theories*, *Nucl. Phys. B* **876** (2013) 556–574, [1307.0478].

[196] E. Fermi, *Tentativo di una Teoria Dei Raggi β*, *Il Nuovo Cimento* **11** (Jan., 1934) 1–19.

[197] UA2 collaboration, M. Banner et al., *Observation of Single Isolated Electrons of High Transverse Momentum in Events with Missing Transverse Energy at the CERN anti-p p Collider*, *Phys. Lett. B* **122** (1983) 476–485.

[198] S. Weinberg, *Baryon and Lepton Nonconserving Processes*, *Phys. Rev. Lett.* **43** (1979) 1566–1570.

[199] W. Buchmuller and D. Wyler, *Effective Lagrangian Analysis of New Interactions and Flavor Conservation*, *Nucl. Phys. B* **268** (1986) 621–653.

[200] B. Grzadkowski, M. Iskrzynski, M. Misiak and J. Rosiek, *Dimension-Six Terms in the Standard Model Lagrangian*, *JHEP* **10** (2010) 085, [1008.4884].

[201] B. Henning, X. Lu and H. Murayama, *How to use the Standard Model effective field theory*, *JHEP* **01** (2016) 023, [1412.1837].

[202] A. Ijjas, P. J. Steinhardt and A. Loeb, *Inflationary paradigm in trouble after Planck2013*, *Phys. Lett. B* **723** (2013) 261–266, [1304.2785].

[203] A. Ijjas, P. J. Steinhardt and A. Loeb, *Inflationary schism*, *Phys. Lett. B* **736** (2014) 142–146, [1402.6980].

[204] A. G. Cocco, G. Mangano and M. Messina, *Probing low energy neutrino backgrounds with neutrino capture on beta decaying nuclei*, *JCAP* **06** (2007) 015, [hep-ph/0703075].

[205] S. Betts et al., *Development of a Relic Neutrino Detection Experiment at PTOLEMY: Princeton Tritium Observatory for Light, Early-Universe, Massive-Neutrino Yield*, in *Community Summer Study 2013: Snowmass on the Mississippi*, 7, 2013. 1307.4738.

[206] A. J. Long, C. Lunardini and E. Sabancilar, *Detecting non-relativistic cosmic neutrinos by capture on tritium: phenomenology and physics potential*, *JCAP* **08** (2014) 038, [1405.7654].

[207] PTOLEMY collaboration, E. Baracchini et al., *PTOLEMY: A Proposal for Thermal Relic Detection of Massive Neutrinos and Directional Detection of MeV Dark Matter*, 1808.01892.

[208] PTOLEMY collaboration, M. G. Betti et al., *Neutrino physics with the PTOLEMY project: active neutrino properties and the light sterile case*, *JCAP* **07** (2019) 047, [1902.05508].

[209] M. Kawasaki and K. Murai, *Lepton Asymmetric Universe*, 2203.09713.

[210] A. G. Cohen, A. De Rujula and S. L. Glashow, *A Matter - antimatter universe?*, *Astrophys. J.* **495** (1998) 539–549, [astro-ph/9707087].

[211] S. Dupourqué, L. Tibaldo and P. Von Ballmoos, *Constraints on the antistar fraction in the Solar System neighborhood from the 10-year Fermi Large Area Telescope gamma-ray source catalog*, *Phys. Rev. D* **103** (2021) 083016, [2103.10073].

[212] W. Hu and S. Dodelson, *Cosmic Microwave Background Anisotropies*, *Ann. Rev. Astron. Astrophys.* **40** (2002) 171–216, [astro-ph/0110414].

[213] C. J. Copi, D. N. Schramm and M. S. Turner, *Big bang nucleosynthesis and the baryon density of the universe*, *Science* **267** (1995) 192–199, [astro-ph/9407006].

[214] A. Coc, E. Vangioni-Flam, P. Descouvemont, A. Adahchour and C. Angulo, *Updated Big Bang nucleosynthesis confronted to WMAP observations and to the abundance of light elements*, *Astrophys. J.* **600** (2004) 544–552, [astro-ph/0309480].

[215] R. H. Cyburt, B. D. Fields, K. A. Olive and T.-H. Yeh, *Big Bang Nucleosynthesis: 2015*, *Rev. Mod. Phys.* **88** (2016) 015004, [1505.01076].

[216] A. D. Sakharov, *Violation of CP Invariance, C asymmetry, and baryon asymmetry of the universe*, *Pisma Zh. Eksp. Teor. Fiz.* **5** (1967) 32–35.

[217] C. Jarlskog, *Commutator of the Quark Mass Matrices in the Standard Electroweak Model and a Measure of Maximal CP Violation*, *Phys. Rev. Lett.* **55** (1985) 1039.

[218] B. Leaf, *Derivation of the boltzmann equation from the liouville equation*, *Physica* **59** (1972) 206–227.

[219] F. Hahn-Woernle, M. Plumacher and Y. Y. Y. Wong, *Full Boltzmann equations for leptogenesis including scattering*, *JCAP* **08** (2009) 028, [0907.0205].

[220] J. S. Schwinger, *Brownian motion of a quantum oscillator*, *J. Math. Phys.* **2** (1961) 407–432.

[221] L. V. Keldysh, *Diagram technique for nonequilibrium processes*, *Zh. Eksp. Teor. Fiz.* **47** (1964) 1515–1527.

[222] E. Calzetta and B. L. Hu, *Nonequilibrium Quantum Fields: Closed Time Path Effective Action, Wigner Function and Boltzmann Equation*, *Phys. Rev. D* **37** (1988) 2878.

[223] B. Garbrecht, *Why is there more matter than antimatter? Calculational methods for leptogenesis and electroweak baryogenesis*, *Prog. Part. Nucl. Phys.* **110** (2020) 103727, [1812.02651].

[224] G. F. Giudice, A. Notari, M. Raidal, A. Riotto and A. Strumia, *Towards a complete theory of thermal leptogenesis in the SM and MSSM*, *Nucl. Phys. B* **685** (2004) 89–149, [hep-ph/0310123].

[225] M. Fukugita and T. Yanagida, *Baryogenesis Without Grand Unification*, *Phys. Lett. B* **174** (1986) 45–47.

[226] M. A. Luty, *Baryogenesis via leptogenesis*, *Phys. Rev. D* **45** (1992) 455–465.

[227] L. Covi and E. Roulet, *Baryogenesis from mixed particle decays*, *Phys. Lett. B* **399** (1997) 113–118, [hep-ph/9611425].

[228] M. Flanz, E. A. Paschos, U. Sarkar and J. Weiss, *Baryogenesis through mixing of heavy Majorana neutrinos*, *Phys. Lett. B* **389** (1996) 693–699, [hep-ph/9607310].

[229] A. Pilaftsis, *CP violation and baryogenesis due to heavy Majorana neutrinos*, *Phys. Rev. D* **56** (1997) 5431–5451, [hep-ph/9707235].

[230] R. Barbieri, P. Creminelli, A. Strumia and N. Tetradis, *Baryogenesis through leptogenesis*, *Nucl. Phys. B* **575** (2000) 61–77, [hep-ph/9911315].

[231] A. Riotto, *Theories of baryogenesis*, in *ICTP Summer School in High-Energy Physics and Cosmology*, pp. 326–436, 7, 1998. hep-ph/9807454.

[232] W. Buchmuller, P. Di Bari and M. Plumacher, *Leptogenesis for pedestrians*, *Annals Phys.* **315** (2005) 305–351, [hep-ph/0401240].

[233] C. S. Fong, E. Nardi and A. Riotto, *Leptogenesis in the Universe*, *Adv. High Energy Phys.* **2012** (2012) 158303, [1301.3062].

[234] A. Pilaftsis and T. E. J. Underwood, *Resonant leptogenesis*, *Nucl. Phys. B* **692** (2004) 303–345, [hep-ph/0309342].

[235] A. Pilaftsis and T. E. J. Underwood, *Electroweak-scale resonant leptogenesis*, *Phys. Rev. D* **72** (2005) 113001, [hep-ph/0506107].

[236] A. G. Cohen, D. B. Kaplan and A. E. Nelson, *Progress in electroweak baryogenesis*, *Ann. Rev. Nucl. Part. Sci.* **43** (1993) 27–70, [hep-ph/9302210].

[237] M. Trodden, *Electroweak baryogenesis*, *Rev. Mod. Phys.* **71** (1999) 1463–1500, [hep-ph/9803479].

[238] D. E. Morrissey and M. J. Ramsey-Musolf, *Electroweak baryogenesis*, *New J. Phys.* **14** (2012) 125003, [1206.2942].

[239] M. E. Shaposhnikov, *Possible Appearance of the Baryon Asymmetry of the Universe in an Electroweak Theory*, *JETP Lett.* **44** (1986) 465–468.

[240] M. E. Shaposhnikov, *Baryon Asymmetry of the Universe in Standard Electroweak Theory*, *Nucl. Phys. B* **287** (1987) 757–775.

[241] M. E. Shaposhnikov, *Standard model solution of the baryogenesis problem*, *Phys. Lett. B* **277** (1992) 324–330.

[242] G. R. Farrar and M. E. Shaposhnikov, *Baryon asymmetry of the universe in the minimal Standard Model*, *Phys. Rev. Lett.* **70** (1993) 2833–2836, [hep-ph/9305274].

[243] V. A. Rubakov and M. E. Shaposhnikov, *Electroweak baryon number nonconservation in the early universe and in high-energy collisions*, *Usp. Fiz. Nauk* **166** (1996) 493–537, [hep-ph/9603208].

[244] K. Kajantie, M. Laine, K. Rummukainen and M. E. Shaposhnikov, *Is there a hot electroweak phase transition at $m_H \gtrsim m_W$?*, *Phys. Rev. Lett.* **77** (1996) 2887–2890, [hep-ph/9605288].

[245] K. Rummukainen, M. Tsypin, K. Kajantie, M. Laine and M. E. Shaposhnikov, *The Universality class of the electroweak theory*, *Nucl. Phys. B* **532** (1998) 283–314, [hep-lat/9805013].

[246] ATLAS collaboration, G. Aad et al., *Observation of a new particle in the search for the Standard Model Higgs boson with the ATLAS detector at the LHC*, *Phys. Lett. B* **716** (2012) 1–29, [1207.7214].

[247] CMS collaboration, S. Chatrchyan et al., *Observation of a New Boson at a Mass of 125 GeV with the CMS Experiment at the LHC*, *Phys. Lett. B* **716** (2012) 30–61, [1207.7235].

[248] P. Huet and E. Sather, *Electroweak baryogenesis and standard model CP violation*, *Phys. Rev. D* **51** (1995) 379–394, [hep-ph/9404302].

[249] G. Servant, *The serendipity of electroweak baryogenesis*, *Phil. Trans. Roy. Soc. Lond. A* **376** (2018) 20170124, [1807.11507].

[250] N. Turok and J. Zadrozny, *Dynamical generation of baryons at the electroweak transition*, *Phys. Rev. Lett.* **65** (1990) 2331–2334.

[251] N. Turok and J. Zadrozny, *Electroweak baryogenesis in the two doublet model*, *Nucl. Phys. B* **358** (1991) 471–493.

[252] J. M. Cline, K. Kainulainen and A. P. Vischer, *Dynamics of two Higgs doublet CP violation and baryogenesis at the electroweak phase transition*, *Phys. Rev. D* **54** (1996) 2451–2472, [hep-ph/9506284].

[253] L. Fromme, S. J. Huber and M. Seniuch, *Baryogenesis in the two-Higgs doublet model*, *JHEP* **11** (2006) 038, [hep-ph/0605242].

[254] K. Enomoto, S. Kanemura and Y. Mura, *Electroweak baryogenesis in aligned two Higgs doublet models*, *JHEP* **01** (2022) 104, [2111.13079].

[255] S. D. Bass, A. De Roeck and M. Kado, *The Higgs boson implications and prospects for future discoveries*, *Nature Rev. Phys.* **3** (2021) 608–624, [2104.06821].

[256] C. Caprini et al., *Science with the space-based interferometer eLISA. II: Gravitational waves from cosmological phase transitions*, *JCAP* **04** (2016) 001, [1512.06239].

[257] LISA collaboration, P. Amaro-Seoane et al., *Laser Interferometer Space Antenna*, 1702.00786.

[258] M. Lewicki, M. Merchand and M. Zych, *Electroweak bubble wall expansion: gravitational waves and baryogenesis in Standard Model-like thermal plasma*, *JHEP* **02** (2022) 017, [2111.02393].

[259] E. K. Akhmedov, V. A. Rubakov and A. Y. Smirnov, *Baryogenesis via neutrino oscillations*, *Phys. Rev. Lett.* **81** (1998) 1359–1362, [hep-ph/9803255].

[260] M. Drewes, B. Garbrecht, P. Hernandez, M. Kekic, J. Lopez-Pavon, J. Racker et al., *ARS Leptogenesis*, *Int. J. Mod. Phys. A* **33** (2018) 1842002, [1711.02862].

[261] H. P. Nilles, *Supersymmetry, Supergravity and Particle Physics*, *Phys. Rept.* **110** (1984) 1–162.

[262] S. Weinberg, *The Quantum Theory of Fields: Volume 3, Supersymmetry*. Cambridge University Press, 2000.

[263] S. Dimopoulos and H. Georgi, *Softly Broken Supersymmetry and SU(5)*, *Nucl. Phys. B* **193** (1981) 150–162.

[264] N. Sakai, *Naturalness in Supersymmetric Guts*, *Z. Phys. C* **11** (1981) 153.

[265] S. Dimopoulos and S. Raby, *Supercolor*, *Nucl. Phys. B* **192** (1981) 353–368.

[266] E. Witten, *Dynamical Breaking of Supersymmetry*, *Nucl. Phys. B* **188** (1981) 513.

[267] H. E. Haber and G. L. Kane, *The Search for Supersymmetry: Probing Physics Beyond the Standard Model*, *Phys. Rept.* **117** (1985) 75–263.

[268] I. Affleck and M. Dine, *A New Mechanism for Baryogenesis*, *Nucl. Phys. B* **249** (1985) 361–380.

[269] R. Allahverdi and A. Mazumdar, *A mini review on Affleck-Dine baryogenesis*, *New J. Phys.* **14** (2012) 125013.

[270] A. Vilenkin and L. H. Ford, *Gravitational Effects upon Cosmological Phase Transitions*, *Phys. Rev. D* **26** (1982) 1231.

[271] A. D. Linde, *Scalar Field Fluctuations in Expanding Universe and the New Inflationary Universe Scenario*, *Phys. Lett. B* **116** (1982) 335–339.

[272] M. Dine, L. Randall and S. D. Thomas, *Baryogenesis from flat directions of the supersymmetric standard model*, *Nucl. Phys. B* **458** (1996) 291–326, [hep-ph/9507453].

[273] M. Dine, L. Randall and S. D. Thomas, *Supersymmetry breaking in the early universe*, *Phys. Rev. Lett.* **75** (1995) 398–401, [hep-ph/9503303].

[274] M. Yoshimura, *Unified Gauge Theories and the Baryon Number of the Universe*, *Phys. Rev. Lett.* **41** (1978) 281–284.

[275] J. R. Ellis, M. K. Gaillard and D. V. Nanopoulos, *Baryon Number Generation in Grand Unified Theories*, *Phys. Lett. B* **80** (1979) 360.

[276] A. Albrecht and P. J. Steinhardt, *Cosmology for Grand Unified Theories with Radiatively Induced Symmetry Breaking*, *Phys. Rev. Lett.* **48** (1982) 1220–1223.

[277] E. W. Kolb and M. S. Turner, *Grand Unified Theories and the Origin of the Baryon Asymmetry*, *Ann. Rev. Nucl. Part. Sci.* **33** (1983) 645–696.

[278] V. A. Kuzmin, V. A. Rubakov and M. E. Shaposhnikov, *Anomalous Electroweak Baryon Number Nonconservation and GUT Mechanism for Baryogenesis*, *Phys. Lett. B* **191** (1987) 171–173.

[279] E. W. Kolb, A. D. Linde and A. Riotto, *GUT baryogenesis after preheating*, *Phys. Rev. Lett.* **77** (1996) 4290–4293, [hep-ph/9606260].

[280] M. Fukugita and T. Yanagida, *Resurrection of grand unified theory baryogenesis*, *Phys. Rev. Lett.* **89** (2002) 131602, [hep-ph/0203194].

[281] S. M. Barr, G. Segre and H. A. Weldon, *The Magnitude of the Cosmological Baryon Asymmetry*, *Phys. Rev. D* **20** (1979) 2494.

[282] J. A. Harvey, E. W. Kolb, D. B. Reiss and S. Wolfram, *Calculation of Cosmological Baryon Asymmetry in Grand Unified Gauge Models*, *Nucl. Phys. B* **201** (1982) 16–100.

[283] A. Riotto and M. Trodden, *Recent progress in baryogenesis*, *Ann. Rev. Nucl. Part. Sci.* **49** (1999) 35–75, [hep-ph/9901362].

[284] S. Dodelson and L. M. Widrow, *Baryogenesis in a Baryon Symmetric Universe*, *Phys. Rev. D* **42** (1990) 326–342.

[285] S. M. Barr, R. S. Chivukula and E. Farhi, *Electroweak Fermion Number Violation and the Production of Stable Particles in the Early Universe*, *Phys. Lett. B* **241** (1990) 387–391.

[286] S. Dodelson, B. R. Greene and L. M. Widrow, *Baryogenesis, dark matter and the width of the Z*, *Nucl. Phys. B* **372** (1992) 467–493.

[287] S. M. Barr, *Baryogenesis, sphalerons and the cogeneration of dark matter*, *Phys. Rev. D* **44** (1991) 3062–3066.

[288] A. Falkowski, J. T. Ruderman and T. Volansky, *Asymmetric Dark Matter from Leptogenesis*, *JHEP* **05** (2011) 106, [1101.4936].

[289] K. Petraki and R. R. Volkas, *Review of asymmetric dark matter*, *Int. J. Mod. Phys. A* **28** (2013) 1330028, [1305.4939].

[290] P.-H. Gu, M. Lindner, U. Sarkar and X. Zhang, *WIMP Dark Matter and Baryogenesis*, *Phys. Rev. D* **83** (2011) 055008, [1009.2690].

[291] Y. Cui, L. Randall and B. Shuve, *A WIMPy Baryogenesis Miracle*, *JHEP* **04** (2012) 075, [1112.2704].

[292] Y. Cui and R. Sundrum, *Baryogenesis for weakly interacting massive particles*, *Phys. Rev. D* **87** (2013) 116013, [1212.2973].

[293] Y. Cui, *A Review of WIMP Baryogenesis Mechanisms*, *Mod. Phys. Lett. A* **30** (2015) 1530028, [1510.04298].

[294] A. Ghosh, D. Ghosh and S. Mukhopadhyay, *Cosmology of complex scalar dark matter: Interplay of self-scattering and annihilation*, *Phys. Rev. D* **104** (2021) 123543, [2103.14009].

[295] A. Ghosh, D. Ghosh and S. Mukhopadhyay, *Asymmetric dark matter from semi-annihilation*, *JHEP* **08** (2020) 149, [2004.07705].

[296] E. Ma, *Common origin of neutrino mass, dark matter, and baryogenesis*, *Mod. Phys. Lett. A* **21** (2006) 1777–1782, [hep-ph/0605180].

[297] S. Kashiwase and D. Suematsu, *Baryon number asymmetry and dark matter in the neutrino mass model with an inert doublet*, *Phys. Rev. D* **86** (2012) 053001, [1207.2594].

[298] S. Kashiwase and D. Suematsu, *Leptogenesis and dark matter detection in a TeV scale neutrino mass model with inverted mass hierarchy*, *Eur. Phys. J. C* **73** (2013) 2484, [1301.2087].

[299] J. Racker, *Mass bounds for baryogenesis from particle decays and the inert doublet model*, *JCAP* **03** (2014) 025, [1308.1840].

[300] J. D. Clarke, R. Foot and R. R. Volkas, *Natural leptogenesis and neutrino masses with two Higgs doublets*, *Phys. Rev. D* **92** (2015) 033006, [1505.05744].

[301] D. Borah, A. Dasgupta and S. K. Kang, *TeV Scale Leptogenesis via Dark Sector Scatterings*, *Eur. Phys. J. C* **80** (2020) 498, [1806.04689].

[302] T. Hugle, M. Platscher and K. Schmitz, *Low-Scale Leptogenesis in the Scotogenic Neutrino Mass Model*, *Phys. Rev. D* **98** (2018) 023020, [1804.09660].

[303] W.-C. Huang, H. Päs and S. Zeißner, *Scalar Dark Matter, GUT baryogenesis and Radiative neutrino mass*, *Phys. Rev. D* **98** (2018) 075024, [1806.08204].

[304] S. Baumholzer, V. Brdar and P. Schwaller, *The New νMSM (ννMSM): Radiative Neutrino Masses, keV-Scale Dark Matter and Viable Leptogenesis with sub-TeV New Physics*, *JHEP* **08** (2018) 067, [1806.06864].

[305] A. D. Dolgov, *NonGUT baryogenesis*, *Phys. Rept.* **222** (1992) 309–386.

[306] W. Buchmuller, *Baryogenesis: 40 Years Later*, in *13th International Symposium on Particles, Strings and Cosmology*, 10, 2007. 0710.5857.

[307] D. Bodeker and W. Buchmuller, *Baryogenesis from the weak scale to the grand unification scale*, *Rev. Mod. Phys.* **93** (2021) 035004, [2009.07294].

[308] G. Elor et al., *New Ideas in Baryogenesis: A Snowmass White Paper*, in *2022 Snowmass Summer Study*, 3, 2022. 2203.05010.

[309] J. L. Barrow et al., *Theories and Experiments for Testable Baryogenesis Mechanisms: A Snowmass White Paper*, 2203.07059.

[310] S. R. Coleman, *Q-balls*, *Nucl. Phys. B* **262** (1985) 263.

[311] K. Enqvist and J. McDonald, *Q balls and baryogenesis in the MSSM*, *Phys. Lett. B* **425** (1998) 309–321, [hep-ph/9711514].

[312] K. Enqvist and J. McDonald, *B - ball baryogenesis and the baryon to dark matter ratio*, *Nucl. Phys. B* **538** (1999) 321–350, [hep-ph/9803380].

[313] K. Benakli and S. Davidson, *Baryogenesis in models with a low quantum gravity scale*, *Phys. Rev. D* **60** (1999) 025004, [hep-ph/9810280].

[314] C. Bambi, A. D. Dolgov and K. Freese, *A Black Hole Conjecture and Rare Decays in Theories with Low Scale Gravity*, *Nucl. Phys. B* **763** (2007) 91–114, [hep-ph/0606321].

[315] C. Bambi, A. D. Dolgov and K. Freese, *Baryogenesis from Gravitational Decay of TeV-Particles in Theories with Low Scale Gravity*, *JCAP* **04** (2007) 005, [hep-ph/0612018].

[316] C. Bambi, A. D. Dolgov and A. A. Petrov, *Black holes as antimatter factories*, *JCAP* **09** (2009) 013, [0806.3440].

[317] A. D. Dolgov and N. A. Pozdnyakov, *Baryogenesis through baryon capture by black holes*, 2009.04361.

[318] A. Ambrosone, R. Calabrese, D. F. G. Fiorillo, G. Miele and S. Morisi, *Towards baryogenesis via absorption from primordial black holes*, *Phys. Rev. D* **105** (2022) 045001, [2106.11980].

[319] A. D. Dolgov and N. A. Pozdnyakov, *Asymmetric baryon capture by primordial black holes and baryon asymmetry of the Universe*, *Phys. Rev. D* **104** (2021) 083524, [2107.08231].

[320] S. W. Hawking, *Particle Creation by Black Holes*, *Commun. Math. Phys.* **43** (1975) 199–220.

[321] J. D. Barrow, E. J. Copeland, E. W. Kolb and A. R. Liddle, *Baryogenesis in extended inflation. 2. Baryogenesis via primordial black holes*, *Phys. Rev. D* **43** (1991) 984–994.

[322] D. Baumann, P. J. Steinhardt and N. Turok, *Primordial Black Hole Baryogenesis*, hep-th/0703250.

[323] A. Hook, *Baryogenesis from Hawking Radiation*, *Phys. Rev. D* **90** (2014) 083535, [1404.0113].

[324] Y. Hamada and S. Iso, *Baryon asymmetry from primordial black holes*, *PTEP* **2017** (2017) 033B02, [1610.02586].

[325] L. Morrison, S. Profumo and Y. Yu, *Melanopogenesis: Dark Matter of (almost) any Mass and Baryonic Matter from the Evaporation of Primordial Black Holes weighing a Ton (or less)*, *JCAP* **05** (2019) 005, [1812.10606].

[326] A. Boudon, B. Bose, H. Huang and L. Lombriser, *Baryogenesis through asymmetric Hawking radiation from primordial black holes as dark matter*, *Phys. Rev. D* **103** (2021) 083504, [2010.14426].

[327] R. Jeannerot, *A New mechanism for leptogenesis*, *Phys. Rev. Lett.* **77** (1996) 3292–3295, [hep-ph/9609442].

[328] N. Sahu, P. Bhattacharjee and U. A. Yajnik, *B - L cosmic strings and baryogenesis*, *Phys. Rev. D* **70** (2004) 083534, [hep-ph/0406054].

[329] R. Jeannerot and M. Postma, *Leptogenesis from reheating after inflation and cosmic string decay*, *JCAP* **12** (2005) 006, [hep-ph/0507162].

[330] N. Sahu, P. Bhattacharjee and U. A. Yajnik, *Baryogenesis via leptogenesis in presence of cosmic strings*, *Nucl. Phys. B* **752** (2006) 280–296, [hep-ph/0512350].

[331] K. Dick, M. Lindner, M. Ratz and D. Wright, *Leptogenesis with Dirac neutrinos*, *Phys. Rev. Lett.* **84** (2000) 4039–4042, [hep-ph/9907562].

[332] H. Murayama and A. Pierce, *Realistic Dirac leptogenesis*, *Phys. Rev. Lett.* **89** (2002) 271601, [hep-ph/0206177].

[333] M. Blennow, B. Dasgupta, E. Fernandez-Martinez and N. Rius, *Aidnogenesis via Leptogenesis and Dark Sphalerons*, *JHEP* **03** (2011) 014, [1009.3159].

[334] K. Fujikura, K. Harigaya, I. R. Wang and I. R. Wang, *Electroweak-like baryogenesis with new chiral matter*, *JHEP* **07** (2021) 224, [2103.05005].

[335] H. Davoudiasl, R. Kitano, G. D. Kribs, H. Murayama and P. J. Steinhardt, *Gravitational baryogenesis*, *Phys. Rev. Lett.* **93** (2004) 201301, [hep-ph/0403019].

[336] B. Feng, H. Li, M.-z. Li and X.-m. Zhang, *Gravitational leptogenesis and its signatures in CMB*, *Phys. Lett. B* **620** (2005) 27–32, [hep-ph/0406269].

[337] H. Li, M.-z. Li and X.-m. Zhang, *Gravitational leptogenesis and neutrino mass limit*, *Phys. Rev. D* **70** (2004) 047302, [hep-ph/0403281].

[338] T. Shiromizu and K. Koyama, *Space-time dynamics and baryogenesis in brane world*, *JCAP* **07** (2004) 011, [hep-ph/0403231].

[339] G. Lambiase, S. Mohanty and A. R. Prasanna, *Neutrino coupling to cosmological background: A review on gravitational Baryo/Leptogenesis*, *Int. J. Mod. Phys. D* **22** (2013) 1330030, [1310.8459].

[340] J. I. McDonald and G. M. Shore, *Leptogenesis and gravity: baryon asymmetry without decays*, *Phys. Lett. B* **766** (2017) 162–169, [1604.08213].

[341] A. D. Linde, *The New Mechanism of Baryogenesis and the Inflationary Universe*, *Phys. Lett. B* **160** (1985) 243–248.

[342] J. R. Ellis, K. Enqvist, D. V. Nanopoulos and K. A. Olive, *Inflationary Fluctuations, Entropy Generation and Baryogenesis*, *Phys. Lett. B* **191** (1987) 343–348.

[343] G. F. Giudice, M. Peloso, A. Riotto and I. Tkachev, *Production of massive fermions at preheating and leptogenesis*, *JHEP* **08** (1999) 014, [hep-ph/9905242].

[344] T. Asaka, K. Hamaguchi, M. Kawasaki and T. Yanagida, *Leptogenesis in inflaton decay*, *Phys. Lett. B* **464** (1999) 12–18, [hep-ph/9906366].

[345] T. Asaka, K. Hamaguchi, M. Kawasaki and T. Yanagida, *Leptogenesis in inflationary universe*, *Phys. Rev. D* **61** (2000) 083512, [hep-ph/9907559].

[346] M. Kawasaki, M. Yamaguchi and T. Yanagida, *Natural chaotic inflation in supergravity and leptogenesis*, *Phys. Rev. D* **63** (2001) 103514, [hep-ph/0011104].

[347] E. J. Copeland, D. Lyth, A. Rajantie and M. Trodden, *Hybrid inflation and baryogenesis at the TeV scale*, *Phys. Rev. D* **64** (2001) 043506, [hep-ph/0103231].

[348] A. Tranberg and J. Smit, *Baryon asymmetry from electroweak tachyonic preheating*, *JHEP* **11** (2003) 016, [hep-ph/0310342].

[349] R. H. Brandenberger and M. Yamaguchi, *Spontaneous baryogenesis in warm inflation*, *Phys. Rev. D* **68** (2003) 023505, [hep-ph/0301270].

[350] S. H.-S. Alexander, M. E. Peskin and M. M. Sheikh-Jabbari, *Leptogenesis from gravity waves in models of inflation*, *Phys. Rev. Lett.* **96** (2006) 081301, [hep-th/0403069].

[351] M. Bastero-Gil, A. Berera, R. O. Ramos and J. G. Rosa, *Warm baryogenesis*, *Phys. Lett. B* **712** (2012) 425–429, [1110.3971].

[352] G. Elor, M. Escudero and A. Nelson, *Baryogenesis and Dark Matter from B Mesons*, *Phys. Rev. D* **99** (2019) 035031, [1810.00880].

[353] G. Elor and R. McGehee, *Making the Universe at 20 MeV*, *Phys. Rev. D* **103** (2021) 035005, [2011.06115].

[354] LHCb collaboration, A. A. Alves, Jr. et al., *The LHCb Detector at the LHC*, *JINST* **3** (2008) S08005.

[355] Belle-II collaboration, W. Altmannshofer et al., *The Belle II Physics Book*, *PTEP* **2019** (2019) 123C01, [1808.10567].

[356] K. S. Babu, R. N. Mohapatra and S. Nasri, *Post-Sphaleron Baryogenesis*, *Phys. Rev. Lett.* **97** (2006) 131301, [hep-ph/0606144].

[357] K. S. Babu, P. S. Bhupal Dev, E. C. F. S. Fortes and R. N. Mohapatra, *Post-Sphaleron Baryogenesis and an Upper Limit on the Neutron-Antineutron Oscillation Time*, *Phys. Rev. D* **87** (2013) 115019, [1303.6918].

[358] A. G. Cohen and D. B. Kaplan, *Thermodynamic Generation of the Baryon Asymmetry*, *Phys. Lett. B* **199** (1987) 251–258.

[359] A. G. Cohen and D. B. Kaplan, *SPONTANEOUS BARYOGENESIS*, *Nucl. Phys. B* **308** (1988) 913–928.

[360] M.-z. Li, X.-l. Wang, B. Feng and X.-m. Zhang, *Quintessence and spontaneous leptogenesis*, *Phys. Rev. D* **65** (2002) 103511, [hep-ph/0112069].

[361] P. Gu, X. Wang and X. Zhang, *Dark energy and neutrino mass limits from baryogenesis*, *Phys. Rev. D* **68** (2003) 087301, [hep-ph/0307148].

[362] R. W. Brown and F. W. Stecker, *Cosmological Baryon Number Domain Structure From Symmetry Breaking in Grand Unified Field Theories*, *Phys. Rev. Lett.* **43** (1979) 315–318.

[363] K. Sato, *Cosmological Baryon Number Domain Structure and the First Order Phase Transition of a Vacuum*, *Phys. Lett. B* **99** (1981) 66–70.

[364] P. J. O'Donnell and U. Sarkar, *Baryogenesis via lepton number violating scalar interactions*, *Phys. Rev. D* **49** (1994) 2118–2121, [hep-ph/9307279].

[365] E. Ma and U. Sarkar, *Neutrino masses and leptogenesis with heavy Higgs triplets*, *Phys. Rev. Lett.* **80** (1998) 5716–5719, [hep-ph/9802445].

[366] A. S. Joshipura, E. A. Paschos and W. Rodejohann, *A Simple connection between neutrino oscillation and leptogenesis*, *JHEP* **08** (2001) 029, [hep-ph/0105175].

[367] T. Hambye and G. Senjanovic, *Consequences of triplet seesaw for leptogenesis*, *Phys. Lett. B* **582** (2004) 73–81, [hep-ph/0307237].

[368] S. Antusch and S. F. King, *Type II Leptogenesis and the neutrino mass scale*, *Phys. Lett. B* **597** (2004) 199–207, [hep-ph/0405093].

[369] W. Rodejohann, *Type II seesaw mechanism, deviations from bimaximal neutrino mixing and leptogenesis*, *Phys. Rev. D* **70** (2004) 073010, [hep-ph/0403236].

[370] T. Hambye, M. Raidal and A. Strumia, *Efficiency and maximal CP-asymmetry of scalar triplet leptogenesis*, *Phys. Lett. B* **632** (2006) 667–674, [hep-ph/0510008].

[371] A. Strumia, *Sommerfeld corrections to type-II and III leptogenesis*, *Nucl. Phys. B* **809** (2009) 308–317, [0806.1630].

[372] T. Hambye, Y. Lin, A. Notari, M. Papucci and A. Strumia, *Constraints on neutrino masses from leptogenesis models*, *Nucl. Phys. B* **695** (2004) 169–191, [hep-ph/0312203].

[373] S.-L. Chen and X.-G. He, *Leptogenesis and LHC Physics with Type III See-Saw*, *Int. J. Mod. Phys. Conf. Ser.* **01** (2011) 18–27, [0901.1264].

[374] E. T. Franco, *Type I+III seesaw mechanism and CP violation for leptogenesis*, *Phys. Rev. D* **92** (2015) 113010, [1510.06240].

[375] T. Hambye, *Leptogenesis: beyond the minimal type I seesaw scenario*, *New J. Phys.* **14** (2012) 125014, [1212.2888].

[376] F. Bonnet, M. Hirsch, T. Ota and W. Winter, *Systematic study of the d=5 Weinberg operator at one-loop order*, *JHEP* **07** (2012) 153, [1204.5862].

[377] D. Aristizabal Sierra, A. Degee, L. Dorame and M. Hirsch, *Systematic classification of two-loop realizations of the Weinberg operator*, *JHEP* **03** (2015) 040, [1411.7038].

[378] R. Cepedello, R. M. Fonseca and M. Hirsch, *Systematic classification of three-loop realizations of the Weinberg operator*, *JHEP* **10** (2018) 197, [1807.00629].

[379] Y. Liao, G.-Z. Ning and L. Ren, *Flavor Violating Transitions of Charged Leptons from a Seesaw Mechanism of Dimension Seven*, *Phys. Rev. D* **82** (2010) 113003, [1008.0117].

[380] M. B. Krauss, D. Meloni, W. Porod and W. Winter, *Neutrino Mass from a d=7 Effective Operator in an SU(5) SUSY-GUT Framework*, *JHEP* **05** (2013) 121, [1301.4221].

[381] L. Lehman, *Extending the Standard Model Effective Field Theory with the Complete Set of Dimension-7 Operators*, *Phys. Rev. D* **90** (2014) 125023, [1410.4193].

[382] Y. Liao and X.-D. Ma, *Renormalization Group Evolution of Dimension-seven Baryon- and Lepton-number-violating Operators*, *JHEP* **11** (2016) 043, [1607.07309].

[383] Y. Liao and X.-D. Ma, *Renormalization Group Evolution of Dimension-seven Operators in Standard Model Effective Field Theory and Relevant Phenomenology*, *JHEP* **03** (2019) 179, [1901.10302].

[384] Y. Liao, X.-D. Ma and Q.-Y. Wang, *Extending low energy effective field theory with a complete set of dimension-7 operators*, *JHEP* **08** (2020) 162, [2005.08013].

[385] S. Bhattacharya and J. Wudka, *Dimension-seven operators in the standard model with right handed neutrinos*, *Phys. Rev. D* **94** (2016) 055022, [1505.05264].

[386] Y. Liao and X.-D. Ma, *Operators up to Dimension Seven in Standard Model Effective Field Theory Extended with Sterile Neutrinos*, *Phys. Rev. D* **96** (2017) 015012, [1612.04527].

[387] V. Cirigliano, W. Dekens, J. de Vries, M. L. Graesser and E. Mereghetti, *Neutrinoless double beta decay in chiral effective field theory: lepton number violation at dimension seven*, *JHEP* **12** (2017) 082, [1708.09390].

[388] Y. Liao, X.-D. Ma and H.-L. Wang, *Effective field theory approach to lepton number violating decays $K^{\pm} \to \pi^{\mp} l_{\alpha}^{\pm} l_{\beta}^{\pm}$: long-distance contribution*, *JHEP* **03** (2020) 120, [2001.07378].

[389] R. Cepedello, M. Hirsch and J. C. Helo, *Lepton number violating phenomenology of d = 7 neutrino mass models*, *JHEP* **01** (2018) 009, [1709.03397].

[390] R. Cepedello, M. Hirsch and J. C. Helo, *Loop neutrino masses from $d = 7$ operator*, *JHEP* **07** (2017) 079, [1705.01489].

[391] J. Herrero-García and M. A. Schmidt, *Neutrino mass models: New classification and model-independent upper limits on their scale*, *Eur. Phys. J. C* **79** (2019) 938, [1903.10552].

[392] I. Brivio and M. Trott, *The Standard Model as an Effective Field Theory*, *Phys. Rept.* **793** (2019) 1–98, [1706.08945].

[393] A. de Gouvea and J. Jenkins, *A Survey of Lepton Number Violation Via Effective Operators*, *Phys. Rev. D* **77** (2008) 013008, [0708.1344].

[394] F. F. Deppisch, L. Graf, J. Harz and W.-C. Huang, *Neutrinoless Double Beta Decay and the Baryon Asymmetry of the Universe*, *Phys. Rev. D* **98** (2018) 055029, [1711.10432].

[395] K. S. Babu and C. N. Leung, *Classification of effective neutrino mass operators*, *Nucl. Phys. B* **619** (2001) 667–689, [hep-ph/0106054].

[396] Y. Liao, X.-D. Ma and H.-L. Wang, *Effective field theory approach to lepton number violating decays $K^{\pm} \to \pi^{\mp} l^{\pm} l^{\pm}$: short-distance contribution*, *JHEP* **01** (2020) 127, [1909.06272].

[397] KATRIN collaboration, A. Osipowicz et al., *KATRIN: A Next generation tritium beta decay experiment with sub-eV sensitivity for the electron neutrino mass. Letter of intent*, hep-ex/0109033.

[398] KATRIN collaboration, J. Wolf, *The KATRIN Neutrino Mass Experiment*, *Nucl. Instrum. Meth. A* **623** (2010) 442–444, [0810.3281].

[399] KATRIN collaboration, M. Aker et al., *Improved Upper Limit on the Neutrino Mass from a Direct Kinematic Method by KATRIN*, *Phys. Rev. Lett.* **123** (2019) 221802, [1909.06048].

[400] KATRIN collaboration, M. Aker et al., *Direct neutrino-mass measurement with sub-electronvolt sensitivity*, *Nature Phys.* **18** (2022) 160–166, [2105.08533].

[401] I. Esteban, M. C. Gonzalez-Garcia, M. Maltoni, T. Schwetz and A. Zhou, *The fate of hints: updated global analysis of three-flavor neutrino oscillations*, *JHEP* **09** (2020) 178, [2007.14792].

[402] H. K. Dreiner, H. E. Haber and S. P. Martin, *Two-component spinor techniques and Feynman rules for quantum field theory and supersymmetry*, *Phys. Rept.* **494** (2010) 1–196, [0812.1594].

[403] BNL-E949 collaboration, A. V. Artamonov et al., *Study of the decay $K^+ \to \pi^+ \nu\bar{\nu}$ in the momentum region $140 < P_\pi < 199$ MeV/c*, *Phys. Rev. D* **79** (2009) 092004, [0903.0030].

[404] NA62 collaboration, E. Cortina Gil et al., *An investigation of the very rare $K^+ \to \pi^+ \nu\bar{\nu}$ decay*, *JHEP* **11** (2020) 042, [2007.08218].

[405] T. Masuda et al., *Long-lived neutral-kaon flux measurement for the KOTO experiment*, *PTEP* **2016** (2016) 013C03, [1509.03386].

[406] A. M. Cooper-Sarkar, J. G. Guy, A. G. Michette, M. Tyndel and W. Venus, *Limits on Neutrino - Anti-neutrinos Transitions From a Study of High-energy Neutrino Interactions*, *Phys. Lett. B* **112** (1982) 97–99.

[407] R. Dutta, A. Bhol and A. K. Giri, *Effective theory approach to new physics in $b \to u$ and $b \to c$ leptonic and semileptonic decays*, *Phys. Rev. D* **88** (2013) 114023, [1307.6653].

[408] M. Coppola, D. Gomez Dumm, S. Noguera and N. N. Scoccola, *Pion-to-vacuum vector and axial vector amplitudes and weak decays of pions in a magnetic field*, *Phys. Rev. D* **99** (2019) 054031, [1810.08110].

[409] M. Doi et al., *Neutrino mass, the right-handed interaction and the double beta decay. i: Formalism*, *Phys. Theor. Phys.* **66** (1983) 1739.

[410] H. Pas, M. Hirsch, H. V. Klapdor-Kleingrothaus and S. G. Kovalenko, *Towards a superformula for neutrinoless double beta decay*, *Phys. Lett. B* **453** (1999) 194–198.

[411] H. Pas, M. Hirsch, H. V. Klapdor-Kleingrothaus and S. G. Kovalenko, *A Superformula for neutrinoless double beta decay. 2. The Short range part*, *Phys. Lett. B* **498** (2001) 35–39, [hep-ph/0008182].

[412] F. F. Deppisch, M. Hirsch and H. Pas, *Neutrinoless Double Beta Decay and Physics Beyond the Standard Model*, *J. Phys. G* **39** (2012) 124007, [1208.0727].

[413] A. Ali, A. Ali, A. V. Borisov, A. V. Borisov, D. V. Zhuridov and D. V. Zhuridov, *Probing new physics in the neutrinoless double beta decay using electron angular correlation*, *Phys. Rev. D* **76** (2007) 093009, [0706.4165].

[414] F. del Aguila, A. Aparici, S. Bhattacharya, A. Santamaria and J. Wudka, *A realistic model of neutrino masses with a large neutrinoless double beta decay rate*, *JHEP* **05** (2012) 133, [1111.6960].

[415] F. del Aguila, A. Aparici, S. Bhattacharya, A. Santamaria and J. Wudka, *Effective Lagrangian approach to neutrinoless double beta decay and neutrino masses*, *JHEP* **06** (2012) 146, [1204.5986].

[416] V. Cirigliano, W. Dekens, J. de Vries, M. L. Graesser and E. Mereghetti, *A neutrinoless double beta decay master formula from effective field theory*, *JHEP* **12** (2018) 097, [1806.02780].

[417] L. Graf, F. F. Deppisch, F. Iachello and J. Kotila, *Short-Range Neutrinoless Double Beta Decay Mechanisms*, *Phys. Rev. D* **98** (2018) 095023, [1806.06058].

[418] F. F. Deppisch, L. Graf, F. Iachello and J. Kotila, *Analysis of light neutrino exchange and short-range mechanisms in $0\nu\beta\beta$ decay*, *Phys. Rev. D* **102** (2020) 095016, [2009.10119].

[419] W. Dekens, J. de Vries, K. Fuyuto, E. Mereghetti and G. Zhou, *Sterile neutrinos and neutrinoless double beta decay in effective field theory*, *JHEP* **06** (2020) 097, [2002.07182].

[420] KamLAND-Zen collaboration, S. Abe et al., *First Search for the Majorana Nature of Neutrinos in the Inverted Mass Ordering Region with KamLAND-Zen*, 2203.02139.

[421] L. S. Littenberg and R. E. Shrock, *Upper bounds on lepton number violating meson decays*, *Phys. Rev. Lett.* **68** (1992) 443–446.

[422] L. S. Littenberg and R. Shrock, *Implications of improved upper bounds on |Delta L| = 2 processes*, *Phys. Lett. B* **491** (2000) 285–290, [hep-ph/0005285].

[423] E. J. Chun, A. Das, S. Mandal, M. Mitra and N. Sinha, *Sensitivity of Lepton Number Violating Meson Decays in Different Experiments*, *Phys. Rev. D* **100** (2019) 095022, [1908.09562].

[424] T. Li, X.-D. Ma and M. A. Schmidt, *Implication of $K \to \pi\nu\bar{\nu}$ for generic neutrino interactions in effective field theories*, *Phys. Rev. D* **101** (2020) 055019, [1912.10433].

[425] J. Aebischer, M. Fael, C. Greub and J. Virto, *B physics Beyond the Standard Model at One Loop: Complete Renormalization Group Evolution below the Electroweak Scale*, *JHEP* **09** (2017) 158, [1704.06639].

[426] E. E. Jenkins, A. V. Manohar and P. Stoffer, *Low-Energy Effective Field Theory below the Electroweak Scale: Operators and Matching*, *JHEP* **03** (2018) 016, [1709.04486].

[427] J. Brod, M. Gorbahn and E. Stamou, *Two-Loop Electroweak Corrections for the $K \to \pi\nu\bar{\nu}$ Decays*, *Phys. Rev. D* **83** (2011) 034030, [1009.0947].

[428] D. M. Straub, *flavio: a Python package for flavour and precision phenomenology in the Standard Model and beyond*, 1810.08132.

[429] T. Felkl, S. L. Li and M. A. Schmidt, *A tale of invisibility: constraints on new physics in $b \to s\nu\nu$*, *JHEP* **12** (2021) 118, [2111.04327].

[430] BaBar collaboration, J. P. Lees et al., *Search for $B \to K^{(*)}\nu\bar{\nu}$ and invisible quarkonium decays*, *Phys. Rev. D* **87** (2013) 112005, [1303.7465].

[431] Belle collaboration, O. Lutz et al., *Search for $B \to h^{(*)}\nu\bar{\nu}$ with the full Belle $\Upsilon(4S)$ data sample*, *Phys. Rev. D* **87** (2013) 111103, [1303.3719].

[432] Belle collaboration, J. Grygier et al., *Search for $B \to h\nu\bar{\nu}$ decays with semileptonic tagging at Belle*, *Phys. Rev. D* **96** (2017) 091101, [1702.03224].

[433] Belle-II collaboration, W. Altmannshofer et al., *The Belle II Physics Book*, *PTEP* **2019** (2019) 123C01, [1808.10567].

[434] N. Gubernari, A. Kokulu and D. van Dyk, *$B \to P$ and $B \to V$ Form Factors from B-Meson Light-Cone Sum Rules beyond Leading Twist*, *JHEP* **01** (2019) 150, [1811.00983].

[435] A. Bharucha, D. M. Straub and R. Zwicky, *$B \to V\ell^+\ell^-$ in the Standard Model from light-cone sum rules*, *JHEP* **08** (2016) 098, [1503.05534].

[436] G. Colangelo and S. Durr, *The Pion mass in finite volume*, *Eur. Phys. J. C* **33** (2004) 543–553, [hep-lat/0311023].

[437] S. N. Gninenko, *Search for invisible decays of π^0, η, η', K_S and K_L: A probe of new physics and tests using the Bell-Steinberger relation*, *Phys. Rev. D* **91** (2015) 015004, [1409.2288].

[438] Belle collaboration, Y. Miyazaki et al., *Search for Lepton-Flavor-Violating and Lepton-Number-Violating $\tau \to \ell hh'$ Decay Modes*, *Phys. Lett. B* **719** (2013) 346–353, [1206.5595].

[439] Belle-II collaboration, D. Rodríguez Pérez, *Prospects for τ Lepton Physics at Belle II*, in *17th Conference on Flavor Physics and CP Violation*, 6, 2019. 1906.08950.

[440] Y. Liao, X.-D. Ma and H.-L. Wang, *Effective field theory approach to lepton number violating τ decays*, *Chin. Phys. C* **45** (2021) 073102, [2102.03491].

[441] A. Atre, V. Barger and T. Han, *Upper bounds on lepton-number violating processes*, *Phys. Rev. D* **71** (2005) 113014, [hep-ph/0502163].

[442] A. Atre, T. Han, S. Pascoli and B. Zhang, *The Search for Heavy Majorana Neutrinos*, *JHEP* **05** (2009) 030, [0901.3589].

[443] A. Abada, V. De Romeri, M. Lucente, A. M. Teixeira and T. Toma, *Effective Majorana mass matrix from tau and pseudoscalar meson lepton number violating decays*, *JHEP* **02** (2018) 169, [1712.03984].

[444] A. Abada, C. Hati, X. Marcano and A. M. Teixeira, *Interference effects in LNV and LFV semileptonic decays: the Majorana hypothesis*, *JHEP* **09** (2019) 017, [1904.05367].

[445] B. Armbruster et al., *Improved limits on anti-nu(e) emission from mu+ decay*, *Phys. Rev. Lett.* **90** (2003) 181804, [hep-ex/0302017].

[446] C. Bouchiat and L. Michel, *Theory of μ-Meson Decay with the Hypothesis of Nonconservation of Parity*, *Phys. Rev.* **106** (1957) 170–172.

[447] Mu2e collaboration, L. Bartoszek et al., *Mu2e Technical Design Report*, 1501.05241.

[448] Y. Kuno, *Rare lepton decays*, *Prog. Part. Nucl. Phys.* **82** (2015) 1–20.

[449] SINDRUM II collaboration, J. Kaulard et al., *Improved limit on the branching ratio of mu- –> e+ conversion on titanium*, *Phys. Lett. B* **422** (1998) 334–338.

[450] COMET collaboration, Y. G. Cui et al., *Conceptual design report for experimental search for lepton flavor violating mu- - e- conversion at sensitivity of 10**(-16) with a slow-extracted bunched proton beam (COMET)*, .

[451] J. M. Berryman, A. de Gouvêa, K. J. Kelly and A. Kobach, *Lepton-number-violating searches for muon to positron conversion*, *Phys. Rev. D* **95** (2017) 115010, [1611.00032].

[452] W.-Y. Keung and G. Senjanovic, *Majorana Neutrinos and the Production of the Right-handed Charged Gauge Boson*, *Phys. Rev. Lett.* **50** (1983) 1427.

[453] J. Harz, M. J. Ramsey-Musolf, T. Shen and S. Urrutia-Quiroga, *TeV-scale Lepton Number Violation: Connecting Leptogenesis, Neutrinoless Double Beta Decay, and Colliders*, 2106.10838.

[454] S. M. Boucenna, S. Morisi and J. W. F. Valle, *The low-scale approach to neutrino masses*, *Adv. High Energy Phys.* **2014** (2014) 831598, [1404.3751].

[455] Y. Cai, T. Han, T. Li and R. Ruiz, *Lepton Number Violation: Seesaw Models and Their Collider Tests*, *Front. in Phys.* **6** (2018) 40, [1711.02180].

[456] P. S. B. Dev, B. Dutta, T. Ghosh, T. Han, H. Qin and Y. Zhang, *Leptonic scalars and collider signatures in a UV-complete model*, *JHEP* **03** (2022) 068, [2109.04490].

[457] F. F. Deppisch, J. Harz and M. Hirsch, *Falsifying High-Scale Leptogenesis at the LHC*, *Phys. Rev. Lett.* **112** (2014) 221601, [1312.4447].

[458] M. Aoki, K. Enomoto and S. Kanemura, *Probing charged lepton number violation via $\ell^{\pm}\ell'^{\pm}W^{\mp}W^{\mp}$*, *Phys. Rev. D* **101** (2020) 115019, [2002.12265].

[459] B. Fuks, J. Neundorf, K. Peters, R. Ruiz and M. Saimpert, *Probing the Weinberg operator at colliders*, *Phys. Rev. D* **103** (2021) 115014, [2012.09882].

[460] B. Fuks, J. Neundorf, K. Peters, R. Ruiz and M. Saimpert, *Majorana neutrinos in same-sign $W^{\pm}W^{\pm}$ scattering at the LHC: Breaking the TeV barrier*, *Phys. Rev. D* **103** (2021) 055005, [2011.02547].

[461] A. Alloul, N. D. Christensen, C. Degrande, C. Duhr and B. Fuks, *FeynRules 2.0 - A complete toolbox for tree-level phenomenology*, *Comput. Phys. Commun.* **185** (2014) 2250–2300, [1310.1921].

[462] J. Alwall, R. Frederix, S. Frixione, V. Hirschi, F. Maltoni, O. Mattelaer et al., *The automated computation of tree-level and next-to-leading order differential cross sections, and their matching to parton shower simulations*, *JHEP* **07** (2014) 079, [1405.0301].

[463] ATLAS collaboration, M. Aaboud et al., *Search for heavy Majorana or Dirac neutrinos and right-handed W gauge bosons in final states with two charged leptons and two jets at $\sqrt{s} = 13$ TeV with the ATLAS detector*, *JHEP* **01** (2019) 016, [1809.11105].

[464] A. Buckley, J. Ferrando, S. Lloyd, K. Nordström, B. Page, M. Rüfenacht et al., *LHAPDF6: parton density access in the LHC precision era*, *Eur. Phys. J. C* **75** (2015) 132, [1412.7420].

[465] T. Sjöstrand, S. Ask, J. R. Christiansen, R. Corke, N. Desai, P. Ilten et al., *An introduction to PYTHIA 8.2*, *Comput. Phys. Commun.* **191** (2015) 159–177, [1410.3012].

[466] DELPHES 3 collaboration, J. de Favereau, C. Delaere, P. Demin, A. Giammanco, V. Lemaître, A. Mertens et al., *DELPHES 3, A modular framework for fast simulation of a generic collider experiment*, *JHEP* **02** (2014) 057, [1307.6346].

[467] M. Cacciari and G. P. Salam, *Dispelling the N^3 myth for the k_t jet-finder*, *Phys. Lett. B* **641** (2006) 57–61, [hep-ph/0512210].

[468] G. Cowan, K. Cranmer, E. Gross and O. Vitells, *Asymptotic formulae for likelihood-based tests of new physics*, *Eur. Phys. J. C* **71** (2011) 1554, [1007.1727].

[469] M. L. Graesser, G. Li, M. J. Ramsey-Musolf, T. Shen and S. Urrutia-Quiroga, *Uncovering a chirally suppressed mechanism of $0\nu\beta\beta$ decay with LHC searches*, 2202.01237.

[470] CMS collaboration, A. M. Sirunyan et al., *Search for heavy Majorana neutrinos in same-sign dilepton channels in proton-proton collisions at $\sqrt{s} = 13$ TeV*, *JHEP* **01** (2019) 122, [1806.10905].

[471] O. Buchmueller, M. J. Dolan and C. McCabe, *Beyond Effective Field Theory for Dark Matter Searches at the LHC*, *JHEP* **01** (2014) 025, [1308.6799].

[472] G. Busoni, A. De Simone, E. Morgante and A. Riotto, *On the Validity of the Effective Field Theory for Dark Matter Searches at the LHC*, *Phys. Lett. B* **728** (2014) 412–421, [1307.2253].

[473] J. Lang, S. Liebler, H. Schäfer-Siebert and D. Zeppenfeld, *Effective field theory versus UV-complete model: vector boson scattering as a case study*, *Eur. Phys. J. C* **81** (2021) 659, [2103.16517].

[474] I. M. Shoemaker and L. Vecchi, *Unitarity and Monojet Bounds on Models for DAMA, CoGeNT, and CRESST-II*, *Phys. Rev. D* **86** (2012) 015023, [1112.5457].

[475] E. J. Chun et al., *Probing Leptogenesis*, *Int. J. Mod. Phys. A* **33** (2018) 1842005, [1711.02865].

[476] F. F. Deppisch, J. Harz, M. Hirsch, W.-C. Huang and H. Päs, *Falsifying High-Scale Baryogenesis with Neutrinoless Double Beta Decay and Lepton Flavor Violation*, *Phys. Rev. D* **92** (2015) 036005, [1503.04825].

[477] F. Bonnet, D. Hernandez, T. Ota and W. Winter, *Neutrino masses from higher than d=5 effective operators*, *JHEP* **10** (2009) 076, [0907.3143].

[478] P. W. Angel, N. L. Rodd and R. R. Volkas, *Origin of neutrino masses at the LHC: $\Delta L = 2$ effective operators and their ultraviolet completions*, *Phys. Rev. D* **87** (2013) 073007, [1212.6111].

[479] Y. Cai, J. D. Clarke, M. A. Schmidt and R. R. Volkas, *Testing Radiative Neutrino Mass Models at the LHC*, *JHEP* **02** (2015) 161, [1410.0689].

[480] J. de Blas, J. C. Criado, M. Perez-Victoria and J. Santiago, *Effective description of general extensions of the Standard Model: the complete tree-level dictionary*, *JHEP* **03** (2018) 109, [1711.10391].

[481] G. Anamiati, O. Castillo-Felisola, R. M. Fonseca, J. C. Helo and M. Hirsch, *High-dimensional neutrino masses*, *JHEP* **12** (2018) 066, [1806.07264].

[482] A. De Gouvêa, W.-C. Huang, J. König and M. Sen, *Accessible Lepton-Number-Violating Models and Negligible Neutrino Masses*, *Phys. Rev. D* **100** (2019) 075033, [1907.02541].

[483] P.-T. Chen, G.-J. Ding and C.-Y. Yao, *Decomposition of d = 9 short-range $0\nu\beta\beta$ decay operators at one-loop level*, *JHEP* **12** (2021) 169, [2110.15347].

[484] U. Banerjee, J. Chakrabortty, S. Prakash, S. U. Rahaman and M. Spannowsky, *Effective Operator Bases for Beyond Standard Model Scenarios: An EFT compendium for discoveries*, *JHEP* **01** (2021) 028, [2008.11512].

[485] M. Chala and A. Titov, *Neutrino masses in the Standard Model effective field theory*, *Phys. Rev. D* **104** (2021) 035002, [2104.08248].

[486] S. Das Bakshi, J. Chakrabortty, S. Prakash, S. U. Rahaman and M. Spannowsky, *EFT diagrammatica: UV roots of the CP-conserving SMEFT*, *JHEP* **06** (2021) 033, [2103.11593].

[487] K. S. Babu, P. S. B. Dev, S. Jana and A. Thapa, *Non-Standard Interactions in Radiative Neutrino Mass Models*, *JHEP* **03** (2020) 006, [1907.09498].

[488] R. Coy and M. Frigerio, *Effective comparison of neutrino-mass models*, *Phys. Rev. D* **105** (2022) 115041, [2110.09126].

[489] J. Gargalionis and R. R. Volkas, *Exploding operators for Majorana neutrino masses and beyond*, *JHEP* **01** (2021) 074, [2009.13537].

[490] B. Henning, X. Lu, T. Melia and H. Murayama, *2, 84, 30, 993, 560, 15456, 11962, 261485, ...: Higher dimension operators in the SM EFT*, *JHEP* **08** (2017) 016, [1512.03433].

[491] L. Lehman and A. Martin, *Low-derivative operators of the Standard Model effective field theory via Hilbert series methods*, *JHEP* **02** (2016) 081, [1510.00372].

[492] B. Henning, X. Lu, T. Melia and H. Murayama, *Hilbert series and operator bases with derivatives in effective field theories*, *Commun. Math. Phys.* **347** (2016) 363–388, [1507.07240].

[493] L. Lehman and A. Martin, *Hilbert Series for Constructing Lagrangians: expanding the phenomenologist's toolbox*, *Phys. Rev. D* **91** (2015) 105014, [1503.07537].

[494] J. Fuentes-Martin, J. Portoles and P. Ruiz-Femenia, *Integrating out heavy particles with functional methods: a simplified framework*, *JHEP* **09** (2016) 156, [1607.02142].

[495] R. M. Fonseca, *Enumerating the operators of an effective field theory*, *Phys. Rev. D* **101** (2020) 035040, [1907.12584].

[496] I. Doršner, S. Fajfer, A. Greljo, J. F. Kamenik and N. Košnik, *Physics of leptoquarks in precision experiments and at particle colliders*, *Phys. Rept.* **641** (2016) 1–68, [1603.04993].

[497] T. Felkl, J. Herrero-Garcia and M. A. Schmidt, *The Singly-Charged Scalar Singlet as the Origin of Neutrino Masses*, *JHEP* **05** (2021) 122, [2102.09898].

[498] Y. Cai, J. Herrero-García, M. A. Schmidt, A. Vicente and R. R. Volkas, *From the trees to the forest: a review of radiative neutrino mass models*, *Front. in Phys.* **5** (2017) 63, [1706.08524].

[499] R. N. Mohapatra, *Mechanism for Understanding Small Neutrino Mass in Superstring Theories*, *Phys. Rev. Lett.* **56** (1986) 561–563.

[500] R. N. Mohapatra and J. W. F. Valle, *Neutrino Mass and Baryon Number Nonconservation in Superstring Models*, *Phys. Rev. D* **34** (1986) 1642.

[501] M. C. Gonzalez-Garcia and J. W. F. Valle, *Fast Decaying Neutrinos and Observable Flavor Violation in a New Class of Majoron Models*, *Phys. Lett. B* **216** (1989) 360–366.

[502] C. Klein, M. Lindner and S. Ohmer, *Minimal Radiative Neutrino Masses*, *JHEP* **03** (2019) 018, [1901.03225].

[503] C. Arbeláez, R. Cepedello, J. C. Helo, M. Hirsch and S. Kovalenko, *How many 1-loop neutrino mass models are there?*, 2205.13063.

[504] O. Catà and T. Mannel, *Linking lepton number violation with B anomalies*, 1903.01799.

[505] N. Kosnik, *Model independent constraints on leptoquarks from $b \to s\ell^+\ell^-$ processes*, *Phys. Rev. D* **86** (2012) 055004, [1206.2970].

[506] S. Bifani, S. Descotes-Genon, A. Romero Vidal and M.-H. Schune, *Review of Lepton Universality tests in B decays*, *J. Phys. G* **46** (2019) 023001, [1809.06229].

[507] S. Fajfer, N. Košnik and L. Vale Silva, *Footprints of leptoquarks: from $R_{K^{(*)}}$ to $K \to \pi\nu\bar{\nu}$*, *Eur. Phys. J. C* **78** (2018) 275, [1802.00786].

[508] S. Descotes-Genon, S. Fajfer, J. F. Kamenik and M. Novoa-Brunet, *Implications of $b \to s\mu\mu$ anomalies for future measurements of $B \to K^{(*)}\nu\bar{\nu}$ and $K \to \pi\nu\bar{\nu}$*, *Phys. Lett. B* **809** (2020) 135769, [2005.03734].

[509] D. Aristizabal Sierra, M. Hirsch and S. G. Kovalenko, *Leptoquarks: Neutrino masses and accelerator phenomenology*, *Phys. Rev. D* **77** (2008) 055011, [0710.5699].

[510] K. S. Babu and J. Julio, *Two-Loop Neutrino Mass Generation through Leptoquarks*, *Nucl. Phys. B* **841** (2010) 130–156, [1006.1092].

[511] I. Doršner, S. Fajfer and N. Košnik, *Leptoquark mechanism of neutrino masses within the grand unification framework*, *Eur. Phys. J. C* **77** (2017) 417, [1701.08322].

[512] M. C. Gonzalez-Garcia, M. Maltoni and T. Schwetz, *NuFIT: Three-Flavour Global Analyses of Neutrino Oscillation Experiments*, *Universe* **7** (2021) 459, [2111.03086].

[513] J. Ellis, M. Madigan, K. Mimasu, V. Sanz and T. You, *Top, Higgs, Diboson and Electroweak Fit to the Standard Model Effective Field Theory*, *JHEP* **04** (2021) 279, [2012.02779].

[514] A. Crivellin, M. Hoferichter, M. Kirk, C. A. Manzari and L. Schnell, *First-generation new physics in simplified models: from low-energy parity violation to the LHC*, *JHEP* **10** (2021) 221, [2107.13569].

[515] J. Ellis, C. W. Murphy, V. Sanz and T. You, *Updated Global SMEFT Fit to Higgs, Diboson and Electroweak Data*, *JHEP* **06** (2018) 146, [1803.03252].

[516] J. Bernon, J. F. Gunion, H. E. Haber, Y. Jiang and S. Kraml, *Scrutinizing the alignment limit in two-Higgs-doublet models: m_h=125 GeV*, *Phys. Rev. D* **92** (2015) 075004, [1507.00933].

[517] S. L. Glashow, J. Iliopoulos and L. Maiani, *Weak Interactions with Lepton-Hadron Symmetry*, *Phys. Rev. D* **2** (1970) 1285–1292.

[518] G. D'Ambrosio and G. Isidori, *CP violation in kaon decays*, *Int. J. Mod. Phys. A* **13** (1998) 1–94, [hep-ph/9611284].

[519] G. Buchalla and A. J. Buras, *The rare decays $K \to \pi\nu\bar{\nu}$, $B \to X\nu\bar{\nu}$ and $B \to l^+l^-$: An Update*, *Nucl. Phys. B* **548** (1999) 309–327, [hep-ph/9901288].

[520] X.-G. He, G. Valencia and K. Wong, *Constraints on new physics from $K \to \pi\nu\bar{\nu}$*, *Eur. Phys. J.* **C78** (2018) 472, [1804.07449].

[521] D. Bryman, A. J. Buras, G. Isidori and L. Littenberg, *K(L) —> pi0 nu anti-nu as a probe of new physics*, *Int. J. Mod. Phys. A* **21** (2006) 487–504, [hep-ph/0505171].

[522] F. Mescia and C. Smith, *Improved estimates of rare K decay matrix elements from $K_{\ell 3}$ decays*, *PrD* **76** (Aug, 2007) 034017, [0705.2025].

[523] A. J. Buras, D. Buttazzo, J. Girrbach-Noe and R. Knegjens, *$K^+ \to \pi^+\nu\bar{\nu}$ and $K_L \to \pi^0\nu\bar{\nu}$ in the Standard Model: status and perspectives*, *JHEP* **11** (2015) 033, [1503.02693].

[524] A. J. Buras, F. Schwab and S. Uhlig, *Waiting for precise measurements of $K^+ \to \pi^+\nu\bar{\nu}$ and $K_L \to \pi^0\nu\bar{\nu}$*, *Rev. Mod. Phys.* **80** (2008) 965–1007, [hep-ph/0405132].

[525] Y. Grossman and Y. Nir, *K(L) —> pi0 neutrino anti-neutrino beyond the standard model*, *Phys. Lett. B* **398** (1997) 163–168, [hep-ph/9701313].

[526] Y. Grossman, G. Isidori and H. Murayama, *Lepton flavor mixing and K —> pi nu anti-nu decays*, *Phys. Lett. B* **588** (2004) 74–80, [hep-ph/0311353].

[527] G. Buchalla and G. Isidori, *The CP conserving contribution to K(L) —> pi0 neutrino anti-neutrino in the standard model*, *Phys. Lett. B* **440** (1998) 170–178, [hep-ph/9806501].

[528] KOTO collaboration, J. K. Ahn et al., *Search for the $K_L \to \pi^0 \nu\bar{\nu}$ and $K_L \to \pi^0 X^0$ decays at the J-PARC KOTO experiment*, *Phys. Rev. Lett.* **122** (2019) 021802, [1810.09655].

[529] S. Shinohara, *Search for the rare decay $k_l \to \pi^0 \nu\bar{\nu}$ at j-parc koto experiment*, KAON2019, Perugia, Italy, 10-13 September, 2019.

[530] T. Kitahara, T. Okui, G. Perez, Y. Soreq and K. Tobioka, *New physics implications of recent search for $K_L \to \pi^0 \nu\bar{\nu}$ at KOTO*, *arXiv e-prints* (Sep, 2019) arXiv:1909.11111, [1909.11111].

[531] X.-G. He, X.-D. Ma, J. Tandean and G. Valencia, *Breaking the Grossman-Nir Bound in Kaon Decays*, *JHEP* **04** (2020) 057, [2002.05467].

[532] X.-G. He, X.-D. Ma, J. Tandean and G. Valencia, *Evading the Grossman-Nir bound with $\Delta I = 3/2$ new physics*, *JHEP* **08** (2020) 034, [2005.02942].

[533] K. Fuyuto, W.-S. Hou and M. Kohda, *Loophole in $K \to \pi\nu\bar{\nu}$ Search and New Weak Leptonic Forces*, *Phys. Rev. Lett.* **114** (2015) 171802, [1412.4397].

[534] M. Fabbrichesi and E. Gabrielli, *Dark-sector physics in the search for the rare decays $K^+ \to \pi^+ \nu\bar{\nu}$ and $K_L \to \pi^0 \nu\bar{\nu}$*, *Eur. Phys. J. C* **80** (2020) 532, [1911.03755].

[535] P. S. B. Dev, R. N. Mohapatra and Y. Zhang, *Constraints on long-lived light scalars with flavor-changing couplings and the KOTO anomaly*, *Phys. Rev. D* **101** (2020) 075014, [1911.12334].

[536] M. Hostert, K. Kaneta and M. Pospelov, *Pair production of dark particles in meson decays*, *Phys. Rev. D* **102** (2020) 055016, [2005.07102].

[537] A. Datta, S. Kamali and D. Marfatia, *Dark sector origin of the KOTO and MiniBooNE anomalies*, *Phys. Lett. B* **807** (2020) 135579, [2005.08920].

[538] NA62 collaboration, E. Cortina Gil et al., *First search for $K^+ \to \pi^+ \nu\bar{\nu}$ using the decay-in-flight technique*, *Phys. Lett. B* **791** (2019) 156–166, [1811.08508].

[539] NA62 collaboration, E. Cortina Gil et al., *Measurement of the very rare $K^+ \to \pi^+ \nu\bar{\nu}$ decay*, *JHEP* **06** (2021) 093, [2103.15389].

[540] NA62 collaboration, R. Fiorenza et al., *Measurement of the very rare $K^+ \to \pi^+ \nu\bar{\nu}$ decay at the NA62 experiment at CERN*, *PoS* **NuFact2021** (2022) 176.

[541] NA62 collaboration, A. Kleimenova, *Latest results from NA62*, *PoS* **DIS2019** (2019) 122.

[542] R.-X. Shi, L.-S. Geng, B. Grinstein, S. Jäger and J. M. Camalich, *Revisiting the new-physics interpretation of the $b \to c\tau\nu$ data*, *arXiv e-prints* (May, 2019) arXiv:1905.08498, [1905.08498].

[543] P. Colangelo, F. De Fazio and F. Loparco, *Probing New Physics with $\bar{B} \to \rho(770)\, \ell^- \bar{\nu}_\ell$ and $\bar{B} \to a_1(1260)\, \ell^- \bar{\nu}_\ell$*, *arXiv e-prints* (Jun, 2019) arXiv:1906.07068, [1906.07068].

[544] Y. Sakaki, M. Tanaka, A. Tayduganov and R. Watanabe, *Testing leptoquark models in $\bar{B} \to D^{(*)}\tau\bar{\nu}$*, *Phys. Rev. D* **88** (2013) 094012, [1309.0301].

[545] A. J. Buras, *Weak Hamiltonian, CP violation and rare decays*, in *Les Houches Summer School in Theoretical Physics, Session 68: Probing the Standard Model of Particle Interactions*, pp. 281–539, 6, 1998. hep-ph/9806471.

[546] D. Z. Freedman, *Coherent Neutrino Nucleus Scattering as a Probe of the Weak Neutral Current*, *Phys. Rev. D* **9** (1974) 1389–1392.

[547] COHERENT collaboration, D. Akimov et al., *Observation of Coherent Elastic Neutrino-Nucleus Scattering*, *Science* **357** (2017) 1123–1126, [1708.01294].

[548] NUCLEUS collaboration, J. Rothe et al., *NUCLEUS: Exploring Coherent Neutrino-Nucleus Scattering with Cryogenic Detectors*, *J. Low Temp. Phys.* **199** (2019) 433–440.

[549] NUCLEUS collaboration, G. Angloher et al., *Exploring CEvNS with NUCLEUS at the Chooz nuclear power plant*, *Eur. Phys. J. C* **79** (2019) 1018, [1905.10258].

[550] T. Schwetz, A. Zhou and J.-Y. Zhu, *Constraining active-sterile neutrino transition magnetic moments at DUNE near and far detectors*, *JHEP* **21** (2020) 200, [2105.09699].

[551] P. Coloma, P. A. N. Machado, I. Martinez-Soler and I. M. Shoemaker, *Double-Cascade Events from New Physics in Icecube*, *Phys. Rev. Lett.* **119** (2017) 201804, [1707.08573].

[552] M. Atkinson, P. Coloma, I. Martinez-Soler, N. Rocco and I. M. Shoemaker, *Heavy neutrino searches through double-bang events at Super-Kamiokande, DUNE, and Hyper-Kamiokande*, *JHEP* **04** (2022) 174, [2105.09357].

[553] B. Kayser and R. E. Shrock, *Distinguishing Between Dirac and Majorana Neutrinos in Neutral Current Reactions*, *Phys. Lett. B* **112** (1982) 137–142.

[554] B. Kayser, *Majorana Neutrinos and their Electromagnetic Properties*, *Phys. Rev. D* **26** (1982) 1662.

[555] G. Magill, R. Plestid, M. Pospelov and Y.-D. Tsai, *Dipole Portal to Heavy Neutral Leptons*, *Phys. Rev. D* **98** (2018) 115015, [1803.03262].

[556] C. Giunti and A. Studenikin, *Neutrino electromagnetic interactions: a window to new physics*, *Rev. Mod. Phys.* **87** (2015) 531, [1403.6344].

[557] M. B. Voloshin, *On Compatibility of Small Mass with Large Magnetic Moment of Neutrino*, *Sov. J. Nucl. Phys.* **48** (1988) 512.

[558] N. F. Bell, V. Cirigliano, M. J. Ramsey-Musolf, P. Vogel and M. B. Wise, *How magnetic is the Dirac neutrino?*, *Phys. Rev. Lett.* **95** (2005) 151802, [hep-ph/0504134].

[559] P. B. Pal and L. Wolfenstein, *Radiative Decays of Massive Neutrinos*, *Phys. Rev. D* **25** (1982) 766.

[560] R. E. Shrock, *Electromagnetic Properties and Decays of Dirac and Majorana Neutrinos in a General Class of Gauge Theories*, *Nucl. Phys. B* **206** (1982) 359–379.

[561] E. Byckling and K. Kajantie, *Particle Kinematics: (Chapters I-VI, X)*. University of Jyvaskyla, Jyvaskyla, Finland, 1971.

[562] D. Gorbunov and M. Shaposhnikov, *How to find neutral leptons of the νMSM?*, *JHEP* **10** (2007) 015, [0705.1729].

[563] P. Ballett, S. Pascoli and M. Ross-Lonergan, *MeV-scale sterile neutrino decays at the Fermilab Short-Baseline Neutrino program*, *JHEP* **04** (2017) 102, [1610.08512].

[564] NUCLEUS collaboration, R. Strauss et al., *Private Communication*, Private Communication.

[565] V. Brdar, A. Greljo, J. Kopp and T. Opferkuch, *The Neutrino Magnetic Moment Portal: Cosmology, Astrophysics, and Direct Detection*, *JCAP* **01** (2021) 039, [2007.15563].

[566] R. Plestid, *Luminous solar neutrinos I: Dipole portals*, *Phys. Rev. D* **104** (2021) 075027, [2010.04193].

[567] I. M. Shoemaker and J. Wyenberg, *Direct Detection Experiments at the Neutrino Dipole Portal Frontier*, *Phys. Rev. D* **99** (2019) 075010, [1811.12435].

[568] A. Dasgupta, S. K. Kang and J. E. Kim, *Probing neutrino dipole portal at COHERENT experiment*, *JHEP* **11** (2021) 120, [2108.12998].

[569] S. N. Gninenko and N. V. Krasnikov, *Limits on the magnetic moment of sterile neutrino and two photon neutrino decay*, *Phys. Lett. B* **450** (1999) 165–172, [hep-ph/9808370].

[570] O. G. Miranda, D. K. Papoulias, O. Sanders, M. Tórtola and J. W. F. Valle, *Low-energy probes of sterile neutrino transition magnetic moments*, *JHEP* **12** (2021) 191, [2109.09545].

[571] K. S. Babu and R. N. Mohapatra, *Determining Majorana Nature of Neutrino from Nucleon Decays and $n - \bar{n}$ oscillations*, *Phys. Rev. D* **91** (2015) 013008, [1408.0803].

[572] P. S. B. Dev et al., *Searches for Baryon Number Violation in Neutrino Experiments: A White Paper*, 2203.08771.

[573] J. M. Arnold, B. Fornal and M. B. Wise, *Simplified models with baryon number violation but no proton decay*, *Phys. Rev. D* **87** (2013) 075004, [1212.4556].

[574] E. Rinaldi, S. Syritsyn, M. L. Wagman, M. I. Buchoff, C. Schroeder and J. Wasem, *Lattice QCD determination of neutron-antineutron matrix elements with physical quark masses*, *Phys. Rev. D* **99** (2019) 074510, [1901.07519].

[575] Super-Kamiokande collaboration, K. Abe et al., *Neutron-antineutron oscillation search using a 0.37 megaton-years exposure of Super-Kamiokande*, *Phys. Rev. D* **103** (2021) 012008, [2012.02607].

[576] M. Baldo-Ceolin et al., *A New experimental limit on neutron - anti-neutron oscillations*, *Z. Phys. C* **63** (1994) 409–416.

[577] DUNE collaboration, R. Acciarri et al., *Long-Baseline Neutrino Facility (LBNF) and Deep Underground Neutrino Experiment (DUNE): Conceptual Design Report, Volume 2: The Physics Program for DUNE at LBNF*, 1512.06148.

[578] A. Addazi et al., *New high-sensitivity searches for neutrons converting into antineutrons and/or sterile neutrons at the HIBEAM/NNBAR experiment at the European Spallation Source*, *J. Phys. G* **48** (2021) 070501, [2006.04907].

[579] L. N. Chang and N. P. Chang, *B-L NONCONSERVATION AND NEUTRON OSCILLATION*, *Phys. Lett. B* **92** (1980) 103–106.

[580] T.-K. Kuo and S. T. Love, *Neutron Oscillations and the Existence of Massive Neutral Leptons*, *Phys. Rev. Lett.* **45** (1980) 93.

[581] S. Rao and R. Shrock, *$n \leftrightarrow \bar{n}$ Transition Operators and Their Matrix Elements in the MIT Bag Model*, *Phys. Lett. B* **116** (1982) 238–242.

[582] S. Rao and R. E. Shrock, *Six Fermion ($B - L$) Violating Operators of Arbitrary Generational Structure*, *Nucl. Phys. B* **232** (1984) 143–179.

[583] W. E. Caswell, J. Milutinovic and G. Senjanovic, *MATTER - ANTIMATTER TRANSITION OPERATORS: A MANUAL FOR MODELING*, *Phys. Lett. B* **122** (1983) 373–377.

[584] M. I. Buchoff and M. Wagman, *Perturbative Renormalization of Neutron-Antineutron Operators*, *Phys. Rev. D* **93** (2016) 016005, [1506.00647].

[585] S. Bethke, *The 2009 World Average of alpha(s)*, *Eur. Phys. J. C* **64** (2009) 689–703, [0908.1135].

[586] K. Griest and D. Seckel, *Three exceptions in the calculation of relic abundances*, *Phys. Rev. D* **43** (1991) 3191–3203.

[587] J. Edsjo and P. Gondolo, *Neutralino relic density including coannihilations*, *Phys. Rev. D* **56** (1997) 1879–1894, [hep-ph/9704361].

[588] J. A. Harvey and M. S. Turner, *Cosmological baryon and lepton number in the presence of electroweak fermion number violation*, *Phys. Rev. D* **42** (1990) 3344–3349.

[589] FCC collaboration, A. Abada et al., *HE-LHC: The High-Energy Large Hadron Collider: Future Circular Collider Conceptual Design Report Volume 4*, *Eur. Phys. J. ST* **228** (2019) 1109–1382.

[590] N. Bernal, F.-X. Josse-Michaux and L. Ubaldi, *Phenomenology of WIMPy baryogenesis models*, *JCAP* **01** (2013) 034, [1210.0094].

[591] T. Asaka, H. Ishida and W. Yin, *Direct baryogenesis in the broken phase*, *JHEP* **07** (2020) 174, [1912.08797].

[592] S. Girmohanta and R. Shrock, *Nucleon decay and n-$\bar{n}$ oscillations in a left-right symmetric model with large extra dimensions*, *Phys. Rev. D* **101** (2020) 095012, [2003.14185].

[593] F. Zwirner, *Observable Delta B=2 Transitions Without Nucleon Decay in a Minimal Supersymmetric Extension of the Standard Model*, *Phys. Lett. B* **132** (1983) 103–106.

[594] R. Barbieri and A. Masiero, *Supersymmetric Models with Low-Energy Baryon Number Violation*, *Nucl. Phys. B* **267** (1986) 679–689.

[595] G. Lazarides, C. Panagiotakopoulos and Q. Shafi, *Baryon Asymmetry, Stable Proton and $n\bar{n}$ Oscillations in Superstring Models*, *Phys. Lett. B* **175** (1986) 309–311.

[596] J. L. Goity and M. Sher, *Bounds on $\Delta B = 1$ couplings in the supersymmetric standard model*, *Phys. Lett. B* **346** (1995) 69–74, [hep-ph/9412208].

[597] K. S. Babu and R. N. Mohapatra, *Observable neutron anti-neutron oscillations in seesaw models of neutrino mass*, *Phys. Lett. B* **518** (2001) 269–275, [hep-ph/0108089].

[598] K. S. Babu, R. N. Mohapatra and S. Nasri, *Unified TeV Scale Picture of Baryogenesis and Dark Matter*, *Phys. Rev. Lett.* **98** (2007) 161301, [hep-ph/0612357].

[599] R. Allahverdi, B. Dutta and K. Sinha, *Baryogenesis and Late-Decaying Moduli*, *Phys. Rev. D* **82** (2010) 035004, [1005.2804].

[600] P.-H. Gu and U. Sarkar, *Baryogenesis and neutron-antineutron oscillation at TeV*, *Phys. Lett. B* **705** (2011) 170–173, [1107.0173].

[601] P.-H. Gu and U. Sarkar, *Inflationary Baryogenesis with Low Reheating Temperature and Testable Neutron-Antineutron Oscillation*, 1110.2926.

[602] R. Allahverdi and B. Dutta, *Natural GeV Dark Matter and the Baryon-Dark Matter Coincidence Puzzle*, *Phys. Rev. D* **88** (2013) 023525, [1304.0711].

[603] P. S. B. Dev and R. N. Mohapatra, *TeV scale model for baryon and lepton number violation and resonant baryogenesis*, *Phys. Rev. D* **92** (2015) 016007, [1504.07196].

[604] M. Dhuria, C. Hati and U. Sarkar, *Explaining the CMS excesses, baryogenesis and neutrino masses in E_6 motivated $U(1)_N$ model*, *Phys. Rev. D* **93** (2016) 015001, [1507.08297].

[605] A. Ghalsasi, D. McKeen and A. E. Nelson, *Baryogenesis via Mesino Oscillations*, *Phys. Rev. D* **92** (2015) 076014, [1508.05392].

[606] P.-H. Gu, E. Ma and U. Sarkar, *Connecting Radiative Neutrino Mass, Neutron-Antineutron Oscillation, Proton Decay, and Leptogenesis through Dark Matter*, *Phys. Rev. D* **94** (2016) 111701, [1608.02118].

[607] L. Calibbi, G. Ferretti, D. Milstead, C. Petersson and R. Pöttgen, *Baryon number violation in supersymmetry: $n - \bar{n}$ oscillations as a probe beyond the LHC*, *JHEP* **05** (2016) 144, [1602.04821].

[608] P.-H. Gu and U. Sarkar, *High-scale baryogenesis with testable neutron-antineutron oscillation and dark matter*, *Phys. Rev. D* **96** (2017) 031703, [1705.02858].

[609] L. Calibbi, E. J. Chun and C. S. Shin, *LSP baryogenesis and neutron-antineutron oscillations from R-parity violation*, *JHEP* **10** (2017) 177, [1708.06439].

[610] R. Allahverdi, P. S. B. Dev and B. Dutta, *A simple testable model of baryon number violation: Baryogenesis, dark matter, neutron–antineutron oscillation and collider signals*, *Phys. Lett. B* **779** (2018) 262–268, [1712.02713].

[611] C. Grojean, B. Shakya, J. D. Wells and Z. Zhang, *Implications of an Improved Neutron-Antineutron Oscillation Search for Baryogenesis: A Minimal Effective Theory Analysis*, *Phys. Rev. Lett.* **121** (2018) 171801, [1806.00011].

[612] R. N. Mohapatra and R. E. Marshak, *Local B-L Symmetry of Electroweak Interactions, Majorana Neutrinos and Neutron Oscillations*, *Phys. Rev. Lett.* **44** (1980) 1316–1319.

[613] R. N. Mohapatra and G. Senjanovic, *Spontaneous Breaking of Global B^-l Symmetry and Matter - Antimatter Oscillations in Grand Unified Theories*, *Phys. Rev. D* **27** (1983) 254.

[614] D. Chang, R. N. Mohapatra, J. Gipson, R. E. Marshak and M. K. Parida, *Experimental Tests of New SO(10) Grand Unification*, *Phys. Rev. D* **31** (1985) 1718.

[615] K. S. Babu, P. S. Bhupal Dev and R. N. Mohapatra, *Neutrino mass hierarchy, neutron - anti-neutron oscillation from baryogenesis*, *Phys. Rev. D* **79** (2009) 015017, [0811.3411].

[616] I. Baldes, N. F. Bell and R. R. Volkas, *Baryon Number Violating Scalar Diquarks at the LHC*, *Phys. Rev. D* **84** (2011) 115019, [1110.4450].

[617] K. S. Babu and R. N. Mohapatra, *Coupling Unification, GUT-Scale Baryogenesis and Neutron-Antineutron Oscillation in SO(10)*, *Phys. Lett. B* **715** (2012) 328–334, [1206.5701].

[618] S. Patra and P. Pritimita, *Post-sphaleron baryogenesis and n - $\overline{n}$ oscillation in non-SUSY SO(10) GUT with gauge coupling unification and proton decay*, *Eur. Phys. J. C* **74** (2014) 3078, [1405.6836].

[619] E. Herrmann, *On Baryogenesis and $n\bar{n}$-Oscillations*, 1408.4455.

[620] K. S. Babu and R. N. Mohapatra, *B-L Violating Proton Decay Modes and New Baryogenesis Scenario in SO(10)*, *Phys. Rev. Lett.* **109** (2012) 091803, [1207.5771].

[621] K. S. Babu and R. N. Mohapatra, *B-L Violating Nucleon Decay and GUT Scale Baryogenesis in SO(10)*, *Phys. Rev. D* **86** (2012) 035018, [1203.5544].

[622] C. Hati and U. Sarkar, *$B - L$ violating nucleon decays as a probe of leptoquarks and implications for baryogenesis*, *Nucl. Phys. B* **954** (2020) 114985, [1805.06081].

[623] W. Buchmuller and M. Plumacher, *Spectator processes and baryogenesis*, *Phys. Lett. B* **511** (2001) 74–76, [hep-ph/0104189].

[624] E. Nardi, Y. Nir, J. Racker and E. Roulet, *On Higgs and sphaleron effects during the leptogenesis era*, *JHEP* **01** (2006) 068, [hep-ph/0512052].

[625] A. Abada, S. Davidson, F.-X. Josse-Michaux, M. Losada and A. Riotto, *Flavor issues in leptogenesis*, *JCAP* **04** (2006) 004, [hep-ph/0601083].

[626] V. Domcke, K. Kamada, K. Mukaida, K. Schmitz and M. Yamada, *Wash-In Leptogenesis*, *Phys. Rev. Lett.* **126** (2021) 201802, [2011.09347].

[627] D. Chang, R. N. Mohapatra and M. K. Parida, *Decoupling Parity and SU(2)-R Breaking Scales: A New Approach to Left-Right Symmetric Models*, *Phys. Rev. Lett.* **52** (1984) 1072.

[628] D. R. T. Jones, *The Two Loop beta Function for a G(1) x G(2) Gauge Theory*, *Phys. Rev. D* **25** (1982) 581.

[629] G. F. Giudice, B. Gripaios and R. Sundrum, *Flavourful Production at Hadron Colliders*, *JHEP* **08** (2011) 055, [1105.3161].

[630] R. N. Mohapatra, N. Okada and H.-B. Yu, *Diquark Higgs at LHC*, *Phys. Rev. D* **77** (2008) 011701, [0709.1486].

[631] S. Atag, O. Cakir and S. Sultansoy, *Resonance production of diquarks at the CERN LHC*, *Phys. Rev. D* **59** (1999) 015008.

[632] O. Cakir and M. Sahin, *Resonant production of diquarks at high energy pp, ep and e^+e^- colliders*, *Phys. Rev. D* **72** (2005) 115011, [hep-ph/0508205].

[633] C.-R. Chen, W. Klemm, V. Rentala and K. Wang, *Color Sextet Scalars at the CERN Large Hadron Collider*, *Phys. Rev. D* **79** (2009) 054002, [0811.2105].

[634] T. Han, I. Lewis and T. McElmurry, *QCD Corrections to Scalar Diquark Production at Hadron Colliders*, *JHEP* **01** (2010) 123, [0909.2666].

[635] I. Gogoladze, Y. Mimura, N. Okada and Q. Shafi, *Color Triplet Diquarks at the LHC*, *Phys. Lett. B* **686** (2010) 233–238, [1001.5260].

[636] E. L. Berger, Q.-H. Cao, C.-R. Chen, G. Shaughnessy and H. Zhang, *Color Sextet Scalars in Early LHC Experiments*, *Phys. Rev. Lett.* **105** (2010) 181802, [1005.2622].

[637] T. Han, I. Lewis and Z. Liu, *Colored Resonant Signals at the LHC: Largest Rate and Simplest Topology*, *JHEP* **12** (2010) 085, [1010.4309].

[638] P. Richardson and D. Winn, *Simulation of Sextet Diquark Production*, *Eur. Phys. J. C* **72** (2012) 1862, [1108.6154].

[639] D. Karabacak, S. Nandi and S. K. Rai, *Diquark resonance and single top production at the Large Hadron Collider*, *Phys. Rev. D* **85** (2012) 075011, [1201.2917].

[640] M. Kohda, H. Sugiyama and K. Tsumura, *Lepton number violation at the LHC with leptoquark and diquark*, *Phys. Lett. B* **718** (2013) 1436–1440, [1210.5622].

[641] R. S. Chivukula, P. Ittisamai, K. Mohan and E. H. Simmons, *Color discriminant variable and scalar diquarks at the LHC*, *Phys. Rev. D* **92** (2015) 075020, [1507.06676].

[642] Y. C. Zhan, Z. L. Liu, S. A. Li, C. S. Li and H. T. Li, *Threshold resummation for the production of a color sextet (antitriplet) scalar at the LHC*, *Eur. Phys. J. C* **74** (2014) 2716, [1305.5152].

[643] Z. L. Liu, C. S. Li, Y. Wang, Y. C. Zhan and H. T. Li, *Transverse momentum resummation for color sextet and antitriplet scalar production at the LHC*, *Eur. Phys. J. C* **74** (2014) 2771, [1307.4341].

[644] B. Pascual-Dias, P. Saha and D. London, *LHC Constraints on Scalar Diquarks*, *JHEP* **07** (2020) 144, [2006.13385].

[645] ATLAS collaboration, M. Aaboud et al., *A search for pair-produced resonances in four-jet final states at $\sqrt{s} = 13$ TeV with the ATLAS detector*, *Eur. Phys. J. C* **78** (2018) 250, [1710.07171].

[646] CMS collaboration, A. M. Sirunyan et al., *Search for narrow and broad dijet resonances in proton-proton collisions at $\sqrt{s} = 13$ TeV and constraints on dark matter mediators and other new particles*, *JHEP* **08** (2018) 130, [1806.00843].

[647] R. M. Harris and K. Kousouris, *Searches for Dijet Resonances at Hadron Colliders*, *Int. J. Mod. Phys. A* **26** (2011) 5005–5055, [1110.5302].

[648] D. B. Clark, E. Godat and F. I. Olness, *ManeParse : A Mathematica reader for Parton Distribution Functions*, *Comput. Phys. Commun.* **216** (2017) 126–137, [1605.08012].

[649] J. Pumplin, D. R. Stump, J. Huston, H. L. Lai, P. M. Nadolsky and W. K. Tung, *New generation of parton distributions with uncertainties from global QCD analysis*, *JHEP* **07** (2002) 012, [hep-ph/0201195].

[650] CMS collaboration, A. M. Sirunyan et al., *Searches for W' bosons decaying to a top quark and a bottom quark in proton-proton collisions at 13 TeV*, *JHEP* **08** (2017) 029, [1706.04260].

[651] FCC collaboration, A. Abada et al., *FCC-hh: The Hadron Collider: Future Circular Collider Conceptual Design Report Volume 3*, *Eur. Phys. J. ST* **228** (2019) 755–1107.

[652] I. Dorsner, S. Fajfer, J. F. Kamenik and N. Kosnik, *Light Colored Scalar as Messenger of Up-Quark Flavor Dynamics in Grand Unified Theories*, *Phys. Rev. D* **82** (2010) 094015, [1007.2604].

[653] A. Lenz, U. Nierste, J. Charles, S. Descotes-Genon, A. Jantsch, C. Kaufhold et al., *Anatomy of New Physics in $B - \bar{B}$ mixing*, *Phys. Rev. D* **83** (2011) 036004, [1008.1593].

[654] G. Senjanović and V. Tello, *Probing Seesaw with Parity Restoration*, *Phys. Rev. Lett.* **119** (2017) 201803, [1612.05503].

[655] G. Senjanovic and V. Tello, *Disentangling the seesaw mechanism in the minimal left-right symmetric model*, *Phys. Rev. D* **100** (2019) 115031, [1812.03790].

[656] UTfit collaboration, M. Bona et al., *Model-independent constraints on $\Delta F = 2$ operators and the scale of new physics*, *JHEP* **03** (2008) 049, [0707.0636].

[657] J. Charles et al., *Current status of the Standard Model CKM fit and constraints on $\Delta F = 2$ New Physics*, *Phys. Rev. D* **91** (2015) 073007, [1501.05013].

[658] C. Hati, G. Kumar, J. Orloff and A. M. Teixeira, *Reconciling B-meson decay anomalies with neutrino masses, dark matter and constraints from flavour violation*, *JHEP* **11** (2018) 011, [1806.10146].

[659] Super-Kamiokande collaboration, J. Gustafson et al., *Search for dinucleon decay into pions at Super-Kamiokande*, *Phys. Rev. D* **91** (2015) 072009, [1504.01041].

[660] Frejus collaboration, C. Berger et al., *Lifetime limits on (B-L) violating nucleon decay and dinucleon decay modes from the Frejus experiment*, *Phys. Lett. B* **269** (1991) 227–233.

[661] Super-Kamiokande collaboration, V. Takhistov, *Review of Nucleon Decay Searches at Super-Kamiokande*, in *51st Rencontres de Moriond on EW Interactions and Unified Theories*, pp. 437–444, 2016. 1605.03235.

[662] K. S. Babu and C. Macesanu, *Two loop neutrino mass generation and its experimental consequences*, *Phys. Rev. D* **67** (2003) 073010, [hep-ph/0212058].

[663] I. S. Gradshteyn and I. M. Ryzhik, *Table of integrals, series, and products*. Elsevier/Academic Press, Amsterdam, seventh ed., 2007.

[664] E. W. Kolb and S. Wolfram, *Baryon Number Generation in the Early Universe*, *Nucl. Phys. B* **172** (1980) 224.

[665] R. Kleiss, W. J. Stirling and S. D. Ellis, *A New Monte Carlo Treatment of Multiparticle Phase Space at High-energies*, *Comput. Phys. Commun.* **40** (1986) 359.